Lecture Notes in Electrical Engineering 795

C. Subramani
K. Vijayakumar
Brayima Dakyo
Subhransu Sekhar Dash *Editors*

Proceedings of International Conference on Power Electronics and Renewable Energy Systems

ICPERES 2021

Springer

Lecture Notes in Electrical Engineering

Volume 795

The book series *Lecture Notes in Electrical Engineering* (LNEE) publishes the latest developments in Electrical Engineering - quickly, informally and in high quality. While original research reported in proceedings and monographs has traditionally formed the core of LNEE, we also encourage authors to submit books devoted to supporting student education and professional training in the various fields and applications areas of electrical engineering. The series cover classical and emerging topics concerning:

- Communication Engineering, Information Theory and Networks
- Electronics Engineering and Microelectronics
- Signal, Image and Speech Processing
- Wireless and Mobile Communication
- Circuits and Systems
- Energy Systems, Power Electronics and Electrical Machines
- Electro-optical Engineering
- Instrumentation Engineering
- Avionics Engineering
- Control Systems
- Internet-of-Things and Cybersecurity
- Biomedical Devices, MEMS and NEMS

For general information about this book series, comments or suggestions, please contact leontina.dicecco@springer.com.

To submit a proposal or request further information, please contact the Publishing Editor in your country:

China

Jasmine Dou, Editor (jasmine.dou@springer.com)

India, Japan, Rest of Asia

Swati Meherishi, Editorial Director (Swati.Meherishi@springer.com)

Southeast Asia, Australia, New Zealand

Ramesh Nath Premnath, Editor (ramesh.premnath@springernature.com)

USA, Canada:

Michael Luby, Senior Editor (michael.luby@springer.com)

All other Countries:

Leontina Di Cecco, Senior Editor (leontina.dicecco@springer.com)

**** This series is indexed by EI Compendex and Scopus databases. ****

More information about this series at https://link.springer.com/bookseries/7818

C. Subramani · K. Vijayakumar · Brayima Dakyo · Subhransu Sekhar Dash
Editors

Proceedings of International Conference on Power Electronics and Renewable Energy Systems

ICPERES 2021

Springer

Editors
C. Subramani
Department of Electrical and Electronics Engineering
SRM Institute of Science and Technology
Kattankulathur, Tamil Nadu, India

K. Vijayakumar
Department of Electrical and Electronics Engineering
SRM Institute of Science and Technology
Kattankulathur, Tamil Nadu, India

Brayima Dakyo
Department of Electrical and Electronics Engineering
University of Le Havre
Le Havre, France

Subhransu Sekhar Dash
Department of Electrical and Electronics Engineering
Government College of Engineering
Keonjhar, Odisha, India

ISSN 1876-1100 ISSN 1876-1119 (electronic)
Lecture Notes in Electrical Engineering
ISBN 978-981-16-4942-4 ISBN 978-981-16-4943-1 (eBook)
https://doi.org/10.1007/978-981-16-4943-1

Preface

This ICPERES 2021 volume contains the papers presented at the International Conference on Power Electronics and Renewable Energy (ICPERES 2021) held during April 21–23, 2021, at SRM Institute of Science and Technology, Kattankulathur, India. ICPERES 2021 is the International conference aiming at bringing together the researchers from academia and industry to report and review the latest progresses in the cutting-edge research on various research areas of power electronics, renewable energy and its applications to create awareness about these domains to a wider audience of practitioners.

ICPERES 2021 received 325 paper submissions, including seven foreign countries across the globe. All the papers were peer-reviewed by the experts in the area in India and abroad, and comments have been sent to the authors of accepted papers. Finally, 63 papers were accepted for oral presentation at the conference and for the publication in *Lecture Notes in Electrical Engineering* (LNEE) series. This corresponds to an acceptance rate of around 20% and is intended to maintain the high standards of the conference proceedings. The papers included in this Springer volume cover a wide range of topics in power electronics, renewable energy and their real-time applications in problems from diverse domains of science and engineering.

The conference was inaugurated by Dean (CET), SRMIST, on April 21, 2021. The conference featured distinguished keynote speakers as follows: Dr. S. Akhtar Kalam, Head of External Engagement Leader—Smart Energy Research Unit, Victoria University, Australia; Dr. Sidhartha Panda, Professor, Electrical Engineering, Veer Surendra Sai University of Technology, Odisha; Dr. S. S. Dash, GCE, Keonjhar, Odisha, India; Dr. Vivekananda Mukherjee, Professor, Electrical Engineering, Indian Institute of Technology Jharkhand; Dr. Ramazan Bayindir, Professor, Electrical Engineering, Gazi University Technology, Turkey; and Dr. Anup Kumar Panda, Professor, Electrical Engineering, National Institute of Technology Rourkela.

We take this opportunity to thank the authors of the submitted papers for their hard work, adherence to the deadlines, and patience with the review process. The quality of a referred volume depends mainly on the expertise and dedication of the reviewers. We are indebted to the technical committee members, who produced excellent reviews in short time frames.

First, we are indebted to the honorable Dr. T. R. Paarivendhar, Chancellor, Mr. Ravi Pachamoothoo, Pro-chancellor (Admin), Dr. P. Sathyanarayanan, Pro-chancellor (Academics), and Dr. R. Shivakumar, Vice President, SRMIST, wholeheartedly for the confidence they entrusted on us for organizing this international conference ICPERES 2021. We sincerely thank our beloved interim Vice Chancellor for their continuous support and guidance in organizing the conference. Our heartfelt thanks to the Registrar, HODs, Professors, and the staff members of SRMIST, Kattankulathur, for their valuable support for the success of this program. We thank the International Advisory Committee members for providing valuable guidelines and inspiration to overcome various difficulties in the process of organizing this conference. We would also like to thank the participants of this conference. The members of faculty and students of SRM Institute of Science and Technology, Chennai, deserve special thanks because, without their involvement, we would not have been able to face the challenges of our responsibilities. Finally, we thank all the volunteers who made great efforts in meeting the deadlines and arranging every detail to make sure that the conference could run smoothly. We hope the readers of these proceedings find the papers inspiring and enjoyable.

Kattankulathur, India — Prof. K. Vijayakumar
Kattankulathur, India — Dr. C. Subramani
Le Havre, France — Brayima Dakyo
Keonjhar, India — Subhransu Sekhar Dash
May 2021

Conference Committee

Organizing Chairs

Prof. K. Vijayakumar
Dr. C. Subramani

Chief Patrons

Dr. T. R. Paarivendhar, Founder Chancellor
Shri. Ravi Pachamoothoo, Pro-Chancellor (Admin)
Dr. P. Sathyanarayanan, Pro-Chancellor (Academic)

Patrons

Dr. C. Muthamizhchelvan, Vice Chancellor, SRMIST
Dr. T. V. Gopal, Dean (Engineering and Technology), SRMIST

General Chairs

Dr. Ramazan Bayindir, Gazi University, Turkey
Dr. Florian Misoc, UWM, USA
Dr. Brayima Dakyo, University of Le Havre, France

Program Chairs

Dr. Valentina Emilia Balas, UOA, Romania
Dr. G. S. Chae, Baekseok University, South Korea
Dr. S. S. Dash, Government College of Engineering, Keonjhar

Organizing Chairs

Prof. K. Vijayakumar, SRMIST
Dr. C. Subramani, SRMIST

Co-organizing Chairs

Dr. A. Rathinam, SRMIST
Dr. R. K. Pongiannan, SRMIST
Dr. N. Chellammal, SRMIST
Dr. C. S. Boopathi, SRMIST

Organizing Committee

Dr. Y. Jeyashree, SRMIST
Dr. D. Suchitra, SRMIST
Dr. R. Sridhar, SRMIST
Dr. D. Sattianadan, SRMIST
Dr. C. Bharatiraja, SRMIST
Dr. J. Preetha Roselyn, SRMIST
Dr. K. Saravanan, SRMIST
Dr. M. Jagabar Sathik, SRMIST
Dr. K. Mohanraj, SRMIST
Dr. Arun Noyal Doss, SRMIST
Dr. S. Padmini, SRMIST

International Advisory Committee

Dr. Akhtar Kalam, Victoria University, Australia
Dr. Arunachalam Sundaram, Jubail Industrial College, Kingdom of Saudi Arabia

Dr. C. A. Vaithilingam, Taylor University, Malaysia
Dr. Diego Bellan, Politecnico di Milano, Italy
Dr. Dirman Hana, Universiti Tun Hussien Onn Malaysia (UTHM), Malaysia
Dr. Eliathamby Ambikairajah, University of New South Wales, Australia
Dr. Jahangir Hossain, Macquarie University, Australia
Dr. Jayashri Ravishankar, University of New South Wales, Australia
Dr. Naayagi Ramasam, Newcastle University, Singapore
Dr. Narottam Das, CQUniversity, Australia
Dr. Prahlad Vadakkepat, National University of Singapore
Dr. Raj Jain, Washington University, St. Louis
Dr. Ramani Kannan, Universiti Teknologi Petronas, Malaysia
Dr. S. Umashankar, Prince Sultan University, UAE
Dr. Ruzairi Abdul Rahim, Universiti Tun Hussein Onn Malaysia (UTHM), Malaysia
Dr. Saad Mekhilef, University of Malaya, Malaysia
Dr. P. Sanjeevikumar, Aalborg University, Denmark
Dr. Siti Hawa Ruslan, Universiti Tun Hussein Onn Malaysia (UTHM), Malaysia

National Advisory Committee

Dr. Kumar Pradhan, IIT Kharagpur
Dr. Bhim Singh, IIT Delhi
Dr. Ganapati Panda, IIT Bhuvaneshwar
Dr. S. Jeevananthan, PEC, Pondicherry
Dr. Debashish Jena, NITK Surathkal
Dr. N. P. Padhy, IIT Roorkee
Dr. S. Chandramohan, Anna University
Dr. G. Uma, Anna University
Dr. K. Udhayakumar, Anna University
Dr. M. Somasundaram, Anna University
Dr. M. Arun Bhaskar, VEC, Chennai
Dr. S. Raghuraman, VEC, Chennai
Dr. D. Kalpana, MIT, Anna University
Dr. M. Jegadeeshkumar, Sairam Institute of Technology
Dr. G. Prakash, Sairam Institute of Technology, Chennai
Dr. Sidhartha Panda, VSSUT EC, Burla
Dr. M. Mohanthy, SOA University, Odisha
Dr. K. Sureshkumar, VEC, Chennai

Paper Selection and Publication Process

Dr. A. Geetha, SRMIST

Dr. T. M. Thamizh Thentral, SRMIST
Dr. S. Usha, SRMIST
Dr. A. Dominic Savio, SRMIST
Dr. R. Brindha, SRMIST
Mr. B. Vinothkumar, SRMIST

Contents

About the Editors

Dr. C. Subramani received Master of Engineering (2006) from Anna University (India), doctoral degree (2012) from SRM University (India) and is Postdoctoral Fellow (2016) from Tshwane University of Technology (South Africa). Professional position: He has joined the SRM University as Assistant Professor from 2009 to till date, in the Department of Electrical and Electronics Engineering, Faculty of Engineering and Technology. He has more than 15 years of teaching experience. Research: Professor Subramani has published and co-authored more than 90 papers in scientific journals and conference proceedings. He has been Advisor of 11 Ph.D. and numerous postgraduate students. He has been acting as Reviewer for many national and international journals. Research areas: His broad areas of research are electric vehicle, energy management control strategy, fuzzy logic controller, particle swarm optimizations, etc.

Prof. K. Vijayakumar has received B.E. degree in Electrical and Electronic Engineering from Annamalai University, M.Tech. (Power Systems) from Annamalai University, and Ph.D. from SRM Institute of Science and Technology. He is currently working as Professor and Head in the Department of Electrical and Electronics Engineering, SRM Institute of Science and Technology (India). His area of research is power electronic applications in power system. His current research is focused on optimizations, hybrid energy systems, and deregulation. He has more than 23 years of teaching experience. Research: Professor Vijayakumar has published and co-authored more than 100 papers in scientific journals and conference proceedings. He has been Advisor of eight

Ph.D. and numerous postgraduate students. He has been acting as Reviewer for many national and international journals. He is also one of the editors of few of the books titled *Basic Electrical Engineering* and *Electrical Engineering Practice Lab Manual* of Vijay Nicole Imprints Private Limited.

Prof. Brayima Dakyo received Engineer Dipl. (1984) and Doctor in Engineering (1987) degrees from Dakar University (Senegal) and Doctoral degree (1988) and Habilitation (1997) from University of Le Havre (France). Professional position: He has joined the University of Le Havre as Assistant Professor (MdC) from 1989 to 1999, in the Faculty of Sciences and Technology. He was Founder and Director of Electrical and Automatic research Laboratory (GREAH) 1999. From 2000 to now, he is Full Professor of Electrical Engineering and Director of Electrical and Automatic Research Team of Le Havre (GREAH) (15 full professors and assistant professors plus 20 Ph.D. students among whom six are averagely involved in renewable energies field). Professor Dakyo is General Advisor of the electrical engineering department, Master's degree and bachelor's degree. Research: Professor Dakyo has published and co-authored more than 180 papers in scientific journals and conference proceedings since 1987. He has been Advisor of 20 Ph.D. and numerous M.Sc. students and Co-Author of three books (power electronic, marine and wind energy, and power management).

Dr. Subhransu Sekhar Dash is presently Professor and Head in the Department of Electrical Engineering, Government College of Engineering, Keonjhar, Odisha, India. He received his Ph.D. degree from College of Engineering, Guindy, Anna University, Chennai, India. He has more than 22 years of research and teaching experience. His research areas are AI techniques application to power system, modeling of FACTS controller, power quality, and smart grid. He is Visiting Professor at Francois Rabelais University, POLYTECH, France. He has published more than 220 research articles in peer-reviewed international journals and conferences. Professor Dash has played a role as Convenor, Program, or General Chair for many International Conferences.

He is also one of the editors of few of the books titled *Introduction to FACTS* and *Power Quality Management* of IRD Publication and Vijay Nicole Imprints Private Limited, respectively.

Deep CNN Depth Decision in Intra Prediction

Helen K. Joy and Manjunath R. Kounte

Abstract The video and its compression become prominent with the emergence of digital video technology and common use of video acquisition devices. The traditional video compression needs upgradation with artificial intelligence, machine learning, neural network, and deep learning. Apart from normal signal processing the deep learning technologies are advantages as they can deal with content analysis than dealing only with neighboring pixels. The initial steps in video compression, intra/inter frame prediction provide a better percentage in overall compression. The computational complexity of existing intra prediction method is more. This paper proposes a deep learning based intra prediction method using CNN. This deep depth prediction algorithm trains the network to provide depth of the CTU with reduced computation and less time. The experimental results show a dip in the encoding time, about 71.3% compared to existing method.

Keywords Deep learning · Video compression · HEVC · CNN

1 Introduction

Various compression methods became so prominent when the transfer of data at a low bit rate became a need, but the quality of the image was also a concern. So, video compression and its variance became an eminent one in the research area. Digging back to the history of video compression the traditional methods started from basic coding like Huffman coding followed by frequency transformation to recent techniques like hybrid video processing techniques, HEVC, and its advanced version. Based on the need of the user and various other features there is various compression.

H. K. Joy (✉)
School of Electronics and Communication, REVA University, Rukmini Knowledge Park, Kattigenahalli, Yelahanka, Bengaluru, Karnataka 560064, India

M. R. Kounte
Department of Electronics and Computer Engineering, School of Electronics and Communication, REVA University, Rukmini Knowledge Park, Kattigenahalli, Yelahanka, Bengaluru, Karnataka 560064, India

C. Subramani et al. (eds.), *Proceedings of International Conference on Power Electronics and Renewable Energy Systems*, Lecture Notes in Electrical Engineering 795,
https://doi.org/10.1007/978-981-16-4943-1_1

1.1 Evolution of Video Compression Development by ISO/IEC/MPEG

"Motion JPEG (M-JPEG or MJPEG) is an initial video compression technique in which each frame in the video or interlaced field of the video in digitalized sequence is compressed separately as an image in jpeg format. It was developed focusing on multimedia personal computer applications, M-JPEG is now used by video-capture devices like digital cameras, webcams IP cameras, etc. and by non-linear video editing systems too. It is supported by QuickTime Player, the PlayStation console, and web browsers such as Microsoft Edge Safari, Google Chrome, Mozilla Firefox, etc." [1]. MPEG-1 standard is the initial version of the MP3 audio format introduced, i.e., best-known part of this format. MPEG-2 came out of the drawbacks of MPEG-1 [2]. "MPEG-2 is used widely in digital television signal which is broadcast by terrestrial, and DBS (direct broadcast satellite television system) followed by MPEG 4, MPEG H has several "parts"—each of them can be considered a different standard [3]. These include a video compression standard, media transport protocol standard, a digital file format container standard, an audio compression standard, three sets of conformance testing standards, set of three reference software packages, and related technologies and technical reports.

1.2 Evolution of Video Compression Development by ITU/VCEG

ITU-T video compression standard introduced H.261 is the year November 1988. In the H.26 × family, first member, H.261 IN "video coding standards in the domain of the VCEG [4] (ITU-T Video Coding Experts Group) then Specialists Group on Coding for Visual Telephony" [1]. MPEG-2 consists of "three different kinds of coded frames: I-frame/intra-coded frames, P -frame/predictive-coded frames, and B-frame/bidirectionally-predictive-coded frames" [1, 5]. H.263 is a member of the H.26 × family of video coding standards in the domain, ITU-T. Like other H.26 × standards, H.263 is also based on (DCT) discrete cosine transform video compression. It was later advanced to add different additional enhanced features in the years 1998 and 2000.H.264 mostly called AVC (Advanced video coding), its block segmentation based, motion compensated with DCT technique. The aim behind AVC was to transfer video at low bit rate with better efficiency for UHD videos. "High Efficiency Video Coding, is also known as HEVC or H.265 [6], is the step in this evolution. It builds off a lot of the techniques used in AVC/H.264 to make video compression even more efficient.

1.3 Evolution of Video Compression Development by SMPTE

"SMPTE 421 M technology was developed with contributions from a number of companies, with the majority of patent contributions from Microsoft, Panasonic, LG Electronics, and Samsung Electronics.VC-1 is supported in the now deprecated Microsoft Silverlight, the now discontinued HD DVD, and in the Blu-ray Disc" [1]. DNxHD is a video coding format intended to be used as both an intermediate format good to use in editing and in presentation format. VC3 data is typical can be stored in an MXF container, still, it can also be saved in a QuickTime container. 1.4 Evolution of video compression development by On2 True Motion.

On2 True Motion's VP3 is a lossy video compression format that is royalty-free and a video codec that focus on web activities. It is an incarnation done by "True Motion video codec; a set of video codecs created by On2 Technologies. There is no standard.

specification for the VP3 bitstream format above the VP3 source code done by On 2 Technologies. It was given to the public as open source, and On2 irrevocably disclaimed all rights to it, granting a royalty-free license grant for any patent claims it might have over the software and any derivatives, allowing anyone to use any VP3-derived codec for any purpose" [1]. VP4 codec and the RealSystem iQ architecture became the only streaming media platform capable of delivering the VP4 codec" [7]. VP7 codec was used by Move Media Player plugin for Internet Explorer, Firefox, and for the streaming of full network shows used by ABC and Fox. VP9 is a royalty-free and open video coding format developed by Google that was mainly used on Google's video platform YouTube. VP9 support is common among web browsers, Android, etc. [1].

Currently, the video compression is mainly focusing on smart compression that is the incorporation of the goodness of Artificial intelligence (AI), Machine learning (ML), Neural network (NN), and Deep Learning (DL). As the scope of machine learning based systems to process the pixels are not bounded to the neighboring pixels, as in general signal processing, the content-based analysis can be considered. This is a major breakthrough in all image and video processing.

Video compression procedure can be mainly made into some general steps that all compression standard follows. The methodology or approach changes but steps remain the same and it follows so, sampling the frames, intra frame prediction, inter frame prediction, Transform, scaling, quantization, entropy coding, and loop filtering.

This paper mainly focuses on how a deep learning based intra frame prediction can be done with less computational complexity. the paper starts with the introduction evolution and steps in video compression. Then the focus will be streamlined to intra frame prediction using neural network and deep learning application with the proposed algorithm and results and concluded finally pointing how deep learning technique can reduce computational complexity in intra frame prediction.

2 Intra Prediction in Video Compression

Intra prediction provides a major role in the compression of video and it's the topic to be taken care when intelligent VC is taken into consideration. Intra prediction is defined as predicting the redundant information within the frame, In recent video systems and commonly used compression tech, the role of intra prediction to compression is good. As the frame is divided into macro blocks in H.264 or CTU in H265, the technique of comparison is of frames similarities. Comparing and encoding same CU helps in better compression efficiency. The recent VC technique, HEVC [8] in market is using Quadra tree structure CTU. CTU is of variable size from 64 × 64 CV to 8 × 8 that is, processing variable depth from larger coding unit (LCU) to smaller coding unit. PU (prediction unit) is defining CTU split is required or not, so PU is the basic deciding unit for intra/inter prediction.

HEVC has proved its capability to reduce bit rate by more than half percentage than its previous encoder [8]. The bit rate reduction HEVC could afford the bit rate saving because of the new encoding method of CTU splitting. But the impact of this is affected on computation, complexity of computing increased as the new CTU encoding was introduced. So, the recent focus is to reduce the complexity by maintaining other parameters. Results have proved that complexities in calculation or more observed in inter/intra prediction, it's 3.2 times complex than H.264. CTU partitioning and prediction are observed as the reason for the encoding. It can be noted that working the process to reduce the CTU partitioning can help the computational complexity and thus fastening up the total encoding process. In HEVC the RD cost of various coding units from LCU is 64*64 to SCV 8*8 is calculated in each CTU with optimism depth. All CU [9] poses a prediction unit that holds the info of intra/inter prediction. Taking into consideration the better compression efficiency, the rate distortion cost is calculated separately and for all the PU modes of depth. This makes the calculation complex but helps to attain better compression than the previous method.

Algorithms are proposed to reduce the complexity in calculation with better encoding efficiency minimum encoding efficiency. To reduce the computational complexity many algorithms were proposed that can be mainly of learning based algorithms or manually tuned algorithms considering various parameters to check complexity reduction. Cho et al. used a Bayesian decision rule that uses the RD cost of full and low complexity CTUS to develop a better CTU splitting of purring. Based on the no of high frequency key points in CU, Kim et. all proposed a CTU spieling algorithm.

Some algorithms were proposed to reduce the comparing the size of PU to have a fast PU six [10] decision. As it is developed manually the trial and error method works more here that is a major disadvantage noted. Taking into consideration one of the parameters to work manually may affect the other dependent parameters and may affect the total RD performance [11]. The next is learning based algorithms.

Learning based algorithms for the intra prediction helps to reduce video coding complexity by learning using the proposed by learning using dataset extensivity and

building a model, Here classification algorithm with logistic regression. Lu et al. SVM support vector margin for classification [12]. These algorithms wanted some features, i.e., inbuilt/manually extracted features to predict the CTU partitioning. Extracting the features may help in future for CNN and deep learning approach to predict actual CTU structure. The CNN tried its best to predict CTU perfectly but the shallow net has its limitation to extract enough features to accurately predict the CTU partition.

The paper proposes a deep layer of learning with an extensive dataset to extract the underlying features to partition the CTU in an effective way using deep CNN network. The proposed system focuses on deep CNN based intra prediction that efficiently predicts the CTU should be split on non split using deep CNN network learning methods. The data base should be created effectively, an efficient database that covers all the 4 quantization parameter ranges are chosen for this analysis. It should be trained effectively to extract the deeper information and multiple information and multiple patterns in the CTU splitting. The model used is deep architect use that uses all suitable kernel sizes to match the CTU splitting from 64*64 to 16*16. Comparing to the computational complexity in HEVC the system architecture will properly predict the inter CTU split/non split by a reduced vector of length 16*1 with the total depth information of the CTU. This will effectively reduce the time taken for encoding and make the total system fast and efficient.

3 Data Set and CTU Splitting

The data set used here contains coding unit and its corresponding intra prediction depth. In HEVC intra frame prediction 64X64 coding tree units and its CU /PU, that constitute the basic block of intra frame prediction can be represented by 16 × 1 vector. In HEVC it is represented by a 16 × 16 matrix with depth values 0,1,2,3. The dataset used is YUV dataset where Y represents the luminance and U and V represent the chrominance of blue and red. The YUV data set has a set of image files of different sizes extracted from video. From that information, the 64 × 64, 32 × 32, 16 × 16, etc. can be extracted. If image files are into 64 × 64 CTUs, the size of the train dataset is around 110 K images. The size of the validation dataset is around 40 K images. Testing validation and training of these datasets will be done as an initial step.

3.1 Idea of CTU Splitting

According to CTU splitting in HEVC, it can be split or non split, i.e., it's a binary classifier. But the 64 × 64 CTU can be split again to 32 × 32, 16 × 16, and 8 × 8 based on split or non split binary consent. So, it's a kind of binary classification at various levels. Let's discuss the CTU split, a 64 × 64 CTU can be regarded to 2

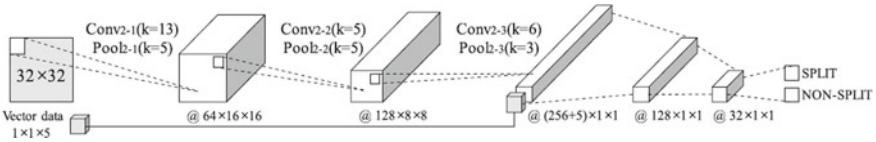

Fig. 1 Concept depth decision algorithm using CNN

levels, split/non split. The spilled one will be four, 32 × 32 cu's. Out of this four,32 × 32 cu, each can be split/non split there are 42 ways to split. Furthermore, if we split 43 split ways are there. Now let's consider the available patterns by this split & non split based on its depth. As it goes deeper to the CTU split for a 16 × 16 cu if we consider it can have only 2 patterns available split/non split pattern. For 32 × 32 its $24 + 1 = 17$ possible patterns and for the next level its $174 + 1 = 83{,}522$ possible patterns are available (Fig. 1).

By observing the depth value many information regarding CTU split can be extracted. Compared to the time taken procedure in the calculation of depth in HEVC, deep learning can train the system in a better way to evaluate it. As in RDO process, it checks each time the cost, compares, and sends back, which consumes time. Instead, it can be segregated into three levels and provide depth. Each level possesses various depth and based on the depth value, the split and non-split can be decoded. For example, if depth is 0 it is non split that is 64 × 64 matrices. If depth is 1 it will possess CU of 32 × 32 in that D1 level will check it is split or non split by a binary.

classifier. In each level the process is repeated, the depth/level of classification can be represented as $[Hd]^3_{.d=0}$ for all $d = 0$, i.e., non split.

so, this case can be ignored and simplify to $[Hd]^3_{.d=1}$. Each depth can be split or non- split.

H1 can be split/non split and need to be represented as H1(x) □ $x = 0$ or 1.

H2(x) have more information so H2(x) should be rewritten as

$$\begin{aligned} &\mathrm{H2}(xi)_{\square} \quad x = 0 \text{ or } 1 \\ &i = 0 - 3 \end{aligned}$$

H3(x i,j) with i,j = 0–3 and can be mathematically represented as

$$\begin{aligned} \mathrm{Yd} = &\mathrm{Hd}(x)_{\square} \quad d = 1 \\ &\mathrm{Hd}(xi)_{\square} \quad d = 2, \mathrm{i} = (0 - 3) \\ &\mathrm{Hd}(xi, j)_{\square} \quad d = 3, i, j = (0 - 3) \end{aligned}$$

So, Yd can give the information about the depth of CU as split or non split. The value gives information about depth and whether it's split or not with a calculation time.

If Yd = 0 it says that the depth d is non split and if Yd = 1 the depth d is split. As we train the network with this information the calculation complexity reduces that saves time too.

3.2 *Deep Depth Decision Algorithm Using Deep Learning*

The deep depth decision algorithm is based on convolutional neural network. Here the input is CU of various size from 32 × 32, 16 × 16, and so on. The 64 × 64 CTU is by default with depth 0 and is not considered, which saves calculation time. The YUV input with 3 channels is given as input to CNN, the convolution layer convert it to 5 × 5 followed by a max pooling to 2 × 2 with activation function as ReLU. The primitive features are extracted with various kernels of size 5, 6, etc. by the deep CNN layers and the training helps it to provide better results. The extracted features are then combined and reduce by the fully connected network to 256 then to 64 and to a vector of 16 elements that provide the information if total CTU split as shown in Fig. 2.

The steps for this will have this work flow initial step is to build a data set, the data set used here are YUV data set and it is available for research purpose. The selected data set are preprocessed by splitting it into image frames with label. These frames and labels are trained and validated using the deep CNN network. The model can be improved by training it again until an optimum is reached. The Convolution process in CNN layer can extract the fine features by using various kernels to achieve better output.

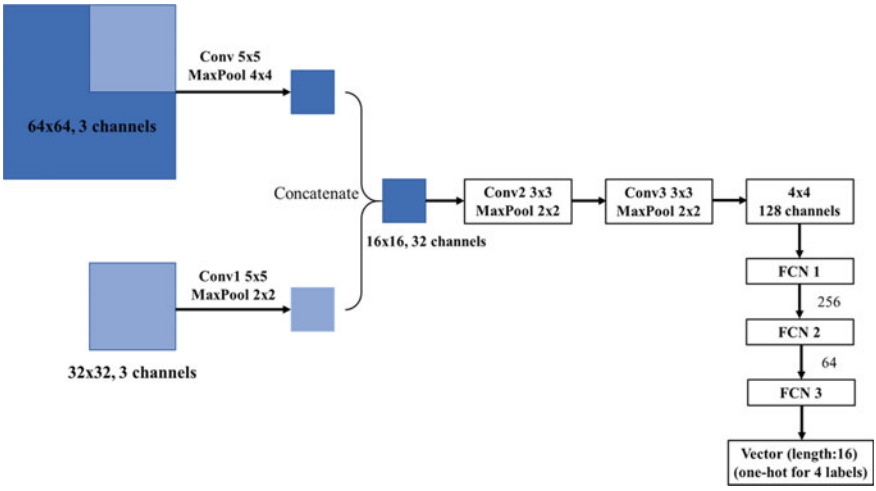

Fig. 2 Deep depth decision algorithm with CNN

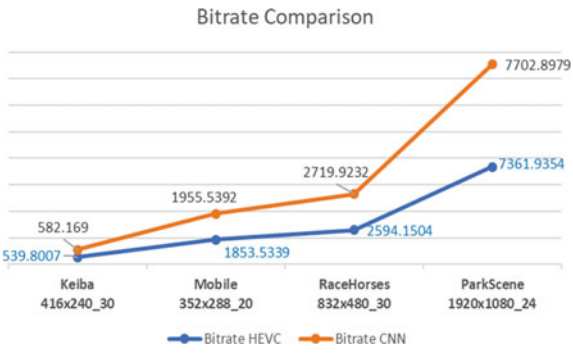

Fig. 3 Bit rate comparison

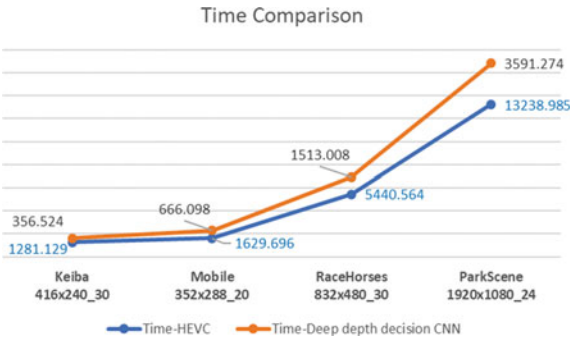

Fig. 4 Time for encoding comparison to analyze complexity

4 Experimental Results

The table shows sample input and its intraframe encoding time using HEVC and the proposed deep depth decision algorithm. A noticeable dip in encoding time can be observed here focusing on the last two columns in the table and the graph in Figs. 3 and 4. The average encoding time reduction is: 71.5%. This point says clearly that the prediction of deep depth decision algorithm is fast and reduced the computational complexity compared to existing technology.

Table 1 showing the input and its intraframe encoding time using HEVC and the proposed deep depth decision algorithm.

5 Conclusion

The video and its compression are a matter of interest with the latest video acquisition devices and the internet. The video processing and its compression were updating its technology with the emergence of artificial intelligence, machine learning, NN, and

Table 1 Bitrate comparison table for various resolutions

YUV sequence with resolution and frame rate	Bitrate HEVC	Bitrate CNN	Time-HEVC	Time-Deep depth decision CNN
Keiba_416 × 240_30	539.8007	582.1690	1281.129	356.524
Mobile_352 × 288_20	1853.5339	1955.5392	1629.696	666.098
RaceHorses_832 × 480_30	2594.1504	2719.9232	5440.564	1513.008
ParkScene_1920 × 1080_24	7361.9354	7702.8979	13,238.985	3591.274

deep learning networks (DL). Intra perdition that is the initial step in video compression helps in a major part of compression in total video compression process. The proposed method trains the deep CNN network with varities of dataset of different dimensions and frame rates. The trained data is validated and tested. This network reduces the computational complexity of intra prediction, if input CTU is given it provides the depth information as a vector of length 16 that provides the total information with less time. The encoding time is calculated and compared with HEVC reference software. The results show 71.3% saving in encoding time. The results can be extended by trying with other deep learning networks like ResNet and compare results.

References

1. Sullivan GJ, Ohm J, Han W-J, Wiegand T (2012) Overview of the high efficiency video coding (HEVC) standard. IEEE TCSVT 22(12):1649–1668
2. Correˆa G, Assuncao P, Agostini L, da Silva Cruz LA (2012) Performance and computational complexity assessment of high efficiency video encoders. IEEE TCSVT 22(12):1899–1909
3. Shen X, Yu L, Chen J (2012) Fast coding unit size selection for HEVC based on Bayesian decision rule. In: PCS
4. Kiho C, Jang ES (2012) Early TU decision method for fast video encoding in high efficiency video coding. Electron Lett 48(12):689–691
5. Yoo HM, Suh JW (2013) Fast coding unit decision algorithm based on inter and intra prediction unit termination for HEVC. In: ICCE
6. Miyazawa K, Murakami T, Minezawa A, Sakate H (2012) Complexity reduction of in- loop filtering for compressed image restoration in HEVC. In: PCS
7. Peixoto E, Shanableh T, Izquierdo E (2014) H.264/AVC to HEVC video transcoder based on dynamic thresholding and content modeling. IEEE TCSVT 24(1):99–112
8. Correˆa G, Assuncao PA, Agostini LV, da Silva Cruz LA (2015) Fast HEVC encoding decisions using data mining. IEEE TCSVT 25(4):660–673
9. Vanne J, Viitanen M, Ham al ainen TD, Hallapuro A (2012) Comparative rate- distortion-complexity analysis of hevc and avc video codecs. IEEE TCSVT 22(12):1885–1898
10. Kim N, Jeon S, Shim HJ, Jeon B, Lim SC, Ko H (2016) Adaptive keypoint-based CU depth decision for HEVC intra coding. In: IEEE BMSB
11. Khan MUK, Shafique M, Henkel J (2013) An adaptive complexity reduction scheme with fast prediction unit decision for HEVC intra encoding. In: IEEE ICIP

12. Hu Q, Shi Z, Zhang X, Gao Z (2016) Fast HEVC intra mode decision based on logistic regression classification. In: IEEE BMSB

Investigation of Electrical Characteristics for Different Geometrical Dimensions of 11 kV Insulators Under Finite Element Method

R. Bharanidharan and R. V. Maheswari

Abstract In the power system, the occurrence of a short circuit in transmission lines is the major challenge in planning, designing, and operating with an excessive high-voltage. The new model incorporates the actual geometrical two dimensions of insulators, property of materials, and self-adaptive measurement of the components. 11-kV non-ceramic insulator designs are simulated using ANSYS software. The insulators are free from contamination. Finite element method (FEM) is a numerical method with 2–3 space variables to solve partial differential equations is employed to identify the electrical stress issues in high-voltage fields. For all surface conditions, the electric field distribution, maximum electrical field strength and its location, voltage distribution, and heat generated on the surface are examined. The simulation findings were introduced and analyzed for non-ceramic insulator designs.

Keywords 11 kV polymeric insulator · Finite element method · Electric field distribution · Voltage distribution

1 Introduction

For the performance of an electric power system, the reliability and consistency of the power system and equipment are very important. Because of damp weather conditions such as dew fog or drizzle, the emission layer becomes conductive, and a leakage current flows through it when combined with moisture [1, 4] Due to their lighter weight, greater mechanical intensity, better anti-pollution performance, and lower maintenance requirements, composite insulators are commonly used in the power system. The distribution and potential of the electrical field can be distorted by flashovers. Dry bands on the insulator surface [2] may form due to the flow of the leakage current. Compared to ceramic insulators, the electrical field distribution of the non-ceramic insulator is distinct. The electric field distribution of a composite insulator is typically more nonlinear than that of a porcelain insulator [3, 7]. Numerical methods such as the Boundary Element Method, the Charge Simulation Method,

R. Bharanidharan (✉) · R. V. Maheswari
Department of EEE, National Engineering College, Kovilpatti, India

C. Subramani et al. (eds.), *Proceedings of International Conference on Power Electronics and Renewable Energy Systems*, Lecture Notes in Electrical Engineering 795,
https://doi.org/10.1007/978-981-16-4943-1_2

the Finite Difference Method, and the Finite Element Method can assess the distribution of the field. Some research has been carried to investigate the AC behavior of hydrophilic and hydrophobic post-insulators [5] while it was raining. Axial and radial elements of electrical field strength along an insulator were determined under dry and rain conditions. FEM was used to conduct an investigation of stress control on polymeric insulators [6]. The optimal installation of an arcing horn close to the end fittings from the investigation has a reduction in the Electric field stress where it is maximum and uniform potential distribution and Electric field for the High-voltage end and earth end Arcing horn installed in a composite insulator. Temperature vulcanizing (RTV) coated insulators usage was increasing in transmission lines [8]. An oversized spectrum of RTV coating damage is currently observed on square measure insulators. Three standard modes of RTV coating damage were simulated, so the characteristics of the electrical discharge emission were investigated. The electric fields of high-voltage insulators were analyzed. This paper involves designing and applying multiple long rod insulators with E-Field analysis. Multiple materials such as ceramic, porcelain, fiberglass, and silicon rubber [9] have been used to model long rod insulators. The effects of the Corona ring on composite polymer insulator strings insulation performance. For the strings, which include corona rings of the respective design specifications, and also for the ring-free strings, experimental investigations were carried out. Test results were discussed from the point of view of discharge development physics and the strings were optimally configured [10].

2 Finite Element Method of Analysis

A simple way to test the distribution of the electric field is to calculate the electric potential distribution initially. Calculation of electric field distribution is done by subtracting the gradient's electrical potential distribution from it and it is expressed in Eq. (1).

$$\text{Electric field} = -\nabla u. \tag{1}$$

where 'u' is the potential gradient. Equation (2) is obtained by applying Maxwell equation where ρ_{vol} is the volume charge density and 'ε' is the permittivity of the medium which is $\varepsilon = \varepsilon_0 \varepsilon_r$ where 'ε_0' is air permittivity and 'ε_r' is the relative permittivity of dielectric material.

$$\nabla(\text{Electric field}) = \frac{\rho_{\text{vol}}}{\varepsilon}. \tag{2}$$

$$\nabla^2 u = -\frac{\rho_{\text{vol}}}{\varepsilon}. \tag{3}$$

With space charges $\rho_{\text{vol}} = 0$, Laplace equation is obtained, and it is expressed in Eq. (4).

$$\nabla^2 u = -0. \tag{4}$$

The Cartesian system of coordinates of two-dimensional function $F(V)$ is expressed in Eq. (5).

$$F(V) = \frac{1}{2} \iint [\varepsilon_e \left(\frac{\mathrm{d}V}{\mathrm{d}e}\right)^2 + \varepsilon_f \left(\frac{\mathrm{d}V}{\mathrm{d}f}\right)^2 \mathrm{d}e\mathrm{d}f. \tag{5}$$

where 'ε_e' and 'ε_f' are the components of the permittivity and the' 'e' and 'f' components of the permittivity of components in the coordinate system of the Cartesian system, and V is the electrical potential. Equation (6) is obtained by assuming the isotropic permittivity distribution $\varepsilon = \varepsilon_e = \varepsilon_f$.

$$F(V) = \frac{1}{2} \int \varepsilon |\nabla V|^2 \mathrm{d}s. \tag{6}$$

Equation (7) represents the effect of conductivity of the pollution layer is considered on the distribution of the electric field then $F(V)$ is

$$F(V) = \frac{1}{2} \iint (\sigma + j\omega\varepsilon)|\nabla V|^2 \mathrm{d}s \tag{7}$$

.

'ω' is the angular frequency and 'σ' is the conductivity of pollution layer μs/cm and '$F(V)$' is the complex function. Assume the 'c' and 'd' are the linear dependencies of each sub-domain of 'V'. it results in the first order approximately in Eq. (8).

$$V_a(c, d) = a_{a1} + a_{a2}c + a_{a3}d, \quad (a = 1, 2, \ldots, h). \tag{8}$$

The measurement of the electrical potential at any node in the total network composed of several triangular elements is performed by minimizing the F function is obtained in Eq. (9). Figure 1 represents the flowchart of the finite element method

$$\frac{\partial F(rV_i)}{\partial V_i} = 0, \quad i = 1, 2, \ldots, h. \tag{9}$$

3 FEM Model of Polymeric Insulator

Polymeric insulators have four major components, they are

a) Fiber-reinforced polymer.

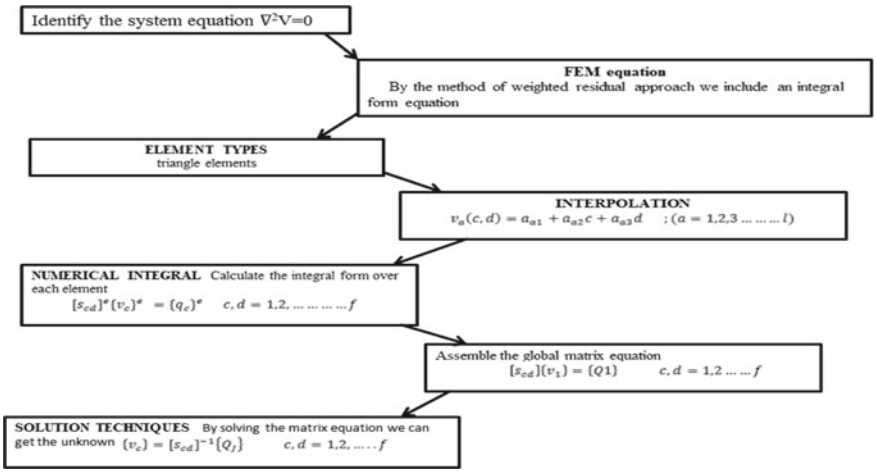

Fig. 1 Flow chart for the FEM

Table 1 Material properties of FEM model

Properties	PEC	Polymer	Air
Relative Permittivity, (ε_r)	4.3	7.2	1
Conductivity, μ s/cm	1	4	0

b) Polymer sheath on the rod.
c) Polymer weather sheds.
d) Metals and fittings.

For the simulation study, an insulator made of polymeric materials was chosen for the current operation dimensions of the 11 kV polymeric insulators used in the simulation analysis, as shown in Table 1. The electric field and voltage distribution (EFVD) of 11 kV polymeric insulators at clean and dry surface conditions are investigated in this paper. The relative permittivity, conductivity, and thickness or height of the contaminated layer and dry band of the materials used in the FEM modeling insulator. Metal fittings are installed at both the line and ground ends of the insulator. Profiles for Test Specimens are shown in Table 2.

4 Simulation Results and Discussion

The potential calculation and distribution of the electric field (E-Field) along the insulator have been constructed. The simulation work is done with the help of software from the ANSYS ELECTROMAGNETIC suite. E-Field distributions for the model were plotted by using 2D axisymmetric tools. Electric potential distributions for the model are plotted by using 2D tools. The relation between the E-Field and

Table 2 Profiles for test specimens

Parameters	Type 1	Type2	Type 3	Type 4	Type 5
Diameter (cm)	5.1	6.1	5.1	6.7	6.5
Total height (cm)	38	40.5	3	31	30
Creepage distance (cm)	34	39	34	30	28
Creepage factor	1.6	2.1	1.6	2.4	2.3
Profile factor	6.2	4.2	6.2	3.9	3.7
Form factor	2.1	2.0	1.9	1.4	1.2
Shed slope angle	28	22	28	20	20

leakage path, electric potential, and leakage path was plotted for each model. The design, operation, and performance of the HV equipment influence the electric field and electric potential distribution. E-Field and Electric potential distribution are the Electrical performance of power equipment. To improve electrical performance, various gases are used. Due to non-uniform electric field distribution, partial and corona discharges occur in the power equipment.

4.1 Type 1 Insulator

Figure 2 shows the results of the Type 1 insulator 2D simulation, such as the distribution of electric potential, the relationship of E-Field distribution between the electric field and the end-to-end arcing distance, the relationship between the electric potential and the end-to-end arcing distance. Figure 2a indicates that the insulator is 2D axisymmetric. Figure 2b indicates that the 2D magnitude of the insulator's distribution of electrical potential. Figure 2c indicates that the magnitude of the distribution of the electric field is more localized around the final fitting. Figure 2d shows that the electrical field distribution vector is more localized around the final fitting. The relationship between the E-Field and the end-to-end arc distance is shown in Fig. 2e, which shows that the field is increased at the end fitting and rises when the end-to-end arc distance approaches the sharp point of the first shed. The relation between the electric potential and the end-to-end arc distance is shown in Fig. 2f, which shows that the potential is reduced from live end fitting to ground end fitting along the insulator.

4.2 Type 2 Insulator

Figure 3 indicates the effects of the Type 2 insulator 2D simulation, such as the distribution of electric potential, the relationship of E-Field distribution between the electric field and the end-to-end arcing distance, and the relationship between the

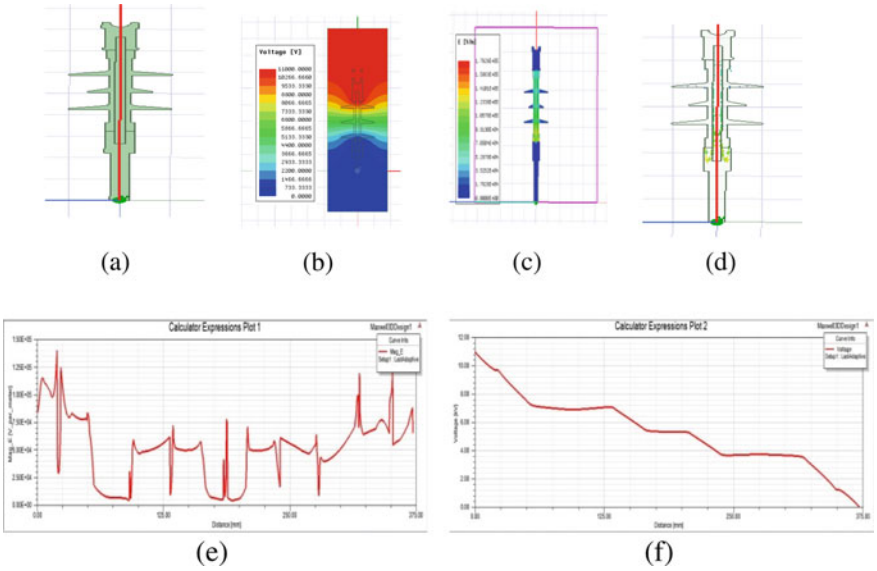

Fig. 2 Results of the Type 1 Insulator, **a** 2D axisymmetric of Type 1 insulator, **b** Potential distribution, **c** Magnitude of E-Field distribution, **d** Vector of E-Field distribution, **e** E-Field versus Arc length, **f** Electric potential versus Arc length

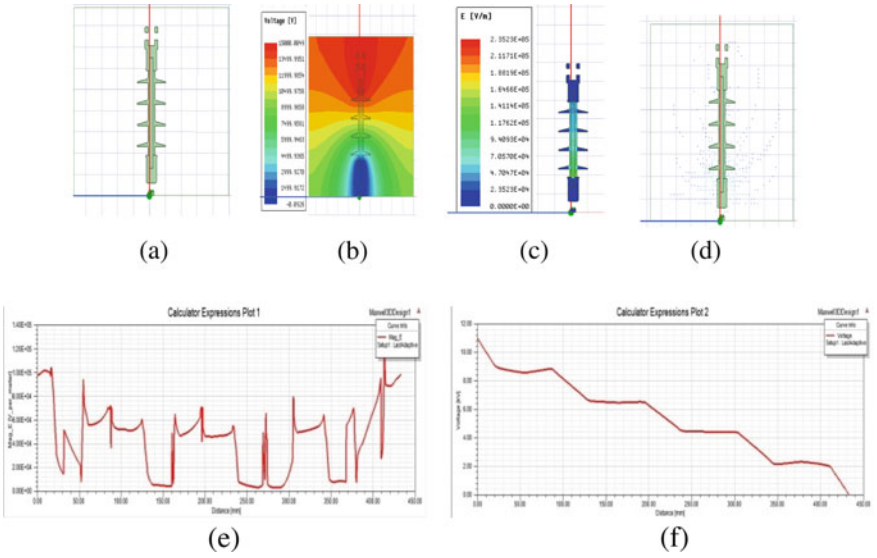

Fig. 3 Results of the Type 2 insulator, **a** 2D axisymmetric of Type 2 insulator, **b** potential distribution, **c** magnitude of E-Field distribution, **d** Vector of E-Field distribution, **e** E-Field versus arc length, **f** electric potential versus arc length

electric potential and the end-to-end arcing distance. Figure 3a indicates that the insulator is 2D axisymmetric. Figure 3b indicates the 2D magnitude of the distribution of the insulator's electrical potential. Figure 3c indicates that the magnitude of distribution of the electric field is more intense around the end fitting. Figure 3d shows that the electric field distribution vector is more intense around the end fitting. The relationship between the E-Field and the end-to-end arc distance is shown in Fig. 3e, which shows that the field is raised at the end fitting and rises when the end-to-end arc distance approaches the sharp point of the first shed. The relation between the electric potential and the end-to-end arc distance is shown in Fig. 3f, which shows that the potential is reduced from live end fitting to ground end fitting along the insulator.

4.3 Type 3 Insulator

Figure 4 indicates the effects of the Type 3 insulator 2D simulation, such as the distribution of electric potential, the relationship of E-Field distribution between the electric field and the end-to-end arcing distance, and the relationship between the electric potential and the end-to-end arcing distance. Figure 4a indicates that the insulator is 2D axisymmetric. Figure 3b indicates the 2D magnitude of the distribution of the insulator's electrical potential. Figure 4c indicates that the magnitude of distribution of the electric field is more intense around the end fitting. Figure 4d

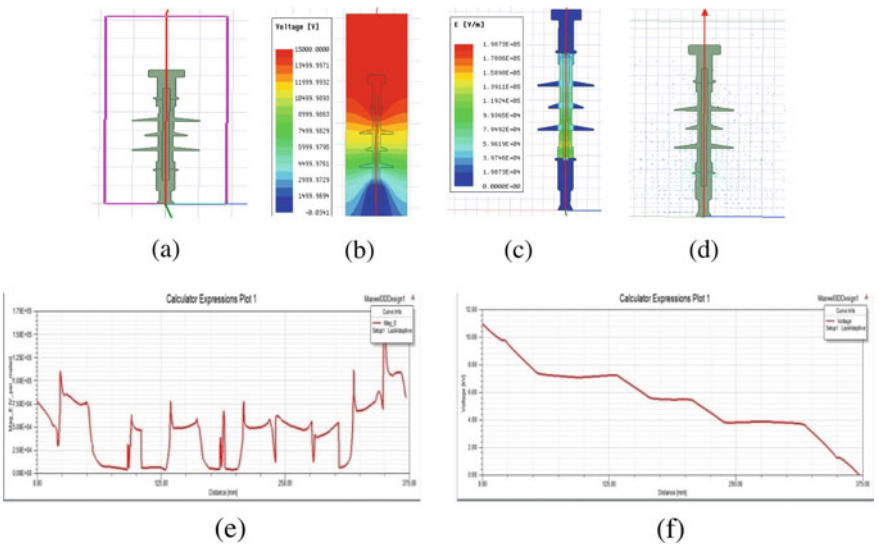

Fig. 4 Results of the Type 3 insulator, **a** 2D axisymmetric of Type 3 insulator, **b** potential distribution, **c** magnitude of E-Field distribution, **d** vector of E-Field distribution, **e** E-Field versus arc length, **f** electric potential versus arc length

shows that the electric field distribution vector is more intense around the end fitting. The relationship between the E-Field and the end-to-end arc distance is shown in Fig. 4e, which shows that the field is raised at the end fitting and rises when the end-to-end arc distance approaches the sharp point of the first shed. The relation between the electric potential and the end-to-end arc distance is shown in Fig. 4f, which shows that the potential is reduced from live end fitting to ground end fitting along the insulator.

4.4 Type 4 Insulator

Figure 5 indicates the results of the Type 4 insulator 2D simulation, such as the distribution of electric potential, the relationship of E-Field distribution between the electric field and the end-to-end arcing distance, and the relationship between the electric potential and the end-to-end arcing distance. Figure 5a indicates that the insulator is 2D axisymmetric. Figure 5b indicates the 2D magnitude of the distribution of the insulator's electrical potential. Figure 5c indicates that the magnitude of distribution of the electric field is more intense around the end fitting. Figure 5d shows that the electric field distribution vector is more intense around the end fitting. The relationship between the E-Field and the end-to-end arc distance is shown in Fig. 5e, which shows that the field is raised at the end fitting and rises when the

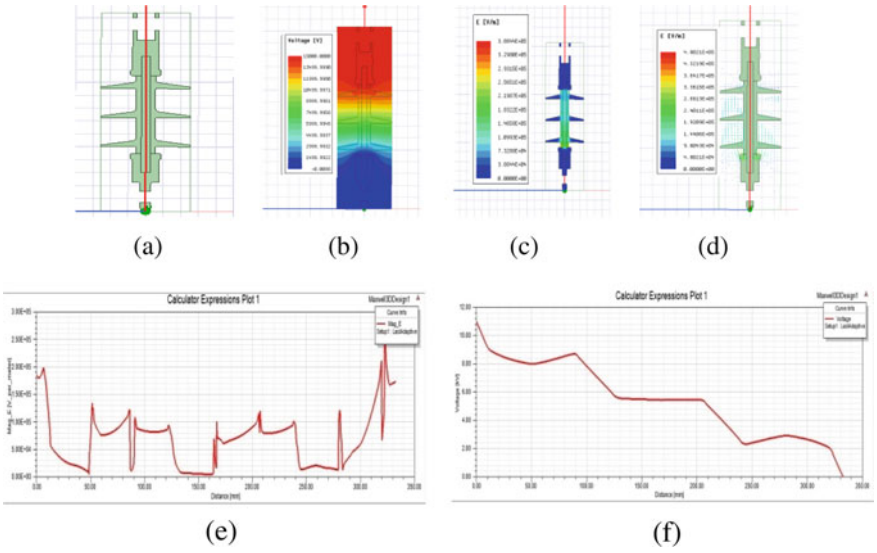

Fig. 5 Results of the Type 4 Insulator, **a** 2D axisymmetric of Type 4 insulator, **b** potential distribution, **c** magnitude of E-Field distribution, **d** vector of E-Field distribution, **e** E-Field versus arc length, **f** electric potential versus arc length

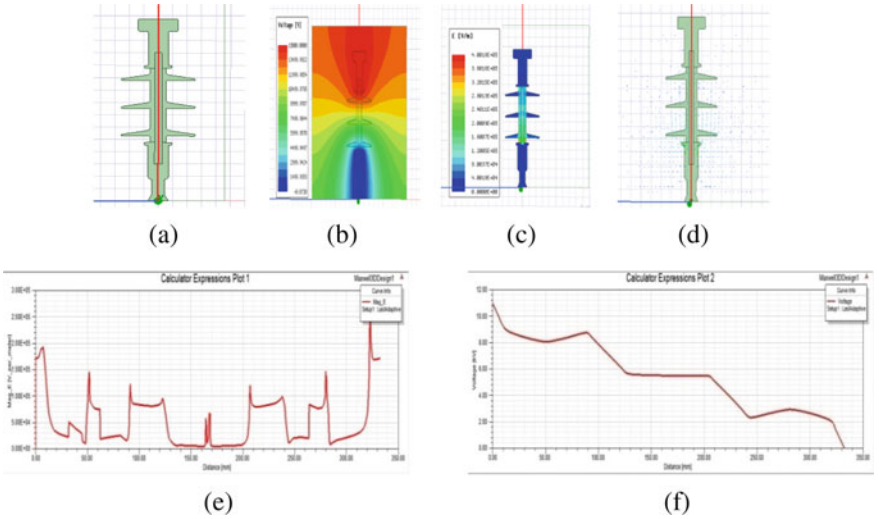

Fig. 6 Results of the Type 5 insulator, **a** 2D axisymmetric of Type 5 insulator, **b** potential distribution, **c** magnitude of E-Field distribution, **d** vector of E-Field distribution, **e** E-Field versus arc length, **f** electric potential versus arc length

end-to-end arc distance approaches the sharp point of the first shed. The relation between the electric potential and the end-to-end arc distance is shown in Fig. 5f, which shows that the potential is reduced from live end fitting to ground end fitting along the insulator.

4.5 Type 5 Insulator

Figure 6 indicates the results of the Type 5 insulator 2D simulation, such as the distribution of electric potential, the relationship of E-Field distribution between the electric field and the end-to-end arcing distance, and the relationship between the electric potential and the end-to-end arcing distance. Figure 6a indicates that the insulator is 2D axisymmetric. Figure 6b indicates the 2D magnitude of the distribution of the insulator's electrical potential. Figure 6c indicates that the magnitude of distribution of the electric field is more intense around the end fitting. Figure 6d shows that the electric field distribution vector is more intense around the end fitting. The relationship between the E-Field and the end-to-end arc distance is shown in Fig. 6e, which shows that the field is raised at the end fitting and rises when the end-to-end arc distance approaches the sharp point of the first shed. The relation between the electric potential and the end-to-end arc distance is shown in Fig. 6f, which shows that the potential is reduced from live end fitting to ground end fitting along the insulator.

5 Conclusion

In this work, E-Field distribution on composite insulators is nonlinear near the end fitting when subjected to the highest magnitude. Electric Field and Electric potential distribution are analyzed along the surface of insulators for 5 different configurations of composite insulators. Type 1 insulators having 3 alternate sheds with ball end fitting shows lower stress compare to others along with higher profile factor, form factor, and dry arcing resistance with solid layer coastal region pollution experiments. Pollution flashover voltages are measured for five kinds of specimen, and it is found the pollution flashover voltage reduces with increasing salt deposit density. The maximum E-field stress is significantly reduced when an arcing horn is installed near the end fittings, according to the analysis.

Acknowledgments The Department of Science and Technology fund for improving S&T infrastructure in universities and higher educational institutions is funding this work (DST-FIST) (SR/FST/College-061/2017) Grant ID and The authors are also grateful to the National Engineering College, Kovilpatti, Tamilnadu, India, for their support.

References

1. Walyo (2007) Study on leakage current waveforms of porcelain insulator due to various artificial pollutants. Int J Math Phys Eng Sci 2(1):27–32
2. Andrew J (2008) Electric fields on ac composite transmission line insulators. IEEE Trans Power Delivery 23(2):823–830
3. Silvester PP, Ferrari RL. Finite elements for electrical engineers, 3rd edn. Cambridge University Press, Cambridge
4. Chandrasekhar S, Sarathi R, Danikas M (2006) Analysis of surface degradation of silicone rubber insulation due to tracking under different voltage profiles. Int J Electrical Eng (Springer)
5. Hartings R (1994) Electric fields along a post insulator: AC-measurements and calculations. IEEE Trans Power Delivery 9(2):912–918
6. Natrajan M, Basharan V, Ganapathyapillai K, Velayutham MR, Mariyasilluvairaj W (2015) Analysis of stress control on 33-kV Non-ceramic insulators using Finite element method. Electric Power Components Syst 43(5):566–577
7. Muniraj C, Chandrasekhar S (2012) Finite element modeling for electric field and voltage distribution along the insulators. World J Modelling Simul 8(4):310–320
8. Zhang Z, Liu X, Jiang X, Hu J, Gao DW (2013) Study on AC flashover performance for different types of porcelain and glass insulators with non-uniform pollution. IEEE Trans Power Deliv 28(3):1691–1698. https://doi.org/10.1109/tpwrd.2013.2245153
9. Jiang X, Yuan J, Zhang Z, Hu J, Sun C (2007) Study on AC artificial-contaminated flashover performance of various types of insulators. IEEE Trans Power Delivery 22(4):2567–2574
10. Ilhan S, Ozdemir A (2015) Impacts of corona rings on the insulation performance of composite polymer insulator strings. IEEE Trans Dielectr Electr Insul 22(3):1605–1612

Non-isolated Multilevel Zeta Converter for MLI Application

Marikannu Marimuthu, Subramanian Vijayalakshmi, B. Paranthagan, R. Venugopal, S. Srinithi, B. Yuvaraj, R. Soundarajan, and S. K. Vasantha Kumar

Abstract A new multilevel zeta converter which converts fixed DC voltage to multilevel DC output voltage is discussed in this paper. Proposed converter has stable voltage feedback capacity and produces high gain output voltages with less input current. Voltage supplied by the PV panel or the fuel cell is at an output of a low voltage. These output voltages can be interfaced with standalone (or) grid connected inverter system by employing the proposed converter. By using a single transistor with the multilevel capacitor geometric structure, the proposed converter is able to generate an output voltage that is much higher and has ripple free output current with a higher step-up conversion ratio. It allows for operation at much higher frequencies for a much longer period of time. Additionally, it does not require for the electrical transformer for high gain. The output of the zeta converter generates four output level voltages which are simulated and verified with theoretical results.

Keywords Zeta converter · High voltage gain · Multilevel voltages · Multilevel Inverter · Self-balancing capacitor

M. Marimuthu (✉) · S. Vijayalakshmi
Department of Electrical and Electronics Engineering, Saranathan College of Engineering, Trichy, India

B. Paranthagan
Associate Professor, Department of Electrical and Electronics Engineering, Saranathan College of Engineering, Trichy, India
e-mail: paranthagan-eee@saranathan.ac.in

R. Venugopal
Assistant Professor, Department of Electrical and Electronics Engineering, Saranathan College of Engineering, Trichy, India

S. Srinithi
PG Scholar, Department of Electrical and Electronics Engineering, Saranathan College of Engineering, Trichy, India

B. Yuvaraj · R. Soundarajan · S. K. Vasantha Kumar
UG Student, Department of Electrical and Electronics Engineering, Saranathan College of Engineering, Trichy, India

C. Subramani et al. (eds.), *Proceedings of International Conference on Power Electronics and Renewable Energy Systems*, Lecture Notes in Electrical Engineering 795,
https://doi.org/10.1007/978-981-16-4943-1_3

1 Introduction

Transportation sector using electric motors is growing exponentially which may be a less contributor to the greenhouse gas emission when compared to conventional transportation system. This reduction is seen as important because it can slow the warming of the planet by lowering pollution and bringing the global temperature closer to normal [1–5]. The burning of petroleum products like petrol, diesel, CNG, etc., is the key reason why we are experiencing a rise of in air pollution due to transport sector, that is why there is some need to modernize the design of the electric vehicles. Electric vehicles will be zero-carbon emission vehicles which will result in no carbon pollution.

Hybrid electric vehicles (plug-in hybrid electric vehicles) are becoming more popular, and more research is being done to develop an efficient, durable, and highly reliable hybrid energy storage scheme with immense power density, a lower price-to-weight ratio, and a longer life cycle. The three phase power electronic converters (PEC) have a significant role to play in regulating the amount of current flowing through an electric hybrid system (HISS). As of today, depending on the type of vehicle that they use energy sources like solar, fuel cells, and ultra-capacitors, all of which are renewable in nature. For utilizing low voltage obtained from renewable sources, the proposed converter will be useful for production of voltages with high gain. Figure 1 shows the overall block diagram of the applications involving multilevel zeta converter.

The proposed converter provides many advantages, such as: (i) a huge conversion ratio with much less duty cycle (ii) increased voltage feedback stability (iii) higher performance and (vi) low EMI noise.

The ultimate goal is to combine the advantages of a zeta converter and a multistage geometric capacitor structure. This combination makes it possible to increase the

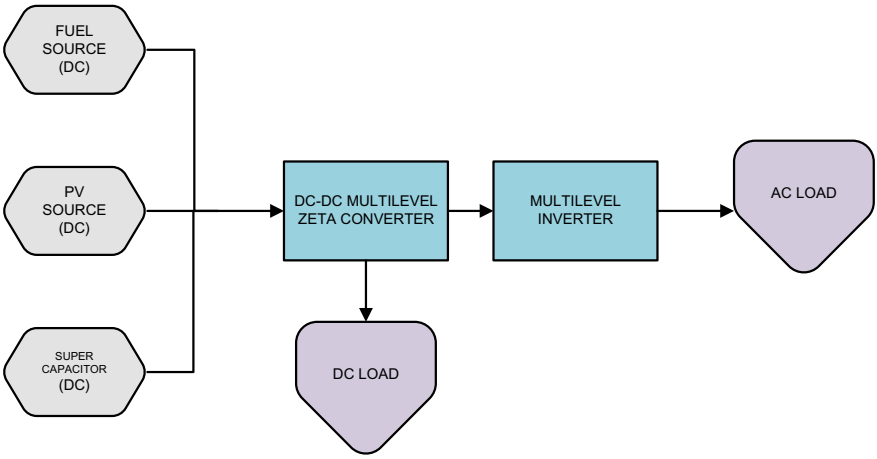

Fig. 1 Application of high gain dc-dc converters

levels by simply inserting a diode and a capacitor. The unique aspect of this proposed zeta is achieving the merits of zeta converter along with high voltage gain [6–8].

2 Design and Operation of Multilevel Zeta Converter

The ultimate idea of this converter is to reduce the number of switches and increase the output voltage gain. In multilevel zeta converter MZC, the circuit is built with single switch only [9–12]. The circuit diagram of the proposed generalized multilevel zeta converter for n levels is shown in Fig. 2.

The duty cycle D for a zeta converter is given by,

$$D = \frac{V_{\text{out}}}{V_{\text{out}} - V_{\text{in}}} \tag{1}$$

$$V_{\text{out}} = \frac{V_{\text{in}} D}{1 - D} \tag{2}$$

The inductor L_1 and L_2 are designed based on the following equation by assuming appropriate duty ratio and output power,

$$L_1 = \frac{V_{\text{in}} D}{F \Delta I_{\text{L}_1}} \tag{3}$$

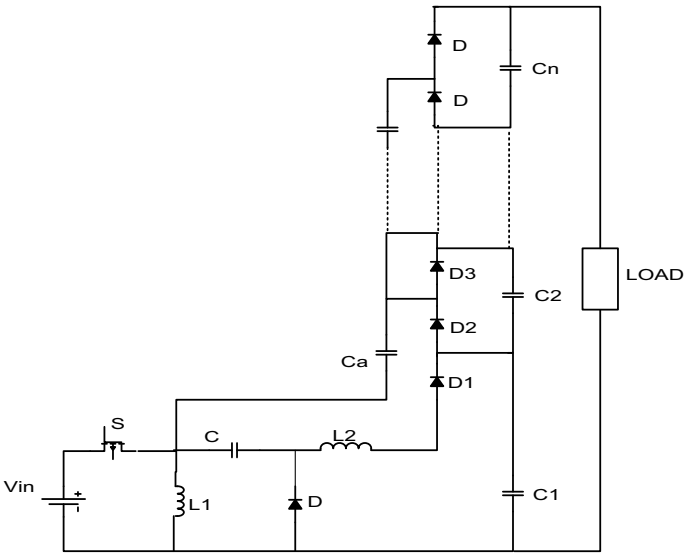

Fig. 2 Generalized structure of MZC

$$L_2 = \frac{V_{\text{in}} D}{F \Delta I_{\text{L}_2}} \tag{4}$$

The capacitor value can be obtained by using following expression,

$$C_1 = \frac{V_{\text{out}} D}{F R \Delta V_{\text{C}_1}} \tag{5}$$

$$C_2 = \frac{V_{\text{in}} D}{8 F^2 L_2 \Delta V_{\text{C}_2}} \tag{6}$$

where F = Switching Frequency.

The multilevel zeta converter with four output levels is shown in Fig. 3.

Operates in various modes which are explained as follows,

Mode 1: The Switch is closed.

When the switch is in the on state, the inductor L_1 is connected to the input voltage and the inductor which is charged in pervious cycle discharges through D_2. As a result, capacitor C_1 is charged which is shown in Fig. 4a.

Mode 2: The switch is closed.

In mode 2 operation, capacitor voltage C_{b} is clamped to C_2 with the help of diode D_4 which is shown if Fig. 4b.

Mode 3: The Switch is closed.

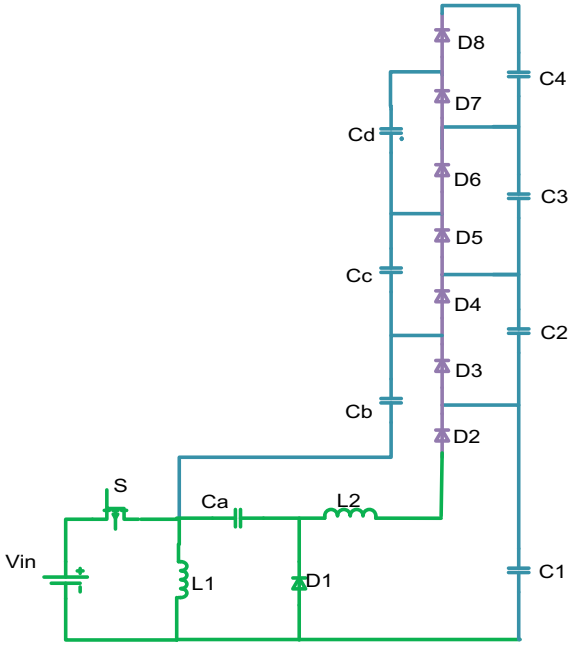

Fig. 3 MZC circuit with four multilevel outputs

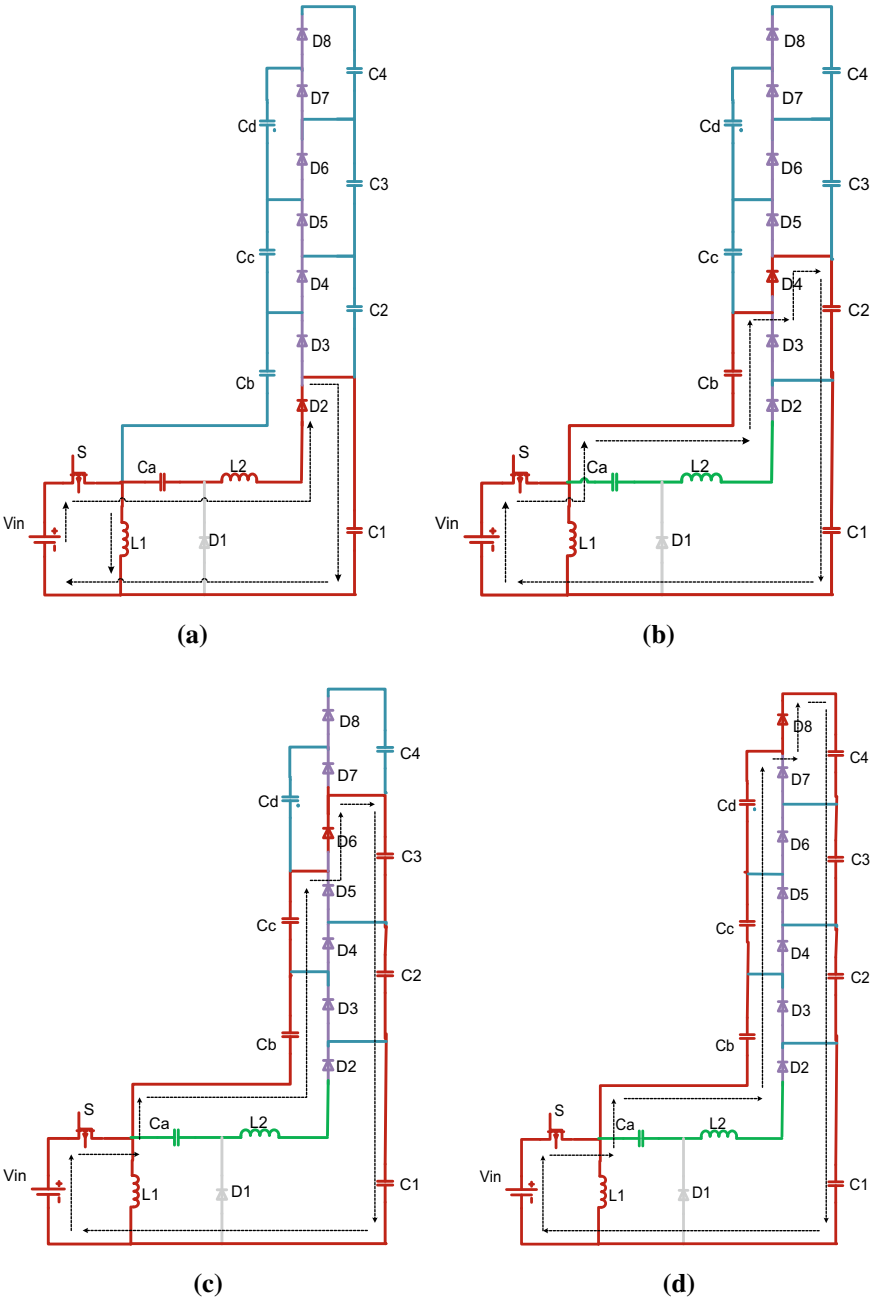

Fig. 4 **a** Mode-1, **b** Mode-2, **c** Mode-3, **d** Mode-4, **e** Mode-5, **f** Mode-6, **g** Mode-7, **h** Mode-8

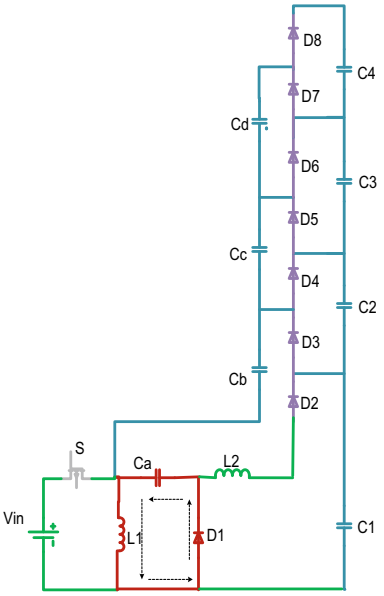

(e)

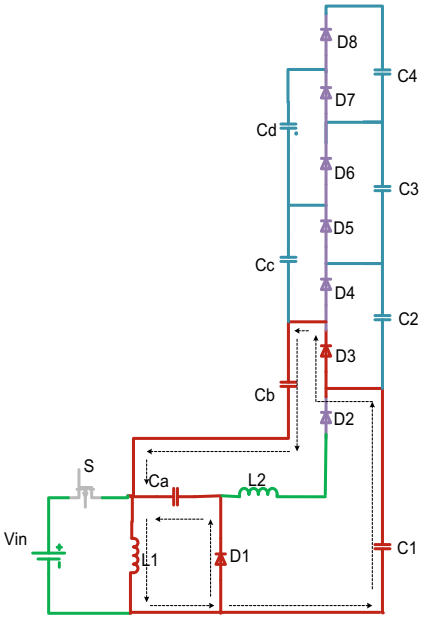

(f)

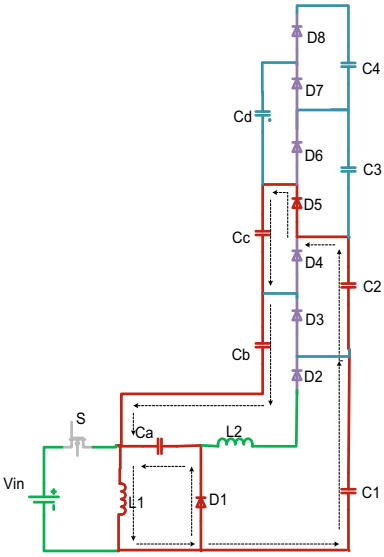

(g)

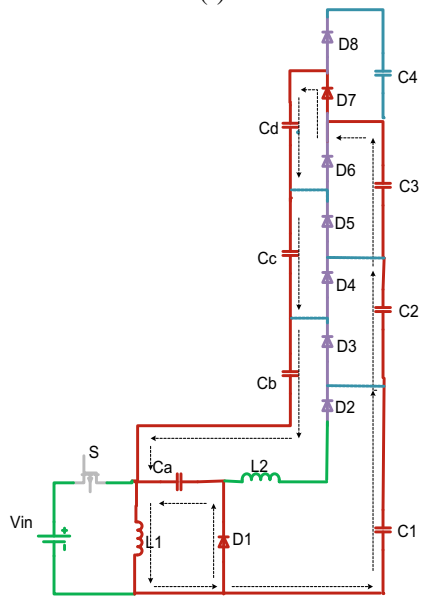

(h)

Fig. 4 (continued)

When the voltage across Vc_b and Vc_c is greater than Vc_2 and Vc_3, then capacitor voltage across C_b is clamped to C_2, and capacitor voltage across C_c is clamped to capacitor voltage C_3 through D_6 which is shown in Fig. 4c.

Mode 4: switch is closed.

When the circuit is in the clamped mode, if the voltage across the C_b, C_c, and C_d are greater than the voltage across C_2, C_3, and C_4, the voltages across C_b, C_c, and C_d are clamped to those values of those voltages across C_2, C_3, and C_4 through the diode D_8 and the key switches S. It can be seen in Fig. 4d.

Mode 5: The switch is open.

During mode 5, Switch S is open condition, and diode D_1 is operates. Inductor L_1 discharges through D_1 which is shown in Fig. 4e.

Mode 6: The switch is open.

When voltage across C_1 is greater than C_b, then voltage between C_1 is clamped to voltage between C_b which is shown in Fig. 4f.

Mode 7: The switch is open.

In mode 7, voltage across C_1 and C_2 is greater than C_b and C_c , and then, the voltage between C_1 and C_2 is clamped to voltage between C_b and C_c with the help of diode D_5 is shown in Fig. 4g.

Mode 8: The switch is open.

In mode 8, the diode D_5 turns ON, hence voltages of C_1, C_2, C_3 are greater than C_b, C_c, C_d. The voltage across capacitors C_1, C_2, C_3 are clamped to voltage across the capacitors C_b, C_c, C_d is shown in Fig. 4h.

3 Simulation Results and Discussion

The simulation has been implemented in MATLAB/Simulink environment. Figure 5 shows the output voltage obtained for the proposed four-level zeta converter. The

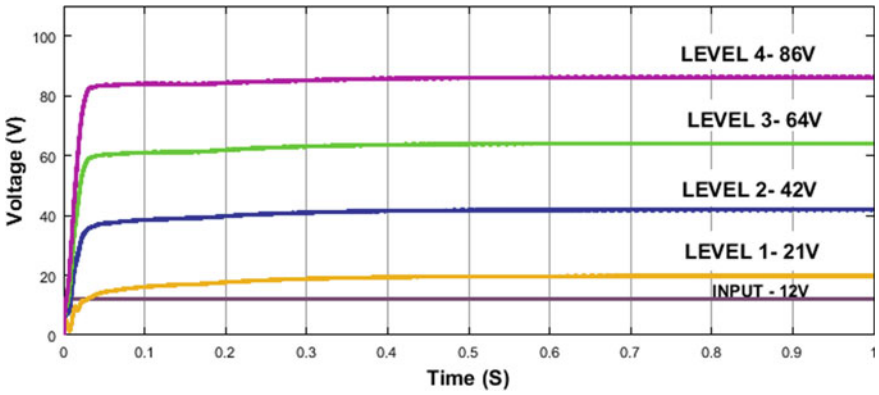

Fig. 5 Load voltage obtained for the proposed MZC

Table 1 Design parameters of proposed zeta converter

Parameter	Value
Input voltage (V_{in})	12 V
Switching frequency	5 kHz
Inductor L_1	1.155 mH
Inductor L_2	1.155 mH
Capacitor C_a	1.846 mF
Self-balancing capacitor (C_b, C_c, C_d, C_1, C_2, C_3)	1.731 mF
Duty ratio (D)	60%

converter is mainly used as a conventional zeta converter, yielding a 21 V output voltage at the first stage. By adding the components to expand the level further, at each level, the converter showed a considerable step-up in the output voltage like 42 V, 64 V, and 86 V, respectively.

The multilevel voltages convergence hold good for all capacitors in the range to be controlled to a standard voltage despite any changes in the source loads or the existence of voltage changes introduced on the board. The parameter values are shown in Table 1.

Finally, when the multilevel converter is powered using zeta, it generates a desired output voltages having less voltage overshoot. In addition, the output has less electromagnetic noise and self-oscillation. The performance parameters including faster settling time and no steady-state error have been greatly improved. Many experiments have been performed to check the supremacy of the zeta is well on the switching element.

4 Application of Multilevel Zeta Converter to Multilevel Inverter Operation

The proposed multilevel zeta converter is used to act as input voltage supply for H-bridge using level circuit as shown in Fig. 6. An H-bridge with level circuit combination generates 9 degree of AC voltage with a frequency of 50 Hz. The nine level MLI output voltages are 0 V, +21 V, +42 V, +64 V, +86 V, −21 V, −42 V, −64 V, −86 V, are shown in Fig. 7. Since these AC waves have less harmonics, they can be used for medium-power applications like computers, telecom power supplies in remote areas, electric vehicles, and uninterruptible power supplies.

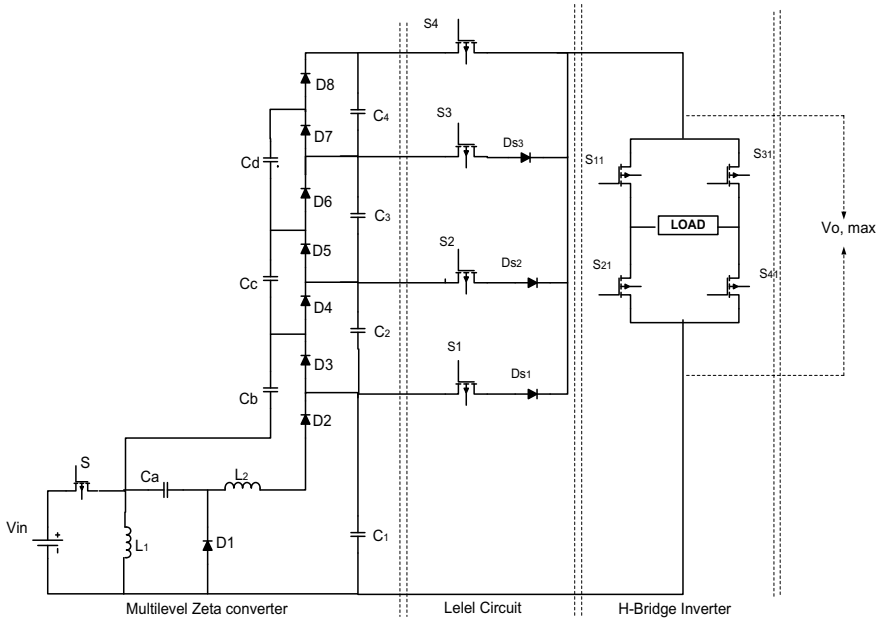

Fig. 6 Multilevel zeta converter with H-bridge inverter

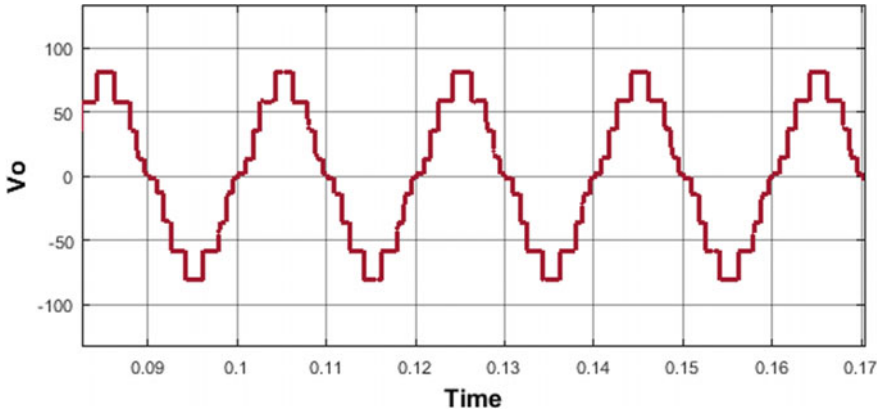

Fig. 7 Output voltage waveform of H-bridge inverter

5 Conclusion

When comparing the output voltage of the single-level zeta converter to that of the multilevel one, it is easier to understand that the number of levels is increased that the maximum output voltage 86 V with 12 V input. The constant input current, the higher degree of output voltage gain obtained by assuming a much shorter duty cycle, the

lower current stress, and the necessity of fewer parts, all without the use of a transformer, are all "special features" of this multilevel zeta converter. The most important advantage is that it is able to raise multilevel output voltages without interruption of the primary elementary circuit. Transistors that are capable of overcoming these electric vehicle problems go a long way in passing the slew of test results.

References

1. Gaurav P, Dhote VP, Modak. Study and analysis of zeta converter fed by solar photovoltaic system using PID controller
2. Manikandan K, Sivabalan A, Sundar R, Sury P. A study of landsman, sepic and zeta converter by particle swarm optimization technique. 978-1-7281-5197-7/20/$31.00 ©2020 IEEE
3. Suresh P, Kirubakaran D (2018) Novel zeta converter with multi level inverter connected to grid. In: IJEECS, vol 11, no 3, September 2018, pp 814–820
4. Falin J (2010) Designing DC/DC converters based on ZETA topology. Analog Appl J
5. Marimuthu M, Vijayalakshmi S, Shenbagalakshmi R (2020) A novel non-isolated single switch multilevel cascaded DC-DC boost converter for multilevel inverter application. J Electrical Eng Technol. The Korean Institute of Electrical Engineers 2020
6. Al Gabri AM, Fardoun AA, Ismail EH (2015) Bridgeless PFC modified SEPIC rectifier with extended gain for universal input voltage applications. IEEE Trans Power Electron 30(8):4272–4282
7. Vuthchhay E, Bunlaksananusorn, Hirata H (2008) Dynamic modeling and control of a zeta converter. In: ECTI-CON 2008, vol 2, 1417 May 2008, pp 969–972
8. Palma L, Todorovic MH, Enjeti P (2005) A high gain transformer less DC-DC Converter for fuel cell applications. In: IEEE Power Electron Jun 2005, p 2514
9. Padmanaban S, Grandi G, Wheeler PW, Blaabjerg F, Loncarski J (2015) A simple MPPT algorithm for novel PV power generation system by high output voltage DC-DC boost converter. In: IEEE (ISIE), pp 214–220
10. Rosas-Caro JC, Sanchez VM, Vazquez-Bautista RF, Morales-Mendoza LJ, Mayo-Maldonado JC, Garcia-Vite PM, Barbosa R(2016) A novel DC-DC multilevel SEPIC converter for PEMFC systems. Int J Hydrogen Energy
11. Alishah RS, Hosseini SH, Babaei E, Sabahi M (2017) Optimal design of new cascaded switch-ladder multilevel inverter structure. IEEE Trans Ind Electron 64(3):2072–2080. https://doi.org/10.1109/TIE.2016.2627019
12. Taghvae A, Adabi J, Renanejad M (2017) A multi- level Inverter structure based on a combination of switched capacitor and DC sources. IEEE Tras. Ind. Informatics 13(5):2162–2171. https://doi.org/10.1109/TII.2017.2710265

Corrupted Image Enhancement Through WaveNet: A Hybrid Approach

C. Vimala and P. Aruna Priya

Abstract A denoising method for medical images through hybrid technique is presented in this paper. The hybrid technique is the combination of wavelet and neural network (WaveNet). Proposed algorithm has been validated through benchmark image, and medical images both are degraded by the variety of noise density through Gaussian noise and visual property. The performances of denoised images are also analyzed with wavelet techniques and compare the results with proposed technique. The proposed strategy is developed in MATLAB platform. Simulation results are evidence for the proposed work

Keywords Wavelet · Neural network · Denoising · Enhancement

1 Introduction

A medical image is corrupted by different reasons, and the removal of the noise is extremely important for correct diagnosis. The process of removing noise from the image is called image denoising. Denoising is basically classified into two types one is filtered method and the other one is transform method. This paper deals with one of the transform methods like wavelet transform [1]. The wavelet transform-based denoising method is concentrated more in the literature. Continuous and discrete are the two different wavelet approaches. The developed version of discrete wavelet transform is the higher density wavelet transform. The higher density wavelet transform that includes double density DWT, double density dual-tree DWT-based image denoising technique will provide good quality of the image. The image quality performance measure values such as peak signal to noise ratio (PSNR), mean square error (MSE), and root mean square error (RMSE) are used to identify the best denoising methods [2]. Digital images are affected by various types of noise. Noise is an

C. Vimala (✉) · P. Aruna Priya
Department of Electronics and Communication Engineering, College of Engineering and Technology, SRM Institute of Science and Technology, Kattankulathur, India

P. Aruna Priya
e-mail: arunaprp@srmist.edu.in

C. Subramani et al. (eds.), *Proceedings of International Conference on Power Electronics and Renewable Energy Systems*, Lecture Notes in Electrical Engineering 795,
https://doi.org/10.1007/978-981-16-4943-1_4

unwanted component, which affects the image. One of the well-known noise that affect the image is additive white Gaussian noise (AWGN), in which the noise probability density function is bell-shaped, and it is uniformly distributed. The additive noise model is represented in Eq. (1) [3].

$$x(m, n) = s(m, n) + \eta(m, n) \tag{1}$$

Removing additive white Gaussian noise (AWGN) from a corrupted signal or image is very interesting. The wavelet-based denoising techniques are mostly implemented for the removal of AWGN [4]. The random variable for Gaussian y is normalized to have zero mean, and variance value is one. The mathematical expression is written in Eq. (2) as shown below

$$f_y(y) = \frac{1}{\sqrt{2\pi}} \exp\left(-\frac{y^2}{2}\right) \tag{2}$$

Therefore, the probability distribution function of random variable Gaussian z of a signal is given in Eq. (3)

$$p(z) = \frac{1}{\sqrt{2\pi}} \exp\left(-\frac{(z-\mu)}{2\sigma^2}\right) \tag{3}$$

where z represents the gray level, μ represents mean value, and σ represents the standard deviation (SD) value. The square of the SD (σ^2) represents variance. The Gaussian noise is normalized to have mean zero and variance one. The standard normal distribution of Gaussian noise is given by $N(0, 1)$, i.e., $N(\mu, \sigma^2)$ it is shown in Fig. 1. Also, the power spectrum of the noise is constant at all frequencies [5]. Image denoising is one of the vital essentials in image processing applications. The degraded images are not useful for any analysis. The researchers have used various methods to improve the degraded images, with appropriate analysis. While implementing the denoising techniques, the prior knowledge on the properties of the distorted images and the noises is assumed [6]. Figure 2 denotes the concept of denoising $s(x, y)$ is the image subjected to blurring through a linear operation. $n(x, y)$ is the noise signal

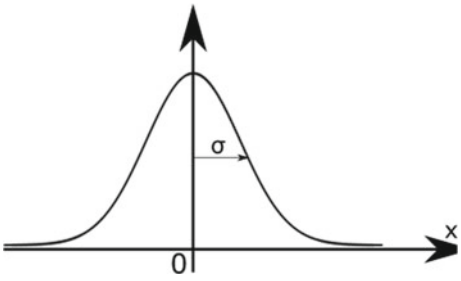

Fig. 1 Normal distribution of Gaussian noise

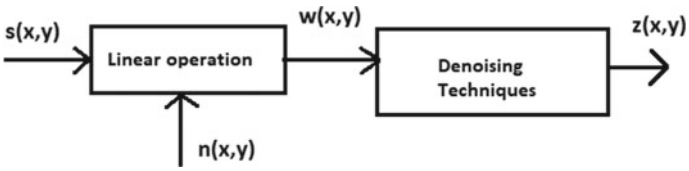

Fig. 2 Denoising process

nique, $z(x, y)$ a restored image is obtained. "Linear operation" considered here can add or multiply the noises with the original image [3].

2 Higher Density Dual-Tree DWT

The dual-tree DWT and higher density will provide higher density. This dual-tree at one level of computation has six dilation and translation coefficients [7, 8]. In this method, the DDDWT technique is applied to the dual-tree DWT. The scaling and wavelet functions are defined absolutely through the dilation and translation it is represented in Eq. (4) to Eq. (6 [9, 10]). The system model for denoising in DDDTDWT is illustrated in Fig. 3.

3 Proposed Denosing Method

Hybrid (wavelet + Neural Network = WaveNet) image denoising technique of WaveNet network. The WaveNet is a combination of both wavelet and neural network. Wavelet is a well-known denoising algorithm for image processing along with this combined neural network, so it is very useful for noise reduction (Fig. 4).

The performance of the hybrid technique is compared with the wavelet-based denoising method. The various noise level of noisy and denoised PSNR values are given in Table 1. With the low-noise level taken as 10, the PSNR improves by 30% by the wavelet method and hybrid method improves PSNR by 35.92%. If the sigma value is 25, the percentage improvement for hybrid method is 50.11%, but wavelet method provides only 41.56%. Table 2 represents the MSE performance of hybrid method, which is compared with DDDTDWT method. The 85.03% of the noise is removed from noisy image by DDDTDWT method, and by the improved hybrid method, 88.92% of the noise is removed from noisy image. The best training performance of hybrid method is shown in Fig. 5. The performance value calculated using the formula Eq. (7)–(9) [11–13].

$$\psi_{h,i}(t), \psi_{g,i}(t), i = 1, 2 \tag{4}$$

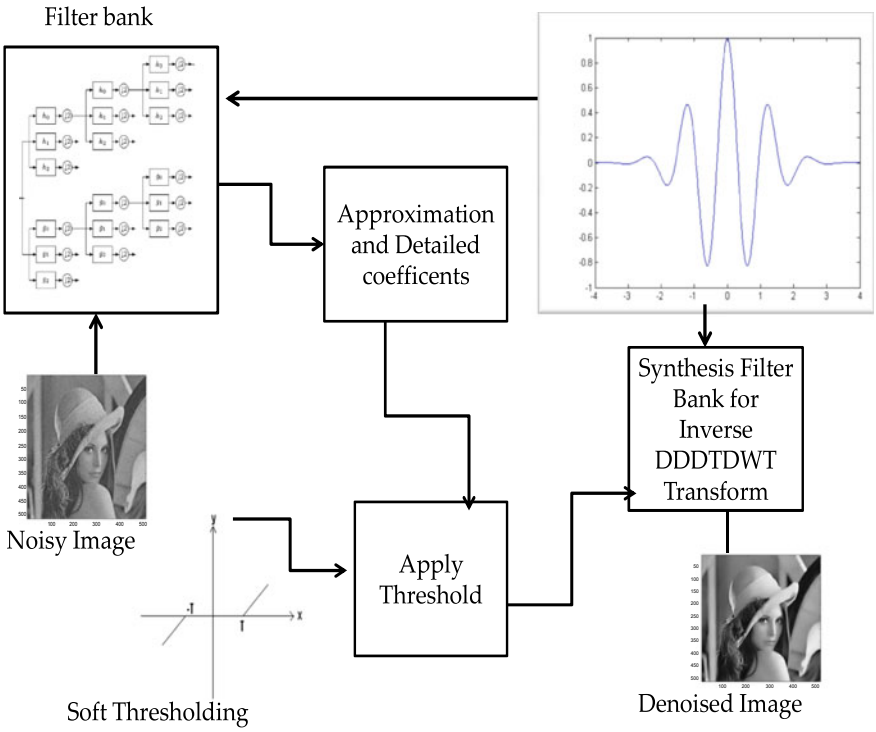

Fig. 3 System model for DDDTDWT denoising method

Fig. 4 Neural network structure

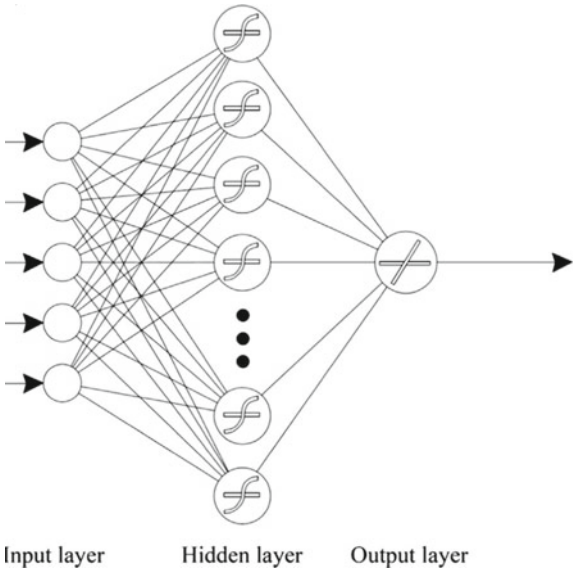

Table 1 Comparison of performance measure for noisy and denoised images using DDDTDWT for high noise = 50

Image	MSE		RMSE		PSNR(dB)	
	corrupted	Enhanced	corrupted	Enhanced	corrupted	Enhanced
Lena	401.8993	**89.2713**	20.0474	**9.4483**	28.1442	**34.6783**
zelda	398.2987	**63.6774**	20.0316	**7.3819**	22.0965	**30.7674**
Mandrill	400.3713	**291.5080**	20.0093	**7.0736**	22.1062	**23.4843**
Peppers	225.8456	**60.8188**	15.0282	**7.7986**	24.5927	**31.9732**

Table 2 PSNR performance comparison

Noisy	DDDWT	DDDTDWT	DDDTDWT + ANN
10	29.55	31.7	**33.56**
15	24.65	30.8	**31.37**
20	22.13	29.81	**30.02**
25	20.58	28.81	**29.97**

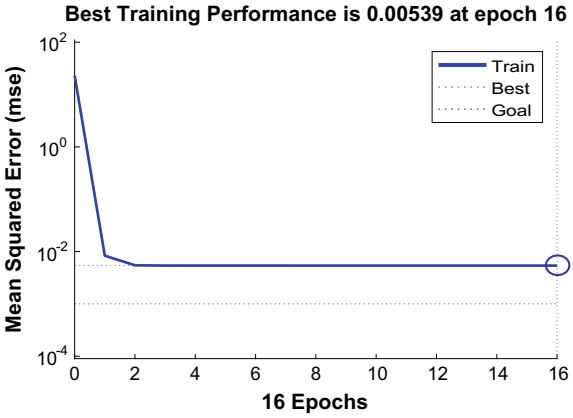

Fig. 5 Training performance using hybrid method

$$\Psi_{h,1}(t) \approx \Psi_{h,2}(t - 0.5) \tag{5}$$

$$\Psi_{g,1}(t) \approx \Psi_{g,2}(t - 0.5) \tag{6}$$

The test images are selected and added with Gaussian white noise with zero mean and different noise variance. The quality of the denoised image is measured, and the values are also tabulated, and the values are compared with DWT and DDDTDWT. Due to more number of detailed coefficients, the DDDTDWT achieves high PSNR. The comparisons are made for a different noise variance, where the denoising methods such as DWT, DDDWT, and DDDTDWT are compared, and the

results show that DDDTDWT performs better than the other two methods.

$$\text{PSNR} = 20\log_{10}\left(\frac{\text{Max}}{\text{RMSE}(x, y)}\right) \tag{7}$$

$$\text{RMSE} = \frac{1}{N}\sqrt{\left(\sum_{i=1}^{N}(x_i - y_i)^2\right)} \tag{8}$$

$$\text{MSE} = \frac{1}{N}\sum_{i=1}^{N}(x_i - y_i)^2 \tag{9}$$

4 Result and Discussion

The proposed system is for medical images like uterus, tooth, lung, and brain. The denoised PSNR value shown in Table 2 and the values are compared with various wavelet denoising algorithms and evident that proposed techniques gives the commendable PSNR values than the existing techniques. The MSE values of proposed and existing techniques are calculated, and the values are given in Table 3. The minimum MSE values yield the proposed system. The minimum MSE is one type of evidence to prove the proposed system. The same measurements are taken for four different noise density values. For evaluation purpose, noisy image with constant noise level and the same image size is used for both existing and proposed. It is seen that the value of MSE is decreased when the noise variance low and increases when the noise variance is high. The proposed method gives the less MSE, and it is given in Fig. 6. The proposed ANN is incorporated with all the above-mentioned noisy medical images through proposed method, and the corresponding denoised MSE value is shown in Table 3, and the improved PSNR value is shown in Table 2.

Table 3 Noisy and denoised MSE, RMSE value comparison

σ	Corrupted image	Enhanced image MSE			
		DWT	DDDWT	DDDTDWT	DDDTDWT + ANN
10	100.631	65	50.763	60.16	**44.54**
15	224.580	90	60.18	50.21	**48.02**
20	398.862	124	77.809	65.23	**52.48**
25	626.233	250	123.786	100.56	**88.35**

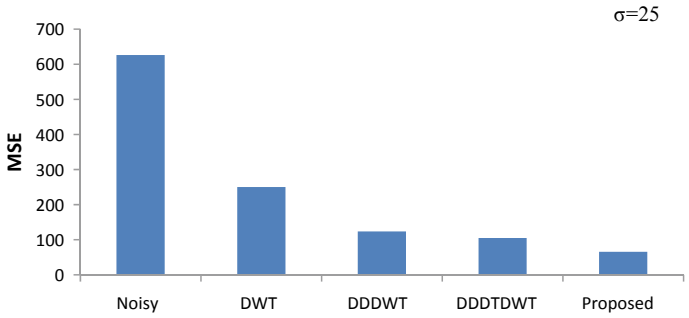

Fig. 6 Graphical representation of enhanced image MSE value

5 Conclusion

The hybrid technique, which is the combination of wavelet and neural network (WaveNet), has been implemented for denoising medical images, and the performance measures such as PSNR, MSE, and RMSE are computed. Four test medical images have been analyzed, and denoised images are applied to image quality assessment which shows improvement in terms of the PSNR increase and the mean square error and RMSE decrease. The obtained results of the proposed method have been compared with results from other wavelet techniques that confirms that the proposed method outperforms the on hand denoising methods.

References

1. Guo L, Chen W, Liao Y, Liao h, Li J (2016) An edge-preserved image denoising algorithm based on local adaptive regularization. J Sensors Article ID 2019569, 6 pages. https://doi.org/10.1155/2016/2019569
2. Liu XW, Huang LH (2014) A new nonlocal total variation regularization algorithm for image denoising. Math Comput Simul 97(3):224–233
3. Kittisuwan P (2016) Image enhancement via MMSE estimation of Gaussian scale mixture with Maxwell density in AWGN. J Innov Optical Health Sci 9(2)
4. Ding Y, Ivan WS (2015) Artifact-free wavelet denoising: Non-convex sparse regularization convex optimization. IEEE Signal Process Lett 22:1364–1368
5. Vimala C, Aruna Priya P (2019) Artificial neural network based wavelet transform technique for image quality enhancement. Comput Electrical Eng 76:258–267
6. Aravind N, Suresh KV (2015) A discontinuity adaptive prior for image denoising. Int J Comput Appl 110:13–19
7. Xu J, Feng A, Hao Y, Zhang X, Han Y (2016) Image deblurring and denoising by an improved variational model. Int J Electronics Commun 70:1128–1133
8. Yan J, Lu WS (2015) Imaging denoising by generalized total variation regularization and least squares fidelity. Multidimension Syst Signal Process 20(1):89–97
9. Wang X, Ou X, Chen B-W, Kim M (2015) Image denoising based on improved wavelet threshold function for wireless camera networks and transmissions. Int J Distributed Sensor Netw. https://doi.org/10.1155/2015/670216

10. Jaiswala A, Upadhyayb J, Somkuwar A (2014) Image denoising and quality measurements by using filtering and wavelet based techniques. Int J Electronics Commun 68:699–705
11. Chinnarao B, Madhavilatha M, Pratap NL (2012) Improved image denoising algorithm using dual tree complex wavelet transform with new thresholding technique. Int J Electronics Eng 4(1):1359
12. Hedaoo P, Swati S, Godbole (2011) Wavelet thresholding approach for image denoising. Int J Netw Security Appl 3(4):16–21
13. Vimala C, Aruna Priya P (2015) Noise reduction based on double density discrete wavelet transform. In: IEEE international conference on smart structures and systems, pp 15–18

Modeling and Control of Cascaded Multilevel Inverter for Harmonics Mitigation of Induction Motor Drive

Ranganathan Selvarasu, C. Kannan, S. Priyadharsini, and Dagne Alemayehu Shiferaw

Abstract Nowadays the majority of the industrial drives are employed with induction motors as a load. Induction motor receives input from the output of MLIs, which requires quality power in terms of lower or negligible total harmonic distortion (THD). In order to provide quality power, in this paper, modeling of cascaded multilevel inverter (MLI) for harmonics mitigation of induction motor is proposed. In recent years, cascaded H-bridge MLI technology has emerged as a crucial to offer a quality output for industrial drives. In this work, three-phase five- and seven-level inverters are developed, modeled and simulation carried out using MATLAB/Simulink. Comparisons of simulation as well as prototype solutions are presented.

Keywords Induction motor · Total harmonic distortion · PWM technique · Cascaded H-bridge multilevel

1 Introduction

In present days, almost ninety percentages of industrial drives are employed with induction motors due to the advantages offered by them, which includes rugged and simple in construction, less maintenance, reliable, offers high efficiency, and cost is less. The variable speed of drive is required in many applications, which is accomplished by induction motor. Nowadays due to the development of semiconductor devices, power electronic devices are playing a vital role for controlling speed of induction motor. In most of the drives, the induction motor speed is controlled by output of voltage source inverters.

The output voltage level of inverters is improved by altering structure of MLI topologies. The conventional inverter offers output voltage with huge total harmonic

R. Selvarasu · D. A. Shiferaw
Adama Science and Technology University, Adama, Ethiopia

C. Kannan (✉) · S. Priyadharsini
Arunai Engineering College, Tiruvannamalai, India

C. Subramani et al. (eds.), *Proceedings of International Conference on Power Electronics and Renewable Energy Systems*, Lecture Notes in Electrical Engineering 795,
https://doi.org/10.1007/978-981-16-4943-1_5

distortion. A multilevel inverter offers output voltages with less total harmonic distortion. A survey has been carried out on multilevel inverter topologies, control, and their applications [1].

A tutorial on multilevel converter has been presented, which includes operating principle of inverter, various topologies for power circuit, methods of modulation, technical issues, and applications at industry [2]. Single- and double-source module for multilevel inverter structure has been proposed to decrease the power electronic switches, and the results have been compared with different topologies [3]. A triple inverter topology has been proposed with multilevel operation. Each inverter has been fed by three isolated PV generators. The simulation and experiment results confirmed the performance of proposed topology of inverter [4]. PI and fuzzy controller have been proposed to develop cascaded H-bridge MLI, which produces output voltages with five levels of reduced total harmonic distortion and the results compared [5]. A new multilevel electromagnetic interference filter has been developed to suppress mutual interference. The resistance to thermal and electromagnetic interference has been improved by the designed filter [6]. The grid-connected PV system reliability has been improved by designing a 27-level cascaded H-bridge MLI. Modified synchronous optimal PWM technique has used to obtain the minimal THD [7]. Six-phase induction generator has been modeled for wind energy conversion system, which uses three-level converters on grid side [8]. Cascaded H-bridge MLI with modified topology has been proposed to provide a staircase shape of DC voltage to the bridge inverter, which in turn offers AC voltage with minimal THD with power loss reduction [9].

A cascaded H-bridge MLI with five levels has been modeled for wind mill applications, which provides reduced total harmonic distortion [10]. A complete review has been presented for newly proposed different MLI topologies [11]. In order to reduce switches and losses, a new tapped source stack succored MLI has been developed [12].

In this paper, three new types of cascaded H-bridge MLI are proposed with multicarrier pulse width modulation. They produce two levels, five levels, and seven levels output voltages. The proposed topologies are modeled and simulated with MATLAB/Simulink environment. In addition to that, prototype model is developed to prove the efficacy of proposed topology. Simulation and prototype result are presented and compared.

2 Basic Structure of Inverter-Fed Induction Motor

Induction motor is supplied from DC supply using proposed five levels and seven levels cascaded H-bridge MLI in order to lessen the THD. The multicarrier PWM scheme is implemented to get the gating signal to control the MOSFET gate. Figure 1 represents the block diagram for induction motor fed by MLI.

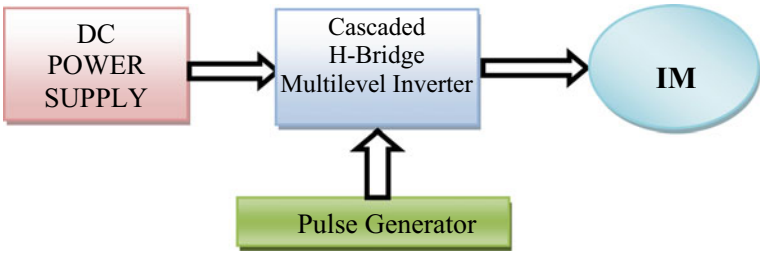

Fig. 1 Block diagram of induction motor fed by inveter

3 Proposed Modeling of Inverter

Cascaded H-bridge MLI is one of the conventional MLI which possesses numerous advantages than other types. The foremost merit of cascaded MLI structure is modular in nature where the entire system that contains identical cell is grouped. However, it requires isolated DC supply of $(2k + 1)$ voltage level. In this work, three different structures are developed and modeled.

3.1 Modeling of Two Levels Inverter with Induction Motor

A three-phase two-level inverter is modeled, which comprises six groups of active switches, S_1 to S_6. The MATLAB/Simulink model of two-level inverter is shown in Fig. 2.

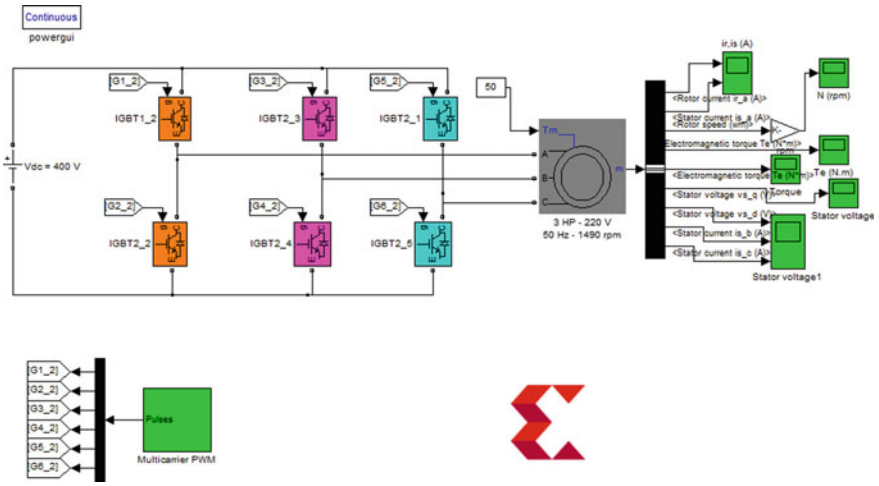

Fig. 2 Simulink model of two-level inverter-fed induction motor

Simulink model of two levels inverter is developed by considering induction motor as a load with rating of 50 HP, 400 V, 1500 rpm. Multicarrier pulsed width modulation is adopted for the developed system. All the carrier waves are formed above zero and arranged in phase with 180°. The stator of induction motor is fed with output of two levels inverter. Three-phase source and load torque are maintained as possible constant. Simulation is performed in phasor mode.

3.2 Modeling of Five Levels Inverter with Induction Motor

A three-phase five-level inverter is modeled. Figure 3 indicates Simulink model of five-level inverter. Induction motor is considered as a load for developed Simulink model of five levels inverter.

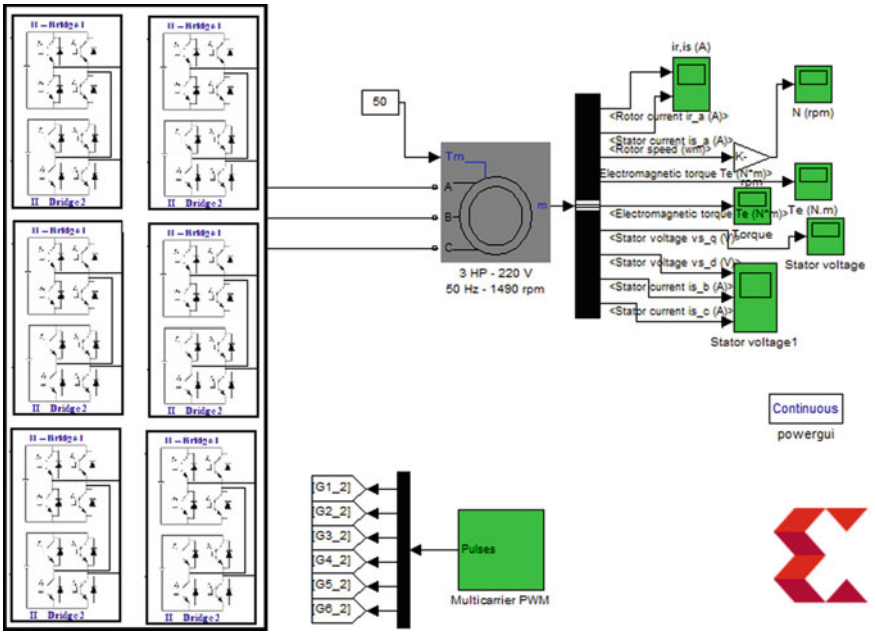

Fig. 3 Simulink model of five-level inverter with induction motor

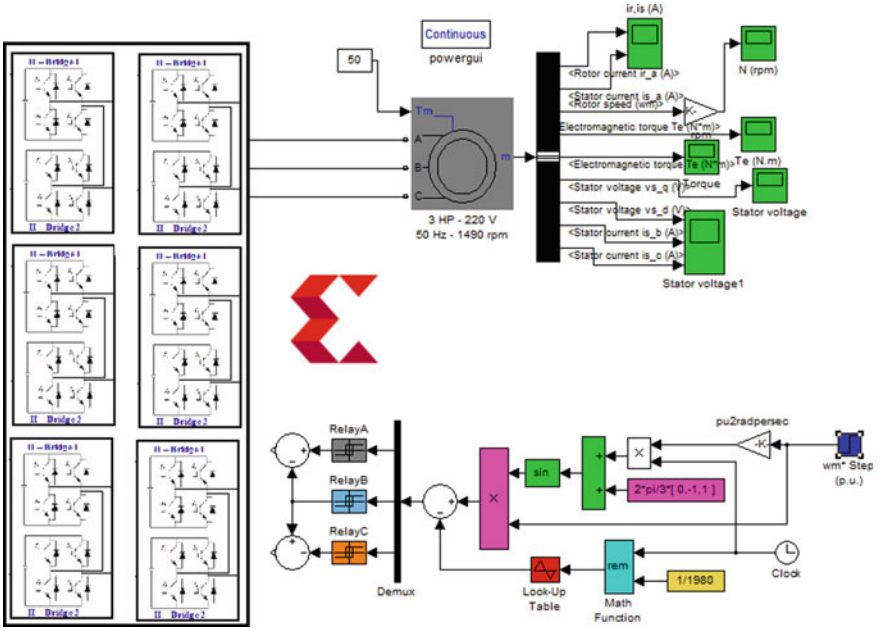

Fig. 4 Simulink model of seven-level inverter with induction motor

3.3 Modeling of Seven-Level Cascaded Inverter with Induction Motor

Figure 4 shows Simulink model of a developed three-phase seven-level inverter-fed induction motor.

4 Results and Discussion

In this work, two, five, and seven levels cascaded H-bridge inverters are modeled. The modeled inverters are fed with induction motor, which is simulated using MATLAB software. The voltage and total harmonic distortion of two-level inverter are presented in Figs. 5 and 6, respectively. Figure 6 shows the two-level inverter harmonic spectrum analyses with THD of 40.48c/o for modulation Index 1.

Figure 7 presents the simulation and hardware result of phase voltage of five-level inverter. Figure 8 represents the five-level inverter harmonic spectrum analysis with THD 35.77c/o for modulation Index 1. Figure 9 indicates speed of induction motor offered by five-level inverter output.

Figure 10 presents simulation and hardware result of phase voltage of seven-level inverter. Simulation and hardware result of FFT analysis of seven levels inverter are

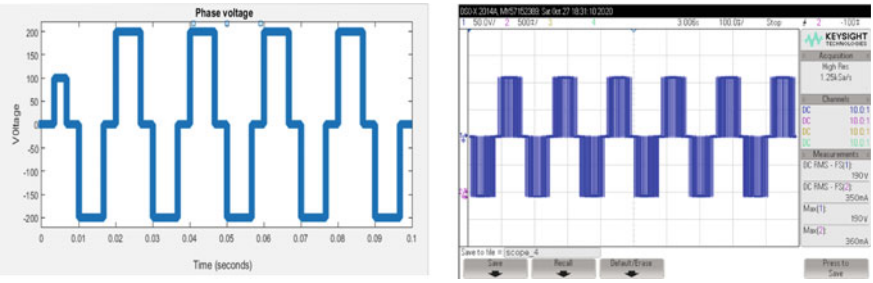

Fig. 5 Simulation and hardware result of phase voltage of two-level inverter

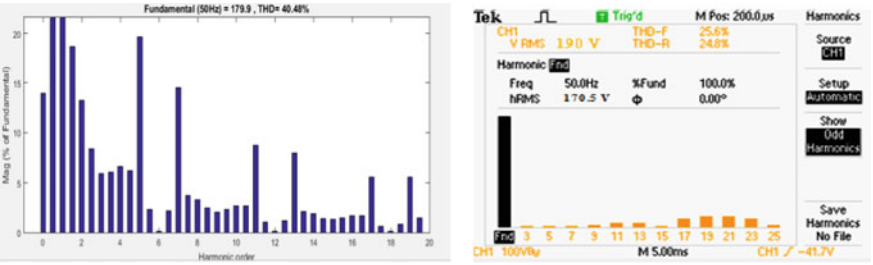

Fig. 6 FFT analysis of two-level inverter offered by simulation and prototype

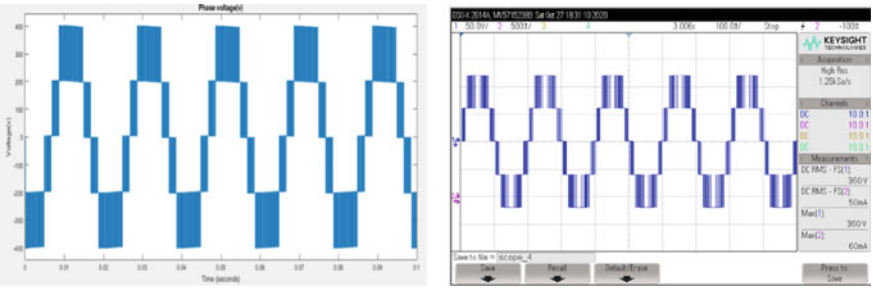

Fig. 7 Simulation and hardware result of phase voltage of five-level inverter

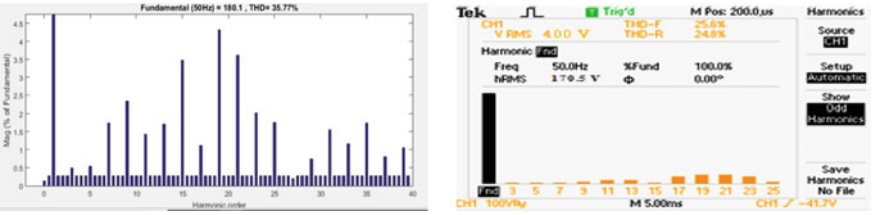

Fig. 8 Simulation and hardware result of FFT analysis of five-level inverter

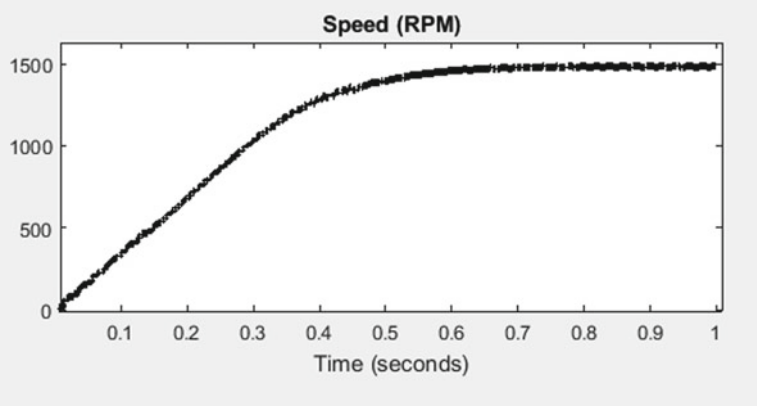

Fig. 9 Induction motor speed obtained by five-level inverter output

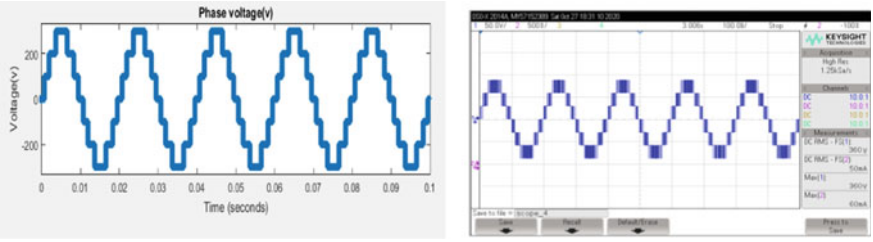

Fig. 10 Simulation and hardware result of phase voltage of seven-level inverter

presented in Fig. 11. In this case, the THD is 11.89c/o for modulation Index 1. It is clear from the figures that THD in output voltage of seven levels inverter is lower than the harmonic distortion in output voltage of five levels inverter. Figure 12 shows the speed of induction motor offered by seven-level inverter output.

Table 1 provides the THD offered by two, five, and seven levels inverter for various modulation index. It is possible to see from the table that seven-level inverter provides lesser THD than two- and five-level inverter. The hardware of prototype model is presented in Fig. 13.

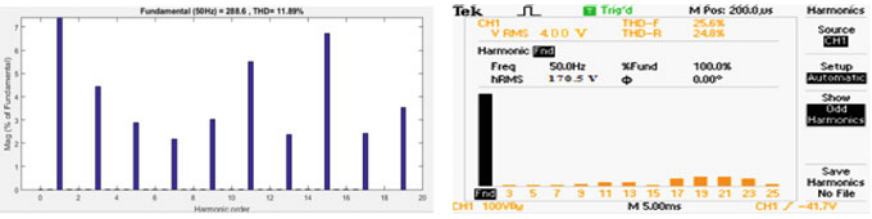

Fig. 11 FFT analysis of seven-level inverter offered by simulation and prototype

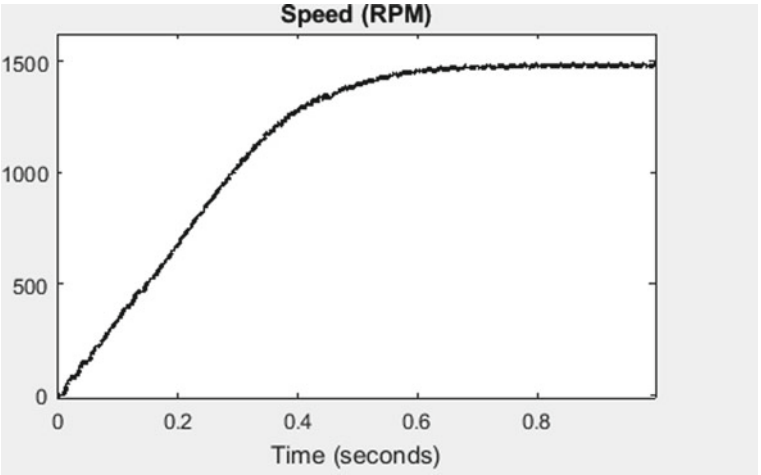

Fig. 12 Induction motor speed obtained by seven-level inverter output

Table 1 Comparison of modulation index versus total harmonic distortion

Modulation index	THD of two-level inverter (%)	THD of five-level inverter (%)	THD of seven-level inverter (%)
1	40.48	35.77	11.89
0.9	43.67	36.64	12.28
0.8	45.98	38.93	14.79
0.7	48.43	41.72	15.74
0.6	51.54	31.39	8.94
0.5	36.74	43.68	13.00
0.4	53.00	46.48	18.36
0.3	55.94	49.87	19.97
0.25	57.24	52.56	21.27

5 Conclusion

In this paper, two-, five-, and seven-level cascaded inverters are developed and modeled. The modeled inverter topologies fed with induction motor are simulated using MATLAB software. The performance of developed inverters in terms of output voltage and THD of modeled inverters is compared with the solutions of prototype model. The THD of two, five, and seven levels inverter is presented with various modulation indexes. It is obvious from the above results and discussions that the seven-level inverter offers low harmonic distortion in their output voltages.

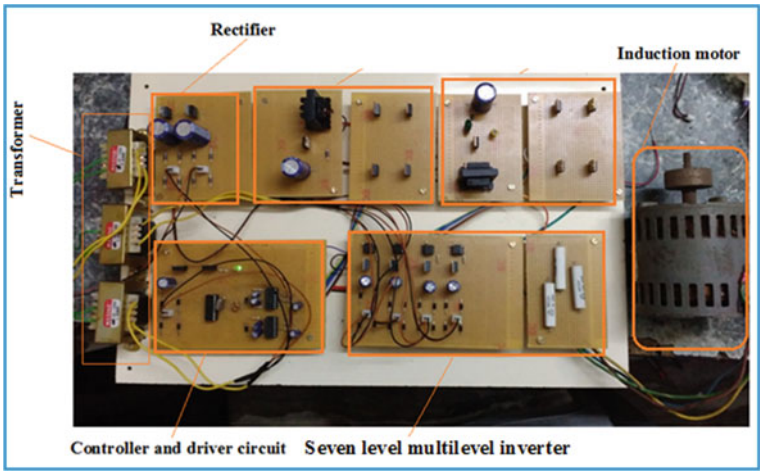

Fig. 13 Hardware proof of concept

References

1. Rodriguez J, Lai J-S, Peng FZ (2002) Multilevel inverters: a survey of topologies, controls, and applicatiosn. IEEE Trans Ind Electron 49:724–738
2. Rodriguez J, Frequelo LG, Kouro S, Leon JI, Portillo RC, Prats MAM, Perez M (2009) Multilevel converters: an enabling technology for high-power applications. IEEE Proc 97(11):1786–1817
3. Vinoth Kumar N, Cinnaiyan VK (2017) Multilevel inverter topology using single source and double source module with reduced power electronic components. J Eng 3:467–480
4. Fernão Pires V, Cordeiro A, Foito D, Fernando Silva J (2018) Three-phase multilevel inverter for grid-connected distributed photovoltaic systems based in three three-phase two-level inverters. Solar Energy 174:1026–1034
5. Kannan C, Mohanty NK, Selvarasu R (2017) A new topology for cascaded H-bridge multilevel inverter with PI and Fuzzy control. Energy Proc 117:917–926
6. Xu S-Z, Peng Y-F, Li S-Y (2019) Suppression effectiveness research on multi-level EMI filter in thermal electromagnetic interactive filed of explosion-proof three-level NPC converter. Case Stud Thermal Eng 15
7. Gayathri Devi B, Keshavan BK (2019) A novel hybrid phase shifted-modified synchronous optimal pulse width modulation based 27-level inverter for grid-connected PV system. Energy 178:309–317
8. Chinmaya KA, Singh GK (2019) Modeling and experimental analysis of grid-connected six-phase induction generator for variable speed wind energy conversion system. Electric Power Syst Res 166:151–162
9. Garapati DP, Jegathesan V, Veerasam M (2018) Minimization of power loss in newfangled cascaded H-bridge multilevel inverter using in-phase disposition PWM and wavelet transform based fault diagnosis. Ain Shams Eng J 9:1381–1396
10. Palanivel P, Selvarasu R, Barani Sundaram B, Alemayehu H (2018) Cascaded hybrid device multilevel converters for wind mill applications. In: International conference on advances of science and technology, pp 93–101
11. Chandrasekaran K, Mohanty NK, Sahoo AK. Performance analysis of modular vs non modular multilevel inverter. In: International Conference on Renewable Energy Integration into Smart

Grids: A Multidisciplinary Approach to Technology Modelling and Simulation (ICREISG), IEEE, pp 61–67.
12. Chandrasekaran K, Mohanty NK. A flexible rung ladder structured multilevel inverter. Tehnički vjesnik 27(4):1044–1049

Assessment of Various Vector Control Schemes for PMSM Drive Application

Kodumur Meesala Ravi Eswar, Chokkalingam Bharatiraja, and Jayakumar Vinoth

Abstract Currently, the operation of Finite Control Set Model Predictive Control (FCS-MPC) schemes in electric motor drives domain is emerging. Its distinguished features are: intuitive, simple and easy insertion of multi-objectives. The application of FCS-MPC in permanent magnet synchronous motor (PMSM) drive has several benefits in terms of improving the performance when compared with direct torque control (DTC)-operated PMSM drive. The FCS-MPC scheme is categorized into two: predictive torque control (PTC) and predictive current control (PCC). This paper deals with comparative evaluation of these control schemes for PMSM drive operation concerning flux and torque ripple, and current THD. Therefore, the gained results are analyzed for PMSM drive highlighting the benefits of FCS-MPC over DTC.

Keywords Direct torque control (DTC) · Finite Control Set Model Predictive Control (FCS-MPC) · Permanent magnet synchronous motor (PMSM) · Predictive current control (PCC) · Predictive torque control (PTC)

1 Introduction

Considering support of fast microprocessor technologies, the AC motor drives are powering the future of industry [1]. Nowadays, PMSM drives are emerging, which is having special advantages in machine point of view [2]. The notable advantages are stated as: high efficiency, high power density and torque-to-weight ratio. To achieve high dynamic performance for motor drives, vector control schemes are

K. M. Ravi Eswar (✉) · C. Bharatiraja · J. Vinoth
Department of Electrical and Electronics Engineering, SRM Institute of Science and Technology, Kattankulathur, India
e-mail: ravieswm@srmist.edu.in

C. Bharatiraja
e-mail: bharatic@srmist.edu.in

J. Vinoth
e-mail: vinothj@srmist.edu.in

C. Subramani et al. (eds.), *Proceedings of International Conference on Power Electronics and Renewable Energy Systems*, Lecture Notes in Electrical Engineering 795,
https://doi.org/10.1007/978-981-16-4943-1_6

preferred. The vector control schemes for motor drives started with introduction of field-oriented control (FOC) in the year 1968 [3]. In beginning, it is implemented for induction motor (IM) drives. Later, its application is extended for PMSM drives [4]. The brief features of FOC operation for PMSM drives are: implementation in rotating reference frame necessitates coordinate frame transformations, indirect control of flux and torque through current components and involvement of current PI regulators. Therefore, the FOC operation is stated to be complex for PMSM drive [5]. Continuing the developments in motor drives, in the year 1986, direct torque control (DTC) is introduced. In [6], DTC is implemented for IM drive. Considering the special benefits of PMSM, DTC operation is applied for PMSM drives [7]. Its operational advantages [7] over FOC are provided as: simple, nonappearance of current PI controllers, performance in stationary frame of reference, straight regulation of flux and torque. However, hysteresis controller existence in digital stage of DTC operation consequences poor steady-state response of flux and torque for PMSM drive [5]. The detailed implementation of DTC and its operational results for PMSM drive are analyzed in this paper.

On the other side, FCS-MPC schemes are providing as promising technology in the domain of motor drives [8]. This modeling-based control is accomplished in stationary/rotating reference frame. The vital operational stages in predictive control are considered as [9]: data measuring and estimating, prediction and cost function (CF) evaluation. The FCS-MPC is classified into two [9], which are stated as PCC and PTC. In both of these control techniques, the mentioned operational stages remain same. However, the control variables differ. In PCC technique [10], stator current is considered as basic control variable, whereas in PTC technique, the basic control variables are flux and torque [11, 12]. In this paper, FCS-MPC (i.e., PCC and PTC) technique implementation and operational results are examined for PMSM drive.

The overall conclusions are drawn from various control responses obtained for PMSM drive. Therefore, in this paper detailed investigations are made for the mentioned control schemes applied to PMSM drive.

2 PMSM Drive Operation

The PMSM drive supplied with two-level voltage source inverter (VSI) is presented in Fig. 1a. Voltage space vector (E_s) is indicated based on switching combinations. Its generalized form is given by (1). As it is familiar that the possible switching combinations are 8, and there are overall 8 voltage vectors (VVs). Their realization is depicted in Fig. 1b.

$$E_s = \frac{2E_{dc}}{3}\left(S_a^+ + S_b^+ e^{j(2\pi/3)} + S_c^+ e^{j(4\pi/3)}\right) \tag{1}$$

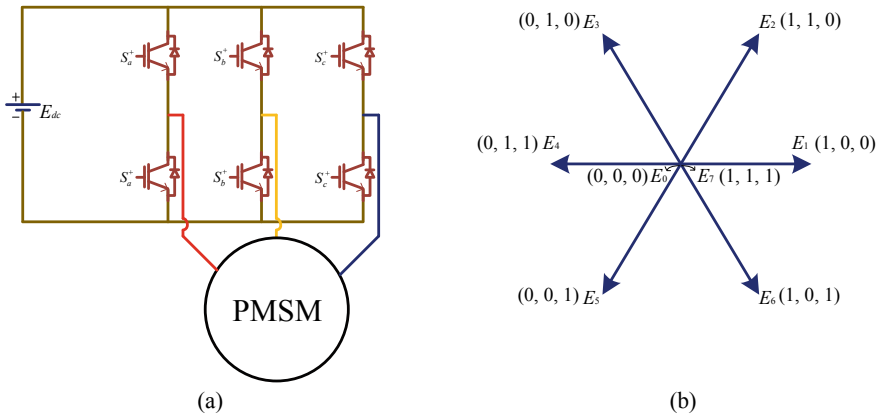

Fig. 1 **a** PMSM supplied from two-level VSI and **b** possible VVs of two-level VSI

2.1 Direct Torque Control (DTC)

PMSM drive is executed with DTC technique in stationary ($\alpha\beta$) reference frame. Its operational block diagram is mentioned in Fig. 2. In first step of its operation, measurement and estimation of PMSM drive variables are required. It is possible to have direct measurement of PMSM speed, current phasor and inverter DC link voltage. The process of present state (k) stator flux estimation is given by (2), where $k - 1$ is previous state data and T_s is sample period. Torque estimation is given by (3), where i_s denotes stator current variable. DTC operation requires stator flux sector information. Among the probable six sectors ($S_1 - S_6$) having 60° span as provided in Fig. 3, the stator flux sector information can be gained by (4). In Fig. 3a, an instant is presented where flux space vector (λ_s) falls in sector 2. The reference flux ($|\lambda_s{}^*|$) during control operation of PMSM drive is set as rated flux value. With

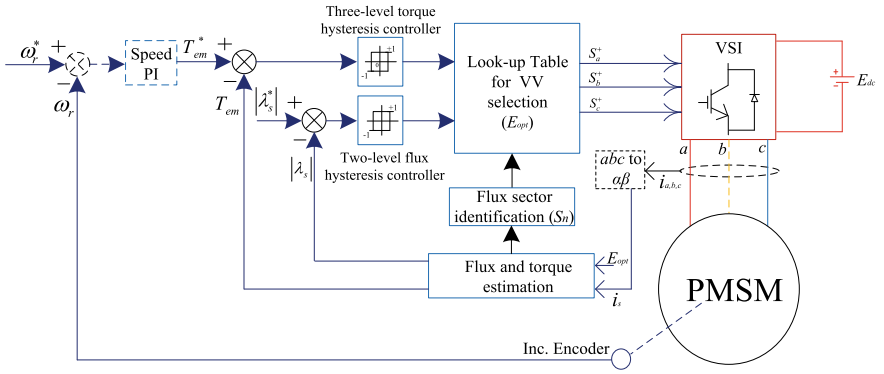

Fig. 2 Block model of PMSM drive operated with DTC technique

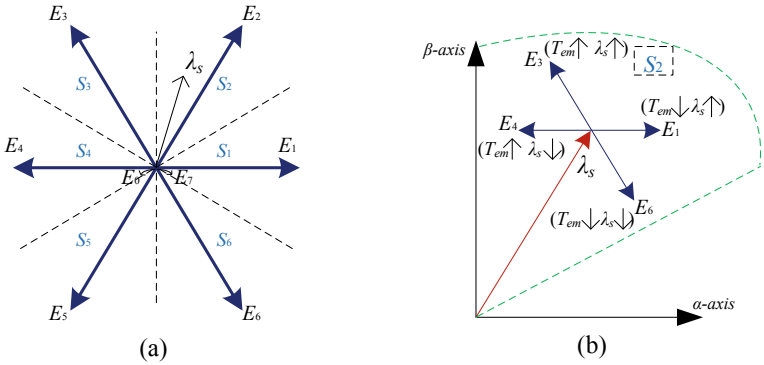

Fig. 3 **a** Possible sectors of voltage space vector plane for two-level VSI and **b** flux space vector in sector-2 and selection of VV for flux and torque control

these, necessary inputs required for operation of DTC technique are fulfilled.

$$\lambda_s(k) = \lambda_s(k-1) + (E_s - R_s i_s)T_s \tag{2}$$

$$T_{em} = 1.5\frac{P}{2}\text{imag}\left(\bar{\lambda}_s * i_s\right) \tag{3}$$

$$\theta = \tan^{-1}\left(\frac{\lambda_{\beta s}}{\lambda_{\alpha s}}\right) \tag{4}$$

During control operation, the speed error (i.e., difference of reference and actual speed) is fed to speed PI controller, which produces required reference torque value ($T_{em}{}^{*}$) to minimize speed error. Torque and flux errors are attained by comparing their reference value with actual.

The torque error is provided to three-level torque hysteresis controller, whose output (H_T) may be -1 or 0 or $+1$, based on its error value crossing boundary conditions. Likewise, two-level flux hysteresis controller is supplied with flux error, whose output (H_λ) may be -1 or $+1$, based on its error value crossing boundary conditions.

The predefined look-up table is framed for VV application in a sample time, which is based on stator flux sector, outputs of flux and torque hysteresis controller. This choice of VV is to reduce errors of flux and torque. In view of flux space vector in sector-2, Fig. 3b shows the effect of VV on flux and torque response. Considering same analysis, Table 1 represents complete look-up table development for application of VV (E_{opt}) in a sample time of DTC operation. Therefore, gaining direct control over flux and torque of PMSM drive.

Table 1 VV selection for flux and torque control in DTC

Sector identification	Hysteresis torque error (H_T)				
	+1		0	−1	
	Hysteresis flux error (H_λ)				
	+1	−1	+1/−1	+1	−1
S_1	E_2	E_3	E_0	E_6	E_5
S_2	E_3	E_4	E_0	E_1	E_6
S_3	E_4	E_5	E_0	E_2	E_1
S_4	E_5	E_6	E_0	E_3	E_2
S_5	E_6	E_1	E_0	E_4	E_3
S_6	E_1	E_2	E_0	E_5	E_4

2.2 *Finite Control Set-Model Predictive Control (FCS-MPC)*

At the present time, FCS-MPC techniques drawing more attention in the field of electrical drives. As the control scheme rely on system model, it is essential to deliver system dynamic model during its operation. Therefore, dynamic equations of PMSM used in FCS-MPC operation are given by (5–8), where λ_f is rotor magnetic flux linkage along d-axis, ω_m is mechanical speed of rotor, L_s and R_s are stator inductance and resistance. These dynamic equations are presented in rotating reference frame (dq).

$$E_s = R_s i_s + \frac{\mathrm{d}\lambda_s}{\mathrm{d}t} + j\lambda_s \omega_r \tag{5}$$

$$\lambda_s = L_s i_s + \lambda_f \tag{6}$$

$$T_{em} = 1.5\frac{P}{2}\mathrm{imag}\left(\overline{\lambda}_s * i_s\right) \tag{7}$$

$$T_{em} - T_l = J\frac{\mathrm{d}\omega_m}{\mathrm{d}t} \tag{8}$$

As control variables are required to be predicted for next sample intervals, prediction model has to be developed based on PMSM dynamic equations. By means of Euler's methodology, prediction equations for control variables are framed at $(k+2)$ sample instant. $(k+2)$ signifies two-step ahead prediction of control variables which obviate sample delay issues during control operation. To execute FCS-MPC, the vital control stages are: measuring and estimation, prediction, and CF optimization. As it is stated that FCS-MPC is categorized into two (i.e., PTC and PCC), the part of first control stage (i.e., measurement) remains same for both. Measuring variables includes PMSM drive speed (ω_r), current phasor (i_s) and DC link voltage (E_{dc}).

The functioning of remaining stages varies based on two subcontrol operations of FCS-MPC. These are presented in detail below.

2.2.1 Predictive Torque Control (PTC)

Using flux and torque as basic control variables, PTC technique for PMSM drive is developed as presented in Fig. 4. PTC functioning is implemented in stationary reference frame to circumvent complexity of coordinate frame transformation. The estimated flux and current phasor at $(k+1)$ sample are given by (9–10), which are utilized in two-step ahead $(k+2)$ prediction of flux (11), current (12) and thereby, torque (13) of PMSM drive is attained. Here, e_r signifies back emf which is $\lambda_f \omega_r e^{j\theta}$, where ω_r and θ are electrical rotor speed and angle, respectively. The predictions at $(k+2)$ are gained with possible 7 (n) VVs of two-level VSI supplying to PMSM drive. Therefore, estimation and prediction of control variables fulfilled two stages of PTC operation.

$$\lambda_s(k+1) = \lambda_s(k) + (E_{\text{opt}} - R_s i_s(k))T_s \tag{9}$$

$$i_s(k+1) = i_s(k)\left(1 - \frac{T_s R_s}{L_s}\right) + (E_{\text{opt}} - e_r)\frac{T_s}{L_s} \tag{10}$$

Prediction of control variables:

$$\lambda_s(k+2)_n = \lambda_s(k+1) + ((E_s)_n - R_s i_s(k+1))T_s \tag{11}$$

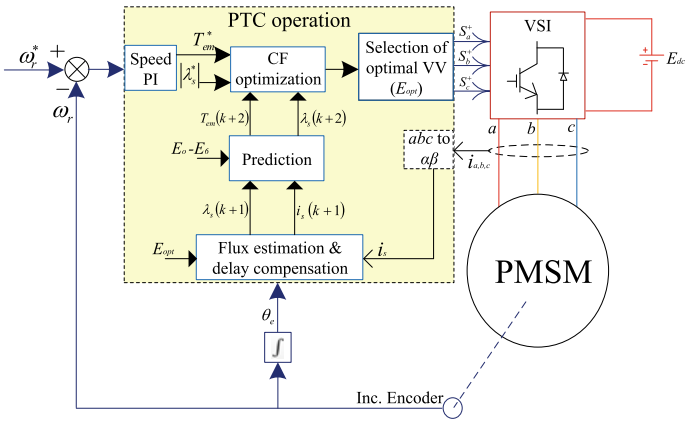

Fig. 4 Block model of PMSM drive operated with PTC technique

$$i_s(k+2)_n = i_s(k+1)\left(1 - \frac{T_s R_s}{L_s}\right) + ((E_s)_n - e_r)\frac{T_s}{L_s} \tag{12}$$

$$T_{em}(k+2)_n = 1.5\frac{P}{2}\text{imag}\left(\bar{\lambda}_s(k+2) * i_s(k+2)\right) \tag{13}$$

The final stage involves in CF optimization, which acts crucial role in optimal VV choice. The basic CF design with control objectives of flux and torque is specified by (14). The predicted variables of flux and torque are compared with their references. The optimal VV serving predicted variable closeness to reference ensures the minimum CF value. Hence, CF optimization is achieved. This evaluated optimal VV is chosen for control action, therefore realizing predictive torque and flux control of PMSM drive.

$$X_n = \left|T_{em}^* - T_{em}(k+2)_n\right| + W\left|\left|\lambda_s^*\right| - \left|\lambda_s(k+2)_n\right|\right| \tag{14}$$

In (14), W is termed as weighting factor, creating relative balance between two dissimilar control objectives (flux and torque).

2.2.2 Predictive Current Control (PCC)

In this control technique, flux and torque of PMSM drive are indirectly controlled by current components in rotating (dq) reference frame. Therefore, basic control variable in PCC is stator current phasor. Its functioning block diagram is presented in Fig. 5. Till the rated speed of PMSM drive, demagnetization of rotor flux is not necessary. Therefore, d-axis reference stator current ($i_{ds}{}^*$) is set to zero. The q-axis reference stator current ($i_{qs}{}^*$) is set by speed PI controller according to speed error minimization. In first stage, current phasor estimation at $(k+1)$ is attained by (15).

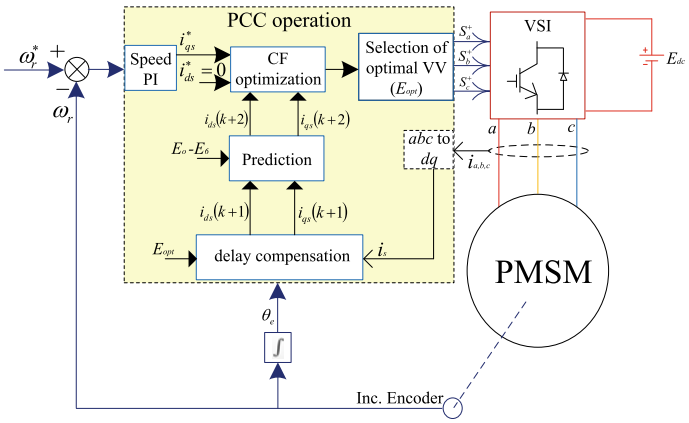

Fig. 5 Block model of PMSM drive operated with PCC technique

With the presented 7 (n) VVs of two-level VSI, measured and estimated data, the current prediction at $(k+2)$ is obtained in second stage as given by (16).

$$i_s(k+1) = i_s(k)\left(1 - \frac{T_s R_s}{L_s} - \mathrm{j}\omega_r T_s\right) + \frac{T_s}{L_s}\left(E_{\text{opt}} - \mathrm{j}\lambda_f \omega_r\right) \tag{15}$$

Prediction of control variable:

$$i_s(k+2)_n = i_s(k+1)\left(1 - \frac{T_s R_s}{L_s} - \mathrm{j}\omega_r T_s\right) + \frac{T_s}{L_s}\left((E_s)_n - j\lambda_f \omega_r\right) \tag{16}$$

In PCC, CF (17) is established with elementary control objectives of stator current components. The optimal VV satisfying closeness of predicted current components with their references guarantees minimum CF value and optimization at final stage of PCC operation. The evaluated optimal VV serves predictive current control and thereby, indirect flux and torque control of PMSM drive.

$$X_n = \left|i_{ds}^* - i_{ds}(k+2)_n\right| + \left|i_{qs}^* - i_{qs}(k+2)_n\right| \tag{17}$$

From this entire discussion, it is summarized that PMSM drive operation is elucidated with various control techniques such as DTC, FCS-MPC: PTC and PCC.

3 Results and Discussion

Using mathematical analysis presented in part-2, MATLAB/Simulink simulations are conducted on existing PMSM drive whose ratings are listed in Table 2. The discussed control techniques are applied for PMSM drive operation.

Table 2 PMSM drive parameters

Parameters	Value
Stator resistance (R_s)	1.12 Ω
Stator inductance (L_s)	10.5 mH
Rated stator flux ($\lvert\lambda_s^*\rvert$)	0.705 Wb
Rated power	5 HP
Rated torque	23.5 N m
Poles (P)	4
Inertia	0.061 kg m^2
Rotor flux (λ_f)	0.7 Wb
Proportional gain	0.2
Integral gain	0.05

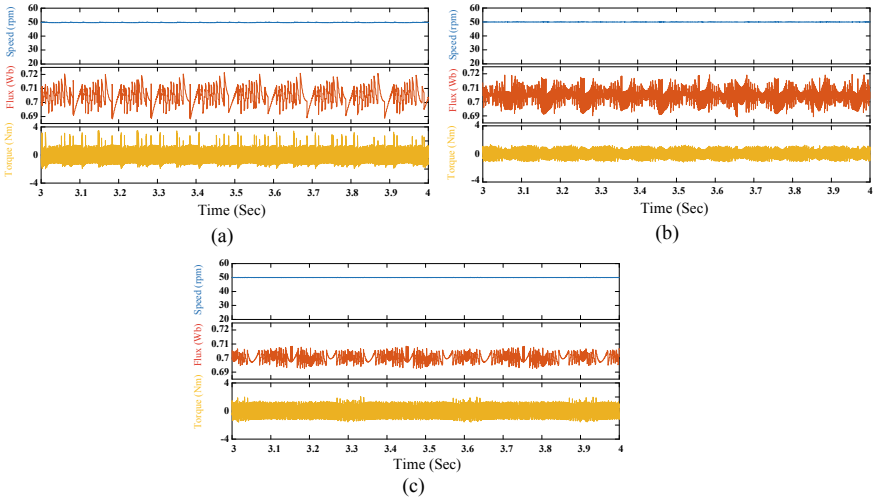

Fig. 6 Response of PMSM drive during low speed (50 rpm) condition **a** DTC, **b** PTC and **c** PCC

In PTC, CF (14) is assigned with weighting factor value of 75, which is designated from heuristic tuning, whereas PCC operation is independent from weighting factor. Considering this simulating environment, various control operation results are presented and discussed in this part of paper.

The simulations are executed on PMSM drive operated with DTC, PTC and PCC techniques. Transition-free response is captured during PMSM drive operation showing speed, flux and torque in Fig. 6. In Fig. 6, low-speed reference (50 rpm) is selected for PMSM drive while observing response of DTC, PTC and PCC techniques. From these tests, it is evident that PTC and PCC techniques exhibits overall improved control response when compared to DTC. In DTC-operated PMSM drive, the existence of hysteresis regulators for flux and torque control is responsible for lack of better response. On the other side, two step ahead prediction, intuitive nature with the consideration of CF optimization in every sample instant made predictive control techniques gaining the benefit of improved motor drive response.

The transition response is analyzed for PMSM drive with sudden variations in speed. In Fig. 7, the reference speed variations are indicated, i.e., from 50 rpm

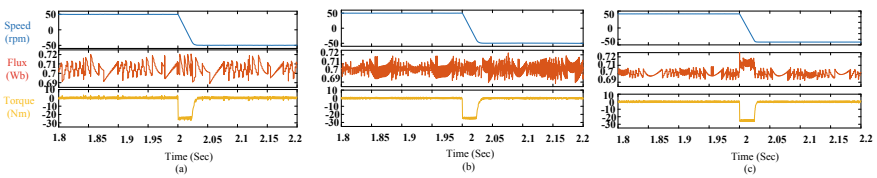

Fig. 7 Response of PMSM drive during speed step change from forward (50 rpm) to reverse (−50 rpm) conditions **a** DTC, **b** PTC and **c** PCC

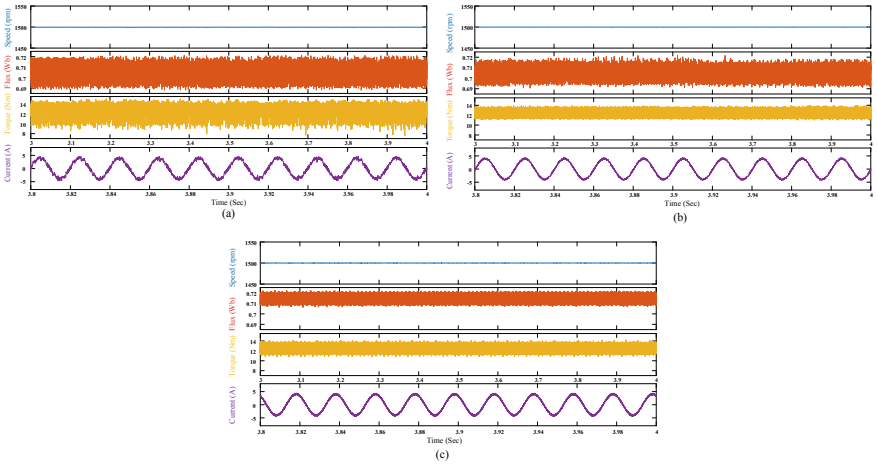

Fig. 8 Response of PMSM drive during loaded condition at 1500 rpm **a** DTC, **b** PTC and **c** PCC

(forward) to −50 rpm (reverse). The executed response of PMSM drive operated with DTC (2 s to 2.023 s), PTC (2 s to 2.023 s) and PCC (2 s to 2.024 s) techniques are presented in Fig. 7. From these, it is verified that all control techniques perform almost similar transition response for PMSM drive. However, PCC-operated PMSM drive has slight variation in dynamic response, i.e., 2 s to 2.024 s, due to indirect control of torque via current space vector.

Under loaded condition (load torque as 12.5 Nm) at rated speed of 1500 rpm, PMSM drive response for DTC, PTC and PCC techniques is presented in Fig. 8. From these tests, it is evident that PTC and PCC techniques exhibit overall improved control response when compared to DTC. The obtained flux and torque ripples (standard deviation values) are presented in Table 3. From this, it is clearly observed that PTC of PMSM drive stands top gaining less torque ripples, followed by PCC and DTC at the end, whereas for current THD observations, PCC stands top with less THD, followed by PTC and DTC at the end. Therefore, in comparison of PTC and PCC techniques, direct involvement of current objective in CF of PCC results less current THD than PTC. While in PTC, CF is structured with flux and torque objectives, which is accountable for less torque ripples than PCC. Flux response is much influenced

Table 3 PMSM drive performance comparison under various control techniques

Control technique	Flux ripple (Wb)	Torque ripple (Nm)	Current THD (%)
DTC	High (0.0067)	High (1.207)	High (15.22)
PTC	Low (0.0053)	Lower (0.615)	Low (7.41)
PCC	Lower (0.0031)	Low (0.681)	Lower (6.70)

by direct control of current component (i_{ds}) which is possible in PCC resulting less flux ripples than PTC.

The outcomes of this entire analysis are listed in Table 3, which differentiates among control techniques by quantitative and qualitative data. Thus, PMSM drive operation with various control techniques is studied.

4 Conclusion

In this paper, the concept and operation of different vector control techniques such as DTC, FCS-MPC (PTC and PCC) for PMSM drive application are studied. PMSM drive is operated with these control techniques in simulation platform. The control responses for different operating conditions of PMSM drive are observed. The presented qualitative and quantitative analysis clearly depicts operational differences among them. In comparison of FCS-MPC with DTC, FCS-MPC techniques serves overall better performance for PMSM drive.

References

1. Samir K, Rodriguez J, Wu B, Bernet S, Perez M (2012) Powering the future of industry: high-power adjustable speed drive topologies. IEEE Ind Appl Mag 18(4):26–39
2. Behzad A, Rahrovi B (2010) Minimum-copper-loss control over full speed range of an IPMSM drive for hybrid electric vehicle application. In: 2010 IEEE vehicle power and propulsion conference, pp 1–6
3. Felix B (1972) The principle of field orientation as applied to the new TRANSVECTOR closed loop control system for rotating field machines. Siemens Rev 34(5):217–220
4. Pradeep K, Dhundhara S, Makin R (2016) Performance analysis of PMSM drive based on FOC technique with and without MRAS method. In: 2016 International Conference on Recent Advances and Innovations in Engineering (ICRAIE), pp 1–6
5. Fatih K, Topaloglu I, Faruk Cakir M, Gurbuz R (2013) Comparative performance evaluation of FOC and DTC controlled PMSM drives. In: 4th international conference on power engineering, energy and electrical drives, pp 705–708
6. Isao T, Noguchi T (1986) A new quick-response and high-efficiency control strategy of an induction motor. IEEE Trans Industry Appl IA-22(5):820–827
7. Mino-Aguilar G et al (2010) A direct torque control for a PMSM. In: 2010 20th international conference on electronics communications and computers, pp 260–264
8. Dehong Z, Zhao J, Li Y (2016) Model-predictive control scheme of five-leg AC–DC–AC converter-fed induction motor drive. IEEE Trans Industr Electron 63(7):4517–4526
9. Jose R, Kazmierkowski MP, Espinoza JR, Zanchetta P, Abu-Rub H, Young HA, Rojas CA (2013) State of the art of finite control set model predictive control in power electronics. IEEE Trans Industrial Informatics 9(2):1003–1016
10. Turker T, Buyukkeles U, Faruk Bakan A (2016) A robust predictive current controller for PMSM drives. IEEE Trans Industrial Electronics 63(6):3906–3914
11. Eshwar K, Ravi Eswar KM, Vinay Kumar T (2020) An effective predictive torque control scheme for PMSM drive without involvement of weighting factors. IEEE J Emerging Selected Topics Power Electronics. https://doi.org/10.1109/JESTPE.2020.2989429

12. Eshwar K, Vinay Kumar T (2020) Effective predictive torque control scheme for four-level open-end winding permanent magnet synchronous motor drive. Int Trans Electrical Energy Syst 30(10):e12536

Design and Implementation of Discrete Controller-Based Zeta Converter for Solar Power Applications

R. Uthirasamy, V. Kumar Chinnaiyan, U. S. Ragupathy, and S. Vishnu Kumar

Abstract In this paper, a closed-loop discrete controller is implemented for Zeta converter modules. Discrete controller offers good dynamic response, fine voltage regulation, and it can be programmable without external passive components. Zeta converter is capable of producing non-pulsating output current and has good adaptability. An analog proportional–integral–derivative (PID) and discrete PID controllers are designed, and their performances are compared. Effectiveness of the controllers is demonstrated and validated with experimental results. Achieved result shows that the discrete controller provides good transient response. Further, the performance of connecting dual snubber with Zeta converter has been analyzed. Dual snubber is connected in the Zeta converter, and the conducted EMI results have been observed. Simulation model of a solar module and Zeta converter to control the voltage to the DC motor has been developed using PSPICE software. From the experimental results, it is inferred that the dual snubber reduces the switching losses and suppresses the dv/dt and di/dt effects.

Keywords Zeta converter · Discrete controller · Electromagnetic interference · Snubber circuit · Switching loss

1 Introduction

DC–DC converters play a major role for the integration of renewable energy resources. The efficiency of DC–DC converter is estimated by its duty ratio and

R. Uthirasamy (✉) · V. Kumar Chinnaiyan
Department of Electrical and Electronics Engineering, KPR Institute of Engineering and Technology, Coimbatore, India

U. S. Ragupathy
Department of Electronics and Instrumentation Engineering, Kongu Engineering College, Erode, India

S. Vishnu Kumar
Department of Electronics and Communication Engineering, Vel Tech Rangarajan Dr. Saguthala R&D Institute of Science and Technology Chennai, Chennai, India

C. Subramani et al. (eds.), *Proceedings of International Conference on Power Electronics and Renewable Energy Systems*, Lecture Notes in Electrical Engineering 795,
https://doi.org/10.1007/978-981-16-4943-1_7

its losses. Zeta converter topology is proposed to interface the solar PV and drive load system. The emerging renewable energy such as solar energy is the feasible solution for today's energy crisis. The output current/power of an individual cell or an array of cells connected in series or in parallel depends on the working voltage available at the terminals. The maximum power produced by the PV system varies with intensity of solar irradiation and temperature. Thus, to raise the competence of PV system, it is essential to operate the system with highest output power. Maximum power point tracking (MPPT) has been implemented with a variety of techniques and power conditioner. The subsystem of the photovoltaic installations is the solar converter. The employment of Zeta converters in the charge controllers is ordinary in a standalone photovoltaic system. Zeta converter is a DC–DC converter having two inductors and two series capacitor. It is accomplished to operate in moreover step-up or step-down manner. It performs a non-inverting buck-boost function similar to that of a SEPIC converter. Zeta converter is one of the best choices to regulate the solar power. Proposed Zeta converter is working in continuous conduction mode (CCM) with a coupled inductor [1–5]. The major challenge in the field of DC to DC converter is the control aspect. The control method necessitates the efficient modeling and enabling systematic study of the converters. In general, the converters are time invariant and nonlinear, and it comprises with the large passive components. In common, analog controller design technique experiences higher complexity in control, lesser flexibility to superior functions and system changes and have lack of consistency. The proposed discrete controller provides lot of advantages than their analog controller. It also offers in its dynamic response as firmness, fast response and fewer peaks overshoot [6]. In this proposed work, high-degree DPWM signals are produced by maintaining high system switching frequency. The main purpose of control of discrete controller has to run the boost converter along with a duty ratio so that the reference voltage and the output voltage of the DC component are equal. The parameter support stability in spite of changes in the load or deviations in the input voltage. The state space model builds the controller and makes simulation much quicker than the other method [7–10]. The Zeta converter is represented by means of state space method, and the simulation is carried out by MATLAB/Simulink software. The block diagram of digitally controlled Zeta converter with entire setup is revealed in Fig. 1.

The output voltage and the reference voltage are compared using comparator, and the output is fed to compensator. Generally, compensators are designed using flip-flops. Desired PWM pulses are generated in the comparator and fed to the zeta converter from side to side the gate driver [11, 12]. Use of buck converter is general in the charge controller of solar-powered DC motors. The converters that control the input voltage of DC motor generate EMI which is conducted all the way through the cables to photo voltaic system; from there on, it is radiated when the solar cells act as antenna. Those unwanted radiations impede with the communiqué structure over and above any receptive tools nearby. To stay away from such unnecessary and unwarranted interference, the finest way is to assail the source of interference, specifically the EMI produced by the Zeta converter switching strategy.

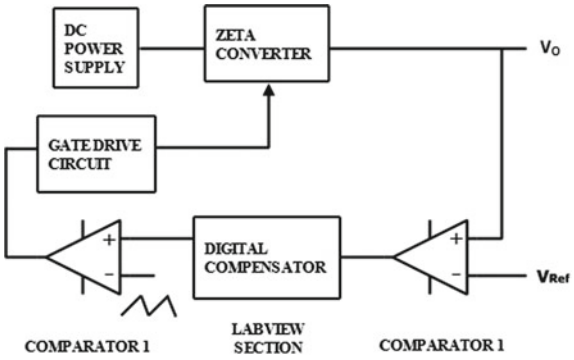

Fig. 1 Digitally controlled block diagram of Zeta converter

2 Zeta Converter

Zeta converter consists of inductors L_1 and L_2 and capacitor c and diode D. Its main advantages is to maintain the output voltage polarity same as the input. As the Zeta is a switch mode circuit, its performance is strongly reliant in the stability of the L current and C voltage. The voltage of the Zeta converter is implicit to activate in the continuous conduction mode (CCM) as shown in Fig. 2. There exist two modes of operation using one switch mode, when it is turned off. It consists of MOSFET as switch, two capacitors C_1 and C_2, diode D, two inductors L_1 and L_2 and load R.

2.1 ON State Condition of Zeta Converter (MODE 1)

While the switch S is turned on (ON-state), the diode D gets reversed biased, and it is in off state as shown in Fig. 3. For the duration of this state, inductor L_1 and L_2 get energize, and the inductor current i_{L1} and i_{L2} increase linearly. The capacitor C_1 will discharge to V_o, and it is associated in sequence with L_2. So the voltage across the inductor (L_2) is V_s and diode is $V_s + V_o$. By applying Kirchoff's voltage law, voltage across L_1 will be,

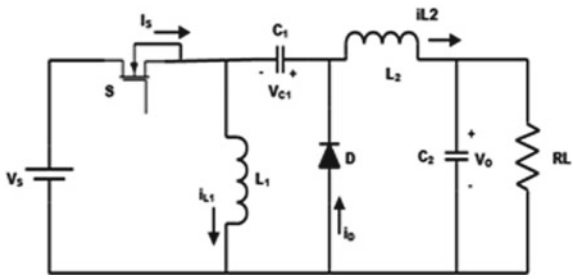

Fig. 2 Circuit diagram of Zeta converter

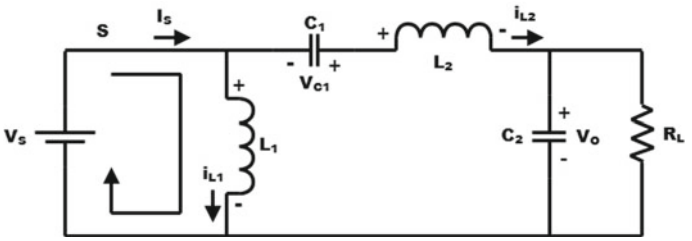

Fig. 3 Mode I operation of zeta converter

$$\frac{\mathrm{d}i_{L1}}{\mathrm{d}t} = \frac{V_s}{L_1} \tag{1}$$

$$\Delta I_{L1} = \left[\frac{V_s}{L_1}\right] T_{\text{on}} \tag{2}$$

And voltage across L_2 will be,

$$\frac{\mathrm{d}i_{L2}}{\mathrm{d}t} = \frac{V_s}{L_2} + \frac{V_{C1}}{L_2} - \frac{V_{C2}}{L_2} \tag{3}$$

$$\Delta I_{L1} = \left[\frac{V_S}{L_2} + \frac{V_{C1}}{L_2} - \frac{Vo}{L_2}\right] T_{\text{on}} \tag{4}$$

By applying Kirchoff's current law, the rate of voltage through the capacitors will be,

$$\frac{\mathrm{d}V_{C1}}{\mathrm{d}t} = -\frac{i_{L2}}{LC1} \tag{5}$$

$$\Delta V_{C1} = -\left[\frac{i_{L2}}{C_1}\right] T_{\text{on}} \tag{6}$$

$$\frac{\mathrm{d}V_{C2}}{\mathrm{d}t} = \frac{i_{L2}}{C_2} - \frac{V_{C2}}{R_L C_2} \tag{7}$$

$$\Delta V_{C1} = \left[\frac{i_{L2}}{C_2} - \frac{V_{C2}}{R_L C_2}\right] T_{\text{on}} \tag{8}$$

2.2 OFF State Condition of Zeta Converter (MODE 2)

While the control switch S is turned OFF (OFF-state), the diode D gets high potential at anode, and it is in ON state. At this condition, inductor L_1 and L_2 are in de-energized. The voltage polarity of the conductor changes, the diode will get forward biased and it will conduct. Energy in inductors is de-energized to capacitor C_1 and load resistance, respectively. Consequently, the energy in the inductor current i_{L1} and i_{L2} is decreasing linearly. By applying Kirchoff's voltage law, voltage across inductor L_1 is expressed as,

$$\frac{\mathrm{d}i_{L1}}{\mathrm{d}t} = -\frac{V_{c1}}{L_1} \tag{9}$$

$$\Delta I_{L1} = \frac{V_{c1}}{L_1} T_{\text{off}} \tag{10}$$

Voltage across inductor L_2 is expressed as,

$$\frac{\mathrm{d}i_{L2}}{\mathrm{d}t} = -\frac{V_{C2}}{L_2} \tag{11}$$

$$\Delta I_{L2} = \frac{V_{C2}}{L_2} T_{\text{off}} \tag{12}$$

3 Simulation Results and Discussion

The proposed Zeta converter is pretend using MATLAB/Simulink and the output voltage attained using discrete PID controller. The controller constraints are in under considerations with steady-state error, settling time, peak time, rise time, ripple output voltage and overshoot which is evaluated alongside its PI, PID controllers are premeditated for the identical Zeta converter. Steady-state error examined for load change is much smaller than 1% and no undershoot or overshoot is clear. The presentation necessities for the Zeta converter with Discrete PID controller are improved than discrete PI, analog PID and analog PI controllers. The results thus accomplished with discrete PID controller for Zeta converter is comparable and agreement with the numerical computation. It is confirmed that the discrete system demonstrates an enhanced outcome than the analog controllers. The input voltage is fixed as 10 V until 0.03 s and then varied to 14, 18, 14 and 10 V throughout the time instance 0.03 s, 0.06 s, 0.09 s, and 0.12 s, respectively. The load resistance is also changed concurrently with an input voltage. The load resistance is fixed as 14 Ω till 0.03 s, and then varied to 18 Ω, 22 Ω, 18 Ω, and 14 Ω during the instance 0.03 s, 0.06 s, 0.09 s and 0.12 s, respectively. The reference voltage is also all together changed up to 0.075 s,

it is 7 V afterward it is 20 V. In the simulated answer, the performance of Buck action up to 0.075 s and then carry out as a boost process in Zeta converter with the changes in input voltage and load resistance. In dual operation, overshoot or undershoots are not observed in the output voltage, and there is no mark for steady-state error, and output ripple voltage is forever smaller than 3%. By changing the capacitance and inductance values of the Zeta converter, the simulated outcomes are tabulated. The system does not prove any steady-state error, undershoot or overshoots, and it settles down at a speedy rate with a settling time of about 4 ms for all the values. Simulation is also brought out by changing the load not limiting to R, it can extend to RL and RLE load. The output voltage has not varied due to the variation in nature of the load. Therefore, the above results confirmed that the designed discrete controller gives tight output voltage regulation, better stability and robustness. The efficiency against load resistance graph of the Zeta converter and the discrete PID controlled Zeta converter is depicted in Fig. 4. The input voltage is 12 V, reference voltage is 21 V, and the changes load resistance is between 2 Ω and 12 Ω, then the efficiency of the discrete PID controlled Zeta converter efficiency has been varied from 97.8 to 96.8%, and the efficiency of the uncontrolled Zeta converter is varied from 84 to 90%.

Figure 5 depicts the output voltage responses of the analog PID controlled and discrete PID controlled Zeta converter. Fix the Zeta converter input voltage is 14 V and the reference output voltage is 21 V, the attained analog PID controlled Zeta has more ripple voltage, overshoot and steady-state error. It has more rise time and less accurate settling time. The discrete PID controlled Zeta has low settling time and rise time, and the peak overshoot is less than 1% with an insignificant steady-state error with no ripple voltage. With this response, it is very well identify that the performance parameters are outstanding in discrete PID controller than in analog PID controller. The output voltage response of the discrete PID controlled Zeta converter for change in load is view sequentially. The nature of load is changed as R, RL and RLE and changing nature has not influenced the output voltage of the converter is clear. The

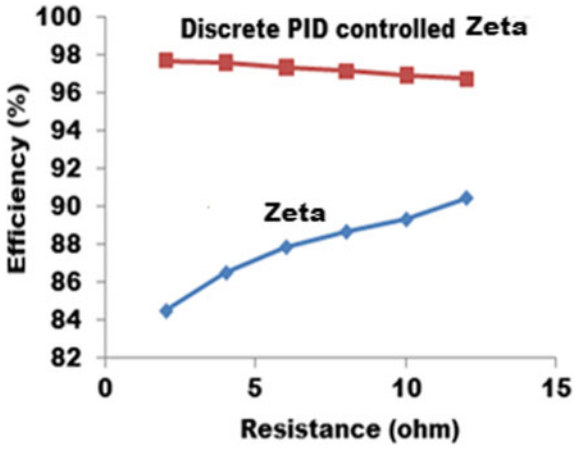

Fig. 4 Comparison of efficiencies for Zeta and discrete PID controlled Zeta converter

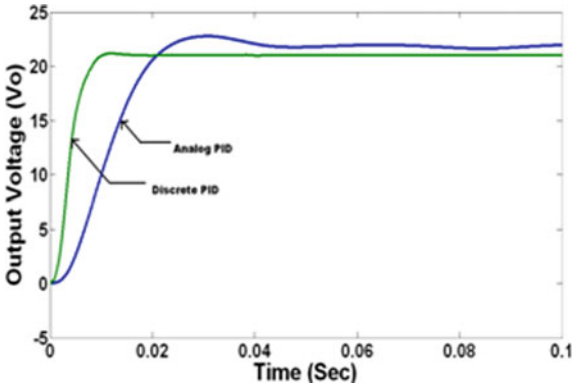

Fig. 5 Comparison between output voltage responses of discrete PID controlled and analog PID controlled Zeta converter

load resistance is differed as 14 Ω, 18 Ω and 10 Ω; the converter will be capable to produce the output voltages as 21 V, 20.998 V and 6.996 V for the reference voltages of 21 V, 21 V and 7 V, respectively. Then the simulation result is taken for the inductance of 5 mH and 10 mH, inserted to the resistance of 14 Ω and 18 Ω, the output voltage is acquired in the order of 7.001 V and 21.002 V, respectively, for the fixed reference of 7 V and 21 V. Again, the output has been obtained using RLE load with a resistance of 20 Ω, inductance of 1 mH and a voltage source of 2 V, the controller is capable to find the output voltage as 20.997 V for the specific reference of 21 V. Similarly, an output voltage of 7.001 V is tracked for the fixed reference of 7 V, whose RLE values are 9 Ω, 5 mH and 3 V.

4 Hardware Results and Discussion

In the hardware setup, the input voltage to the discrete PID controlled Zeta converter is 12 V, reference voltage is fix as 21 V and the resistance of load is considered as 14 Ω; the obtained output voltage is 21.1 V as depicted in Fig. 6. It has smaller settling time and rise time for the time period of 1.5 ms and has oscillation at the initial time period, but it has settled shortly. No undershoot or overshoot is evident. The input voltage is obtained at channel 2 and the output voltage is obtained at channel 3. In the output voltage response, steady-state error is 0.1 V which is lesser than 1%.

In the same way, the input voltage is 18 V, for 21 V reference and the load resistance is 14 Ω; the resultant voltage is illustrated in Fig. 7.

5 Conclusion

In this paper, the discrete PID controller for Zeta converter has been designed and implemented. The discrete PID controlled Zeta converter has improved efficiency

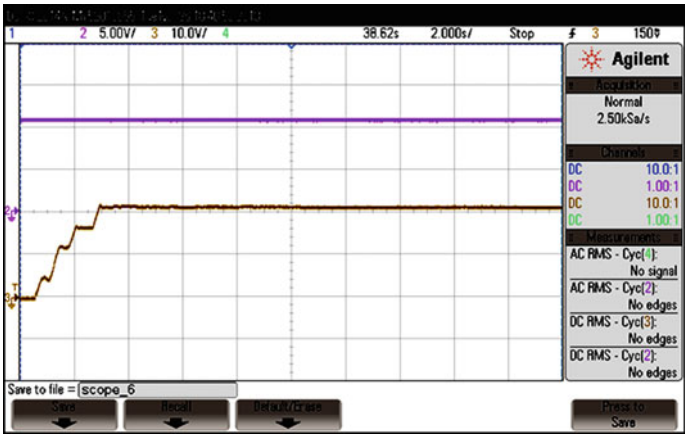

Fig. 6 Output voltage response for 12 V input, $R_0 = 14\ \Omega$, and $V_{\text{ref}} = 21$ V

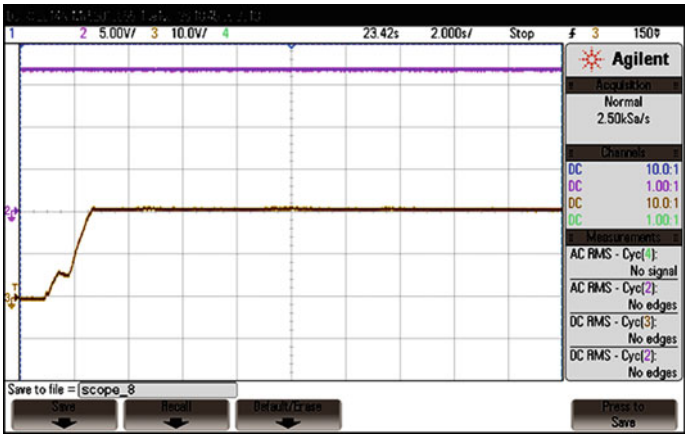

Fig. 7 Output voltage acquired for 18 V input, $R_0 = 14\ \Omega$, and $V_{\text{ref}} = 21$ V

than the conventional Zeta converter. The results attained with the proposed discrete PID controller for DC–DC converter are in concurrence with the arithmetic computation and also better perform than the existing analog controllers. Simulation results divulge that the converters not only illustrate the evidence of the steady state and transient performance but also enhance the efficiency of the Zeta converter. The numerical investigation, simulation results and the investigational response reveal that the controller attains high output voltage regulation, good stability, superior dynamic performances and more efficiency. This topology is well-suited with all other DC–DC converter and also can be extended for any of the applications such as PV, Wind, telecommunication applications and speed control of DC motor drives.

References

1. Maki A, Valkealahti S (2012) Power losses in long string and parallel connected short strings of series-connected silicon-based photovoltaic modules due to partial shading conditions. IEEE Trans Energy Convers 27(1):173–183
2. Walker GR, Sernia PC (2004) Cascaded dc-dc converter connection of photovoltaic modules. IEEE Trans Power Electron 19(4):11301139
3. Walker GR, Pierce J (2006) Photo voltaic DC–DC module integrated converter for novel cascade and bypass grid connection topologies-design and optimization. In: Proceeding of power electronics specialist conference-PESC pp. 1–7, 18–22 (June 2006)
4. Kaushika N, Gautam N (2003) Energy yield simulations of interconnected PV arrays. IEEE Trans Energy Convers 18(1):127–134
5. Lee J, Min B, Kim T, Yoo D, Yoo J (2009) High efficient interleaved input-series-output-parallel-connected converter for photovoltaic power conditioning system. In: Proceedings of energy conversion congress and exposition, pp 327–329
6. Chen L, Wu H, Xu P (2015) A high step-down non-isolated bus converter with partial power conversion based on synchronous LLC resonant converter. In IEEE conferences applied power electronics conference and exposition
7. Ahmad MdW, Anand S (2016) Power decoupling in PV system using partial power processing converter. IEEE conference in compatibility, power electronics and power engineering (2016)
8. Zapata JW, Renaudineau H (2016) Partial power DC–DC converter for photovoltaic microinverters. IEEE Ind Electron Soc
9. Zhao J, Yeates K, Han Y (2013) Analysis of high efficiency converter processing partial input/output power. IEEE control and modeling for power electronics
10. Agamy MS (2014) An efficient partial power processing converter for distributed PV architectures. IEEE Trans Power Electron 29(2) (2014)
11. Agamy MS, Chi S, Elasser A, Harfman-Todorovic M, Jiang Y, Mueller F, Tao F (2013) A high power density DC–DC converter for distributed PV architectures. IEEE J Photovolt 3(2):791–798
12. Suntio T (2015) Comments on an efficient partial power processing converter for distributed PV architectures. IEEE Trans Power Electron 30(4)

Structural Optimization of LMS Adaptive Filter Using Multi-stage Cascaded Configuration

S. Hannah Pauline, Samiappan Dhanalakshmi, and R. Kumar

Abstract In telecommunication systems, the most crucial challenge is to recover a signal corrupted by noise. Adaptive filters are widely utilized for signal de-noising applications with least mean square adaptive algorithm being the most desired. Even though LMS algorithm is simple in structure and robust; it suffers from slow convergence speed and has high mean square error (MSE) value. Therefore, in this paper, we introduce a structural optimization of adaptive filters using conventional LMS adaptive algorithm. Here, a multi-stage cascaded LMS adaptive filter model is proposed for adaptive noise cancellation (ANC) systems, and the novelty is that the number of filter stages to be cascaded is adjusted automatically to provide optimum performance. The simulation is carried out for a signal de-noising application and the efficiency of the proposed filter model is tested with regards to MSE, SNR and ANR. The advantages of the proposed filter model are proved in the results.

Keywords LMS · MSE · Signal de-noising · Adaptive noise cancellation · SNR

1 Introduction

Noise is one of the causes for signal quality loss, rendering it useless for further processing. Signal de-noising is therefore applied in many areas, including telecommunications and biomedical applications. Before the signal is further processed for advanced applications, the signal de-noising mechanism should be applied which is

S. Hannah Pauline · S. Dhanalakshmi (✉) · R. Kumar
Department of Electronics and Communication Engineering, College of Engineering and Technology, Faculty of Engineering and Technology, SRM Institute of Science and Technology, SRM Nagar, Kattankulathur, Kanchipuram, Chennai, Tamil Nadu 603203, India
e-mail: dhanalas@srmist.edu.in

S. Hannah Pauline
e-mail: hannahps@srmist.edu.in

R. Kumar
e-mail: kumarr@srmist.edu.in

C. Subramani et al. (eds.), *Proceedings of International Conference on Power Electronics and Renewable Energy Systems*, Lecture Notes in Electrical Engineering 795,
https://doi.org/10.1007/978-981-16-4943-1_8

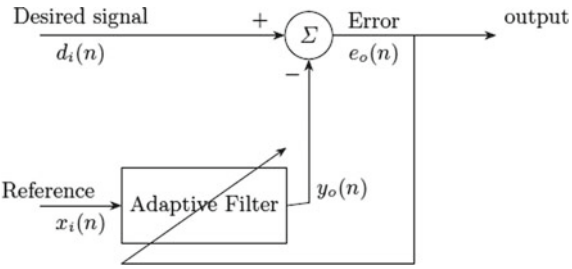

Fig. 1 General block representation of ANC

done by adaptive noise canceller (ANC). For ANC, adaptive filters are more desirable because, depending on the error signal, they can change their coefficients, and no prior knowledge is needed. Adaptive filters [1] are used in numerous applications including echo [2] and noise cancellation [3]. Fig. 1 depicts the fundamental ANC.

The primary input signal provided to the ANC is the noisy signal $d_i(n)$ defined as

$$d_i(n) = a(n) + n(n), \tag{1}$$

where $a(n)$ is the noise-free signal and $n(n)$ is the added noise. $a(n)$ and $n(n)$ are not time correlated to each other and the input to the filter $x_i(n)$ is a noise in time correlated to $n(n)$. The adaptive filter gives the replica of the noise signal $\hat{n}(n)$ as

$$y_o(n) = \mathbf{w}^T(n)\mathbf{x}_i(n), \tag{2}$$

where $\mathbf{w}(n) = [w_0, w_1, \ldots w_{M\text{-}1}]^T$ and $\mathbf{x}_i(n) = [x_0(n), x_1(n-1), \ldots x_{M\text{-}1}(n\text{-}M+1)]^T$ are weights of the filter and its input, respectively, M is the order of filter and the error is computed as

$$e_o(n) = d_i(n) - y_o(n) = d_i(n) - \hat{n}(n), \tag{3}$$

such that the effect of noise is minimal. The efficiency of the adaptive filter is improved by the using suitable algorithms like LMS and its variants. Due to its feasible implementation and robustness, the LMS adaptive algorithm [4] is commonly used. The LMS algorithm, however, suffers from low convergence speeds. The filter structure can be adjusted as suggested by several researchers to achieve optimum performance with regard to steady-state MSE and convergence speed. Cascade configuration [5] of adaptive filter has demonstrated optimal performance and is successfully used in ANC systems. The cascaded filter structure was first proposed by [6] to boost the broadband noise signal and its tracking of multiple sinusoids. A reduction of MSE for linear prediction application is achieved by the FIR cascaded structure proposed by Prandoni and Vetterli [7]. Cascaded LMS adaptive filter models have been successfully used also for motion artefact deletion from ECG [8] and EEG [9] signals. Compared to traditional LMS adaptive filters, the 2-stage [10] and 3-stage [11] cascaded LMS adaptive filter architectures used for

ANC systems provide better efficiency with regard to SNR. For successful removal of impulse noise from speech signals with reduced computational complexity, the multi-stage cascaded adaptive filter structure proposed in [12] is used.

The above studies show that a cascaded adaptive filter model performs better than conventional single stage adaptive filter in regards to convergence speed and MSE. Therefore, in this paper, we have explored the efficacy of multi-stage cascaded LMS filter model for signal de-noising application. Also, we have introduced automatic control logic to adjust the number of stages to be cascaded to obtain optimal performance in terms of MSE and convergence speed. The proposed multi-stage cascaded LMS adaptive filter model is detailed in Sect. 2. Section 3 includes the MATLAB simulation results, thus verifying the proposed method's effectiveness, and a conclusion with the future scope is included in Sect. 4.

2 Proposed Multi-stage Cascaded LMS Adaptive Filter Model with Automatic Stage Control

Conventional LMS algorithm is preferred due to its simple structure and superior stability. But its convergence speed is low and has high MSE value. Cascaded LMS filter structures have proved to increase the speed of convergence and provides lower MSE values. We present the multi-stage cascaded LMS adaptive filter structure using a cascaded connection of the conventional LMS adaptive filter for signal de-noising application. Also. we have implemented an automatic control logic which controls the number of stages to be cascaded. Figure 2 represents the schematic diagram of the proposed multi-stage cascaded LMS filter model for ANC system.

The primary input signal $d_L(n)$ to each stage, as depicted in the figure, is the error e_{L-1} of the previous stage ANC. The reference residual noise signal from previous stage $x_{L-1}(n) - y_{L-1}(n)$ is given as the filter input $x_L(n)$ for the next stage ANC. The primary input signal $d_1(n)$ to stage I ANC wherein has the clean signal $a(n)$ corrupted by additive noise $n(n)$

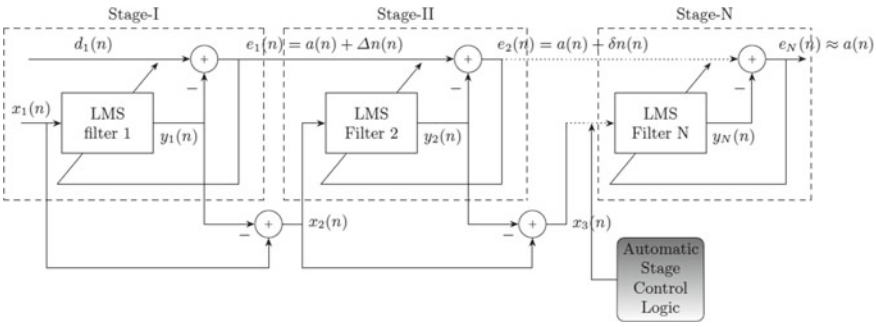

Fig. 2 Schematic diagram of proposed multi-stage cascaded LMS adaptive filter

$$d_1(n) = a(n) + n(n). \tag{4}$$

The stage I filter is given a reference input signal $n'(n)$ correlated in time to the noise $n(n)$. $a(n)$ and $n(n)$ are assumed to be uncorrelated, and the noise signal from $d_1(n)$ is eliminated using $n'(n)$.

$$x_1(n) = n'(n). \tag{5}$$

Stage I filter output is

$$y_1(n) = \mathbf{w}_1^T(n)\mathbf{x}_1(n) = \mathbf{w}_l^T(n)\mathbf{n}'(n) = \hat{n}(n), \tag{6}$$

where $\mathbf{w}_1(n) = [w_0, w_1, \ldots w_{M-1}]^T$ and $\mathbf{x}_1(n) = [x_0(n), x_1(n-1), \ldots x_{M-1}(n\text{-}M+1)]^T$ are weights of the filter and its input, respectively, at stage I, M is the filter order. LMS algorithm is employed to adjust the filter weights as

$$\mathbf{w}_1(n+1) = w_1(n) + \mu e_1(n)\mathbf{n}'(n), \tag{7}$$

μ is the step-size parameter and the error of stage I is

$$e_1(n) = d_1(n) - y_1(n) = a(n) + n(n) - \hat{n}(n) = a(n) + \Delta n(n), \tag{8}$$

where $\Delta n(n) = n(n) - \hat{n}(n)$ is the residual noise to be reduced. The error signal $e_1(n)$ of stage-I ANC is applied to stage-II ANC as its primary input signal $d_2(n)$

$$d_2(n) = e_1(n) = d_1(n) - \hat{n}(n) = a(n) + \Delta n(n), \tag{9}$$

and the input $x_2(n)$ to the stage-II filter is the difference between the input signal and output signal of stage-I filter $x_1(n) - y_1(n)$.

$$x_2(n) = x_1(n) - y_1(n) = n'(n) - \hat{n}(n) = \Delta n'(n). \tag{10}$$

The residual noise signal $\Delta\hat{n}(n)$ is

$$y_2(n) = \mathbf{w}_2^T(n)\mathbf{x}_2(n) = \mathbf{w}_2^T(n)\Delta\mathbf{n}'(n) = \Delta\hat{n}(n), \tag{11}$$

where $\mathbf{w}_2(n) = [w_0, w_1, \ldots w_{M-1}]^T$ and $\Delta\boldsymbol{n}'(n) = [\Delta n_0'(n), \Delta \mathrm{n}_1'(n-1), \ldots \Delta n'(n-M+1)]^{\mathrm{T}}$ are weights of the filter and its input, respectively, at stage II. The weight update equation of stage-II LMS filter is

$$\mathbf{w}_2(n+1) = \mathbf{w}_2(n) + \mu \mathrm{e}_2(n)\Delta\mathbf{n}'(n), \tag{12}$$

The stage-II ANC error signal $e_2(n)$ is

$$e_2(n) = d_2(n) - y_2(n) = a(n) + \Delta n(n) - \Delta\hat{n}(n) = a(n) + \delta n(n) \tag{13}$$

where $\delta n(n) = \Delta n(n) - \Delta\hat{n}(n)$ is the residual noise that is to be reduced. Furthermore, the error signal of the previous stage is the primary input signal for each stage. The input signal to the Nth stage filter is the reference residual noise from the $N-1$th stage ANC. The number of stages required to give optimal performance is adjusted automatically, and at the optimal Nth stage, the error from stage-(N-1) constitutes the primary input signal of the Nth stage given by,

$$d_N(n) = e_{N-1}(n) = a(n) + \gamma n(n), \tag{14}$$

where γ is a minimal noise. The reference noise input to Nth stage filter is the reference residual noise from the preceding $(N-1)$th stage ANC.

$$x_N(n) = x_{N-1}(n) - y_{N-1}(n) = \gamma n'(n). \tag{15}$$

The stage-N adaptive filter output $y_N(n)$ gives the estimate of the remaining noise $\gamma\hat{n}(n)$ at the N_{th} stage.

$$y_N(n) = \mathbf{w}_N^T(n)\mathbf{x}_N(\vec{n}) = \mathbf{w}_N^T(n)\gamma\mathbf{n}'(n) = \gamma\hat{n}(n), \tag{16}$$

where $\mathbf{w}_N(n) = [w_0, w_1,\ldots w_{M-1}]^T$ and $\gamma\mathbf{n}\prime(n) = [\gamma n_0'(n), \gamma n_1'(n-1), \ldots\gamma n'_{M-1}(n-M+1)]^T$ are the coefficients of the filter and its input, respectively, at stage N. Stage-N filter co-efficient update is

$$\mathbf{w}_N(n+1) = \mathbf{w}_\mathbf{L}(n) + \mu e_N(n)\mathbf{x}_N(n). \tag{17}$$

The error $e_N(n)$ of stage-N ANC is calculated by

$$e_N(n) = d_N(n) - y_N(n) = a(n) + \gamma n(n) - \gamma\hat{n}(n) \approx a(n). \tag{18}$$

$\gamma n(n) - \gamma\hat{n}(n) \approx 0$; therefore, $e_N(n) \approx a(n)$. We conclude from the above analysis that as the filter approaches its optimal stage the clean signal is estimated with minimal noise. To minimize the noise and thus improve the steady-state MSE, it is necessary to automatically change the number of stages to its optimal $N = N_{\text{opt}}$ stage. We employ an automatic selection of stages (refer Sect. 2.2) to attain optimal performance.

2.1 Mean Square Error (MSE)

The error at the optimal stage is

$$e_N(n) = d_N(n) - y_N(n) = a(n) + n(n) - [y_1(n) + y_2(n) + \cdots + y_N(n)]. \tag{19}$$

At the optimal stage N of the ANC, $y_1(n)+y_2(n)+\cdots+y_N(n)=\tilde{n}(n)$ (estimate of n(n)) and the MSE is denoted as:

$$\begin{aligned} E\left[|e_N(n)|^2\right] &= E\left[|a(n)|^2\right] + E[|n(n)-\tilde{n}(n)|^2] - 2E[|a(n)(n(n)-\tilde{n}(n))|] \\ &= E\left[|a(n)|^2\right] + E[|n(n)-\tilde{n}(n)|^2] - 2E[|a(n)n(n)|] + 2E[|a(n)\tilde{n}(n)|] \end{aligned} \tag{20}$$

The following equation is obtained due to the uncorrelation between added noise $n(n)$ and the uncorrupted signal $a(n)$.

$$2E\,[|a(n)n(n)|] = 0 \tag{21}$$

Meanwhile, $a(n)$ and $\hat{n}(n)$ are also uncorrelated; hence, the following is stated,

$$2\,E[|a(n)\tilde{n}(n)|] = 0 \tag{22}$$

Inserting Eqs. (21) and (22) in (20)

$$E\left[|e_N(n)|_2\right] = E\left[|a(n)|_2\right] + E[|n(n)-\tilde{n}(n)|^2] \tag{23}$$

Also, we note that the replica of the noise-free signal $a(n)$ is achieved as. $E[|n(n)-\tilde{n}(n)|^2]$ is minimized. It means that at the optimal filter stage N, $y_1(n)+y_2(n)+\cdots+y_N(n)$ is as close to $n(n)$ as possible, and hence $E[|n(n)-\tilde{n}(n)|^2]$ is minimized (i.e.),

$$[y_1(n)+y_2(n)+\cdots+y_N(n)] \approx n(n) \tag{24}$$

The above analysis proves that the noise signal can be removed from the input signal $d_1(n)$ by adjusting the number of stages of the filter, and the $O(n)$ represents the de-noised from the ANC.

$$O(n) = e_N(n) \approx a(n) \tag{25}$$

Thus, we infer that the de-noised signal $O(n)$ is obtained as the number of stages in the cascaded filter structure approaches its optimal value.

2.2 Control Logic for Automatic Stage Selection

The MSE value reaches its minimal value only at the filter's optimal stage as proved in the above section. The Pearson cross-correlation function is computed between the error of each stage L, $e_L(n)$ and the reference input noise $n'(n)$. This value is used to compute the optimum filter stage. It is presumed that the noise signal $n'(n)$ which is the reference noise is in time correlated to the added noise signal $n(n)$ but

is not correlated to the uncorrupted signal $a(n)$. The error output of each stage ANC is the replica of the uncorrupted signal (i.e.) $e_L(n) = \hat{a}(n)$; therefore, the correlation between $e_L(n)$ and $n'(n)$ reduces as the filter reaches its optimal stage. The estimated correlation coefficient between $e_L(n)$ and $n'(n)$ is defined as

$$\rho_{eLn'} = Cov\left(eL, n'\right)/\sigma_{eL}\sigma_{n'} \tag{26}$$

where $\rho_{eL,n'}$ is the Pearson product–moment correlation coefficient Cov(eL,n') is the co-variance of variables eL and n', σ_{eL} and $\sigma_{n'}$ are the standard deviation of eL and standard deviation of n'. In the proposed method, $eL(n)$ is the estimate of the uncorrupted signal at each stage and $n'(n)$ is the reference noise used at stage-I. Since we have assumed that the information signal $a(n)$ and the added noise are in time uncorrelated, the value of $\rho_{eL,n'}$ should be low. The estimated correlation function $\rho_{eL,n'}$ is investigated at each stage and further adaptive filter stages are added until the value of $\rho_{eL,n'}$ reaches a minimal threshold value at the optimal cascaded filter stage.

3 Results and Discussion

The proposed filter structure is applied to signal de-noising application for extracting the uncorrupted signal. The primary input signal to stage-I ANC is $d_1(n) = a(n) + n(n) = A\sin(2\pi f_1) + B\sin(2\pi f_2)$ where $f_1 = 10$ Hz is the low-frequency information signal, and $f_2 = 100$ Hz is the high frequency additive noise signal. The amplitudes of A and B are 1 and 0.5, respectively. The reference input signal to stage-I filter is a noise signal correlated to $n(n)$ given by $n'(n) = B_1\sin(2\pi f_2)$ where B_1 has an amplitude of 0.35. The filter length is taken as 4, and the initial filter weights are assumed to be zero. The value of μ is taken as 0.01. The performance criteria utilized to validate the proposed multi-stage (M-S) cascaded LMS filter model are the MSE, SNR and average noise reduction (ANR) (in dB). Figure 3 presents the MSE performance for the above specifications such that the input SNR = 13 dB. The speed of convergence is significantly improved and the MSE is further minimized by using the proposed multi-stage cascaded LMS adaptive filter.

The proposed filter model is tested by adjusting the input SNR to be 21 dB and the MSE performance of the proposed multi-stage cascaded LMS adaptive filter model as compared to the existing cascaded models is presented in Fig. 4. We observe that for an input SNR of 21 dB, the proposed filter attains minimum MSE value and faster convergence speed.

From Table 1, we infer that the proposed multi-stage cascaded LMS adaptive filter framework in ANC systems outperforms the existing single stage and 2-stage cascaded LMS adaptive filter models in terms of SNR and ANR (average noise reduction). The proposed adaptive filter structure in ANC gives an output SNR value of at least 3–4 dB higher than the existing cascaded adaptive filters and achieves

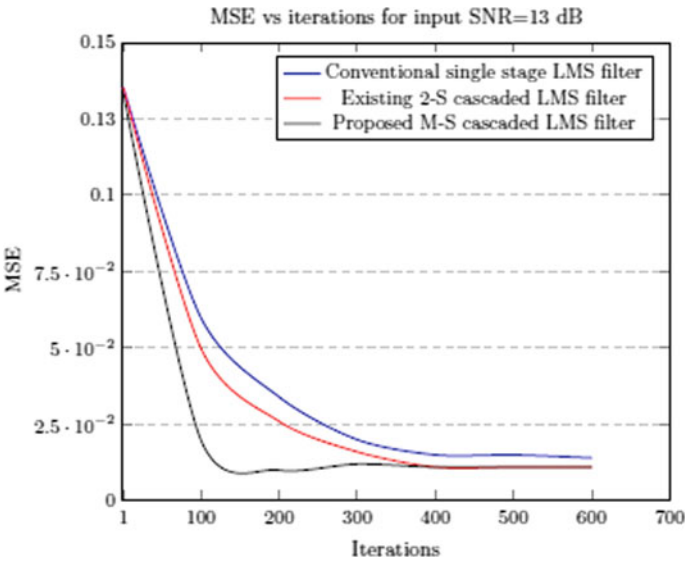

Fig. 3 Convergence of MSE with iterations for an input SNR = 13 dB

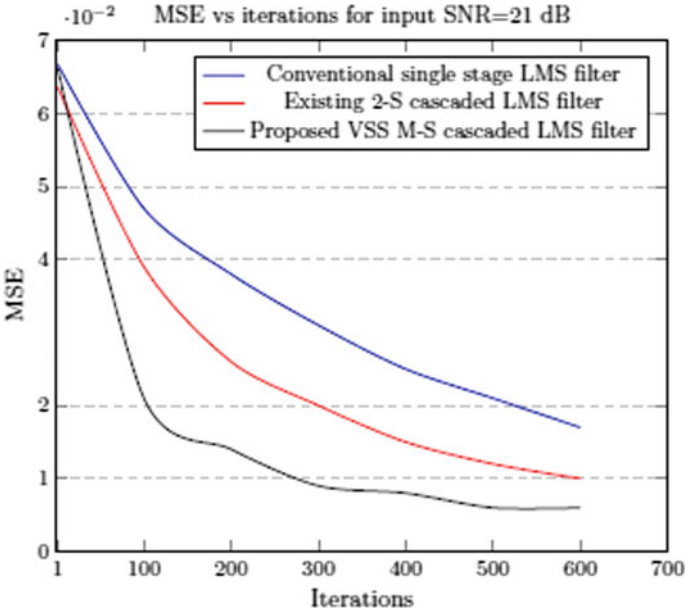

Fig. 4 Convergence of MSE with iterations for an input SNR = 21 dB

Table 1 Comparison of MSE, SNR and ANR for various adaptive filter models

Input SNR	Filter structure	MSE	SNR (dB)	ANR (dB)
13 dB	LMS adaptive filter	0.0328	27.23	29.46
	Existing 2-S cascaded LMS filter	0.0265	29.35	30.03
	Proposed M-S cascaded LMS filter	**0.0200**	**32.16**	**32.62**
21 dB	LMS adaptive filter	0.0329	27.19	28.35
	Existing 2-S cascaded LMS filter	0.0244	30.17	30.83
	Proposed M-S cascaded LMS filter	**0.0154**	**34.80**	**35.18**

higher average noise reduction levels as compared to the use of conventional LMS adaptive filter and 2-stage LMS cascaded adaptive filter structure in ANC systems.

4 Conclusion and Future Scope

A multi-stage cascaded LMS adaptive filter model is presented in this paper based on automatic control of stages to be cascaded. The proposed multi-stage(M-S) cascaded LMS adaptive filter model used in ANC systems offers an improved solution to achieve higher convergence speed and a minimal MSE value by automatically adjusting the number of filter stages to be cascaded. From the simulation results, we infer that that the proposed variable stage filter gives good performance as compared to the conventional LMS and the existing 2-stage cascaded LMS adaptive filter structure. Using such structures, cost-effective hardware ANC systems can be implemented in future.

References

1. Sayed AH (2003) Fundamentals of adaptive filtering (1st ed). Wiley Interscience
2. Sankaran SG, Beex AA (1997). Acoustic echo and noise canceler improvements for hands free telephones. IEEE Southeastcon' 97, New York 148–150
3. Sambur M (1978) Adaptive noise canceling for speech signals. IEEE Trans Acoust Speech Sig Proc 26(5):419–423
4. Haykin S, Widrow B (2003) Least-mean-square adaptive Filters, 1st edn. Wiley, Newyork
5. Poularikas AD (2014) Adaptive filtering: fundamentals of least mean squares with MATLAB®, 1st edn. CRC Press, Taylor and Francis Group
6. Ahmed N, Hush D, Elliott G, Fogler R (1984) Detection of multiple sinusoids using an adaptive cascaded structure. In: IEEE International Conference on Acoustics, Speech, and Signal Processing, USA pp 199–202
7. Prandoni P, Vetterli M (1998) An FIR cascade structure for adaptive linear prediction. IEEE Trans Signal Process 46(9):2566–2571
8. Kim H, Kim S, VanHelleputte N, Berset T, Geng D, Romero I, Yazicioglu RF (2012) Motion artifact removal using cascade adaptive filtering for ambulatory ECG monitoring system. In: IEEE biomedical circuits and systems conference, Taiwan, pp 160–163

9. Garcés Correa A, Laciar E, Patiño HD, Valentinuzzi ME (2007) Artifact removal from EEG signals using adaptive filters in cascade. In: 16th argentine bioengineering congress and the 5th conference of clinical engineering, Journal of Physics, IOP Publishing
10. Dixit S, Nagaria D (2017) Design and analysis of cascaded LMS adaptive filters for noise cancellation. Circ Syst Signal Proc 36(2):1–25
11. Maurya AK (2018) Cascade-cascade least mean square (LMS) adaptive noise cancellation. Circ Syst Sig Proc 37(9):3785–3826
12. Awad A (2019) Impulse noise reduction in speech signal through multi-stage technique. Eng Sci Technol Int J 22:629–636

THD Optimization with Low Switching Frequency Control for 15-Level Reduced Switch Asymmetric Multilevel Inverter

Gireesh Kumar Devineni, Aman Ganesh, Neerudi Bhoopal, and D. S. N. M. Rao

Abstract The switching modulation techniques of high switching frequencies are not recommended in medium voltage drive applications with a power of megawatts because of high power losses and low converter performance. Fundamental strategies like selective harmonic elimination (SHE) are a popular alternative. Since the transcendental equations formulated by SHE are simply nonlinear in nature, it has proven to be an important challenge for the scientists to achieve a viable solution on the desired modulation index. This article presents the comparison analysis of the GA and PSO approach with good initial guess, and its hybrid optimization of PSO-GA is used for solution of the SHE equation set to various modulation index values. The %THD generated at various modulation index values is also consistent with the harmonic standards of IEEE 519-1992.

Keywords GA · PSO · PSO-GA · Hybrid Algorithms · THD · SHEPWM

1 Introduction

Multilevel inverter technology has grown in popularity in recent decades due to its advantages of producing increased levels of output voltages using less power switch requirements for medium voltage and high-power applications. Multilevel inverters are currently available in three topologies: DC MLI, CHB MLI, and FCMLI. H-bridge MLI is typically favored for various industrial uses among all these topologies [1–3]. Low-frequency switching and high-frequency switching controls are two types of

G. K. Devineni · A. Ganesh (✉)
School of Electronics and Electrical Engineering, Lovely Professional University, Phagwara, Punjab, India
e-mail: aman.23332@lpu.co.in

G. K. Devineni · N. Bhoopal
Department of Electrical and Electronics Engineering, B V Raju Institute of Technology, Narsapur, Telangana, India

D. S. N. M. Rao
Department of Electrical and Electronics Engineering, Gokaraju Rangaraju Institute of Engineering and Technology, Hyderabad, India

C. Subramani et al. (eds.), *Proceedings of International Conference on Power Electronics and Renewable Energy Systems*, Lecture Notes in Electrical Engineering 795,
https://doi.org/10.1007/978-981-16-4943-1_9

modulation techniques used to control multilevel inverters [4]. The following effects can be caused by high frequency modulation in inverters, such as carrier-based pulse width modulation schemes.

- Reduced system efficiency due to increased thermal losses.
- Motor bearing failure and insulation damage in case of drive control due to high dv/dt.
- Effect of electromagnetic interference due to the power frequency of sidebands in the order 10–30 kHz.
- Ripples and harmonics in voltage and current waveforms.

However, low-frequency switching modulation methods such as SHE have key features, like the less thermal loss, control on harmonic o/p voltage, and a better harmonic profile. To generate an optimal solution at a specific modulation index for low percent of THD to satisfy the harmonic standards of IEEE 519-1992, SHE methodology is suffering from the cumbersome nature to deal with the SHE equations. This problem has received considerable attention in recent years, and many computational algorithms are being used to address SHE equations to achieve improved solutions with little time and effort in computation. The viable solutions for the nonlinear SHE equations are sought using stochastic optimization techniques such as genetic algorithms, species-based modified optimization techniques, and firefly algorithms. Recently, Manasrah et al. [5] have suggested the new PSO-GA algorithm with the combined merits of both GA and PSO algorithms, which incorporates the efficient, scalable, and compact coding of GA and PSO algorithms to address the problem of workflow forecasting. This article compares the feasibility of the PSO-GA algorithm with that of conventional GA and PSO algorithms in solving a set of SHE equations that are developed in the control of single-phase switched-diode 15-level inverter [6].

2 Problem formulation for SHEPWM

The selective harmonic elimination technique is often termed the low-frequency switching method according to harmonic elimination theory. It aims to find the suitable switching angles of the converter, to eliminate the selected lower harmonics, so that THD can be mitigated on the load voltage and current. SHE has numerous advantages, including good control on harmonics, lower thermal losses, and triple harmonics that are multiple harmonics of the third order. The SHE methodology may also be referred to as the coded PWM method and was typically used in application areas including improvements to the power quality, effective medium voltage control, HVDC, and distribution systems [7].

High-frequency switching methods like carrier-dependent PWM and SVPWM generate bands across the carrier frequencies, resulting in a high THD percentage. In addition to that, the system with a switched frequency of 500 Hz results in significant thermal loss if multilevel inverters are run at an output level of more than

1 MW. For this reason, one of the common strategies at MW rated power is the low-frequency switching technique such as selective harmonic elimination. In the other hand, for decades, scholars are forced to have potential alternatives to the transcendental, nonlinear SHE set. The increase in voltage levels also increases the amount of variables in SHE formulations, increasing the computing complexity [8]. Among the most common topology is switched-diode asymmetric 15-level inverters for solar PV applications. For analysis, thus, 3-source, 7-switch 15-level single-phase inverter is considered in this article [9]. Figure 1 shows the proposed asymmetric 15-level inverter circuit which has two units named primary circuit which is responsible for level generation, and other is auxiliary circuit which is used for polarity reversal. Using Fourier series analysis of 15-level output of the inverter in Fig. 1, the output voltage equation is represented by

$$V(\omega t) = \sum_{k=1,3,5,....}^{\infty} \frac{4V_{dc}}{k\pi}[\cos(k\alpha_1) + \cos(k\alpha_2) + \cdots + \cos(k\alpha_n)]\sin(k\omega t) \quad (1)$$

where $n =$ number of switching angles.

The range of switching angles between 0° and 90° ($0° < \alpha < 90°$) is taken as constrain in the SHE technique. Dividing the square wave output into Fourier

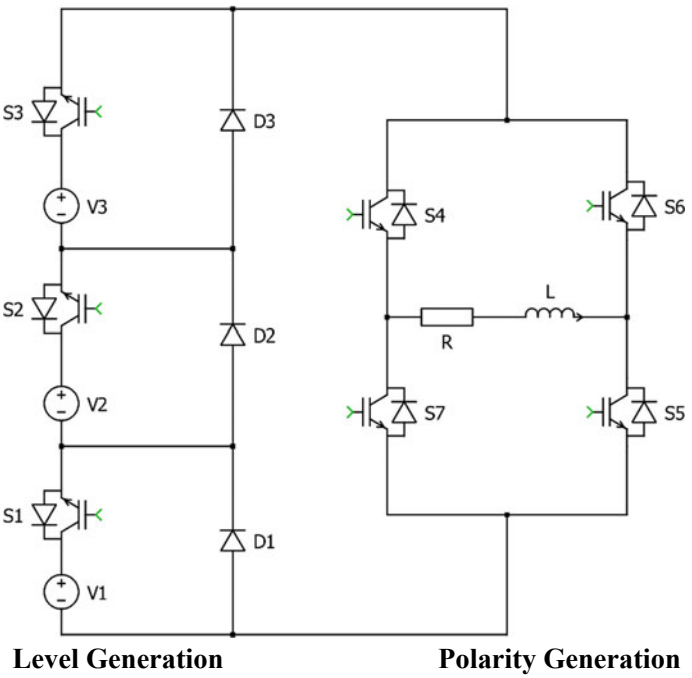

Fig. 1 Proposed 15-level multilevel inverter with reduced number of switches

components of sine wave in compliance with the Fourier series, there are even no harmonics due to its symmetry. The triplen harmonics were omitted by varying the modulation index in multiples of 3. In terms of switching angles, it is necessary to show the fundamental output voltage (V_1) as

$$\frac{4V_{\text{dc}}}{\pi}[\cos(k\alpha_1) + \cos(k\alpha_2) + \cdots + \cos(k\alpha_n)] = V_1 \tag{2}$$

The maximum fundamental voltage $V_{1\text{max}}$ can be written as follows:

$$V_{1\text{max}} = \frac{4V_{\text{dc}}}{\pi} \tag{3}$$

Therefore, the modulation index M_i can be represented as

$$M_i = \frac{\pi V_1}{4V_{\text{dc}}} (0 \leq M_i \leq 1) \tag{4}$$

The switched-diode 15-level inverter consists of 7 degrees of freedom. One of those seven is generated from fundamental voltages, and the other six degrees are used to eliminate other odd harmonics of order: 5th to 19th. In multilevel inverters, modulation processes may be categorized by switching frequency. The key purpose is to improve maximum fundamental voltage by reducing harmonic content of lower order. Combining Eqs. (2) and (4), the transcendental equations can be written as

$$\left.\begin{aligned}
&\cos(\alpha_1) + \cos(\alpha_2) + \cos(\alpha_3) + \cos(\alpha_4) + \cos(\alpha_5) + \cos(\alpha_6) + \cos(\alpha_7) = M_i \\
&\cos(5\alpha_1) + \cos(5\alpha_2) + \cos(5\alpha_3) + \cos(5\alpha_4) + \cos(5\alpha_5) + \cos(5\alpha_6) + \cos(5\alpha_7) = 0 \\
&\cos(7\alpha_1) + \cos(7\alpha_2) + \cos(7\alpha_3) + \cos(7\alpha_4) + \cos(7\alpha_5) + \cos(7\alpha_6) + \cos(7\alpha_7) = 0 \\
&\cos(11\alpha_1) + \cos(11\alpha_2) + \cos(11\alpha_3) + \cos(11\alpha_4) + \cos(11\alpha_5) + \cos(11\alpha_6) + \cos(11\alpha_7) = 0 \\
&\cos(17\alpha_1) + \cos(17\alpha_2) + \cos(17\alpha_3) + \cos(17\alpha_4) + \cos(17\alpha_5) + \cos(17\alpha_6) + \cos(17\alpha_7) = 0 \\
&\cos(19\alpha_1) + \cos(19\alpha_2) + \cos(19\alpha_3) + \cos(19\alpha_4) + \cos(19\alpha_5) + \cos(19\alpha_6) + \cos(19\alpha_7) = 0
\end{aligned}\right\} \tag{5}$$

Fitness can be achieved by adding the intended objective to the penalty factor. The consistency of the solution for the initial target is the fitness value. The principle goal here is to obtain a set of switching angles to achieve the optimal value of the magnitude of the fundamental harmonic. The fitness function is determined accordingly for each solution.

3 Control Algorithms

The switching angles of proposed inverter are optimized by nature-inspired optimization algorithms. The following algorithms of GA, PSO, and hybrid GA-PSO algorithms were used in this research for solving the nonlinear equations generated from SHEPWM as given in Eq. (5).

3.1 Genetic Algorithm

Genetic algorithms (GAs), based on biological evolution, are computerized search methods. Genetic algorithms are based on the population size of pre-selected candidates. The implementation of genetic algorithms takes place following phases for selective harmonic elimination problem [10, 11].

1. Initialization: Initial population of any candidate solution in the search space can be developed by the following equation, close to the middle of each switching boundary. For each solution set, the number of populations was calculated as 20.

$$\alpha_{ij}^{\mathrm{IP}} = \alpha_{ij} + \left[\alpha_{ij}^{L} \pm \mathrm{rand}_j \left\{ \frac{\left(\alpha_{ij}^{U} - \alpha_{ij}^{L} \right)}{2} \right\} \right] \tag{6}$$

where $\alpha_{ij}^{\mathrm{IP}}$ represents initial population matrix, and α_{ij}^{L} represents initial guess of solutions from α_1 to α_7.

2. Evaluation: The fitness values of the candidate solutions are determined using the pre-formulated objective function as seen in the equation until the population for each switching angle is initialized or the offspring population is set.

$$F_{\mathrm{OBJ}}(\alpha) = \frac{1}{1 + F(\alpha)} \tag{7}$$

where

$$F(\alpha) = \mathrm{mod}\, f_1(\alpha) + \mathrm{mod}\, f_2(\alpha) + \mathrm{mod}\, f_3(\alpha) + \cdots$$

3. Selection: The selection to produce offspring was made by assigning more instances of these solutions with higher fitness values to the candidate's solutions and applying a survival mechanism. This was accomplished by calculating the fitness of each population and by comparing it with a random number of (0, 1) that is determined by the collection of roulette wheels.

4. Crossover or Recombination: Two or three parental solutions are summarized to create new solutions, which can be theoretically enhanced (e.g., offspring). Any solution is converted to an 11-bit binary, pairs have been randomly selected from parental crossover solutions, and a random number 'r' has been generated for each pair in a random version of (1, 1) to align 'r' with a specified probability crossover (here 0, 6) to establish whether or not the pair is to be perforated, over point was found. A single-point crossover was used here.

5. Mutation: Although two or more chromosomes are recombined, localized yet random mutations change the solution. Here too, for every descendant a random number 'r' is created, in which 'r' contrasts with the pre-defined probability of mutation (here 0, 1). If the mutation was deemed suitable, a random number was

established between (1.10) to determine the mutation rate, complementing this single bit.

6. Replacement: To replace the parents of the second generation, the first generation's parental population was selected, recombined, and mutated.

7. Termination: If the termination criterion is not reached, then repeat steps 2 to 6.

3.2 Particle Swarm Optimization

Kennedy and Eberhart suggested PSO in 1995, and it is defining Swarms' sociological behavior [12]. The phases in PSO algorithm for solving SHEPWM problem are given below.

Step 1: Initialize the parameters of particle vectors X_i, V_i, P_{best}, G_{best}, and inertia weight of the particle C_0. Choose number of generations as 100, size of population as 40, cognitive parameter C_1 as 0.5, and social parameter C_2 as 1.25.

Step 2: Test the conditions for $0 < (C_1 + C_2) < 2$ and $(C_1 + C_2)/2 < C_0 < 1$. The system would then be guaranteed to converge to a stable equilibrium position if the two conditions were met. If false, go to Step 1.

Step 3: The new position and velocity vectors of particles were determined using the following equation.

$$v_l^i(t+1) = w(t).v_l^i(t) + C_{\text{ind}}.\text{rand1}, (p_l^i - x_l^i(t) + C_{\text{soc}}.\text{rand2}.\left(G^i - x_l^i(t)\right) \quad (8)$$

Then, the new position is defined as

$$x_l^i(t+1) = x_l^i(t) + v_l^i(t+1) \quad (9)$$

Step 4: Evaluate the objective function of the particles using

$$\text{OF} = \min_{\alpha_k}\left\{\left(100 * \frac{V_1^* - V_1}{V_1^*}\right)^4 + \sum_{K=2}^{N} \frac{1}{h_k}\left(50 * \frac{V_{h_k}}{V_1}\right)^2\right\} \quad (10)$$

Step 5: Check for the constraint on fitness function as

$$\alpha_1 < \alpha_2 < \alpha_3 < \alpha_4 < \alpha_5 < \alpha_6 < \alpha_7 < \frac{\pi}{2} \quad (11)$$

Step 6: Check for $P(xi) < P(Pi)$, if not then $i = i + 1$ go to step 3.

Step 7: Update the particle's best local position if the best local position is better than before. Thus $Pi = Xi$ replaces the local best position.

Step 8: $Pg = \min$ (P neighbor).

Step 9: Terminate the process if the optimal switching angles achieved.

3.3 PSO-GA Hybrid Algorithm

A hybrid approach is proposed which combines genetic algorithm (GA) with PSO. This hybrid algorithm combines GA and PSO principles and produces individuals not only through the GA crossover and mutations but also through PSO processes in the new generation. It can solve the problem of local minima of the PSO and has greater search accuracy.

The algorithm of GA_PSO with combined accuracy is given below:

Step 1: Initialization of variables for GA.

Step 2: Initialization of variables for PSO.

Step 3: Arrange the PSO group, and determine the optimal GA solution coefficient for each condition.

Step 4: Impose GA's optimal location condition, and perform GA mutations and crossover.

Step 5: Select the best solution and stop when the best individual in GA or PSO has met the termination criteria.

Step 6: If the PSO's condition is met (target value or iteration number), the reproduction process is stopped. If not, it will go step 3.

Step 7: Perform a hybrid method if generations could be precisely segregated by the iterative items *N*. Select *P* individuals arbitrarily according to their fitness from each sub-system.

Figure 2 presents the comparison between convergence characteristics of GA, PSO, and GA-PSO hybrid algorithms. The convergence characteristics show the number of iterations required for a given algorithm to evaluate the fitness function. Compared to GA and PSO, the hybrid PSO-GA algorithm converges at a faster rate for the 65 iterations.

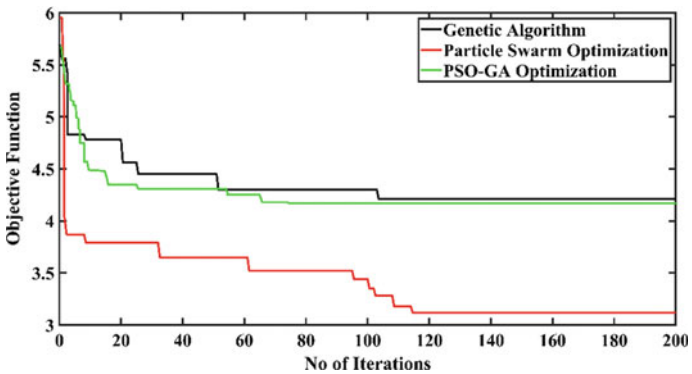

Fig. 2 Objective function versus number of iterations

4 Results and Discussions

Using MATLAB Simulink, the suggested asymmetrical structure is developed with GA, PSO, and combined PSO-GA hybrid algorithms, as well as the SHE PWM technique. The proposed asymmetrical structure's input DC sources are 37 V, and the measured peak voltage (Vpeak) is 259 V. The desired inverter's switching frequency is 50 Hz, the harmonic frequency is 1 kHz, and the Nyquist frequency with total harmonics is 5 kHz. The RL load is considered with $R = 26.8\ \Omega$ and $L = 9.9$ mH. For a modulation index of 0.9, the switching angles are obtained. The proposed asymmetric multilevel inverter's switching pulses are shown in Fig. 3 for both primary circuit (level generation) and auxiliary circuit (polarity generation). The proposed inverter can generate 15 levels of output voltage with 7 steps in each half cycle, each having a voltage magnitude of 37 V.

Figure 4(a) represents load voltage waveform, and Fig. 4(b) represents the load current waveform of 15-level output. The THDs of voltage and current harmonic waveforms were evaluated (Figs. 5 and 6) for GA, PSO, and PSO-GA hybrid algorithms. The PSO-GA algorithm has given a less voltage THD of 5.34% and current THD of 2.66% compared to GA and PSO algorithms. The comparative analysis of

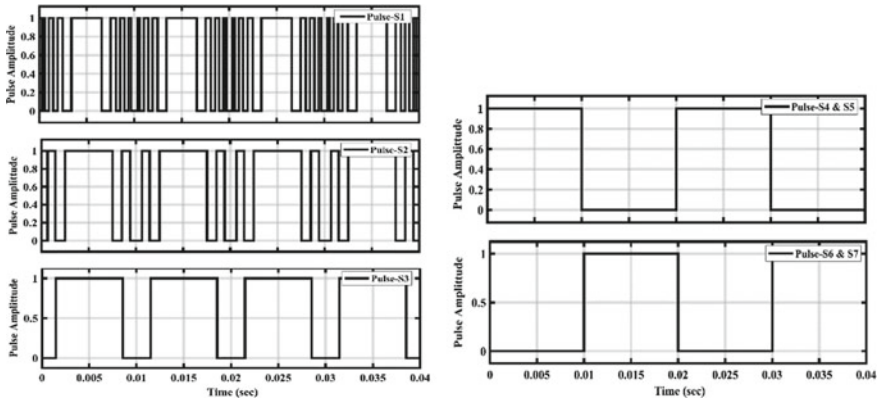

Fig. 3 Gating pulses for the primary and auxiliary circuit

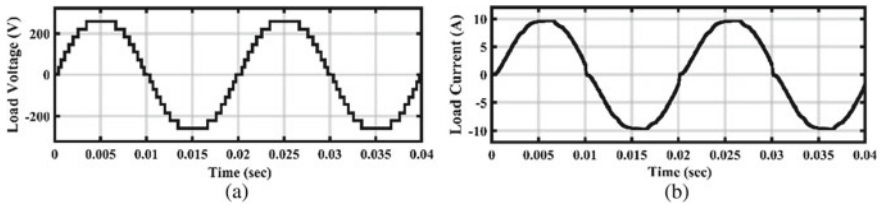

Fig. 4 **a** Load voltage and **b** Load current waveforms of proposed inverter

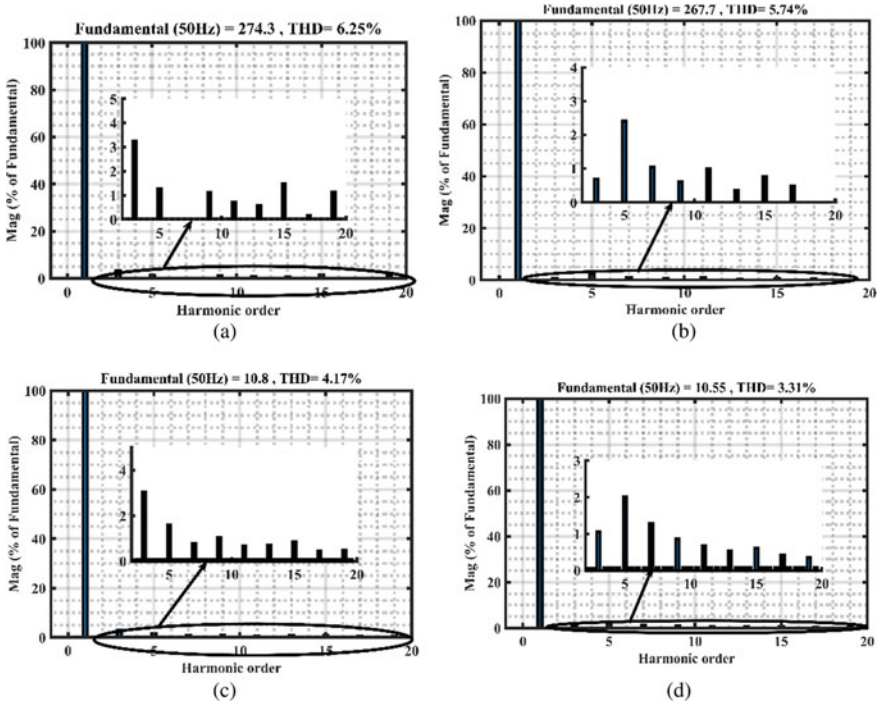

Fig. 5 Voltage harmonic distortion **a** GA **b** PSO and current harmonic distortion **c** GA **d** PSO

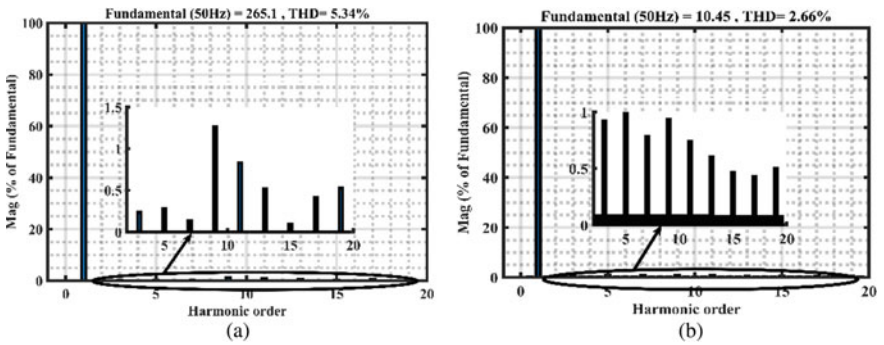

Fig. 6 **a** Voltage harmonic distortion with PSO-GA **b** Current harmonic distortion with PSO-GA

these three algorithms for % voltage and current harmonic distortion is given in Fig. 7.

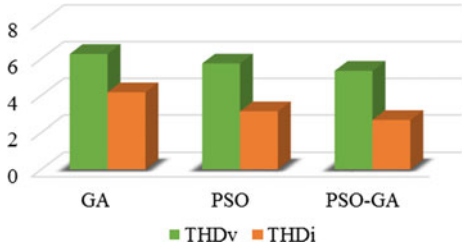

Fig. 7 Comparison of THD for GA, PSO, and their hybrid PSO-GA algorithm

5 Conclusions

This work focused primarily on comparative analysis of GA, PSO, and their hybrid PSO-GA algorithms for solving nonlinear transcendental SHE equations, which were built in the single-phase asymmetric inverter to achieve the appropriate switching angles. PSO-GA is a robust and efficient algorithm that has solved SHE equation set from 0.5 to 1.0 modulation index values with less computational effort. The comparative analysis is done for the total harmonic distortion in an asymmetric 15-level inverter for different modulation indexes using SHEPWM control. The THD estimated at the inverter output using PSO-GA algorithm is 5.34% without using any filter at the inverter output, which is comparatively less than the individual GA and PSO algorithms. Hence, this research concludes that the PSO-GA hybrid algorithm will give optimal switching angles for the 15-level asymmetric multilevel inverter using (SHEPWM) low-frequency switching control.

References

1. Rodríguez J, Lai JS, Peng FZ (2002) Multilevel inverters: a survey of topologies, controls, and applications. IEEE Trans Ind Electron. https://doi.org/10.1109/TIE.2002.801052
2. McGrath BP, Holmes DG (2002) Multicarrier PWM strategies for multilevel inverters. IEEE Trans Ind Electron. https://doi.org/10.1109/TIE.2002.801073
3. Mekhilef S, Abdul Kadir MN (2011) Novel vector control method for three-stage hybrid cascaded multilevel inverter. IEEE Trans Ind Electron https://doi.org/10.1109/TIE.2010.2049716
4. Mittal N, Singh B, Singh SP, Dixit R, Kumar D Multilevel inverters: a literature survey on topologies and control strategies. https://doi.org/10.1109/ICPCES.2012.6508041
5. Manasrah M, Ali HB (2018) Workflow scheduling using hybrid GA-PSO algorithm in cloud computing. Wirel Commun Mob Comput 2018. https://doi.org/10.1155/2018/1934784
6. Bharath VS, Gopinath M (2014) Tumbling total harmonic distortion in multi inverter with the aid of hybrid (GA-PSO). J Theor Appl Inf Technol 62(1):131–138
7. Devineni GK, Ganesh A (2020) Problem formulations, solving strategies, implementation methods & applications of selective harmonic elimination for multilevel converters. J Eur des Syst Autom 53(6):939–952. https://doi.org/10.18280/jesa.530620
8. Manohar VJ, Trinad M, Ramana KV (2016) Comparative analysis of NR and TBLO algorithms in control of cascaded MLI at low switching frequency. Procedia Comput Sci 85(Cms):976–986. https://doi.org/10.1016/j.procs.2016.05.290

9. Kumar DG, Ganesh A, Naga Malleswara Rao DS (2021) Design and analysis of a novel cascaded 15-level asymmetric inverter using PSO and whale algorithms. In: 2021 international conference on sustainable energy and future electric transportation (SEFET), Hyderabad, India, 2021, pp 1–6. https://doi.org/10.1109/SeFet48154.2021.9375752
10. El-Naggar K, Abdelhamid TH (2008) Selective harmonic elimination of new family of multi-level inverters using genetic algorithms. Energy Convers Manag 49(1):89–95. https://doi.org/10.1016/j.enconman.2007.05.014
11. Anjali Krishna R, Padmasuresh L, Muthukumar P (2018) Genetic algorithm based 15 level multilevel inverter with SHE PWM. Int J Eng Technol 7(2.33) Special Issue 33:893–897
12. Rasheed M, Omar R, Sulaiman M, Halim WA (2019) Particle swarm optimisation (PSO) algorithm with reduced numberof switches in multilevel inverter (MLI). Indones J Electr Eng Comput Sci 14(3):1114–1124. https://doi.org/10.11591/ijeecs.v14.i3.pp1114-1124

Signal Conditioning Circuits for GMR Sensor in Biomedical Applications

G. Anand, T. Thyagarajan, B. Aashique Roshan, L. Rajeshwar, and R. Shyam Balaji

Abstract Superparamagnetic nanoparticles offer a wide range of applications in the emerging field of electronic devices. Recent developments have identified them as components for a new type of magnetoresistance sensor. A novel measuring method is used where increased field sensitivity is bought at the value of an inherent device noise. The proposed GMR sensor has many advantages, yet its output is feeble due to noise, and hence, there is a requirement for designing a signal conditioning circuit to improve the signal strength. The objective is to analyze the low concentration (sample) with a better signal conditioning circuit for the GMR sensor.

Keywords Superparamagnetic nanoparticles · Magnetoresistance sensor · Signal conditioning circuit

1 Introduction

Nanotechnology and microtechnology have rapid progress and influence over the scientific developments which improve the standard of life [1]. Superparamagnetic nanoparticles have a good vary of applications in a trend of electronic devices [2]. Recent developments have identified them as components for a replacement style of magnetoresistance sensor. Resistive sensors are an inevitable part of many instrumentation systems and play an essential role in the measurement of physical quantities like pressure, force, temperature, etc., [3]. Resistive sensors range from the potentiometer, strain gauge (traditional types) to anisotropic magnetic resistance (AMR) and giant magnetoresistance (GMR) sensor (conventional) [4]. To improve sensitivity, accuracy, compatibility, and reduced size with electronic systems, magnetic field measurement has been developed [5]. GMR sensors have taken a most important role in the field of magnetic sensing due to their high signal strength, quick response under a lower magnetic field, small size, high sensitivity, frequency response, reduced power consumption, and low cost [6, 7]. These merits of GMR sensors are counterbalanced with a demerit that makes it hard to assess the accurate reading at the

G. Anand (✉) · T. Thyagarajan · B. Aashique Roshan · L. Rajeshwar · R. Shyam Balaji
Department of Instrumentation, Anna University, MIT Campus, Chennai, India

C. Subramani et al. (eds.), *Proceedings of International Conference on Power Electronics and Renewable Energy Systems*, Lecture Notes in Electrical Engineering 795,
https://doi.org/10.1007/978-981-16-4943-1_10

output. The output obtained will be feeble [8]. To overcome this demerit, there is a need to design an advanced signal conditioning circuit.

A basic instrumentation system consists of a sensor, signal conditioning unit, and process unit. A non-electrical signal is converted to an electrical signal to the signal conditioning unit by the sensing element [9]. The signal conditioning unit converts the electrical signal to the anticipated voltage level. Accurate signal conditioning is a key to any industrial data acquisition or industrial control application. Many sensors do not provide a clean and clear signal due to various reasons such as electrical or RF noise or wire loss. Such signals require a signal conditioning unit before being captured and processed by a data acquisition device [10]. Signal conditioning includes various processes, but a number of the foremost common are amplification, isolation, filtering, coupling, and linearization. To this, the main aim of this paper is to design a signal conditioning unit for a GMR sensor by comparing and analyzing a couple of filters, AC/DC coupling, and amplifiers. LTspice® simulation tool is employed for circuit analysis and implementation. LTspice® is a high-performance SPICE simulation software, schematic capture, and waveform viewer with enhancements and models for easing the simulation of analog circuits. LTSpice is a flexible, accurate, and free circuit simulator available for Windows and Mac [12]. It is easy-to-use circuit designing software and may be applied for analysis for sort of circuit. It is less time-consuming, and all circuits can be executed accurately.

2 Methodology

To design a signal conditioning unit, the schematic arrangement and selection of active and passive elements of a circuit play a foremost role. It influences the overall functioning of the system. The success of the designed measurement system depends on the design and performance of the signal conditioning unit [11]. The selection of filters and amplifiers was decided by the electrical output characteristics. The filters selected for comparison are the band-stop filter, band-reject filter, and notch filter. The instrumentation amplifiers used for comparison are OP07, AD822, and INA118. Qualitative and quantitative analyses were performed, and therefore, the preferred amplifier and filter were selected.

2.1 Comparison of Instrumentation Amplifiers

OP07 has an exceptionally low input offset voltage, and high open-loop gain makes it beneficial for high-gain instrumentation applications. The minimal input voltage range of ± 13 V was attained with a high CMRR of 106 dB and high accuracy due to its high input impedance.

Figure 1 describes the OP07 amplifier circuit implemented using the LTspice® simulation tool.

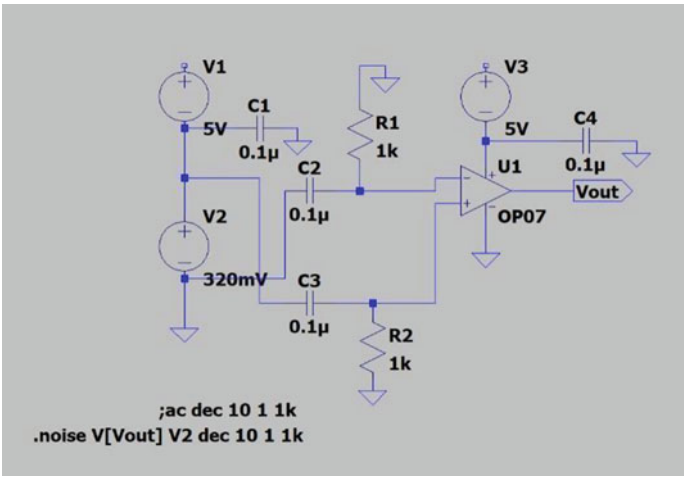

Fig. 1 OP07 amplifier circuit implemented

The AD822 is a low-power FET input op-amp, dual precision which will function from a single supply of 5 V till 30 V. It has a single-supply capacity with an input voltage range extending below the negative rail, allowing the AD822 to adapt input signals below ground. Output voltage swing extends to within 10 mV of each rail, providing the maximum output dynamic range. Figure 2 illustrates the AD822 amplifier circuit implemented using the LTspice® simulation tool.

The INA118 is an instrumentation amplifier for general purpose with excellent accuracy and low power consumption. It is a three op-amp design, flexible, and small that makes this device an excellent choice for a wide range of applications. Current-feedback input provides wide bandwidth, even at high gain. Internal input protection could withstand till ±40 V devoid of loss. This amplifier has been utilized to have

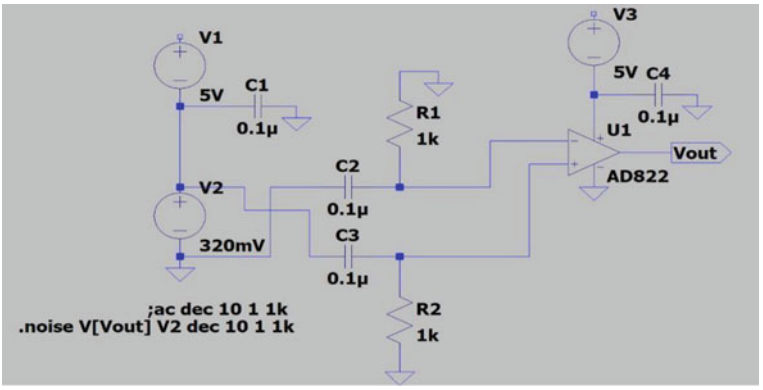

Fig. 2 AD822 amplifier circuit implemented

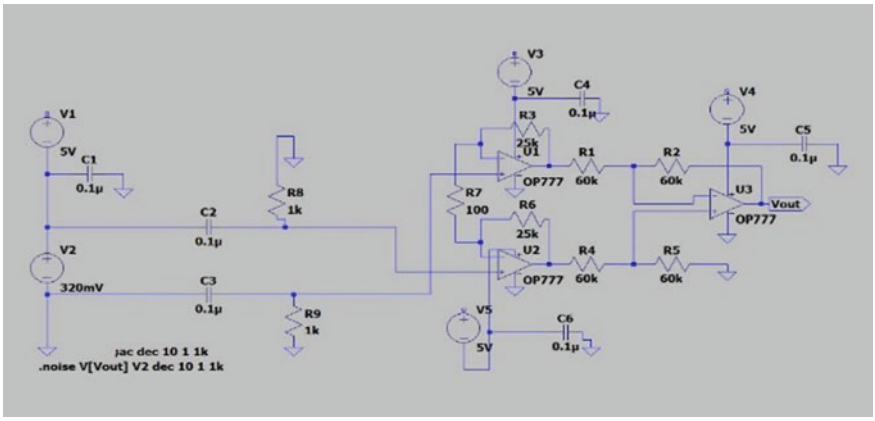

Fig. 3 INA118 amplifier circuit implemented

low offset voltage, high common-mode voltage, and drift voltage. Figure 3 explains the INA118 amplifier circuit implemented using the LTspice® simulation tool.

2.2 Comparison of Filters

Band-stop filter (BSF) is a frequency selective circuit that operates exactly in reverse to the band-pass filter. The band-stop filter is called a band-reject filter which passes all frequencies apart from those within a specified stopband. If the stopband is highly attenuated and very narrow for few hertz, the band-stop filter is known as a notch filter. Figure 4 refers to the filter implementation using the LTspice® simulation tool.

A band-rejection filter allows to pass most of the frequencies unaltered, but it mitigates a specific range to extremely low levels. It operates exactly in reverse to the band-pass filter. The word band rejection refers to the deliberate removal of a known frequency in signal processing. Figure 5 refers to the filter implementation using the LTspice® simulation tool.

Notch filters are similar to the band-pass filter that has a combination of low- and high-pass filters in the circuit design. The distinction is that it features a twin-T parallel resistance-capacitance (RC) network as in Fig. 6 circuit to acquire a deep notch. A professionally designed notch filter can produce an attenuation of more than −60 dB at the notch frequency. It eliminates a frequency of a narrow band and allows frequencies above and below of that band. This filter is also known as a band-reject filter as it eliminates frequencies. Figure 6 refers to the filter implementation using the LTspice® simulation tool.

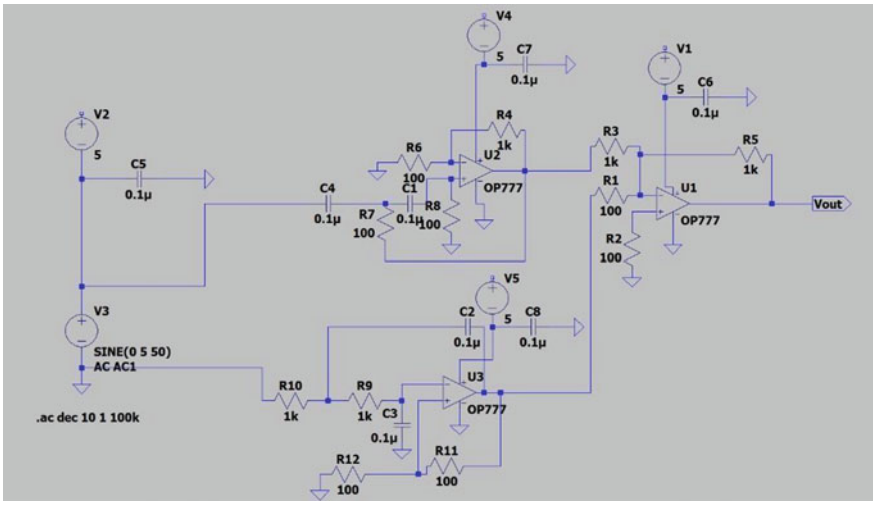

Fig. 4 Band-stop filter implementation

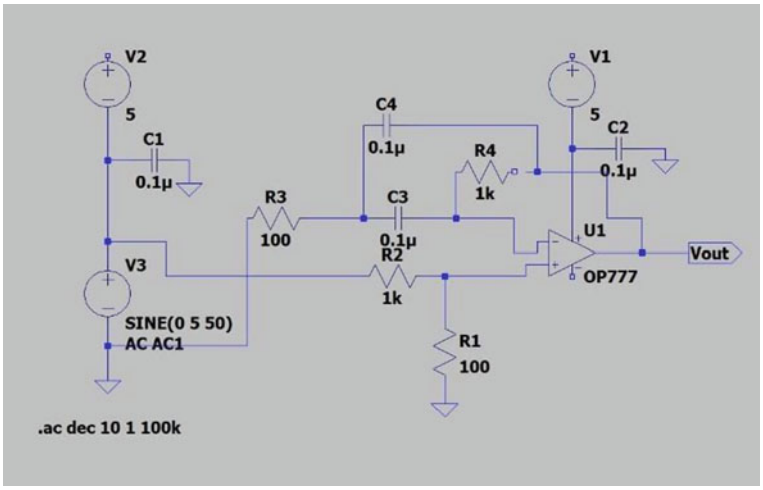

Fig. 5 Band-reject filter circuit implementation

2.3 Analysis of the Instrumentation Amplifiers

Quantitative Analysis: The parameter considered to compare the above circuits is power dissipation.

Power dissipation is a measure of the rate at which energy is dissipated, or lost, from an electrical system. The internal energy increases, causing its temperature to

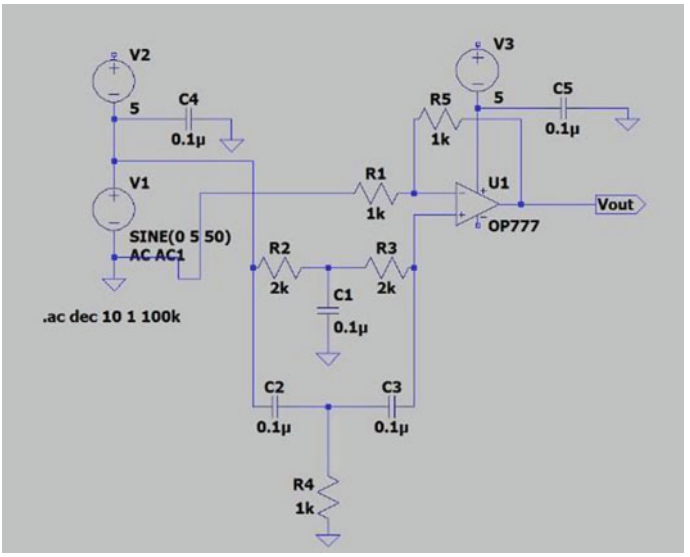

Fig. 6 Notch filter implementation

rise above the ambient (surrounding) temperature. This causes energy to dissipate away from the conductor into the surroundings, through the process of heat transfer.

Qualitative Analysis: The desired instrumentation amplifier is selected based on the power dissipation which provides the high output gain amplification.

2.4 Analysis of the Filters

Quantitative Analysis: The parameters considered to compare the above circuits are signal-to-noise ratio (SNR) and common-mode rejection ratio (CMRR).

Qualitative Analysis: The total harmonic distortion (THD) is the parameter used in this analysis. Harmonic distortion is a common form of distortion in applications where the peaks of the output signal get "clipped." As listed in Table 2, a filter with a lower percentage of THD is preferable.

2.5 AC/DC Coupling

The alternating coupling circuit in Fig. 7 permits only AC signals to pass through a connection, and it removes the DC offset by a DC blocking capacitor. Normalizing the signal to a mean of zero, the DC component is rejected by the AC coupling.

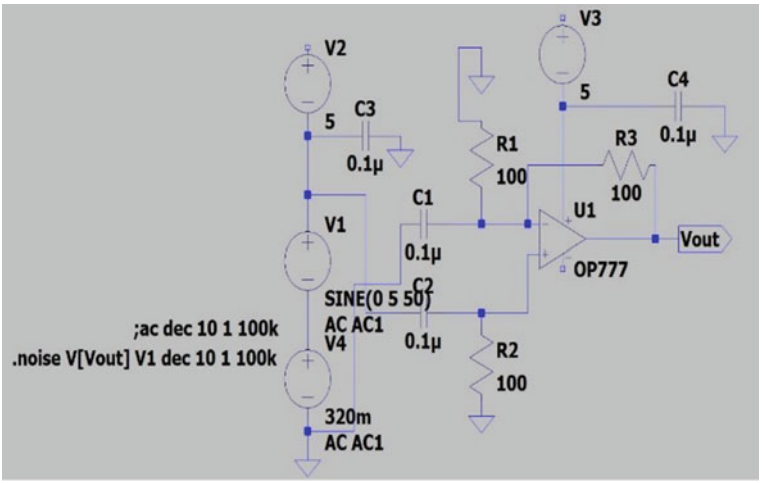

Fig. 7 AC coupling circuit implementation

The direct coupling circuit in Fig. 8 permits both AC and DC signals to pass through a connection. The DC element is a 0 Hz signal which acts as an offset about which the AC component of the signal fluctuates.

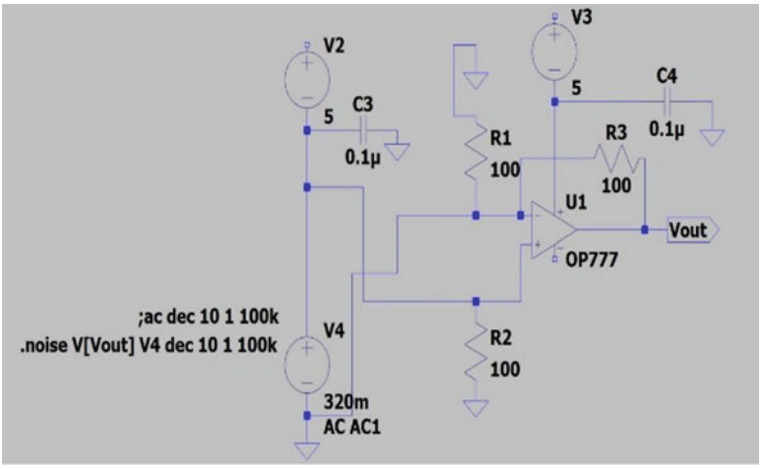

Fig. 8 DC coupling circuit implementation

3 Results and Discussions

3.1 Comparison and Analysis of Instrumentation Amplifiers

The output of the OP07 and AD822, which give less gain amplification, is shown in Figs. 9 and 10. From Fig. 11 there is a high gain amplification in INA118 which

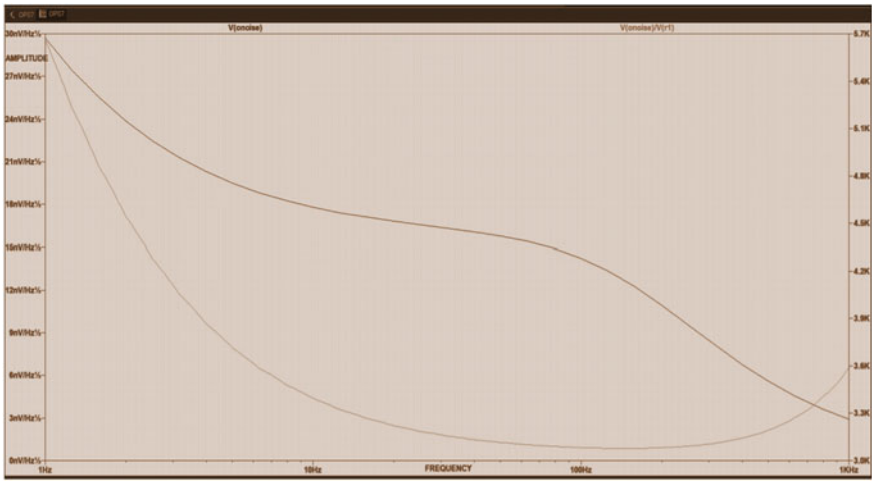

Fig. 9 OP07 amplification circuit output

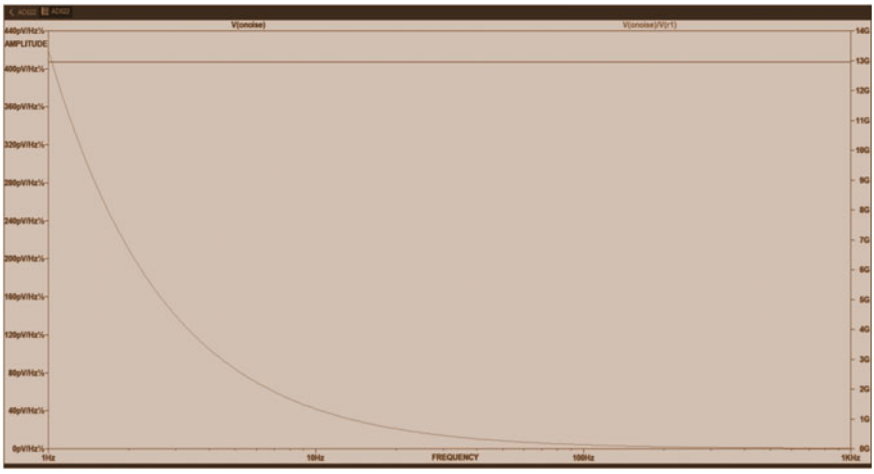

Fig. 10 AD822 amplification circuit output

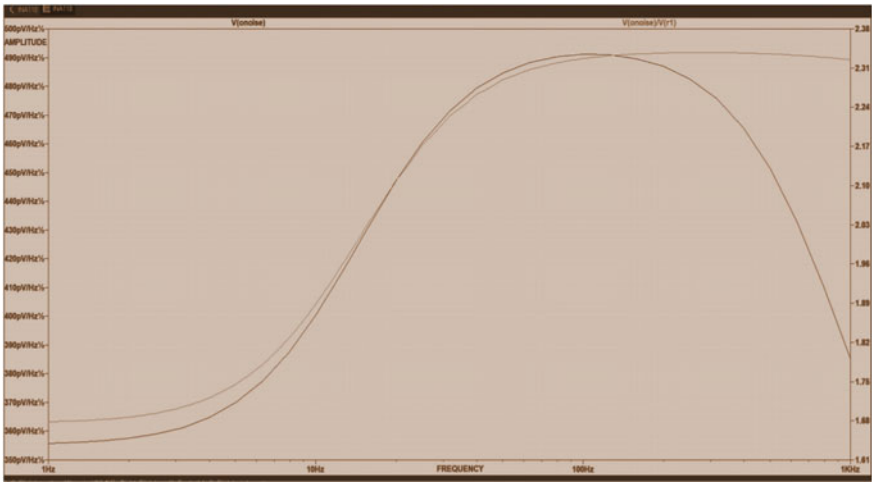

Fig. 11 INA118 amplification circuit output

serves the purpose of amplifying the feeble signal which is required. Hence, the INA 118 is selected as the preferred Instrumentation Amplifier for future processes.

Thus, by analyzing the above three circuits' power dissipation from Table 1, it is found out that INA 118 instrumentation amplifier satisfies both quantitatively and qualitatively.

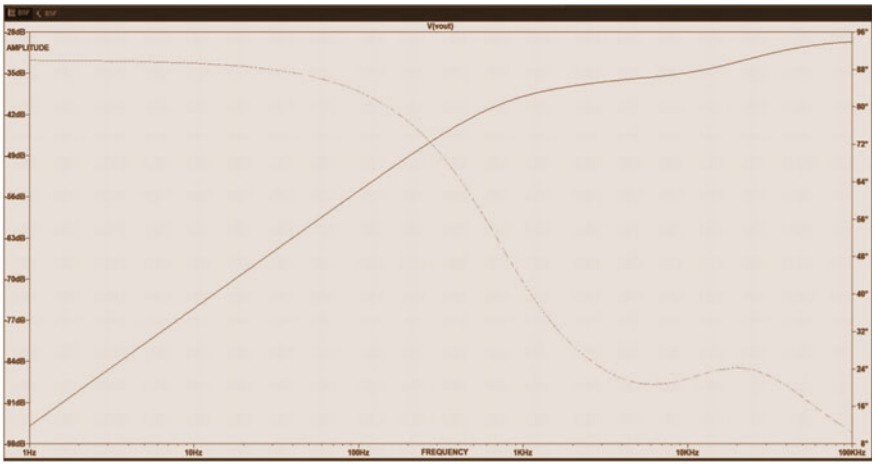

Fig. 12 Band-stop filter output

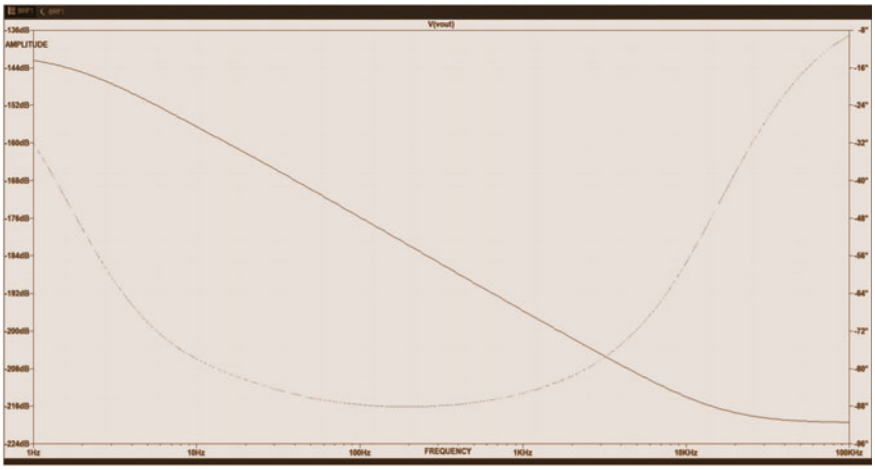

Fig. 13 Band-reject filter output

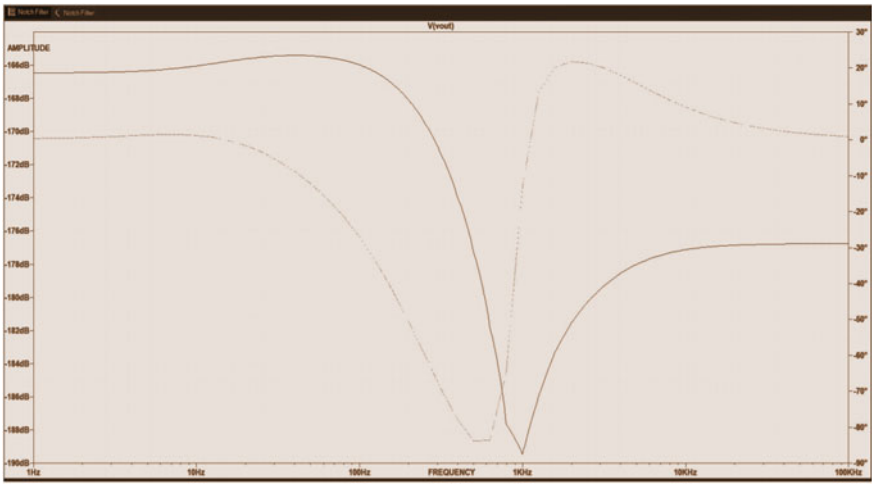

Fig. 14 Notch filter output

Table 1 Power dissipation

Instrumentation amplifier	Power dissipation (mW)
OP07	227
AD822	162
INA118	90

Table 2 Total harmonic distortion

For 50 Hz	SNR (in dB)	CMRR (in dB)
Band-stop filter	19.5	−63
Band-reject filter	42	−65
Notch filter	6	−67.5

3.2 Comparison and Analysis of Filters

The output of the BSF and BRF which allows or completely do not reject the noise, are shown in Figs. 12 and 13. From Fig. 14 there is a sharp curve in the notch filter output which rejects the noise at that frequency that is exactly required. Hence, the notch filter is selected for future processes. Thus, from analyzing the above Table 2 it is found that the Notch filter satisfies both Quantitatively and Qualitatively.

3.3 AC/DC Coupling

From Figs. 15 and 16, AC/DC coupling is used to eliminate the DC offset voltage, and hence, sensor output always generates the actual output without the necessity for any biasing.

Based on the studies carried out for various analog sections, the final signal conditioning circuit has been formulated and simulated as shown in Fig. 17. The output of the simulation in Fig. 18 provides a better result for the GMR sensor compared with any signal conditioning circuits.

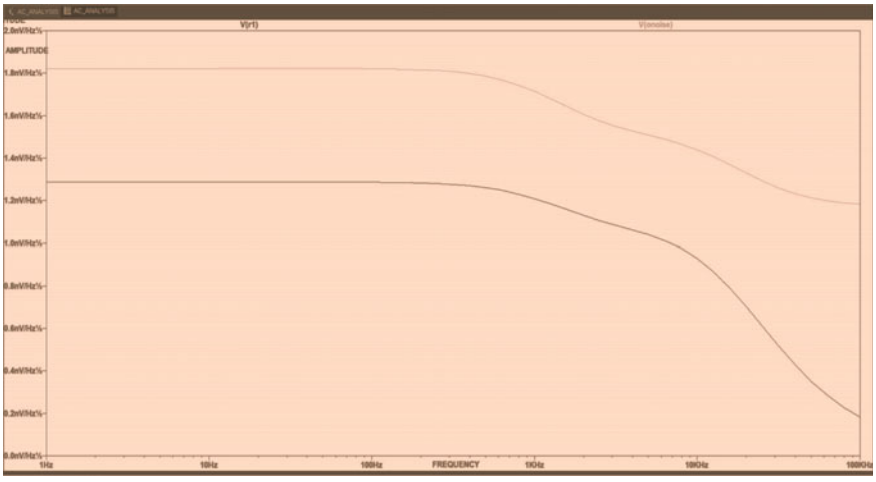

Fig. 15 AC coupling output

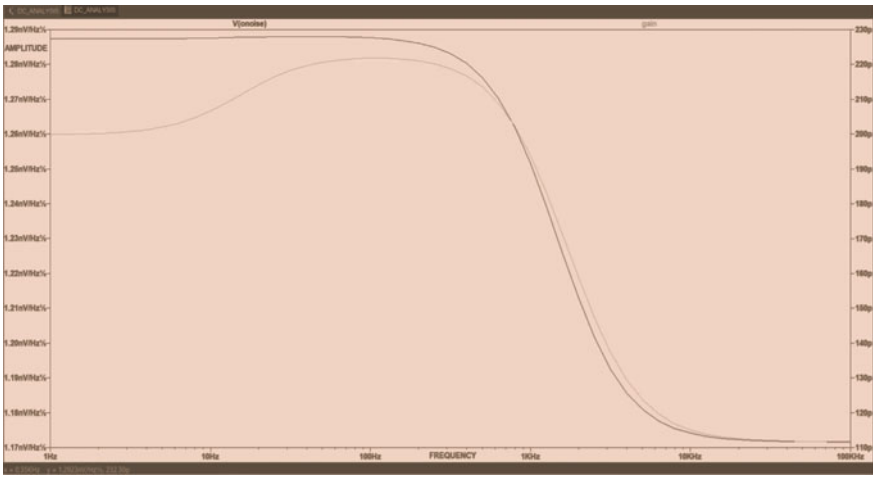

Fig. 16 DC coupling output

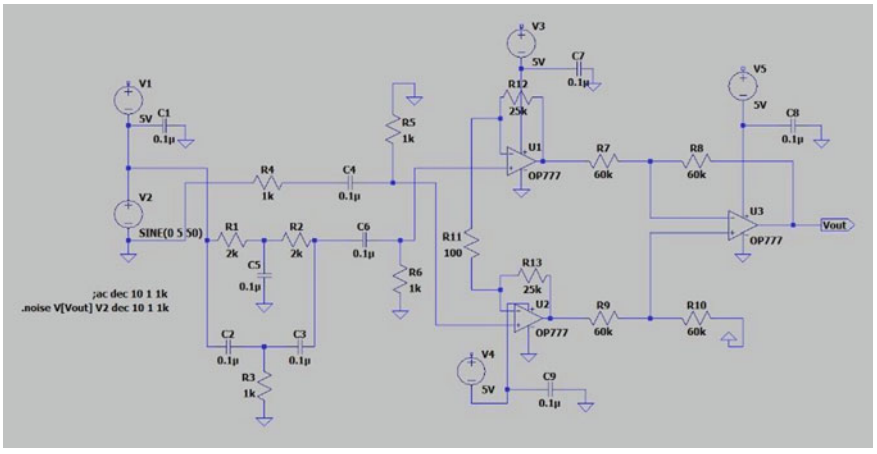

Fig. 17 Signal conditioning circuit implementation

4 Conclusion

The output from GMR sensors is very feeble which might be affected by the noise. Hence, there is a need for a signal conditioning circuit for better output. Based on various simulation studies for noise filtering, AC and DC coupling and amplification circuits for biomedical applications have been carried out, and the desired signal conditioning circuit is finalized to overcome the demerit of the GMR sensor. Now, signal conditioning circuit is ideally implemented in a software simulation platform. Further, it will be implemented in real time.

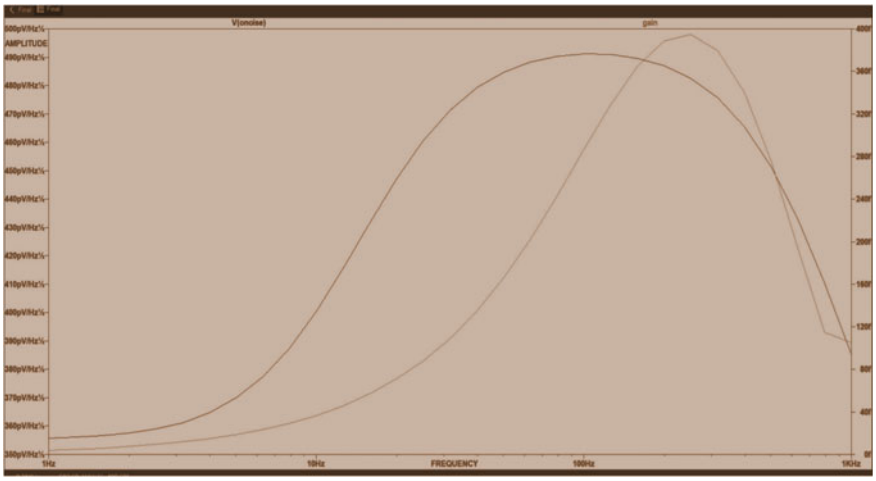

Fig. 18 Signal conditioning circuit output

References

1. S. Cardoso et al (2017) Challenges and trends in magnetic sensor integration with microfluidics for biomedical applications. J Phys D Appl Phys 50(21). https://doi.org/10.1088/1361-6463/aa66ec.
2. Park J (2015) Superparamagnetic nanoparticle quantification using a giant magnetoresistive sensor and permanent magnets. J Magn Magn Mater 389:56–60. https://doi.org/10.1016/j.jmmm.2015.04.049
3. Murzin D et al (2020) Ultrasensitive magnetic field sensors for biomedical applications. Sensors (Switzerland) 20(6):1–32. https://doi.org/10.3390/s20061569
4. Chugh VK, Kalyan K, Anoop CS, Patra A, Negi S (2017) Analysis of a GMR-based plethysmograph transducer and its utility for real-time blood pressure measurement. Proc Annu Int Conf IEEE Eng Med Biol Soc EMBS pp 1704–1707. https://doi.org/10.1109/EMBC.2017.8037170
5. Bernieri GB, Ferrigno L, Laracca M (2013) Improving performance of gmr sensors. IEEE Sens J 13(11):4513–4521. https://doi.org/10.1109/JSEN.2013.2271275
6. Daughton JM (2000) GMR and SDT sensor applications. IEEE Trans Magn 36(5):2773–2778. https://doi.org/10.1109/20.908586.
7. Smith CH, Schneider RW (1998) Magnetic field sensing utilizing GMR materials. Sens Rev 18(4):230–236. https://doi.org/10.1108/02602289810240592
8. Zhang D, Pan Z, Zhou H, Zhang W (2016) Magnetic sensor based on giant magneto-impedance effect using the self-regulating technology on the bias magnetic field. Sens Actuators, A Phys 249:225–230. https://doi.org/10.1016/j.sna.2016.09.005
9. Bhaskarrao NK, Anoop CS, Dutta PK (2017) A simple signal conditioner for tunneling magneto-resistance based angle sensor. In: 2016 IEEE annual India conference (INDICON), pp 1–6, 2017. https://doi.org/10.1109/INDICON.2016.7839065
10. Elangovan K, Anoop CS (2020) A digital signal-conditioner for resistive sensors and its utility for linearizing GMR-based magnetometer. 2020 IEEE Sens Appl Symp SAS 2020 - Proc, https://doi.org/10.1109/SAS48726.2020.9220031
11. Juárez-Aguirre R et al (2013) Digital signal processing by virtual instrumentation of a MEMS magnetic field sensor for biomedical applications. Sensors (Switzerland) 13(11):15068–15084. https://doi.org/10.3390/s131115068

12. Aminudin RDH, Iryanti M (2019) The characterization of giant magnetoresistance sensor for prototype of bridge deflection measurement. J Phys Conf Ser 1280(2). https://doi.org/10.1088/1742-6596/1280/2/022065

Modeling and Simulation of SPVGC System Using Conventional Controller

P. Chandra Babu, B. Venkata Prasanth, and P. Sujatha

Abstract This article addresses the system connected to the solar PV grid by the DC to DC converter and inverter (VSC) for the supply of electricity to the power grid, addressing the major device elements, which include the first one 20-kW solar array, second one grid side inverter and third one boost converter, mathematical modeling and THD change by irradiation effect. This paper begins with a PV system model, simulation circuit and discussion. This paper has a concise overview of all part included in this system and considers environmental temperature and solar radiation practical data at BVRIT campus. It also addressed a common algorithm for MPP monitoring. The results of simulations demonstrate how the variations in solar radiations will influence the production of any PV module and shows THD of the photovoltaic-grid connected.

Keywords DC–DC Converter · THD · P&O · SPV · VSC inverter

1 Introduction

Photovoltaic (PV) is the name of a method to convert solar energy into direct electrical energy using semi-conductive materials which exhibit the photovoltaic effect, a physical, photochemical and electrochemical phenomenon commonly studied. Solar panels consisting of multiples of solar cells can be used for supplying effective solar

P. Chandra Babu (✉)
Department of Electrical and Electronics Engineering, JNTUA College of Engineering, Anantapuram, India

Department of Electrical and Electronics Engineering, B V Raju Institute of Technology, Narsapur, Telangana, India

B. V. Prasanth
Department of Electrical and Electronics Engineering, QIS College of Engineering & Technology, Ongole, A.P, India

P. Sujatha
Department of Electrical and Electronics Engineering, JNTUA College of Engineering, Anantapuram, A.P., India

C. Subramani et al. (eds.), *Proceedings of International Conference on Power Electronics and Renewable Energy Systems*, Lecture Notes in Electrical Engineering 795,
https://doi.org/10.1007/978-981-16-4943-1_11

power in a photovoltaic system. The first stage includes the photoelectric effect from which a second electrochemical mechanism takes place involving the ionization of crystallized atoms in a series, producing an electric current.

Solar panels have variety of solar cells with different materials are used in PV power generation. Like silicone-based monocrystalline, polycrystalline, amorphous, copper indium sulfides and cadmium telluride products currently used in photovoltaic content. Solar cable copper links modules (cable modules), arrays (cable arrays) and subfields. The development of different solar cells has progressed rapidly in recent decades due to the rising demands for green energy [1, 2].

The lower the cost of solar energy, the more favorable it is relative to conventional energy, and the more attractive it is to electricity and energy users all over the world. In California, solar power is currently cheaper than most other peak generators, including those operating on low-cost natural gas, at prices far below USD 100/MWh ($0.10/kWh). Lower energy costs also boost demand for energy consumption, as the cost of renewable energy is very attractive relative to retail electricity prices. PV prices dropped considerably by 2011 and will continue to fall. The solar cell's average retail price under Solar buzz has fallen from $3.50 per watt to $2.43 per watt during 2011[3]. The "Best Class" price was expected to decline to $0.50/Watt at the end of 2012 and was anticipated to decline to $0.36/Watt before 2017. Many locations PV utilization increased and is usually defined as photovoltaic cost at or below the retail energy prices. Further, the conversion efficiency from solar to electricity is very low, with a figure of only 9–17%. So, similarly MPPT is a key part of a solar pv grid-based system that ensures that the maximum available energy is always extracted from the PV panel at all times and driven to the AC grid, an ideal infinite power sink [1, 2, 4–12]. The literature presents various MPPT algorithms, including P&O and Hill Climbing (H&C) [4], grid-related PV-connected power plants which operate parallel to conventional electrical sources and are primarily used as grid power supplies [4, 13].

The simplest grid connection system is implemented in MATLAB/Simulink, this model is similar to all practical residence use model having a PV array, and a converter unit connected at point of connection. The 3-phase grid-connected PV system with a widely used perturb and observe technique [4, 5] for maximum power point tracking (MPPT) used to evaluate model performance under variable irradiation condition.

2 System Description of PV Grid-Connected System

Figure 1 displays the components used in the proposed model of 20 kW PV arrays connected to a 25 kV grid. Perturbation and observation technology is being introduce for MPP. The major devices are (1) The utilities grid. (2) PV arrays with a power of 20 kW. (3) DC–DC boost converters (magenta block) which are used to raise the PV output to 500 V DC. (4) 3-phase VSC inverter (orange blocks) which is used to transform the DC voltage supplied by arrays (500 V) to an AC voltage of 260 V.

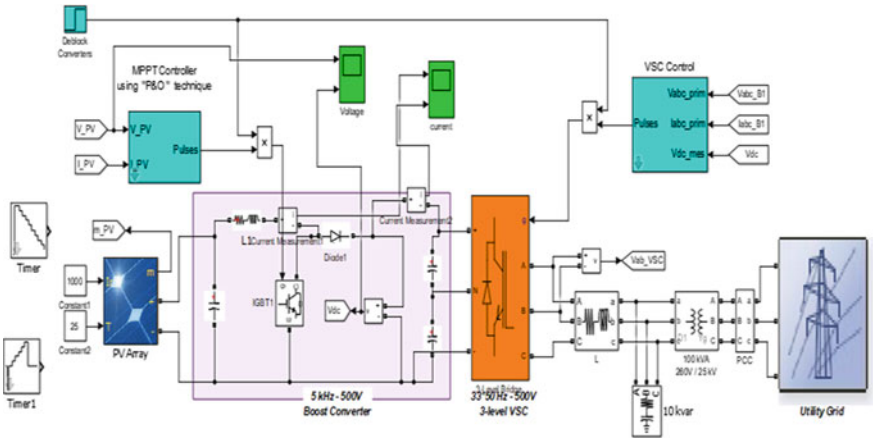

Fig. 1 PV system with grid connection

(5) A 100 kVA three-phase coupling transformer. 260/25 kV. (6) Capacitor banks 10 kVar used to damp out the harmonics generated by the VSC.

3 Modeling of PV Array and MPPT

3.1 PV Array Modeling

The solar cell is the solar panel's building block. The mathematical model is developed and derived to better understand the PV module. The performance characteristics of the PV module are highly dependent on three important factors, namely solar radiation, cell temperature and PV module output voltage.

The mathematical modeling of the solar panel (module) is evaluated in order to obtain the performance characteristics of the PV module. The parameters of voltage, current and power output vary according to radiation, temperature and load current. The impact of these three variations is taken into account in the simulation process such that temperature and solar shifts arise. In view of PV cell output power (P) and voltage, the PV cell performance is calculated under solar (S) radiation and temp. (T). Relevant equations can be obtained on the basis of Kirchhoff's first law. The performance characteristics of PV cell models can be described in these equations.

3.1.1 Ideal Solar Cell Model

Analogous circuit in illustration 2 can be interpreted as an ideal solar cell. A solar cell equation shown in Eq. 1 defines the IV characteristic.

$$I = I_{\text{ph}} - I_o(\text{ekT}^{\text{qv}} - 1) \tag{1}$$

3.1.2 Practical Solar Cell Model

The I–V properties of a true solar cell differ from the properties of the ideal solar cell. The functional solar cell can have a set of parallel resistors (circuit see Fig. 2).

$$I = \text{Iph} - \text{Id} - \text{Ish} \tag{2}$$

The current flow creates voltage drop in the elements of the identical circuit. Voltage is obtained between the diode and resistor is

$$\text{Vj} = V + \text{IRc} \tag{3}$$

The photon generated current can be expressed by

$$\text{Iph} = \text{NpIg} \tag{4}$$

$$\text{Ig} = \text{NpIg} \tag{5}$$

$$I_G = \frac{\text{Icc Gi}}{1000} + I(T_t - T_r) \tag{6}$$

The current transferred more to the diodes, after the series resistance is ignored.

$$I_D = N_p I_{\text{cat}} \left\{ \text{exe}\left(\frac{qV0}{N_c \text{AEkT}} \right) - 1 \right\} \tag{7}$$

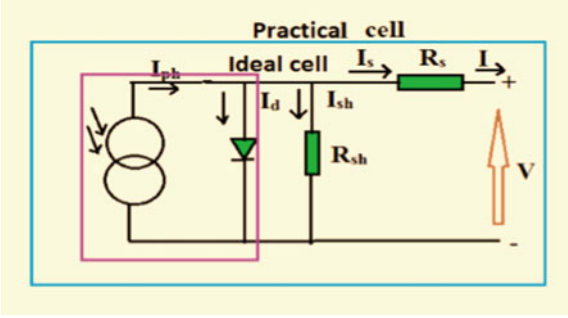

Fig. 2 PV cell equivalent circuit

In the above-mentioned equation, the saturation rate is the Icat, A is the ideal component, k is the Boltzmann constant, N_c the series number of cells, q is the electron load, V_0 is the PV module output voltage, N_p is the number of cells.

Reverse saturation current (RSC) is provided

$$I_{\text{sat}} = I_{\text{or}} \frac{T^3}{T_r} \exp\left[\frac{qE_g}{kT}\left(\frac{1}{T_r} - \frac{1}{T}\right)\right] \tag{8}$$

The current is delivered by the shunt resistor

$$I_{\text{sh}} = \frac{\text{Vo}}{\text{Ns Rsh}} \tag{9}$$

The complete output current from the PV module is, substitute Eqs. 7, 8 and 9 in 2

$$I = N_p I_g - N_p I_{\text{sat}} \left\{\exp\left[\frac{qV_{\text{o}}}{N_s \text{AkT}}\right] - 1\right\} - I_{\text{sh}} \tag{10}$$

The cell diode saturation current depends on the cell temperature and is described by

$$I_{\text{sat}} = I_{\text{or}} \frac{T^3}{T_r} \exp\left[\frac{qE_g}{kT}\left(\frac{1}{T_r} - \frac{1}{T}\right)\right] \tag{11}$$

The fill factor of solar cell is calculated as a division of the maximum power that is converted into electrical power and described as

$$\text{Fill Factor} = \text{FF} = \frac{\text{VMP IMP}}{\text{VOC ICC}} \tag{12}$$

Solar cell efficiency is calculated as a fraction of converted power to input power, see Eqs. 13 and 14

$$P_{max} = V_{\text{oc}} I_{\text{sc}} \text{FF} \tag{13}$$

$$\eta = \frac{V_{\text{oc}} * I_{\text{sc}}\ \text{FF}}{P_{\text{in}}} \tag{14}$$

In the above equation, V_{oc}, ISC, FF are the voltage of the opening circuit, short-circuit current and fill factor, η is the efficiency. Manufacturer specifications for the module «1Soltech 1STH-215-P» are listed in Table 1, the 20 k-Watts grid-connected PV array composed of 10 parallel strings and each string having 10 series connected modules, total 100 modules connected, each one produce 213.15 W, total power is 21.315 KW, i.e., (10 * 10 * 213.15 W = 21.315 kW).

Table 1 PV module configuration details

Selected parameters	Values
Parallel String	10
Series connected modules per string	10
Module	1Soltech 1STH-215-P
Max. Power	213.15 W
Voc	36.3 V
Isc	7.84 A
Vmp	29 V
Imp	7.35 A
Ncell	60

3.2 Maximum Power Point Tracking (MPPT)

PV module efficiency is an issue that limit the large utilization of PV systems so a DC–DC is installed into any MPPT system using an MPP controller. It can run the PV systems for a certain set of conditions at the maximum power point and optimize the array performance. This is achieved by the MPPT by continuously regulating the voltage or current irrespective of the attached load attached. As a result, several MPP tracking (MPPT), the most common method used in the present analysis, was developed and implemented, namely perturb and observe [3, 13–15]. MPPT techniques vary in complexity, needed sensors, convergence speed, cost, efficiency range, hardware implementation, popularity, and in other respects [3, 15].

The ability to track the maximum power point (MPP) for the uniform solar irradiation has proved traditional MPPT technique. However, traditional techniques have struggled to detect the true MPP under rapidly changing environments and partly shaded conditions [12]. The P&O and H&C are widely used and popular because they are easy to apply [3, 14] in this paper, P&O is considered for implementing MPPT in PV system.

In general, the following properties should be given by a good MPPT algorithm, which also succeeds in partial shading conditions [11]. (1) Monitoring MPP easily to achieve high performance, (2) Simple to use with a low device load, (3) The need for fewer and less costly sensors (removing boost conversion sensors reduces cost significantly) (4) Impose minimum disruption at grid side. [11]

3.2.1 P&O MPPT

The output voltage of the PV array is interrupted by a small rise in the P&O algorithm resulting in a power shift (Del P). When the Del P is positive, the voltage adjusts to the MPP. It was in the same direction. If the negativity of Del P is reached, the device is not running at the optimum location, so it is necessary to reduce the size of the device to return the operating point to the MPP [13].

3.3 Boost Converter

The diagram shows the simple boost converter in Fig. 3. It is used if the output voltage is greater than the input voltage. The inductor current flows through the diode with $V_x = V_{o,}$ while the transistor is ON $V_x = V_{\text{in}}$. It is assumed that the current is still flowing for this analysis (continuous conduction). The voltage around the inductive system is shown in Fig. 4, and the average voltage must be zero for the constant average current.

$$V_{\text{in}} t_{\text{on}} + (V_{\text{in}} - V_0) t_{\text{off}} = 0 \tag{15}$$

You can change this to the following

$$\frac{V_o}{V_{\text{in}}} = \frac{T}{t_{\text{off}}} = \frac{1}{(1 - D)} \tag{16}$$

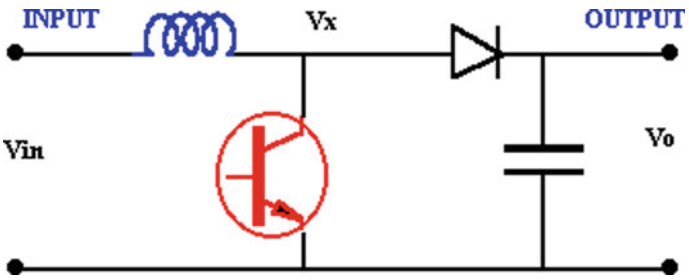

Fig. 3 Boost converter circuit

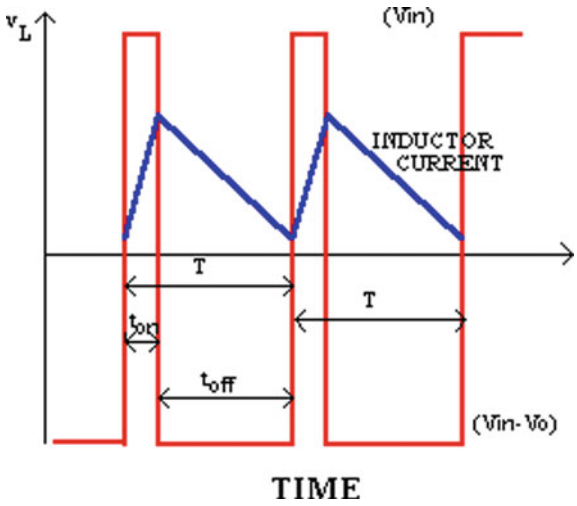

Fig. 4 Voltage and current waveforms

and the power balance provides for a lossless circuit is

$$\frac{I_O}{I_{\text{in}}} = (1 - D) \tag{17}$$

The voltage output must be greater than the input voltage, as the duty ratio "D" is 0 to 1. A negative sign means that the voltage is inverted. Input voltage for a converter is $V_{\text{in}} = 290$ V, then output voltage $V_{\text{o}} = 290/(1–0.42) = 500$ V.

3.4 VSC Inverter

Direct power (DC) and voltage are provided by PV modules. However, alternating current (AC) and voltage (AC) are required in order to feed the electricity to the grid. Inverter is the unit for converting DC to AC. They may also be responsible for maintaining the PV array operating point on the MPP. It is also done with MPP monitoring algorithms for controlling purposes. The VSC converts 500 V DC voltages to 260 V AC and retains the unit power factor. The control mechanism of VSC consists of 2 control loops, which are (a) external & (b) internal control loops, in both cases PI controller was implemented.

a. A loop regulates DC link voltage to ±250 V. (Read color)
b. B loop provides current components (Yellow color) by regulates grid currents, see Fig. 5 control circuit.

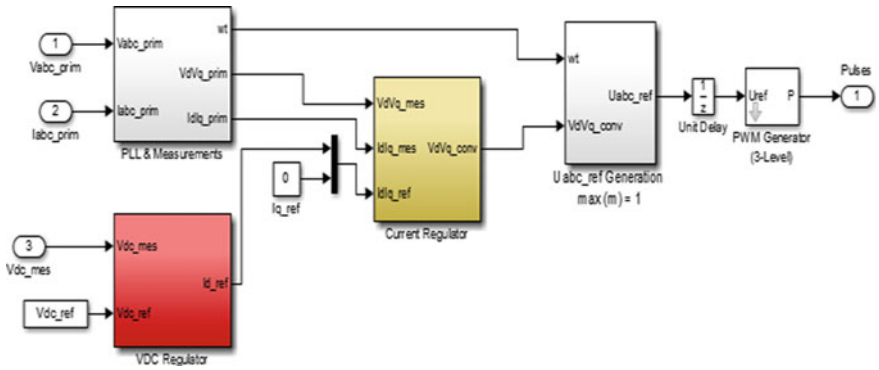

Fig. 5 control circuit of VSC

4 Simulation Results

4.1 Simulink Model of PV Cell

In the present model, 60 cells are connected in series, each cell voltage is 0.605 V, a simple PV module circuit as shown in Fig. 2. To compare the operational behavior of PV cell module, the simulation is performed with different solar irradiations like 250, 500, 850 W/m^2 and 1000 W/m^2 with constant temperature 25 °C, the corresponding MPP changes from 5.342 kw, 10.8 kw, 18.22 kw and 21.32 kw, respectively, see Fig. 6. For different irradiation conditions, the performance characteristics (current vs voltage curve) of PV array are shown in Figs. 6a. The MPP is changes from 19.54 kw, 20.86 kw to 21.32 kw when temp changes from 45 °C, 35 °C and 25 °C, respectively, with constant 1000 W/m^2. As it can be seen from current vs voltage curves, the PV cell current is highly dependent on the value of solar irradiation. The output power is reduced when irradiation is reduces from 1000 to 250 W/m^2. Figure 1 shows the simple circuit diagram of PV grid-connected system, through dc–dc converter and inverter.

In this paper, standard test condition and practical test conditions are considered for performance evaluation. In the standard test condition, solar irradiance is taken as 1000 W/m^{2,} and temperature is taken as 25 ∘C as shown in Fig. 7a. In the practical test condition, solar irradiance and temperature one year from September 2018 to August 2019 is logged at B V Raju Institute of Technology, Narsapur, Medak, Telangana as shown in Fig. 7b. Month wise mean values of solar irradiance and temperature are calculated as shown in Fig. 7c and with this data performance of proposed grid-connected PV system is evaluated.

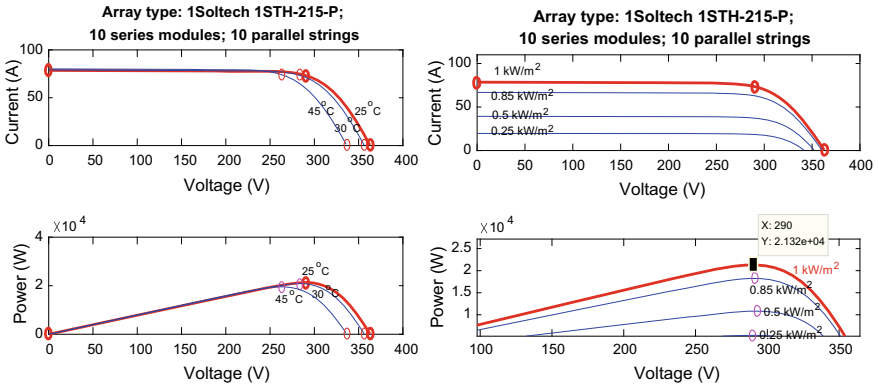

Fig. 6 I–V and P–V curve at **a** different temperatures 25, 30 and 45 degrees at 1000 irradiation **b** different irradiation 1000, 850, 500 and 250 W/m^2 at 25°

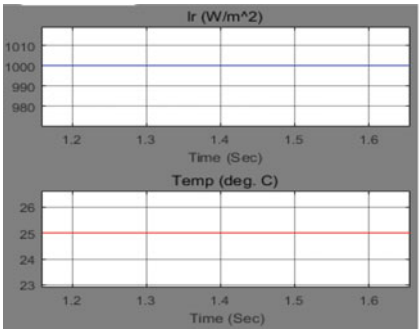

(a) STC condition

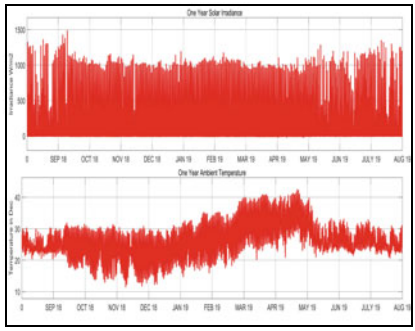

(b) PTC Condition

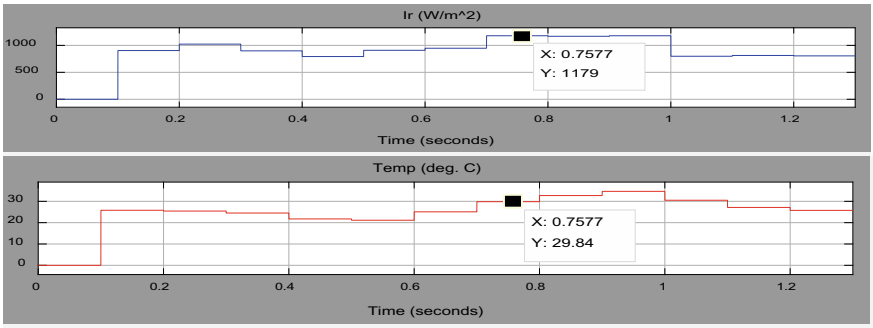

(c) Simplified Temperature and Irradiation

Fig. 7 Simulation diagram of irradiation and temperature in different condition

4.2 STC Condition

In the standard test conditions, PV voltage (V) and PV current (A) are show in Fig. 8a, b, respectively, actual and reference DC link voltages are compared and plotted in Fig. 8c. Since the solar irradiance and temperature are constant at all instances, PV output also constant at all the instances. The PV output power and grid power are compared and plotted in Fig. 9. Power difference of 2 kW is recorded between output power and grid power and considered as converter losses. Grid current and voltage are plotted in Fig. 10a, b, Fig. 11 represents inverter line to line voltage.

4.3 Dynamic Condition

In the dynamic test conditions, PV voltage (V) and PV current (A) are not changed, and actual and reference DC link voltages are compared and plotted in Fig. 12. Since the solar irradiance and temperature are variable at all instances, PV output also varies at all the instances. The PV output power and grid power are compared and

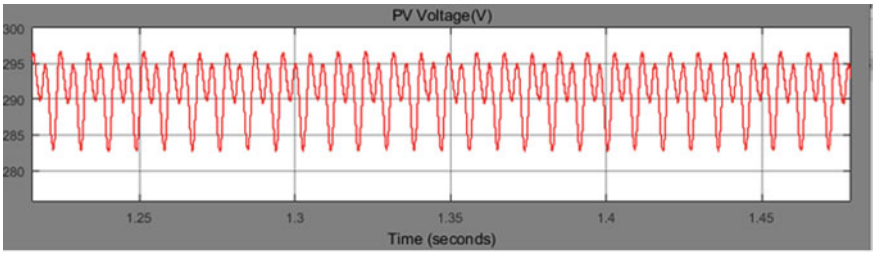

(a)

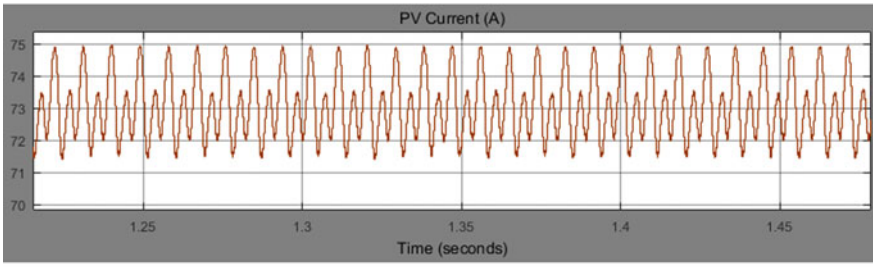

(b)

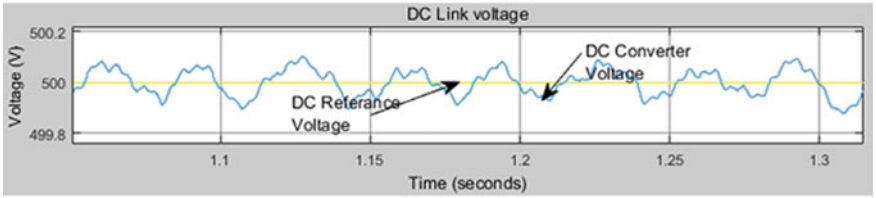

(c)

Fig. 8 **a** Voltage and **b** current generated by PV **c** DC Link voltage comparing with reference voltage

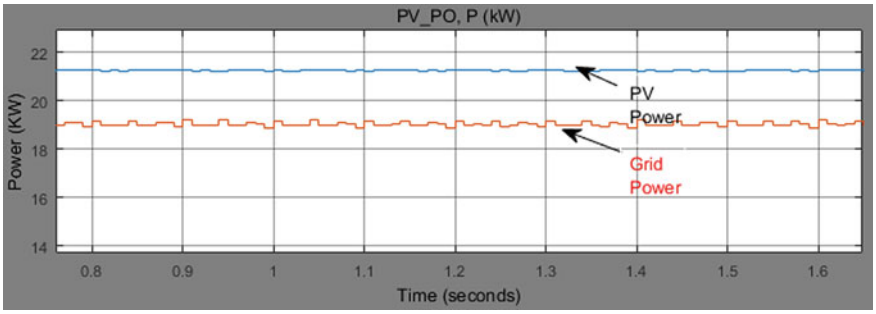

Fig. 9 Powers generated by the PV and grid power

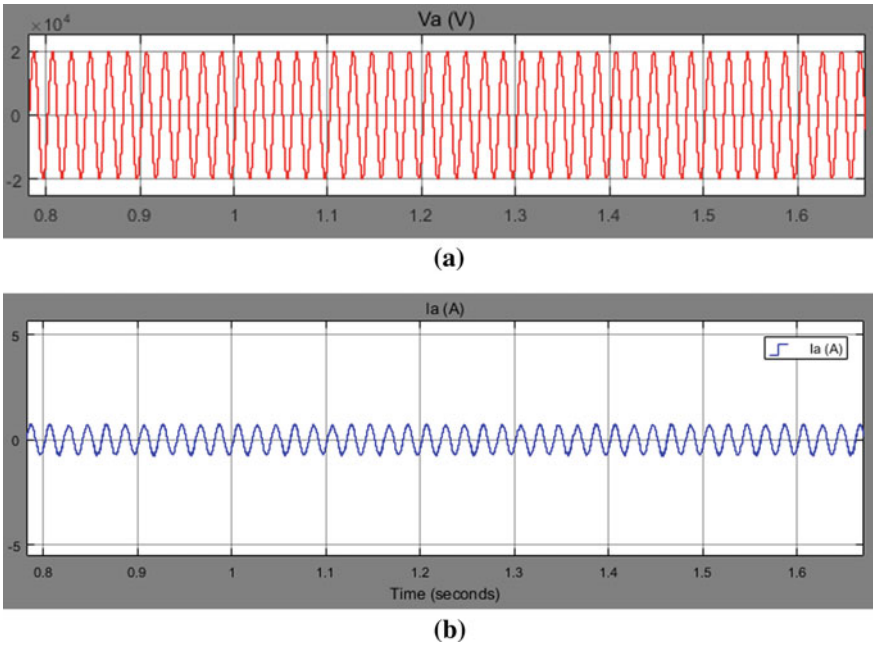

Fig. 10 Current and voltage injected into the grid **a** grid voltage **b** current

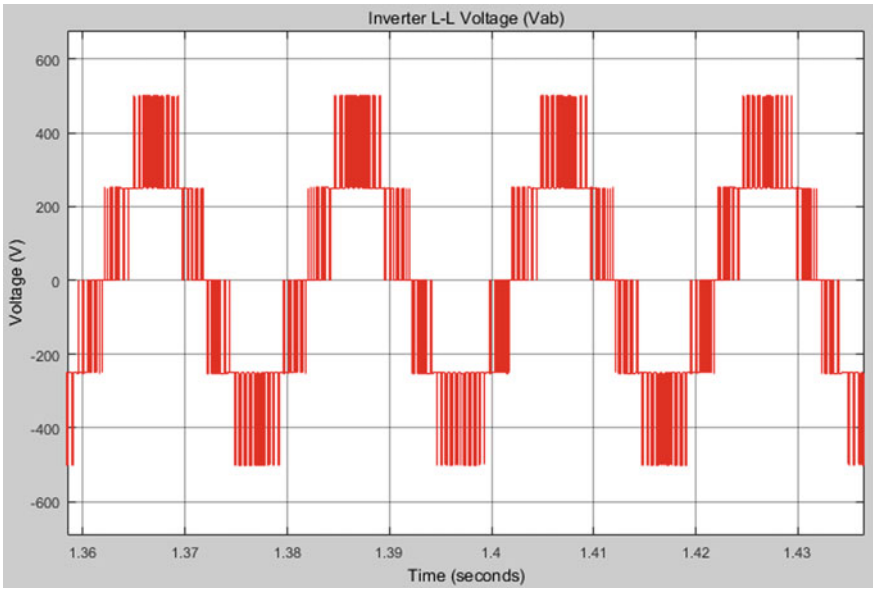

Fig. 11 DC–AC inverter line to line voltage

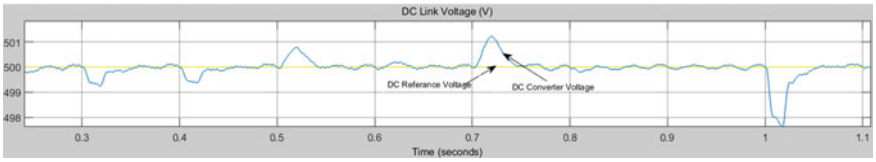

Fig. 12 PV output characteristics DC link voltage

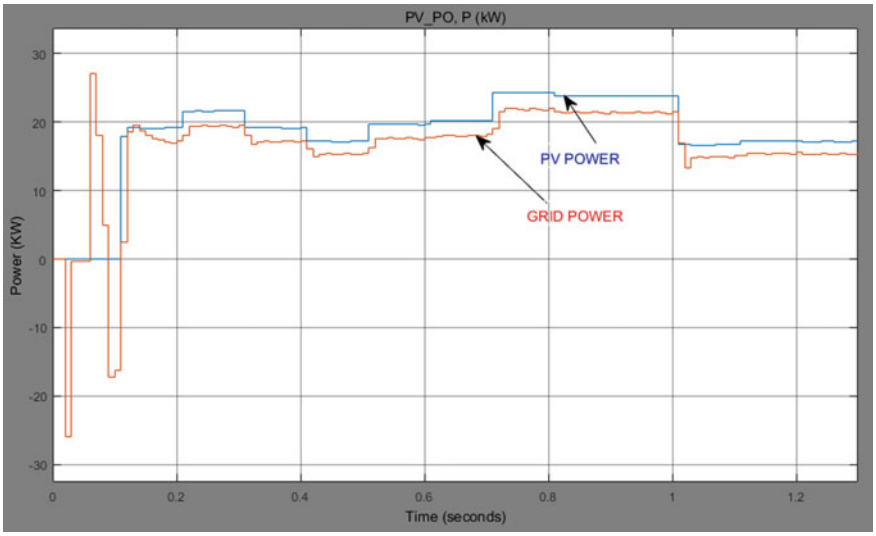

Fig. 13 Power flow at grid side and source side

plotted in Fig. 13. Power difference at 0.76 s is 2.6 kW is recorded between output power and grid power and considered as converter losses.

The THD analysis in the both cases are analyzed, in the STC conditions, the grid current THD is reported as 9.67%, similarly in PTC grid current THD is reported as 15.77%. Hence, significant amount of THD is varied from STC to PTC conditions see Fig. 14. Nevertheless, control topologies need to be enhanced to overcome this.

5 MPPT Performance Key Points

5.1 Tracking

The GMPP Access: Since solar photovoltaic systems do not even obtain uniform sunshine for a short period of time between very near areas, partial shading is also possible due to inevitable conditions [12, 16]. These situations can lead to multiple

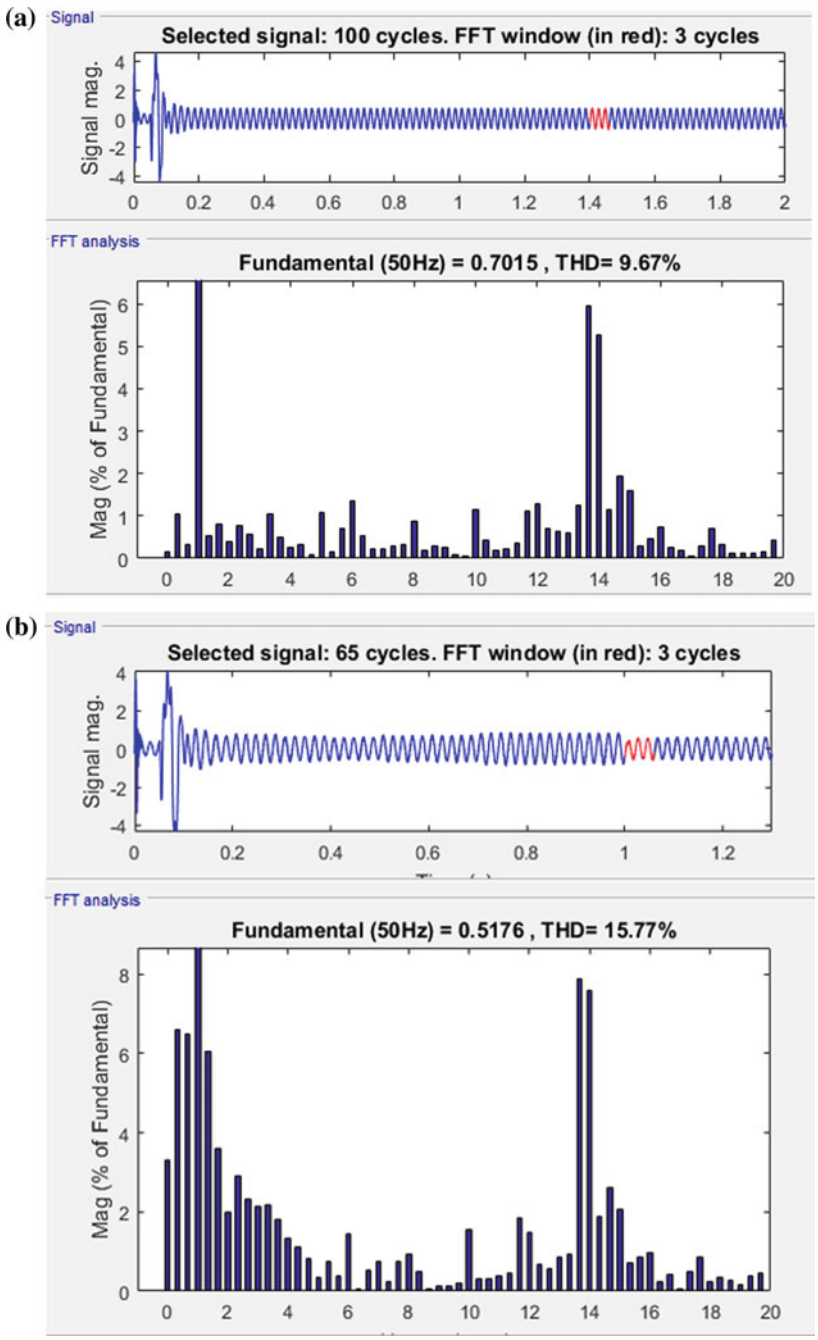

Fig. 14 THD analyses of 50 Hz grid current wave form **a** THD at STC. **b** THD at dynamic conditions

LMPPs, which are based on the IV–PV feature, affecting the MPPT tracking performance. Traditional MPPT algorithms are ineffective for monitoring and shading GMP PCs, while intelligent MPPT for optimization are designed to track GMPP over several LMPPs.

5.2 Convergence Speed

A strong MPPT algorithm needs to converge at the appropriate current and voltage with good speed and accuracy, regardless of the constant or dramatic change in solar irradiance. Reasonably, the GMPP takes more time than the hybrid solution to adopt a traditional maximum power point. In addition, the GMPP incorporates hybrid algorithms with limited or reduced oscillations [12, 16].

5.3 Sensitivity

An effective MPPT algorithm must be sufficiently adaptive to handle any conditions and changes in the atmosphere. It needs to be able to respond quickly and track the GMPP in a particular PV system [17].

5.4 Design Complexity

One of the important factors is the selection of an adaptable MPPT which is retained due to the difficulty of its development for a specific PV device [12, 16]. How successful the algorithm searches for the real GMPP in the life of various LMPPs depends on how complex the MPPT technique is. In addition, the photovoltaic system does not harvest the entire solar energy.

6 Conclusion

Due to the abundance of sunlight, SPV is the best and important source of electricity in the renewable energy system. But it has some disadvantages, such as weather interference, poor efficiency. For this function, a power electronics interfaced MPPT is used to obtain maximum power from a photovoltaic system. In this paper, we have discussed and analyzed the modeling of PV array, most recent technique, i.e., P&O based MPPT and grid-connected system output power, I–V, P–V characteristics, PV power, THD at STC and practical condition and required performance key points for any MPPT are discussed. THD verified with real PV input data, it changed from

9.67% to 15.77% due to source side disbalances caused due to change in irradiation and temperature.

References

1. Technical Report, "Growth of electricity sector in India from 1947–2012", Central Electricity Authority (CEA) of India
2. Doolla S Grid connection issues for distributed generation—review & standards. Department of Energy Science and Engineering, Indian Institute of Technology Bombay
3. Subudhi B, Pradhan R (2013) A comparative study on maximum power point tracking techniques for photovoltaic power systems. IEEE Trans Sustaine Energ **4**(1)
4. Sera D et al (2013) On the perturb-and-observe and incremental conductance MPPT methods for PV systems. IEEE J Photovoltaics 3(3):1070–1078
5. Zope PH et al (2010) Performance and simulation analysis of single-phase grid connected PV system based on source inverter. In: International conference on power electronics, drives and energy system
6. Kasera J et al Design of grid connected photovoltaic system employing incremental conductance MPPT algorithm. J Electr Eng
7. Sujatha P et al (2020) Implementation of anfis-mptc for 20 kwp spv power generation and comparison with flmppt under dissimilar conditions. Int J Amb Energy 41(1):1–11. https://doi.org/10.1080/01430750.2019.1707117
8. Ram JP Rajaseka N, Miyatake, M (2017) Design and overview of maximum power point tracking techniques in wind and solar photovoltaic systems: a review. Renew Sustainable Energ Rev 73:1138–1159. https://doi.org/10.1016/j.rser.2017.02.009
9. Adly M, Strunz K (2018) Irradiance-adaptive PV module integrated converter for high efciency and power quality in standalone and DC microgrid applications. IEEE Trans Industr Electron 65(1):436–446. https://doi.org/10.1109/TIE.2017.2723860
10. Technical Report, "Monthly all india installed generation capacity report, June 2014", Central Electricity Authority (CEA) of India
11. https://energyeducation.ca/encyclopedia/Photovoltaic_cell.
12. Ghasemi MA, Foroushani HM, Parniani M (2016) Partial shading detection and smooth maximum power point tracking of PV arrays under PSC. IEEE Trans Power Electron 31(9):6281–6292
13. "Photovoltaic Cell Conversion Efficiency," U.S. Department of Energy, Retrieved, 19 May 2012
14. Kamarzamana NA, Tanb CW (2014) A comprehensive review of maximum power point tracking algorithms for photovoltaic systems. Renew Sustain Energ Rev 37:585–598
15. Onat N (2010) Recent developments in maximum power point tracking technologies for photovoltaic systems. Int J Photoenergy 1–10
16. Ali A et al (2020) Investigation of MPPT techniques under uniform and non-uniform solar irradiation condition–A Retrospection. IEEE Access 8:127368–127392. https://doi.org/10.1109/ACCESS.2020.3007710
17. Venkata Prasant B (July 2019) Performance evaluation of MPPT in a PVG with conventional and intelligent controllers under STC and DTC. Int J Recent Technol Eng ISSN: 2277-3878, 8(2):4984–4991. https://doi.org/10.35940/ijrte.b1075.078219

Study of the Operating Parameters of a Two-Bed Adsorption System: Comparison Between the Silica–Gel–Water and Zeolite–Water Pairs

Mouhamadou Lamine Cisse and Biram Dieng

Abstract The aim of this work is to model firstly the different components of a two-bed adsorption cooling system with continuous cold production fed by hot water from biogas or thermal sensors, then in a second step, to the numerical resolution in order to determine the evolution of the various temperatures at the level of the adsorber, the desorber, and to evaluate the COPs. For the validation of the model, the zeolite–water couple was compared with the literature. The results of the analysis show that the COP of zeolite–water is 0.38, lower than that of silica–gel–water which is 0.62. The evaporating temperature reached is between 0 and 5 °C and the cooling temperature between 8.01 and 8.55 °C. This temperature range is acceptable as it is intended for dairy products. The variation in the desorbed fraction is between 1.36 and 1.47 kg/kg s (decrease in the desorbed fraction), during adsorption, it is between −1.1 and −1.05 kg/kg s (increase in the adsorbed fraction). The desorption temperatures reached are 56.8 °C for silica–gel and 51.25 °C for zeolite–water.

Keywords Simulink · Zeolite · Water · Dormand–Prince · Temperature · Desorption

1 Introduction

The demand for energy, especially in refrigeration, is considerable [1].

Adsorption systems have received a lot of attention in recent years because of their environmental friendliness. This study is interested in the production of cold by adsorption with biogas and thermal sensors as energy source. It is a two-bed system. It is used for the preservation of dairy products with a temperature range of 4–8 °C. This type of system constitutes a promising application for solar cooling in general

M. L. Cisse (✉) · B. Dieng
Research Team in Renewable Energies, Materials and Lasers, Department of Physics UFR SATIC, University Alioune Diop of Bambey Senegal (UADB), Campus, Diourbel BP 30, Bambey, Senegal

B. Dieng
e-mail: biram.dieng@uadb.edu.sn

C. Subramani et al. (eds.), *Proceedings of International Conference on Power Electronics and Renewable Energy Systems*, Lecture Notes in Electrical Engineering 795,
https://doi.org/10.1007/978-981-16-4943-1_12

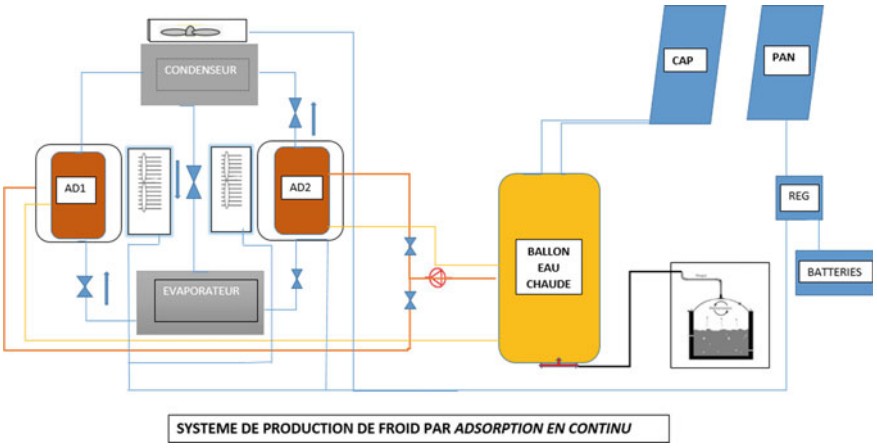

Fig. 1 Study system

and for the adsorption system in particular. The coefficient of performance will thus be the subject of a determination, as will the other operating parameters (Fig. 1).

2 System Description

The heat is supplied by hot water produced either from the thermal sensor, more precisely the vacuum sensor, or from biogas. The hot water enters the desorber (E2) and transmits its heat to the adsorbent. The latter begins the desorption of the refrigerant contained within it as soon as it reaches the desorption temperature. Then the desorbed fluid being in the form of vapor will condense in the condenser with rejection of heat. Finally, when it reaches saturation pressure, the fluid is passed to the evaporator.

During this time, the adsorber (E1) cooled by fans begins an adsorption phase of the evaporated fluid at the level of the evaporator allowing continuous cold production. The two elements work alternately.

The system will be controlled by valves.

3 Mathematical Model

3.1 Adsorbent Bed

Many studies have focused on mathematical modeling, especially for a cylindrical generator, which is the typical configuration, both for the arts and the basic structure of other complex generators [2, 3]. Because adsorption refrigeration is essentially a phenomenon involving heat and mass transfer processes, the modeling work is primarily concerned with adsorption performance, heat transfer in the adsorbent bed, and the transfer process coupled mass. Among the different adsorption performance models, non-equilibrium adsorption models (nonlinear equations) have become increasingly dominant [4, 5], while equilibrium adsorption models have received less attention [6, 7].

3.2 Energy Balance

The mathematical model of the physical problem stated below is presented as follows.

Energy balance is at the level of the adsorber and desorber.

The heat transfer can be described as follows where $\delta = 0$ if the concerned compartment operates as a desorber and $\delta = 1$ if the concerned compartment operates as an adsorber.

If $\varphi = 1$, the adsorber is connected to the evaporator, and if $\varphi = 0$, the adsorber is connected to the desorber.

$$\begin{aligned}(m_{\text{ad}} * C_{\text{ad}} + m_a * C_a + m_a * w * Cp_r) * \frac{\mathrm{d}T_a}{\mathrm{d}t} &= m_a * \Delta H_{\text{ads}} * \frac{\mathrm{d}w}{\mathrm{d}t} \\ &+ \delta m_a * Cp_{r,v} * \left[\varphi(T_{\text{ev}} - T_a) + (1-\varphi)\left(T_{r,v} - T_a\right)\right] * \frac{\mathrm{d}w}{\mathrm{d}t} \\ &+ \dot{m}_{f,\text{ad}} * Cp_f\left(T_{j,\text{in}} - T_{j,\text{out}}\right) \end{aligned} \quad (1)$$

Condenser

$$\begin{aligned}\left(m_{r,\text{cd}} * Cp_r + m_{\text{cd}} * C_{\text{cd}}\right) * \frac{\mathrm{d}T_{cd}}{\mathrm{d}t} &= -m_a * \frac{\mathrm{d}w_{\text{des}}}{\mathrm{d}t} * L_v \\ &- m_a * cp_{r,v} * \frac{\mathrm{d}w_{des}}{\mathrm{d}t}\left(T_{\text{gn}} - T_{\text{cd}}\right) \\ &+ \dot{m}_{f,\text{cd}} * \text{cp}_f(T_{j,\text{in}} - T_{j,\text{out}}) \end{aligned} \quad (2)$$

Evaporator

$$\left(m_{\text{ev}} * m_{r,\text{ev}} * C_{p,r}\right)\frac{\mathrm{d}T_{\text{ev}}}{\mathrm{d}t} = -m_a * \frac{\mathrm{d}w_{\text{ads}}}{\mathrm{d}t} * \text{Lv}$$

Table 1 Parameters

Symbol	Value	Unit
ma	50	kg
Mf, ad	1.6	m^3/h
mr, ev	10	kg
Ca	0.924	Kj/kg K
Cpr, v	1.85	kJ/kg K
Cad	0.905	Kj/kg/K
ΔHads	2800	KJ
Lv	2500	KJ
UAcd	6090	W/K-
Mf, ev	2	m^3/h
Mf, cd	3,7	m^3/h
Tev, in	9	°C
Tcd, in	30	°C
Tg, in	70	°C
UAev	3420	W/K
Ccd, Cev	0.386	Kj/kg/K
mad	64.04	kg
Mcd	24.28	kg
mev	12.45	kg

$$- m_a * \frac{\mathrm{d}w_{\mathrm{des}}}{\mathrm{d}t} * \mathrm{Cp}_r * (T_{\mathrm{cd}} - T_{\mathrm{ev}}) + \dot{m}_{f,\mathrm{ev}} * \left(T_{j,\mathrm{in}} - T_{j,\mathrm{out}}\right)(\mathrm{kW}) \tag{3}$$

Calculation of COP.

$$\mathrm{COP} = \frac{Q_{\mathrm{ev}}}{Q_{\mathrm{des}}} \tag{4}$$

3.3 Numerical Solution

The numerical method used is that of Dormand–Prince. This method is nothing other than that of EULER of order 45. The primary data used in the numerical calculations are given in Table 1.

4 Simulations

This curve Fig. 2 shows that the desorption temperature varies between 49 and 56.8 °C. It reaches a maximum value equal to 56.8 °C. The adsorption temperature has an initial value of 55 °C, then it decreases to 49.2 °C considered as the end of adsorption value. After these two phases, preheating (from 49.2 to 50.8 °C) and precooling are observed.

An increase in the variation dw/dt of the desorbed fraction is observed Fig. 3. This shows that the desorbed fraction decreases over time. The minimum value of the variation is 1.36 kg/kg s, and the maximum value of the variation is evaluated at 1.47 kg/kg s. This evolution is justified because the desorption being progressive, the fraction decreases over time. It stops at the end of the desorption.

A negative growth is observed in the variation dw/dt of the adsorbed fraction Fig. 4. This shows that the adsorbed fraction increases over time. The minimum value of the variation is −1.1 kg/kg s, and the maximum value of the variation is evaluated at −1.05 kg/kg s.

The simulation shows a constant condensing temperature equal to 30 °C. Figure 5.

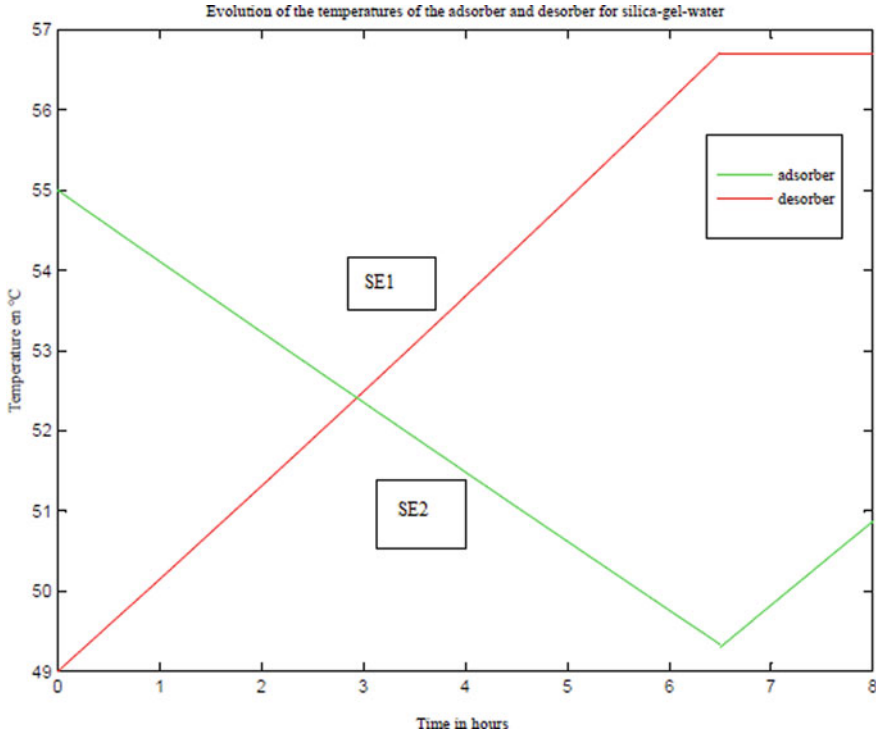

Fig. 2 Temperature evolution at the adsorber and desorber as a function of time for the silica–gel water

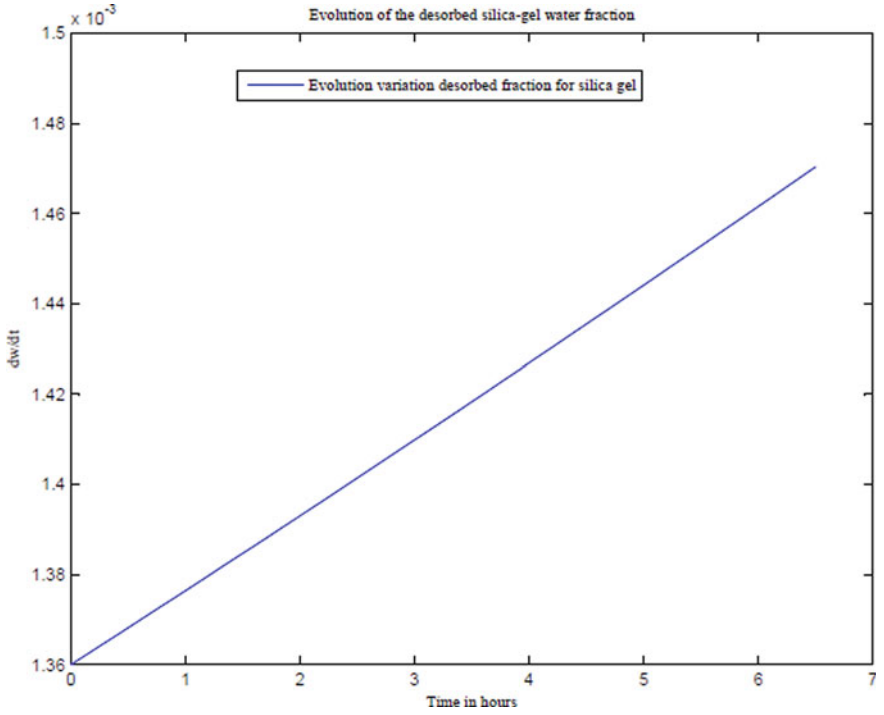

Fig. 3 Evolution of the variation of the desorbed fraction over time for silica–gel water

This curve Fig. 6 shows that the desorption temperature varies between 49 and 51.25 °C. The adsorption temperature, for its part, has an initial value of 52 °C, then it decreases to 50.9 °C considered as the end of adsorption value. After these two phases, preheating and precooling are observed. The comparison with Fig. 7 shows the same pattern, in particular with regard to the temperatures of SE1 (adsorption) and SE2 (desorption). This model in Fig. 7 has already been validated [8].

The evolution of the COP shows a maximum value of 0.38 at the end of the cycle. This is compared with Fig. 9. We see an increasing evolution like that observed for a two-bed system using the same couple with a COP of 0.56 Fig. 9 [8].

An evaporation temperature is observed which varies between 0 and 5 °C Fig. 10. It is equal to 5 °C over 6.5 h then reaches 0 °C for the rest of the cycle. This value obtained is relatively low and favors a cooling temperature below 10 °C.

It can be seen that the cooling temperature Fig. 11 varies between 8.01 and 8.55 °C. This relatively low value is suitable for cooling dairy products.

The curve shows an increase in COP over time Fig. 12. It reaches a maximum value of 0.38 for zeolite–water and 0.62 for silica–gel–water. The latter is close to 0.6 in [9]. This value is low in the case of adsorption systems, compared to absorption systems.

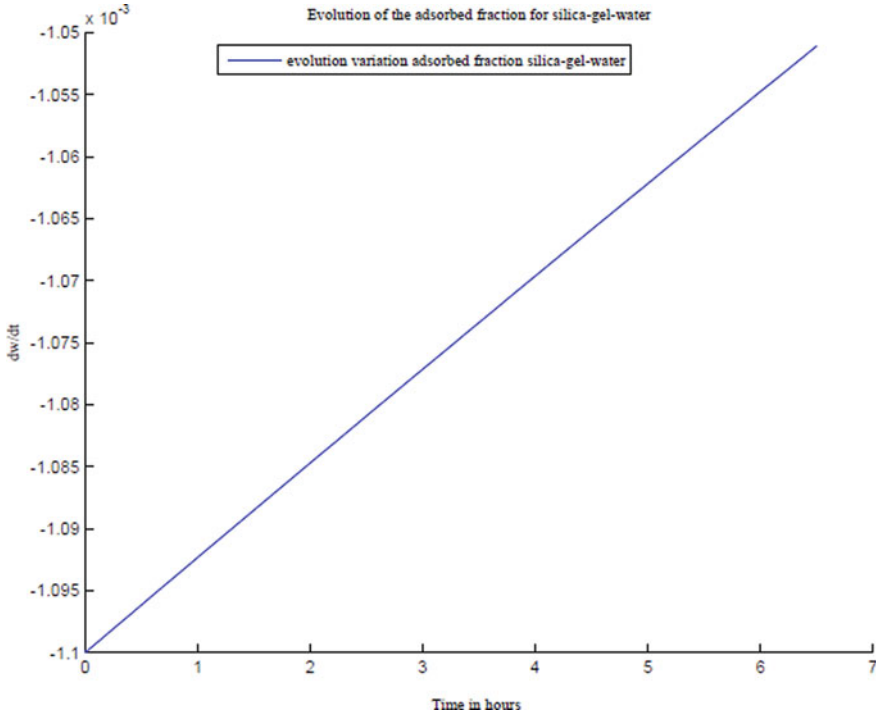

Fig. 4 Evolution of the variation of the adsorbed fraction over time for silica–gel water

5 Conclusion

This modeling and simulation work made it possible to determine the evolution of desorption, condensation, and evaporation temperatures in the case of an adsorption system with two adsorption beds. This after inserting the input parameters of our model, these results were subsequently compared with that of other studies to measure validity. A comparison between the couples was made.

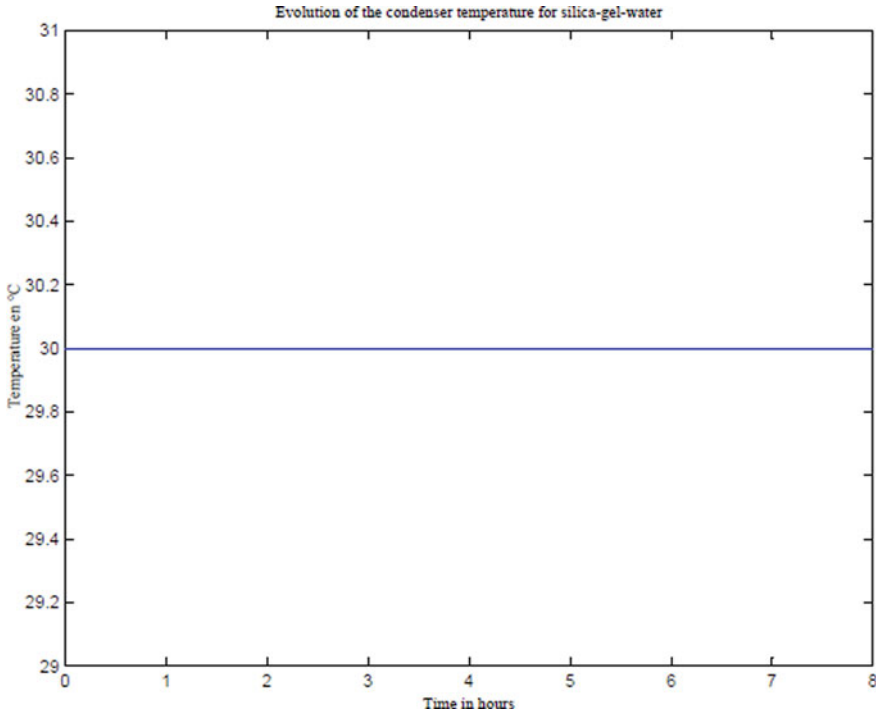

Fig. 5 Evolution of the condenser temperature for silica-gel-water

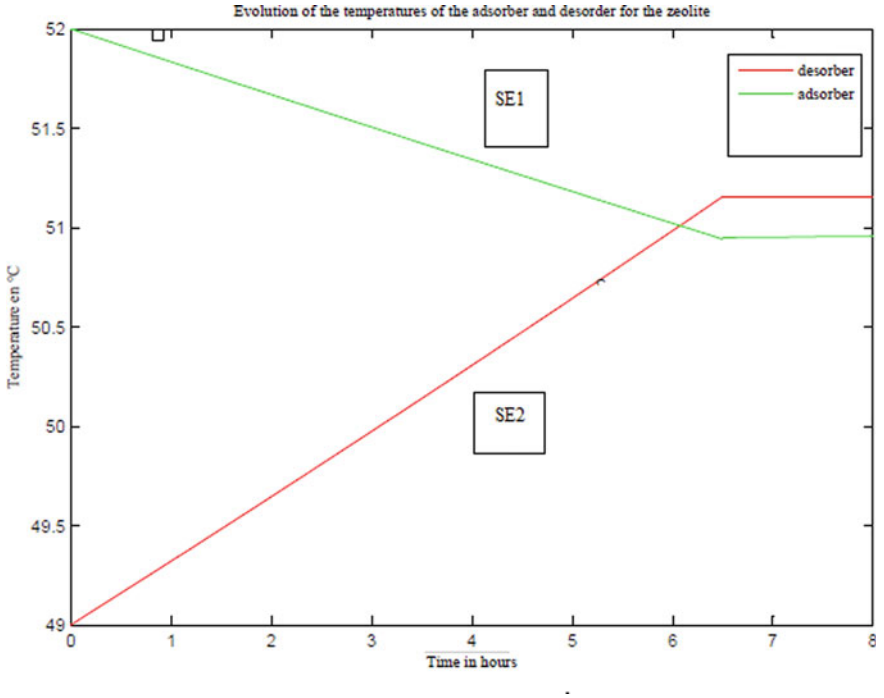

Fig. 6 Evolution of the adsorber and desorber temperatures for zeolite–water

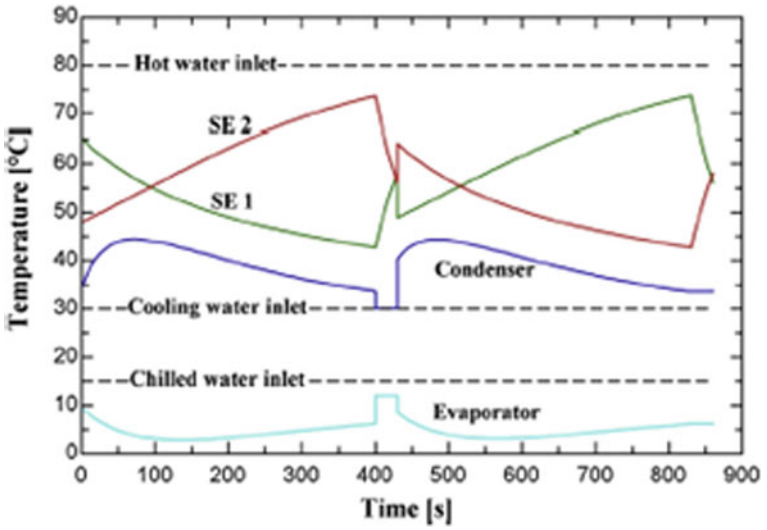

Fig. 7 Profiles of the different temperatures of 13X/cacl2–water–zeolite [8]

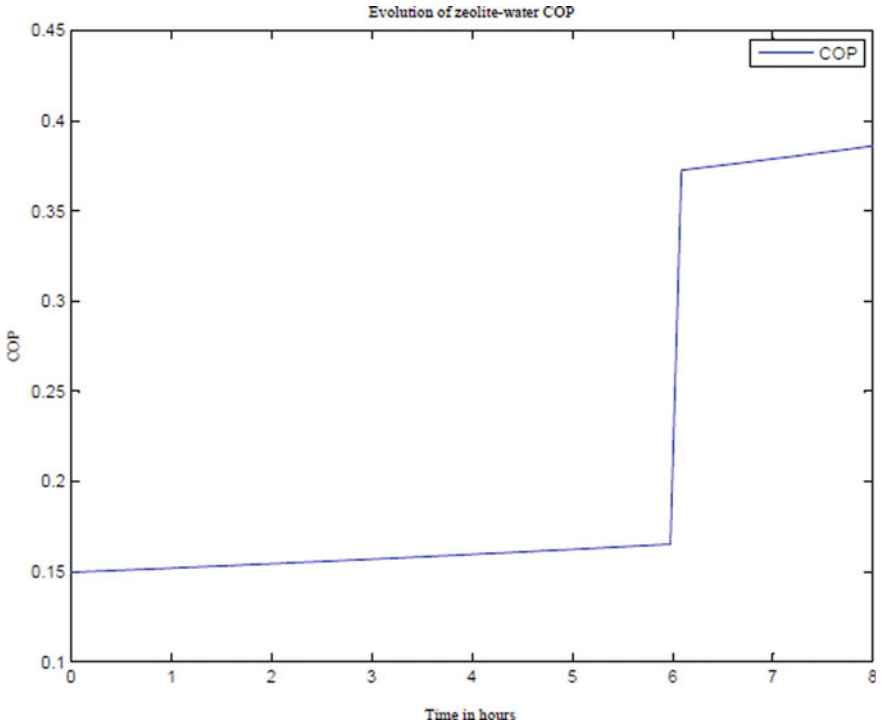

Fig. 8 Variation COP for zeolite–water over time

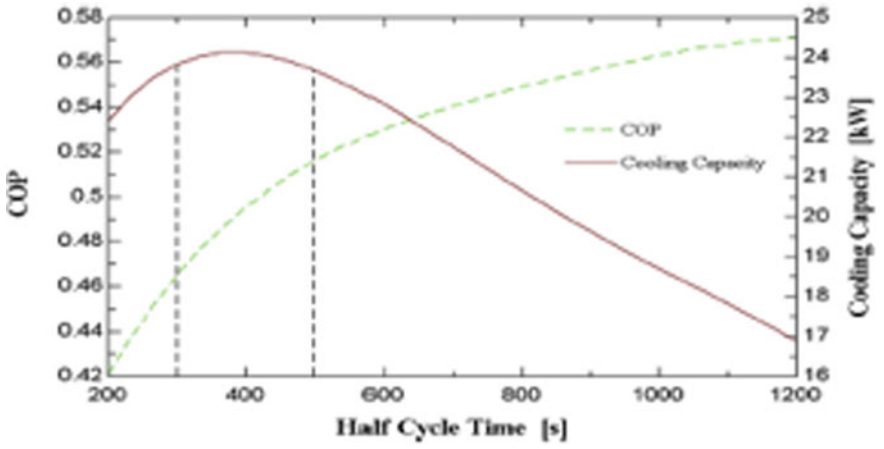

Fig. 9 Evolution of the COP of the Zeolite 13X/ $CaCl_2$–water pair [8]

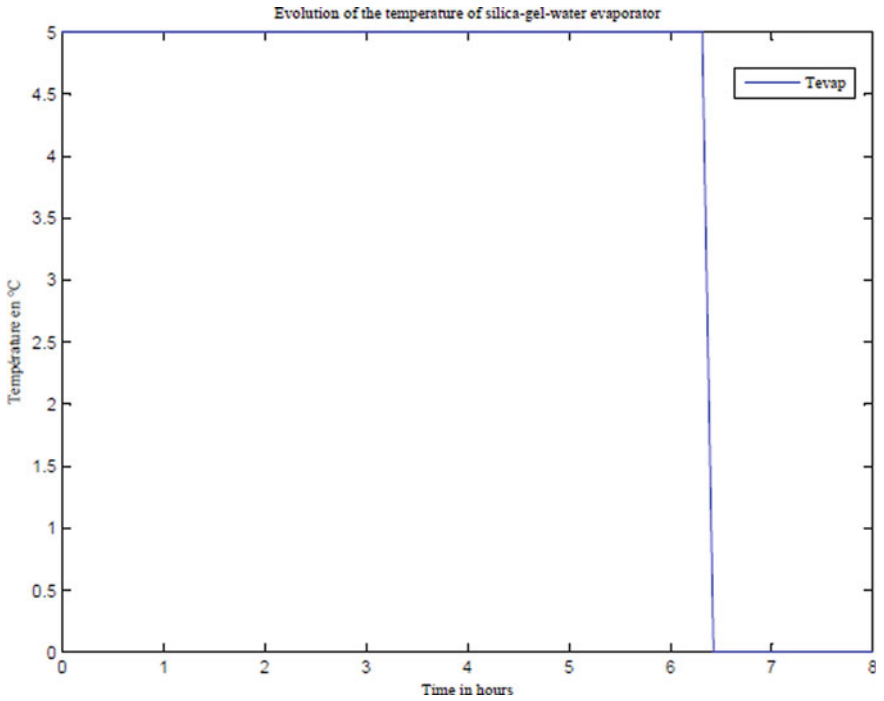

Fig. 10 Variation of the evaporator temperature for silica–gel over time

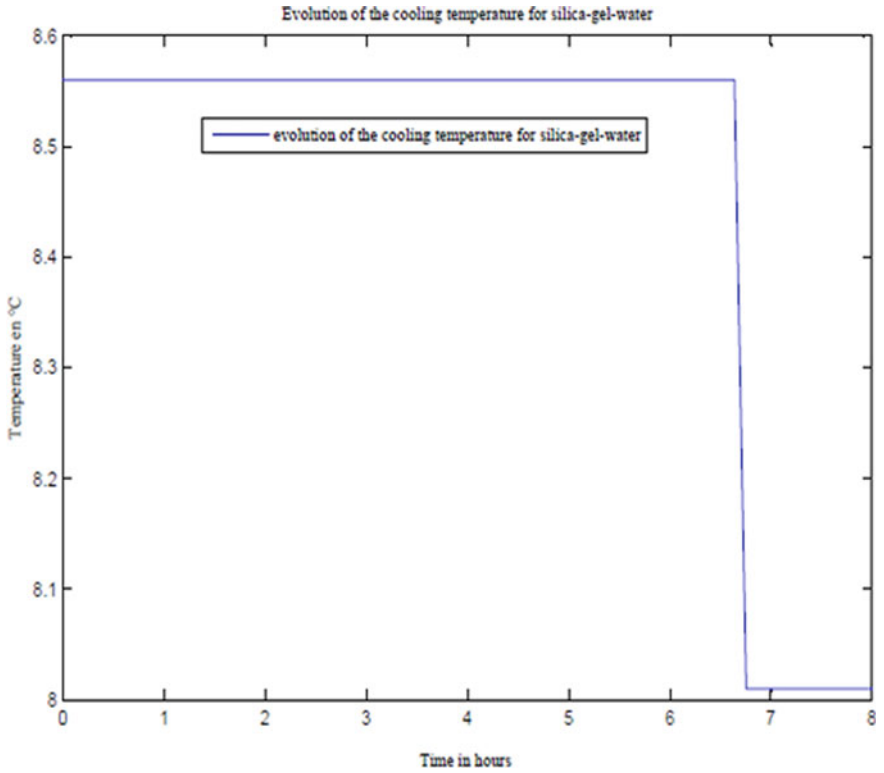

Fig.11 Variation of the cooling temperature for silica–gel water over time

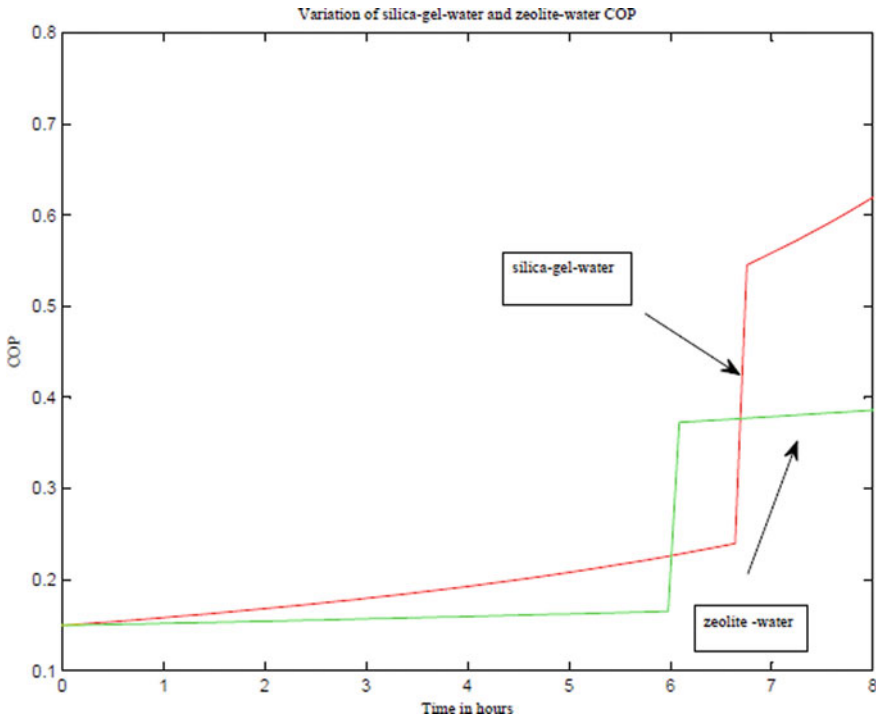

Fig. 12 Variation of silica–gel–water and zeolite–water COP as a function of time

References

1. Clito FA (1961) Afonso, recent advances in building air conditioning systems. Appl Therm Eng 26(2006):1971
2. Zhao HZ, Zhang M, Liu ZY, Liu YL, Ma XD (2008) Mechanical and experimental study on freeze proof solar powered adsorption cooling tube using active carbon/ methanol working pair. Energy Convers Manage 49:2434–2438
3. Mers AA, Azzabakh A, Mimet A, Kalkha HE (2006) Optimal design study of cylindrical finned reactor for solar adsorption cooling machine working with activated carbon-ammonia pair. Appl Therm Eng 26:1866–1875
4. Leong KC, Liu Y (2004) Numerical modeling of combined heat and mass transfer in the adsorbent bed of a zeolite/water cooling system. Appl Therm Eng 24:2359–2374
5. Yang PZ (2009) Heat and mass transfer in adsorbent bed with consideration of non-equilibrium adsorption. Appl Therm Eng 29:3198–3203
6. Zhang XJ, Liu HX, Wang RZ, Shi F (2002) Numerical simulation of heat transfer in regenerator of solid adsorption refrigeration system. Renew Energy 26:599–610
7. Hu J, Exell RHB (1994) Simulation and sensitivity analysis of an intermittent solar powered charcoal/methanol refrigerator. Renew Energy 4:133–149
8. Alizera et al (2014) Performance evaluation of Zeolite 13X/$CaCl_2$ two-bed adsorption Refrigeration system. Int J Thermal Sci 80:76–82
9. Alam KCA et al (2013) Solar adsorption cooling: a case study on the climatic condition of dhaka. J. Comput. 8(5)

Investigation of Hybrid Fault Ride Through Control Strategies in Grid-Connected Wind Energy Conversion Systems

J. Preetha Roselyn, C. R. Raghavendran, and D. Devaraj

Abstract The significant issues which are associated with grid code during grid fault are the fault ride through (FRT) capability of wind farms. This paper presents a detailed investigation of different hybrid fault ride through schemes in DFIG-based wind system under both symmetrical and unsymmetrical fault conditions. This work analyzed the performance of hybrid FRT combinations like crowbar resistance with RL circuit, DC chopper associated with crowbar resistance, DC chopper connected with series dynamic resistor, voltage control scheme with crowbar resistance are developed and studied under symmetrical and unsymmetrical fault conditions. The simulation results are obtained using MATLAB Simulink version 2019b, and the hardware real-time simulation is implemented in OPAL-RT real-time simulator. The proposed hybrid FRT schemes provide promising results improving the system parameters under different fault scenarios in grid-connected wind system.

Keywords Doubly fed induction generator · Fault ride through · Grid code compliance · Grid faults · DC link voltage control

1 Introduction

Renewable energies play a vital role in modern power grid of which wind energy has the fastest deployment in many countries. Various operational guidelines have been developed for the integration of distributed generation by several countries according to different grid codes [1–3]. Doubly fed induction generators (DFIGs) are the most widely used wind energy conversion system due to its special features like variable speed and real-reactive power control [3–6]. The control of DC link voltage and real

J. Preetha Roselyn (✉) · C. R. Raghavendran
Department of Electrical and Electronics, SRM Institute of Science and Technology, Kattankulathur, Chennai, India

D. Devaraj
Department of Electrical and Electronics, Kalasalingam Academy of Research and Education, Srivilliputhur, India

C. Subramani et al. (eds.), *Proceedings of International Conference on Power Electronics and Renewable Energy Systems*, Lecture Notes in Electrical Engineering 795,
https://doi.org/10.1007/978-981-16-4943-1_13

power transfer is carried out using the grid side power converter, whereas the rotor-side converter is used for reactive power control in the grid during normal operating conditions [7–9]. During fault conditions, the DFIG-based wind system is usually disconnected from the grid to protect the rotor-side power converter and DC link capacitor [10, 11]. But according to grid code requirements, the distributed generation should be connected to the grid during fault conditions till a certain extent and hence support the grid. The suitable fault ride through (FRT) schemes are essential for DGs to support the DG-connected grid system by regulating the real and reactive power and also to protect the power electronic components in the system. Many conventional FRT methods, namely crowbar protection circuit, dynamic voltage restorer (DVR), superconducting fault current limiters (SFCL), series damping resistors (SDRs) are mentioned in literature. In this paper, the different conventional FRT schemes such as crowbar resistance, DC chopper, series dynamic resistor and voltage control scheme and hybrid schemes such as crowbar resistance with RL, crowbar resistance with series dynamic resistor and series dynamic resistor with DC chopper and voltage control with crowbar protection scheme are exhaustively investigated under symmetrical fault conditions for all grid parameters like voltage at the point of common coupling, DC link voltage, stator current, rotor current, post fault transient current, real and reactive power injection. The paper is organized as follows: The paper is organized as follows: FRT grid codes are detailed in Sect. 2. The details of the hybrid FRT methodologies are explained in Sect. 3. The results and discussions of simulation and hardware are detailed in Sect. 4. The conclusion and future scope are represented in Sect. 5.

2 FRT Grid Requirement

The grid code requirement during fault conditions is provided in Fig. 1. The curve represents that the wind turbine should stay connected to the grid during the abnormal condition and supports grid stability. Table 1 represents the fault clearing time, the nominal system voltage, and the duration of the fault clearing. The V_f specifies that 15% of nominal system voltage should be maintained during the fault condition, and the V_{pf} signifies the minimum voltage under normal operation of the wind system.

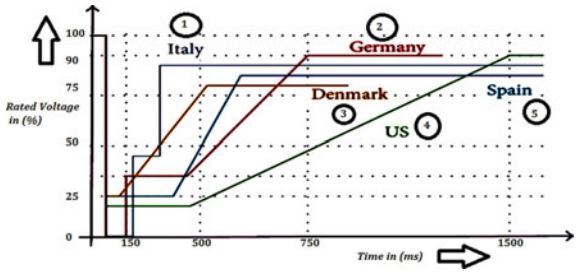

Fig. 1 Grid code FRT curve in various constrains

Table 1 Indian grid code requirement

Nominal system voltage (kV)	Clearing time (ms)	V_{pf} (kV)	V_f (kV)
400	100	360	60
220	160	200	33
132	160	120	19.8
110	160	96.25	16.5
66	300	60	9.9

3 Framework of Hybrid FRT Schemes

3.1 Proposed Hybrid FRT Strategies

To get the best characteristics of each FRT scheme, the conventional FRT strategies are combined in a proper way for better FRT capability of the system. The proposed hybrid FRT schemes developed and implemented in this work are crowbar resistance with RL circuit, DC chopper with crowbar resistance, DC chopper with the series dynamic resistor and voltage control scheme with crowbar resistance.

3.1.1 Hybrid Crowbar Resistance with RL Circuit

The hybrid crowbar protection circuit is designed with thyristor bypass resistors as shown in Fig. 2. This combination helps in diminishing the rotor current and helps in suppressing the DC link voltage. When the value of the terminal voltage decreases below the threshold value of the comparator, the FRT scheme will be activated and the rotor controller is turned off. When the terminal voltage exceeds the threshold value, the crowbar will be deactivated and the rotor controller will be activated.

3.1.2 Hybrid DC Chopper with Crowbar Resistance

Crowbar resistance is incorporated with DC chopper and is shown in Fig. 3. This hybrid controller protects the DC link capacitor from overvoltage during grid fault conditions. The combination of dc chopper and crowbar resistance helps in reducing DC link voltage to the permissible value, and the crowbar resistance helps in maintaining the rotor currents. This combination thus helps in controlling DC link voltage, rotor currents and active power.

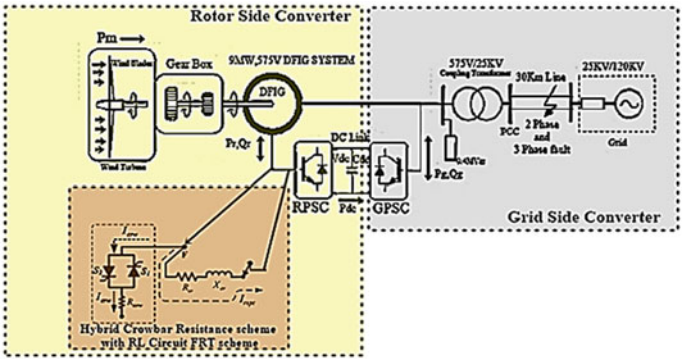

Fig. 2 Hybrid crowbar resistance with RL circuit FRT strategy

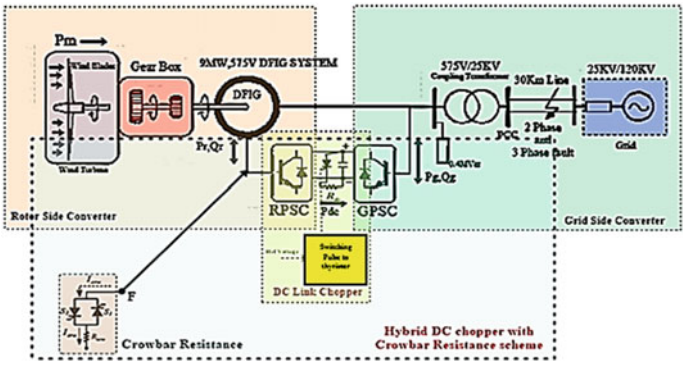

Fig. 3 Hybrid DC chopper with RL circuit FRT strategy

3.1.3 Hybrid Voltage Control Scheme and Crowbar Resistance

The combination of the voltage control scheme with crowbar resistance as shown in Fig. 4 helps in reducing the oscillation of the real power and rotor current. The crowbar resistance is adequate in damping the oscillations in the rotor current, and the voltage control scheme helps in regulating the PCC voltage during grid faults.

3.1.4 Hybrid DC Chopper with SDR

In this combination, when the DC link voltage exceeds the limit, the chopper will be turned on. Additionally, with this hybrid DC chopper as shown in Fig. 5, SDR can restrict the rotor overvoltage and also limit the high rotor current. The rotor current can decrease the charging current to the DC link capacitor and hence reduces the DC link overvoltage.

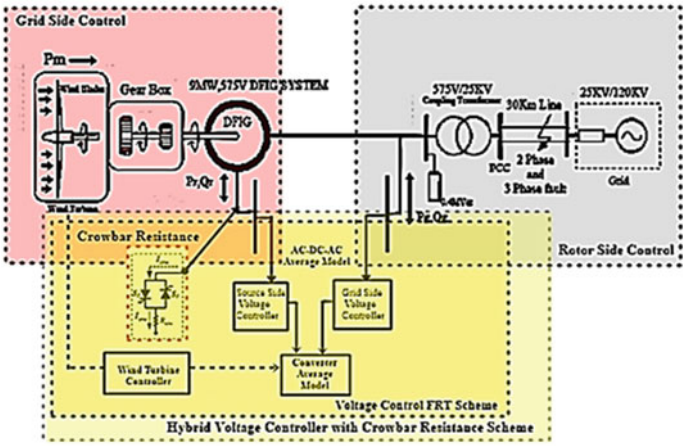

Fig. 4 Hybrid voltage control scheme with Crowbar Resistance FRT strategy

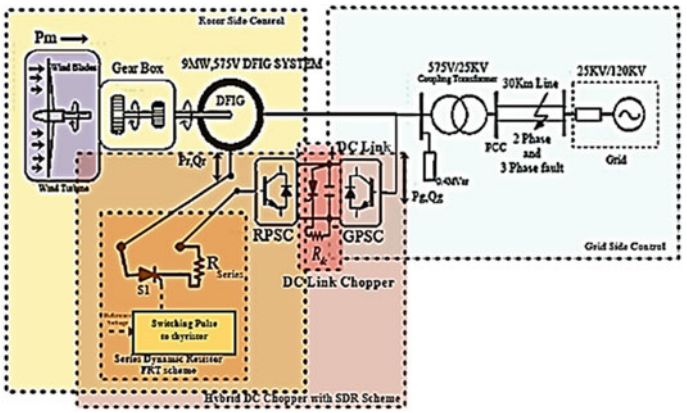

Fig. 5 Hybrid DC chopper with SDR FRT strategy

4 Results and Discussion

The performance of the hybrid FRT strategies is tested in a grid-connected 9 MW, DFIG-based wind system in MATLAB 2019b version. The proposed FRT strategy is validated in OPAL-RT HIL platform. The DFIG is operated at an average wind speed of 12 m/s. The transient behaviors of the DFIG-based grid-connected system are studied under different fault conditions such as symmetrical and unsymmetrical faults, and the results under symmetrical faults are provided in this section.

4.1 Simulation Results

The hybrid FRT strategies, namely (a) combined crowbar resistance with RL circuit, (b) DC chopper with crowbar resistance, (c) DC chopper interlinked with SDR and (d) voltage control scheme with crowbar resistance are developed and implemented in test system as shown in Fig. 6. The different parameters are DC link voltage, real and reactive power, stator and rotor currents, the voltage at PCC is measured and analyzed under symmetrical fault condition.

4.1.1 Performance of Hybrid FRT Schemes Under Symmetrical Faults

Under this scenario, a three-phase short-circuit fault is simulated which produces low-voltage fault behaviors in DFIG-WECS. The system parameters under symmetrical fault are discussed as follows:

(i) ***DC link Voltage***
Figure 7 shows the DC link voltage which rises instantaneously because of the rotor inrush currents injected from the RSC into the DC link capacitor. The hybrid FRT controllers are more effective in suppressing the DC link voltage than conventional FRT scheme. Various hybrid schemes are introduced to recognize which hybrid FRT scheme is more effective in reducing the DC link voltage. The DC link is suppressed to 1155 V by using DC chopper with series dynamic resistor, which is very less when compared to other combinations. DC chopper with crowbar resistance is the next effective method in maintaining the DC link voltage within the permissible limit.
(ii) ***Voltage at Point of Common Coupling***
Figure 8 shows illustrates the dip in voltage, at the point of common coupling during the short-circuit fault. By introducing the hybrid FRT scheme, the dip in the voltage is reduced better than conventional FRT schemes and the DC chopper

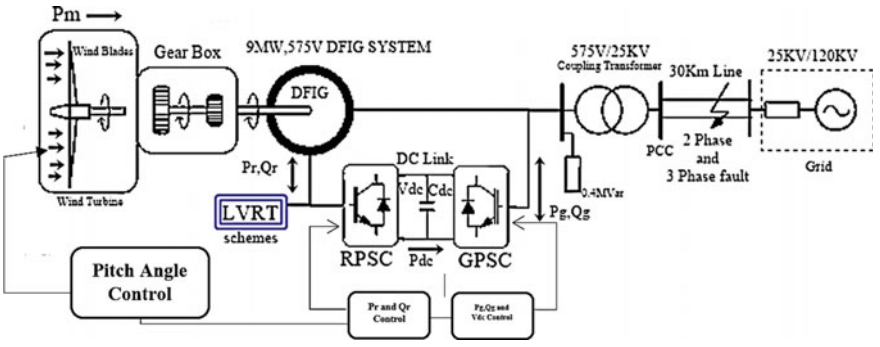

Fig. 6 Single line diagram of 9 MW grid-connected wind system

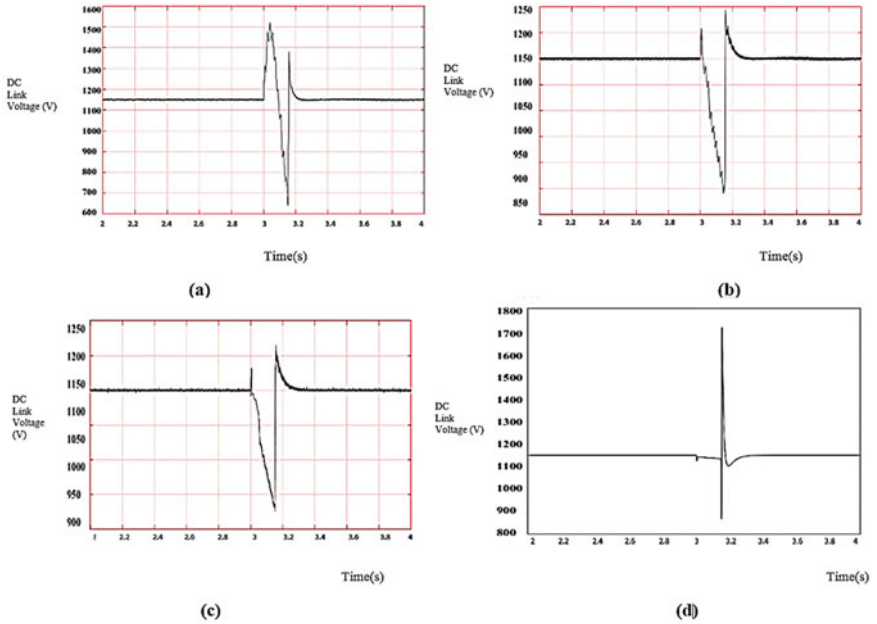

Fig. 7 DC link voltage of the DFIG-WECS under symmetrical fault: **a** crowbar resistance with RL, **b** DC chopper with CBR, **c** DC chopper with SDR, **d** voltage control scheme with CBR

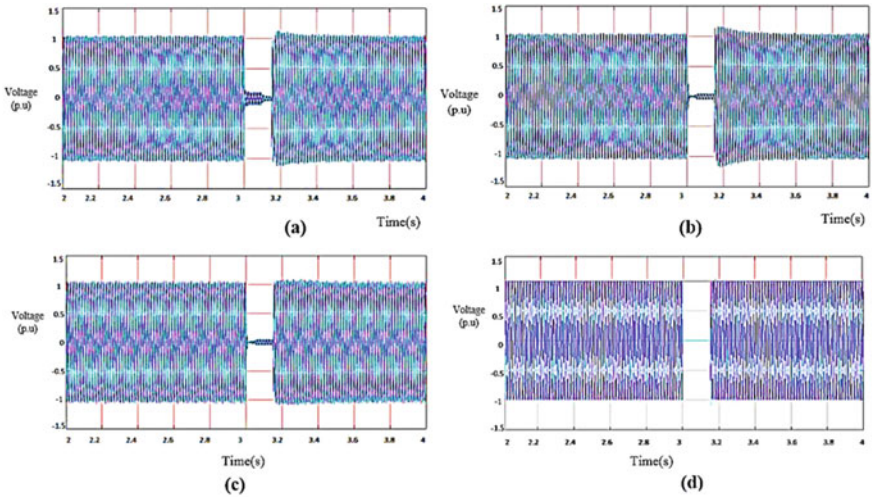

Fig. 8 Voltage at PCC of the DFIG-WECS under symmetrical fault: **a** crowbar resistance with RL, **b** DC chopper with CBR, **c** DC chopper with SDR, **d** voltage control scheme with CBR

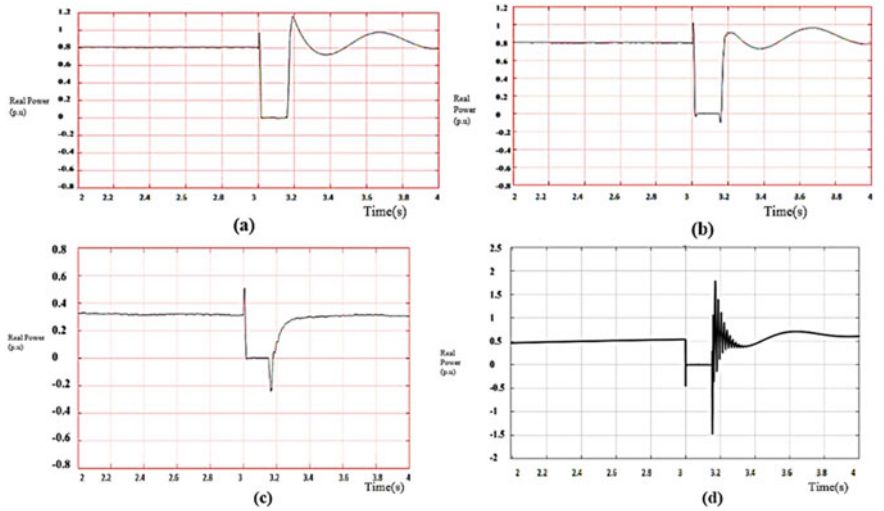

Fig. 9 Real power of the DFIG-WECS under symmetrical fault: **a** crowbar resistance with RL, **b** DC chopper with CBR, **c** DC chopper with SDR, **d** voltage control scheme with CBR

with SDR scheme helps in reducing the voltage dip to 0.2 p.u with a recovery time of 3.17 s and hence the transient behavior of the system.

(iii) ***Real Power***

Figure 9 illustrates the real power of the system when the system is subjected to symmetrical fault condition. When the voltage control scheme is introduced in the system, the oscillation is reduced and reaches 0.8 p.u during the fault clearing time. When the hybrid voltage control scheme with crowbar resistance is introduced in the system, the real power reaches to 0.5p.u and oscillation is also less.

(iv) ***Reactive Power***

Figure 10 illustrates the reactive power injected into the system when it is subjected to symmetrical fault condition. When the DC chopper FRT scheme is introduced to the system, the reactive power injection levels reach the value of 0.1p.u, and when hybrid FRT scheme like DC chopper combined with SDR is introduced under the same condition, it can be seen that the reactive power injection is increased to 0.5p.u. This hybrid combination is verified as the potential hybrid FRT scheme when compared to the other FRT schemes in case of reactive power support.

The performance comparison of different hybrid FRT schemes developed for the test system is shown under symmetrical fault conditions. From the figures, it is clear that the voltage control scheme with crowbar resistance and DC chopper with SDR schemes is good in reducing the post fault transient current.

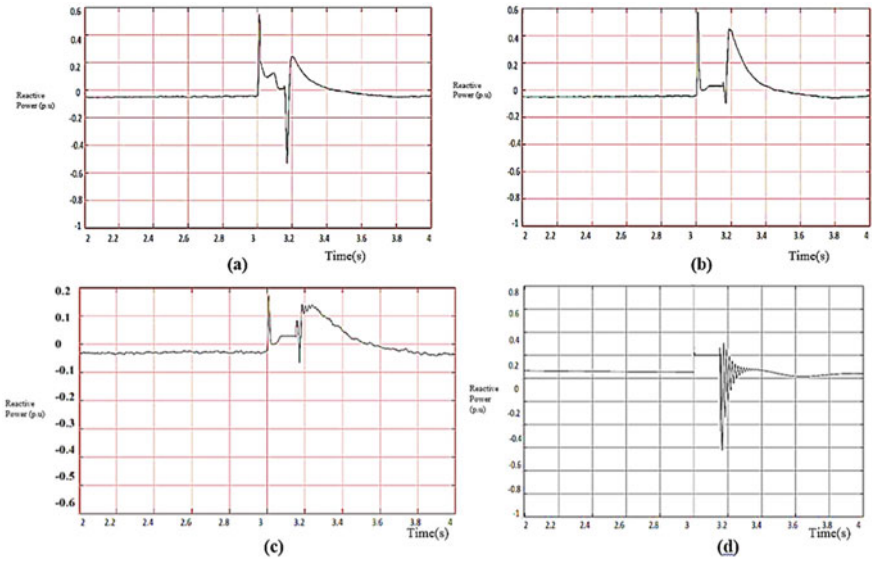

Fig. 10 Reactive power of the DFIG-WECS under symmetrical fault: **a** crowbar resistance with RL, **b** DC chopper with CBR, **c** DC chopper with SDR, **d** voltage control scheme with CBR

4.2 Real-Time Simulation Results

The hardware simulator is composed of OPAL-RT interconnected with the PC in which the wind system of maximum power of 9 MW is generated at the wind speed of 12 m/s. The power coefficient C_p is maintained to be 0.323. The performances of the proposed configuration under real-time environment are evaluated under the fault conditions and are discussed in following subsections. In the proposed hybrid controller, DC chopper with SDR which performs better in FRT capability in the simulated environment is tested in the hardware setup. A hardware simulator was designed and built on OPAL-RT RCP/HIL[Version-OP4510] interconnected with the RT lab simulator software installed PC, and the waveforms are observed using the oscilloscope shown in Figs. 11 and 12. The performance of the proposed FRT controller under real-time environment is evaluated under the unsymmetrical LLG fault condition. In OPAL-RT platform, the SimPower Systems model is used with subsystem blocks, wind system as the Master Subsystem (SM) and the FRT controller in the Slave Subsystem (SS).

Under this scenario, unsymmetrical LLG fault is simulated which produces low-voltage fault behaviors in DFIG-WECS. It has been analyzed that the hybrid controllers are more effective in suppressing the DC link voltage (Fig. 13) than conventional schemes. DC chopper with SDR hybrid FRT scheme is more effective in suppressing the DC link voltage. The DC link is suppressed to 1150 V by using DC chopper combined with series dynamic resistor, and hence selected as the suitable hybrid FRT scheme in suppressing the DC link voltage. Figure 14 shows the real

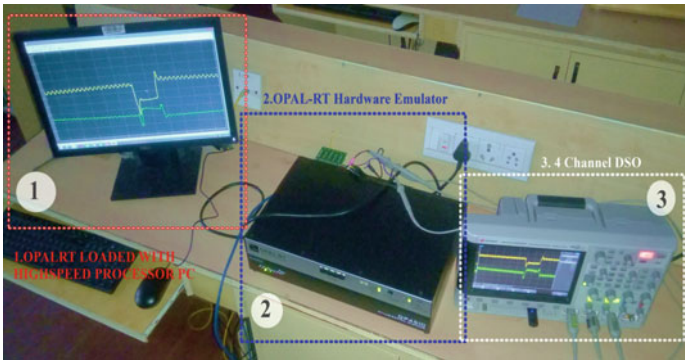

Fig. 11 Hardware setup for FRT controller

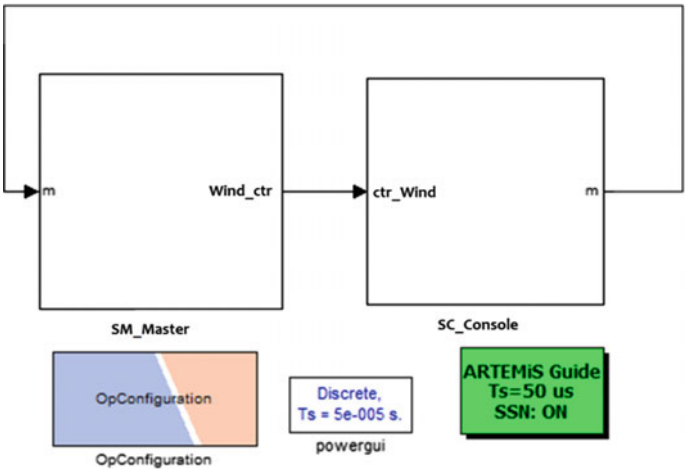

Fig. 12 Hardware configuration

power absorbed by the system when it is subjected to unsymmetrical fault condition. When the DC chopper with SDR is introduced in the system at that condition, the real power reaches to 0.5 p.u and oscillation is less when compared to the conventional FRT scheme. Figure 15 illustrates the voltage dip in the point of common coupling during the unsymmetrical fault condition. The rotor current increases which lead to heavy dip in the PCC point. By selecting DC chopper with SDR scheme, the voltage level is reduced only to 0.7 p.u and recovery with 3.16 s. This hybrid scheme is the best one when compared to other FRT schemes by reducing the voltage sag at the PCC point (Table 2).

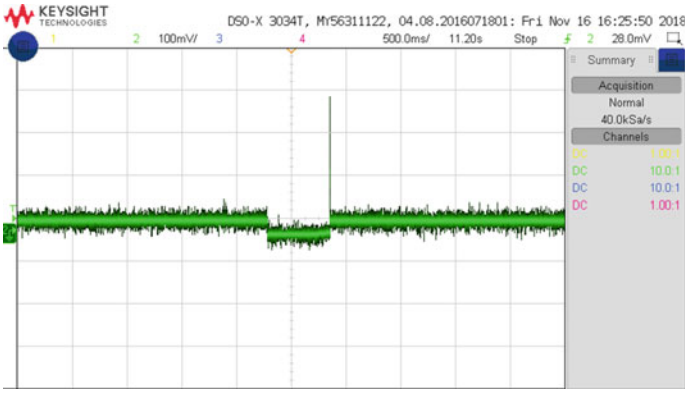

Fig. 13 DC link voltage

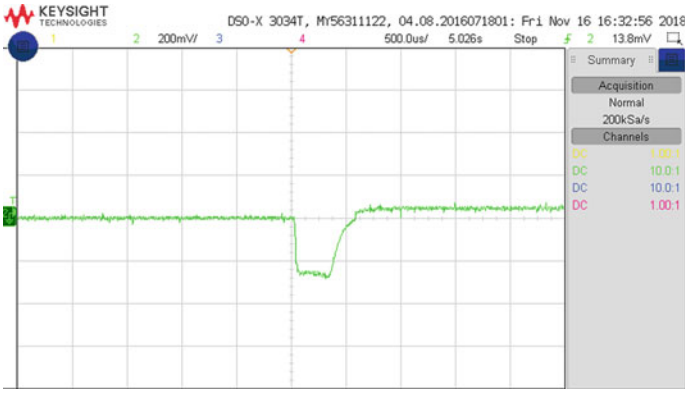

Fig. 14 Real power

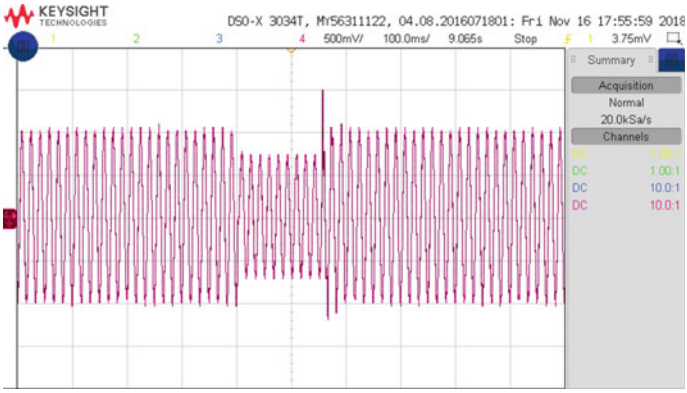

Fig. 15 Voltage at PCC

Table 2 Experimental results of hybrid FRT controllers under unsymmetrical fault condition

Voltage at PCC	DC Link Voltage	Real Power
Dips to 0.7 pu and recovered at 3.16 s	Peak value of 1150 V	Oscillations reached 0.5pu during fault clearing

5 Conclusion

The hybrid FRT schemes are studied under different system parameters such as oscillations in the active and reactive power, rotor and stator currents, DC link voltage, etc. which are successively improved. In addition, different combinations of hybrid FRT schemes are designed and analyzed on different system parameters which will improve the consistency of both the wind farm and the power system. From the comprehensive analysis on different hybrid FRT schemes, it is understood that DC chopper with SDR schemes perform well in improving the system conditions and supporting the grid under symmetrical faults. In future, new control schemes incorporated with intelligent control techniques like artificial neural network and fuzzy logic could be implemented for the wind turbines to enhance the stability of the system.

References

1. Zeng Z, Yang H, Zhao R, Cheng C (2013) Topologies and control strategies of multi- functional grid-connected inverters for power quality enhancement: a comprehensive review. Renew Sustain Energy Rev 24(5):223–270
2. Lund H, Munster E (2006) Integrated energy systems and local energy markets. Energy Policy 34(10):1152–1160
3. Tazil M, Kumar V, Bansal RC, Kong S, Dong ZY, Freitas W, Mathur HD (2010) Three-phase doubly fed induction generators: an overview. IET Electr Power Appl 4(2):75–89
4. Asuhaini AB, Zin BM, Pesaran MHA, Khairuddin AB (2013) An overview on doubly fed induction generators control and contributions to wind based electricity generation. Renew Sustain Energy Rev 27:692–708
5. Mwasilu F, Justo JJ, Ro KS, Jung JW (2012) Improvement of dynamic performance of Doubly Fed Induction Generator-based wind turbine power system under an unbalanced grid voltage condition. IET Renew Power Gener 6(6):424–434
6. Eriksen PB, Ackermann T, Abildgaard H, Smith P, Winter W, Rodriguez G (2005) System operation with high wind penetration. IEEE Power Energ Mag 3(6):65–74
7. Pannel G, Atkinson DJ, Zahawi B (2010) Minimum-threshold crowbar for a fault-ride- through grid-code-compliant DFIG wind turbine. IEEE Trans Energy Conserv 25(3):750–759
8. Noureldeem O (2012) Behavior of DFIG wind turbines with crowbar protection under short circuit. Int J Electr Comput Sci 12(3):32–37
9. Jadhav HT, Roy R (2013) A comprehensive review on the grid interaction of doubly fed induction generator. Int J Electr Power Energy Syst 49:8–18
10. Morren J, De Haan SW (2005) ride through of wind turbines with doubly-fed induction generator during a voltage dip. IEEE Trans Energy Convers 20(2):435–441

11. Lopez J, Gubia E, Olea E, Ruiz J, Morroyo L (2009) Ride through of wind turbines with doubly fed induction generator under symmetrical voltage dips. IEEE Trans Industr Electron 56(10):4246–4254

Performance Analysis of Single-Axis Solar Tracker Using IoT Technique

S. Usha, A. Geetha, T. M. Thamizh Thentral, C. Subramani, R. Ramya, and C. S. Boopathi

Abstract To empower the abstraction of maximum power from the solar panel using MPPT with P&O algorithm, this proposed work enlightens the practice of single-axis solar tracker exploitation by Arduino Uno. The introduction of IoT into the project helps in remote monitoring of the entire system and also the analysis with the neat graphical representation of the data over a course of time. The significant characteristic for monitoring, supervising and performances estimations of integration of Internet of Things (IoT) technology which is an efficient wireless communication technology is considered which disables the difficulties faced in physical monitoring of solar photovoltaic (PV) and getting the values of voltage and current.

Keywords Arduino · Node MCU · Illumination · Power generation · Internet of Things · Wireless communication

1 Introduction

In this contemporary world of globalization, the growth of mankind leads to increasing demand of energy consumption which affects the conventional sources of electricity [1, 2]. Keeping in mind, man has discovered several techniques of harnessing electrical energy from renewable resources. The renewable resources are naturally replenished. The most suitable of them is solar energy which is free and provides us with light and heat, being pollution-free. It is an eco-friendly supply [3–5].

Despite of solar being a promising source of energy, there is a need of improving method to harness the energy. With being variable weather condition, a limitation affecting solar module, different maximum power point tracking methods are used [6]. The easiest to implement method is perturb and observe (P&O) which yields highly efficient output. MPPT is used in the extraction of the maximum. DC-DC converter act as an interference between the PV module and the load. By varying the

S. Usha (✉) · A. Geetha · T. M. T. Thentral · C. Subramani · R. Ramya · C. S. Boopathi
Department of Electrical and Electronics Engineering, SRM Institute of Science and Technology, Tamil Nadu, Kattankulathur 603203, India

C. Subramani et al. (eds.), *Proceedings of International Conference on Power Electronics and Renewable Energy Systems*, Lecture Notes in Electrical Engineering 795,
https://doi.org/10.1007/978-981-16-4943-1_14

duty cycle, the load impedance is varied to match the peak point of power with the source [7–10].

Instead of a fix system, a single-axis solar tracker has been implemented in the project using Arduino, light detecting resistors (LDR) and a motor. Solar panel is assembled with connecting a motor to track the maximum sunlight which will shine on the panel directly at any time of the year and day [11, 12].

System characteristic is being monitored and optimized using perturb and observed technique and by the use of boost converter. The source impedance is adjusted to match the load impedance by varying the duty cycle. The purpose of this project is to also develop a solar tracker based on the intensity of light, to increase the output voltage, current and power [13–16].

2 Description of Block Diagram

Figure 1 tells about the basic of the entire project. It consists of Arduino for all the calculation of the voltages, for integrating with the IoT and also helps with the automatic solar tracking. The energy received from the solar panel goes directly into the DC-DC boost converter in which the duty cycle changes according to the varying input voltage. It is done using the MPPT algorithm based on the perturb & observe (P&O) method. It is also called hill climb method which adjusts the duty cycle and then by comparing, it moves towards maximum power point. The system also consists of IoT platform which uses things peak platform for connecting the

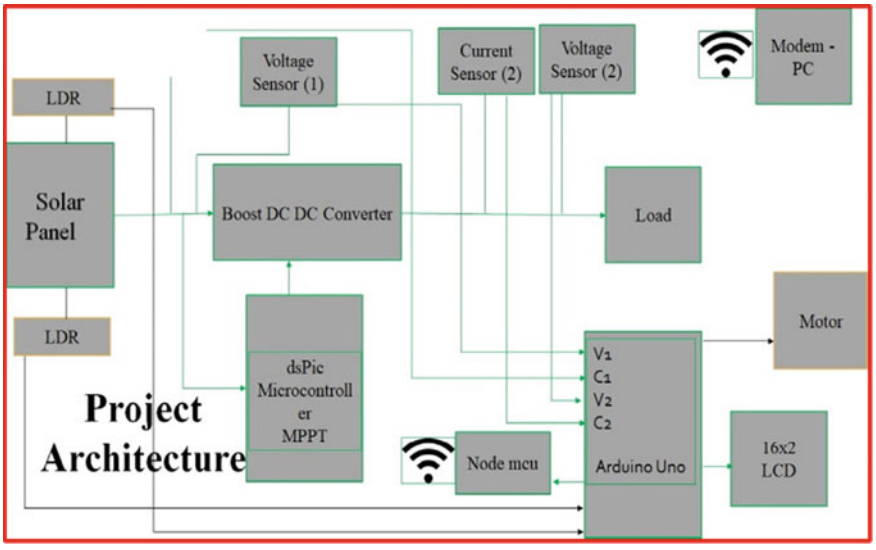

Fig. 1 System architecture

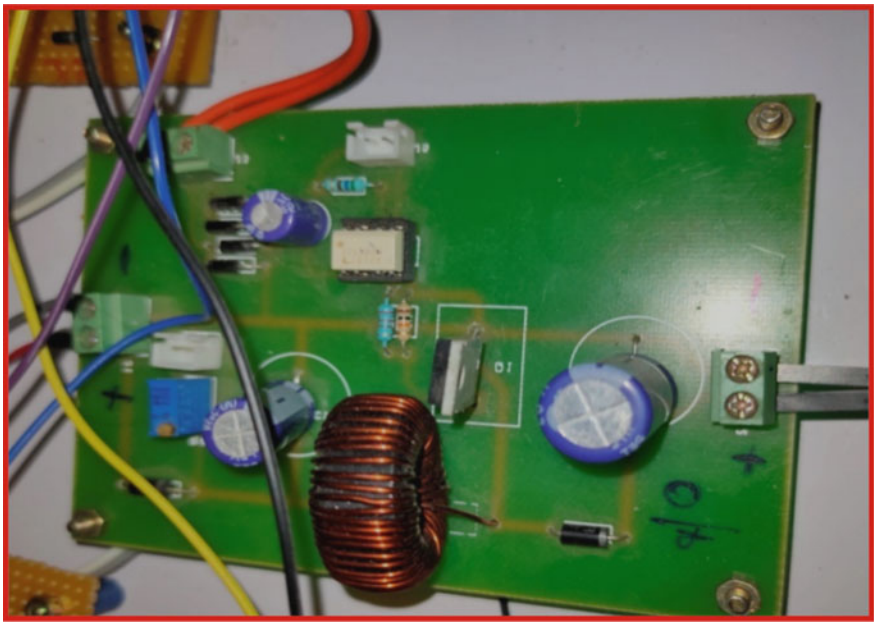

Fig. 2 Boost converter

system to internet. All the readings for the voltage and current are uploaded onto the platform which then can be viewed from anywhere just by accessing the platform. The tracking is facilitated by using two LDRs in combination with motor which asses the current light situation in the area and accordingly control the panel orientation. By using the solar tracking, the overall power generation can be increased by almost 10% to 25%, hence, lowering per unit cost.

3 DC-DC Boost Converter

A boost converter, whose output voltage is higher than input voltage. It steps up the voltage and consists of two semiconductors with one energy storing element like capacitor or inductor or the combination of the mentioned elements (Figs. 2 and 3).

4 P&O MPPT Algorithm Analysis and Implementation

In the P&O algorithm, small increments are added until the maximum power point is reached, and this is how PV array is perturb; initially, the power is calculated by values of V1 and I1 simultaneously calculating V2 and I2 for P2. If P2 is positive,

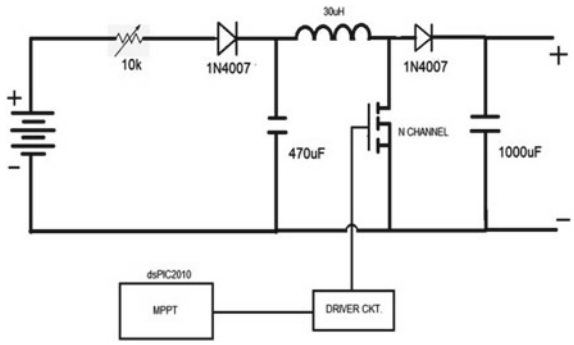

Fig. 3 DC-DC boost converter

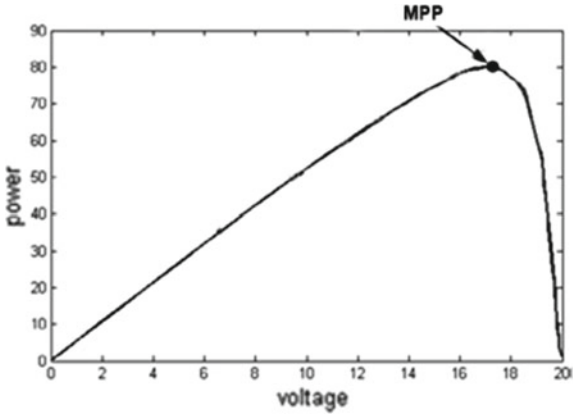

Fig. 4 MPPT tracking curve

then it goes in the same direction; once P2 reads negative, the output power is flowing back towards the maximum power point by adding a negative increment. At the time of maximum power point, the system oscillates between point. The controller tracks operating point and brings the voltage of the solar module to operate around MPP. DC module output is located with DC-DC converter. The circuit model also sends real-time data to a free IoT platform for analytical approach (Figs. 4 and 5).

5 Analysis and Simulation

The simulation for the solar and MPPT module is done using MATLAB Simulink 2013. The PV cell, i.e. independent source supplies the proposed circuit; the input is given by the output, and PV terminals provide duty cycle for the boost converter. The PV panel used is 12v, and the output voltage is boosted up to 27 V. The output voltage by varying the duty cycle k whose value is 0.67 which is calculated by using

Fig. 5 P&O algorithm

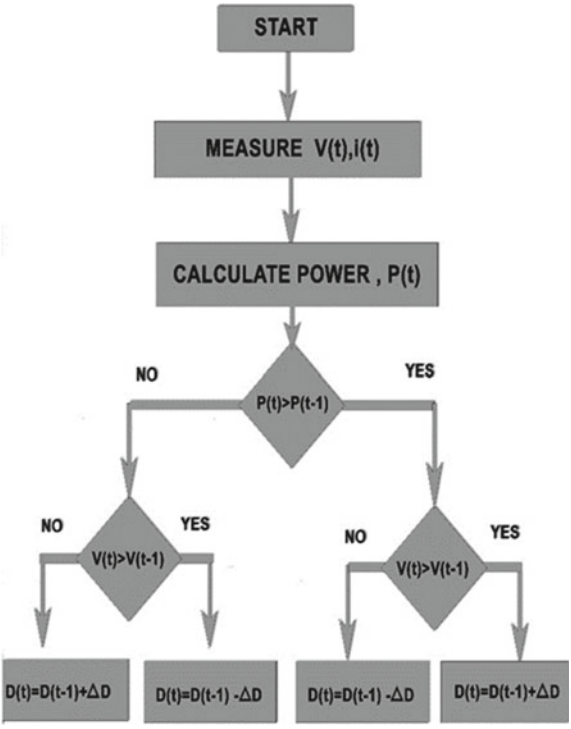

the formula Vo = Vs./1-k the pulse width of the pulse generator is varied, and various voltage ranges at the output can be obtained.

For entire duration of the simulation, the cell temperature for photovoltaic cell is maintained at constant 250 C with a mean of 4000 lumens (Fig. 6 and 7).

Once the power from the solar panel is injected into boost converter, the dsPIC controller starts functioning. The dsPIC works by varying the duty cycle based on the input voltage sensed by the MPPT, therefore, by which the output voltage gets boosted to maximum power point (Figs. 8, 9 and 10; Table 1).

6 Solar Tracker

We have used LDRs which help in controlling the rotation of the servo motor based on the light intensity of the area. The circuit consists of two LDRs, servomotor, motor driver, Arduino UNO and PV panel; the flowchart for the mechanism is given (Fig. 11).

As seen in the diagrams, the solar panel will get orientated towards the sunlight as we know the sun rises in the east and sets in west, so we can easily place the

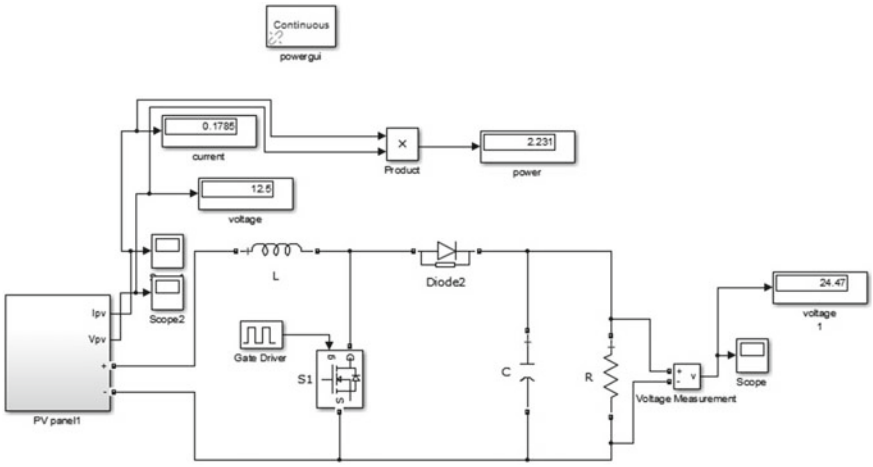

Fig. 6 Simulink circuit

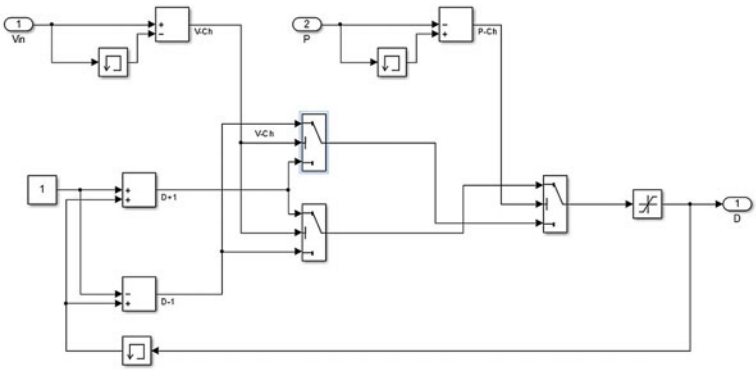

Fig. 7 Simulink MPPT circuit

prototype to track the sunlight all day out producing maximum outputs (Figs. 12, 13, 14 and 15).

7 Conclusion

This project deals with the entire process of solar generation in which the production can be increased by using algorithms. The modified IoT into the project helps in remote monitoring of the entire system, and also the analysis with the neat graphical representation of the data over a course of time was analysed. The P&O algorithm

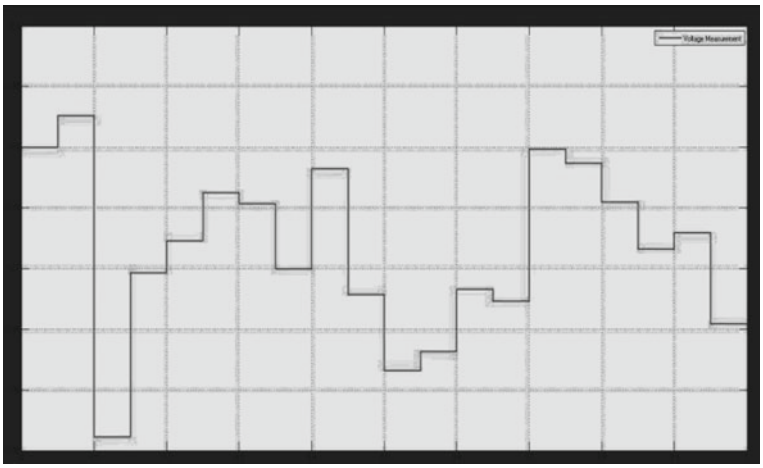

Fig. 8 PV panel voltage

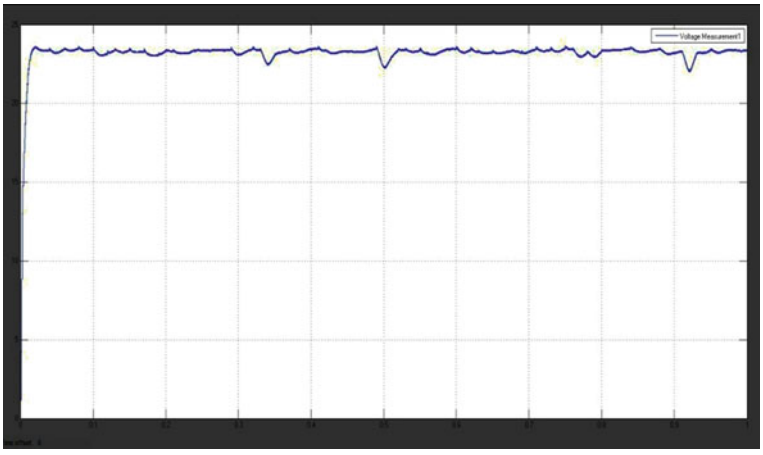

Fig. 9 Output voltage

varies the duty cycle of the boost converter based on the voltage and current calculation and keeps the voltage production around the maximum point so as to maximize the power generation. The tracking system used also helps by increasing the overall power generation of the system and helps in reducing the overall unit generation cost in a large-scale project.

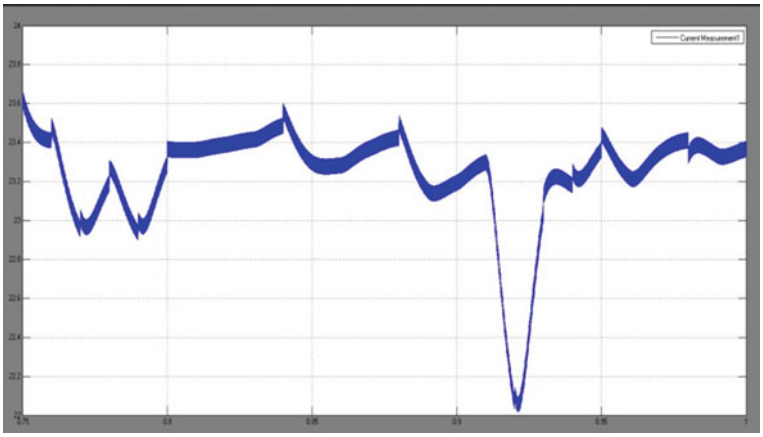

Fig. 10 Output current

Table 1 Output parameters

MPPT method	Output voltage	Output current	Output power
Perturb & observe	23.78 V	9.7A	232.37 W

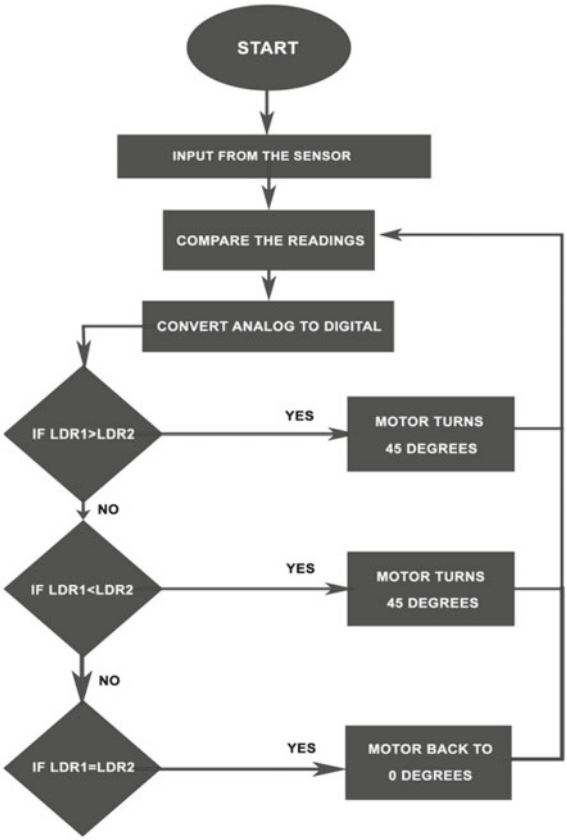

Fig. 11 Flowchart of horizontal-axis solar tracker

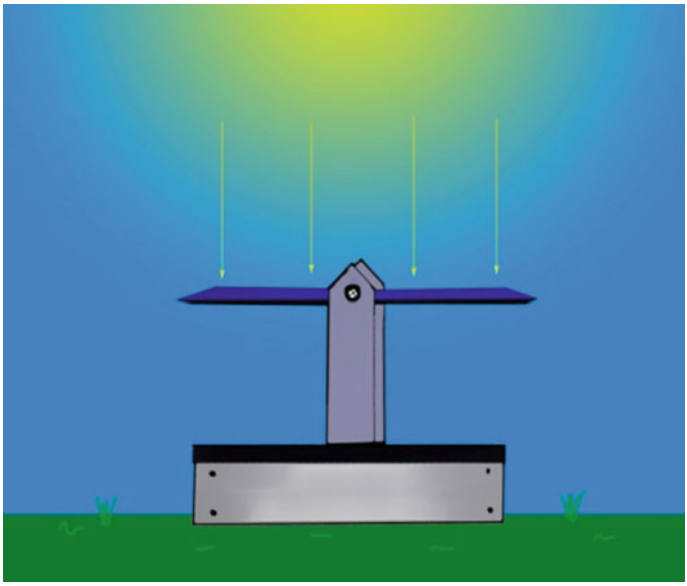

Fig. 12 Side view (panel horizontal)

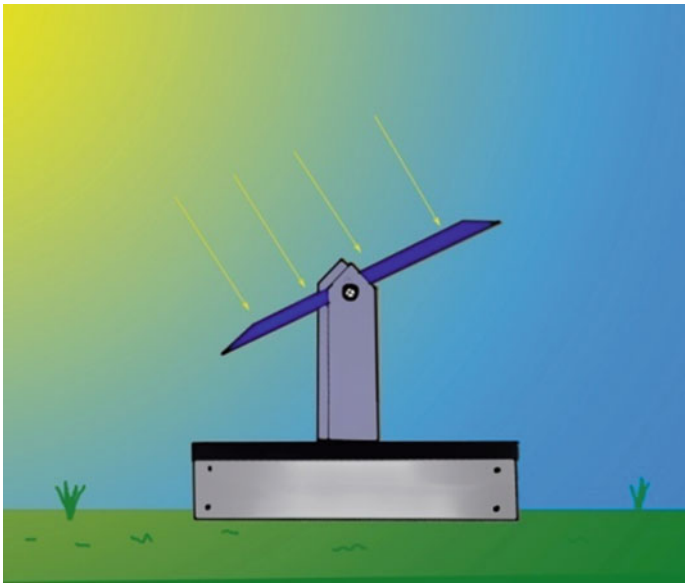

Fig. 13 Panel titled 45 degrees in NW direction

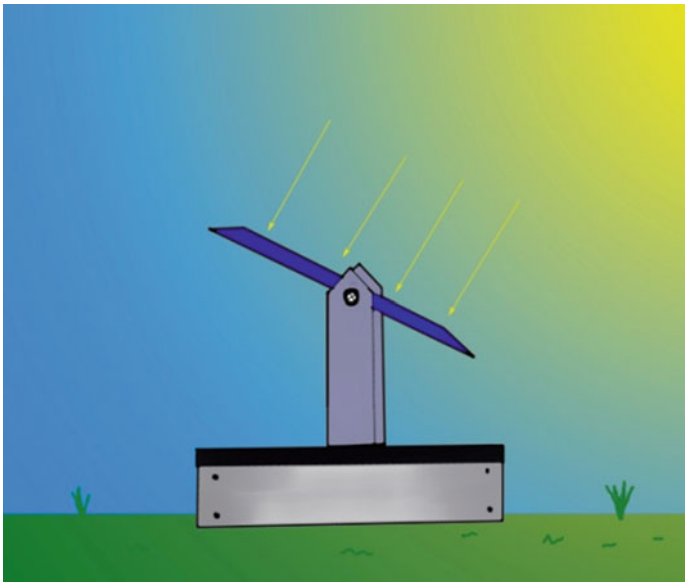

Fig. 14 Panel titled 45 degrees in NE direction

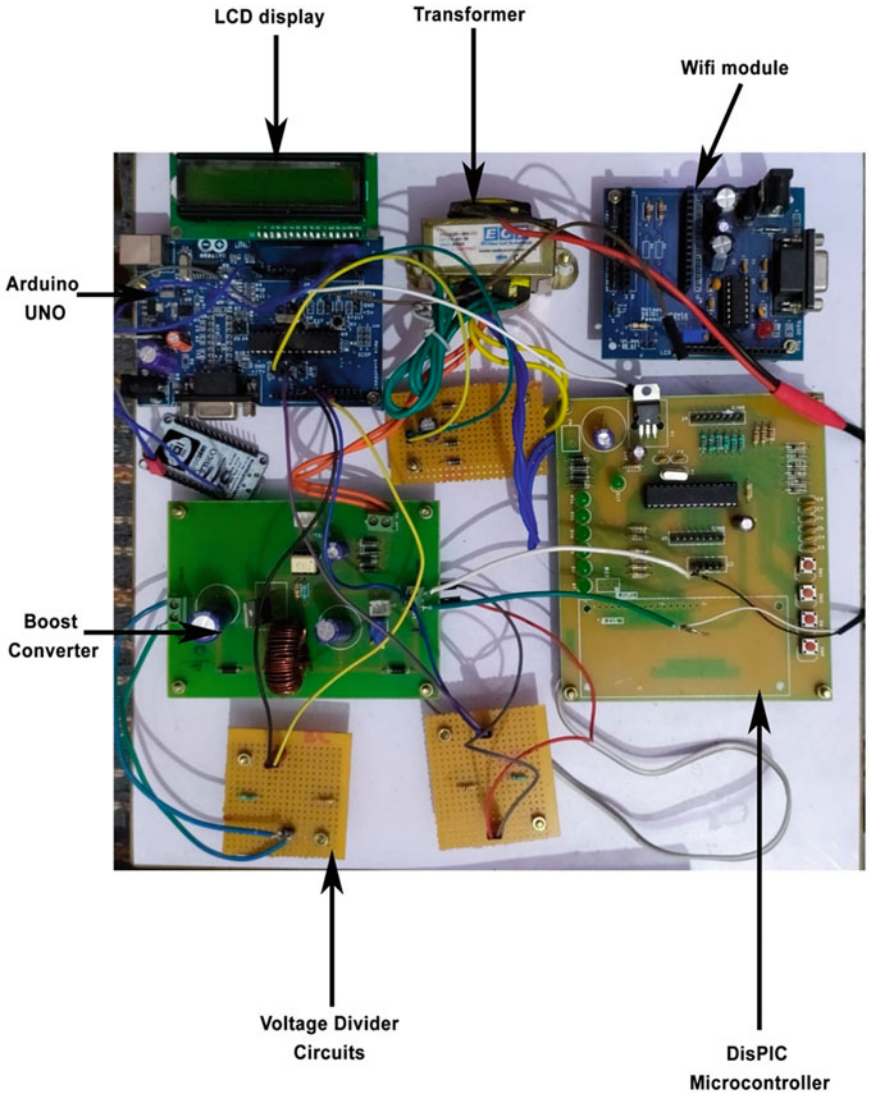

Fig. 15 Hardware setup of proposed method

References

1. Suruhanjaya Tenaga (Energy Commission) Malaysia Energy Statistic Handbook, (2015)
2. Y.-H. Chang and C.-Y. Chang, "A Maximum Power Point Tracking of PV System by Scaling Fuzzy Control," presented at International Multiconference of Engineers and Computer Scientists, Hong Kong, (2010)
3. S. Chin, J. Gadson, and K. Nordstrom, "Maximum Power Point Tracker," Tufts University Department of Electrical Engineering and Computer Science, (2003), pp. 1–66

4. Faranda R, Leva S (2008) Energy Comparison of MPPT techniques for PV Systems. WSES Transaction on Power Systems 3:446–455
5. T. P. Nguyen, "Solar Panel Maximum Power Point Tracker," in Department of Computer Science & Electrical Engineering: University of Queensland, (2001), pp. 64
6. Ayushi Nitin Ingole., "Arduino based Solar Tracking System",. International Conference on Science and Technology for Sustainable Development, Kuala Lumpur, Malaysia, (2016) May 24 – 26
7. Gagari Deb, Arijit Bardhan Roy. Use of Solar Tracking System for Extracting Solar Energy. International Journal of Computer and Electrical Engineering, vol. 4, no. 1, (2009), 42–46
8. Esram T, Chapman PL et al (2007) Comparison of photovoltaic array maximum power point tracking techniques. IEEE Transactions on Energy Conversion EC 22(2):439–445
9. D. Hohm and M. Ropp, "Comparative study of maximum power point tracking algorithms using an experimental, programmable, maximum power point tracking test bed," in Proc. 28th IEEE Photovoltaic specialists conference. IEEE, (2000), pp. 1699–1702
10. Femia N, Granozio D, Petrone G, Spagnuolo G, Vitelli M (2006) Optimized one-cycle control in photovoltaic grid connected applications. IEEE Trans Aerosp Electron Syst 42(3):954–972
11. A. N. A. Ali, M. H. Saied, M. Mostafa, and T. Abdel-Moneim, "A survey of maximum ppt techniques of pv systems," in IEEE Energy tech, (2012)
12. C. Hua and C. Shen, "Comparative study of peak power tracking techniques for solar storage system," in Proc. APEC'98, vol. 2. IEEE, (1998), pp. 679–685
13. K. Irisawa, T. Saito, I. Takano, and Y. Sawada, "Maximum power point tracking control of photovoltaic generation system under non-uniform insolation by means of monitoring cells," in Proc. IEEE 28th Photovolt. Spec. Conf., (2000), pp. 1707–1710
14. S. Yuvarajan and S. Xu, "Photovoltaic power converter with a simple maximum power point tracker," in Proc. Int. Symp. Circuits Syst., vol. 3, (2003), pp. III-399–III-402
15. Rai AK, Kaushika ND, Singh B, Agarwal N (2011) Simulation model of ANN based maximum power point tracking controller for solar PV system. Sol Energy Mater Sol Cells 95(2):773–778
16. S. K. Kollimalla and M.K. Mishra, "Novel adaptive P&O MPPT algorithm for photovoltaic system considering sudden changes in weather condition" in Proc. Int. Conf. Clean Elect. Power, (2013), pp. 653–658

Wireless Power Transfer for Electric Vehicles with Better Ground Clearance

A. Geetha, S. Usha, T. M. Thamizh Thentral, C. Subramani, J. Santha Kumar, and C. S. Boopathi

Abstract In modern era, in electric vehicles charger regularization, the following phase to make the charging procedure more convenient is to eradicate the usage of wired cable sandwiched by linking the electric vehicles and charger to accomplish wireless charging of electric vehicles, and a wireless power transfer (WPT) system ought to be depicted with respective ground clearance of electric vehicle. It is an innovation technology which can be applied for all electric vehicles (EVs) as it helps to get rid of user involvement. The crucial impediment for acquiring wireless charging is ground clearance which downgrades the power transfer efficiency. The theory of WPT for different ground clearance is elucidated, and the corresponding cordless charger device is analysed. The portrayed cordless charger device has capacity to distribute the power of about 45v utmost ground clearance of 20 cm. The battery designed is 4.5KWh and the super capacitor (SC) of 3.8KWh which is sufficient to charge electric vehicle.

Keywords Electric vehicle · Wireless power transfer · Ground clearance · Power converter · Vehicle charging

1 Introduction

The trade market of electric vehicles (EVs) has gradually begun to grow. To revive the vehicle within a short span, high-power charging devices or charging stations are required by the existing conductive charging method. Additional inconvenience is

A. Geetha · S. Usha (✉) · T. M. Thamizh Thentral · C. Subramani · C. S. Boopathi
Department of Electrical and Electronics Engineering, SRM Institute of Science and Technology, Kattankulathur 603203, Tamil Nadu, India

C. S. Boopathi
e-mail: boopathc1@srmist.edu.in

J. Santha Kumar
Department of Mechanical Engineering, SRM Institute of Science and Technology, Kattankulathur 603203, Tamil Nadu, India
e-mail: santhakj@srmist.edu.in

C. Subramani et al. (eds.), *Proceedings of International Conference on Power Electronics and Renewable Energy Systems*, Lecture Notes in Electrical Engineering 795,
https://doi.org/10.1007/978-981-16-4943-1_15

caused by incompatible plugs receptacles between different EV models. Charging infrastructure can be shared by different EV models as for the wireless charging technologies [1, 2].

The deployment of 85 million autonomous vehicles is expected by 2035; hence, establishment of wireless charging is needed, to incorporate in such vehicles [2]. WPT makes the system simplified, automatic, secure, economical and more efficient, whereas using of cables makes system so expensive. For instance, at the time of placing EVs for little while in parking lot, wireless charger systems enable automated charging. It eradicates the need for pilot interruption in course of charging. Main hindrance for acquiring wireless charging are coil misalignment and large air gap. To improve misalignment tolerance, various coil structures are used. The radial coil is pre-owned based on its unsophisticated erection [3–6]. Using miscellaneous coils, like double D-type [8, 9] and solenoid type, [10] leads to increased air gap between transmitter and receiver coils.

The reduction of coil misalignment before WPT's commencement improves transfer efficiency. In [11], the wireless charger was demonstrated by using conveyors and servo motors which helps in positioning the receiver to the transmitter. Air gap between the charging pad and the EV underbody is another limitation in WPT. In [12], a wireless charger was developed for ground clearance of 20 cm, which removes transporting data through amplitude modulation of the coil current.

As a result of numerous stances of vehicles and ground clearance, magnetic coupling is varied. This succumbs the power efficiency. To specify this significance, using of high reactive power and resonant elements is strongly recommended in both transmitter and receiver side. By using power conversion technique, the contactless coupler and the power electronics system, the battery is charged [13].

This system was designed with and supercapacitor and a lithium-ion battery. This cordless charger comprises of rectifier and LC filter. This algorithm used here is constant voltage and constant current, which compensates the transient state and to achieve more stability. This wireless charger with lithium-ion battery of 4.5 KWh and supercapacitor of 3.8KWh was analysed with efficiency of 86%.

2 Proposed Work

In recent trend, wireless power transfer is initializing to seek more and more attention. The block diagram comprises of grid, rectifier, inverter, LC filter, linear transformer, supercapacitor and battery as shown in Fig. 1. The low-frequency AC supply is supplied by grid and is rectified and inverted to high-frequency AC supply. In order to evict the harmonics, LC filter is brought into use. The high-frequency AC supply is provided to transmitter coil, and an emf is induced.

Due to the principle of Faraday's law of electromagnetic induction, the induced emf energizes the receiver coil. On account of magnetic field as shown in Fig. 2, the variations in the coupling factor k which are calculated by

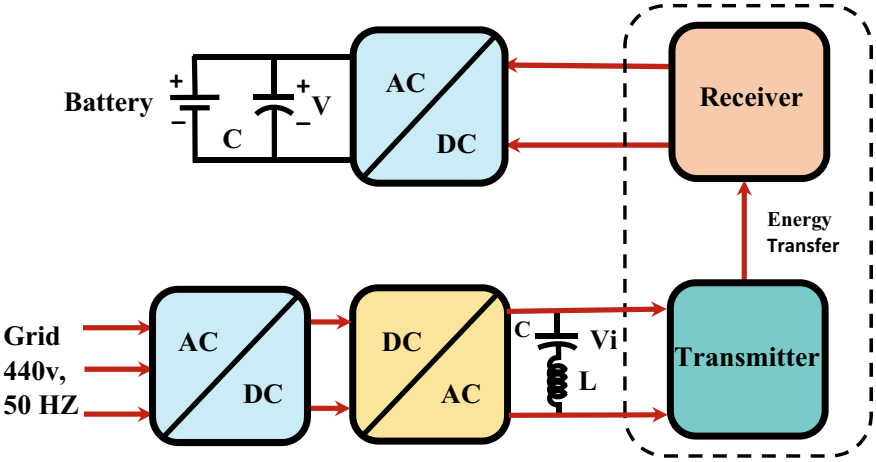

Fig. 1 Schematic layout of the proposed system

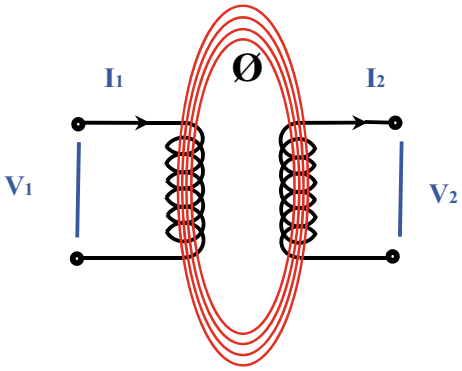

Fig. 2 Two magnetically coupled coils with good coupling

$$K = \frac{M}{L_1 L_2} \tag{1}$$

It is led by variations in the ground clearance, where the mutual inductance is M, and the transmitter and receiver coil inductances are L1 and L2, respectively. The received AC supply is rectified and supplied to the battery through the supercapacitor. In order to preserve the battery from catastrophic damage eruption by abrupt vehicle moving while charging, supercapacitor is applied.

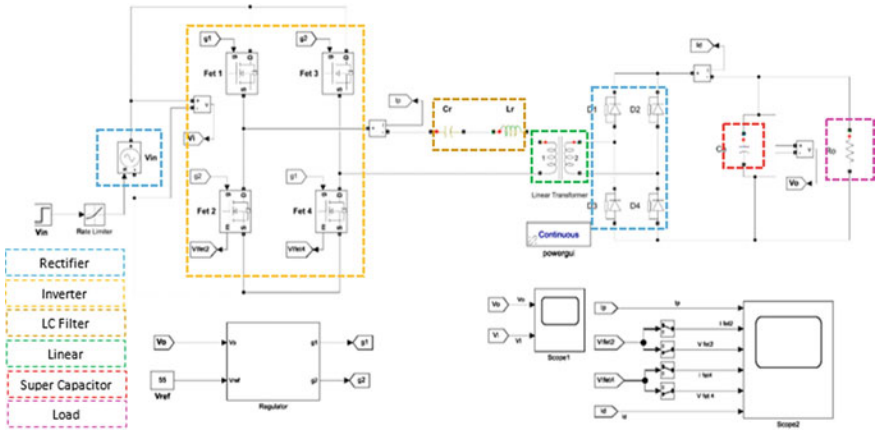

Fig. 3 Simulink diagram of the proposed system

3 Circuit Analysis

In the context of wireless transmission system, efficiency of whole system is dependent on ground clearance of electric vehicles. Since in case of wireless transmission, the transmitter is present in the atmosphere, which terrifically reduces the coupling factor. Now here, it is earnestly indispensable to examine the coupling coefficient (k) by adjusting the number of turns and distances between the transmitter and receiver coil. Figure 3 depicts the simulation diagram of the proposed system. It comprises of rectifier, inverter, LC filter, supercapacior and load. The proposed system tries to optimize the ground clearance during wireless charging of the electric vehicle.

The vital part in the determination of coupling coefficient is ground clearance, but for realistic motive, the number of turns will not be changing automatically as is the case of other parameters. So, in this content, we have concentrated on the dependence of coupling coefficient on the number of turns and distance between the coils. In the event of change in the coupling coefficient, efficiency of the system appropriately varies. In the designing of system parameters, coupling coefficient is useful.

4 Simulation Results

The reference voltage (constant value) and gate pulse were given by PWM technique. The PWM's advantage is low power loss in the switching devices.

There is an absence of current when the switch is in zeroth condition, and the power is transferred to the load when the switch is in the first condition, and also there is zero voltage drop between the switches. The input and output currents and the pulses offered to the power switches are as shown in Fig. 4.

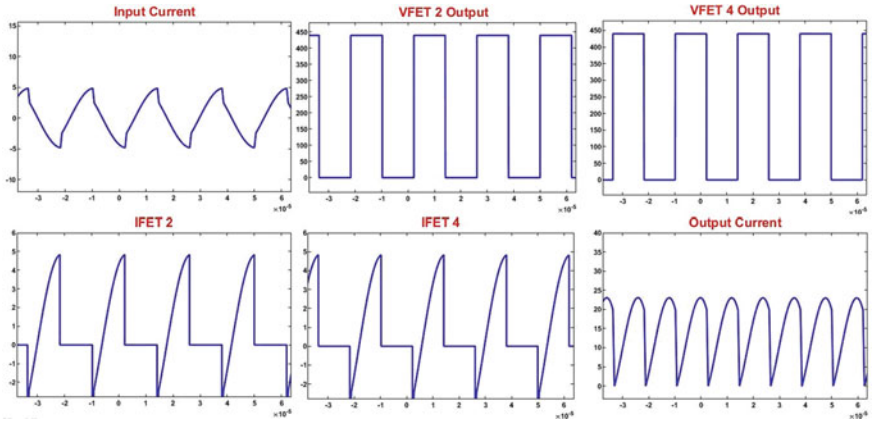

Fig. 4 PWM pulses, input current and output current

Table 1 provides the details of the components used and the corresponding values used for the system. A detailed information about the transmitter and receiver as well as the sub-system is provided with their scope of usage (Fig. 5).

Table 1 Details of the components used

Stage	Component	Symbol	Value	Unit	Scope
Transmitter	MOSFET	FET1-FET4	1	mΩ	Inverter
	Capacitor	Cr	160	nF	LC filter
	Inductor	Lr	37.5	μH	
	Regulator				
	Primary winding	1	52	V	Transmitter
			0.01	Ω	
			75	μH	
Receiver	Receiver winding	2	6	V	Receiver
			0.01	Ω	
			1.36	μH	
	Diode	D1-D4	1	mΩ	Rectifier
	Capacitor	C0	100	μH	Supercapacitor
	Resistor	R0	3	Ω	Load
Sub-system	Diode	D5-D8	1	mΩ	Rectifier
	Inductor	L1-L4	152	μH	Filter
	Diode	D9-D12	1	mΩ	Rectifier
	Capacitor	Cf	47	μH	RC filter
	Resistor	Rf	150	Ω	

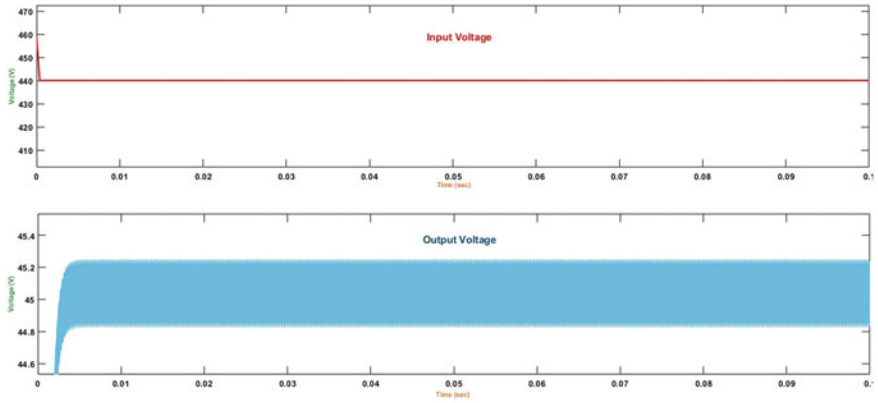

Fig. 5 Input and output voltages of the proposed system

An input supply voltage of 440 V is provided to the proposed system as shown in figure. The power converter designed will offer an output voltage of 45 V is obtained. Hence, a suitable voltage for the wireless charging of the vehicle is obtained with good efficiency.

5 Conclusion

In this material, an authentic method is portrayed to handle different ground clearance in wireless power transfer systems. The measurements used for the above parameters show reliable results for proposed theme. In the prototype, zero visible heating of the used relays was notified. Several simulations were performed. Regardless of previous studies, we inspected with some real-world charger placement limitations in the surveillance area such as walls and ground clearance. The above delivered system is economical and highly beneficial because it uses inverters, rectifiers and filters to handle a different coupling factor. Separate control system is enrolled, where the transmitter coil is automatically tapped for transferring the power to the battery based on the ground clearance within 200 mm. Eventually, this paper contributes to the typical hindrance of varying ground clearance. The wireless charger was procedurally verified for the battery at 4.5 kWh and supercapacitor at 3.8KWh with a peak efficiency of 86%.

References

1. Geetha A, Subramani C, Thamizh Thentral TM (2018) An efficient wireless power transfer using class E2 converter for electric vehicle. J Adv Res Dyn Control Syst 10:1–7

2. Qiu C, Chau KT, Ching TW, Liu C (2014) Overview of wireless charging technologies for electric vehicles. J Asian Electr Veh 12(1):1679–1680
3. Wu Y, Zhang C, Liu B (2018) Research on the quick charging method of wireless power transfer system for supercapacitor. In: 2018 13th IEEE conference on industrial electronics and applications (ICIEA), pp 582–587
4. Sample AP, Meyer DT, Smith JR (2011) Analysis, experimental results, and range adaptation of magnetically coupled resonators for wireless power transfer. IEEE Trans Industr Electron 58(2):544–554
5. Low ZN, Chinga RA, Tseng R, Lin J (2009) Design and test of a high-power high-efficiency loosely coupled planar wireless power transfer system. IEEE Trans Industr Electron 56(5):1801–1812
6. Kim J, Kim J, Kong S, Kim H, Suh IS, Suh NP, Cho DH, Kim J, Ahn S (2013) Coil design and shielding methods for a magnetic resonant wireless power transfer system. Proc IEEE 101(6):1332–1342
7. Miller JM, Onar OC, Chinthavali M (2015) Primary-side power flow control of wireless power transfer for electric vehicle charging. IEEE J Emerg Selected Topics Power Electron 3(1):147–162
8. Budhia M, Boys JT, Covic GA, Huang CY (2013) Development of a single-sided flux magnetic coupler for electric vehicle ipt charging systems. IEEE Trans Ind Electron 60(1):318–328
9. Covic GA, Boys JT (2013) Modern trends in inductive power transfer for transportation applications. IEEE J Emerging Selected Topics in Power Electron 1(1):28–41
10. Budhia M, Covic G, Boys J (2010) A new ipt magnetic coupler for electric vehicle charging systems. In: IECON 2010—36th annual conference on IEEE industrial electronics society, pp 2487–2492
11. Elliott GAJ, Boys JT, Covic GA (2006) A design methodology for flat pick-up icpt systems. In: 2006 1ST IEEE conference on industrial electronics and applications, pp 1–7
12. Omori H, Inoue M, Kimura N, Morizane T, Nakaoka M (2017) A new large-gap wireless ev charger with a power superimposition communication. In: 2017 19th International conference on electrical drives and power electronics (EDPE), pp 65–69
13. Schneider J, O'Hare J (2017) Alignment, verification, and optimization of high-power wireless power charging systems. US Patent 9637014B2

Five-Level PUC Inverter-Based Shunt Active Power Filter for Harmonic Elimination

T. M. Thamizh Thentral, K. Vijayakumar, S. Usha, A. Geetha, and C. S. Boopathi

Abstract The five-level packed U-cell (PUC) inverter topology is designed as an active power filter to reduce the harmonics present in the nonlinear system. The packed U-cell is a newly emerged multilevel inverter that can generate different levels by utilizing capacitors at the output side. It is called packed U-cell since it has a capacitor and a couple of power switches arranged in U shape. The energy conversion takes place using a limited number of power semiconductor devices and capacitors, thus reducing the cost of production. The model of a five-level PUC inverter is designed, and the simulated waveforms along with their THD are discussed.

Keywords PUC5 inverter · Total harmonic distortion · Shunt active power filter · Harmonics

1 Introduction

Distribution network is one of the most important and complex parts of the power system. Transmitting power from the distribution transformer to the power point has challenging problems regarding reactive power and unbalance. Using more number of switches and DC sources in power electronic converters by generating more voltage levels with lower harmonics and smaller size of components is a field of research still going on [1]. In many traditional multilevel converters topology such as flying capacitors, neutral point clamped converts or classical cascaded H bridges which have lesser total harmonic distortion (THD) in current and voltage mostly have many switches required for the operation which results in complexity of circuit, increasing the cost decreasing the reliability [2].

Most problems arise due to the presence of power electronic converters as these converters generate harmonics in the source current and increase relative currents. The main concerns with power converters are maintenance of unity power factor throughout the operation and a relatively low total harmonic distortions of the input

T. M. Thamizh Thentral (✉) · K. Vijayakumar · S. Usha · A. Geetha · C. S. Boopathi
Department of Electrical and Electronics Engineering, SRM Institute of Science and Technology, Kattankulathur 603203, Tamil Nadu, India

C. Subramani et al. (eds.), *Proceedings of International Conference on Power Electronics and Renewable Energy Systems*, Lecture Notes in Electrical Engineering 795,
https://doi.org/10.1007/978-981-16-4943-1_16

AC waveforms [3]. By producing more levels of voltage, the multilevel converters are able to decrease the current and voltage harmonics while keeping a low switching frequency. To overcome various drawbacks of multilevel inverter, the packed U-cell inverter was designed that offers the advantage of less number of switches, thereby reducing switching losses and production cost. A five-level voltage waveform is obtained at the output by applying various voltage balancing techniques for the capacitor. By making use of redundant switching states, the capacitance can be reduced, and hence, small size capacitors can be used [4].

In this paper, the active power filter role in harmonic distortion is discussed in Sect. 2. The PUC5 configuration and switching states are discussed in Sects. 3and 4, respectively. The modeling of a single-phase inverter with feedback is simulated with the help of MATLAB/Simulink as discussed in Sect. 5.

2 Active Power Filters for Harmonic Elimination

Active power filters are now being utilized to compensate for both current and voltage harmonics (depending on connection—shunt or series), power factor correction and power quality improvement in power system networks. The active power filters are made up of power converters and passive devices that have been designed to eliminate harmonic content and improve power quality [5]. They started to gain more popularity recently due to their ability to compensate for harmonics demanded by various nonlinear loads. Current harmonics caused due to distortion by nonlinear loads results in decrease of power quality due to high THD. In order to solve these problems, active filters are introduced in the grid to reduce harmonics and improve the power factor [6].

Active filters are widely classified into three types, namely shunt, series and hybrid. The shunt active filter purpose is to cancel load harmonics present in the current fed to the supply. The advantage of using shunt apart from reactive power compensation is that it can transfer the compensation current with small amounts of active fundamental current so as to compensate for the losses in the systems [7]. The shunt active power filter is commonly composed of a voltage-source converter (VSC) or a current-source converter with DC link capacitors mainly [8].

APFs can be controlled by two methods, i.e., direct mode or indirect mode. In direct mode, the reference current is taken as the extracted harmonic components of the load current. The harmonic extraction can be done by filters, power theories, neural networks, fast individual harmonic extraction technique, Park transformation, wavelet transformation, etc. [9]. In indirect mode, the AC input current is in phase with the standard voltage without having to use any harmonic extraction component. This mode has simpler system structure and better harmonic performances, and hence, the one controller that it used for generating a signal for reference is modulated and sent to switches with required pules. The PUC converter here acts as an active power filter connected in shunt, hence bringing about harmonic elimination in the load current [10].

3 PUC5 Configuration Design

The PUC5 consists of packed U-cells in which each cell has an arrangement of two switches and one capacitor.

The number of levels can be obtained by the relation:

$$2^{(N+1)} - 1 = \text{Number of levels}$$

where $N = 1,2,3$.

The number of capacitors is obtained by the relation:

$$N = 2^{(Nc+1)} - 1$$

where N is the number of voltage levels and Nc is the number of capacitors required.

From the equations, it is understood that the topology not only uses a single DC source, but also reduces the number of switches to obtain the required voltage levels.

4 PUC5 Configuration Design

Figure 1 shows the single-phase PUC5 inverter topology. The different possible switching states are listed in Table 1. The on state of the switches is represented with "*" in the table, and off state is mentioned as "-". Although the PUC7 inverter has a number of components as compared to other converters, switching frequency is high and regulation of capacitor voltage becomes complicated. Hence, it is easier to go with five-level converters, where the capacitor voltage is regulated at half of dc supply value, thus eliminating current and voltage sensors.

From the following eight switching states, eight different paths of current flow are obtained through the system. For generating five levels, six switches and two capacitors are arranged in a U-cell in such a way, that in each half cycle, a total of three switches conduct and a single switch in each leg.

The different levels in output waveform are obtained by using unequal DC sources. Assuming that the capacitor voltages V1 = 2V2 = 2E, the PUC inverter will operate as a five-level inverter with the output voltage as 0, ±E, ±2E. To obtain a voltage level of say +2E, the switches S1, S5 and S6 must be on. Similarly, to get voltage level −2E, the switches S3, S2 and S4 must be triggered. To obtain five levels, there will be a total of eight different possible switching states. The capacitor can be charged in one half cycle and discharged in next or vice versa. In order to fix the voltage of the capacitor constant, the capacitor here is charged at each positive half cycle and discharged in the negative half cycle.

To produce the desired voltage level, the source voltage is fixed at twice the input DC source E, so that the capacitor can be charged up to E. To produce equivalent

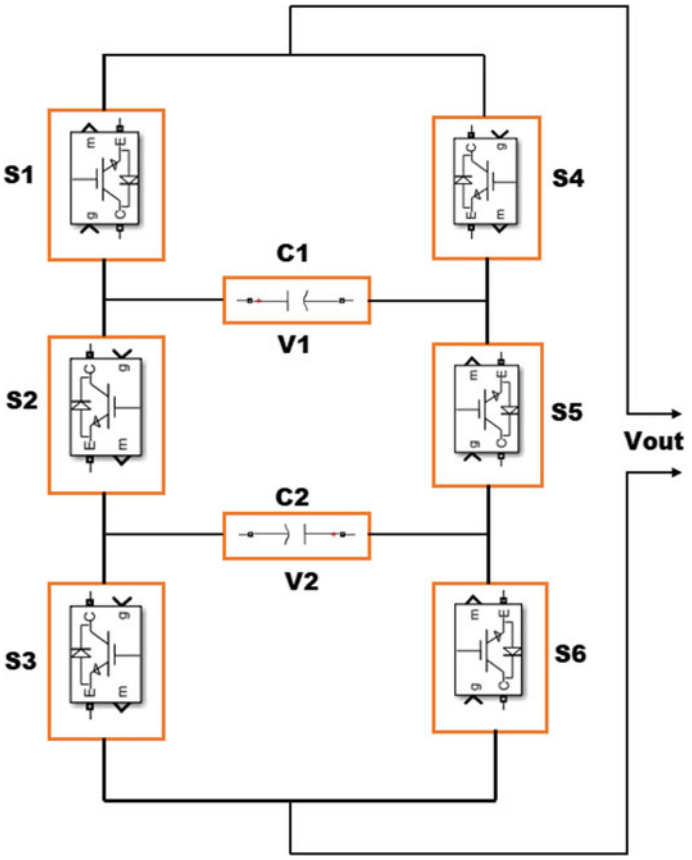

Fig. 1 Per-phase PUC5 converter topology

Table 1 Switching states of PUC inverter

States	S1	S2	S3	Output voltage	V_t
1	*	–	–	V1	2E
2	*	–	*	V1–V2	E
3	*	*	–	V2	E
4	*	*	*	0	0
5	–	–	–	0	0
6	-	–	*	– V2	– E
7	–	*	–	V2–V1	– E
8	–	*	*	– V1	– 2E

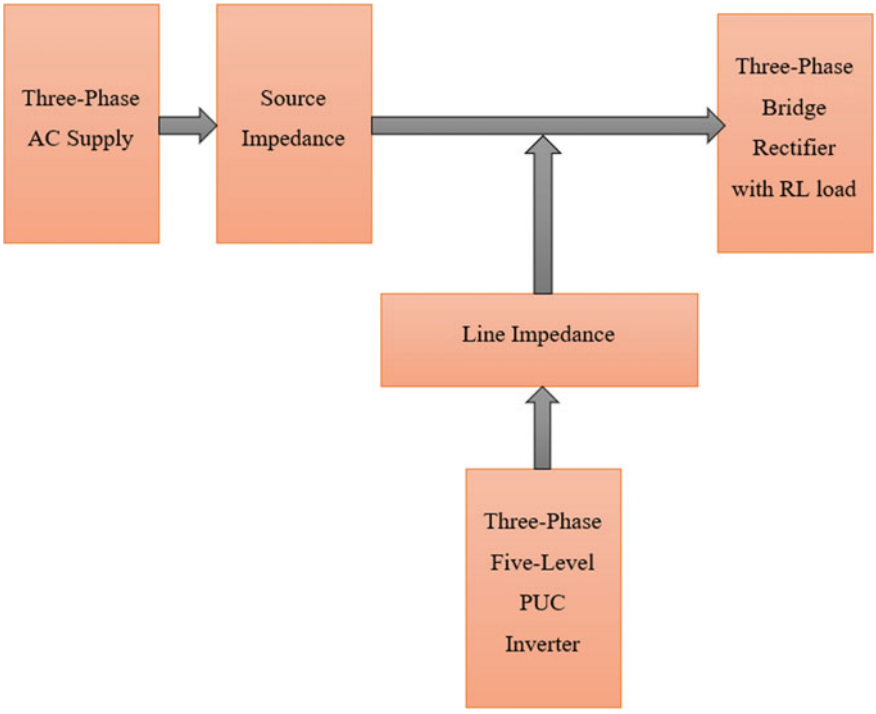

Fig. 2 Block diagram representation of three-phase PUC5 inverter with nonlinear load

charging and discharging times in one period, here in state 2, the capacitor charges from source while it is discharged in the next negative half cycle. The charging of capacitor and discharging time depend on the load value only. This in turn also affects the size of capacitor as larger loads will need small-sized capacitors in DC link and thus also reducing the cost. The block diagram of the proposed three-phase PUC5 inverter-based nonlinear system proposed in this paper is shown in Fig. 2.

5 Experiment Results

The five-level PUC converter in shunt to the AC source system shown in Fig. 3 has been built in MATLAB/Simulink. The PI controller is used for generating the waveform which is obtained from the difference of the reference and carrier signal and injected between the load and AC source. The test parameters are as shown in Table 2. The source currents and voltage waveforms and also output voltage and current waveforms are shown in Fig. 4. The load, filter-side voltage and current are also shown. The THD levels before and after introducing the converter are illustrated in Fig. 5.

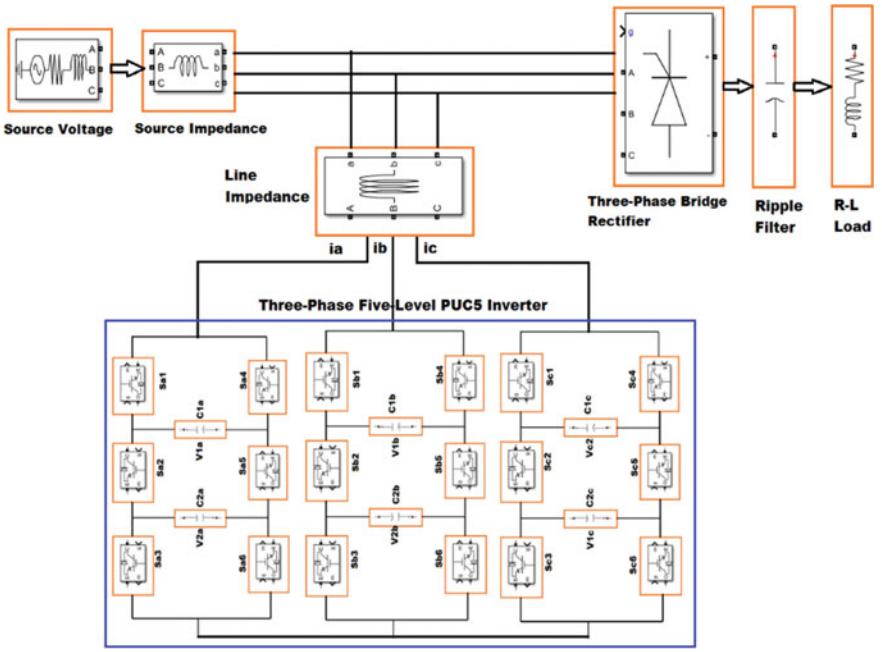

Fig. 3 Three-phase five-level PUC5 inverter with nonlinear load

Table 2 PUC5 inverter parameter values

Parameter	Parameter value
AC grid voltage	110 V
AC grid frequency	50 Hz
Filter-side inductor (Lf)	2.3 mH
Load-side inductor (Ll)	30 mH
Load-side resistance (Rl)	30 Ω
Load-side capacitance	600 μF

The positive and negative sides are equal and opposite to each other and together form the upper and lower switches which in total forms an eight-switch combination. The vector values are generated from the respective voltage outputs from the eight combinations which are zero in two cases and positive or negative in six of them. A hexagon with an equal angle of sixty degree is formed with the nonzero vectors. Therefore, space vector modulation technique generates a voltage in accordance with the vectors calculated and generated due to the eight combinations. The implementation of space vector modulation is found to be very adaptable to changing supply configuration. Since the injection point is independent of load configuration in this closed loop system, space vector modulation provides high accuracy in this implementation. Eight possible combinations of on and off patterns may be achieved.

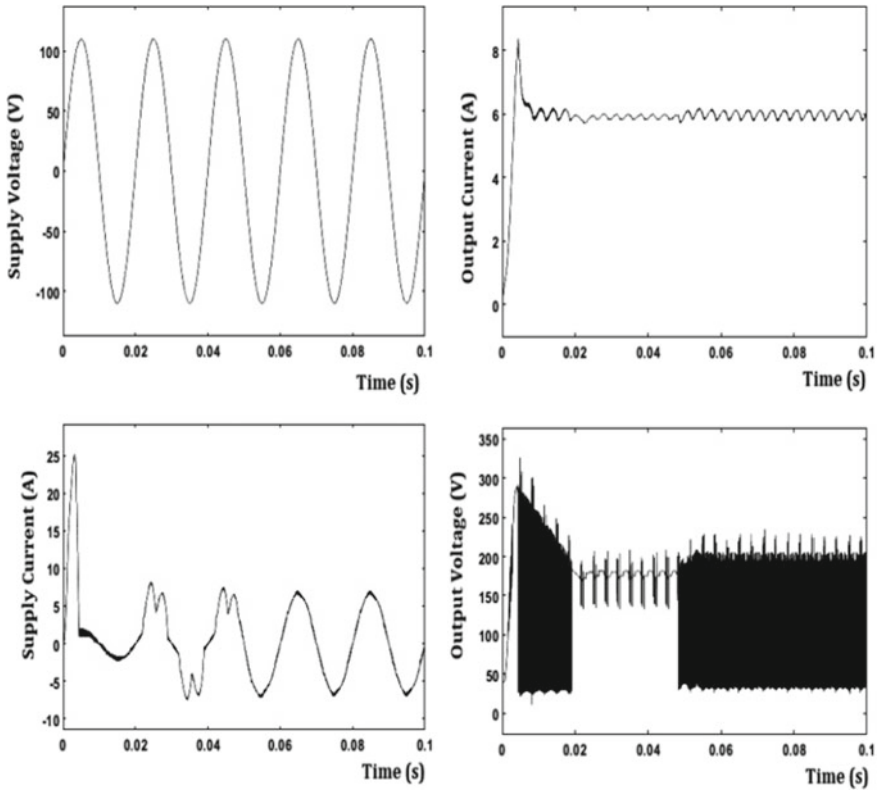

Fig. 4 Input and output current and voltage waveform

The on and off states of the lower switches are the inverted states of the upper ones (Fig. 6).

It is clear that the, since the converter is introduced in shunt, there is significant compensation by the APF in the current harmonics at the load side. Initially, before the converter was introduced, the THD factor was found to be 23.25%. After the introduction of the PUC5 converter, the THD level has dropped down to 2.03%. On observing the waveforms for current on the load side, the harmonics are reduced considerably. Since there is feedback given, according to changes in the load side, then the compensation current will be injected to the load side at the point of common coupling. The filter-side current which is responsible for the compensation harmonics is shown in Fig. 5.

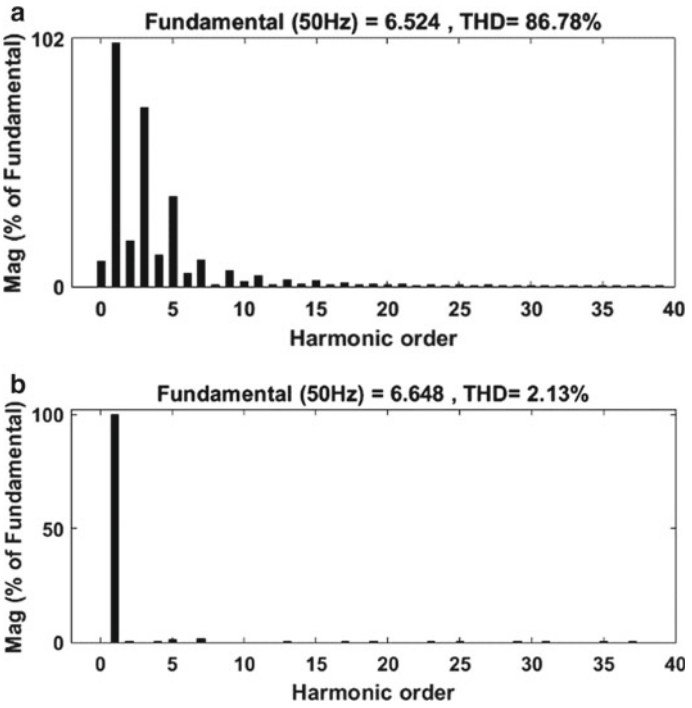

Fig. 5 **a** Source current % THD before filter, **b** source current % THD before filter

6 Conclusion

In this paper, the new technology converter, PUC5 was designed integrated with a proportional and integral controller providing a feedback in a closed loop system and studied. The PUC5 converter is connected in the AC grid in parallel with constant load in order to reduce the current harmonics. The harmonics in the current are observed to be reduced from 23.25 to 2.03% with the injection of current waveform which is a negation of the reference current signal waveform and the carrier waveform. This result is obtained when the load is operated at a value of 100%, and it varies with the intake of load current by a variable nonlinear load if connected at the load side. The PUC5 converter, therefore, would be highly advantageous as it is very easy to be retrofitted in any kind of existing load configuration without the need to be modified and executing the elimination of harmonics in AC power grid systems.

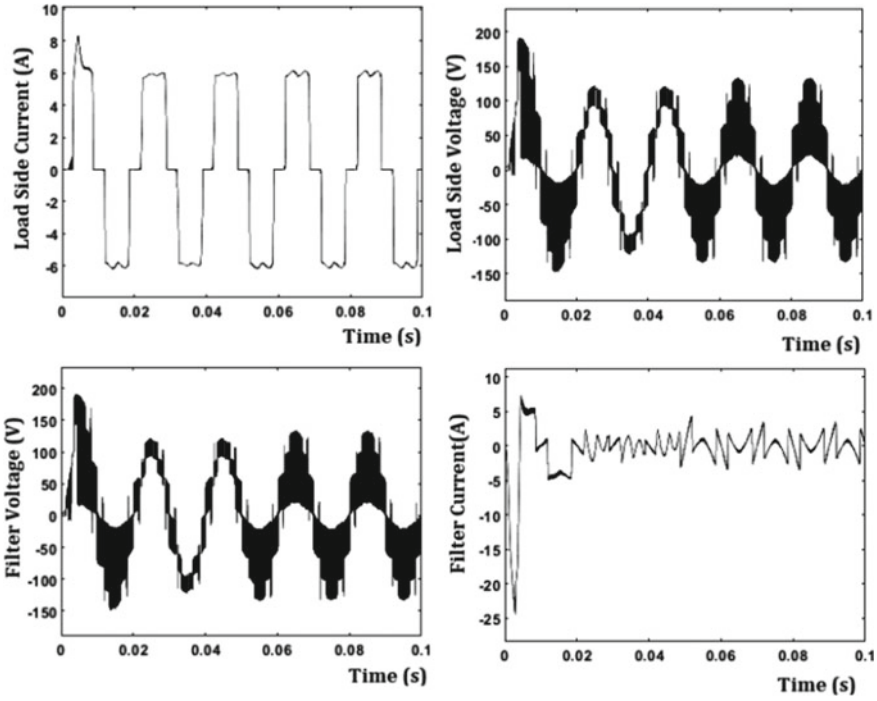

Fig. 6 Load and filter current and voltage

References

1. Vahedi H, Labbé PA, Al-Haddad K (2016) Sensor-Less five-level packed U-Cell (PUC5) inverter operating in stand-alone and grid-connected modes. IEEE Trans Ind Informatics 12(1)
2. Tariq M, Meraj M, Azeem A, Maswood AI, Iqbal A, Chokkalingam B (2018) Evaluation of level-shifted and phase-shifted PWM schemes for seven level single-phase packed U cell inverter. PSS Trans Power Electron Appl 3(3)
3. Abarzadeh M, Vahedi H, Al-Haddad K (2019) Fast sensor-less voltage balancing and capacitor size reduction in PUC5 converter using novel modulation method. IEEE Trans Ind Inf 15(8)
4. Vahedi H, Al-Haddad K () PUC5 inverter—a promising topology for single-phase and three-phase applications. In: Conference: IECON 2016—42nd annual conference of the IEEE industrial electronics society, October 2016
5. Wu JC, Jou HL, Feng YT, Hsu WP, Huang MS, Hou WJ (2017) Novel ciruit topolgy for three phase active power filter. IEEE Trans Power Delivery 22(1)
6. Kocaeli University, Technical Education Faculty, Electrical Education Department (2009) Operation of shunt active power filter under unbalanced and distorted load conditions
7. Jacob A, Abraham BT, Prakash N, Philip R (2014) A review of active power filters in power system applications. Int J Adv Res Electr Electron Instrum Eng 3(6)
8. de Almeida Carlos GA, Jacobina CB, Me´llo GPRA, dos Santos EC Jr (2017) Shunt active power filter based on cascaded transformers coupled with three-phase bridge converters. IEEE Trans Ind Appl 53(5)
9. Busawon K, Putrus GA, Ran L (2005) Fast-individual-harmonic-extraction technique. Proc Gener Transm Distrib 152(4)

10. Vahedi H, Shojaei AA, Chandra A, Al-Haddad (2016) Five-Level reduced-switch-count boost PFC rectifier with multicarrier PWM. IEEE Trans Ind Appl 52(5)

Performance of 100-kW Rooftop PV Plant in Library Building—A Case Study in SRMIST

J. Divya Navamani, Tanmay Padhi, Aditi Kumari, and A. Lavanya

Abstract In this paper, performance analysis of 100-kW rooftop PV plant in library building of SRM Institute of Science and Technology, Kattankulathur, Chennai, is carried out. The site description and the plant capacity are mentioned as the details obtained by the department, and calculation was performed on the same data. The performance of the system over last three academic years has been compared. Furthermore, the analysis is extended by comparing this 100-kW PV plant with the similar PV plant in the institute. The configuration of the PV plant taken for the comparison is the same 100-kW with similar structure. The findings from the study and comparison are added finally with the causes of the shortfall in the performance of the system. Finally, the inferences are concluded which will guide the researchers to find the solutions for the cause and effect observed in this 100-kW PV plant.

Keywords PV · Energy yield · Performance assessment

1 Introduction

As the modern world focuses more and more on renewable energy sources, solar energy has become one of the most used energy forms across the world. Many researches are going on to enhance its use in everyday life and how uses of this energy can be further more expanded. It has been witnessed that a solar thermal collector is used to convert energy into heat and simultaneously panels are used

J. Divya Navamani (✉) · T. Padhi · A. Kumari · A. Lavanya
Department of Electrical and Electronics Engineering, SRM Institute of Science and Technology, Kattankulathur, India
e-mail: divyanaj@srmist.edu.in

T. Padhi
e-mail: tp2737@srmist.edu.in

A. Kumari
e-mail: ak5060@srmist.edu.in

A. Lavanya
e-mail: lavanyaa@srmist.edu.in

C. Subramani et al. (eds.), *Proceedings of International Conference on Power Electronics and Renewable Energy Systems*, Lecture Notes in Electrical Engineering 795,
https://doi.org/10.1007/978-981-16-4943-1_17

for generating electricity [1]. Since PV modules are made up of silicon cell with lesser efficiency, it is necessary to work on the efficiency of the PV module to attract many investors [2]. The system, however, needs to be sustainable and reliable, and it totally depends on the optimization which can meet the demands of load [3]. The performance is also dependent on the environment, location and plant types, so these things are important during installation for any system [4]. Recently, many initiatives have been taken by the Government to install the panels over the roof in many of the offices and institutions which can help to tackle the crisis [5]. Also, it can reduce the effect of greenhouse gas produced through fossil fuel. The PV energy is comparatively less expensive than any other renewable source, and it has been found to be more profitable in rural areas [6]. Another factor which creates impact on the performance is shading effect on the system, and it can influence the output power and output energy of the PV system connected [7].

Various studies are performed in this literature on performance analysis of PV. This study has been done on the PV system present on rooftop of library building of SRM Institute of Science and Technology, Kattankulathur, India. There are 20 strings, and each string has 20 panels connected to it. The details of the plant and the size have been given in the below part. Also, in the later part of this literature, comparative study has been done. Performance for three PV plants was taken, and energy yield and other parameters were calculated.

2 Description of the Plant

The PV power plant was installed in 2014 on rooftop of library building of SRM Institute of Science and Technology, Kattankulathur-603,203. The grid-connected plant consists of 20 strings each of which has 20 panels connected in series. The overall installed capacity is 100-kW. The PV strings are connected to nine inverters out of which four strings are connected to Inverter 1 and remaining eight inverters are each connected with two strings. The rating of each panel is 250 W, and it has 400 panels which are put together to get 100-kW rating. The schematic diagram of the modules connected and the sizing of inverter is given in Fig. 1a.

The photographs of the mono and polycrystalline solar PV module installed in the plant are depicted in Fig. 1b, c. The nine inverters which are connected to the strings of the PV module are illustrated in Fig. 1 d, e. The rating of each inverter with their model/make is also presented in Table 1.

Initially, we started the study by analysing all the influencing parameters of the energy yield from the solar PV plant. Solar irradiation data obtained from the PVsyst 7.1 are analysed from January to December, and the observations are plotted in Fig. 2a, b.

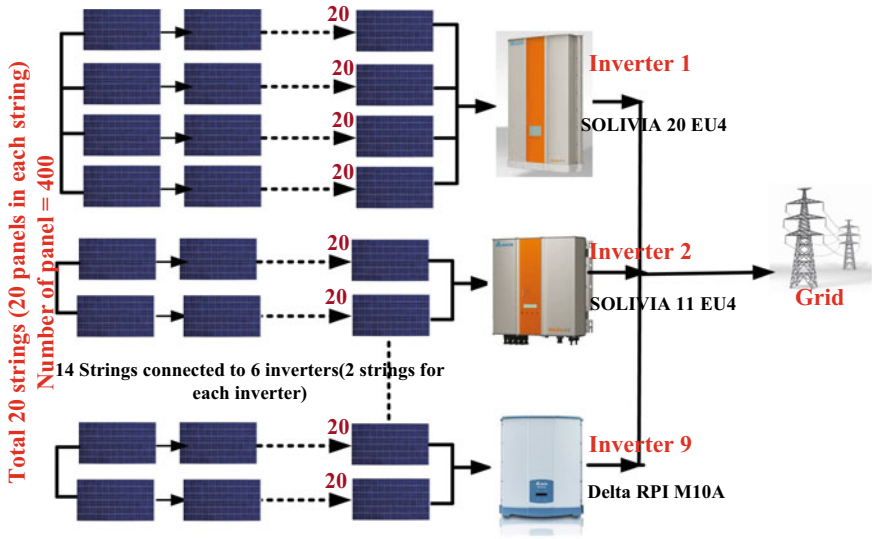

(a)

(b)

(c)

(d)

(e)

Fig. 1 (**a**) Schematic diagram of 100-kW plant, (**b**) and (**c**) solar PV module connected (**d**) and € Inverter connected to the strings

Table 1 Details of the inverters in the plant

Name	Type	Size (kWp)
Inverter 1	SOLIVIA 20 EU4	20
Inverter 2	SOLIVIA 11 EU4	9
Inverter 3	SOLIVIA 11 EU4	11
Inverter 4	SOLIVIA 11 EU4	7
Inverter 5	SOLIVIA 11 EU4	11
Inverter 6	SOLIVIA 11 EU4	11
Inverter 7	SOLIVIA 11 EU4	11
Inverter 8	RPI M10A	10
Inverter 9	RPI M10A	10

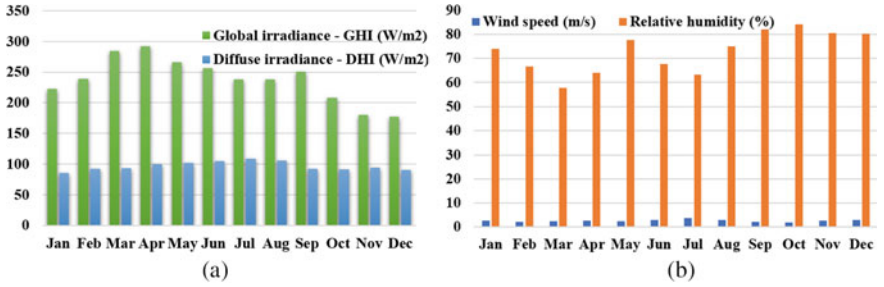

Fig. 2 **a** Solar irradiation in the location, **b** wind speed and relative humidity

3 Performance Analysis of the Plant

This section compares the performance of 100-kW PV plant in the library building for the year 2018–2020. Figure 3a, b presents the graphical representation of the plant for all the year from January to December. From this comparative study, it is observed that the performance of the plant in the year 2018 is poor compared to next two consecutive years. The average performance ratio of this plant for the year 2018 is 41% whereas for the year 2019 and 2020 is 70% and 64%, respectively.

4 Comparative Analysis

In the comparative study, the first comparison is carried out for the 100-kW PV plant for the year 2018–2020. Secondly, the same plant is compared with the similar plant for the year 2020.

A. Comparative study on the PV plant in Library Building:

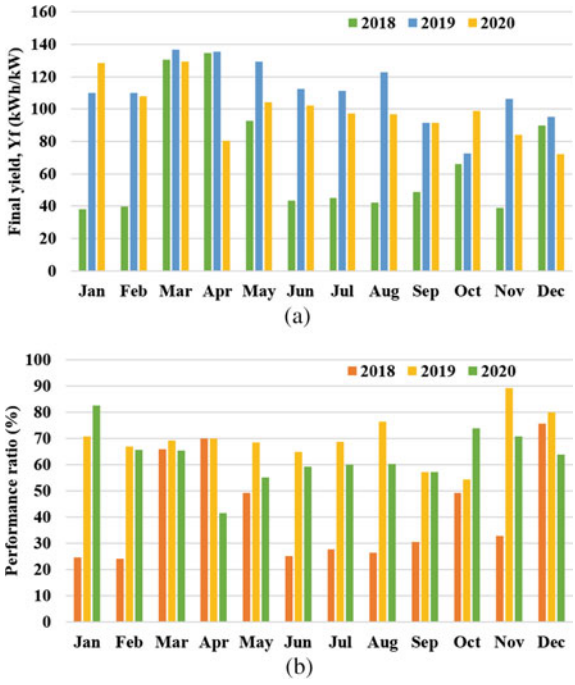

Fig. 3 **a** Final yield for last three years (2018–2020), **b** comparison of performance ratio for three years (2018–2020)

Table. 2 Energy yield and energy produced by 100-kW solar system for the year 2018–2020

Date	Total Yield in Wh	Date	Total Yield in Wh	Date	Total Yield in Wh
01-01-2018	3,822,359	01-01-2019	11,002,279	01-01-2020	12,855,238
01-02-2018	3,972,767	01-02-2019	11,008,333	01-02-2020	10,793,741
01-03-2018	13,041,601	01-03-2019	13,673,836	01-03-2020	12,922,897
01-04-2018	13,458,374	01-04-2019	13,527,115	01-04-2020	8,044,220
01-05-2018	9,293,124	01-05-2019	12,933,989	01-05-2020	10,422,097
01-06-2018	4,328,229	01-06-2019	11,228,847	01-06-2020	10,218,172
01-07-2018	4,491,192	01-07-2019	11,133,617	01-07-2020	9,713,176
01-08-2018	4,222,856	01-08-2019	12,275,602	01-08-2020	9,690,844
01-09-2018	4,896,087	01-09-2019	9,164,699	01-09-2020	9,149,403
01-10-2018	6,605,451	01-10-2019	7,277,069	01-10-2020	9,897,554
01-11-2018	3,891,626	01-11-2019	10,623,177	01-11-2020	8,427,585
01-12-2018	8,989,861	01-12-2019	9,508,014	01-12-2020	7,583,870

This section discusses about the comparison of performance of library building for last three (2018, 2019 and 2020) years. The 100-kW PV plant in library building

was installed in the year 2014. Table 2 presents the total energy yield in Wh for three years. The graphical representation of this comparison is illustrated in Fig. 4.

In this section, three 100-kW PV plants are compared, and their performances were studied. Table 3 depicts the energy yield for the year 2020 along with kWh/kWp of all the PV plant in the institute. All the three PV plants are installed in the same latitude and longitude with 500 m distance between them. The solar irradiation on all the three plants is more or less the same when we observed the NREL data from PVsyst 7.1 software. To deliberately observe the energy yield output of the plant from January to December 2020, a graphical representation is presented in Fig. 5. From this figure, it is noted that the performance of the three plants is quite closer

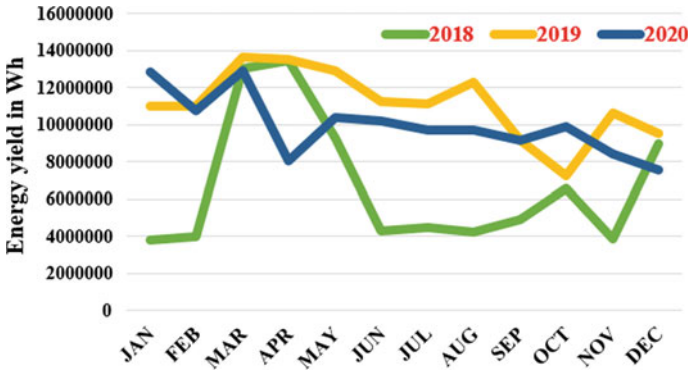

Fig. 4 Comparison of energy yield for three years (2018–2020)

Table 3 Energy yield and energy produced by solar array in the year 2020

Date	Library Building (Wh)	Library Building (kWh/kWp)	Dental College (Wh)	Dental College (kWh/kWp)	Medical College (Wh)	Medical College (kWh/kWp)
Jan-20	12,855,238	128.55	11,358,200	113.58	12,974,100	129.74
Feb-20	10,793,741	107.94	12,370,000	123.7	12,669,400	126.69
Mar-20	12,922,897	129.23	13,624,300	136.24	13,668,900	136.69
Apr-20	8,044,220	80.44	4,098,000	40.98	12,191,800	121.92
May-20	10,422,097	104.22	11,406,900	114.07	10,723,600	107.24
Jun-20	10,218,172	102.18	11,395,400	113.95	9,058,000	90.58
Jul-20	9,713,176	97.13	11,188,500	111.89	9,580,700	95.81
Aug-20	9,690,844	96.91	10,890,100	108.9	10,710,900	107.11
Sep-20	9,149,403	91.49	7,340,900	73.41	10,058,900	100.59
Oct-20	9,897,554	98.98	10,434,400	104.34	10,719,100	107.19
Nov-20	8,427,585	84.28	9,232,800	92.33	9,951,800	99.52
Dec-20	7,583,870	75.84	8,127,300	81.27	4,684,300	46.84

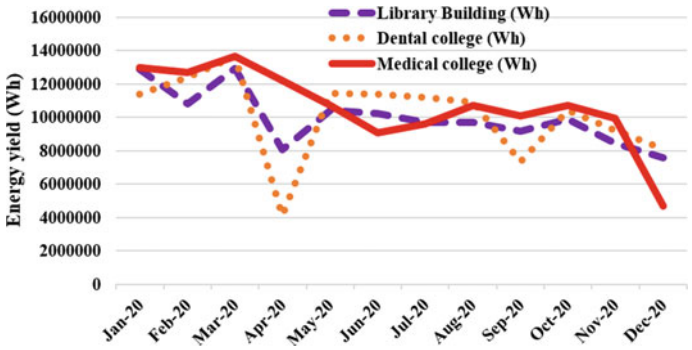

Fig. 5 Comparison of energy yield in Wh for three 100-kW PV plants (2020)

in the month of January, May, July, October and November. It is also observed that the performance of dental college is poor compared to other two plants due to the obstacles and other shading related issues by nearby building. The altitude of library and medical college is also noted to be high compared to the dental college.

5 Inference from the Study

We made a complete analysis on the PV plant installed in library building of SRMIST. It has 400 PV panels. This plant is installed in the year 2014. Initially, it is installed with 400 numbers of monocrystalline PV modules with the rating of 250 W which is conveyed to the total of 100-kW.

Figure 6a, b presents the picture of the library building and satellite image of the building with solar panel where the 100-kW plant is installed. Figure 6c illustrates the changes made in the solar PV module in the year 2017–18. It was reported that the speed of Vardah cyclone was 155 km/hour and it causes $1 billion worth destruction in Tamil Nadu. The hurricane strength uprooted many tress and poles in the state. In SRMIST, it uprooted the installed PV array from the rooftop of the building, and it falls on the other PV modules nearby. This damages around 45-kW of the 100-kW PV system.

6 Conclusion

This paper elaborates the study carried out on the 100-kW solar PV plant in library building in SRM Institute of Science and Technology. The plant has 400 number of PV panel with 250 W rating, and it has nine inverters with different ratings. The performance of this plant is studied, and major findings from this study are as follows.

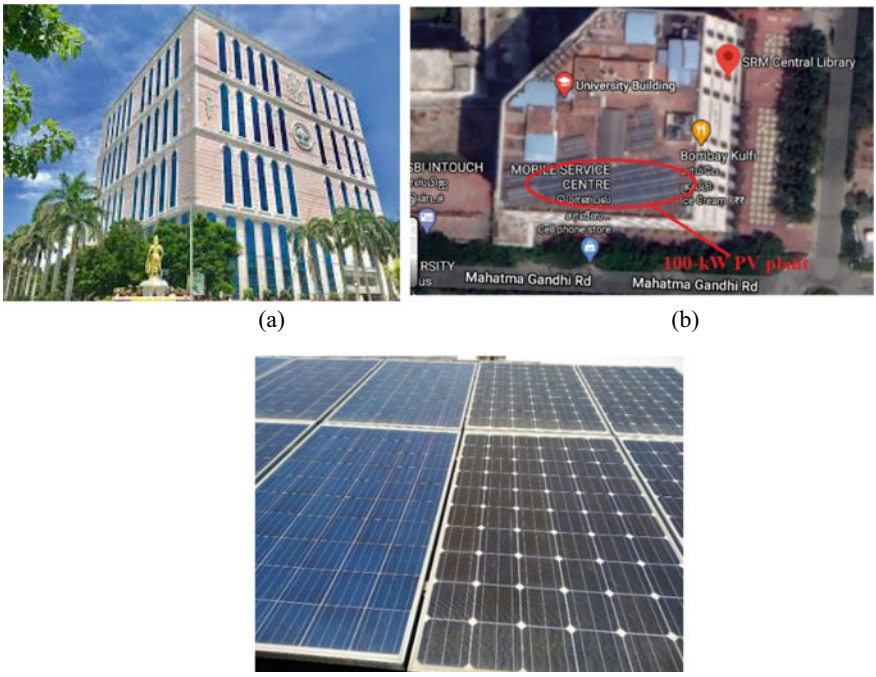

(a) (b)

(c)

Fig. 6 **a** Library building in SRMIST, **b** satellite image of library building with 100-kW PV plant, **c** changes made in the PV panels after cyclone in the year 2016

- Initially, the plant consists of monocrystalline PV panel, and it was installed in the year July 2014.
- The plant was exposed to two cyclones which were occurred in the year 2016 and 2020.
- Due to Vardah cyclone, around 40–45 kW of PV plant was damaged completely. After a year, the damaged PV module is replaced with polycrystalline PV panel.
- After the replacement, there was several issues in the plant, and the performance of the plant in the year 2018 is 41%.

It is observed that the plant performance degrades after it was subjected to the cyclone. The other comparison reveals that the performance of 100-kW plant in dental college is quite low compared to 100-kW plant in library and medical college in SRMIST.

References

1. Tarigan E (2020) Hybrid PV-T solar collector using amorphous type of solar cells for solar dryer. In: 2020 International seminar on intelligent technology and its applications (ISITIA), Surabaya, Indonesia, pp 352–356. https://doi.org/10.1109/ISITIA49792.2020.9163789
2. Ashwini K, Raj A, Gupta M (2016) Performance assessment and orientation optimization of 100-kWp grid connected solar PV system in Indian scenario. In: 2016 International conference on recent advances and innovations in engineering (ICRAIE), Jaipur, pp 1–7. https://doi.org/10.1109/ICRAIE.2016.7939505.
3. Husain NS, Zainal NA, Mahinder Singh BS, Mohamed NM, Mohd Nor N (2011) Integrated PV based solar insolation measurement and performance monitoring system. In: 2011 IEEE colloquium on humanities, science and engineering, Penang, Malaysia, pp 710–715https://doi.org/10.1109/CHUSER.2011.6163827
4. Zou X, Jiang F, Liu H (2016) Performance analysis of a rooftop PV plant and a desert PV plant. In: 2016 Chinese control and decision conference (CCDC), Yinchuan, China, pp 6173–6176https://doi.org/10.1109/CCDC.2016.7532107
5. Sharma R, Goel S (2017) Performance analysis of a 11.2 kWp roof top grid-connected PV system in Eastern India. Energy Rep 3:76–84. ISSN 2352-4847. https://doi.org/10.1016/j.egyr.2017.05.001.
6. Maammeur H, Hamidat A, Loukarfi L, Missoum M, Abdeladim K, Nacer T (2017) Performance investigation of grid-connected PV systems for family farms: case study of North-West of Algeria. Renew Sustain Energy Rev 78:1208–1220. ISSN 1364-0321. https://doi.org/10.1016/j.rser.2017.05.004.
7. Dabou R et al (2017) Impact of partial shading and PV array power on the performance of grid connected PV station. In: 2017 18th International conference on sciences and techniques of automatic control and computer engineering (STA), Monastir, Tunisia, pp 476–481. https://doi.org/10.1109/STA.2017.8314901

Design and Implementation of a Low-Cost Mini Heliostat Solar Tracking System in West Africa

Marie Pascaline Sarr, Ababacar Thiam, Biram Dieng, and El Hadji Ibrahima Cisse

Abstract This paper proposes the design and implementation of a low-cost automatic mini heliostat solar tracker system. The tracking system is designed as open loop control based on astronomical equations. The experimental device consists of a 0.3×0.3 m^2 reflector, 3-mm thick with an Arduino card and two stepper motors. The prototype tracking system has been tested during three days. The influence of the different parameters like number of the day, time, heliostat position and references of the tracking axis was analysed. The results obtained show some improvement with RMSE of 0.050 and 0.085, respectively, for the altitude and azimuth. This system can be used for small applications in rural areas

Keywords Mini heliostat · Solar tracking · Open loop control · Astronomical equations · Experimental

1 Introduction

The lack of access to reliable and affordable energy electricity remains a key constraint to achieving economic and social development of the West African. Access to electricity in this region is at 52% with a great inequality between rural and urban areas [1]. Demand in rural zones is too low to be satisfied and considered like losses by the national electricity companies. With the significant solar potential of this region, 5.5 kWh/m^2/day [2], the concentrating solar power (CSP) technologies constitute an excellent alternative to satisfy energy needs in electricity, hot water, cold, cooking,

M. P. Sarr (✉) · A. Thiam
Efficacité et Systèmes Energétiques, Alioune Diop University of Bambey, Bambey, Sénégal
e-mail: mariepascaline.sarr@uadb.edu.sn

A. Thiam · E. H. I. Cisse
Laboratoire Eau, Energie, Environnement et Procédés Industriels, Ecole Supérieure Polytechnique, Dakar, Sénégal

B. Dieng
Energies Renouvelables, Matériaux et Laser, Alioune Diop University of Bambey, Bambey, Sénégal

C. Subramani et al. (eds.), *Proceedings of International Conference on Power Electronics and Renewable Energy Systems*, Lecture Notes in Electrical Engineering 795,
https://doi.org/10.1007/978-981-16-4943-1_18

drying of products [3–5]. Among CSP technologies, solar tower power (STP) is identified as the most efficient way for capturing and converting solar energy into heat and electricity [6, 7]. However, the high cost of these plants due to their large size makes this technology non-existent in West Africa [8]. The apparition of micro solar tower power generates growing interest because of their high flexibility and low-investment costs [9]. The small size heliostats are easier to be manufactured, installed and cleaned. Moreover, the mini heliostats can be designed with local low-cost materials creating job opportunities for local people. However, the only major challenge remains the mastery of heliostats tracking in West Africa [10]. Accurate tracking is essential for a better efficiency of STP. Nevertheless, improving precision of heliostat tracking increases the complexity and cost of tracking. To reduce the cost of heliostat tracking, error correction algorithms are often incorporated in the tracking program in order to obtain and maintain good accuracy. Several studies have carried on the different error sources and their correction strategy.

Baheti and Scott [11] have developed an error correction method to compensate mechanical errors related to the heliostats movement. This model included base tilt, azimuth and elevation bias offsets, and non-orthogonal drive axes. A closed-loop solar sensor was used to periodically point the normal vector of the heliostat directly to the sun. The tracking errors of the heliostat were obtained by comparing the commanded position of the heliostat at each interval with the actual solar position as calculated by the solar algorithm. These data were used to estimate the error model coefficients and resulted in final RMS error reductions of 10:1 and 5:1 for azimuth and elevation tracking, respectively. Stone and Jones [12] studied the geometric errors that reduced the tracking accuracy of the heliostat at solar two. Three dominant sources of error with their effect on heliostat tracking were described. These are the tilt of the axis of rotation in azimuth, the encoder reference position error and the non-orthogonality errors. The beam characterization system (BCS) is used to measure heliostat tracking errors and improve heliostat tracking accuracy by adjusting the encoder reference position errors. The strategy presented has been able to minimize but not correct these sources of error. Khalsa et al. [13] studied the effect of non-random physical errors (baseplate tilt about the East–West axis, baseplate tilt about the North–South axis, azimuth reference bias, elevation reference bias, azimuth linear error, elevation linear error, drive axis non-orthogonality and aiming error) on heliostat tracking. The data was obtained by directing a single-test heliostat at a large white target on the tower. The offset between the center of the reflected beam and the center of the target was determined using optical image analysis to calculate tracking errors. This technique was effective in correcting errors for a single-summer day. However, an accuracy reduction in winter was observed. Berenguel et al. [14] have described a method for automatic correction of angular offset with heliostat reflected image processing techniques. A CCD camera is placed in front of the tower just before the solar field in order to photograph the images reflected by the heliostats. For each reflected image, its centroid is calculated and compared to the center of the receiver. The distance between these two points constitute the error to be rectified. A maximum distance of 7.4 cm has been obtained. Malan and Gauché [15] performed a method of estimating and correcting tracking errors similar to [13] by adding errors related to very

small installation and manufacturing tolerances. Using image processing techniques, the tracking error offsets of each individual heliostat are determined periodically to estimate the coefficients of the error model. Prototype experiments indicate a daily open loop tracking error of the RMS normal vector of less than 1 mrad. Tracking errors may also be caused by disagreements between the coordinate systems used by solar engineers, civil engineers and surveyors, during the process of surveying a CSP site as discussed by Gross and Balz [16]. To avoid this, transformations between the different geodetic, Cartesian and Universal Transverse Mercator coordinate systems have to be performed. Sun et al. [17] presented a strategy for correcting heliostat tracking errors based on beam characterization system. The Hartley-Meyer algorithm, which is a Gauss–Newton algorithm modified to solve nonlinear least squares equations, is used to determine the six angular tracking parameters of a specific heliostat. A reduction in tracking errors is noted from 3.14 to 0.73 mrad. However, after six months of operation, the tracking accuracy decreases.

The purpose of this paper is to identify and study the different sources of errors in the tracking of an experimental setup of mini heliostat in West Africa. An open loop tracking system with some adjustments is proposed. Errors due to axis reference and mirror tilt have been determined and taken into account after several tests based on repeatability. The influence of the day and the heliostat position on the evolution of the beam reflected has been studied.

2 Materials and Methods

The optical performance of the tracking system is evaluated using a mini heliostat with a reflective surface of $0.3 \times 0.3\ m^2$. An algorithm based on astronomical equations is used to determinate the sun and mini heliostat position according to the geographical coordinates of the site, the day and the tower position. A command is sent to the engines every 5 min. Errors are estimated by comparing between centroid of beam reflected and target center so that this error signal can be used for adjustment purposes. After several days of testing, systematic errors due to reference and sensor tilt problems are corrected.

The heliostat tracking is done in open loop with the astronomical equations. Firstly, solar vector S is determined with geographic coordinates and number of the day. The sun position is identified by the altitude and azimuth angles obtained from Eqs. (1–4) [18] as illustrated in Fig. 1:

$$\overrightarrow{S} = S_z \overrightarrow{i} + S_e \overrightarrow{j} + S_n \overrightarrow{k} \tag{1}$$

where

$$S_z = \sin \alpha \tag{2}$$

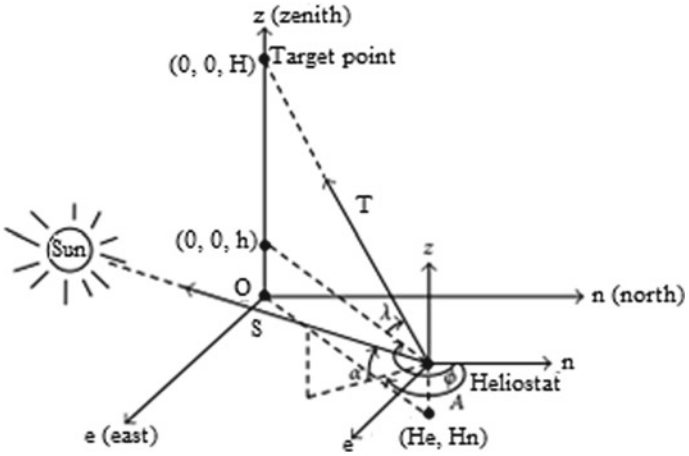

Fig. 1 Coordinates of the sun, heliostat and beam reflected on the tower

$$S_e = \cos\alpha \sin A \tag{3}$$

$$S_n = \cos\alpha \cos A \tag{4}$$

The tower is placed to south of the mini heliostat and is the origin. It is defined by (5):

$$\overrightarrow{T} = T_z \overrightarrow{i} + T_e \overrightarrow{j} + T_n \overrightarrow{k} \tag{5}$$

where

$$T_z = \sin\lambda \tag{6}$$

$$T_e = \cos\lambda \sin\phi \tag{7}$$

$$T_n = \cos\lambda \cos\phi \tag{8}$$

After, the mirror position is determined according to the law of Snell Descartes knowing the position of the tower

$$\overrightarrow{H} = \frac{\overrightarrow{S} + \overrightarrow{T}}{2\cos\theta} \tag{9}$$

This vector can be defined by the altitude αh and azimuth Ah angles of the mirror

$$\sin \alpha_h = \frac{\sin \alpha + \sin \lambda}{2 \cos \theta} \tag{10}$$

$$\sin A_h = \frac{\cos \alpha \sin A + \cos \lambda \cos \phi}{2 \cos \theta} \tag{11}$$

where Θ represents the incidence angle

3 Description of Experimental Setup

The setup on which the experimentation performed is shown in Fig. 2. The experimental tests were conducted at Dakar, Senegal with latitude: 14.7°N and longitude: 17.4°W. The reflected surface is a mirror of 0.3 × 0.3 m^2 with a thickness of 3 mm. The mechanism of each axis is driven by a stepper motor of 400 steps per rotation via a 10:1 transmission system to achieve a final output axis resolution of 4000:1. The required motor torque has been calculated for an efficiency factor of 0.45 N.m. Limit switches are installed at each axis of rotation to prevent mechanical movements from exceeding the predefined limits.

To evaluate tracking performance, graduations of 5 cm per unit were made on the target. The center of the target represented by the white point has coordinates (0, 0, H). On the mirror surface, diagonals were made to detect the mirror center point for evaluating easily the distance between target point and reflected beam (Fig. 3).

Every five minutes, a command is sent to the stepper motors to evaluate the tracking errors (Fig. 4) using the method of Chiesi et al. [19]:

$$\varepsilon_A = a \tan\left(\frac{d_A}{d}\right) \tag{12}$$

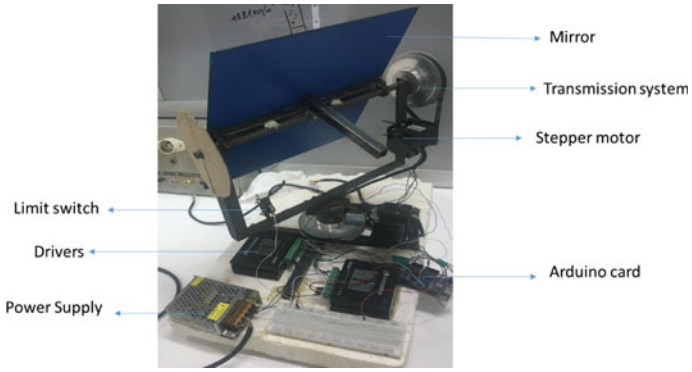

Fig. 2 Components of system

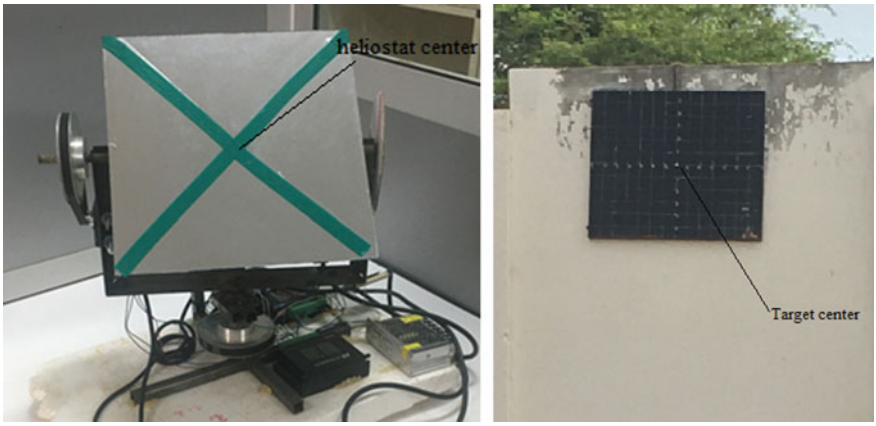

Fig. 3 Identification of heliostat and target centers

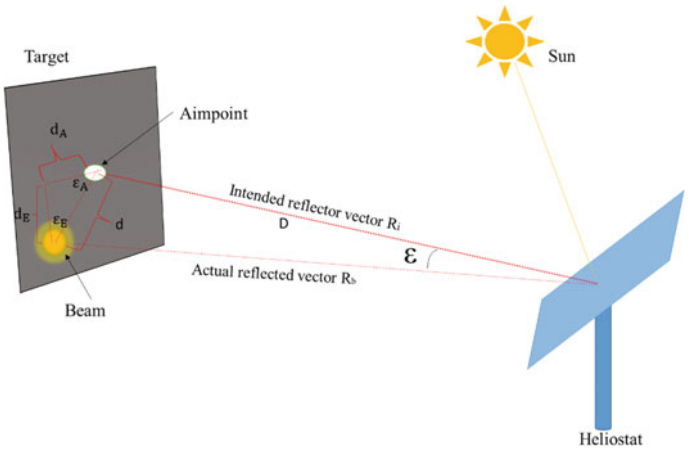

Fig. 4 Illustration of heliostat tracking error

$$\varepsilon_E = a\tan\left(\frac{d_E}{d}\right) \tag{13}$$

$$\varepsilon = a\tan\left(\frac{d}{D}\right) \tag{14}$$

where $d = \sqrt{{d_A}^2 + {d_E}^2}$

d_A azimuth error in cm.
d_E altitude error in cm.
D distance between heliostat tower centers obtained by the laser distance meter (m).

Table 1 Setup parameters of experiment

Parameters	
Height of heliostat (m)	1.10
Height of tower (m)	4.02
Heliostat surface (m^2)	0.3 × 0.3
Distance between heliostat and tower's center D (m)	4.56
Distance heliostat—tower (m)	3.50

Parameters of the experiment are presented in Table 1

4 Results and Discussions

An evaluation of the accuracy of the program is made by comparing the program with the online calculator [20] as shown in Figs. 5, 6 and 7 for three different days. The results obtained gave a mean absolute error (MAE) of 0.83, 0.43, and 0.32 for the days 03/11, 10/11 and 14/11/2020. Tracking errors vary from day to day and can therefore affect the optical performance of the tracking system.

The altitude and azimuth errors obtained experimentally for 03/11/2020 are reported in Fig. 8. The target center was not reached with significant spills at the end of the day. RMSE of 0.168 and 0.201 were obtained for the altitude and azimuth, respectively. After many calibrations, an inconsistency in the references was noted and taken into account at the tracking program. The absolute error was taken into account at the algorithm level to try to reduce it. A second test was performed on the day of 10/11/2020. Figure 9 shows the results obtained. The task was maintained on the target center for a certain period of time. RMSE of 0.0486 and 0.113 were found for the elevation and azimuth, respectively.

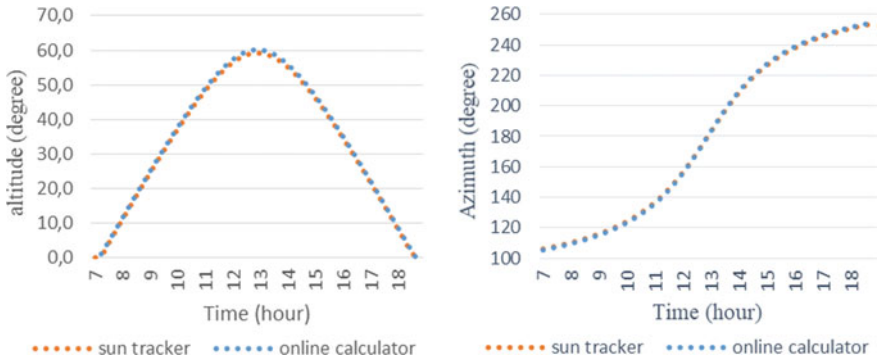

Fig. 5 Solar path of 03/11/20

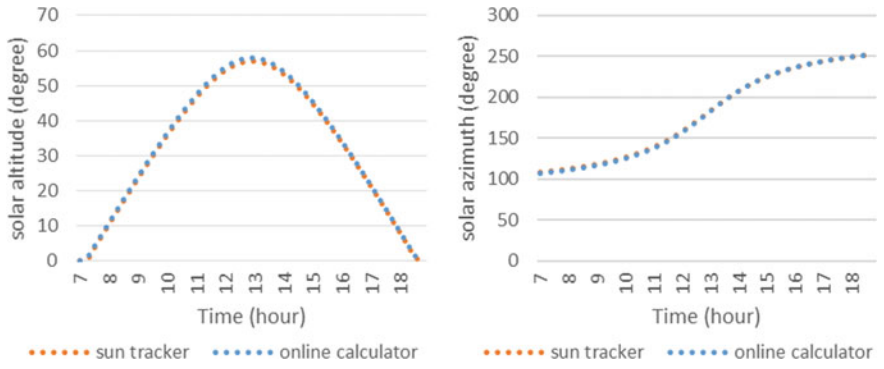

Fig. 6 Solar path of 10/11/2020

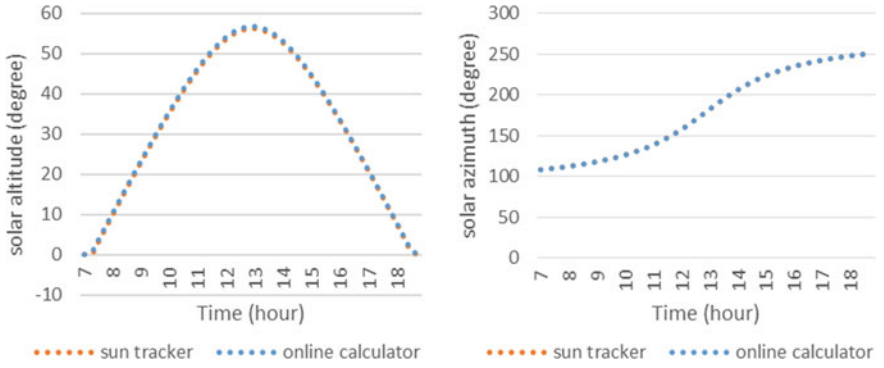

Fig. 7 Solar path of 14/11/2020

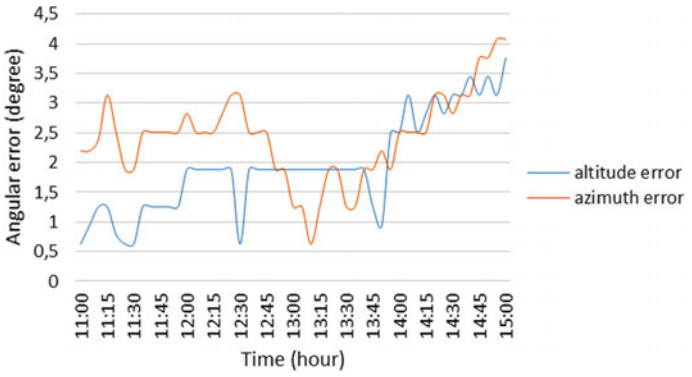

Fig. 8 Tracking error obtained for 03/11/2020

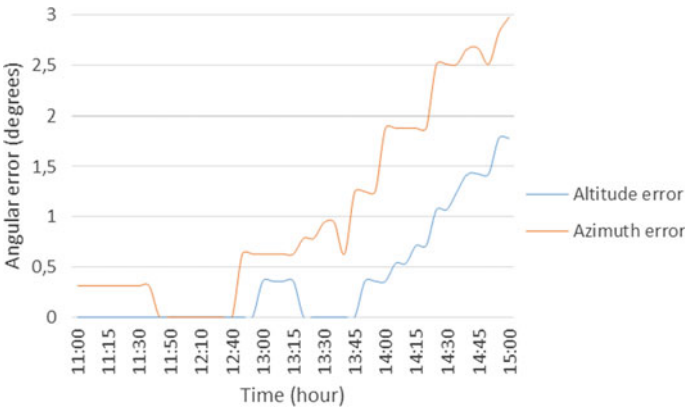

Fig. 9 Tracking error obtained for 10/11/2020

Figure 10 illustrates the results obtained for the day of 14/11/2020. The spot was held at the target for approximately 2 h. The RMSE obtained are 0.050 and 0.085 for elevation and azimuth, respectively.

The results obtained during these days show a reduction in errors. However, a slight increase for the RMSE of the altitude of 14/11/2020. In addition, during the experiments an evolution of the task was noted in one direction only, down and to the right during the day as shown in the pictures in Fig. 11. An appropriate correction can therefore easily be made. Analysis of the results of the experiments showed that the azimuth axis recorded many more errors than the elevation axis. This may be due to the fact that the wind acts more on the azimuth displacement than altitude.

A change of reflector shape is noted during the day on the receiver. Indeed, the shape is normal until solar noon and then begins to distort afterward. This variation of the shape depends on the heliostat position in the field and the time. During the experiments, an error was noted on the conversion of the heliostat angles into steps.

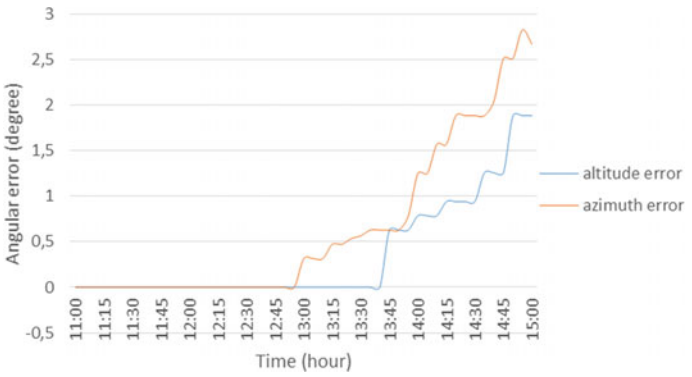

Fig. 10 Tracking error obtained for 14/11/2020

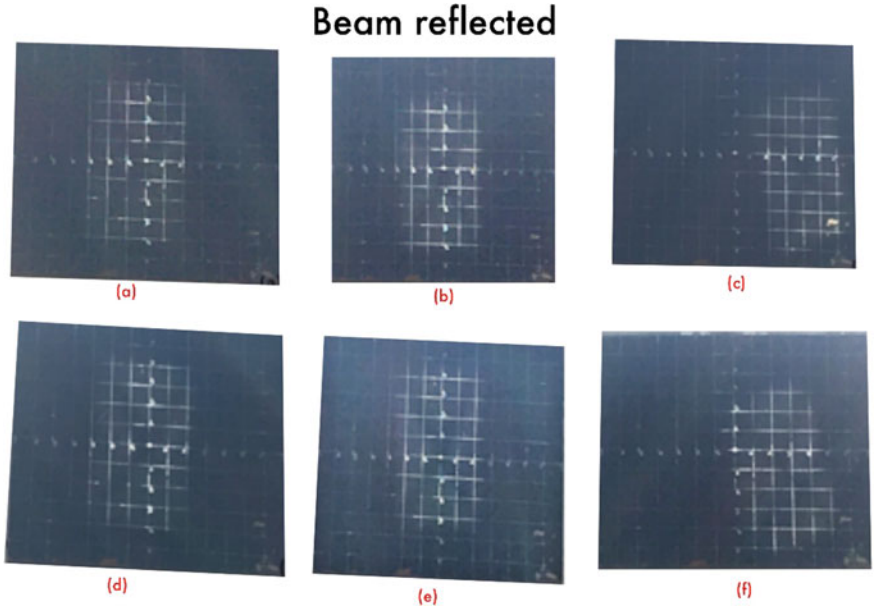

Fig. 11 Optical images of the heliostat reflection on the target 10/11/2020 11h35. **a**, 12h30 **b,** 2h30 PM **c**, 14/11/20 à 11h35 **d**, 12h30 **e,** 2h30 PM **f**

In fact, one step is equal to 0.09°. If the decimal part is inferior at the one step, there is not considered in the conversion. For a significant reduction, it is necessary to take into account in the tracking algorithm the main sources of errors such as mechanical design errors, leap seconds and computation time errors, approximations made during the conversion of heliostat angles into steps, transmission systems.

5 Conclusion

In this paper, an experimental study of the optical performance of a mini heliostat was carried out. The results obtained show a maximum deviation of the reflected beam of 0.15 m and 0.2 m, RMSE of 0.050 and 0.085 for altitude and azimuth. Analysis of the results obtained showed that parameters such as daylight, references and mechanical design errors influence the mini heliostat tracking. The evolution of the reflected image at the receiver is highly dependent on the position of the heliostat relative to the tower. The error variation is much faster for the day of 03/11 and 10/11 than 14/11/20. An improvement is noted, but a better accuracy could be obtained by taking into account more error sources in the algorithm. The development of the mini heliostat will raise awareness about the integration of CSP for the satisfaction of the

thermal energy needs of the rural sub-Saharan population particularly conservation of cereal and dairy products, water pasteurization.

Acknowledgements We are grateful to the WFS (Word Federation of Scientists) for the support.

References

1. Énergie solaire en Afrique, un avenir rayonnant ? https://www.lemondedelenergie.com/energie-solaire-afrique-avenir/2019/02/14/ (consulté le nov. 02, 2020).
2. Azoumah Y, Ramde EW, Tapsoba G, Thiam S (2010) Siting guidelines for concentrating solar power plants in the Sahel: case study of Burkina Faso. Sol Energy 84:1545–1553. https://doi.org/10.1016/j.solener.2010.05.019
3. Al-Amayreh MI, Alahmer A, Manasrah A (2020) A novel parabolic solar dish design for a hybrid solar lighting-thermal applications. In: 2020 7th International conference on power and energy systems engineering (CPESE 2020), 26–29 September 2020, Fukuoka, Japan. Energy Reports 6(9):1136–1143 https://doi.org/10.1016/j.egyr.2020.11.063
4. Mekonnen BA, Liyew KW, Tigabu MT (2020) Solar cooking in Ethiopia: experimental testing and performance evaluation of SK14 solar cooker. Case Studies Thermal Eng 22:100766. https://doi.org/10.1016/j.csite.2020.100766
5. Brouche M, Lahoud C, Lahoud MF, Lahoud C (2020) Solar drying simulation of different products: Lebanese case, Tmrees, EURACA, 25–27 June 2020, Athens, Greece. Energy Reports 6(6):548–564. https://doi.org/10.1016/j.egyr.2020.09.032
6. Bhargav KR, Gross F, Schramek P (2014) Life cycle cost optimized heliostat size for power towers. Energy Procedia 49:40–49. https://doi.org/10.1016/j.egypro.2014.03.005
7. Agyekum EB, Velkin VI (2020) Optimization and techno-economic assessment of concentrated solar power (CSP) in South-Western Africa: a case study on Ghana. Sustain Energy Technol Assess 40:100763. https://doi.org/10.1016/j.seta.2020.100763
8. Seshie YM, N'Tsoukpoe KE, Neveu P, Coulibaly Y, Azoumah YK (2018) Small scale concentrating solar plants for rural electrification. Renew Sustain Energy Rev 90:195–209. https://doi.org/10.1016/j.rser.2018.03.036
9. Renzi M, Egidi L, Cioccolanti L, Comodi G (2017) Performance simulation of a small-scale heliostat CSP system: case studies in Italy. Energy Procedia 105:367–372. https://doi.org/10.1016/j.egypro.2017.03.327
10. Abu-Hamdeh NH, Alnefaie KA (2016) Design considerations and construction of an experimental prototype of concentrating solar power tower system in Saudi Arabia. Energy Convers Manag 117. https://doi.org/10.1016/j.enconman.2016.02.077
11. Baheti R, Scott P (1980) Design of self-calibrating controllers for heliostats in a solar power plant. IEEE Trans Autom Control 25:1091–1097. https://doi.org/10.1109/TAC.1980.1102527
12. Jones SA, Stone KW (1999) Analysis of solar two heliostat tracking error sources. In: ASME international solar energy conference. https://digital.library.unt.edu/ark:/67531/metadc687954
13. Khalsa SS, Ho CK, Andraka CE (2011) An automated method to correct heliostat tracking errors. SolarPACsES 2011
14. Berenguel M et al (2004) An artificial vision-based control system for automatic heliostat positioning offset correction in a central receiver solar power plant. Solar Energy 76:563–575. https://doi.org/10.1016/j.solener.2003.12.006
15. Malan K, Gauché P (2014) Model based open-loop correction of heliostat tracking errors. Energy Procedia 49:2118–2124. https://doi.org/10.1016/j.egypro.2014.03.224
16. Gross F, Balz M (2020) Potentially confusing coordinate systems for solar tower plants. SolarPaces 2020. In: AIP conference proceedings, vol 2303, no 1, Dec 2020

17. Sun F et al (2015) Study on the heliostat tracking correction strategies based on an error-correction model. Sol Energy 111:252–263. https://doi.org/10.1016/j.solener.2014.06.016
18. William B (2001) Stine and michael geyer power from the sun. Netbook http://www.powerfromthesun.net/book.html
19. Chiesi M, Scarselli E, Guerrieri R (2017) Run-time detection and correction of heliostat tracking errors. Renew Energy 105. https://doi.org/10.1016/j.renene.2016.12.093
20. SunCalc sun position- und sun phases calculator. https://www.suncalc.org

Power-Domain NOMA for Massive Connectivity in Smart Grid Communication Networks

M. Jayachandran and C. Kalaiarasy

Abstract The exploitation of information and communication technology (ICT) and the development of smart electricity networks have become the main concerns worldwide. To leverage ICT in the existing electrical power network, 5G wireless systems are integrated toward the development of smart grid networks. For reliable, efficient, and secure communication infrastructure in a smarter electricity network, the non-orthogonal asynchronous transmission is essential. Besides, a massive number of smart meters (SMs) measure energy consumption and convey instantaneous information to the utility through communications networks. However, data rates beyond 10 Gbps, connectivity to support 1 million per sq km device density, and sub-millisecond latencies are challenging issues when implementing a smart distribution grid. Therefore, this paper presents the non-orthogonal multiple access (NOMA) scheme and optimized power control strategy for smart microgrids to integrate numerous sensor devices with higher data transfer rates and lower latencies. This new microgrid configuration enables multiple electricity users to transmit and receive data simultaneously using the same frequency and enables optimized power flow with high flexibility.

Keywords 5G technology · NOMA · ICT

1 Introduction

The increase of power demand in the existing power network causes severe challenges in ensuring reliable, efficient, and economic operation. Lack of intelligent mechanisms, the conventional grids prone to power outages and blackouts. Therefore, smart grids have gained significant popularity in recent years [1]. Smart grid is an advanced electricity supply network that enables monitoring, sensing, control, and

M. Jayachandran (✉) · C. Kalaiarasy
Puducherry Technological University, Puducherry 605014, India
e-mail: jayachandran.escet@pec.edu

C. Kalaiarasy
e-mail: kalaidivi043@pec.edu

C. Subramani et al. (eds.), *Proceedings of International Conference on Power Electronics and Renewable Energy Systems*, Lecture Notes in Electrical Engineering 795,
https://doi.org/10.1007/978-981-16-4943-1_19

communication for improving the reliability, safety, and efficiency of power system operation. In this regard, modern digital communication technologies are essential for the reliable and efficient functioning of the smart grid network (SGN) [2, 3].

Wireless communication technologies are becoming more popular for smart grid applications due to their flexibility and low infrastructure costs. Compared with the 4G technology, 5G has higher system capacity, throughput, and energy efficiency per service. Multiple access (MA) techniques can be regarded as one of the most fundamental enablers in wireless networks. They can be categorized into orthogonal multiple access (OMA) and NOMA methods. In OMA schemes like FDMA, TDMA, CDMA, and OFDMA, multiple users are not permitted to share the same resource concurrently in frequency, time, code, and subcarrier domains, respectively. On the contrary, simultaneous sharing of resources leads to signal interference resulting in loss of data. For instance, an OFDMA network with 64 subcarriers allows only 64 users simultaneously. This orthogonality imposes the capacity limitation. This problem can be resolved by allowing the simultaneous transmission of multiple users in the same frequency carrier which is termed as NOMA. Recently, NOMA has been recognized as one of the promising multiple access techniques for 5G wireless networks. NOMA utilizes the power division multiple access techniques (PDMA) which allocate different power to different users and depends on their distance from the base station (BS) and channel condition [4]. NOMA schemes can be classified into two categories, namely code-domain NOMA and power-domain NOMA. Recently, power-domain NOMA has been proposed which exposes superior capacity than OMA. [5] The fundamental concept of power-domain NOMA is to ascertain that multiple users can be shared simultaneously within the same radio spectrum [6]. The successful operation of NOMA is to form clusters of users with different channel gains and allow them to transmit on the same radio spectrum with appropriate power using superposition coding (SC) at the transmitter and decode the message signal of different users at the receiver using successive interference cancelation (SIC) [7].

Considering the performance of NOMA in fading channels, NOMA in additive white Gaussian noise (AWGN) channels has recently investigated to exploit the time-varying nature of multi-user channels. It has been reported that NOMA achieves superior performance than OMA for various distances [8]. Recently, hierarchical control is proposed for the microgrids. Energy management system (EMS) in microgrids consists of three levels of hierarchical control system, namely primary, secondary, and tertiary control. To optimize the microgrid resources and manage the power flow between the microgrid and the grid, tertiary control is performed.

In this paper, a communication-enabled smart microgrid infrastructure along with an optimized control technique using model predictive control (MPC) for the tertiary control level is proposed. This smart microgrid configuration and the associated control aim to achieve a fast and smooth grid connection of renewable as well as a distributed power source.

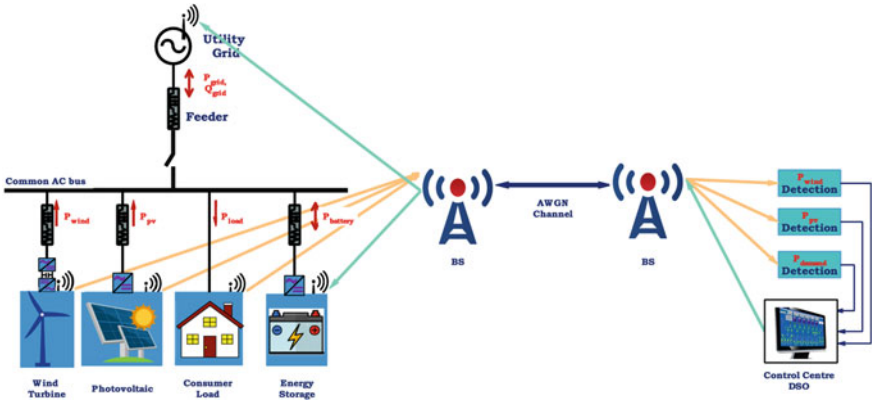

Fig. 1 Schematic diagram of smart microgrid system with wireless communication

2 System Description

The proposed smart microgrid configuration comprises a solar PV array, a wind turbine, a battery energy storage system, and an electric load. All the units in this system are parallelly connected to the common AC bus and rely on wireless communication as shown in Fig. 1. Solar PV and wind turbine are renewable power generation units. The battery bank is an energy storage system that can smooth the intermittent performance of RES and fluctuating load profile. To monitor the smart grid, smart meters are installed for monitoring and measuring the real power, reactive powers, and power flows. In this system, the power converters play a key role to optimize the power flow between renewable sources and the grid.

3 a Typical NOMA Scheme

Concerning uplink transmission with a base station and N devices, smart grid units send messages U_1, U_2, … U_n to the base station. Then, the base station performs superposition coding with these data and transmits the following NOMA signal into the channel:

$$U_{\text{NOMA}} = \sqrt{p}[\sqrt{p}U_1 + \sqrt{p}U_2 + \cdots + \sqrt{p_n}U_n] \tag{1}$$

where P is the total transmit power. Since the channel conditions are arranged as $|g_1|^2 < |g_2|^2 < \ldots |g_n|^2$, the power allocation coefficients must be ordered as $p_1 > p_2 > \ldots p_n$. At the receiving end, device 1 with channel h_1 is farthest from the base station which receives the weakest signal. Device 2 is the next and so on. Device N is the nearest base station that receives the strongest signal. The received

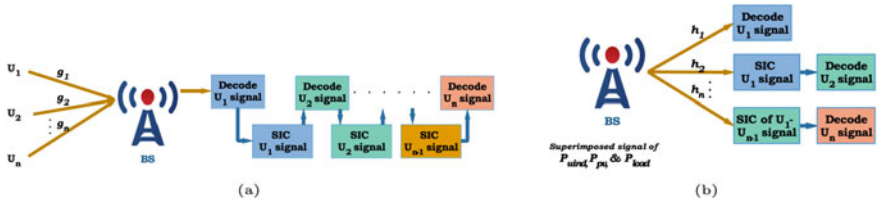

Fig. 2 **a** Uplink NOMA transmission, **b** downlink NOMA transmission

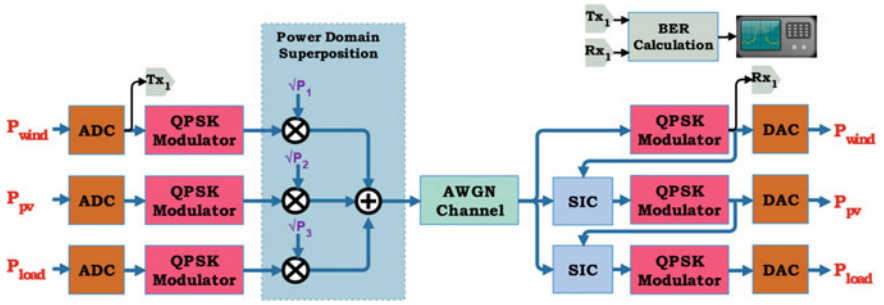

Fig. 3 NOMA with QPSK modulation in AWGN channel

signal at the device i is given by

$$Y_{i,\text{NOMA}} = U_{\text{NOMA}} \times h_i + w_i$$
$$Y_{i,\text{NOMA}} = \sqrt{p}\left[\sqrt{p_1}U_1 + \sqrt{p_2}U_2 + \cdots + \sqrt{p_n}U_n\right] \times h_i + w_i \quad (2)$$

where w_i is the additive white Gaussian noise. The channel conditions are arranged as $|h_1|^2 < |h_2|^2 < \ldots |h_n|^2$. Since the highest power is allotted to device 1, this message dominates the received signal. Hence, decoding is performed to obtain the message. Next, the device 2 signal is directly decoded device 1's message, and then, perform successive interference cancelation (SIC) to remove device 1 message. After SIC, the device 2 message is dominating term. Then, perform direct decoding to obtain the device 2 message. This decoding process can be extended to obtain all messages from smart grid units (Figs. 2 and 3).

4 The Proposed Power Control Strategy

With the knowledge of power demand (P_{demand}), the solar PV power (P_{pv}), and wind turbine power (P_{wind}), the net power available in the common AC bus as shown in Fig. 4 can be calculated as

Fig. 4 Model predictive control for power management strategy

$$P_{\text{net}} = P_{\text{pv}} + P_{\text{wind}} - P_{\text{demand}} \tag{3}$$

For energy saving considerations, this net power must be balanced through battery energy storage system (BESS) power (P_{BESS}) and the utility grid power (P_{grid}). When inverter power is negative, the battery absorbs power from renewable energy sources. Conversely, when inverter power is positive, the battery supplies power to the load. In discharging mode operation, a battery with the higher state of charge (SoC) supplies more power, whereas lower SoC supplies less power. The converse is also true in the charging process. The SoC of BESS can be obtained as

$$\text{SoC}(k+1) = \frac{\text{SoC}(k) + P_{\text{BESS}}(k+1) \times Ts}{C_{\text{BESS}}} \tag{4}$$

where C_{BESS} is the capacity of the batteries. The battery power and utility grid power can be predicted at the next control instant as

$$P_{\text{BESS}}(k+1) = u(k+1) + P_{\text{BESS}}(k) \tag{5}$$

where the control variable $u(k+1)$ is the change of battery power. The required battery power (P_{net}) is obtained by minimizing the following cost function to keep the power balanced within microgrid as

$$J = |P_{\text{net}}(k+1) - P_{\text{BESS}}(k+1)| \tag{6}$$

In general, the microgrid and utility can operate at different frequencies. The transition from islanded to the grid-connected mode and grid-connected to islanded mode are typically planned. To realize a smooth mode transfer, a synchronization procedure is performed to synchronize the voltage, phase angle, and frequency of the DG unit to the common AC bus at the utility side. The proposed control strategy maintains the terminal voltage and frequency of the units to their nominal values. Hence, the units deliver their nominal active and reactive power to load.

5 Simulation Results

Due to simultaneous transmission, NOMA suffers from interference. As a result, OMA performs slightly better than NOMA at low SNR as shown in Fig. 5a. However,

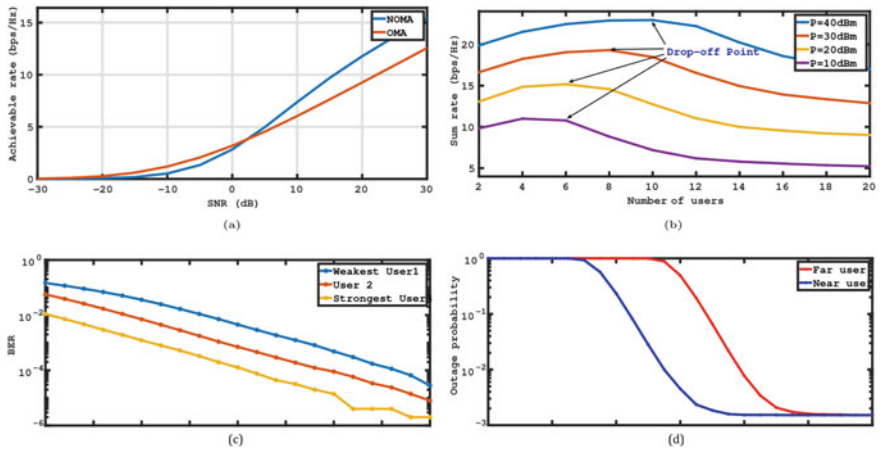

Fig. 5 **a** Capacity performance comparison of NOMA vs OMA, **b** A power allocation method for multiple user single-carrier NOMA, **c** BER performance of multiple user NOMA with QPSK modulation in AWGN channel; **d** Outage probability of uplink NOMA

NOMA outperforms OMA by offering high capacity at high SNR. As a consequence of the number of users (i.e., smart grid devices) of single-career NOMA is increased, the capacity of the network initially increases as shown in Fig. 5b. The drop-off point may be regarded as the maximum limit on the number of devices that can be admitted into the network without any performance degradation. Beyond the drop-point capacity falls. The drop-off point can be changed by varying transmit power. In order to enhance the network capacity without performance degradation, transmit power should be increased. However, the fixed power allocation scheme affects the BER performance as shown in Fig. 5c. The weakest signal has the highest bit error rate, while the strongest signal has the lowest BER and is free from interference. The outage probability is high for both near and far users as shown in Fig. 5d. Thus, NOMA gives superior performance when the channel conditions between the users are more distinct.

Besides, the performance of the proposed control strategy is analyzed in a case study. A typical load profile consumption per day is depicted in Fig. 6a. The power demand throughout the year is also presented in Fig. 6b, and the average load demand for this site is approximately 4 kW. The wind and solar meteorological data for Sundarban (India) location are considered for the case study as shown in Fig. 6c, d. It is observed from Fig. 6g that the power generated by PV is more than the power demand during June–September (3651-6570 h). Hence, the utility grid has not contributed. This excess energy is utilized to charge the battery and distribute it into the dump load as shown in Fig. 6e. It is noted that high quantities of dump energy are stored in the battery (77.19 kW). It can be utilized for street lighting, heating, water pumping, and refrigeration. It is clear from Fig. 6f that the depth of discharge is maintained up to 80% and the state of charge of the battery is not less than 20%

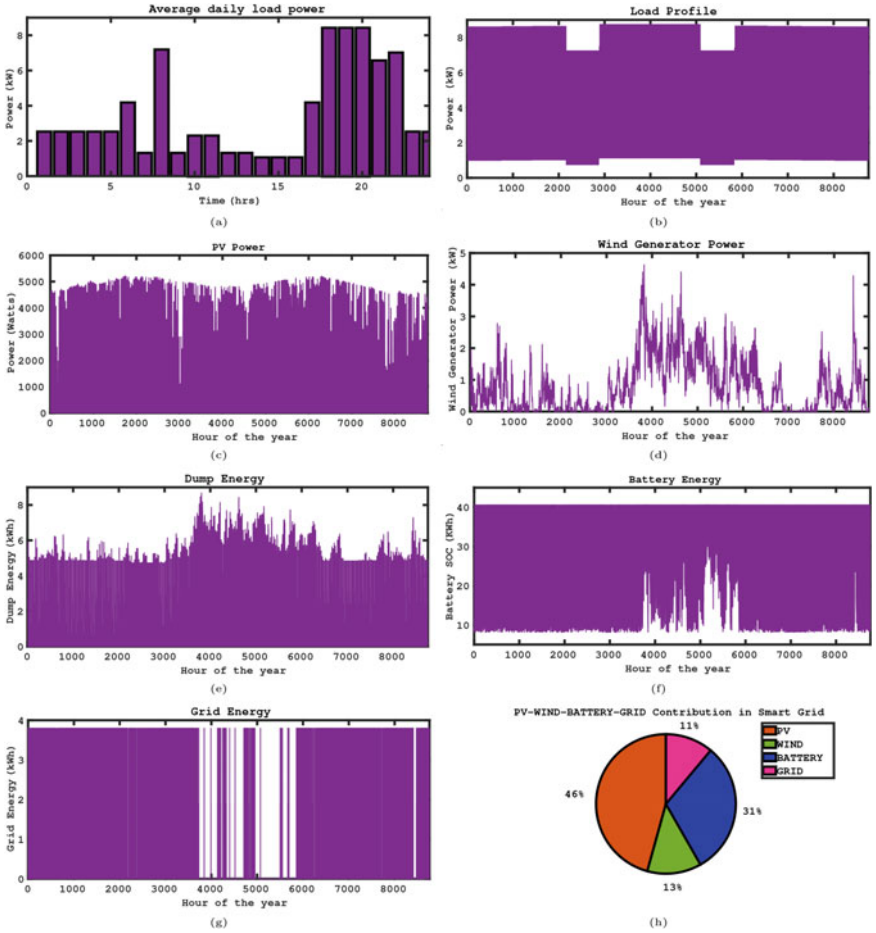

Fig. 6 **a** Typical load profile consumption per day, **b** hourly power demand, **c** hourly PV power, **d** hourly wind turbine power, **e** battery dump energy during the year, **f** battery energy during the year, **g** utility output energy; **h** energy contribution of PV, WT, BESS, and utility grid

of charge level. The percentage of contribution of units over a year is depicted in the pie chart in Fig. 6h.

6 Conclusion

A NOMA-based smart microgrid configuration and MPC-based power control scheme are proposed for future microgrids. The performance and benefits of adopting NOMA can support massive connectivity with high data rates and low latencies for smart grid communication systems. Besides, the proposed power management

strategy optimizes power flow within the microgrid and between renewable energy sources and the utility grid. Thus, the proposed smart microgrid system provides high-quality and reliable electricity to the customers irrespective of the fluctuated renewable energy sources.

References

1. Baldonado, Ahmad A, Rehmani MH, Tembine H, Mohammed OA, Jamalipour A (2017) IEEE access special section editorial: optimization for emerging wireless networks: IoT, 5G, and smart grid communication networks. IEEE Access 5:2096–2100
2. Kuzlu M, Pipattanasomporn M, Rahman S (2014) Communication network requirements for major smart grid applications in HAN NAN and WAN. Comput Netw 67:74–88
3. Hussain M, Rasheed H (2019) Communication infrastructure for stationary and organized distributed smart meters. In: 2019 2nd International conference on communication, computing and digital systems (CCODE), pp 17–22
4. Rabie KM, Adebisi B, Yousif EHG, Gacanin H, Tonello AM (2017) A comparison between orthogonal and non-orthogonal multiple access in cooperative relaying power line communication systems. IEEE Access 5:10118–10129
5. Islam SMR, Avazov N, Dobre OA, Kwak K (2017) Power-domain non-orthogonal multiple access (NOMA) in 5G systems: potentials and challenges. IEEE Commun Surv Tutorials 19(2):721–742
6. Agarwal A, Chaurasiya R, Rai S, Jagannatham AK (2020) Outage probability analysis for NOMA downlink and uplink communication systems with generalized fading channels. IEEE Access 8:220461–220481
7. Ali MS, Tabassum H, Hossain E (2016) Dynamic user clustering and power allocation for uplink and downlink non-orthogonal multiple access (NOMA) systems. IEEE Access 4:6325–6343
8. Shahab MB, Kader MF, Shin SY (2016) Simulink implementation of non-orthogonal multiple access over awgn and rayleigh fading channels. In: 2016 International conference on smart green technology in electrical and information systems (ICSGTEIS), pp 107–110

Power Management in DC Microgrid

B. Balaji and S. Ganesan

Abstract A microgrid can be characterized as force group of disseminated generation, burden, and energy stockpiling gadget gathered together nearby to one another. It offers freedom to use sustainable power hotspots for green and clean climate. This work mainly deals with the analysis, modeling and simulation of DC microgrid with solar powered system alone, DC microgrid with battery alone, DC microgrid with wind alone, DC microgrid with solar powered system and battery, DC microgrid with solar powered system and airstream & DC microgrid with solar powered system, battery and wind. The outcomes are compared in terms of output voltage and output power. The outcome represents the superior performance of DC microgrid through solar powered system, battery and wind sources.

Keywords DC Microgrid · Solar powered system (PV) · Wind · Battery and distributed generation

1 Introduction

The idea of microgrid network was first evolved by RH. Lassete in 2002, that was an example of appropriated age covering assortment of fuel sources from fossil fuel sources to environmentally friendly power sources (sun based, wind and biogas). Microgrid is an organization framework interconnected from assortment of appropriated fuel sources into a little organization which can be worked autonomously or associated with utility matrix. The examination of ac microgrid had been completed yet there are as yet numerous issues that ought to be tackled identified with strength

B. Balaji (✉)
Department of Electrical Engineering, Annamalai University, Chidambaram, India

Department of Electrical and Electronics Engineering, IFET College of Engineering, Villupuram, India

S. Ganesan
Department of Electrical and Electronics Engineering, Government College of Engineering, Salem, India

C. Subramani et al. (eds.), *Proceedings of International Conference on Power Electronics and Renewable Energy Systems*, Lecture Notes in Electrical Engineering 795,
https://doi.org/10.1007/978-981-16-4943-1_20

of activity of inverter, similar to resemble component, solidness of frequency and power supply.

Likewise, the price of inverter was generally costly, particularly for family application. Technique for inverter equal had been done, for example, utilization of stage look circle (PLL) strategy and Droop Voltage. Nonetheless, another issue actually showed up as well, like difference in recurrence and receptive force because of progress and sort of utilized burden. It will end up being its own concern in the microgrid framework. A few explores related with direct current had been created to defeat issues happened in the substituting current like estimation of misfortunes in the organization and proportion of effectiveness of rotating current and direct current.

As of late, the DML-family was presented as a better energy-defer elective than CMOS. DML entryways use 2 distinct methods of activity, dynamic and static, to specifically accomplish either superior or low-energy activity. Hand crafts of DML circuits had been demonstrated to be very efficient Emadi [1]. A solitary transport DC microgrid can address a wide scope of utilizations. Control targets of such frameworks incorporate elite transport voltage guideline and legitimate burden dividing between numerous DG's under different working conditions Peng [2].

A microgrid was difficult to control because of its decreased dormancy and expanded vulnerabilities. To defeat the difficulties of microgrid control, progressed regulators should be created. In this, a circulated, 2 level, correspondence financial control plot, was introduced for numerous transport miniature lattices with each transport having different DG's associated in equal. The control objective of the upper level was to figure the voltage references for one transport subsystems Qinmin [3]. This geography, - because of a-thunderous L-C-tank-associated—among the channel terminals of the switches of 2 inter leaved boost-cells, accomplishes 0 voltage and 0 current—replacements, all things considered, autonomously of the heap current, with a decreased dv/dt crossways the switches Giorgio Spiazzi [4].

The interleaving method was a notable strategy functional in high force claims to divide the yield power among 2 modules though diminishing the info current and yield current wave. Additionally, 0 current exchanging procedure can be utilized to diminish the exchanging misfortunes and increment influence density Bahrami [4]. A hilter kilter forward-flyback dc–dc converter had high-force transformation proficiency 'ηe' over wide yield power range. To tackles issue of clear in the voltage rectifier diodes & the issue obligation misfortune in ordinary deviated half-connect converter, the anticipated converter utilized a voltage doubler construction with forward inductor Lf in the subsequent juncture, rather than utilizing transformer spillage inductance that control yields current Lee [5] (Fig. 1).

An advancement of twofold booming DC–DC converter with 0 voltage trading and 0 current supplanting features proposed. This geography contained-switches and capacitors cuts at the significant feature of the separation transformer. 2 switches were worked in a corresponding manner under a PWM conspire Tahavorgar [6]. Another transformer-less BBC with positive yield voltage was introduced by Miao-2016. Another transformer-less BBC with straightforward design was proposed in this examination. Juxtaposed & the routine BBC, the anticipated BBC voltage acquire was squared junctures of the previous' and its revenue voltage margin were affirmative [7].

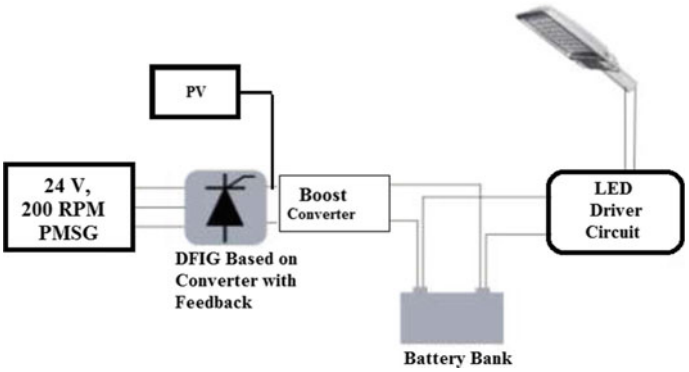

Fig. 1 Block diagram of-AC-DC microgrid-system

Exchanged capacitor based Z source identical DC–DC help converter geographies were anticipated. Reason on the topological developments was moved LCD cubicle of 4th request support converter on anterior side a control siphon cell upstream side Veeracheary [8]. A usable and flexible family energy the executive's framework was proposed to create and carry out request reaction (DR) projects. These were under the half and half age energy stockpiling framework solar powered system, and green vehicle in the keen network (SG). Prevailing family energy the board frameworks can't offer its clients a decision to guarantee client comfort (UC) and not give a practical arrangement as far as diminished carbon emission [9].

Meanwhile a DC microGrid is comprised of force converters associated from side to side various line impedances, tuning voltage regulator gave straightforward & instinctive transaction among clashing objectives voltage guideline & current sharing. Profoundly adaptable circulated governor system was anticipated to accomplish adjusted governor between two control goals, incorporates regulation voltage regulator and consensus based cc Renke [10].

2 System Description

Block diagram of DC microgrid system is exposed in Fig. 2. Various sources are solar powered system, wind generator and battery.

3 Simulation Results

Figure 3 outlines the simulink diagram of DC microgrid with battery alone. Figure 4 outlines the Input voltage and its value is 14 V. Figure 5 outlines the circuit diagram

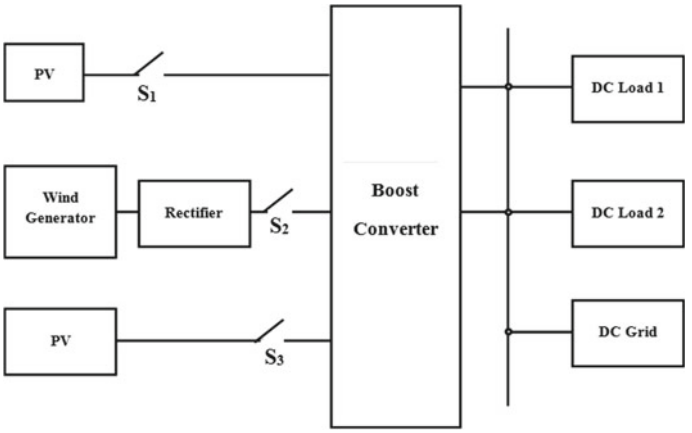

Fig. 2 Block diagram of DC microgrid system

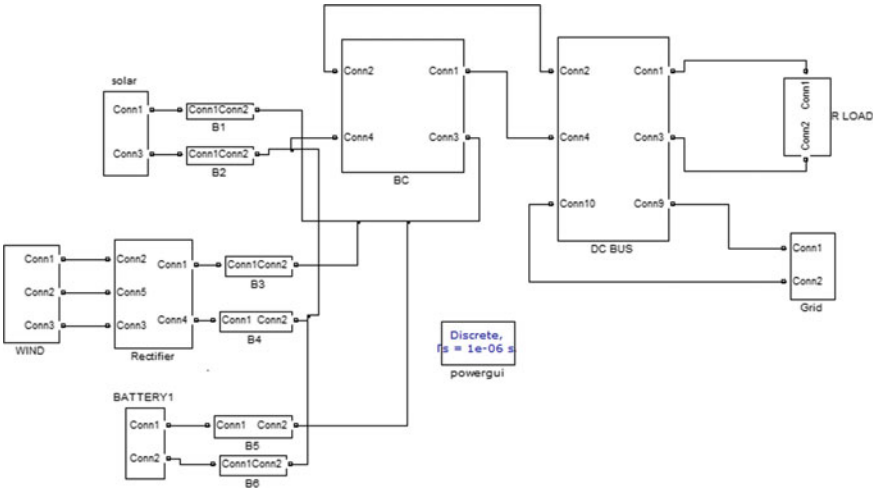

Fig. 3 Simulink diagram of DC microgrid with Battery alone

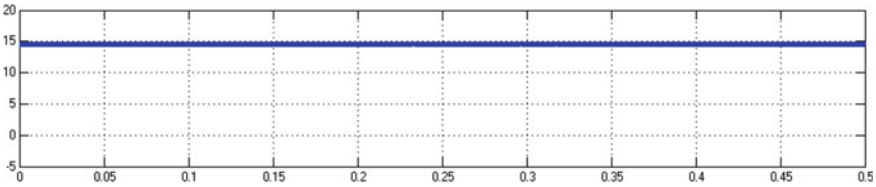

Fig.4 Input voltage

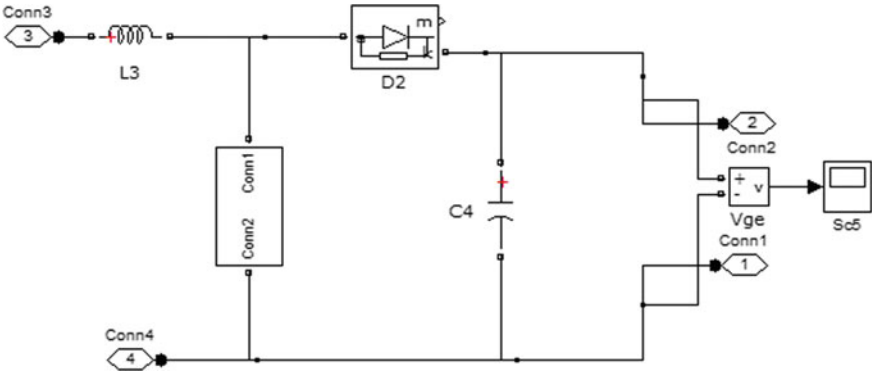

Fig. 5 Circuit diagram of boost converter

of boost converter with silicon carbide mosfet. Figure 6 outlines the switching pulse S1 of boost converter and its value lies between 0 and 1 unit. Figure 7 outlines the voltage across R-load with battery alone, and its value is 81 V. Figure 8 outlines the

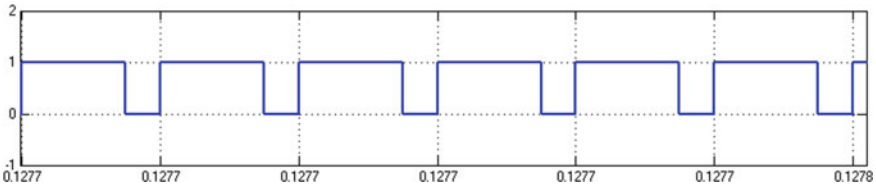

Fig. 6 Switching pulse for-S1 of boost converter

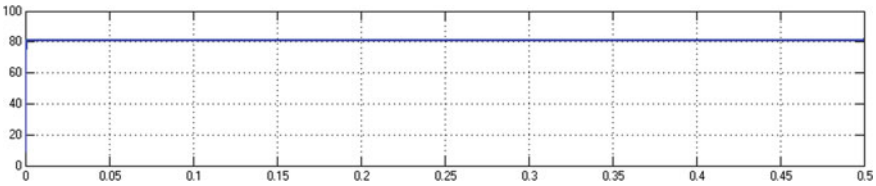

Fig. 7 Voltage across R-load with battery alone

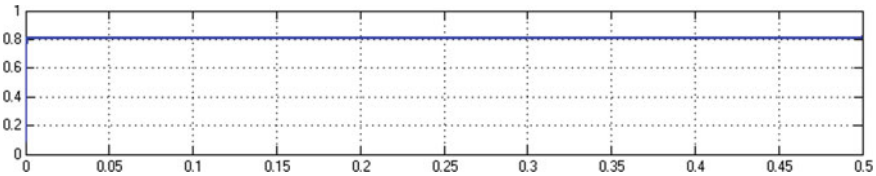

Fig. 8 Current through R-load with battery alone

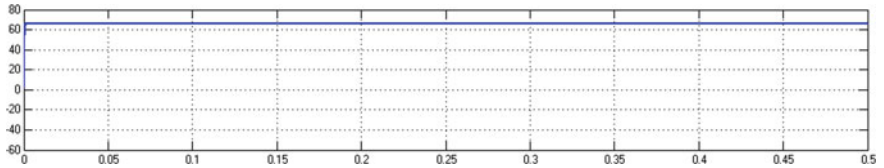

Fig. 9 Output power with R-load with battery alone

current through R-load with battery alone, and its value is 0.82A. Figure 9 outlines the output power with battery alone, and its value is 65 W.

Figure 10 outlines the simulink diagram of DC microgrid with PV alone. Figure 11 outlines the input voltage, and its value is 16 V. Figure 12 outlines the Voltage across R-load, and its value is 86 V. Figure 13 outlines the current through R-load with PV alone, and its value is 0.8A. Figure 14 outlines the output power with PV alone with PV alone, and its value is 74 W.

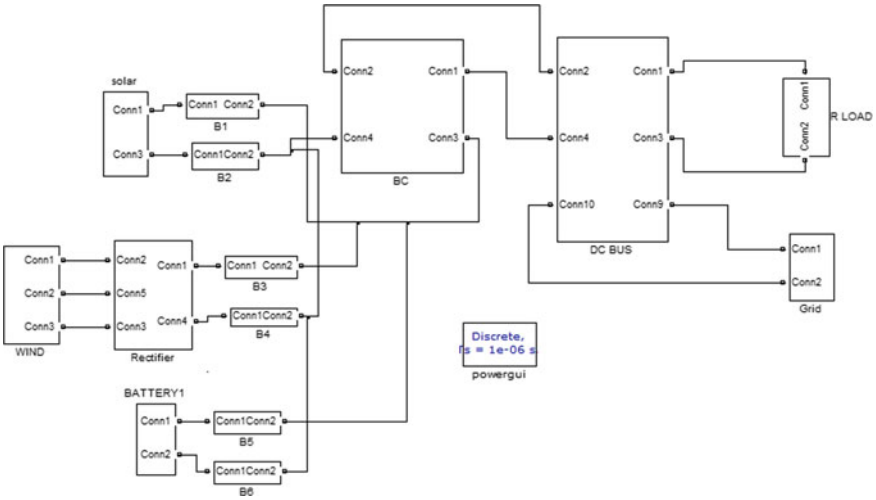

Fig. 10 Simulink diagram DC microgrid with PV alone

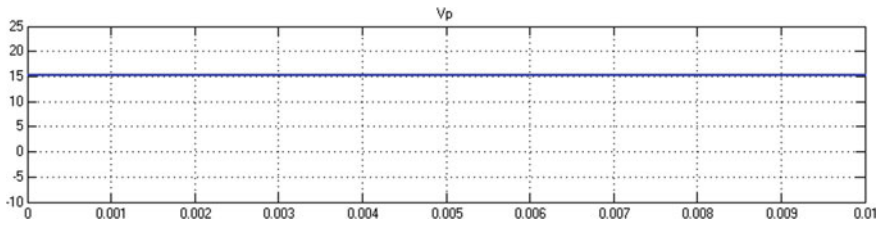

Fig. 11 Input voltage

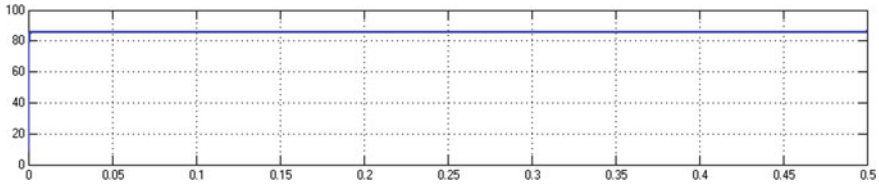

Fig.12 Voltage across R-load with solar powered system alone

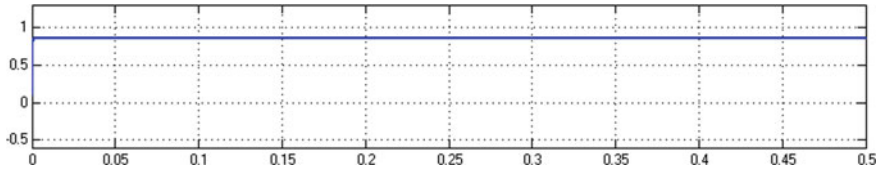

Fig. 13 Current through R-load with solar powered system alone

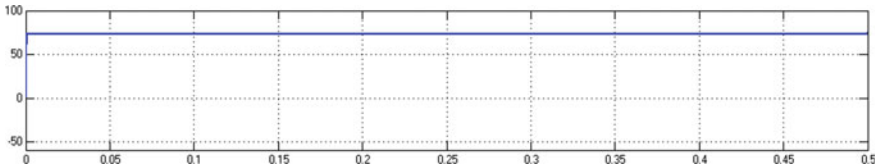

Fig. 14 Output power with solar powered system alone

Figure 15 outlines the simulink diagram of DC microgrid with wind alone. Figure 16 outlines the Input voltage, and its value is 15 V. Figure 17 outlines the voltage across R-load with wind alone, and its value is 90 V. Figure 18 outlines the current through R-load with wind alone, and its value is 0.8A. Figure 19 outlines the output power with wind alone, and its value is 85 W.

Figure 20 outlines the simulink diagram of DC microgrid with solar powered system and battery. Figure 21 outlines the input voltage, and its value is 16 V. Figure 22 outlines the Voltage across R-load with solar powered system and battery, and its value is 100 V. Figure 23 outlines the current through R-load with solar powered system and battery, and its value is 1A. Figure 24 outlines the output power with solar powered system and battery, and its value is 100 W. Figure 25 outlines the simulink diagram of DC microgrid with solar powered system and wind generator. Figure 26 outlines the input voltage, and its value is 16 V. Figure 27 outlines the voltage across R-load with PV and wind generator, and its value is 105 V. Figure 28 outlines the current through R-load with PV and wind generator, and its value is 1.2A. Figure 29 outlines the output power with PV and wind generator, and its value is 110 W.

comparison of output voltage and output power is given in Table 1. By using DC microgrid with solar powered system, battery and wind, the output voltage is

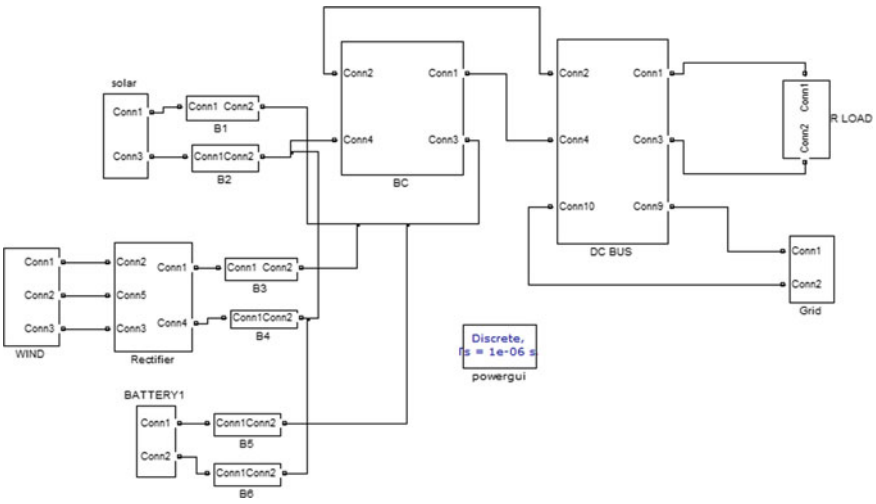

Fig. 15 Simulink diagram of DC microgrid with wind alone

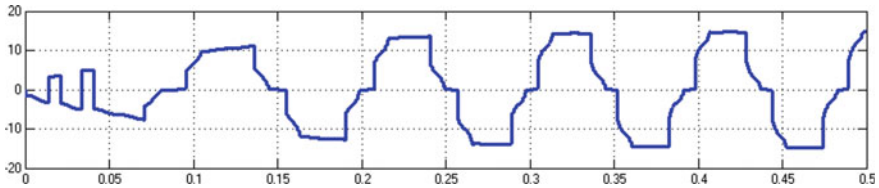

Fig. 16 Input voltage

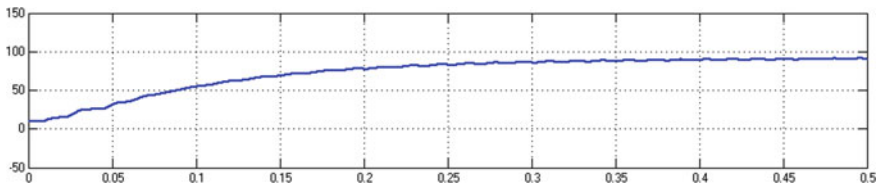

Fig. 17 Voltage across R-load with wind alone

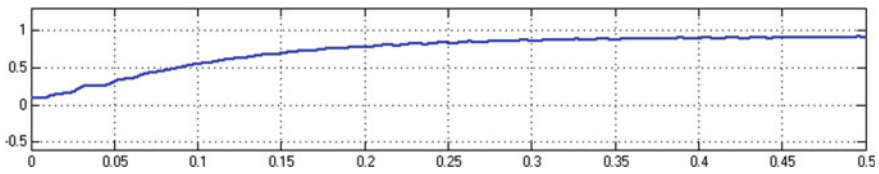

Fig. 18 Current through R-load with wind alone

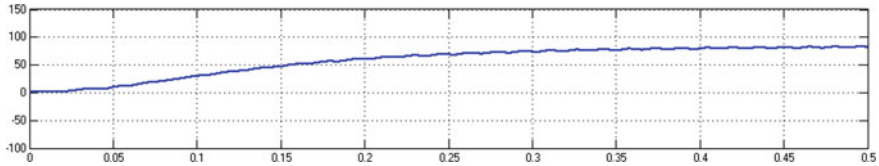

Fig. 19 Output power with wind alone

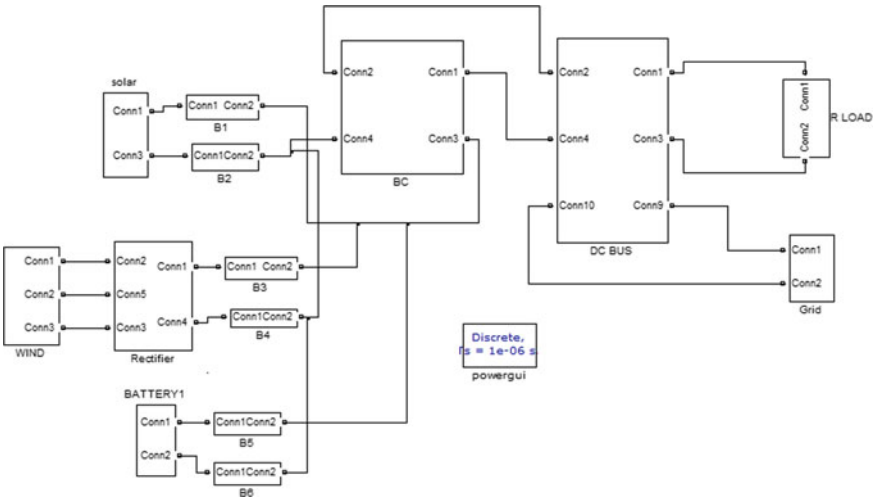

Fig. 20 Simulink diagram of DC microgrid with solar powered system and battery

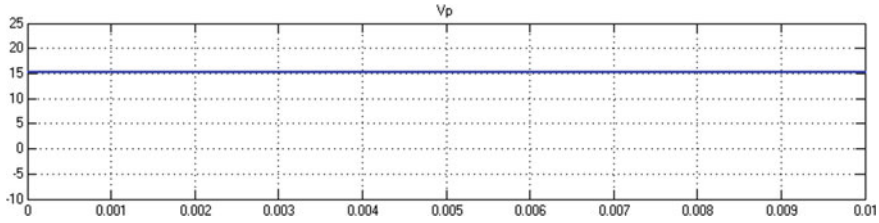

Fig. 21 Input voltage

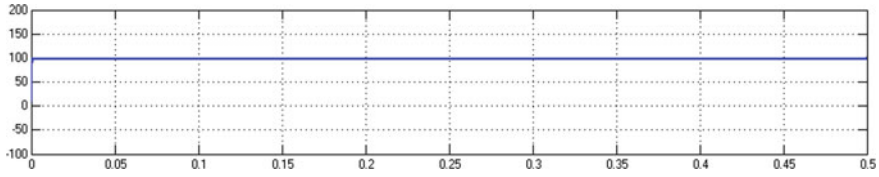

Fig. 22 Voltage across R-load with solar powered system and battery

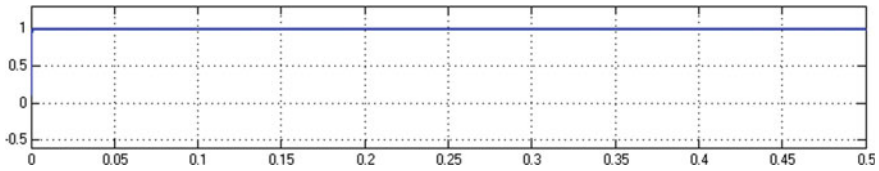

Fig. 23 Current through R-load with solar powered system and battery

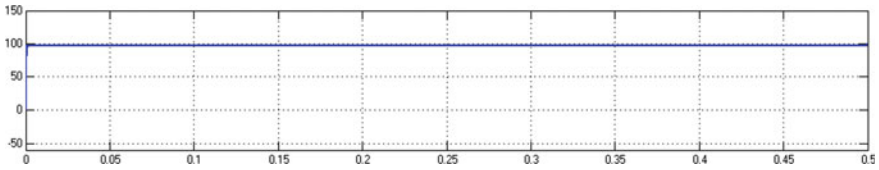

Fig. 24 Output power with solar powered system and battery

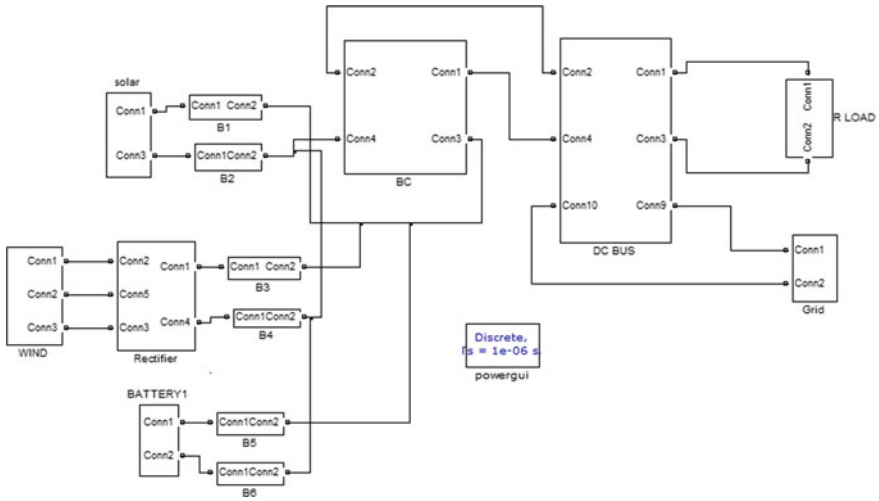

Fig. 25 Simulink diagram of DC microgrid with solar powered system and wind generator

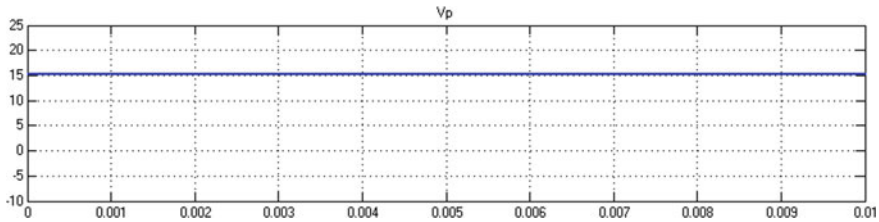

Fig. 26 Input voltage

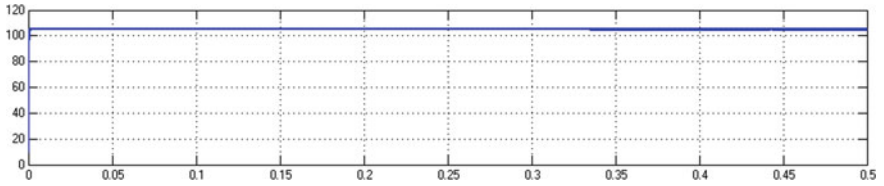

Fig. 27 Voltage across R-load with solar powered system and wind generator

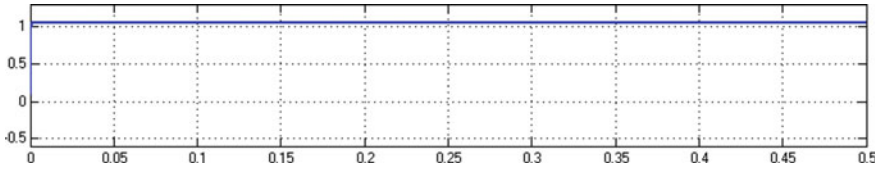

Fig. 28 Current through R-load with solar powered system and wind generator

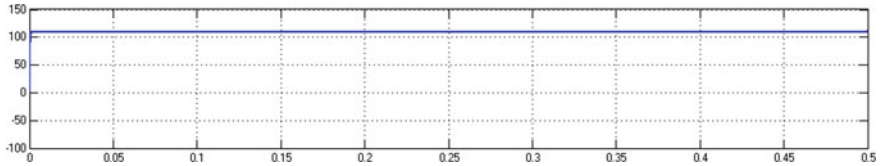

Fig. 29 Output power with solar powered system and wind generator

Table 1 Font sizes of headings. Table captions should always be positioned *above* the tables

Case	Output voltage (V)	Output power (W)
PV (solar powered system)	86	74
Battery	81	65
Wind	90	85
Solar powered system (PV)+Battery	98	97
Solar powered system (PV)+Wind	105	110
PV+Battery+wind	114	130

enhanced from 86 to 114 V; output power is enhanced from 74 to 130 W. Hence, the outcome represents that the DC microgrid with solar powered system, battery and wind is superior to DC microgrid with PV alone, DC microgrid with battery alone, DC microgrid with wind alone, DC microgrid with PV and battery and DC microgrid with PV and wind.

4 Conclusion

DC microgrid with PV alone, DC microgrid with battery alone, DC microgrid with wind alone, DC microgrid with solar powered system and battery, DC microgrid with PV and wind & DC microgrid with PV battery and wind are modeled, analyzed and simulated. The outcomes are compared in terms of output voltage and output power. By using DC microgrid with PV battery and wind, the output voltage is enhanced from 86 to 114 V; output power is enhanced from 74 to 130 W. Hence, the outcome represents that the DC microgrid with PV, battery and wind are superior to DC microgrid with PV alone, DC microgrid with battery alone, DC microgrid with wind alone, DC microgrid with PV and battery and DC microgrid with PV and wind. This work mainly deals with the simulation of DC microgrid with PV, battery and wind. The simulation of DC microgrid with PV battery and wind in closed loop system can be done in future.

Case	Output voltage (V)	Output power(W)
PV (solar powered system)	86	74
Battery	81	65
Wind	90	85
PV+Battery	98	97
PV+Wind	105	110
PV+Battery+wind	114	130

References

1. Azer P, Emadi A (2020) Generalized state space average model for multi phase inter leaved buck, boost and buck-boost DC-Dc converters:-transient steady state and switching dynamics. IEEE Access 77735–77745https://doi.org/10.1109/ACCESS.2020.2987277
2. Peng J, Fan B, Duan J, Yang Q, Liu W (2019) Adaptive decentralized output-constrained control of single-bus DC microgrids. IEEE/CAA J Automatic Sinica 6(2):424–432
3. Fan B, Peng J, Duan J, Yang Q, WLiu (2019) Distributed control of multiple-bus microgrid with paralleled distributed generators. IEEE/CAA J Automatic Sinica 6(3):676–684
4. Bahrami H, Adib E, Farhangi S, Iman-Eini H, Golmohammadi R (2017) ZCS-PWM interleaved boost converter using resonance-clamp auxiliary circuit. IET Power Electron 10(3):405–412
5. Bahrami H, Adib E, Farhangi S, Iman-Eini H, Golmohammadi R (2017) ZCS-PWM interleaved boost converter using resonance-clamp auxiliary circuit. IET Power Electron 10(3):405–412. https://doi.org/10.1049/iet-pel.2016.0267
6. Lee HS, Choe HJ, Ham SH, Kang B (2017) High-efficiency asymmetric forward-flyback converter for wide output power range. IEEE Trans Power Electron 32(1):433–440
7. Tahavorgar A, Quaicoe JE (2017) A dual series-resonant DC–DC converter. IEEE Trans Power Electron 32(5):3708–3718
8. Miao S, Wang F, Ma X (2016) A new transformerless buck–boost converter with positive output voltage. IEEE Trans Ind Electron 63(5):2965–2975

9. Veerachary M, Kumar P (2020) Analysis-and-design of-quasi-z-source equivalent DC-DC boost converters. IEEE Trans Ind Appl 2:1–1. https://doi.org/10.1109/TIA.2020.3021372
10. Imran A, Hafeez G, Khan I, Usman M, Shafiq Z, Qazi AB, Khalid A, Thoben K-D (2020). Heuristic based programable controller for efficient energy management under renewable energy sources and energy storage system in smart grid. IEEE Access 8(2):39587–139608https://doi.org/10.1109/-ACCESS.2020.3012735

Embedded System for Lethal Gas Leakage Exposure and Forewarning System Using Arm Processor

M. Nirmala and S. Durga Shree

Abstract All over the world various semiconductor manufacturing industries dealing with the accidents that occur due to the leakage of hazardous or lethal gases that are involved in the process of making semiconductors and accidents due to the noise of the machineries used. As it is an emerging problem in the production of semiconductor, a safety system is being proposed. The proposed embedded based safety indication system would ensure that the leakage of gas such as hydrogen and any deviation from the safety limit of sound, accidents happening all over without any leakage of gases is being detected and an immediate alert to this leakage or deviation is being sent to the representative of the industry. The message may be sent to their number, displaying the alert, turning off the supply to the system and ringing an alarm to indicate the above cases of accident. In this paper, the effectiveness of the proposed ARM controller-based safety system is implemented using proteus virtual system modelling is using, would ensure the absolute safety.

Keywords ARM based embedded system · Hazardous gases · Proteus virtual platform · Global System for Mobile Communication (GSM) · Arduino IDE

1 Introduction

In general, more than 35% of gas concerned accidents happens in industries because of gas leakage. The real concern is the spillage of hydrogen and sound related accidents in industries. Various rules and regulations are executed for the gas spillage and abnormal noise identification system. The Proposed model gives an alert message which is fundamentally required to differentiate a Gas leakage in the commercial premises. An alert message is sent on to the Liquid Crystal display and a sign with

M. Nirmala · S. Durga Shree (✉)
Electrical and Electronics Engineering Department, Kumaraguru College of Technology, Coimbatore 641049, India
e-mail: durgashree.19mes@kct.ac.in

M. Nirmala
e-mail: nirmala.m.eee@kct.ac.in

C. Subramani et al. (eds.), *Proceedings of International Conference on Power Electronics and Renewable Energy Systems*, Lecture Notes in Electrical Engineering 795,
https://doi.org/10.1007/978-981-16-4943-1_21

the assist of GSM unit is skilled to articulate messages to the desired member about the spillage of Hydrogen and shortly kill the furnish of gas [1]. The wi-fi based carbon dioxide (CO_2) monitoring system with GPS receiver is used to acquire statistics information about the gas leakage. But challenge of this gadget is that it makes use of web for monitoring, also it needs to have 24/7 web connection. This System solely raises an alarm when gas is leaked, but it cannot perform any motion to forestall or decrease any the harm [2] Fuel leakage is to installation a fuel leakage detector at inclined locations. The advantage of the system is computerized alarming system, which can observe liquefied petroleum fuel leakage in quite a number of locations [3]. In [4], the GSM based an embedded machine for Gas Cylinder maintenance where its detection section become aware of the fuel leakage and sends SMS to the customer via GSM about the gas leakage. A wi-fi LPG leakage monitoring detects the leakage of the LPG and signals the client the use of GSM about the leakage and controls exhaust fan [5]. Whenever the device detects the enlarge in the attention of the LPG leakage it straight away indicators via activating an alarm and concurrently sending message to the specific cell phones. The fan is switched on to exhaust gasoline and an LPG secure valve geared up to the cylinder is closed thru alerts to keep away from similarly leakage. The machine assures protection and prevents explosion [6]. A microcontroller totally based gadget the place a fuel sensor (MQ6) is used in detection of LPG leakage [7]. This unit is additionally built-in with an alarm unit, to sound an alarm or provide a visible indication of the leakage. The sensor has excessive sensitivity with rapid response time at low priced cost. If leakage is detected, message to the unique consumer or to household member the use of mobile community referred to as GSM is dispatched automatically [8]. It additionally measures the weight of LPG cylinder and displayed in LCD display. A fuel volume of much less or equal to 10 kg, it requests for the new cylinder through robotically sending textual content message to a distributor [9]. Also, when cylinder weighs much less than or equal to 0.5 kg, it informs the patron by way of sending a message to fill up the cylinder [10].

Gas leakages and accidents due to noise that exceeds human audible vary are one of the major causes at the behind of industrial accidents. The leakage of fuel is robotically detected with the aid of the detection system. The probabilities of furnace accident are prevented through the gadget which would have been delivered on thru the leakage of gas [11]. The fuel sensor observes the occurrence of hydrogen gasoline and sound sensor senses the variation of the sound, then the ARM cortex controls the stepper motor and also flash this information as a display which strengthen this industrial accident quitter system [12]. The proposed system is an automatic fuel exposure, sound revealing and accident prevention system. The fuel leakage is routinely detected with the aid of ARM system. The exhaust fan is routinely switched ON if a leakage is detected. To force out the gas from the room, the exhaust is used. Simultaneously sending an alert message to turn off the supply of gas. The chances of fire accident are efficiently avoided by the system. ARM controller along with a gas sensor to identify the presence of hydrogen gas around the surroundings and its range. A GSM module conveys a warning message to the respective person responsible. The ARM Microcontroller has low number of transistors and these

transistors are cost effective. One of the most advanced form of these microcontrollers is a cortex controller, it is mostly used in wireless communication technologies and other embedded system due to benefits such as low power consumption, etc. ARM Controller is an energy efficient Microcontroller. It is a high performance 32-bit processor which offers numerous benefits to the developers. It collectively directs the data over the web for throwing gasoline out after few milliseconds lag and continue send messages as "Gas Leakage Detected" to mobile phone.

2 Proposed Lethal Gas Leakage Exposure and Forewarning System

The main objectives of the proposed system are: (i) To develop a system which detects the leakage of Hazardous gas like HYDROGEN and alert people quickly using effective controller as a medium to prevent any kind of accidents. (ii). To prevent the upshot of any blast in the industry by alerting the area of accident and to maintain the safety range of sound audible to human ears. (iii) The alerting includes displaying 'There is a leakage', sending a message regarding the leakage (to the respective representative of the gas unit in the industry), cutting-off the supply immediately, giving an alarm, turning the exhaust gas shown in Fig. 1.

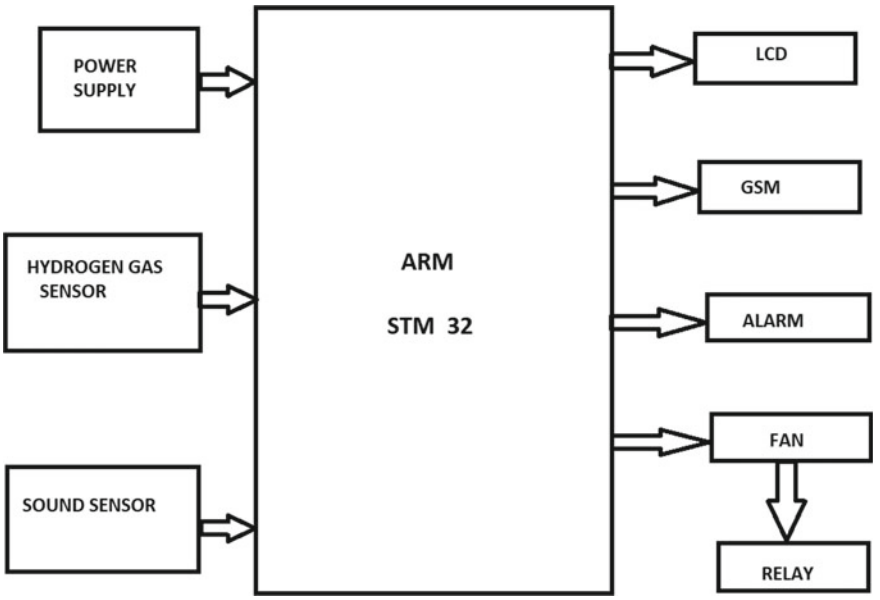

Fig. 1 Block diagram of the proposed lethal gas leakage exposure and forewarning system

The entire block incorporates the detection of the gasoline sensor, then there is a block manner in which there is an Arduino microcontroller issue which acts to acquire the cost dispatched by means of the gasoline sensor and eventually the output block shows the output in the structure of LED lights SMS gateway. The entire block right here is the gasoline sensor that reads the analog facts enter value, in this situation the sensor will flip on if the Arduino microcontroller has power, the sensor will then begin studying and sending analog records to the microcontroller and then enter the block process. The block manner acts as the recipient of statistics that is dispatched from the enter block and then processed to do the conditioning that was once in the past programmed the use of the Arduino IDE software. After conditioning, the output will be persevered to the output block. The output block consists of a led mild as a warning of a fuel leak in the room then the fan features as a gasoline suction in the fan room will mechanically flip on if the block manner sends a command that is when there is a fuel leak in the room, the fan will mechanically flip off if the analog cost is the enter block has back to regular and the closing one is the GSM SIM800l module which features as a message sending media in the tournament of a fuel leak in the room, sending messages will show up persistently with a prolong of 5 s if the gasoline prerequisites in the room are nonetheless excessive intensity.

2.1 ARM Based Indication System

The circuit diagram for the proposed ARM based indication system is shown in Fig. 2.

The proposed device consists of the GSM module, LCD, relay circuit and sensors as hydrogen sensor and sound sensor which affords greater security to the enterprise

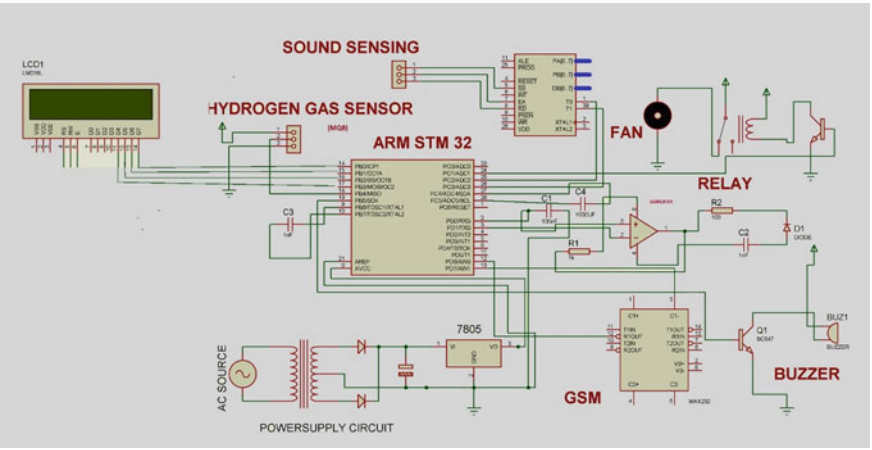

Fig. 2 ARM based indication system

and hence to will increase the effectivity of the system. The gasoline detector has quite a few advantages, some are convenient installation, low cost and honestly convenient to use. Another essential gain of the detector is that even if fuel leaks happens when no people is in the inside of building, GSM module could ship on the spot messages to stakeholders related to the gasoline leakage and for this reason it helps in warding off the accidents at the earliest. The proposed gadget is to make certain the protection restriction and discover the quantity of hydrogen fuel in the ecosystem and the stage of noise in the environment (human audible range) and to realize the unit (in the industry) in which a blast has come about except any leakage in gasoline.

The power supply required to run the prototype is very minimum. The selected components in a way that consumes lesser power than those present in the existing system. Figure 3 shows the work flowchart of the proposed system. The GSM module is controlled by the ARM microcontroller. The module indicates an ALERT, when the gas is leaked. Here alerting system is sending an alert message saying "LEAKAGE ALERT" to the respective representative of the respective firm which is not a part of any existing system. The GSM module is provided with a SIM CARD with the registered number of the respective representative to receive an alert message. A relay is generally connected here to the hydrogen gas sensor and sound sensor. The function of the relay is to turn the system into an open system from a closed system and abruptly turn OFF of the supply. When the system becomes a closed one the leakage of the respective gas also stops as the system has no supply. The relay receives an interrupt signal to turn OFF. Safety is assured when a relay is included as the preventing the leakage of gas would also make a root to get rid of an accident.

3 Simulation Results

Figure 4 shows the simulation circuit of proposed system. The simulation circuit consists of an M8 hydrogen gas sensor, a sound sensor, and the power supply on the input side. The power supply is the available AC source which being stepped down from 230 to 11 V using an step down transformer which is further fed into a rectifier which converts the AC voltage to pulsating DC and then into pure DC using a capacitor. Certain level of gas and sound has be coded to the ARM in which whenever the limit exceeds the coded level the ARM would give signal to the components in the output side. The GSM module to send an alert message to the particular representative of the particular unit, the LCD to display 'ABNORMAL ALERT', the relay to make the system an open circuit and thus cut off the supply, the exhaust fan goes on in order to let the gas into the atmosphere and finally the alarm goes on to indicate that there is a gas leakage or there is a noise disturbance in the industry.

Figure 5 shows that the simulation results of ARM based system under normal operating condition. Figures 6 and 7 illustrates that output of hydrogen sensor and sound sensor under abnormal conditions.

At certain level of hydrogen gas (500) and sound (3000 dB) has be coded to the ARM in which whenever the limit exceeds the coded level the ARM would give signal

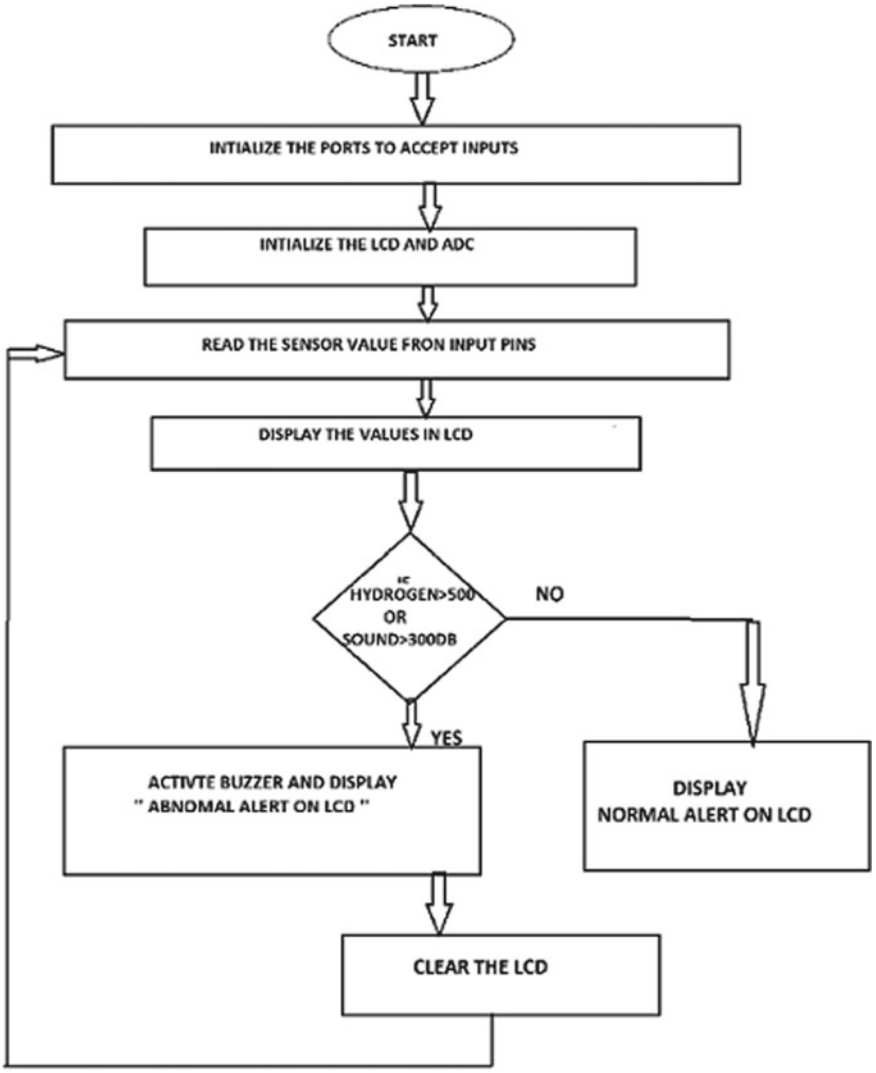

Fig. 3 Flowchart of ARM based indication system

to the components in the output side. The GSM module to send an alert message to the particular representative of the particular unit, the LCD to display 'ABNORMAL ALERT', the relay to make the system an open circuit and thus cut off the supply, the exhaust fan goes on in order to let the gas into the atmosphere and finally the alarm goes on to indicate that there is a gas leakage or there is a noise disturbance in the industry. And if the condition is normal it displays NORMAL CONDITION.

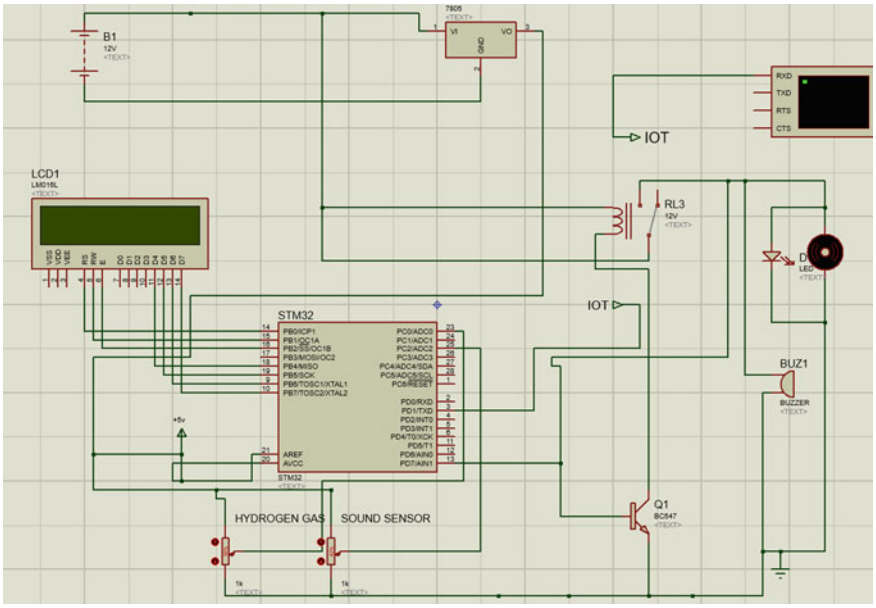

Fig. 4 Simulation circuit of ARM based indication system

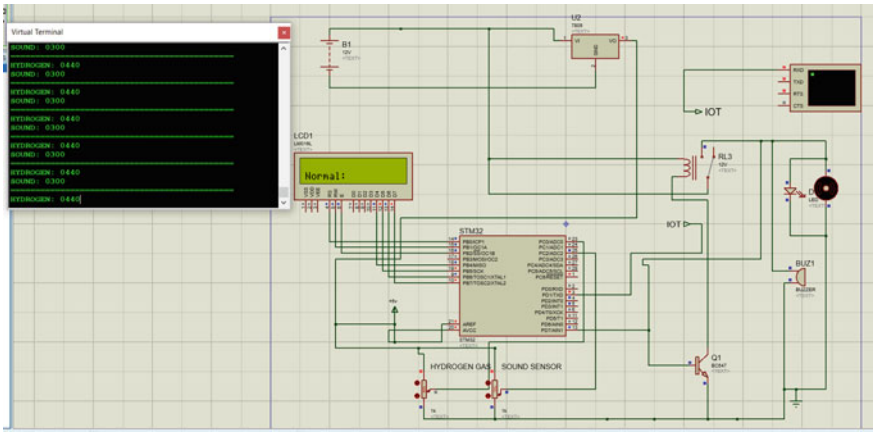

Fig. 5 Simulation result under normal operating conditions (No leakage)

4 Conclusion

As it is known that the leakage of gases in industries and it's aftermath is an emerging problem which has even caused many life, the future scope of the proposed system would be that it would reduce the number of accidents happening all over world due

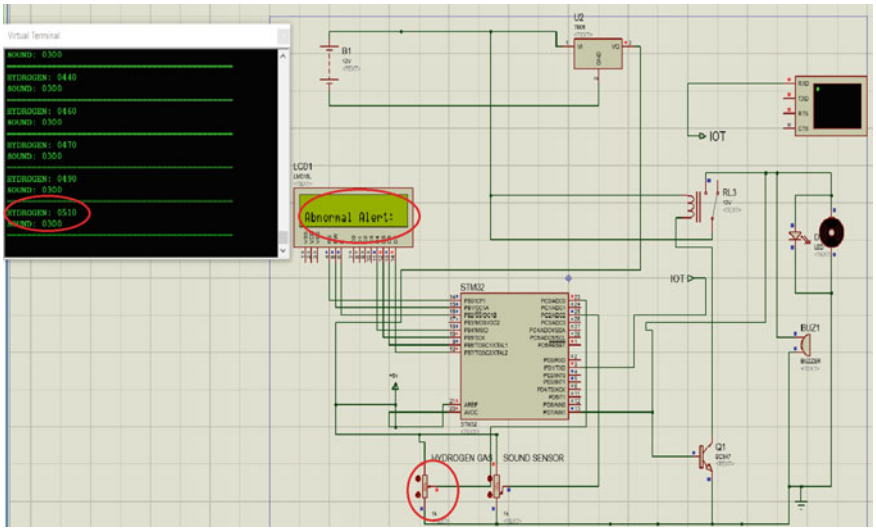

Fig. 6 Hydrogen sensor output under abnormal condition

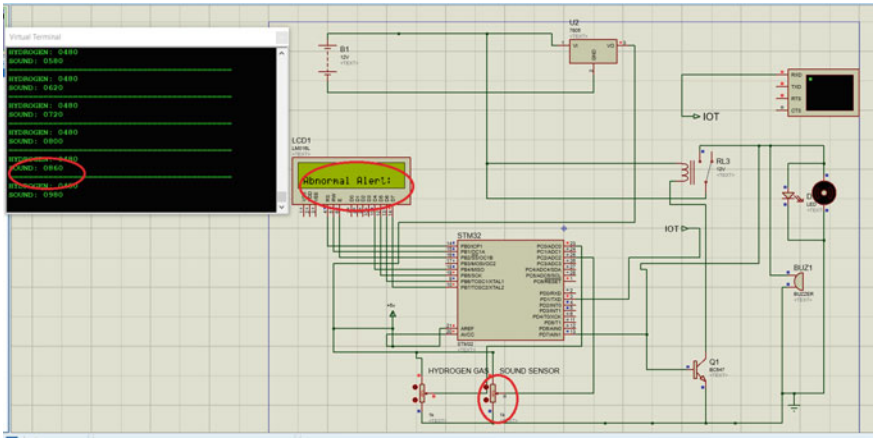

Fig. 7 Sound sensor output under abnormal condition

to the leakage of gas in the industries and accidents that happen due to the sound that exceeds the safety level. Thus, as a result of the proposed system is implemented using proteus virtual platform and safety can be ensured in the future to the entire semiconductor company (Einfochips) for which the system is being proposed. More of modifications can be made in the future to the prototype as a retrofittable device to the gas tubes in the industry which use hydrogen and in industries which machines used produce more noise.

References

1. Bhamare P, Dalvi S, Bhamare M, Dube D, Bhonsale M (2016) A survey on GasBo for LPG gas detection using mobile. Int J Adv Res Dev 4:27–32
2. Falohun AS, Oke AO, Abolaji BM, Oladejo OE (2016) Dangerous gas detection using an integrated circuit and MQ9. Int J Innov Res Eng Manag 4:197–200
3. Katole KR, Bagade V, Bagade B, Soni A, Kamde H (2016) Hazardous gas detection using ARDUINO. Int J Innov Res Eng Manage 4:597–600
4. Kasar MS, Dhaygude R, Godse S, Gurgule S (2016) Automatic LPG gas booking and detection system. Int J Innov Res Eng Manag 4:297–300
5. Amsaveni M, Anurupa A, Preetha RSA, Malarvizhi C, Gunasekaran M (2015) GSM based LPG leakage detection and controlling system. J VLSI Des Sig Process 3:55–65
6. Keluskar H, Chavan P, Sonalikudale, Salunke GD, Pawar S (2015) GSM based home safety. Int J Innov Res Eng Manag 4:68–71
7. Soundarya T, Anchitaalagammai JV, Deepa Priya G, Karthick Kumar SS (2014) Cylinder LPG gas leakage detection for home safety. IOSR J Electron Commun Eng (IOSR-JECE) 9:53–58
8. Prabhu AD, Pathak AD (2017) Gas leak detector using Arduino UNO microcontroller. Int J Res Appl Sci Eng Technol (IJRASET) 5:45–48
9. Putra MF, Kridalaksana AH, Arifin Z (2017) Designing an LPG gas leak detector with MQ6 sensor microcontroller-based via android smartphone as an information media. Jurnal Informatika Mulawarman 12:71–75
10. Yang M, Zhao W, Xu W, Feng Y, Zhao Z, Chen X, Lei K (2019) Multitask learning for cross-domain image captioning. IEEE Trans Multimedia 21:82–87
11. Hidayat I (2018) Gas leak system using MQ-6 based on wireless sensor network. 17:355–364
12. Parwati CI, Suseno HP, Fatkhiyah E (2015) Modeling telemetry system “Multi-Node” early warning ammonia gas leak based SMS gateway. Jurnal Teknologi 8:151–160

A Trasformerless Buck-Boost Converter as Maximum Power Point Tracker for Battery Charging

C. Balaji, O. Hemakesavulu, A. Dominic Savio, B. Vinothkumar, S. Sakthi, and P. Sivaperumal

Abstract DC-DC converters are utilized to interface the Photovoltaic source to the battery for charging purposes. A non-isolated (NI) DC-DC buck-boost converter has been employed as a maximum power point tracking (MPPT) system to derive the photovoltaic power present. The MPPT control is utilized to extricate the greatest power available from the photovoltaic source. The MPPT gets the solar irradiation and solar cell temperature as contributions to decide the optimized duty cycle to acquire maximum power. In this work, a non-isolated buck-boost converter is utilized as MPP tracker for battery charging applications. The performance of the converter is simulated and validated through the experimental results.

Keywords PV source · Buck-boost converter · Maximum power point tracker · Battery charging

1 Introduction

Solar energy has shown promising results and is economic. However, PV cell/module shows non-linear I-V and P-V characteristics which rely on temperature and solar insolation [1]. The stochastic nature of PV system has energy conversion problems, which result lower efficiency of approx. 18% [2]. To increase efficiency and overcoming the problems in energy conversion, MPP control is used to drive the PV

C. Balaji (✉) · A. Dominic Savio · B. Vinothkumar
School of Electrical Engineering, SRM Institute of Science and Technology (Formerly Known As SRM University), Kattankulathur Campus, Chennai 603203, India

B. Vinothkumar
e-mail: vinothkb@srmist.edu.in

O. Hemakesavulu
Department of EEE, AITS, Rajampet, AndhraPradesh, India

S. Sakthi
Department of EEE, Jeppiaar Engineering College, Chennai, India

P. Sivaperumal
Department of EEE-Marine, AMET University, Chennai, India

C. Subramani et al. (eds.), *Proceedings of International Conference on Power Electronics and Renewable Energy Systems*, Lecture Notes in Electrical Engineering 795,
https://doi.org/10.1007/978-981-16-4943-1_22

modules at their maximum power point [3]. As in [4], a DC-DC power converter acts as MPPT (maximum power point tracker) that optimizes the power flow between PV system and load. Generally, Batteries are connected to the converter to maintain the required charge voltage for the batteries. A charge controller helps in achieving higher efficiency in PV battery charging systems [5].

In most of the commercial PV system fed battery applications, the MPP fixed above the charging voltage of batteries [6]. A buck conversion is needed in this but with high temperature and low insolation condition, the MPP goes below the required charging voltage which requires a boost operation [7]. As in [6], to achieve a steady voltage from an input supply which is lower or greater than the yield especially in MPPT application, a buck-boost converter is required to harvest maximum possible power from solar modules at all times irrespective of the type of load being used. In battery charging applications, if a battery is directly attached to a solar-based module with no converter, it will harm the battery because of the variances in the voltage provided to the battery. Many converters are reported in literature for the application of buck-boost converters as a MPP tracker [8, 9].

This paper presents a MPP tracker realized by a transformerless buck-boost converter having positive output voltage. Many algorithms are reported in the literature for tracking MPP. Simple and a popular perturb and observe (P&O) procedure is adopted [10]. Experiment analysis is done by implementing this converter to a standalone PV system.

2 The Photovoltaic Power System

PV power conversion system converts energy from the sun into the electricity by solar cells and supplies power to the load in demand. The block diagram in Fig. 1. illustrates the components of a typical PV conversion system feeding a DC load. The components include a PV panel (solar array), DC-DC power electronic converter and

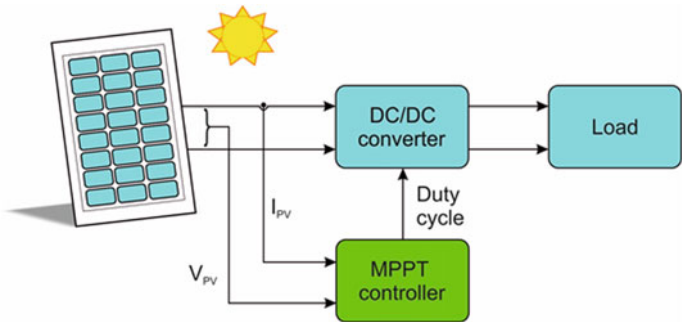

Fig. 1 Components of a typical PV conversion system

a DC load. Additionally, to extract maximum available power, an MPPT controller is used.

2.1 P-V and V-I Characteristics of the PV Cell

The attributes of a PV cell can be determined from P-V and V-I plots. The voltage Vs current plot is shown in Fig. 2a. Current corresponding to V_{max} is noted. This current is referred to as the current at MPP. A typical P-V plot is shown in Fig. 2b. For various voltages at different temperatures and irradiance. The MPP is located as a point at which the voltage increases and power decreases. Since the P-V characteristics depends on temperature and irradiance, the MPP must be tracked for changing temperature and irradiance to harvest maximum power from PV cell. The attributed curve of PV cell in Fig. 2c. It shows two points; short circuit current I_{sc} and open circuit voltage V_{oc}. The point where I_{mp} and V_{mp} meet is the maximum power point, which corresponds to maximum power available from the PV cell. The greatest possible power can be transmitted to the load if the load line crosses this instantaneous point exactly.

The value of this load resistance can be determined using (1).

$$R_{mp} = \frac{V_{mp}}{I_{mp}} \tag{1}$$

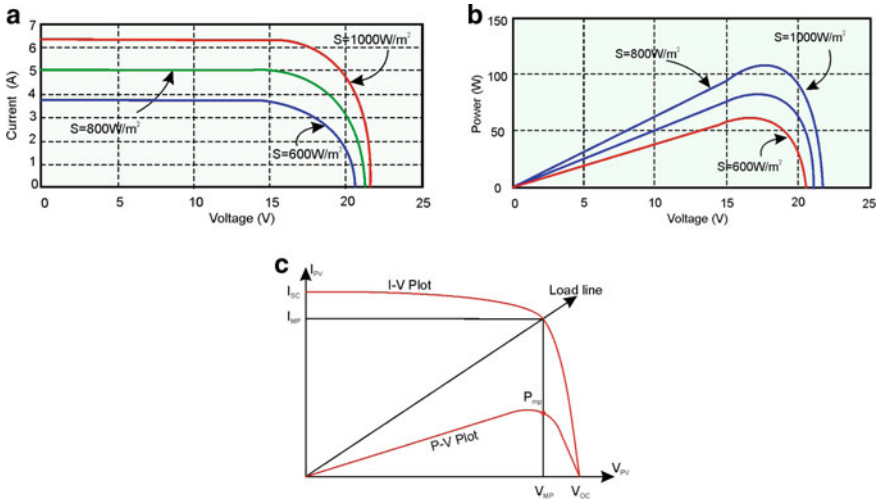

Fig. 2 **a** I-V characteristics, **b** P-V characteristics of PV cell, **c** V-I and P-V characteristics of a PV cell

2.2 Maximum Power Point

The maximum power point tracking (MPPT) guarantees the extraction of the peak possible power from the solar arrangement and transmission to the load [10]. So as to transmit most of the power, a DC-DC power converter is employed between PV module and the load. The load impedance as observed by the supply source is balanced by controlling the duty cycle and coordinated at the instance of the maximum power with the source.

3 Buck-Boost Converter

The simple block diagram in Fig. 3. shows the battery charging using PV panel. The circuit of NI buck-boost converter [11] is shown in Fig. 4a. It comprises of two MOSFET switches S_1 and S_2, pair of diodes D_1 and D_2, two capacitors C_1 and C_2,

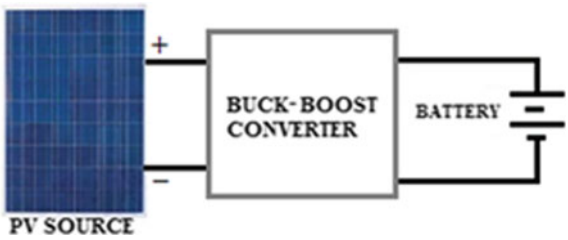

Fig. 3 Block diagram of PV fed battery charging

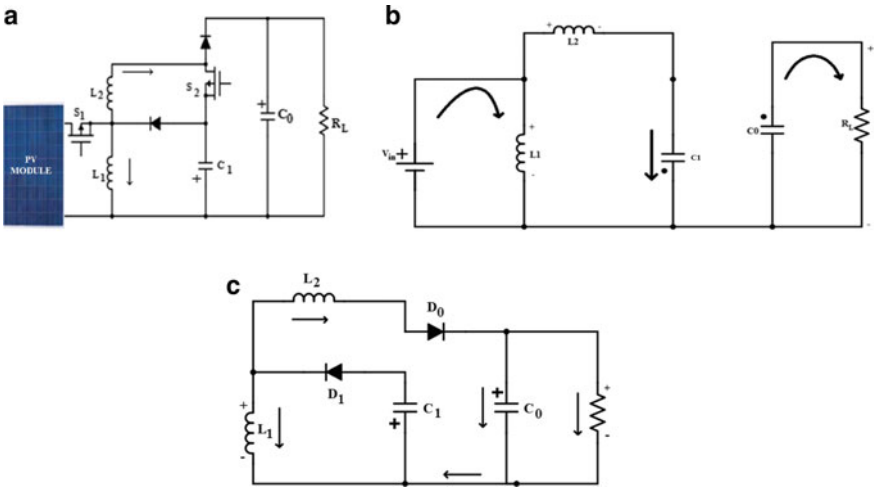

Fig. 4 **a** Buck-Boost converter, **b** equivalent circuit of state 1, **c** state 2

two ferrite core inductors L_1 and L_2 and a load. MOSFET switching devices S_1 and S_2 are operated synchronously.

The PV is a source and a battery is a load. The converter can be operate in buck and boost mode. The NI buck-boost converter works in two states.

State 1: In this state, the MOSFET switching devices S_1 and S_2 are closed and the pair of diodes D_1 and D_2 are reverse biased. The wound inductors L_1 and L_2 are magnetically charged and the parallel plate capacitors C_1 and C_0 are allowed to drain. The input voltage V_{pv} magnetizes the inductor L_1. Also, V_{pv} and V_{C_1} magnetizes the inductor L_2.The polarity and current directions in this state are marked in Fig. 4b. The expressions are given in (2)

$$\frac{di_{L_1}}{dt} = \frac{v_{in}}{L_1}, \frac{di_{L_2}}{dt} = \frac{v_{in} + v_{C_1}}{L_2}, \frac{dv_{C_1}}{dt} = -\frac{i_{L_2}}{C_1}, \frac{dv_0}{dt} = -\frac{v_0}{C_0 R} \tag{2}$$

State 2: In this state, the MOSFET switching devices S_1 and S_2 are opened and the pair of diodes D_1 and D_2 conduct in forward bias. The inductors L_1 and L_2 are magnetized and the parallel capacitors C_1 and C_0 are dissipated. The capacitor C_1 is powered by the energy stored in industry L_1 through D_1. The parallel plate capacitor C_0 and the load are supplied by the energy stored in inductor L_2. The current directions and polarity are marked in Fig. 4c. The expressions are given in (3)

$$\frac{di_{L_1}}{dt} = -\frac{v_{C_1}}{L_1}, \frac{di_{L_2}}{dt} = -\frac{v_{C_1} + v_0}{L_2}, \frac{dv_{C_1}}{dt} = -\frac{i_{L_1} + i_{L_2}}{C_1}, \frac{dv_0}{dt} = \frac{i_{L_2}}{C_0} - \frac{v_0}{C_0 R} \tag{3}$$

3.1 Time Domain Waveforms

It is taken into an assumption that the equipment employed are conventional, capacitors are adequately bigger to keep up the consistent voltage across it and the converter works in steady and stable state for ease of analysis. For the suggested NI buck-boost converter working in continuous conduction mode (CCM), time-domain waveforms are presented in Fig. 5a.

The voltage boost of the suggested converter is derived and presented in (4).

$$\frac{V_o}{V_{pv}} = \left(\frac{D}{1 - D}\right)^2 \tag{4}$$

It is obvious from (12) that when duty cycle $D > 0.5$ the suggested converter works in boost mode. Else, it operates in buck mode. The converter can also be employed to regulate the output voltage as it has higher gain. The comparison of voltage gains of

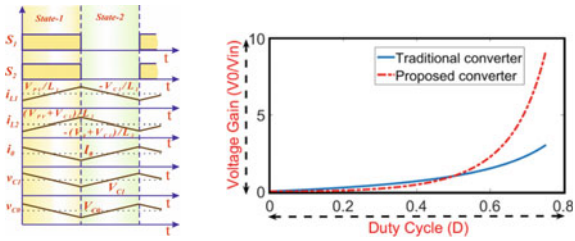

(a) (b)

Fig. 5 **a** Characteristic waveforms under steady state, **b** comparison of voltage gains

buck-boost converter in this work and the traditional buck-boost converter are shown in Fig. 5b.

3.2 Modelling of the Converter

The model of the converter is obtained by solving the state equations obtained from analyzing equivalent circuits of state 1 and state 2. The model is presented in (5).

$$A = \begin{bmatrix} 0 & 0 & \frac{d-1}{L_1} & 0 \\ 0 & 0 & \frac{2d-1}{L_2} & \frac{d-1}{L_2} \\ \frac{1-d}{C_1} & \frac{1-2d}{C_1} & 0 & 0 \\ 0 & \frac{1-d}{C_0} & 0 & \frac{-1}{C_0 R} \end{bmatrix}, B = \begin{bmatrix} \frac{d}{L_1} \\ \frac{d}{L_2} \\ 0 \\ 0 \end{bmatrix}, X = \begin{bmatrix} i_{l1} \\ i_{l2} \\ C_1 \\ C_2 \end{bmatrix},$$
$$D = [0], C = \begin{bmatrix} 0 & d-1 & 0 & 2d+1 \end{bmatrix} \tag{5}$$

3.3 Design of Inductors and Capacitors

The capacitor voltage ripples and inductor current ripples are calculated using Charge-Sec Balance and Volt-Sec balance respectively.

$$\left.\begin{aligned} \Delta i_{L_1} &= \frac{V_{\mathrm{PV}}}{L_1} d_1 T_S, L_1 = \frac{V_{\mathrm{PV}}}{\Delta i_{L_1} \times f_s} d_1 \\ \Delta i_{L2} &= \frac{V_{\mathrm{PV}} + V_{C_1}}{L_2} d_1 T_S, V_{C_1} = \frac{d_1}{1-d_1} V_{\mathrm{PV}}, L_2 = \frac{2-d_1}{(1-d_1)\Delta i_{L_2} \times f_s} V_{\mathrm{PV}} \\ \Delta V_{C_1} &= \frac{i_{L_2}}{C_1} d_1 T_S, C_1 = \frac{V_0}{R \Delta V_{C_1} f_s (1-d_1)} d_1 \\ \Delta V_{C_0} &= \frac{V_0}{R C_0} d_1 T s, C_0 = \frac{V_0}{R \Delta V_{C_0} f_s} d_1 \end{aligned}\right\} \text{and} \tag{6}$$

Table 1 Buck-boost converter parameters

Inductor (L_1)	1.3 mH	Capacitor (C_1)	7.5 pF
Inductor (L_2)	3.3 mH	Switching frequency	20 kHz
Capacitor (C_0)	18.75 pF	Load	40 Ω

If the inductor ripple current, the input and output voltages V_{in} and V_0 respectively, the duty ratio D, the Load Resistance R, and the switching frequency f_s are familiar, the inductance and capacitor values can be calculated using (6). The designed values are shown in Table 1.

4 Simulation

The PV system with proposed DC-DC buck-boost Converter as Maximum Power Point Tracker is shown in Fig. 6. The converter is designed for the maximum output power of 100 W.

The converter is simulated using MATLAB. The voltage of PV panel at MPP is set at 30 V, and the module voltage is fixed at 24 V. The load resistance of 40 Ω is used. The circuit is simulated with different duty cycles. Waveforms of voltage in boost operation is shown in Fig. 7. Variation of output voltages from a converter with a fixed input at various duty cycles are displayed in Table 2.

A 24 V and 7 Ah lead-acid battery has been employed as a load in buck operation. The initial charge of the battery is fixed at 50%. The state of charge has been increased

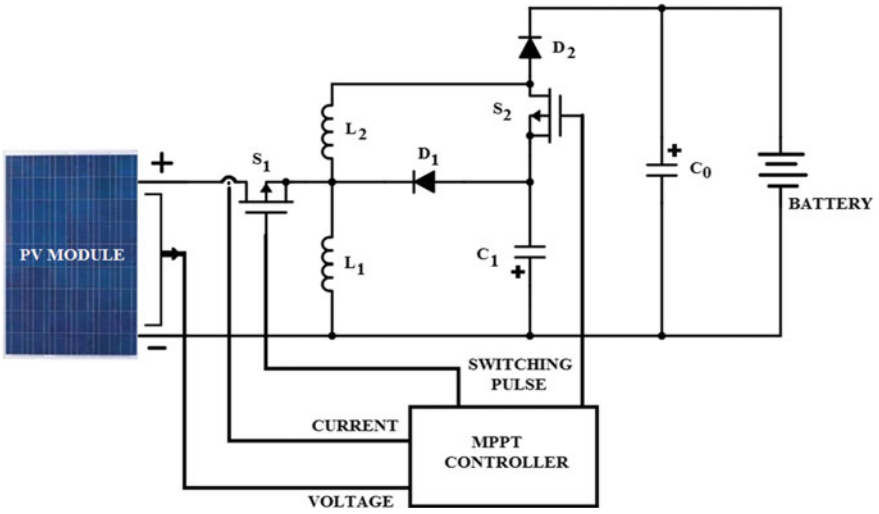

Fig. 6 PV system with proposed MPP tracker and battery

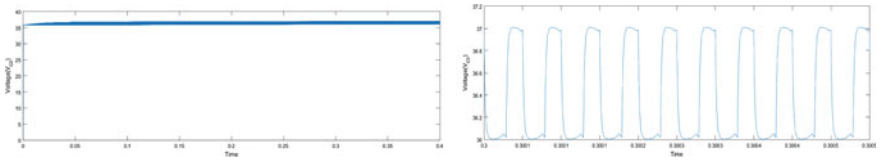

Fig. 7 Waveforms of voltage in boost mode

Table 2 Variation of output voltages from a converter with a fixed input at various duty cycles

Duty cycle (%age)	Input voltage (V)	Output voltage (V)	Output current (A)
40	24.9	18.9	0.153
45	24.6	21.8	0.1745
50	24.7	24.85	0.199
55	24.3	32.2	0.258
60	24.4	41.9	0.335

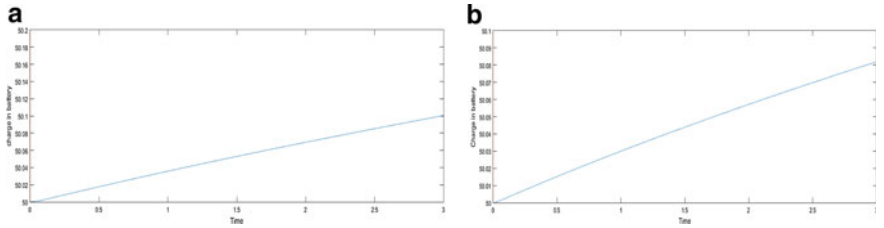

Fig. 8 **a** State of charge of 24 V battery, **b** state of battery charge of 24 V battery

from 50 to 50.1 in 3 s of simulation time. The state of charge waveform is displayed in Fig. 8a.

A 24 V and 7 Ah lead-acid battery has been utilized as a load during boost mode. The initial charge of the battery is set at 50%. The state of charge has been increased from 50 to 50.08 in 3 s simulation time. The state of battery charge is shown Fig. 8b.

5 Experiment Verification

A laboratory prototype with MPPT system and a battery as a load were built to check the operational performance of the suggested converter as shown in Fig. 9. The switching signals are generated using FPGA SPARTAN6 controller board. A hall-effect sensor (ACS-712) and voltage divider circuit are used to sense current and voltage respectively. The parameters of the proposed prototype are given in Table 1. Tests have been done to show the vitality of the proposed buck-boost converter. A 75 W PV module is utilized at standard test conditions with insolation of 1000 W/m^2

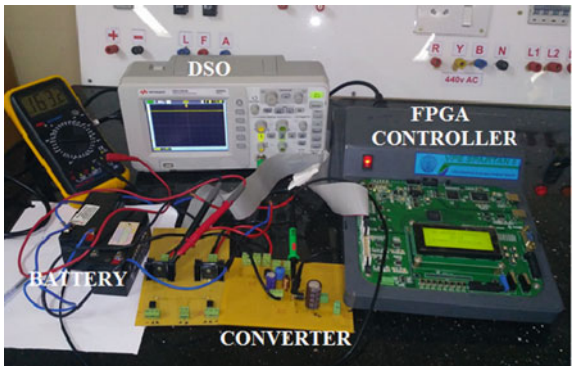

Fig. 9 Digital photograph of the experimental setup

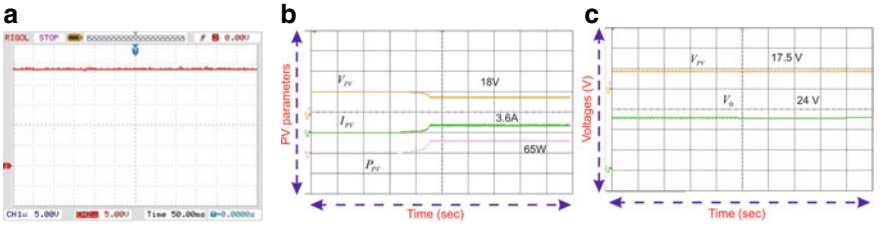

Fig. 10 **a** Battery voltage under charging condition, **b** PV voltage (Ch 1) 20 V/div, PV current (Ch 2) 10A/div, PV power (Ch M) 100 W/div, $T = 2$ s/div, **c** PV voltage (Ch 1) 20 V/div, output voltage (Ch 2) 10 V/div, $T = 1$ s/div

and a temperature of 25 °C. At the point when a battery is directly tied to the PV module, it is seen that the power extracted from the module is 52 W. However, a system with the converter as MPP tracker produces 65 W.

The charging voltage that appears across the battery terminals is shown in Fig. 10a. It shows that the proposed converter serves as a MPP tracker and charges the battery effectively. The battery is charged using 24 V supply from PV panel.

The PV voltage, current and power when the PV module generates 65 W are shown in Fig. 10b, c. It can be seen that the MPP tracker continuously tracking and the PV power is reaching maximum value i.e., 65 W. The experimental test results of the suggested buck boost converter as a MPP Tracker prove that it could improvise the energy transmission efficiency effectively.

6 Conclusion

The PV fed battery charging is a developing area of research in the recent years in the field of photovoltaic based energy generation technologies. This work utilized a

Non-inverting Buck-Boost topology between PV and the battery. The circuit configuration and operation of converter has been explained for which theoretical investigation, simulation, and tests were conducted. From the experimental results, it can be concluded that the converter is a good candidate for PV system fed battery charging applications. It works effectively as MPP Tracker.

References

1. Chandrasekar B, Nallaperumal C, Padmanaban S, Bhaskar MS, Holm-Nielsen JB, Leonowicz Z, Masebinu SO (2020) Non-isolated high-gain triple port DC–DC Buck-Boost converter with positive output voltage for photovoltaic applications. IEEE Access 8:113649–113666
2. Chandrasekar B, Nallaperumal C, Dash SS (2019) A nonisolated three-port DC–DC converter with continuous input and output currents based on Cuk topology for PV/fuel cell applications. Electronics 8(2):214
3. Sridhar R, Jeevananthan S, Dash SS, Selvan NT (2014) Unified MPPT controller for partially shaded panels in a photovoltaic array. Int J Autom Comput 11(5):536–542
4. Mahapatro SK (2013) Maximum power point tracking (MPPT) Of solar cell using buck-boost converter. Int J Eng Res Technol 2(5):1810–1821
5. Savio DA, Juliet VA, Chokkalingam B, Padmanaban S, Holm-Nielsen JB, Blaabjerg F (2019) Photovoltaic integrated hybrid microgrid structured electric vehicle charging station and its energy management approach. Energies 12(1):168
6. Sujitha N, Krithiga S (2017) RES based EV battery charging system: a review. Renew Sustain Energ Rev 75:978–988
7. Chandrasekar B, Chellammal N, Nallamothu B (2019) Non-isolated unidirectional three-port Cuk-Cuk converter for fuel cell/solar PV systems. J Power Electron 19(5):1278–1288
8. He X, Zhang X, Liu H, Zhang H (2015) Application of an integrated transformerless buck-boost converter in photovoltaic MPPT systems. In: 2015 IEEE 11th international conference on power electronics and drive systems. IEEE, pp 692–695
9. Vivek P, Ayshwarya R, Amali SJ, Sree AN (2016) A novel approach on MPPT algorithm for solar panel using buck boost converter. In: 2016 international conference on energy efficient technologies for sustainability (ICEETS). IEEE, pp 396–399
10. Blange R, Mahanta C, Gogoi AK (2015) MPPT of solar photovoltaic cell using perturb & observe and fuzzy logic controller algorithm for buck-boost DC-DC converter. In: 2015 international conference on energy, power and environment: towards sustainable growth (ICEPE). IEEE, pp 1–5
11. Miao S, Wang F, Ma X (2016) A new transformerless Buck-Boost converter with positive output voltage. IEEE Trans Ind Electron 63(5). In some cases, it is the contact volume editor that checks all the pdfs. In such cases, the authors are not involved in the checking phase

A Feed-Forward Neural Network Based MPPT Controller for PEMFC System with Ultra High Step Up Converter

B. Karthikeyan, D. Karthikeyan, V. P. Arumbu, K. Sundararaju, R. Palanisamy, and P. Divya

Abstract In the proposed work, a feed forward neural network (FFNN) based MPPT controller is implemented in which back-propagation algorithm is used to extract maximum power and reduce peak overshoot from 1.26 kW PEMFC. To step up the PEMFC voltage, an Ultra High Step Up converter (UPHC) is designed and its steady state analysis is carried out. The duty cycle of UPHC is controlled using FFNN MPPT controller to extract optimum power from fuel cell whose result is compared with conventional Fuzzy Logic controller. A simulation work has been carried out using MATLAB/Simulink environment and discussed the results.

Keywords Feed-forward Neural Network · MPPT · PEMFC · Step up converter · Fuzzy logic controller

1 Introduction

Fossil fuel contribution to the energy economy for fast decades is remarkable but it is going to be exhausted in near future due to increasing energy demand. Hence the researchers are focusing on green energy which is pollution free, free of cost, long existence etc. Among the renewable energy series, fuel cell is fascinating technology makes the researchers to look into it. There is a wide variety of fuel cell, in that Polymer Exchange Membrane Fuel Cell is differing because it's operating parameters. Some of the notable unique operating parameters are low temperature operation, efficient, can be started quickly, noiseless operation, harmless by-product.

B. Karthikeyan (✉)
Department of Electrical and Electronics Engineering, K. Ramakrishnan College of Technology, Trichy, India
e-mail: karthikeyanb.eee@krct.ac.in

D. Karthikeyan · V. P. Arumbu · R. Palanisamy · P. Divya
Department of Electrical and Electronics Engineering, SRM Institute of Science and Technology, Chennai, India

K. Sundararaju
Department of Electrical and Electronics Engineering, M. Kumarasamy College of Engineering, Karur, India

C. Subramani et al. (eds.), *Proceedings of International Conference on Power Electronics and Renewable Energy Systems*, Lecture Notes in Electrical Engineering 795,
https://doi.org/10.1007/978-981-16-4943-1_23

Even though it has lot attractive features, there will be negative side of PEMFC which makes not suitable for electric vehicle application [1, 2].

The voltage and current relationship for PEMFC is non-linear in V-I plane. There will be a point in V-I characteristics at which maximum output power is available. To make it suitable for any practical application, it is required to incorporate a controller that makes maximum output power at any operating condition. Hence there is need for Maximum Power Point Tracking Controller (MPPT) to ensure optimum output power to load. In literate various MPPT controllers were proposed and discussed the performance of controller, some of noticeable controllers are discussed here [3, 4].

Incremental conductance algorithm using neural network was proposed [5]. A 7 kW PEMFC feeding resistive load through step up converter was studied using MATLAB/Simulink platform. It was proved that the proposed controller performed better in terms of fast convergence, reduced peak overshoot and steady state operation compared to fixed step size IC, variable step size controllers without using neural network. Extended sliding mode controller was proposed in extracting maximum power from 200 W PEMFC during dynamic operating condition [6]. The improvements listed in this study compared to conventional controllers are increased tracking speed, increased boost converter efficiency. To overcome electrical non linearity of PEMFC, a dedicated power converter for each fuel cell in an array was proposed [7]. It is a different approach because maximum fuel operating point was implemented instead of maximum power point strategy. There were some improvements done like 20% more power could be extracted than conventional method.

A high voltage gain boost converter along with RBFN controller was proposed for electric vehicle application [8]. In this analysis, temperature was considered to be time varying operating parameter. During the dynamic operating condition, the proposed controller was able to reduce input current ripple content, reduced voltage stress across the active switches and track the optimum power effectively than conventional fuzzy based controller. To improve both static and dynamic performance of the converter, a variable step size IC controller was proposed in which varying operating parameters are hydrogen partial pressure and temperature [9]. In both the cases, the effectiveness of proposed controller was better in terms of reduced peak overshoot, fast response time, reduced ripple content.

A genetic algorithm based optimum algorithm was proposed to extract maximum power from PEMFC during variation of hydrogen pressure, oxygen pressure and temperature [10]. The proposed controller could achieve better accuracy, fast response and less fluctuation of power under different operating condition. Sun flower optimization algorithm was proposed to reduce sum of squared error between calculated and actual output voltage [11]. The result obtained is compared with conventional methods for two practical systems of Nedstack PS6 PEMFC and Horizon 500 W PEMFC in which it was proved that the proposed system gives good convergence, accurate and precision. Water cycle algorithm was proposed to tune PID controller which ensures maximum power extraction from PEMFC [12].

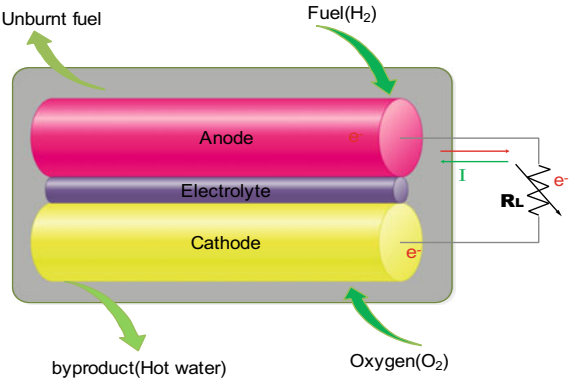

Fig. 1 PEM fuel cell

2 PEM Fuel Cell

Fuel cell is the recent technology in which chemical energy is directly converted into electrical energy without polluting the environment. Its features like quick start up, noise free operation, low operating temperature and high efficiency are fascinating the researchers to use it for electric vehicle application as well as stationary power production. Among the various types of fuel cells, Proton Exchange Membrane Fuel Cell (PEMFC) is abrupt choice for electric vehicle application because of its temperature about 60–90 °C. The platinum catalyst makes the fast reaction rate to regulate the constant output voltage. As shown in Fig. 1, Hydrogen (H_2) rich fuel is supplied at anode to oxidize the hydrogen ions. On the other hand, oxygen (O_2) rich atmospheric air is supplied at cathode to reduction reaction take place. At the end, heat and hot water are obtained as by-product which can re-circulate after cooling process.

3 Ultra High Step up Converter

The proposed converter consists of three active switches S_1, S_2, S_3 in which S_1, S_2 are triggered simultaneously and switch S_3 is triggered asymmetrically. Two inductors L_1, L_2 are placed in series with each Switch S_1, S_2 respectively in parallel connected arms. Diodes D_1, D_2 are connected in parallel arms as shown in Fig. 2 which avoids current reversal during the main switches are turned off. Capacitor C_1 is connected in parallel with load to make continuous load current.

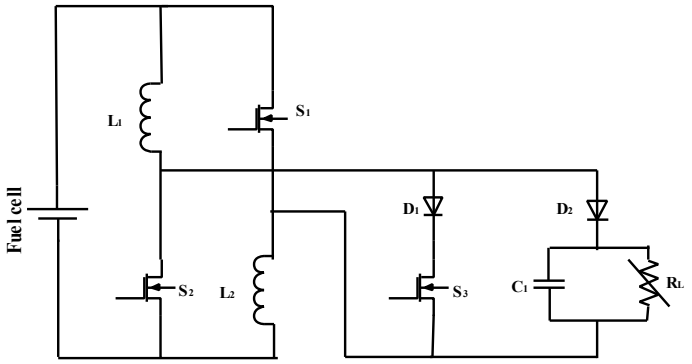

Fig. 2 Ultra high step up converter

3.1 Mode of Operation

During the mode 1, both the switches S_1, S_2 are turned on and inductor L_1, L_2 store energy. The energy stored in capacitor C_1 at previous mode supply the load as shown in Fig. 3.

During mode 2, both switches S_1 and S_2 are turned off and triggering pulse is applied to the switch S_3. The energy stored in inductor L_1, L_2 is released through Switch S_3 and diode D_1 as shown in Fig. 4. The load is supplied from capacitor C_1 which is charged previously.

During this mode, all switches S_1, S_2, S_3 are turned off and energy stored in inductor L_1, L_2 are released to load which makes high output voltage. The corresponding current path is shown in Fig. 5.

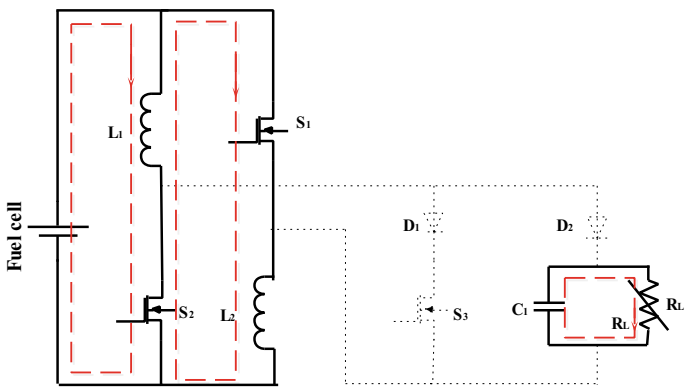

Fig. 3 Mode 1

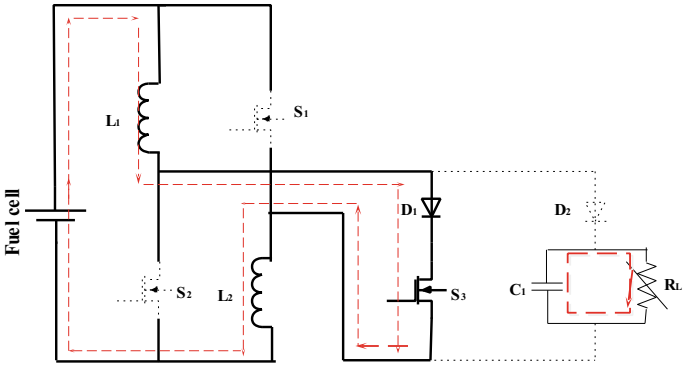

Fig. 4 Mode 2

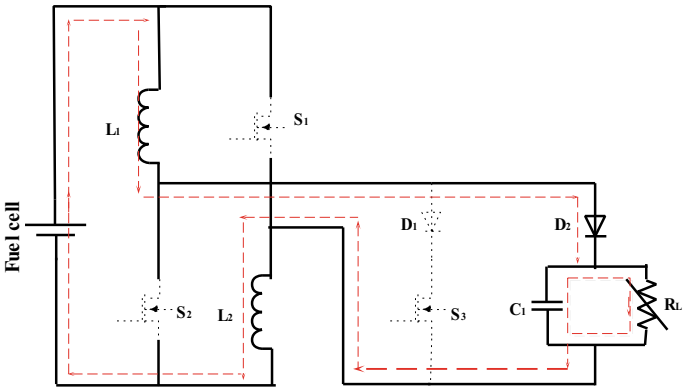

Fig. 5 Mode 3

3.2 Voltage Gain

The conventional boost converter gain is

$$M = 1/(1 - D) \tag{1}$$

The proposed converter voltage conversion gain can be written as

$$M = (1 + D_1)/D_2 \tag{2}$$

The voltage gain of proposed converter is compared with conventional step up converter as shown in Fig. 6 by changing the values of duty cycle d_1 and d_2 is kept constant. Both the duty cycle can be varied according to the conversion requirement.

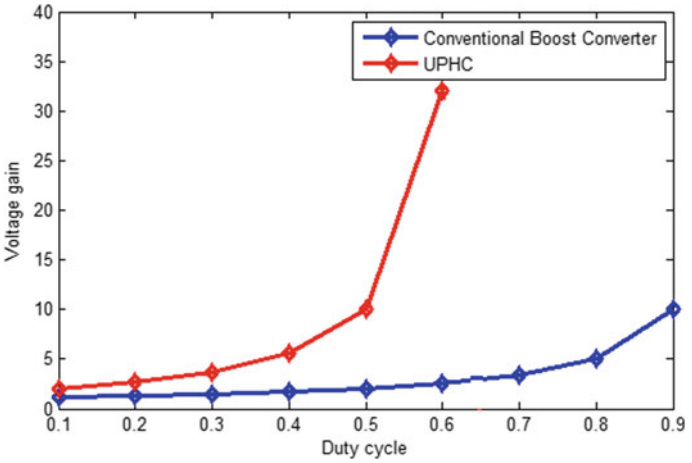

Fig. 6 Voltage gain comparison

It is obvious that the proposed UPHC converter provides high voltage gain compared to conventional converter.

4 Feed-Forward Neural Network Controller

To extract the maximum power output from UPHC converter and reduce peak overshoot at the time of starting, a feed forward neural network as shown in Fig. 7 based

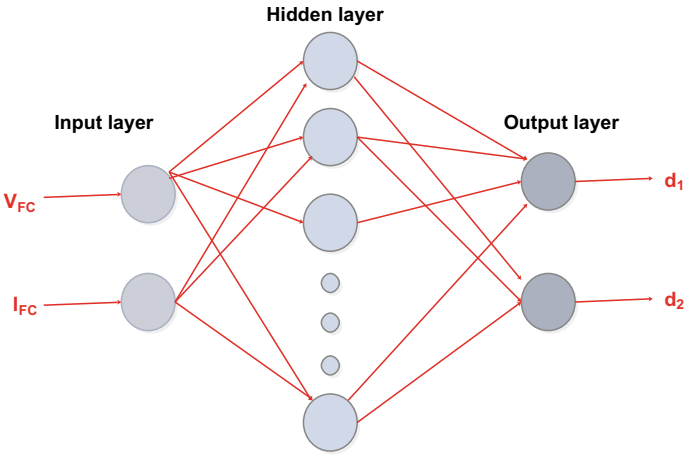

Fig. 7 Feed-forward neural network

MPPT controller is implemented in which voltage from fuel cell (V_{FC}) and current from the fuel cell (I_{FC}) are fed as input in the input layer. In the input layer linear activation function is used to map the input which is given to next layer nodes. The weight in the hidden layer is found by applying tan sigmoid membership function. At the output layer linear activation function is used to calculate duty cycle d_1 and d_2. The trained network is tested using back propagation algorithm by updating weight after each epochs.

5 Simulation Results and Discussion

The simulation work has been carried out using MATLAB/Simulink platform in which fuel cell parameters are pre-specified values. The characteristics of 1.26 kW PEMFC is analyzed. The inference made from analysis is the fuel cell is operated at 24.23 V, 52 A to give maximum power output of 1259.6 W.

The proposed Ultra-High Step up Converter fed from 1.26 kW circuit is constructed by using the hardware components. The operating frequency of the converter is kept at 50 kHz while the duty cycle is maintained at $d_1 = 0.5$ and $d_2 = 0.35$. The average output voltage obtained at steady state is shown in Fig. 8. The fuel cell output voltage is influenced by the operating temperature and variation of temperature is considered as 328 K for (0–0.6 s), 361 K for (0.6–1.2 s) and 338 K for (1.2–2.4 s) which corresponds to variation of output voltage, current and power as shown in Fig. 9. While the operating temperature is varied, the output power of UPHC is also varied in which peak overshoot is present which is shown in Fig. 10. The peak overshoot of DC link power is reduced by 21.5% with respect to steady state power 565 W corresponding maximum power reached during first time is 687 W shown in Fig. 11. From the Fig. 11, it is inferred that Feed Forward Neural Network outperforms the conventional Fuzzy based controller.

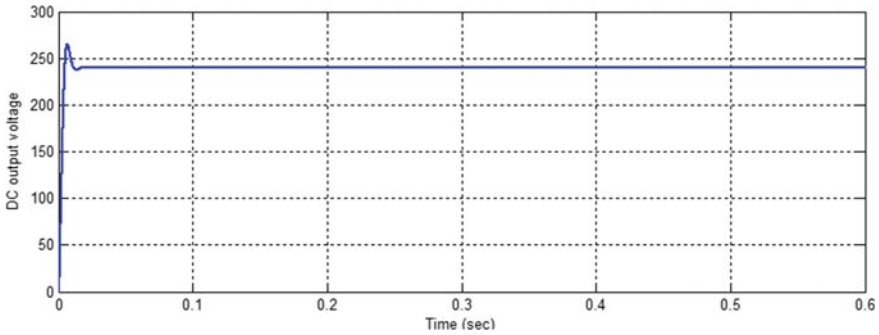

Fig. 8 Output voltage of UPHC converter

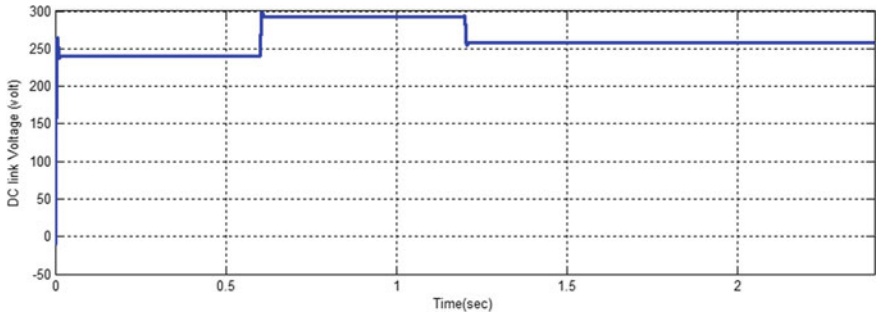

Fig. 9 DC link voltage

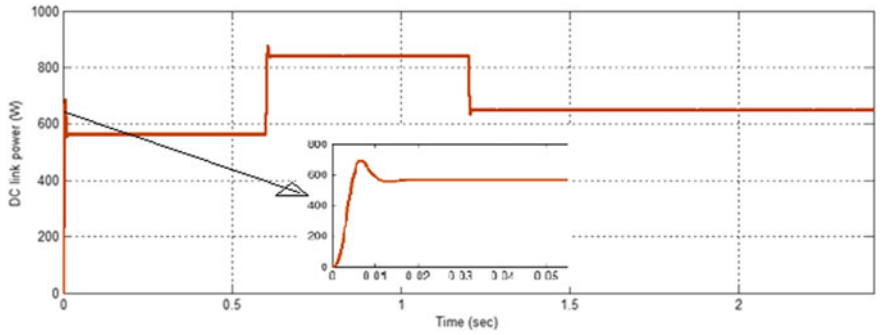

Fig. 10 DC link power

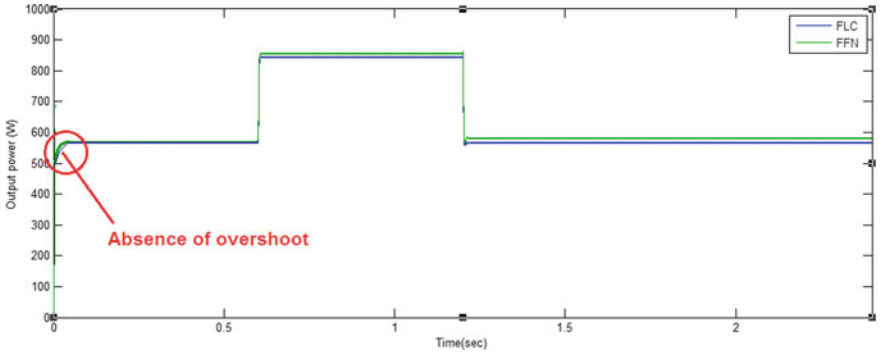

Fig. 11 DC link power output comparison

6 Conclusion

In the proposed work, Feed-forward Neural Network based MPPT controller was implemented to extract maximum power from 1.26 kW PEMFC. The Ultra High Step Up converter (UHSC) was designed and steady state analysis of the step up converter was done. The switching pulses of UPHC were generated by the FFNN based MPPT controller thereby optimum power extraction was ensured. A simulation work was carried out using MATLAB/Simulink environment also implemented hardware prototype and the following highlights were observed.

- A 1 kW UPHC converter was designed and analyzed the steady state operation. The proposed converter provides better performance than conventional converter.
- Feed forward Neural Network based MPPT controller performs well than conventional Fuzzy Logic controller.
- Peak overshoot in DC link power was reduced by 21.5% with reference to steady state power; average time to reach optimum power is reduced by 20.5%.

References

1. Sammes N (2006) Fuel cell technology, reaching towards commercialization. Springer, United Kingdom
2. Larminie J, Dicks A (2003) Fuel systems explained. J. Wiley, pp 207–225
3. Spiegel C (2011) PEM fuel cell modeling and simulation using MATLAB. Elsevier
4. İnci M, Ömer T (2019) Review of fuel cells to grid interface: configurations, technical challenges and trends. J Cleaner Prod 213:1353–1370
5. Reddy, Jyotheeswara K, Sudhakar N (2018) Energy sources and multi-input DC-DC converters used in hybrid electric vehicle applications—a review. Int J Hydrogen Energ 43:17387–17408
6. Harrag A, Bahri H (2017) Novel neural network IC-based variable step size fuel cell MPPT controller: performance, efficiency and lifetime improvement. Int J Hydrogen Energ 42:3549–3563
7. Wang MH, Huang ML, Jiang WJ, Liou KJ (2016) Maximum power point tracking control method for proton exchange membrane fuel cell. IET Renew Power Gener 10:908–915
8. Somaiah B, Agarwal V (2016) Distributed maximum power extraction from fuel cell stack arrays using dedicated power converters in series and parallel configuration. IEEE Trans Energ Convers 31:1442–1451
9. Reddy KJ, Sudhakar N (2018) High voltage gain interleaved boost converter with neural network based MPPT controller for fuel cell based electric vehicle applications. IEEE Access 6:3899–3908
10. Harrag A, Messalti S (2017) Variable step size IC MPPT controller for PEMFC power system improving static and dynamic performances. Fuel Cells 17:816–824
11. Ahmadi S, Abdi Sh, Kakavand M (2017) Maximum power point tracking of a proton exchange membrane fuel cell system using PSO-PID controller. Int J Hydrogen Energ 42:20430–20443
12. Harrag A, Messalti S (2018) How fuzzy logic can improve PEM fuel cell MPPT performances? Int J Hydrogen Energ 43:537–550

Predictive Maintenance of Industrial Equipment's Using IOT

S. Nithya, K. Vijayalakshmi, and M. Parimala Devi

Abstract Internet of Things (IOT) is swiftly increasing technology nowadays global in internet world. IOT is mixture of communication system and embedded device that is used to attach hardware devices to the community or net. IOT is used for transmission and reception of information. These structures are used to check the processes in industries and its applications were through implementing industry standard protocols using IOT. In this machine small scale commercial packages like liquid level control, power monitoring and so on can be analyzed wirelessly via Wi-Fi gadgets, mobiles and laptops. The principle purpose is to epitomize the importance of IOT as a way to survey small scale commercial packages.

Keywords IoT · PLC · Wi-Fi · GSM · Sensors

1 Introduction

Nowadays, business tracking has important function location to monitor and manipulate the industrial applications or appliances and apparatuses. Business tracking is exercised for recognising the enterprising of heavy industrial appliances or apparatuses. Commercial tracking is used to perform quick processing, decrease energy utilization and usage, to enhance quality, lessen highly-priced systems and international control of enterprise [1, 2]. Many strategies have been conducted and performed which are to be had to reveal and manipulate industrial approaches. Nowadays, "net of things" is the most favourable technique for commercial process tracking [3].

S. Nithya (✉) · K. Vijayalakshmi
Department of Electrical and Electronics Engineering, SRM Institute of Science and Technology, Ramapuram, Chennai, India
e-mail: nithyas@srmist.edu.in

K. Vijayalakshmi
e-mail: vijayalk1@srmist.edu.in

M. Parimala Devi
Department of Electronics and Communication Engineering, Velalar College of Engineering and Technology, Erode, India

C. Subramani et al. (eds.), *Proceedings of International Conference on Power Electronics and Renewable Energy Systems*, Lecture Notes in Electrical Engineering 795,
https://doi.org/10.1007/978-981-16-4943-1_24

IOT is aggregate of ingrained machine and verbal exchange gadget wherein business equipments are related to internet with the assist of wireless sensor network [4] and gadgets or commercial utility can monitor and manipulate via mobiles and laptops.

Forms of items, sensors, electrical apparatuses and items are attached to net very easily with IOT. IOT is even employed for data transfer and accumulation of records from electrical appliances or gadgets and connect it to the IOT dashboard via certain communication protocols [5]. May be connected the use of Bluetooth, Ethernet, Wi-Fi and so forth to the internet. An arrangement to raise cautions in the event of discovery of lethal gases, fuel spillage over the safe breaking point can assist with maintaining a strategic distance from mishaps [6, 7]. A model dependent on ARDUINO/IOT module has been created dependent on the above idea for location and ongoing checking of the modern floor. IOT gadgets for the most part have some cloud administration to oversee the gadget from the web or versatile applications [8]. The purpose of a gadget being arranged and it can get to easily from anyplace through web association.

On applied to reveal numerous commonplace parameters utilized in industries which include strength, liquid degree and dc motor pace manipulate [9]. On this paper, factory and manufacturing technique tracking is finished by IOT in unique implementation. On this paper eWON Flexy IoT module as shown in Fig. 1, CPU 315 DP PLC is used for accumulating facts from equipments and transfer it right into

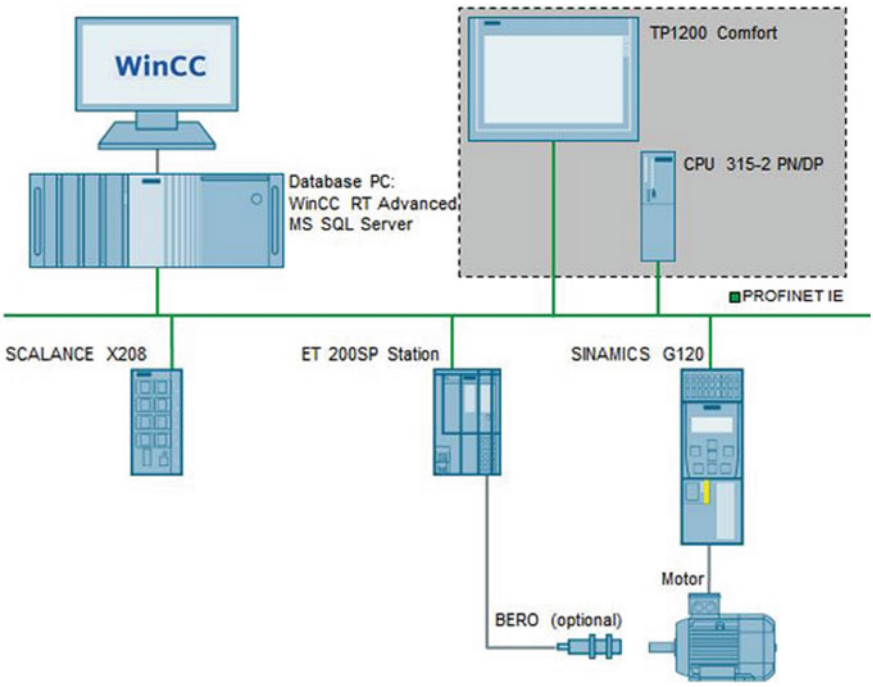

Fig. 1 Concept layout

the cloud. eWON Flexy is the IoT module [10]. Business process tracking device includes 4 application percent based coloration mixing, liquid stage manage and tracking, dc motor velocity manipulate and electricity monitoring.

2 Methodology

The proposed solution is the vision of any organization have to be to maximize productiveness with guaranteed employee safety and environmental obligation. A gadget for actual time monitoring is proposed through deployment of sensors at exclusive points of the company premises as in Fig. 2. The first rate sensors come across the level of emissions, misalignment, temperature, frequency, current, voltage and lots of others factors that might also send notification to the ground manager through Google Cloud. An arrangement to raise cautions in the event of discovery of issues and damages over the safe breaking point can assist with maintaining a strategic distance from mishaps. A model dependent on ARDUINO/IOT module has been created dependent on the above idea for location and ongoing checking of the modern floor. IOT gadgets for the most part have some cloud administration to oversee the gadget from the web or versatile applications. The purpose of a gadget being arranged and it can get to easily from anyplace through web association. on the web regulating of mechanical procedure have gotten most extensive angle for modern development and benefit all things considered used to diminishes production, and costs just like maintenance issue. Right now, forms like meter observing, load, speed

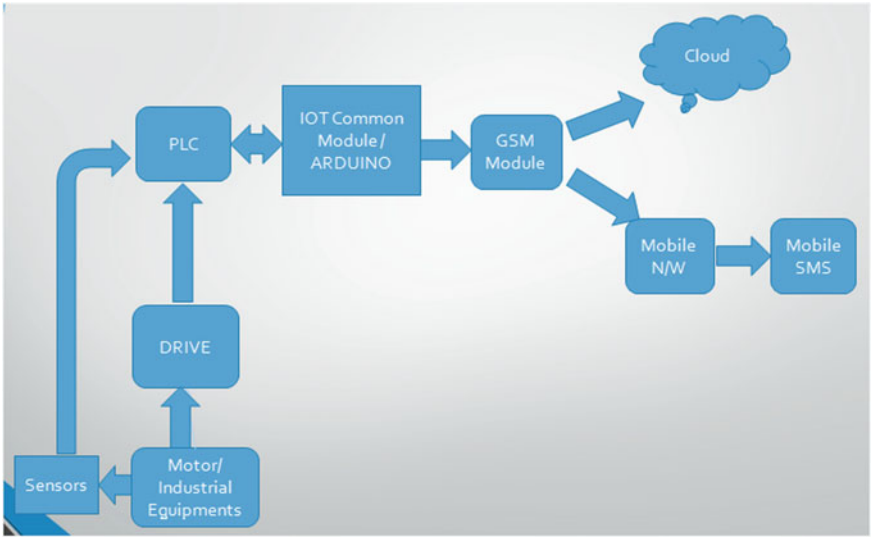

Fig. 2 Concept block diagram

control of motors, PLC processes and analog controls are observed through android mobiles, PCs etc. using IOT. We use the concept of Machine Management System (MMS) to control and supervise the facilities remotely and with better efficiency.

IoT gadgets, motors and equipment in industries are prone to wear and tear over a period of usage. Industrial motors are used for heavy machinery equipments and use a lot of load and stress to do the required job properly. Hence in this paper we will talk about the prevention of wear and damage and reduce the downtime and also increase the up time. The motors in industries are equipped with a smart sensor. The sensors we will be:

- Vibration sensor
- Temperature sensor.

The sensors are attached on to the motor or any industrial equipment that we need to monitor. The vibration sensor that is used is a accelerometer sensor. When the motor undergoes a slight misalignment or a spike in temperature that causes it to work vigorously, the sensors senses the change in frequency of its rotation in its radial or axial position in the form of analog waves. The same is applied to the temperature sensors. The frequency read is sent into the A/D converter that converts the input signals from analog to digital signals. The Variable frequency drive (VFD) is kept attached to the motor for controlling the frequency of the motor speed as per the needs of the industrial needs. The VFD can also show the current and voltage at which the motor is running.

After the conversion of the signals into digital format, the signals are sent from the sensors and VFD to the PLC for processing. The signals received are analysed in the PLC. The signals are compared with the ladder program that is build with the help of SIMATIC manager. PLC framework has the fundamental practical section of processor, memory, power gracefully, input/yield interface, interchanges, and industrial equipment devices. The PLC framework works only if the user inputs the required instructions and algorithms of work into the program that helps it perform the needed process executions and atomization. These instructions are input into the PLC by the user or officials during handling. The info/yield channels give disengagement and sign molding capacities so sensors and actuators can frequently be straightforwardly associated with them without the requirement for other hardware. Yields are indicated as being of hand-off sort, transistor type, or triac type. The interchanges interface is utilized to get and transmit information on correspondences systems from or to other remote PLCs.

2.1 Ladder Logic

LCs frequently use “Ladder Logic Programming” a short-sighted programming language that is appropriate for modern applications. Ladder logic is similar to stacking up relay circuits. The program involves the use of relay circuits to form connection to various sensors in the system linking to the motors or any industrial

equipment. Presently in our case the ladder logic uses bit logic operation. The LD is the standardized PLC programming operation. The program uses different graphical elements in contrast to other coding softwares. Ladder logic symbols look like electric symbols that gives better user interface that will help the engineers to assign different symbols. The lines in the PLC ladder logic programme are called rungs. These rungs can be as many in relation to the number of equipments that is connected to the rungs. During execution the ladder logic rungs are read and executed one rung at a time, the PLC executes one symbol at a time. There are many symbols like normally open, normally closed, output coil etc. as in Fig. 3. The normally open contact specifies the switched off state, normally closed consists of the closed contact through which the current flows and the output coil consists of the motor or any equipment. When the programme is running, it reads the states of these symbols then convert it into binary values of 0's and 1's also considered as low and high respectively.

The program build is used for analysing the values that the PLC receives. The program has functions known as counter and comparators. The counter will count the input signal value and the then sends it to the comparator. The comparator is another function that compares the values of the input digital signals with the safe running values inputed by the industrial user with the help of SIMATIC manager. If the values analysed by the PLC from the sensors are found to be abnormally high or low compared to the values set by the user then the PLC send the processed data to the IOT. The signals are sent to the IOT which triggers a prompt to send a message to the GSM module. A software called eBuddy is used for generating the message that is needed to be sent to the maintenance officials or any other higher authority manager.

2.2 Vibration Monitoring

Speed and quickening are the two generally normal parameters that are checked with vibration sensors to distinguish issues on turning hardware. Speed is the speed estimated a solitary way. It is estimated in 'mm/sec'. Speeding up is the pace of progress of speed.

Vibration sensors shown in Fig. 4 are devices or apparatus that measures a wide range of readings and values that include speed, frequency, velocity, strain, etc. These sensors utilize the piezoelectric impact by changing over them to an electrical charge these sensors can also help in finding out the cracks, wears and tears that the machines undergo if it has any faulty motors. These sensors can be used in many industries and facilities. There are two types of vibrations axial vibration and radial vibration. Notwithstanding the sensor qualities, you should think about the necessary equipment and programming to appropriately condition, procure, and imagine accelerometer estimations. For instance, you have to perform signal handling on crude vibration signs to show the information in a progressively significant arrangement, for example, the recurrence range. To all the more likely acquaint yourself with

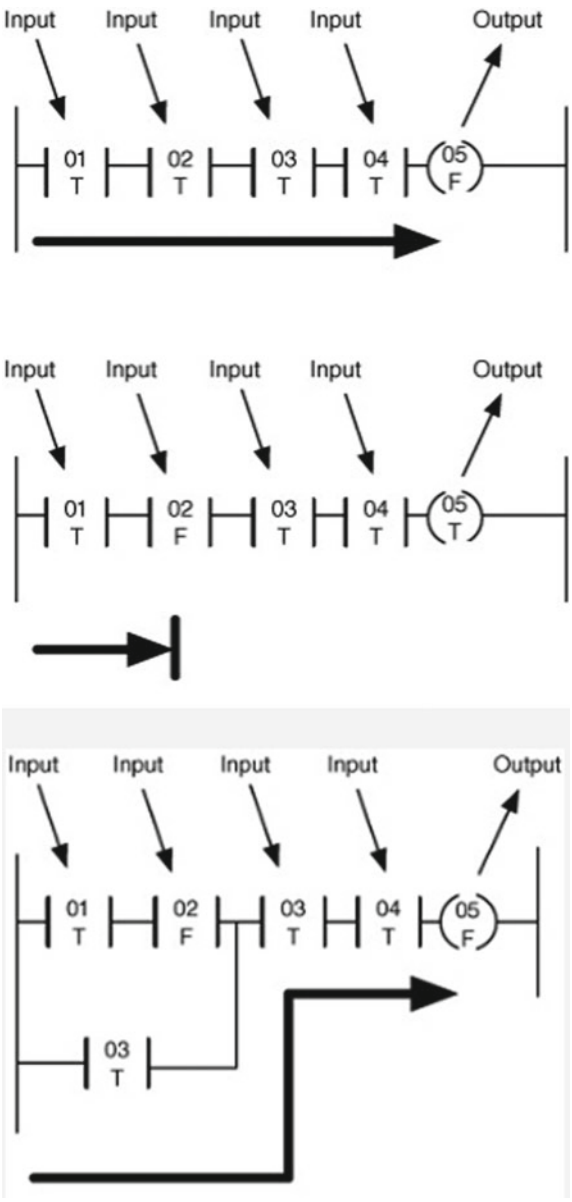

Fig. 3 Ladder Logic

the estimation equipment and programming handling essential for accelerometer estimations, download the Engineer's guide to accurate sensor measurements.

With speeding up we can screen a lot higher frequencies. We use speeding up estimations to identify issues that apply a power, for example, little stuns and effects

Fig. 4 Vibration sensors

that happen at the beginning of bearing harm, gearbox shortcomings, and siphon cavitation and so on.

2.2.1 Different Levels of Monitoring

i. **Machinery Protection sensor**
Basic apparatus assurance sensors offer checking of the general vibration levels, estimated in speed (mm/sec). These are regularly applied to the ISO 10816 norm. This degree of checking won't analyze a particular machine issue, yet will distinguish an adjustment in the general vibration level brought about by deficiencies, for example, unbalanced, misalignment, looseness, belt drives.

ii. **Intelligent Vibration Sensor**
Smart vibration sensors encourage checking of both the speed levels (mm/sec) also, increasing speed levels (g). This degree of observing won't ordinarily analyze a explicit machine shortcoming. In any case, by observing both speed and increasing speed it is conceivable to recognize vibration increments brought about by a more extensive scope of issues, for example, Unbalance, Misalignment, looseness, belt drives, Bearing defects, Rubbing, Gears, Fluid noise, Impact detection.

iii. **Fault analysis**

Flaw examination frameworks can be customized to distinguish explicit hardware issues by checking the individual deficiency frequencies that identify with these different vibration issues. When distinguished, the client would then be able to be advised which flaw is beginning to create on the machine. This degree of point by point examination takes into consideration progressively proficient support systems to happen. These frameworks can be modified to analyze explicit machine blames, for example, Unbalance Misalignment, Looseness, Belt drives, bearing defects, Rubbing, Gears, Fluid noise, Impact detection (Fig. 5).

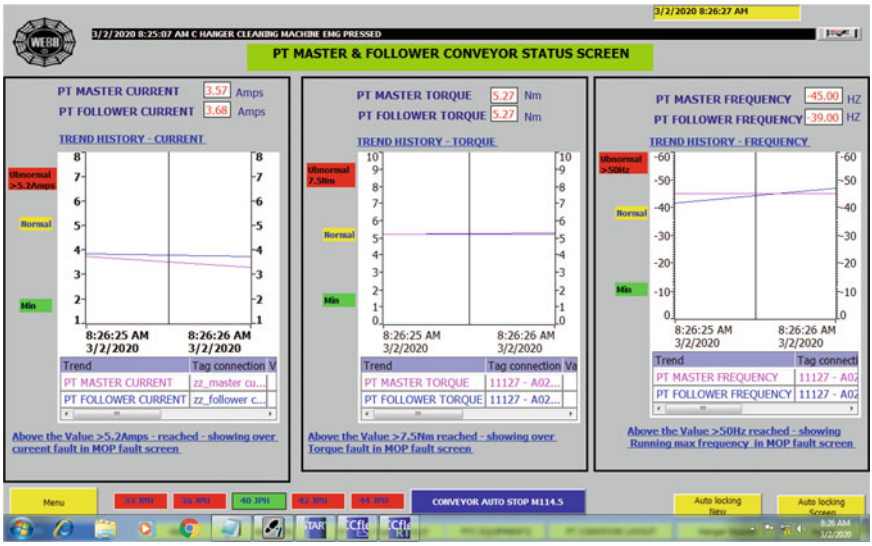

Fig. 5 Screenshot of conveyor status screen

2.3 Wireless Monitoring

An IOT module is a device that is installed in various devices and appliances in today's technological world. It helps in interconnecting and linking different machinery in industries or factories with each other that when combined forms a cyber physical system. The IOT helps in sending receiving and transferring information with all of these devices or machinery. In general it helps in the autonomous communication between each of these devices without human intervention. The IOTs always depend on the internet for the transfer of information consistently on network. This is on the grounds that IOT applications need to send information naturally, progressively without any sort of user interface with the devices in order to transfer data. These devices have good reliability, cost effectiveness, and rigidness. Not at all like customer gadgets that are ordinarily conveyed by the end-client and utilized in controlled conditions, IOT gadgets are regularly sent in extraordinary situations and remote like transportation holders or under seawater in harbor the executives arrangements. IOT situations can be immensely requesting with outrageous temperatures, vibration, and mugginess.

A GSM module shown in Fig. 6 is a chip or circuit that can provide a connection between the module and the remote operator or overseer who has established the connections. The connections can be between any portable devices like tablets, phones, laptops, chrome books, etc. for interactions between the module and GSM framework. The modem is a basic part here. A GSM includes a GSM module alongside some different parts like correspondence interface power gracefully and a few markers. The Ethernet cables and wireless connection based on wifi and internet

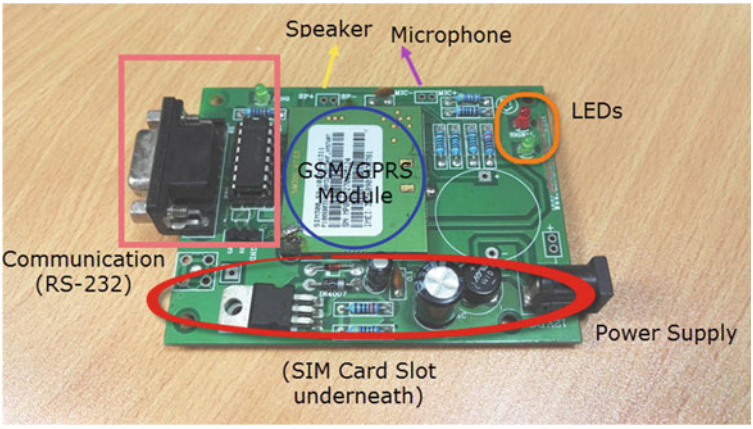

Fig. 6 GSM/GPRS module

we can link these devices together without much issues as it has a wide range of compatibility. GSM Modules permit remote correspondence with different gadgets and instruments. Since this technology allows us to remotely and securely connect to various devices and monitor the company activities it is easier to perform the security monitoring, hoe automation, automotive GPS tracker, online and e commerce transactions. GSM module associates with the network utilizing a SIM cards from any companies like airtel Vodafone, etc. The basic radio frequencies where a run of the mill GSM Module works are 900 and 1800 MHz.

Previously mentioned errands, cultivated with the assistance of AT Commands. AT Commands are pieces of Command Set, which are characterized initially for a modem. GSM Network likewise actualizes a comparable AT like orders for its GSM Modules. The processor or controller to which the GSM/GPRS Module is associated with, is answerable for sending the AT Commands to the module. Accordingly, the GSM Module performs order explicit errands like noting a call, send a SMS Message, etc. Even through the AT Commands may appear to be nonexclusive, it is fitting to allude with the information gave by the maker of the GSM Module for right and complete rundown of AT Commands.

2.4 Wireless Communication

Nowadays, The eBuddy software must be installed in every official's phones or tables to receive the messages. The message is sent to the GSM module that sends it to the cloud or user. The user receives the messages through the eBuddy app. The messages sent depends on the gravity of the situation i.e. if the problem faced by the motor or equipment is low then the messages are only sent to the lower maintenance officials and if the problem persists for a longer time or if it's more grave and precarious

then the messages are sent even to the higher officials who can get the details of the matter and tend to it as soon as possible which prevents any further troubles and circumstances. The user gets the message in the form of Email or SMS. The received data is stored in the cloud in the form of spreadsheet. The database of every ongoing or previous operations of the equipments are stored in the cloud and the officials or managers can get a monthly or yearly data report on the equipments and its values. A vitality observing dependent on IoT is utilized to improve the vitality the executives framework.

3 Results and Discussion

The proposed framework can screen and measure the situations and state progressively inside the plant. By determination of exact and precise sensors, a test arrangement to measure the gases was created. The information from the sensors were gathered progressively and transferred in Google spread sheet shown in Fig. 7.

The communication between PLC and VFD is done with the help of a STARTER software through an IP gateway. The gateway is a device for controlling and translating CIP protocol to SEIMENS profibus protocols. Then we configure the VFD to the SEIMENS starter software in the form of a profibus slave. We have to enter the motor or equipment details like the power rating, current ratings and voltage ratings and the type of motor (Figs. 8 and 9).

This product particularly intended for administrator control and observing in SIMATIC. Procedure perception framework is a standard administrator Interface with all the significant administrator control and observing capacities which can be utilized in any part any innovation. SIMATIC software is present day devices for

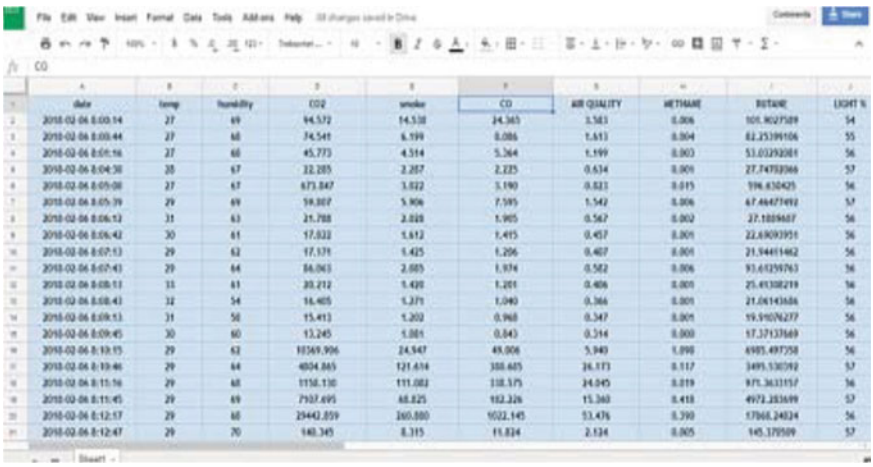

Fig. 7 Google spread sample

Fig. 8 Light and harmful gases

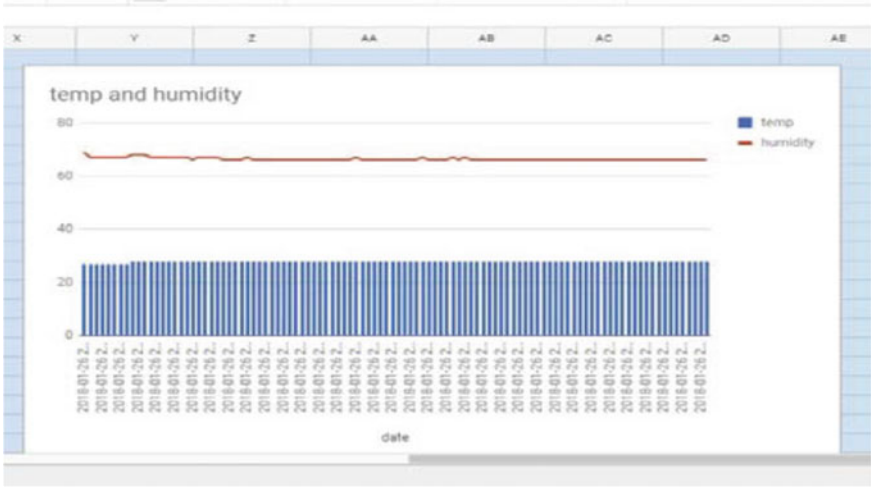

Fig. 9 Temp and humidity graph

arranging SIMATIC administrator board's conservative gadgets. Programming that secures data on the area and reason for mistakes in plants and apparatus and along these lines offers quick and pointed procedure diagnostics.

The proposed structure can assist with forestalling industry related mishaps because of gas and fuel spillage by legitimate recognizable proof and cautioning the individuals around. The proposed configuration can likewise be made appropriate for recognizing the contamination level from vehicles and to keep a mind the smoke outlet from processing plants. The plan can be altered to identify the level of gases inside pit openings with the goal that valuable lives can be spared. Utilization of IOT in relationship with ARDUINO/IOT module makes the framework modest and moderate. The light weight framework can be installed in Jacket, Helmet and Wrist observes which can be worn by labourers to investigate the highlights of Wearable

Technology [11]. The framework likewise empowers basic man to screen the nature of air in their region by means of cell phone application.

4 Conclusion and Future Work

In this paper an Intelligent Industry Monitoring framework in light of IOT is proposed which can successfully screen the Mechanical floor. A model dependent on ARDUINO/IOT module was created which could detect the centralization of current, vibrations and temperature. The continuous information acquired from the various sensors has been transferred to Google cloud. Notwithstanding this other parameters like temperature, dampness and light force were estimated. For simplicity of investigation the above information got were plotted. Arrangements were likewise made to alarm the labourers if there should be an occurrence of any crisis. The framework gives solid, precise investigation to forestall any instance of mishaps. This framework utilizes ARDUINO/IOT module giving modest arrangements for security. Slight adjustment of the model empowers the client to adjust it to any condition. Prescient support is an up and coming modern need, for which the proposed model can be ad libbed. If there should arise an occurrence of misalignment and damage we need to access the issues from point to point which must be broke down further. Also, the gases diffusing out during spillage may likewise join among themselves delivering different results which must be managed in detail. These cases can open an eye for the sprouting analysts.

References

1. Leman AM, Hidayah N (2013) Occupational safety and health: workers and industrial safety monitoring for sustainable work environment development. Health and Safety, AET
2. Wu-Zhao, Lei-Hong L, Yue-shan H, Xiao-ming W (2013) A community health service architecture based on the Internet of Things on health-care. In: World congress on medical physics and biomedical engineering, vol 39, pp 1317–1320
3. Nayak R, Panigrahy MR, Rai VK, Rao TA (2017) IoT based air pollution monitoring system. Imperial Jo Interdisc Res 3(4)
4. Deshmukh MR, Renuka SJC, Chavan A, Atarde G (2018) IoT based air & sound pollution monitoring system. IJRIIE 4(3)
5. Xiaojun C, Xianpeng L, Peng X (2015) IoT based air pollution monitoring and forecasting system. In: International conference on computer and computational sciences (ICCCS), pp 257–260
6. Ramagiri R, Reddy SCM, Reddy S (2015) Development of IoT based vehicular pollution monitoring system. In: International conference on green computing and internet of things, (ICGCIoT)
7. Spachos P, Song L, Hatzinakos D (2014) Gas leak detection and localization system. In: 2014 IEEE 11th consumer communications and networking conference (CCNC), Las Vegas, NV, pp 1130–1131. https://doi.org/10.1109/CCNC.2014.6994392

8. Han H, Kang H, Son J (2017) Intelligent operation monitoring IoT tag for factory legacy device. In: 2017 international conference on information and communication technology convergence (ICTC)
9. Siddula SS, Babu P, Jain PC (2018) Water level monitoring and management of dams using IoT. In: 2018 3rd international conference on internet of things: smart innovation and usages (IoT-SIU)
10. Lee J-L, Tyan Y-Y, Wen M-H, Wu Y-W (2017) Development of an IoT-based bridge safety monitoring system. In: 2017 international conference on applied system innovation (ICASI)

A Simplified Beginner's Guidelines for Design and Fabrication of Prototype Electrical Vehicle

P. Ramesh Babu, P. Vigneshwar, R. Udaya Simha, S. Tanweer Ahamed, S. Vengatesh, and V. Vijay

Abstract The aim of this paper is to build a prototype electric vehicle out of structural materials. It is influential in the development of a modern, safe, and environmentally sustainable mode of public mobility. The objective of its design is to create a lightweight, compact three-wheeled electric vehicle frame. The design phase entails the creation of a 3D model, a practical prototype, and frame refinement using CAD software and the material parameters. The electrical and mechanical study is performed, the results recorded 125 km per charge, and the weight of the vehicle is 180 kg. The top speed is 40kmph along with >80% efficiency of the BLDC hub motor.

Keywords Electric vehicle · Lithium-ion battery · BLDC hub motor · Suspension · Steering

1 Introduction

We breathe contaminants in excess of the air we require; as a community, we are planting trees and adhering to rules to mitigate this problem; however, pollution emitted by automobiles has a detrimental effects which could lead to health problems including certain tiredness, and even respiratory issues. Adopting sustainability implies not only the plantation of more trees, as such as the use of clean energy for a healthier atmosphere and emissions reductions. It'll last up to 39 years depending on the (R/P) ratio for fossil fuels (approx.). Green technology should be used now just to ensure that natural resources are protected for subsequent generations. Electric cars were favored because they were comfortable, safe to drive, also did not release any pollutants. Thomas Alva Edison was researching on enhancing energy effectiveness

P. Ramesh Babu (✉) · P. Vigneshwar · R. Udaya Simha · S. Tanweer Ahamed · S. Vengatesh · V. Vijay
Saranathan College of Engineering, Trichy, Tamil Nadu, India

P. Vigneshwar
e-mail: vigneshwar-mech@saranathan.ac.in

C. Subramani et al. (eds.), *Proceedings of International Conference on Power Electronics and Renewable Energy Systems*, Lecture Notes in Electrical Engineering 795,
https://doi.org/10.1007/978-981-16-4943-1_25

of a battery in 1901. Meanwhile, Ferdinand Porsche builds the world's first hybrid-electric vehicle, powered by a battery and a gasoline engine. There were downtimes for electric vehicles, as combustion engines were used often but they were affordable and plentiful, and gas-powered vehicles became successful that they pushed up the price of fossil fuels. Then NASA came up with the concept of using Lunar Rovers to operate solely on electricity in order to promote electric vehicles, which narrowed the odds of electric vehicles. The CitiCar by Sebring-Vangaurd was a notable electric vehicle with a range of 50–60 miles, and it wasn't enough. Electric vehicles with the same range and acceleration as combustion engines are being produced again after several years of testing.

2 Design and Fabrication

Electric vehicles are classified into three categories: two-wheelers, three-wheelers, and four-wheelers. The three-wheelers are preferred because they are lightweight and have a robust build. The number of front and rear wheels on a three-wheeler defines the vehicle's stability. Figures 1 and 2 shows the designs of electric three wheeled vehicle.

2.1 Chassis

Chassis is the metal frame of the vehicle without the body. The frame is an integral part of vehicle design and fabrication because it determines factors such as vehicle safety, stability, balance, and ergonomics [1].

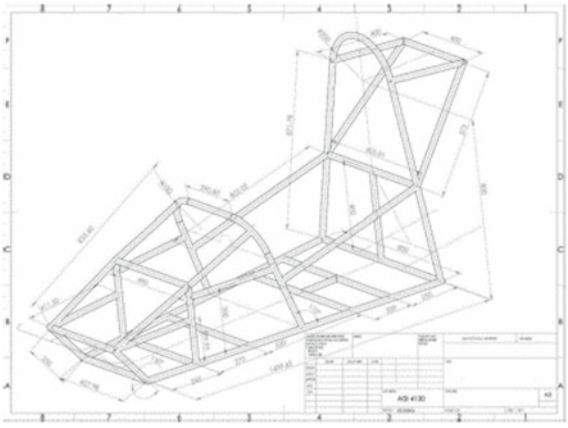

Fig. 1 The frame drawing of roll cage

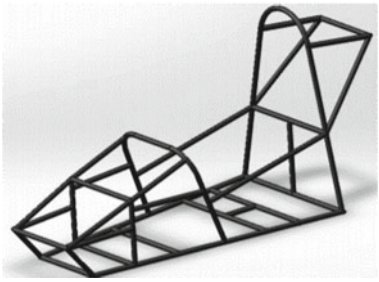

Fig. 2 The CAD model of the roll cage

2.2 Frame Definition

The design of the vehicle implies a light weight and safe. The chassis must withstand the weight applied and must not fail at any instant. There are two wheels on the front and one wheel on the rear which decides the overall stability and balanced weight.

2.3 Frame Dimensions

The overall length of the chassis is 2047.18 mm, overall width is 800 mm, and the overall height of the chassis is 1000 mm. The wheelbase length is 1600 mm. Since there are two wheels on the front side, the wheel track length is 1400 mm. The ground clearance of a vehicle is 150 mm. The total weight of the roll cage is 23.729 kg with firewall clearance of 55 mm (Fig. 3).

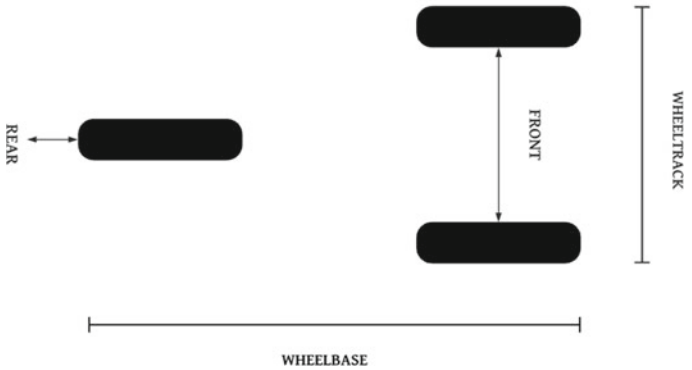

Fig. 3 Wheelbase and wheel track of the prototype model

3 Aisi 4130

The vehicle's roll cage is made up of metal bars in the form of pipes. Cold drawn steels costs around Rs. 80–Rs. 200 per kg, which is why it is preferred. AISI 4130 (American Iron and Steel Institute) alloy steel is used which has extraordinary welding steel that can be welded in all commercial methods and good mechanical properties. Tungsten Inert Gas (TIG) welding is used for this type of alloy steel. The properties is mentioned in the below table,

Properties	
Chemical composition	Chromium, Cr 0.80–1.10 Manganese, Mn 0.40–0.60 Carbon, C 0.280–0.330 Silicon, Si 0.15–0.30 Molybdenum, Mo 0.15–0.25
Yield strength	460 MPa
Tensile strength	560 MPa
Young's modulus	210 GPa
Poisson ratio	0.3
Density	7.85 g/cm^3

4 Stress Analysis

The impact of force is analyzed using ANSYS 17.2 software and the vehicle's parameters, which necessitates the calculation and display of stress effects on the vehicle using the maximum principle stress, deformation. The final results will be used to evaluate what changes can be made to the frame to increase the effect on the driver's safety (Figs. 4, 5, 6, 7, 8 and 9).

5 Mechanical Systems

We encounter bumps and speed breakers when driving on the highways, so steering and suspension help. The tires appear to slip while driving around a curve. To prevent this, we used the Ackerman mechanism, which reduces it. A few parameters in steering systems must be determined in order for them to operate correctly. The Hydraulic suspension system supports the vehicle and reduces the bumps that shocks absorb when driving on a rough road (Figs. 10 and 11).

Let us see the calculation and formulas for the steering mechanism,

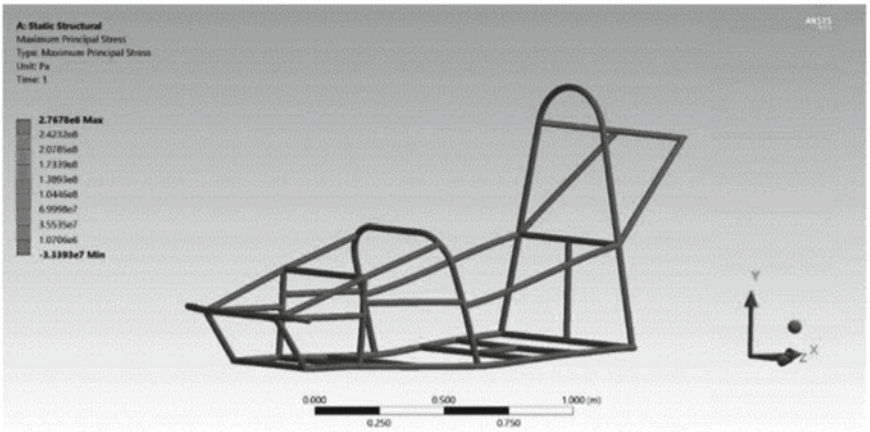

Fig. 4 Front impact on stress

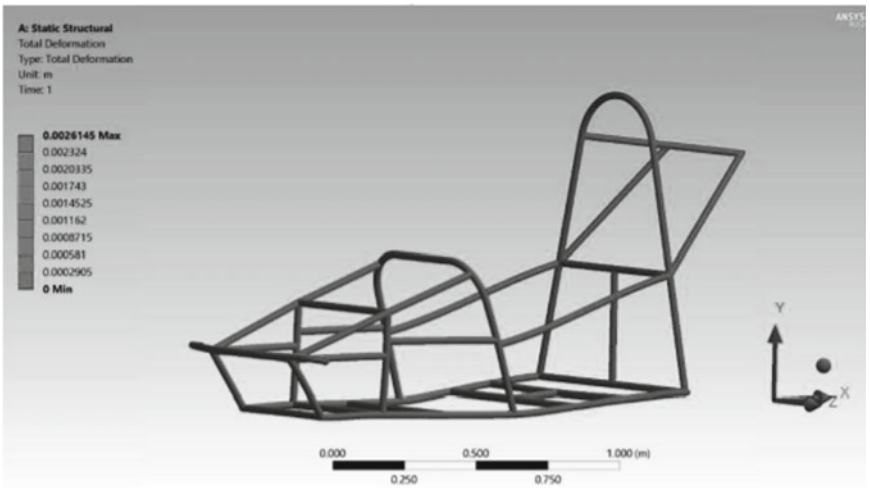

Fig. 5 Front deformation

$$\text{Ackerman} = \tan^{-1}\left(\frac{\text{wheelbase}}{\frac{\text{wheelbase}}{\tan\delta_{\text{outside}}} - \text{track}_{\text{front}}}\right) \tag{1}$$

$$\text{Ackerman}_{\text{percentage}} = \left(\frac{\delta_{\text{inside}}}{\text{Ackerman}}\right) \times 100\% \tag{2}$$

Using the formula,

$$\tan\theta_o = \frac{a}{d+a} \tag{3}$$

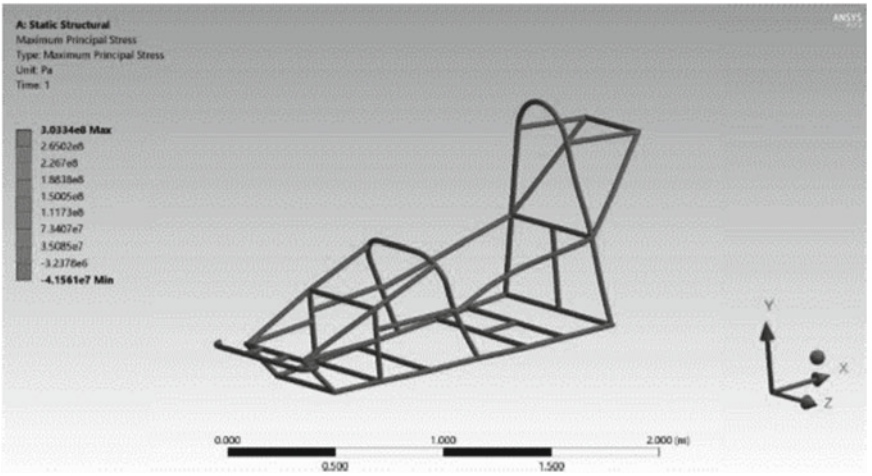

Fig. 6 Side impact on stress

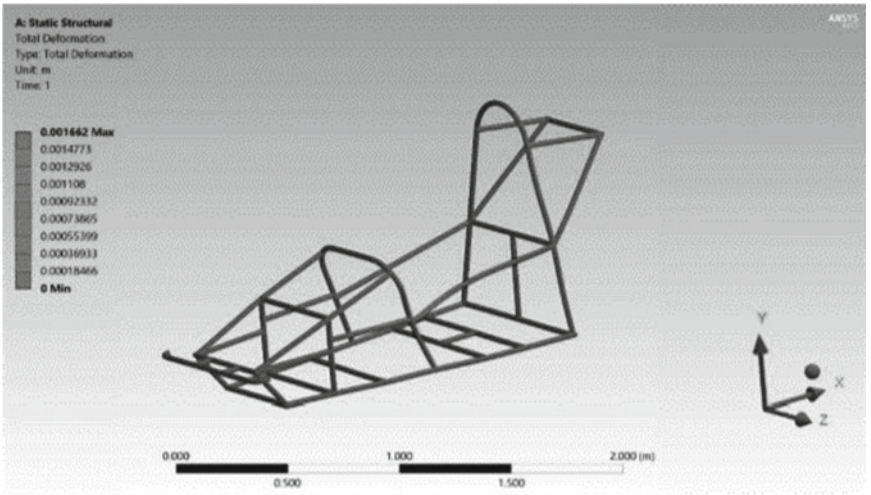

Fig. 7 Side deformation

$$\tan\theta_i = \frac{a}{d+a} \tag{4}$$

where θ_o, θ_i are outside and inside angles.

For acceleration of the prototype,

$$\text{Air resistance}(R_a) = (K_a \times A \times V^2)\, N \tag{5}$$

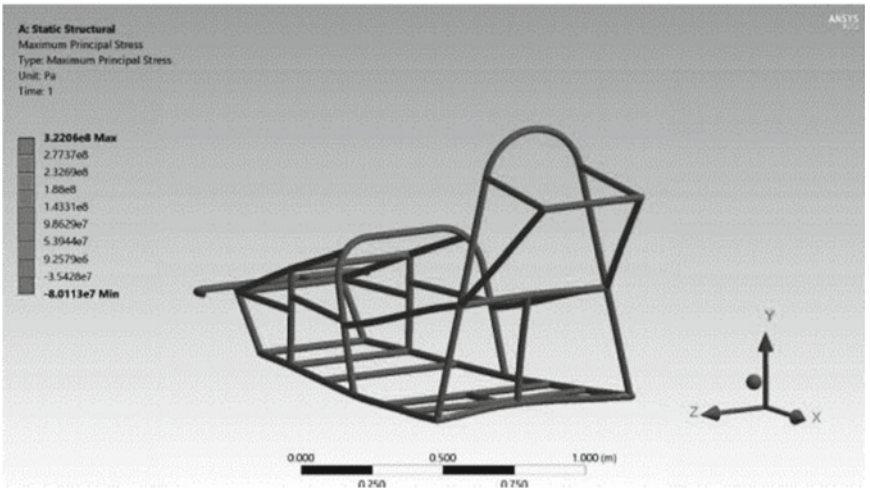

Fig. 8 Rear impact on stress

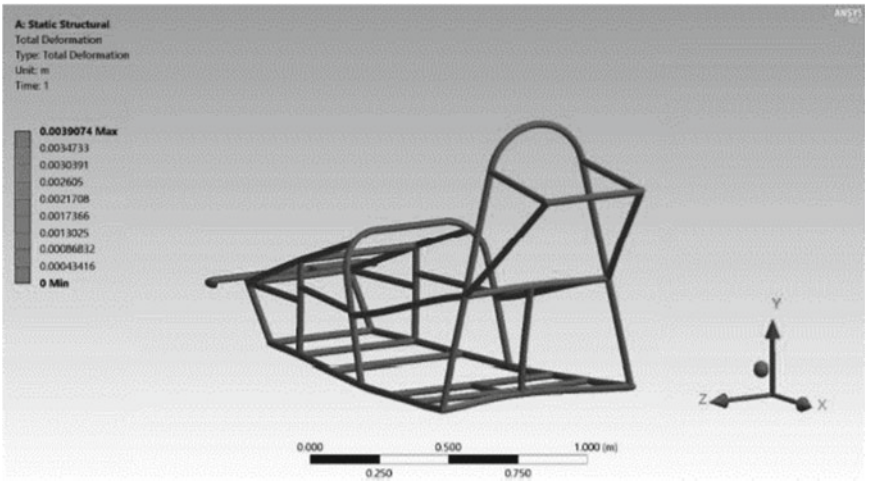

Fig. 9 Rear deformation

where K_a is proportionality constant of acceleration, A is acceleration and V is velocity.

$$\text{Rolling resistance}(R_r) = (K \times W \times g)N \tag{6}$$

where K depends on nature of the load, W is total weight and g is gravitational acceleration constant.

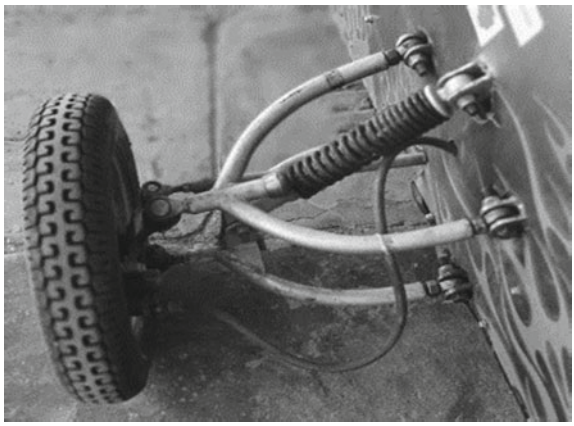

Fig. 10 Double wishbone suspension

Fig. 11 Dual suspension with swing arm

$$\text{Traction force } F = \frac{T_e \times \text{Gear ratio} \times \text{Transmission efficiency}}{\text{Wheel Radius}} \tag{7}$$

where T_e is torque.

$$\text{Acceleration } a = \frac{F - R}{m} \text{ in m/s} \tag{8}$$

where

$$R = R_a + R_r \tag{9}$$

Disc brakes mainly focuses on squeezing the pairs of pads against a disc using calipers. This slows down the rotational speed and hold it stationary. We use brake oil dot 3 in our electric vehicle [4].

6 Design of Electrical Systems

6.1 Selection of Electric Drive

The electric vehicle system is divided into four sections, which describes how a concept vehicle works. The four sections are namely—Battery, motor, motor controller, and Dashboard. The motor requirements are 1 kW, 48 V hub motor, and their capability determines the prototype vehicle's performance efficiency and speed. Normally, we use a regular motor, but to keep it small and lightweight. The formula for finding current I is,

$$P_{\text{in}} = (V \times I) \text{ in W} \tag{10}$$

$$I = \left(\frac{P_{\text{in}}}{V}\right) \text{ in A} \tag{11}$$

In order to find the value of P_{in}, We can apply the values of Efficiency E and Output Power P_{out} in the formula of efficiency.

$$\eta = \left(\frac{P_o}{P_{\text{in}}}\right)$$

$$P_o = (P_{\text{in}} \times \eta) \text{ in W} \tag{12}$$

$$P_{\text{out}} = \left(\frac{2 \times \pi \times N \times T}{60}\right) = T = \left(\frac{P_{\text{out}} \times 60}{2 \times \pi \times N}\right) \text{ in Nm} \tag{13}$$

6.2 Selection of Battery

Lithium-ion battery, they are rechargable battery, cylinderical in shape, and the rating we are using is 48 V, 75 Ah. It is a closed battery pack with Battery Management System (BMS) in it. BMS is a electronic integrated circuit that monitors the battery. It weighs around 19 kg which is 30% less compared to Lead acid batteries [5].

6.3 Power Line Diagram

We used safety devices like fuses, MCB (C-type), and kill switches.

$$\text{Fuse rating} = \left(125\%\left(\frac{P_{\text{in}}}{pf \times V}\right)\right)\text{in A} \tag{14}$$

$$\text{MCB rating} = 125\% \text{ of } I_{\text{max}} \text{ in A} \tag{15}$$

7 Final Prototype of Electric Vehicle—Photographs

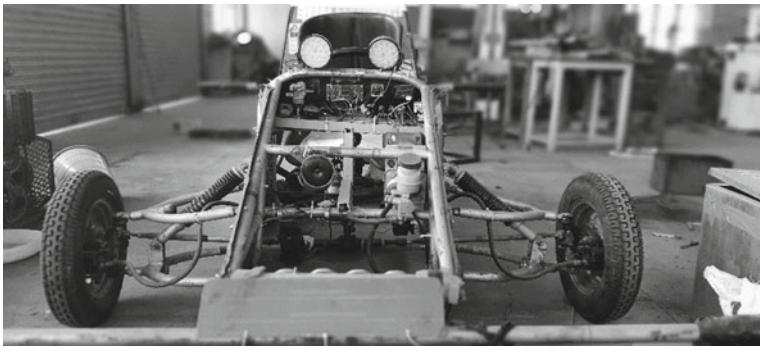

8 Conclusion

This document's conclusion is solely for the purpose of designing and fabricating a prototype electric vehicle as a beginner. Electric cars should be prioritized as the cost of gasoline rises and pollutes the environment. Until developing the prototype,

this analysis demonstrates the basic specifications. Prototypes will be needed in the coming years for larger companies to test new EVs concepts.

Acknowledgements The authors would like to express their gratitude to the National Solar Vehicle Challenge (NSVC) and the Saur Urja Vehicle Challenge (SUVC) for validating our prototype electric vehicle through competition in India. And we'd like to thank our college for supporting us to work in various aspects, as well as fabricate the completed prototype vehicle.

- 2nd Runner-up in NATIONAL SOLAR VEHICLE CHALLENGE 2019
- Runner-up in SAUR URJA VEHICLE CHALLENGE 2020.

References

1. Nabil T, El-Naghi BE, Saeed M, Kamal A, Gharib E, Mohsen M, Ahmed I (2019) Design and fabrication of prototype battery electric three wheeled vehicles. J Asian Electr Veh 17(2):1823–1834
2. Casalino G, Moradi M, Moghadam MK, Khorram A, Perulli P (2019) Experimental and numerical study of AISI 4130 steel surface hardening by pulsed Nd: YAG laser. Materials 12(19):3136
3. Wilhelm E, Bornatico R, Widmer R, Rodgers L, Soh GS (2012) Electric vehicle parameter identification. World Electr Veh J 5(4):1090–1099
4. Paterson J, Ramsay M (1993) Electric vehicle braking by fuzzy logic control. In: Conference record of the 1993 IEEE industry applications conference twenty-eighth IAS annual meeting. IEEE, pp 2200–2204
5. Yoshio M, Brodd RJ, Kozawa A (2009) Lithium-ion batteries, vol 1. Springer, New York, pp 2–3
6. Petrushov VA (1998) Improvement in vehicle aerodynamic drag and rolling resistance determination from coast-down tests. Proc Inst Mech Eng Part D J Autom Eng 212:369–380
7. Nian X, Peng F, Zhang H (2014) Regenerative braking system of electric vehicle driven by brushless DC motor. IEEE Trans Ind Electron 61(10):5798–5808
8. Sciarretta A, Guzzella L (2007) Control of hybrid electric vehicles. IEEE Control Syst Mag 27(2):60–70
9. Ehsani M, Gao Y, Miller JM (2007) Hybrid electric vehicles: architecture and motor drives. Proc IEEE 95(4):719–728
10. Duncan J (1983) Linear induction motor equivalent-circuit model, electric power applications. IEE Proc B 130(1):51–57
11. Chan CC, Chau KT (2001) Modern electric vehicle technology (No. 47). Oxford University Press on Demand
12. Prabhu VN, Manigandan N (2014) Design and fabrication of solar transport vehicle. OSR J Mech Civ Eng 11:14–19

Performance Analysis of IPT with DC to DC Converter for E-Vehicle Application

V. Senthil Nayagam and L. Premalatha

Abstract This work proposes the utilization of Inductive Power Transmission (IPT), for charging the E-Vehicle's battery with the help of an efficient DC TO DC converter. In this IPT method, the DC TO DC converter is operated with the inclusion of transmitting and receiving coils. The required power for transmitting coil from the input source (AC Source or solar energy) is controlled and supplied by the DC TO DC converter 1. Meanwhile from the receiving coil side of IPT system, the obtained power supply will be controlled by DC TO DC converter 2 for charging the battery. In order to identify the efficient DC TO DC converter, two types of converters namely VMC (Voltage multiplier cell) based DC TO DC converter and LUO converters are taken into account for comparison.

Keywords DC-DC converter · LUO · IPT · E-vehicle · Battery

1 Introduction

1.1 Existing System Methodology

Most of us in this modern world use a traditional vehicle that uses fossil fuel, which is the primary factor that causes harmful damage to the ozone layer. It is therefore, proposed traditional vehicles will be replaced by electric vehicles (EV) [1] to maintain the quality of the air around us. This solution of using battery-operated vehicles [2, 3] leads the automobile industries to manufacture various cars and two wheelers which are more luxurious thus replacing the engines of the conventional vehicles by motors. This is named as the E-Vehicle [4] and it is popular in the market but not affordable for

V. Senthil Nayagam (✉)
Department of Electrical and Electronics Engineering, Sathyabama Institute of Science and Technology, Chennai, India

L. Premalatha
School of Electrical and Electronics Engineering, VIT Institute of Science and Technology, Chennai, India
e-mail: premaprak@yahoo.com

C. Subramani et al. (eds.), *Proceedings of International Conference on Power Electronics and Renewable Energy Systems*, Lecture Notes in Electrical Engineering 795,
https://doi.org/10.1007/978-981-16-4943-1_26

all consumers due to its heavy initial cost. All these luxurious E-vehicles are with one touch control which requires separate source for the control circuit and also supply required for motor driving. Therefore heavy battery utilization is required for long travel. Those control circuits consist of inverters and efficient DC to DC converters [5–7] with high voltage conversion ratio in the input and output stages of the inverter according to the supply and load demand, so that the battery life can be extended and cooling arrangements for the battery can be minimized. But the major issue is that the charging station is supposed to have a variety of charging points for various types of E-vehicles [8, 9] and its battery capacities. Therefore in order to avoid this issue, single charging point has to be designed to charge the variety of batteries of various vehicles. To design this kind of charging point we need to incorporate the efficient DC to DC converter [10–12] with fewer ripples in the dc supply input for the E-vehicle battery. If the main source of supply is AC with reduced voltage, then for charging the battery, boost converter is required for the battery charging of various E-vehicles. If in case, the main source voltage level is very high than the required charging voltage level, then step down DC to DC converter used to charge the battery to apply required voltage to the battery of the various E-vehicle. A single buck-boost converter can be used to charge the variety of battery range of E-vehicle with variety of input source but if incase there is failure in the converter any kind of battery charging can be stopped. So it is recommended to use separate buck converter and boost converter so as to increase the lifetime and uninterrupted charging of the battery. But there are some challenges in the implementation of battery-operated vehicles which are charging the battery with wired connection for a moving vehicle, which is impossible for longer distance; increasing the life span and reliability; and low-maintenance operation of the battery. But there are some challenges in the implementation of battery operated vehicles. For long distance travel, charging the wired battery is difficult which lessens the battery's durability and low maintenance of the battery. Further problems are that the traditional boost converter's voltage gain will be high with high duty ratio, diode reverse recovery issue that leads to large current ripples, high conduction losses, plugging charger manually / unplug operation and wired charging chances of electrical shock. Inductive charging of battery with a charge controller such as a powerful DC to DC converter successfully meets the above-mentioned challenges and their solutions. LUO converter (boost converter) output, interleaved coupled inductor dependent DC to DC converter (boost converter), buck converter, boost converter with voltage multiplier cell performance are tested for battery charging in our work. In addition to this, inductive wireless charging is tested and its performances are analyzed for various distances between transmitting and receiver coils. In the process of inductive type of charging the battery, as the distance between transmitting (primary) and receiving (secondary) coil increases there is a decrease in output voltage (secondary side) this is due to coupling coefficient factor. Hence sufficient power can be obtained with the aid of the LUO converter or interleaved coupled inductor boost converter to charge the vehicle battery. In the existing system of wireless charging the voltage control takes place only in the transmitting (primary) side of the coil, because the inverter in primary coil side is operated in fixed frequency. Hence in the process of E-vehicle battery charging, the

secondary side voltage is unable to control. This causes poor performance and less efficiency of the battery charging. And also as the inverter is a square wave type, the harmonics content will be rich in the supply. This leads to the failure of existing wireless battery charging system.

In the existing inductive charging system without secondary side control of voltage system consists of AC supply source, rectifier block which will convert AC to DC and it is supplied as an input to the inverter controlled by DSPIC30F2010 controller. Then the transmitting coil with compensation network will transfer AC supply from transmitting coil to receiving coil through air gap. Finally, the battery will receive the power from the receiving coil through an uncontrolled rectifier. In this system the voltage on the secondary side is not controlled with respect to the battery. Therefore uninterrupted charging of battery is not ensured and hence it is difficult to drive effectively under load varying conditions. Moreover losses associated with the inductive power transfer (IPT) method are very high.

Therefore, in overcoming the above mentioned issues related to the effective charging of battery, this research work concentrates on proposed technique of novel wireless charging with reduced losses and also on efficient control of secondary side wireless transmitted supply.

2 Proposed Methodology

2.1 Process of Identifying Effective DC to DC Converter for Battery Charging by Receiver Coil of IPT System

The block diagram of coupled inductor based interleaved boost converter with voltage multiplier cell in IPT implementation shows the overall circuit implementation with their connection between every circuit unit is presented in the Fig. 1. The AC input source of 48 V is converted as DC supply using rectifier and this DC supply is fed to the controlled inverter which is used to convert as AC supply and it is controlled by the DSPIC30F2010 controller in order to maintain the primary coil voltage according to the requirement.

The controlled output from the transmitter coil is transmitted wirelessly with the aid of compensation network to the receiver coil. This received AC supply from the receiver coil is further converted as DC supply by the rectifier in order to control the secondary voltage as DC supply and to maintain the required level of voltage for E-Vehicle battery charging requirement by the coupled inductor based interleaved boost converter with voltage multiplier cell. This controlled secondary voltage is applied to the battery to charge or for DC load requirement according to the supply availability in the feedback voltage of the input side of the coupled inductor based interleaved boost converter with voltage multiplier cell.

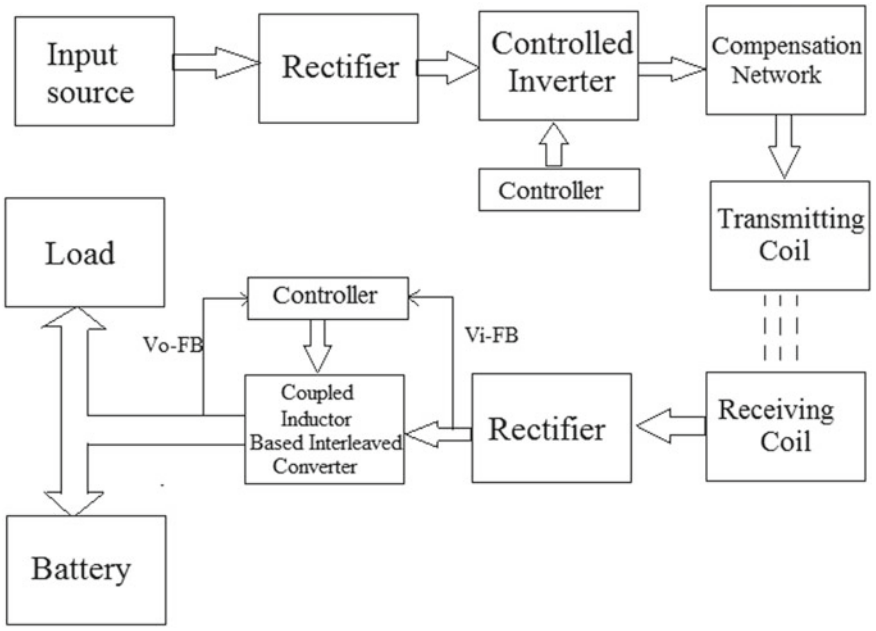

Fig. 1 Block diagram of coupled inductor based interleaved DC to DC converter in IPT implementation

2.2 Simulation Circuit Coupled Inductor Based Interleaved DC to DC Converter in IPT

Simulation diagram of coupled Inductor based interleaved DC to DC converter with voltage multiplier cell is shown in the Fig. 2 that is simulated with the specification shown in Table 1 and measures various voltage in the circuit.

Simulation diagram of LUO DC to DC converter is shown in Fig. 3. It is simulated with the specification shown in Table 2 and measures various voltage in the circuit.

Table 3 shows the resonance condition changes of the IPT coils, by the input and output voltage variation of the coupled inductor based interleaved DC to DC converter for varying load conditions and duty ratio. From this table, it is clearly indicated that, the wireless transmitter coil input and receiver coil output voltages are drastically reduced, as long as, there is an increase in the duty ratio and the load.

Table 4 shows the resonance condition changes as the input and output voltage varies by the LUO DC to DC converter for varying load conditions and duty ratio. From this table, it is clearly indicated that, wireless transmitted input and output voltages are slightly reduced as the duty ratio and load increases when compare to coupled inductor based interleaved DC to DC converter.

From the waveform shown in Fig. 4, it is observed that, without LUO converter (without secondary side control), the inverter's closed loop control (only primary

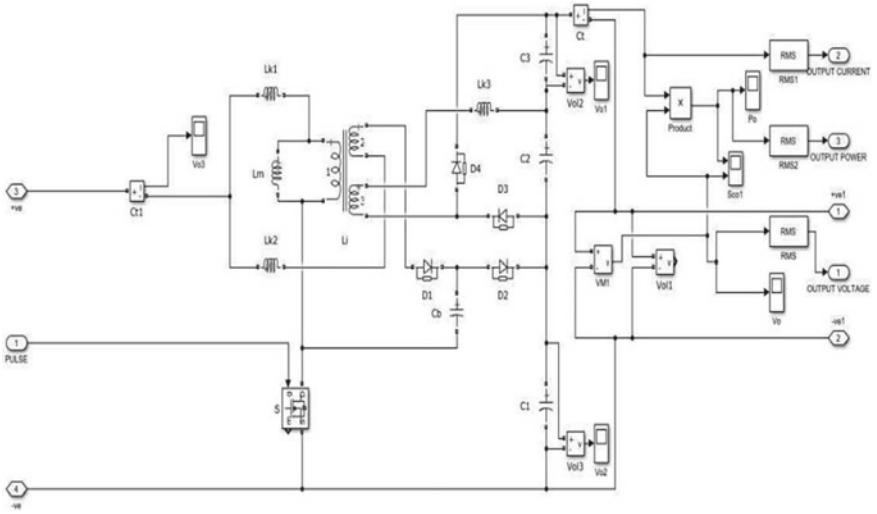

Fig. 2 Simulation diagram of coupled inductor based interleaved DC to DC converter in IPT implementation

Table 1 Simulation specifications of interleaved coupled inductor based DC to DC converter

Simulation Parameters	Value
Switching frequency	15 kHz
Input voltage	12~40 V
Output voltage	20~65 V
Output power	40 W
Inductor value	0.150 uH
Capacitor value	1500 uF
MOSFET	IRF840 (400 V, 8 A)
DIODE	MUR460 (600 V, 4 A)

control) is insufficient to charge the battery connected on the secondary side. Therefore there will not be any flow of current into the battery to charge the battery.

3 Conclusion

From the obtained simulation results of coupled inductor based interleaved DC to DC converter with VMC and LUO dc- dc converter in the implementation of WPT system, for finding effective DC to DC converter −2 in the secondary coil of IPT system, it is observed that coupled inductor based interleaved converter with VMC DC to DC converter produced high output voltage for the duty ratio compared to

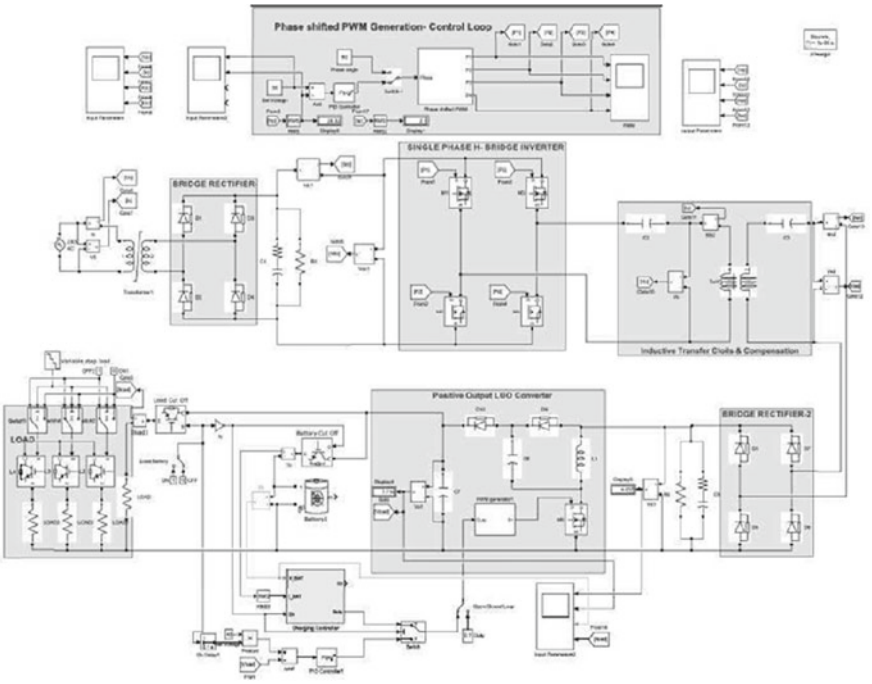

Fig. 3 Simulation diagram of LUO converter with IPT Implementation

Table 2 Simulation specifications of LUO DC to DC converter

Switching frequency	15 kHz
Input voltage	12~40 V
Output voltage	20~65 V
Output power	40 W
Inductor value	0.150 uH
Capacitor value	1500 uF
MOSFET	IRF840 (400 V, 8 A)

Table 3 Response of coupled inductor based interleaved DC to DC converter according to variation of duty ratio and load

Load	Duty cycle	0.1	0.15	0.2	0.25	0.3	0.4	0.5
100 Ω	Input voltage	30.76	30.26	29.35	28.58	24	24.72	21.28
	Output voltage	62.95	63.37	63.89	64.06	56.52	64.09	62.48
50 Ω	Input voltage	22.56	21.92	20.86	20.06	15	16.26	13.39
	Output voltage	34.29	45.19	44.92	44.42	43.97	41.15	38.25

Table 4 Response of LUO converter according to variation of duty ratio and load

Load	Duty cycle	0.1	0.15	0.2	0.25	0.3	0.4	0.5
100 Ω	Input voltage	17.22	15.85	13.22	11.71	9.98	7.82	6.05
	Output voltage	56.86	55.54	52.09	49.47	46	41.1	36.06
50 Ω	Input voltage	13.77	10.21	8.79	7.83	6.61	5.02	3.84
	Output voltage	36.28	31.8	29.88	28.34	26.06	22.55	19.54

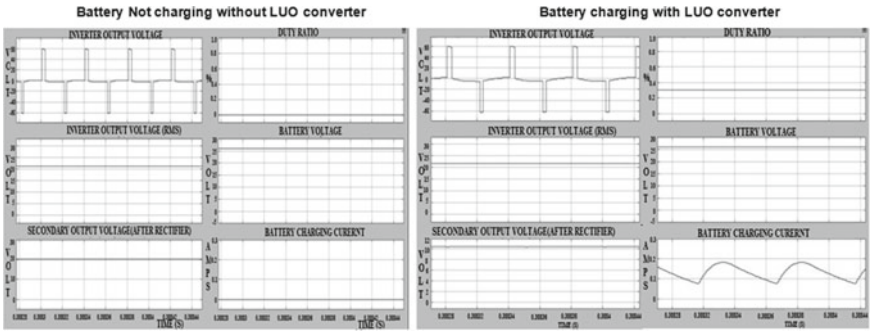

Fig. 4 Secondary side control waveform without and with LUO converter

the LUO DC to DC converter. But during variation of load, distance between the transmitter and receiver coils, it is found that, high output voltage which is usually obtained in the coupled inductor based interleaved DC to DC converter with VMC is reduced drastically when compared to the LUO DC to DC converter. Because, LUO converter is not much affects the resonance condition, which is the main factor for efficient wireless power transfer. The comparative results from Tables 3 and 4 which shows the effect of converters on the resonance condition changes between the WPT coils, which leads to reduction of input voltage of the transmitting coil. Henceforth, output voltage of the receiver coil is also reduced, because the WPT coils are works under mutual inductance principle. During the LUO converter operation of increasing the receiver coil voltage to the required level of battery charging, which is not much reduce the input voltage of the WPT transmitting coil when compare to drastic reduction of input voltage of WPT transmitting coil under VMC based Interleaved coupled inductor DC to DC converter operation. So, LUO DC to DC converter performs better than the coupled inductor based interleaved converter with VMC DC to DC converter in the implementation of IPT for E-Vehicle battery charging. Therefore LUO DC to DC converter is preferred for wireless power transmission of battery charging. Similarly, from the primary side control (inverter output control) and secondary side control (LUO converter output control), it is observed that, both control is required under closed loop mode of operation, for proper charging of the battery.

References

1. El-Shahat A, Ayisire E, Yan Wu, Rahman M, Nelms D (2019) Electric vehicles wireless power transfer state-of-the-art. Energ Procedia 162:24–37
2. Huang C-Y, Boys JT, Covic GA, Budhia M (2009) Practical considerations for designing IPT system for EV battery charging. IEEE 6:402–407
3. Hoang DT, Wang P, Niyato D, Hossain E (2017) Charging and discharging of plug-in electric vehicles (PEVs) in vehicle-to-grid (V2G) systems: a cyber insurance-based model. IEEE Access 5:732–754
4. Manshadi SD, Khodayar ME, Abdelghany K, Üster H (2018) Wireless charging of electric vehicles in electricity and transportation networks. IEEE Trans Smart Grid 9:4503–4512
5. Berkovich Y, Axelrod B (2011) Switched-coupled inductor cell for DC to DC converters with very large conversion ratio. IET Power Electron 4(3):309–315
6. Makowski MS, Maksimovic D (1995) Performance limits of switched capacitor DC to DC converters. In: Proceedings of IEEE 26th power electronics specialist, pp 1215–1221
7. Kumar MK, Sekhar P (2012) High step up voltage gain achieved in DC TO DC converters using Linear Peak Current Mode control technique. Int J Mod Eng Res 2(3):870–875
8. Jeong S, Jang YJ, Kum D, Lee MS (2019) Charging automation for electric vehicles: is a smaller battery good for the wireless charging electric vehicles? IEEE Trans Autom Sci Eng 16:486–497
9. Castiglia V, Noia LD, Livreri P, Miceli R, Pellitteri F, Viola F (2017) An efficient wireless power transfer prototype for electrical vehicles. In: International conference on renewable energy research and application (ICRERA), vol 10, pp 1215–1220
10. Yie-Tone C, Zong-Xing Lu, Liang R-H (2018) Analysis and design of novel high step-up DC TO DC converter with coupled inductors. IEEE Trans Power Electron 33(1):425–436
11. Tofoli FL, de Souza Oliveria D, Torrico-Bascope RP Jr, Alcazar YJA (2012) Novel non isolated high voltage gain DC to DC converters based on 3SSC and VMC. IEEE Trans Power Electron 27:743–749
12. Torrico-Bascope GV, Vasconcelos SA, Torrico-Bascope R, Fernando LM, de Oliveira DS, Carlos GC (2006) A high step-up DC TO DC converter based on three-state switching cell. IEEE, pp 998–1003

Operating Cost Analysis of Microgrid Including Renewable Energy Sources and a Battery Under Dynamic Pricing

Hephzibah Jose Queen, J. Jayakumar, and T. J. Deepika

Abstract In this paper, minimization of operating cost of DC microgrids is formulated. Utility grid, solar, wind and battery is associated with this formulation. In this optimization problem, both with and without losses are considered in the power flow model. Impact of renewable energy sources on reduction in operating cost is discussed. Based on the solar radiation and air density, power generation from solar and wind are calculated respectively. Heuristic method is used to solve this minimization problem. To analyze the operating cost, a six-bus customized system is used. To calculate the cost structure, three different cases are considered. The first case considers the system without any renewable energy sources or battery storage. In the second case, a solar and a Wind Energy Conversion system are added to the system and in the third case, the battery is included with the existing system. With the inclusion of renewable energy system, dynamic pricing and various load conditions, the proposed algorithm is minimizing the operating cost considerably.

Keywords Microgrid · Solar power · Wind turbine · Battery and dynamic pricing

1 Introduction

The upcoming energy revolution entails the integration of various distributed energy sources. This means an integration of renewable energy sources like solar and wind power. Chendal [1] in his paper states the establishment of micro girds is one option to integrate these new distributed energy sources in an effective way. Strunz et al. [7] describes a micro grid is an almost autonomous working, low voltage electricity network including different residential loads and generating units. To guarantee a

H. J. Queen (✉) · J. Jayakumar
Department of Electrical and Electronics Engineering, Karunya Institute of Technology and Sciences, Coimbatore, India

J. Jayakumar
e-mail: jayakumar@karunya.edu

T. J. Deepika
Department of Electrical and Electronics Engineering, Sona College of Technology, Salem, India

C. Subramani et al. (eds.), *Proceedings of International Conference on Power Electronics and Renewable Energy Systems*, Lecture Notes in Electrical Engineering 795,
https://doi.org/10.1007/978-981-16-4943-1_27

stable operation of the microgrid, there is one connection point to the utility grid. If the energy generation in the microgrid is higher than the demand, electrical energy is feed in the utility grid respectively if the energy generation in the microgrid is lower than the required demand, additional energy is needed from the utility grid. To minimize the operating costs of the system, a battery storage unit can be added to the grid. Furthermore, dynamic pricing represents a good opportunity to minimize the total operating costs for a specific time-period (here: 24 h). Dynamic pricing means that the electricity price varies depending on supply and demand instead of being fed.

The following calculations show the cost benefit of the integration of renewable energy sources and the effect of a battery storage unit added to the micro grid. Hephzibah et al. [2] designed a system to simplify the optimization model, the micro grid is reduced to a one-bus-system with several units. Therefore, the line losses can be neglected, and no power flow calculation is needed. Thus, the line losses are not considered in the optimization model of the operating costs. In a second step, the line losses of an electricity network with the same units are determined and the costs for the losses are added to the total operating costs of the grid.

The available units are a PV Panel and a Wind Energy Conversion system, two residential loads, a battery storage and the connection point to the utility grid. The input data are the same in systems, the one-bus-system and the six-bus-system. To run the load flow calculation, the results of the optimization model of the one-bus-system are used as input values for the battery. The one-bus-system represents a DC bus, whereas the six-bus-system are an ac network. Therefore, the load flow calculations are also calculated for an AC system.

2 Input Data

2.1 Solar Panel

The available solar power is dependent on the direct solar radiation $\text{sun}_{\text{direct}}$, the diffuse solar radiation $\text{sun}_{\text{diffuse}}$, the size of the solar panel area A and the efficiency of the solar panel η_{solar}. This relation is described by Eq. (1)

$$P_{\text{Solar}} = \eta_{\text{solar}} A (\text{Sun}_{\text{direct}} + \text{Sun}_{\text{diffuse}}) \tag{1}$$

A monocrystalline solar cell has an average effciency of 20%. A solar panel with an area of $A = 80\ \text{m}^2$ is connected to the grid via converter with an efficiency of around 96%. Thus, the overall efficiency of the solar panel is taken as $\eta_{\text{solar}} = 19.2\%$. The German weather service measures weather data in 15 different climate regions in Germany. Data used in this study case belongs to the first climate region which is located at the north-sea cost. The measuring station is Bremerhaven, Germany. Table 1 lists the measured sun radiation values of region one for the 1st September

Table 1 Solar radiation data and output power

Time of day	Radiation (W/m^2)		Solar power (kW)	Time of day	Radiation (W/m^2)		Solar power (kW)
	Direct	Diffuse			Direct	Diffuse	
1:00	0	0	0	13:00	54	284	5.19168
2:00	0	0	0	14:00	49	265	4.82304
3:00	0	0	0	15:00	39	228	4.10112
4:00	0	0	0	16:00	131	238	5.66784
5:00	0	0	0	17:00	40	159	3.05664
6:00	0	2	0.03072	18:00	14	67	1.24416
7:00	13	77	1.38240	19:00	0	0	0
8:00	45	171	3.31776	20:00	0	0	0
9:00	112	256	5.65248	21:00	0	0	0
10:00	203	298	7.69536	22:00	0	0	0
11:00	249	332	8.92416	23:00	0	0	0
12:00	109	348	7.01952	24:00	0	0	0

[3]. The results of the calculated solar power by Eq. (1) are also shown in the same table.

2.2 Wind Power

The wind turbine is connected to the bus via a generator and a rectifier. Due to mechanical (e.g. gearbox and bearings) and electrical (e.g. generator, rectifier and cables) losses and the coefficient of power (max. 16/27) of a wind turbine, the overall efficiency η_{wind} of the turbine, the generator and the rectifier is assumed to be 33%. Furthermore, the generated power is dependent on the air density ρ_{air} (1.225 kg/m^2) the swept area of the blades A (2827 m^2) and the wind speed v. The wind power can be calculated using Eq. (2).

$$P_{\text{wind}} = \eta_{\text{wind}}.1/2.\,\rho_{\text{air}}.A.v^3. \tag{2}$$

The wind speed data is taken from the same data base as the solar radiation data by Kothari [8]. The used wind speed data and the resulting wind power values are listed in Table 2.

Table 2 Wind speed data and wind power

Time of day	Speed (m/s)	Power (kW)	Time of day	Speed (m/s)	Power (kW)	Time of day	Speed (m/s)	Power (kW)	Time of day	Speed (m/s)	Power (kW)
1:00	5.1	75.81	7:00	2.0	4.57	13:00	2.0	4.57	19:00	3.0	15.43
2:00	4.3	45.44	8:00	1.0	0.57	14:00	5.0	71.44	20:00	2.0	4.57
3:00	3.7	28.95	9:00	2.0	4.57	15:00	7.0	196.02	21:00	3.0	15.43
4:00	3.6	26.66	10:00	4.0	71.44	16:00	5.0	71.44	22:00	2.0	4.57
5:00	3.3	20.54	11:00	4.0	196.02	17:00	3.0	15.43	23:00	3.0	15.43
6:00	3.0	15.43	12:00	4.0	71.44	18:00	3.0	15.43	24:00	3.0	15.43

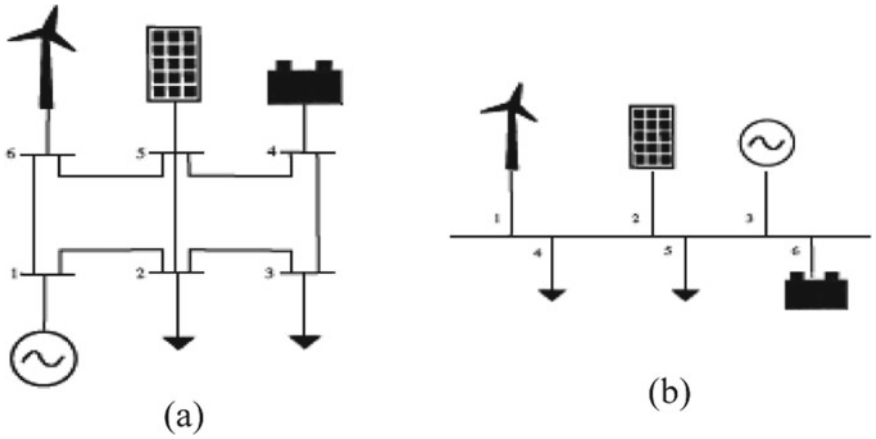

Fig. 1 **a** Structure of six-bus-system**, b** structure of one-bus-system (lossless 6 bus)

2.3 Battery Storage Wind Power

The technical data of the battery storage are in accordance with the Tesla Powerwall 2.0. The maximum power is 3.3 kW and the DC energy is 13.5 kWh [5]. The assumed efficiency for the charging (η_{charge}) and discharging ($\eta_{\text{discharge}}$) process is 93% each. The Tesla Powerwall is a lithium-ion battery pack with an integrated DC/DC converter. Therefore, the system is very easy to install. Moreover, this battery type is mainly used as a residential storage system in combination with solar panels.

2.4 Residential Loads

The considered 6 bus system with PV, wind, battery, loads and grid connection is shown in Fig. 1a. The same system is reduced to a one-bus-system as in Fig. 1b when losses are ignored. Table 3 shows the residential load data. There is one fixed value for each hour of the day. The load data is in accordance with the values from Chendan et al. [1].

2.5 Electricity Prices

The electricity prices are in accordance with the prices price$_t$ publish by the European Energy Exchange for the 1st September 2017 [4]. The prices are listed in Table 4.

Table 3 Residential load data

Time of day	Load (kW)		Time of day	Load (kW)		Time of day	Load (kW)		Time of day	Load (kW)	
	1	2		1	2		1	2		1	2
1:00	10.84	20.39	7:00	12.03	21.76	13:00	12.98	24.30	19:00	26.50	47.42
2:00	9.35	17.74	8:00	15.58	28.59	14:00	12.60	23.39	20:00	26.02	46.42
3:00	8.78	16.67	9:00	15.07	27.64	15:00	12.44	23.40	21:00	24.17	43.41
4:00	8.67	16.36	10:00	13.00	24.41	16:00	13.28	25.05	22:00	22.11	40.27
5:00	8.61	16.26	11:00	13.14	25.43	17:00	16.50	30.51	23:00	18.31	33.90
6:00	9.24	17.30	12:00	13.41	25.83	18:00	22.77	41.35	24:00	14.60	27.52

Table 4 Dynamic electricity prices

Time of day	Price (EUR/MWh)	Time of day	Price (EUR/MWh)	Time of day	Price (EUR/MWh)	Time of day	Price (EUR/MWh)
1:00	33.09	7:00	36.04	13:00	44.87	19:00	42.20
2:00	31.07	8:00	43.46	14:00	43.09	20:00	43.74
3:00	29.89	9:00	45.83	15:00	39.91	21:00	43.95
4:00	29.64	10:00	45.12	16:00	38.93	22:00	39.40
5:00	29.65	11:00	44.90	17:00	38.56	23:00	36.21
6:00	31.71	12:00	45.02	18:00	40.36	24:00	34.51

3 Cost Analysis: Six-Bus System Without Line Losses

A six-bus system is considered with wind turbine connected at bus one, solar panel at bus two and battery at bus six. The connection point of the microgrid and the utility grid is at bus three. Bus four and five represent two residential loads. As the line losses of the microgrid are neglected, the grid is reduced to a one-bus-system as in Fig. 1b.

3.1 Mathematical Model of Lossless System

The optimization problem of minimizing the operating costs of the microgrid can be modeled by the following equations. The objective function (Eq. 3) depends on the electricity price and power drawn from utility grid. The operating costs of renewable energy sources are assumed to be zero. Power feed into the system is positive and drawn power is negative. Equation 4 is the power balance. The system is reduced to one-bus with several connected units as there are no line losses. At every time step, the stored energy in the battery must be within its minimum and maximum capacity $\text{energy}_{\max}$ modeled in Eq. 6. The power of the battery is thus divided into charging and discharging power (Eq. 5). According to Eqs. 7 and 8 the charging and discharging power has to be within the technical limits of the battery.

$$\min \sum_{t=0}^{T} \text{price}_t . P_{\text{utility},t} . \tag{3}$$

$$0 = P_{\text{utility},t} + P_{\text{load1},t} + P_{\text{load2},t} + P_{\text{solar},t} + P_{\text{wind},t} + P_{\text{battery},t} . \tag{4}$$

$$P_{\text{battery},t} = P_{\text{charge},t} + P_{\text{discharge},t} . \tag{5}$$

$$0 \leq \sum_{t=0}^{T} \left(-P_{\text{charge},t}.\eta_{\text{charge}} - P_{\text{discharge},t}/\eta_{\text{discharge}}\right).\text{period} < \text{energy}_{\max}. \quad (6)$$

$$P_{\text{batterymin}} \leq P_{\text{charge},t} < 0. \quad (7)$$

$$0 \leq P_{\text{discharge},t} \leq P_{\text{batterymax}}. \quad (8)$$

3.2 Lossless System—Case Studies

To evaluate the cost structure of the microgrid, three different cases are considered. The first case considers the micro grid without any renewable energy sources or battery storage. The residential loads are met by the utility grid. In the second case, a PV Panel and a Wind Energy Conversion system are added to the system [9] and in the third case, the system is enhanced by a battery [7].

3.3 Results—Lossless System Analysis

The results of the optimization model for the three cases are listed in Table 5. The operating costs obtained in Cases 1, 2 and 3 are €40.84, €8.41 and €8.29 respectively.

4 Cost Analysis: Six-Bus System with Line Losses

A six-bus-system with the same generating units and loads is considered as in Fig. 1a.

4.1 Mathematical Model of System with Loss

The load buses and the battery bus are modeled as PQ buses and the wind turbine and the solar panel are modeled as PV buses. Thus, the connection point to the utility grid represents the slack bus. The bus types are listed in Table 6. By means of the load flow calculation, the required power from the utility grid can be identified. The original values of R and X are also listed in Table 6. The MVA Base is 100 MV A, the system frequency 50 Hz and the nominal voltage 11 kV.

Subsequently, the line losses $p_{\text{loss},t}$ at the time t, as in Eq. (9) is the difference between the injected power into the system and the power drawn from the system.

Table 5 Utility power and power stored for 3 case studies

Time of day	P_{Utility} (kW)			P_{Battery} (kW)	Time of day	P_{Utility} (kW)			P_{Battery} (kW)
	Case 1	Case 2	Case 3			Case 1	Case 2	Case 3	
1:00	31.23	−44.58	−44.58	0	13:00	37.28	27.52	27.52	0
2:00	27.09	−18.35	−18.35	−3.3	14:00	35.99	−40.27	−40.27	0
3:00	25.45	−3.50	−3.50	−3.3	15.00	35.84	−164.28	−164.28	0
4:00	25.03	−1.63	−1.63	−3.3	16.00	38.33	−38.77	−38.77	0
5:00	24.87	4.33	4.33	−3.3	17.00	47.01	28.52	28.52	0
6:00	26.54	11.08	11.08	−1.316	18.00	64.12	47.45	47.45	0
7:00	33.79	27.84	27.84	0	19.00	73.92	58.49	58.49	0
8:00	44.17	40.28	40.28	0	20.00	72.44	67.87	67.87	0
9:00	42.71	32.49	32.49	3.3	21.00	67.58	52.15	52.15	0
10:00	37.41	−6.86	−6.86	3.3	22.00	62.38	57.81	57.81	0
11:00	38.57	−6.93	−6.93	2.655	23.00	52.21	36.78	36.78	0
12:00	39.24	−4.36	−4.36	3.3	24.00	42.12	26.69	26.69	0

Table 6 Six bus system data

Bus No.	Description	Bus type	To Bus	Resistance	Reactance
1	Utility grid	Slack	2	0.05	0.20
2	Load 1	PQ	3	0.10	0.50
			5	0.20	0.50
3	Load 2	PQ	4	0.20	0.80
4	Battery	PQ	5	0.10	0.30
5	Solar panel	PV	6	0.20	0.40
6	Wind turbine	PV	1	0.10	0.15

Simply said the difference between generation and demand. The parameter $p_{b,t}$ symbolizes the power injected or drawn from the system at bus b at the time t. For instance, this value is negative for all load buses and positive for all buses with generating units. The cost incurred due to losses is computed as in Eq. (10). The line losses are drawn from the utility grid. The parameter dt symbolizes the time period of 1 h.

$$p_{\text{loss},t} = \sum_{b=1}^{n\text{bus}} p_{b,t} \quad \forall t \in T. \tag{9}$$

$$\text{cost}_{\text{loss},t} = p_{\text{loss},t} * \text{price}_t * \text{d}t \quad \forall t \in T. \tag{10}$$

4.2 Results—Six Bus System Analysis with Loss

The cases considered in the six-bus-system are in accordance with those mentioned in Sect. 3.2. The calculated line losses of the system and the associated costs for the losses are shown in Table 7. The line losses are very small in comparison to the load and the generated power by a PV Panel and a Wind Energy Conversion system.

5 Conclusion

An Optimization algorithm is developed to attenuate the operating cost of micro grid. The cost function is dependent not only the utility power but also the real time pricing. A six-bus system without losses and with losses is tested to authenticate the considered algorithm.

The integration of renewable energy sources provides the opportunity to reduce the operating costs. In this case the operating costs are reduced to less than a fourth of the

Table 7 Line losses and cost for 3 case studies

Time of day	Losses (kW)			Cost (EUR)		
	Case 1	Case 2	Case 3	Case 1	Case 2	Case 3
1:00	0.99	4.29	4.29	0.000033	0.000142	0.000142
2:00	0.82	1.95	1.97	0.000025	0.000061	0.000061
3:00	0.76	1.17	1.22	0.000023	0.000035	0.000036
4:00	0.74	1.08	1.13	0.000022	0.000032	0.000033
5:00	0.74	0.91	0.97	0.000022	0.000027	0.000029
6:00	0.80	0.86	0.88	0.000025	0.000027	0.000028
7:00	1.10	1.03	1.03	0.000040	0.000037	0.000037
8:00	1.71	1.58	1.58	0.000074	0.000069	0.000069
9:00	1.61	1.40	1.29	0.000074	0.000064	0.000059
10:00	1.30	1.88	1.88	0.000059	0.000085	0.000085
11:00	1.38	1.95	1.94	0.000062	0.000088	0.000087
12:00	1.42	1.95	1.93	0.000064	0.000088	0.000087
13:00	1.29	1.13	1.13	0.000058	0.000051	0.000051
14:00	1.22	4.14	4.14	0.000053	0.000178	0.000178
15.00	1.22	23.53	23.53	0.000049	0.000939	0.000939
16.00	1.36	4.22	4.22	0.000053	0.000164	0.000164
17.00	1.92	1.77	1.77	0.000074	0.000068	0.000068
18.00	3.44	3.21	3.21	0.000139	0.000130	0.000130
19.00	4.55	4.33	4.33	0.000192	0.000183	0.000183
20.00	4.37	4.42	4.26	0.000191	0.000193	0.000186
21.00	3.80	3.62	3.62	0.000167	0.000159	0.000159
22.00	3.26	3.18	3.18	0.000128	0.000125	0.000125
23.00	2.33	2.24	2.24	0.000084	0.000081	0.000081
24.00	1.59	1.56	1.56	0.000055	0.000054	0.000054

original operating costs. This shows that there is a high potential of saving money and reducing the power drawn from the utility grid. The integration of a battery does not reduce the costs by a significant value. Although the battery has a very small impact in this study case, it could have a bigger influence by using another electricity price profile. Finally, the simulation results show that the developed algorithm depreciates the operating cost in both the cases (with and without losses) (Table 8).

Table 8 Comparison of Results

Case study	With losses		Without loss	
	Loss (kW)	Cost (Euro)	Loss (kW)	Cost (Euro)
1	43.72	0.001765	40.80	40.8018
2	77.40	0.003080	8.41	8.4131
3	77.30	0.003072	8.29	8.2931

References

1. Chendan Li FC, de Bosio F (2016) Economic Dispatch for operating cost minimization under real− time pricing in droop−controlled dc microgrid. IEEE J Emerg Sel Top Power Electron 5:587–595
2. Queen HJ, Jayakumar J (2018) Operating cost analysis of a Microgrid including renewable energy sources without considering the losses. Int J Pure Appl Math 118(20):745–750
3. Federal OCE for building and regional planning in Germany. http://www.bbsr.bund.de/EnEVPortal/DE/Regelungen/Testreferenzjahre/Testreferenzjahre/03_ergebnisse.html?nn=436654. Accessed: 2017-10-04
4. eex. https://www.eex.com/de/marktdaten/strom/spotmarkt/auktion#!/2017/09/01. Accessed: 2017-10-06
5. \teslapowerwall2.0dc. https://www.solahart.com.au/media/2849/powerwall-2-dc_datasheet_english.pdf. Accessed: 2017-10-07.
6. Strunz K, Abbasi E, Huu DN (2014) DC microgrid for wind and solar power integration. Emerg Sel Top Power Electron IEEE J 2:115–126
7. Barelli L, Bidini G, Bonucci F (2016) A microgrid operation analysis for cost effective battery energy storage and RES plants integration. J Energ 113:831–844
8. Kothari JDP (2004) Power system optimization
9. Brini S, Abdallah HH, Ouali A (2009) Economic dispatch for power system included wind and solar thermal energy. Leonardo J Sci 14:204–220

A Comparative Study of Field Distribution Properties of Different Types of Oils Using Comsol

M. Divya Bharathi, R. V. Maheswari, and S. Senthil Kumar

Abstract Nature ester oil is the alternative to mineral oil in transformer for cooling purposes. This paper mainly focuses on a comparative study of field distribution properties of three types of oil (coconut oil, peanut oil, sunflower oil) with different gap spacing values. The three types of oil have different conductivity and permittivity values. The electrodes are immersed in oils. The electrodes are made of copper material. The arc length versus electric potential graph is obtained. Using comparative study analysis we find out the oil which has the best field distribution properties. Electrical breakdown or dielectric breakdown is a cycle that happens when an electrical protecting material, exposed to a sufficiently high voltage, out of nowhere turns into an electrical channel and electric flow moves through it. All protecting materials go through a breakdown when the electric field brought about by an applied voltage surpasses the material's dielectric quality. The voltage at which a given protecting article becomes conductive is called its breakdown voltage and relies upon its size and shape. Under adequate electrical potential, an electrical breakdown can happen inside solids, fluids, gases, or vacuum. Notwithstanding, the particular breakdown components are diverse for every sort of dielectric medium. The electrical breakdown might be a flashing occasion (as in an electrostatic release) or may prompt a persistent electric curve if defensive gadgets neglect to intrude on the flow in a force circuit. For this situation, an electrical breakdown can cause calamitous disappointment of electrical hardware, and fire risks.

Keywords Natural ester · Electrical Field Distribution · Dielectric medium · Arc length · Electric Potential

M. Divya Bharathi (✉) · R. V. Maheswari
Department of Electrical and Electronics Engineering, National Engineering College, Kovilpatti, India

S. Senthil Kumar
Department of Electrical and Electronics Engineering, New Prince Shri Bhavani College of Engineering and Technology, Chennai 600073, India

C. Subramani et al. (eds.), *Proceedings of International Conference on Power Electronics and Renewable Energy Systems*, Lecture Notes in Electrical Engineering 795,
https://doi.org/10.1007/978-981-16-4943-1_28

1 Introduction

The transformer assumes a significant function in giving a solid what's more, effective power flexibly and is one of the most basic types of gear in electric force transmission and conveyance frameworks [1, 2].

Most of the high voltage transformers are loaded up with fluid that functions as electrical protection just as a warmth move medium. The most ordinarily utilized fluid in power transformers is mineral oil because of its ease and great properties [3, 5]. Anyway, the execution of mineral oil begins to be restricted because of ecological thought. Initially, traditional transformer oils are generally non-biodegradable; they can pollute soil and water at the point when a genuine spill happens [4, 6].

This may upset the manor and different creatures. Besides, the mineral oils were separated from the oil, which will run out later on since oil is non-renewable [5, 7]. Normal ester protecting liquid offers fire security, climate, also, protection maturing points of interest over mineral oil and are discovered to be appropriate for the utilization in transformer protection framework. Past fixed cylinder maturing contemplates showing that the warm maturing pace of paper protection in regular ester is fundamentally more slow than that in mineral oil. These two characteristic esters have presently been utilized in little force and appropriation transformers over the US, and further upgrades are progressing in the trust that they will be generally applied in enormous force transformers [8, 9]. Moore introduced the prerequisites and desires for regular ester liquids for application in power transformers. It has become evident that more examination is needed to learn the drawn-out safe activity of transformers where the common ester is utilized.

2 Methodology

Analyze the field distribution properties of three kinds of oil (ex. coconut oil (saturated oil), sunflower oil (unsaturated oil), peanut oil (monosaturated oil) using COMSOL multiphysics software.

In COMSOL the HV electrode applied potential (50, 70, 80 and 100 V). The ground electrode was at 0 potential. The electrodes are immersed in these three types of oil. The distance between the electrodes is varied in the form of 2, 4, 6 and 10 cm. The electrodes are made of copper material. The conductivity and permittivity values of the three types of oil are shown in Tables 1 and 2.

Table 1 Oil conductivity values

S. No.	Oil	Conductivity
1	Coconut oil	$2.09*10^{-7}\ \Omega^{-1}\ m^{-1}$
2	Sunflower oil	$2.48*10^{-7}\ \Omega^{-1}\ m^{-1}$
3	Groundnut oil	$1.74*10^{-7}\ \Omega^{-1}\ m^{-1}$

Table 2 Oil permittivity values

S. No.	Oil	Permittivity
1	Coconut oil	2.9
2	Sunflower oil	3.35
3	Groundnut oil	2.64

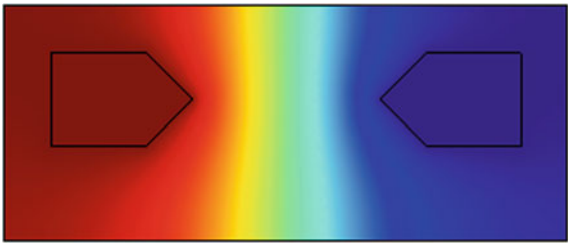

Fig. 1 Coconut oil with a point to point Electrode in 2 cm gap spacing

The values of permittivity of three kinds of oil are shown in Table 2.

3 Results and Discussion

This paper deals with the field distribution of three types of oil with different voltage and different gap spacing. The electrode configuration is the point to point, sphere to sphere, plane to plane, plate to plate.

3.1 Coconut Oil (Point to Point Electrode Configuration)

Here the field distribution of coconut oil with a point to point electrode configuration using different voltage and different gap spacing results using COMSOL is given Fig. 1.

In Fig. 2a the *x*-axis is arc length and *y*-axis is electric potential. The point to point 50 V 2 cm gap spacing has the lowest arc length versus electric potential curve. The point to point 100 V 10 cm gap spacing curve has the highest magnitude in this arc length versus electric potential graph.

3.2 Coconut Oil (Sphere to Sphere Configuration)

In Fig. 2b sphere to sphere electrode configuration, the all curves starting point has applied voltage. Then time elapses the value of arc length versus electric potential

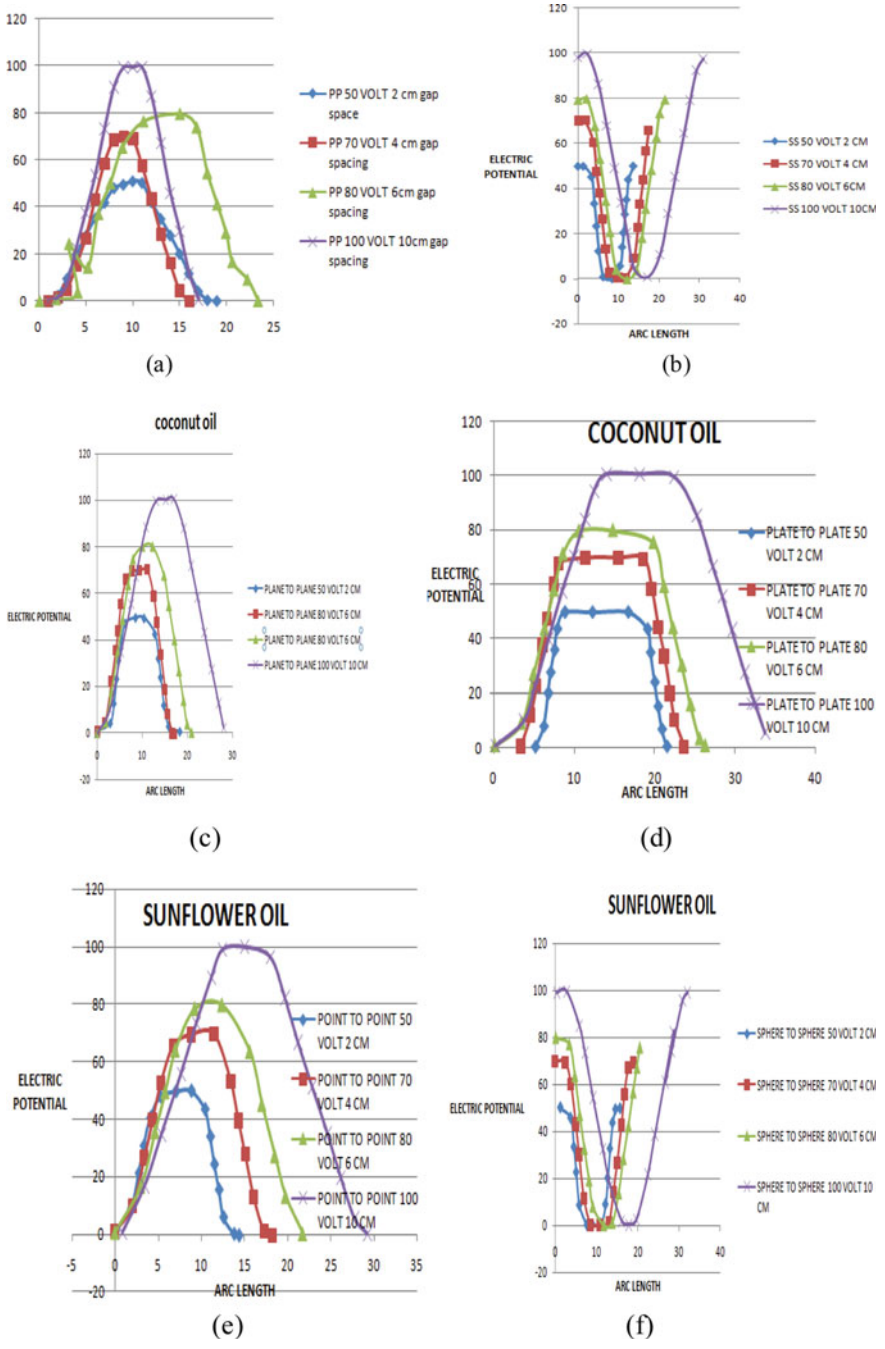

Fig. 2 Simulation result. **a** Coconut oil point to point configuration, **b** coconut oil sphere to sphere, **c** coconut oil plane to plane, **d** coconut oil plate to plate, **e** sunflower oil point to point, **f** sunflower oil sphere to sphere

of all these curves drastically down to 0. Then all the curves are rise up to the given potential of that considered voltage.

Dielectric breakdown is additionally significant in the plan of coordinated circuits and other strong state electronic gadgets. Protecting layers in such gadgets are intended to withstand ordinary working voltages, however higher voltage, for example, from electricity produced via friction may demolish these layers, delivering a gadget pointless. The dielectric quality of capacitors restricts how much energy can be put away and the sheltered working voltage for the gadget.

3.3 Coconut Oil Plane to Plane Electrode

In Fig. 2c all these curves start from 0 electric potentials then all these curves are increased up to consider electrode given potential then all the curves are linearly decreasing to 0 electric potentials. The gap spacing is increased then the electric potential decreases.

Utilizing present-day limited component procedures, the electric fields created by anodes can be precisely determined. This permits plans to be tried and improved before produce. Extraction and pillar speeding up cathodes can be demonstrated and reproduced radiates followed through them.

3.4 Coconut Oil Plate to the Plate Electrode

In Fig. 2d the arc length versus electric potential curves starts from 0 then it was increasing linearly then reach the particular electrode configuration given electric potential. Then the voltage is stable at a particular time. Then the electric potential is linearly reduced to 0. Corona shields are a kind of field molding cathode used to shield sharp focuses that would somehow experience the ill effects of the corona. The sharp focuses are generally unavoidable parts like jolts or different installations and fittings.

A corona shield builds the range of these focuses by in a real sense concealing them with adjusted terminals that are electrically associated so they are successful at a similar potential. Different names for corona shields are monitor rings and stress rings. Faltering is the place where particles assault cathode surfaces, thumping molecules off the surface. This cycle causes the disintegration of the terminal surface. Cathodes in plasmas experience the ill effects of faltering.

3.5 Sunflower Oil Point to Point

In Fig. 2e the high voltage electrode the voltages are applied is 50, 70, 80 and 100 V. The gap spacing is increased linearly. The arc length versus electric potential graph has these characteristics point to point 50 V 2 cm < point to point 70 V 4 cm < point to point 80 V 6 cm < point to point 100 V 10 cm.

3.6 Sunflower Oil Sphere to Sphere

In Fig. 2f at 17–18 cm arc length, the sphere to sphere 100 V 10 cm gap spacing has 0 electric potential then the configuration has linearly increases and reaches 100 V. In sphere to sphere 50 V 2 cm configuration at arc length 7 cm to 11 cm, the value of electric potential is 0 V. Then that curve increases and reaches 50 V.

The plan and manufacture of electrodes for direct current (dc) high voltage photoemission electron firearms can fundamentally impact their presentation, most prominently regarding the greatest attainable inclination voltage. Legitimate electrostatic plan of the triple-point intersection shield anode limits the danger of electrical breakdown (arcing) along with the protector link plug interface, while the cathode shape is intended to keep up <10 MV/m at the ideal working voltage focusing on almost no field discharge once molded.

3.7 Sunflower Oil Plane to Plane

In Fig. 3a the plane to plane 80 V 6 cm electrode configuration 10–12 cm arc length the electric potential is 80 V then that curve decreases linearly. In this graph plane to plane 70 V 4 cm electrode configuration at 2 cm arc length, the electric potential is 13 V. At 3 cm arc length, the electric potential is 25 V. At 9–11 cm arc length the electric potential remains 70 V then the electric potential decreases depending upon arc length.

3.8 Sunflower Oil Plate to Plate

In Fig. 3b plate to plate 50 V 2 cm electrode configuration 8–15 cm arc length, the electric potential is maximum almost close to 50 V. Then it linearly decreases. At 19.93 cm arc length, the electric potential is 0 V. The plate to plate 100 V 10 cm electrode configuration 13–23 cm arc length the electric potential is near to 100 V. Then the curve linearly decreases.

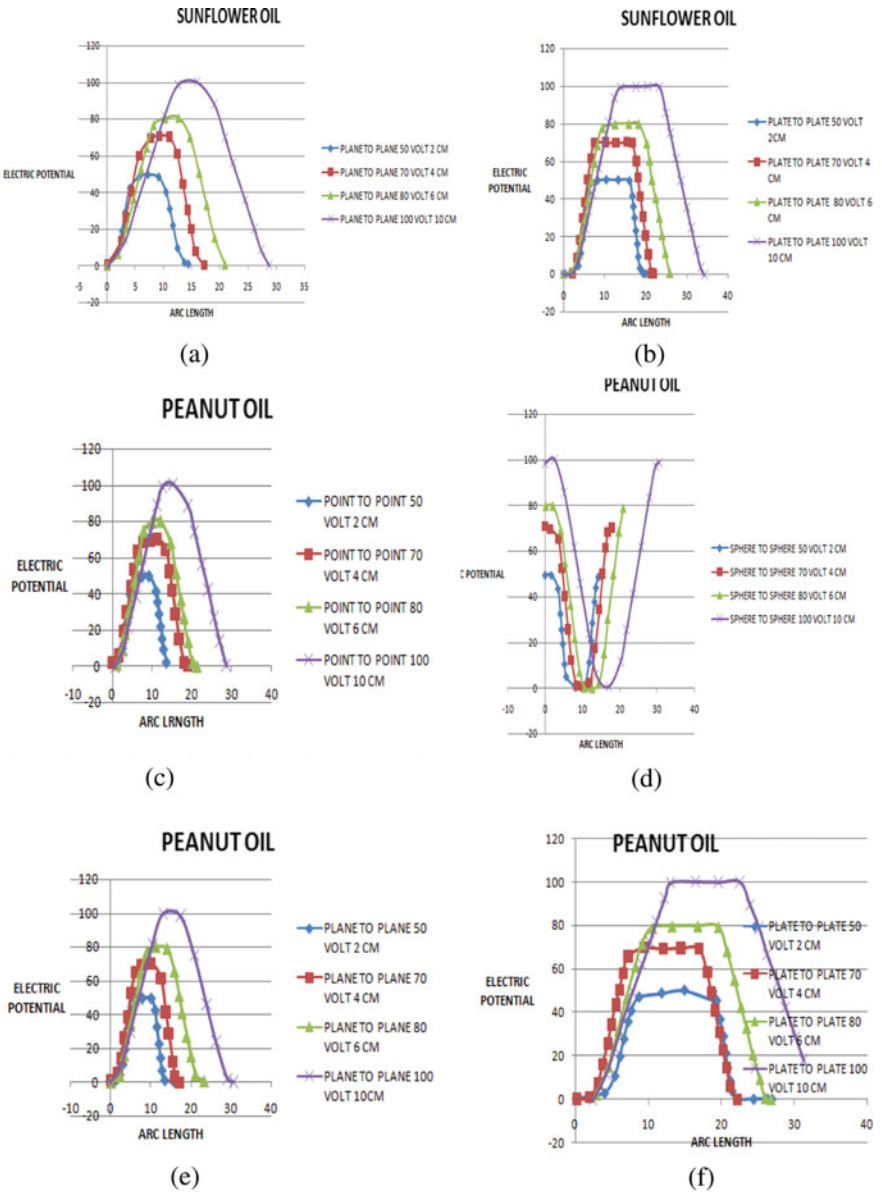

Fig. 3 Simulation result. **a** sunflower oil plane to plane, **b** sunflower oil plate to plate, **c** peanut oil point to point, **d** peanut oil sphere to sphere, **e** peanut oil plane to plane, **f** peanut oil plate to plate

The shape and material of the high-voltage electrode of an air pressure plasma age framework were advanced. The exploration was performed to accomplish the greatest consistency of plasma treatment of the outside of the low-voltage cathode with a measurement of 100 mm. To create low-temperature plasma with a volume of around 1 cubic decimetre, a beat volume release was utilized started with a corona release. The consistency of the plasma in the district of the low-voltage cathode was evaluated utilizing a framework for estimating the appropriation of release current thickness. The framework's low-voltage Electrode-gatherer—was a plate of 100 mm in distance across, the directing surface of which was isolated into 64 radially found sections of the equivalent surface region. The current at each portion was enlisted by a fast estimating framework constrained by an ARM-based 32-digit microcontroller. To encourage the understanding of results got, a PC program was created to imagine the outcomes. The program gives a 3D picture of the current thickness circulation on the outside of the low-voltage cathode.

3.9 Peanut Oil Point to Point

In Fig. 3c point to point 70 V 4 cm electrode configuration the maximum voltage almost equal to 70 V occurring at the arc length value of 7–11 cm. In point to point 80 V 6 cm electrode configuration. The maximum voltage almost 80 V occurring at 10–12 cm arc length. Then the curve linearly decreases.

3.9.1 Peanut Oil Sphere to Sphere

In Fig. 3d sphere to sphere 50 V 2 cm electrode configuration 1 and 14 cm arc length electric potential is maximum between 1 and 14 cm arc length points the electric potential value decreases. Sphere to sphere 100 V 10 cm electrode configuration the maximum electric potential occurring at 2 and 30 cm arc length. The response can be begun and halted by interfacing or detaching the two anodes. On the off chance that we place a variable opposition in the circuit, we can even control the pace of the net cell response by basically turning a handle. By interfacing a battery or other wellspring of current to the two anodes, we can drive the response to continue in its non-unconstrained, or invert course. By putting an ammeter in the outer circuit, we can quantify the measure of electric charge that goes through the terminals, and consequently the number of moles of reactants that get changed into items in the cell response.

3.9.2 Peanut Oil Plane to Plane

In Fig. 3e plane to plane 70 V 4 cm electrode configuration the maximum electric potential of 70 V occurring at the arc length value of 7–10 cm arc length. Plane

to plane 80 V 6 cm electrode configuration the maximum electric potential 80 V occurring at the arc length value of 11–14 cm arc length.

In most electrochemical tests our premium is focused on just one of the anode responses. Since all estimations must be on a total cell including two anode frameworks, it is normal practice to utilize a reference terminal as the other portion of the cell. The significant prerequisites of a reference cathode are that it be anything but difficult to get ready and keep up, and that it's likely to be steady.

3.9.3 Peanut Oil Plate to Plate

In Fig. 3f plate to plate 50 V 2 cm electrode configuration the maximum voltage of 50 V occurring at the arc length value of 14.92 cm. In plate to plate 100 V 10 cm electrode configuration the maximum voltage of 100 V occurring at the arc length values of 13–22 cm arc length.

A galvanic cell (here and there more suitably called a voltaic cell) comprises two half-cells joined by a salt extension or some other way that permits particles to pass between the different sides to look after electroneutrality. The customary method of speaking to an electrochemical cell of any sort is to compose the oxidation half response on the left and the decrease on the right.

4 Conclusion

A comparative study using three kinds of oil with different conductivity and permittivity and find out the field distribution of those oil using comsol software. From these results, coconut oil has the highest field distribution results compared to peanut oil and sunflower oil. Peanut oil has followed after coconut oil. The sunflower oil has the least field distribution values. So the result is coconut oil > peanut oil > sunflower oil.

Acknowledgements The authors are also grateful to the National Engineering College, Kovilpatti, Tamilnadu, India, for their support.

References

1. Cui Y, Ma H, Saha T, Ekanayake C, Martin D (2016) Particle tracing modelling on moisture dynamics of oil-impregnated transformer. IET Sci Meas Technol 10(4):335–343
2. Madavan R, Balaraman S (2017) Comparison of antioxidant influence on mineral oil and natural ester properties under accelerated aging conditions. IEEE Trans Dielectr Electr Insul 24(5):2800–2808. https://doi.org/10.1109/TDEI.2017.006527
3. Liao R, Lin Y, Zhang Y, Xia H (2016) Independent effects of aged oil and aged paper on moisture evaluation of power transformers. Electr Power Components Syst 44(5):556–564

4. Mariprasath TS, Victor K (2015) Pongamia Pinnata as alternate liquid dielectrics in distribution transformer: a critical study on the property of viscosity. Adv Energ Power 3:1–7. https://doi.org/10.13189/aep.2015.030101
5. Rao UM, Sood YR, Jarial RK (2016) Performance analysis of alternate liquid dielectrics for power transformers. IEEE Trans Dielectr Electr Insul 23(4):2475–2484. https://doi.org/10.1109/TDEI.2016.7556527
6. Al-Amin H, O'Brien J, Lashbrook M (2013) Synthetic ester transformer fluid: a total solution to windpark transformer technology. Renew Energ 49
7. Bakrutheen M, Karthik R, Madavan R (2013) Investigation of critical parameters of insulating mineral oil using semiconductive nanoparticles. In: Proceedings of IEEE international conference on circuit, power and computing technologies, ICCPCT 2013, pp 294–299. https://doi.org/10.1109/ICCPCT.2013.6529039
8. Thien YV, Azis N, Jasni J, Kadir Z, Yunus R, Ishak M, Yaakub Z (2016) The effect of polarity on the lightning breakdown voltages of palm oil and coconut oil under a non-uniform field for transformers application. Ind Crops Prod 89:250–256. https://doi.org/10.1016/j.indcrop.2016.04.061
9. Mehta DM, Kundu P, Chowdhury A, Lakhiani VK, Jhala AS (2016) A review of critical evaluation of natural ester vis-a-vis mineral oil insulating liquid for use in transformers: Part II. IEEE Trans Dielectr Electr Insul 23(3):1705–1712. https://doi.org/10.1109/TDEI.2016.005371

Managing the Smart Grid with Demand Side Management Using AntLion Optimization

Banala Venkatesh and S. Padmini

Abstract The demand Side Management (DSM) considered as the utmost key strategy applied to a Smart Grid (SG), which prepares consumers to yield accurate results regarding their consumption of electrical energy and supports the utility to curtail the peak load demand and restructure the demand curve. In this paper, a load shifting strategy has been applied for the DSM with huge number of controllable devices. To curtail the peak demand, decrease the electricity bill and to minimize the PAR, the load-shifting problem has been approached in hourly manner, throughout the 24 h in a day. Antlion Optimization (ALO) algorithm has been used to accomplish the objective of load shifting through minimization problem to the DSM and has been employed in residential loads of SG.

Keywords Smart Grid · Demand side management · Appliance scheduling · ALO algorithm · Load shifting

1 Introduction

In the modern age, things surrounding are getting smarter with respect to time. In near prospect, all our traditional power girds will convert to smart grids. The demand of electricity growing day by day will provide opportunities for future innovation to design our system very much effective, capable and smart. The main theme of converting the traditional grid to smart grid is to raise demand in calculation, computerization and communication to maintain the network by monitoring and controlling with the minimal manual interference.

The main features of the smart grid are capability, consistency; effectiveness, sustainability and consumer participation. Huge size grids has been mandatory for improved consistency. With the better quality, sustainability of assets beside with

B. Venkatesh (✉) · S. Padmini
SRM Institute of Science and Technology, Kattankulathur, Chengalpattu, India
e-mail: bv1006@srmist.edu.in

S. Padmini
e-mail: padminis@srmist.edu.in

C. Subramani et al. (eds.), *Proceedings of International Conference on Power Electronics and Renewable Energy Systems*, Lecture Notes in Electrical Engineering 795,
https://doi.org/10.1007/978-981-16-4943-1_29

consumer participation practical capability can be enlarged by means of Demand side management (DSM) [1]. The adjustment of customer demand for Electrical energy over different methods such as economic encouragements and interactive alteration over teaching is called DSM [2]. In DSM, customers are motivated to alter its regular electricity consumption plan on the source of power saving techniques, electric billing and economic encouragements [3]. So a practical generation capability has made and which reduces the dependency for large production. By applying demand side management, carbon emissions will get decreased by less utilization of peak load Generating plants, for example Diesel generators in peak load hours. Peak load hour and off-peak load hour are the two different kinds of energy demand. Peak load hours are from 11 am to 3 pm and from 6 to 9 pm and the remaining time is off peak load hours. Excess generation must be provide in order to meet the peak demand. DSM is the best option to reduce the necessity of more generation in the peak load hours.

The various techniques are used to apply DSM for the smart grid system as shown in Fig. 1. DSM is applied to various functions of SG in areas of electrical power market, infrastructure construction and electrical vehicles, by this way a DSM leads to most important parameter in SG [4]. By controlling and manipulating the energy demand, modified demand profile reduced maximum load demand can be obtained, that leads to the better stability of the system less cost of generation and less environment pollution. Energy utilization of customer is affected by penalties and emoluments in perfect levels of supply chain by means of smart tariff with

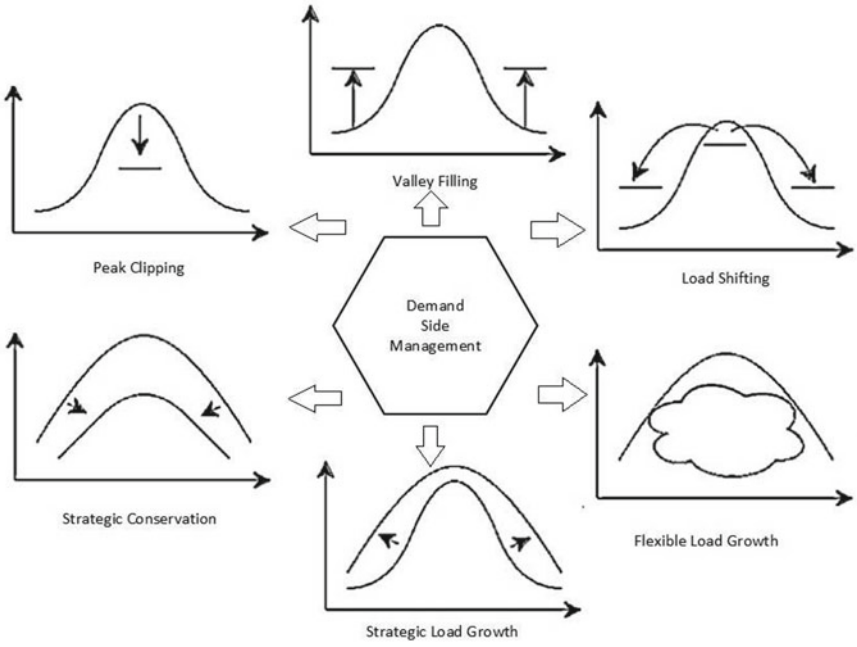

Fig. 1 Techniques of demand side management

DSM. However, DSM provides an opportunity to enhance the system performance, stability and security by improving the present infrastructure capability by helping to minimize the carbon technology throughout the system by playing an important role.

DSM helps in improving load factor that is accountable for maintain low electricity prices [5]. For reducing the highest demand through load shifting schemes are used which takes the advantage of loads altering from high load hours to off high load hours, strategic conversion is a non-traditional method which reduce the total consumption after the load shape changes at consumers. In recent years, Several DSM schemes and algorithms are evolved [6–9]. Traditional methods are dynamic programing and linear programming are mostly used. A huge variety of devices along with several metaheuristic methods, such as computational methods could not tackle such a huge number of controllable devices.

In this manuscript, we have articulated the problems of reduction of the peak load, electricity bill and Peak to average ratio, which will be conversed in later sections. A related method has been discoursed in paper offered by Logenthiran [10]. In this paper, an advanced method is proposed using Antlion optimization technique (ALO) for solving the DSM problem. The data of load and devices of smart grid, mentioned in paper [10] has been taken.

2 Problem Formulation

2.1 Minimization Function

The primary gaol in the DSM is to make the initial load curve as similar to our objective load curve. The modification can be done by applying DSM Techniques. Let us take the initial load curve as load_{in}. Let us assume the altered load curve obtained as load_{fi} by applying the techniques of DSM [11]. So, Then our objective can be framed as

$$\text{minimization } F_1 : \text{Max}\left(\text{Load}_{fi}\right) \tag{1}$$

$$\text{minimization } F_2 : \sum_{H=1}^{h}\left(\text{Load}_{fih}.E_h\right) \tag{2}$$

$$\text{minimization } F_3 : \text{Min(PAR)} \tag{3}$$

From the above functions, F_1 represents the highest peak value of final load curve, that we want to be minimized laterally with the function F_2 denoting the final cost of energy over a Twenty fourhour duration interval and E_h is the electricity price in hth hour and Function F_3 denotes the peak to average ratio of the system.

From the above Eqs. 1 and 2 the final load curve is obtained as by estimation the load alteration as function F_h

$$\min F_h : [|\mathrm{RLM}_h| - |\Delta \mathrm{Load}_h|] \tag{4}$$

Subject to for all $h = 1, 2, 3, \ldots, N$. where N is the time step number in hour wise block.

The estimated load correction for each time step hour h can be obtained from RLM i.e., Reducible load Margin, which is given by

$$\mathrm{RLM}_h = \mathrm{Forecast}_h - \mathrm{obj}_h \tag{5}$$

Equation (5) governs the estimated load, which desires to be remove fully or partially or added to the initial load curve at various hour slots that makes it as close as to objective load curve.

$$\mathrm{RLM}_h = \begin{cases} \geq 0 \ \mathrm{Forecast}_h > \mathrm{obj}_h \\ \leq 0 \ \mathrm{Forecast}_h < \mathrm{obj}_h \end{cases} \tag{6}$$

The minimization of Peak to Average ratio leads to improvement in system performance and system stability, it is expressed as

$$\mathrm{PAR} = \frac{\mathrm{Load}_{\max}}{\mathrm{Load}_{\mathrm{mean}}} = \frac{\mathrm{Load}_{\max}}{\frac{\sum_n \mathrm{Load}}{N}} \tag{7}$$

Here, total hourly time slot is denoted as N, peak load is denoted as $\mathrm{Load}_{\max}$, Average value of the load is represented as $\mathrm{Load}_{\mathrm{mean}}$.

2.2 Constraints

The following are the constraints developed for the above minimization problem.

- The type of the shifted device should be greater than zero always in all time slots [11]

$$x_{kh} > 0 \quad \forall k, h \tag{8}$$

- The available number of controllable devices of that particular must always be less than the number of devices to be shifted

$$\sum_{k=1}^{h} x_k \leq \mathrm{controllable}(k) \tag{9}$$

2.3 Calculation of Controllable Devices

There are two types of controllable devices are there in the DSM scheme which is a most important thing. One is Non-shiftable devices, those are fixed to run under defined time slot e.g. refrigerator, T.V. etc. Another one is Shiftable devices, which are flexible to run under any time slot e.g. washing machine, dryer, dishwasher etc. in this work the shiftable devices from residential area of the smart grid test system is considered for solving the DSM Problem. The devices setup in the residential areas for controlling the load typically consumes less amount of power and the running time slot is very slow. In residential area, 2604 manageable devices contains of 14 various devices are installed [10].

3 AntLion Optimization (ALO)

Here antlion method is taken which is referred from the paper [12]. The technique ALO is a newly designed Evolutionary metaheuristic searching method, which imitates the antlions hunting method in nature. By this method, ant and antlions defined by means of searching managers are represented to discover answers by stages of capturing the target prey, which contains the arbitrary walking direction of ants, construction of setups, making the ants to fall in trap, capturing the target prey, and reconstruction the traps.

Ants passage randomly in Wildlife while hunting for nutrition, so at each step an arbitrary walk by an ant is represented as

$$Z_k = [0; p(1) + p(2); \ldots; \sum_{j=1}^{N-1} p(j); \sum_{j=1}^{N} p(j) \tag{10}$$

where $k = 1, \ldots,$ dimen, dimen is the dimension of ant, N is the iteration number, $Z = [Z_1; \ldots; Z_{\text{dimen}}]$, Z_k is a $(N + 1) \times 1$ matrix, and $p(j)$ is a Random function and can be expressed as:

$$p = \begin{matrix} 1 & \text{if rand} > 0.5 \\ -1 & \text{if rand} < 0.5 \end{matrix} \tag{11}$$

Here rand is a arbitrary number produced by even spreading among 0 to 1.

The walking of ants has to be altered to the accurate position in actual search space permitting to the limited boundaries. Position can be calculated using Eq. (12):

$$Y_k = \left(\frac{Z_k - l_k}{m_k - l_k} \right) * (o_k - n_k) + n_k \tag{12}$$

where l_k and m_k is the min and max values of Z_k, n_k, and o_k denotes the min and max of antlion in the kth dimension respectively, $Y = [Y_1; \ldots; Y_{\text{dim}}]$,

Y_k is a $(N + 1) \times 1$ matrix. Z_k is normalized in range of [0, 1] using $Z_k - l_k / Z_k - m_k$, then it is converted into domain $[n_i, o_i]$ using Eq. 12.

The ants' movements are affected by antlions' traps. This can be described as:

$$n = n^0 + \text{Antlion}, \quad o = o^0 + \text{Antlion} \tag{13}$$

where n' and o' is the min and max of varying boundary at current iteration,

In the ALO algorithm, Elitism procedure is used. That means that a Global best antlion is chosen as elite antlion during process of optimization.

Random walking of the ant will be governed by the position update of each ant, which is selected by Roulette wheel and elite. It can be found as:

$$\text{Ant} = \frac{R_A + R_E}{2} \tag{14}$$

where Ant is the novel location, R_A is the Roulette wheel nominated antlion, R_E is elite antlion. Updated position of ant must be change if the ant crosses its boundaries.

The antlion should takes its position when the ant grasps the quarry and is greater than the antlion. This procedure is known as prey catching, and it is given as:

$$\text{Antlion} = \text{Ant}, \text{ if } f(\text{Ant}) < f(\text{Antlion}) \tag{15}$$

4 Test Smart Grid System

To validate the efficiency of the suggested method, the proposed DSM strategy is applied on residential area smart grid. Figure 2 shows the Utility of the smart grid. The operating voltage of electrical network is 400 V. The connection among the two grids has a 0.003 pu resistance, 0.01 pu. reactance. The residential area system microgrid length is 2 km. This network data is for utilized for planning of resources without any congestion (Table 1).

The main goal of DSM is decrease the utility bills of customers in all the three areas. Therefore, a nonlinear relationship should be there between objective load curve and electricity tariff. The equal electricity tariffs are applicable to all areas in the smart grid. Simulations were carried out with a maximum allowable delay of 12 h. The performance of the algorithm would be better if there is a longer delay, since the number of loads related to load shifting increases, leads to improved results.

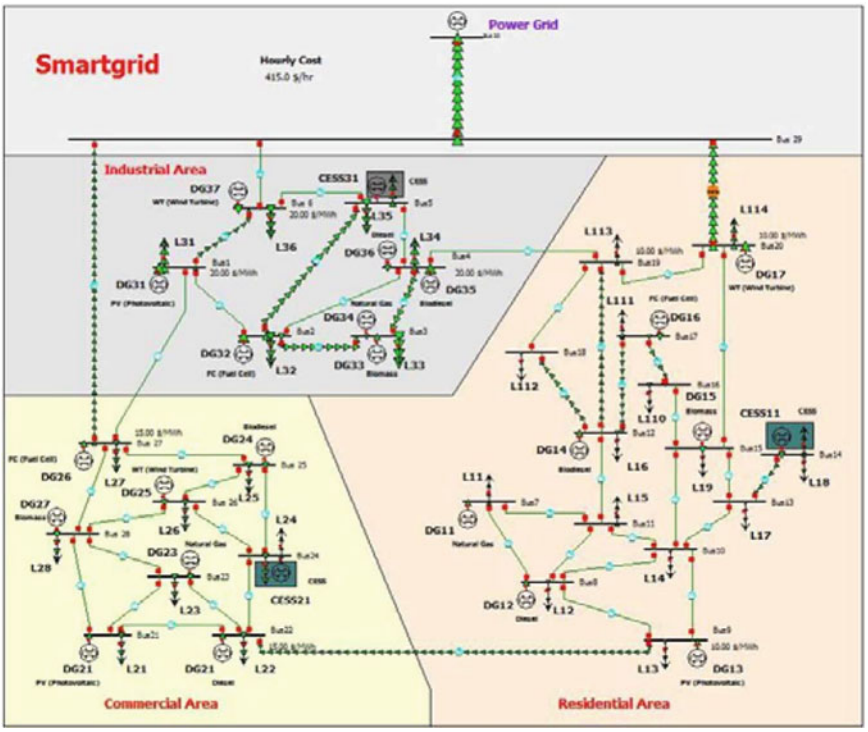

Fig. 2 Smart grid network

Table 1 Data for the residential smart grid area

Name of the device	Hourwise power utilization of each Device (kW)		
	1st hour	2nd hour	3rd hour
Dryer	1.2		
Dish washer	0.7		
Washing machine	0.5	0.4	
Oven	1.3		
Iron	1.0		
Vaccum	0.4		
Fan	0.20	0.20	0.20
Kettle	2.0		
Toaster	0.9		
Rice cooker	0.85		
Hair dryer	1.5		
Blender	0.3		

5 Results and Discussions

ALO Technique has been applied for the residential area for the DSM problem in Sect. 3. Different set of devices are there in each section with various features like different operating hours, schedule and power consumption.

Figure 3 Show the power analysis of demand for 24 h duration. From the graph the maximum energy consumption by the device is 2000 W and minimum consumption of the device is 40 W. Figure 4 shows the power consumption analysis of various devices (Table 2).

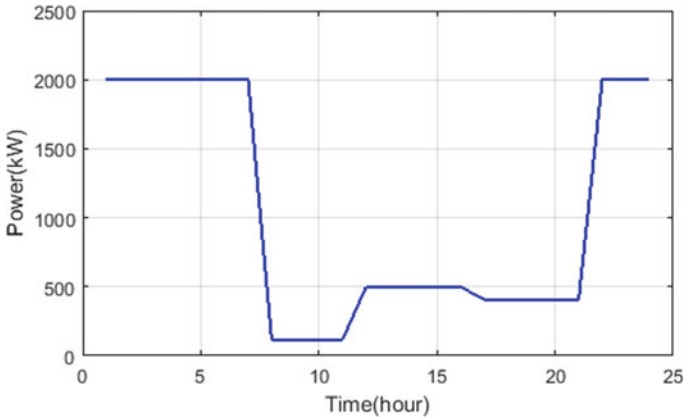

Fig. 3 Demand analysis

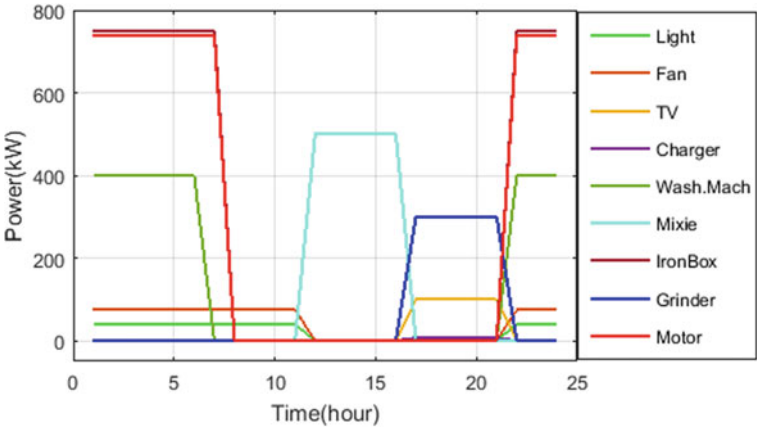

Fig. 4 Individual power analysis

Table 2 Maximum load and electricity bill reduction

Technique	Maximum load without DSM (KW)	Maximum load with DSM (KW)	Percentage of reduction (%)	Electricity bill without DSM (rupees)	Electricity bill DSM (Rupees)	Percentage of reduction (%)
PSO	1540	1334.1	15.4	3080	2668.2	15.4
ALO	1540	1309.4	17.64	3080	2618.8	17.64

6 Conclusion

DSM technique in SG is presented in this paper with ALO technique. DSM has gaining a lot of attention, because of its benefits in smart grid. During peak hours, extra demand of power gets reduces, reduces the electricity bill of the customers and reduction in the PAR value. In this paper, ALO algorithm has been adopted which obtains a better result compared to PSO and reduces the peak demand, substantial savings in energy bill and PAR value, carried on residential loads of the smart grid.

References

1. Guelpa E et al (2019) Demand side management in district heating networks: a real application. Energy 182:433–442
2. Tang R, Wang S, Li H (2019) Game theory based interactive demand side management responding to dynamic pricing in price-based demand response of smart grid. Appl Energ 250:118–130
3. Khan A, Javaid N, Ahmad A, Akbar M, Khan Z, Ilahi M (2018) A priority-induced demand side management system to mitigate rebound peaks using multiple knapsack. J Ambient Intell Humanized Comput 10(4):1655–1678
4. Su H, Zio E, Zhang J, Chi L, Li X, Zhang Z (2019) A systematic data-driven Demand Side Management method for smart natural gas supply systems. Energ Convers Manag 185:368–383
5. Kumar K, Saravanan B (2019) Day ahead scheduling of generation and storage in a microgrid considering demand Side management. J Energ Storage 21:78–86
6. Yilmaz S, Chambers J, Patel M (2019) Comparison of clustering approaches for domestic electricity load profile characterisation—implications for demand side management. Energy 180:665–677
7. Walzberg J, Dandres T, Merveille N, Cheriet M, Samson R (2019) Accounting for fluctuating demand in the life cycle assessments of residential electricity consumption and demand-side management strategies. J Cleaner Prod 240:118–251
8. Luo X, Fong K (2019) Development of integrated demand and supply side management strategy of multi-energy system for residential building application. Appl Energ 242:570–587
9. Peltokorpi A, Talmar M, Castrén K, Holmström J (2019) Designing an organizational system for economically sustainable demand-side management in district heating and cooling. J Cleaner Prod 219:433–442
10. Logenthiran T, Srinivasan D, Shun T (2019) Demand side management in smart grid using heuristic optimization. IEEE Trans Smart Grid 3(3):1244–1252

11. Gupta I, Anandhini GN, Gupta M (2016) An hour wise device scheduling approach for demand side management in smart grid using Particle swarm optimization. In: National power systems conference. https://doi.org/10.1109/npsc.2016.7858965
12. Mirjalili S (2015) The ant lion optimizer. Adv Eng Softw 83:80–98

Comparison of PI Based and ANN Based Dynamic Voltage Restorer Controller for Voltage Sag Mitigation in Distribution System

T. Jane Tracy and N. Rathina Prabha

Abstract In recent years, one of the major concerns in the distribution system is the quality of power at the consumer side. Out of all power quality issues, voltage sag is the most frequent one. The Dynamic Voltage Restorer (DVR) is one of the effective ways for protecting sensitive loads from Voltage sag/swell conditions. In this paper design and analysis of DVR for mitigating voltage sag is done by means of MATLAB/SIMULINK. The results of conventional DVR controller using PI are compared with Artificial Neural Network (ANN).

Keywords Artificial Neural Network (ANN) · Custom Power System Devices (CUPS) · Dynamic Voltage Restorer (DVR) · Total Harmonic Distortion (THD)

1 Introduction

Nowadays the interest on power quality has increased very high. This is mainly due the problems created by the poor power quality by the consumers and the utilities [1]. Among the entire power quality disturbance Voltage Sag is considered as the most frequently occurring one in a distribution system. The major features that categorize the voltage sag are its magnitude and duration of occurrence.

There are many custom power devices used to mitigate the voltage sag. Among this DVR is considered as the most effective way to protect the sensitive loads in a power system from voltage sag and swell [4, 5]. DVR is the series connected custom power device used for the injection of required voltage in series to the system to regulate the load.

T. Jane Tracy (✉) · N. Rathina Prabha
Department of Electrical and Electronics Engineering, Mepco Schlenk Engineering College, Sivakasi, India

N. Rathina Prabha
e-mail: nrpeee@mepcoeng.ac.in

C. Subramani et al. (eds.), *Proceedings of International Conference on Power Electronics and Renewable Energy Systems*, Lecture Notes in Electrical Engineering 795,
https://doi.org/10.1007/978-981-16-4943-1_30

2 Analysis of Voltage Sag

Voltage sag indices are experienced by customers when they share a common supply impedance with an over current event on the supply system [7]. The voltage dip must be quantified using some of the indices. Some of the important indices are as follows.

2.1 Detroit Edison Sag Score (SS)

The Detroit Edison sag score is defined as follows

$$S = \frac{V_a + V_b + V_c}{3} \tag{1}$$

where V_a, V_b, V_c are the RMS value of the phase voltage in terms of per unit. This method does not consider the time duration of voltage sag.

2.2 Voltage Sag Lost Energy Index (VSLEI)

When there is a three phase fault in a distribution system the Voltage Sag Lost Energy Index can be given as [10].

$$W = \left\{1 - \frac{V_a}{V_{\text{nom}}}\right\}^{3.14} \times T_a + \left\{1 - \frac{V_b}{V_{\text{nom}}}\right\}^{3.14} \times T_b + \left\{1 - \frac{V_c}{V_{\text{nom}}}\right\}^{3.14} \times T_c \tag{2}$$

where V_a, V_b, V_c are the voltages in three different phases. The value of T_a, T_b, T_c represent the time duration of sag for all the three phases.

3 Schematic Diagram of Dynamic Voltage Restorer

Figure 1 shows the schematic diagram of DVR. The DVR injects the missing voltage caused due to the disturbance, faults or any problem caused in the distribution system. The components of DVR are as follows [4]:

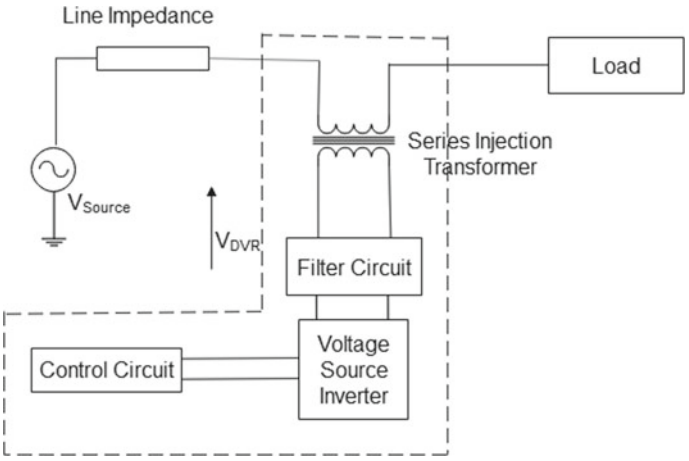

Fig. 1 Schematic diagram of DVR

3.1 DC Energy Storage Device

The source for the VSI is given from a DC energy storage device. These energy storage devices are used to supply the required real power when DVR is providing compensation.

3.2 Control Circuit

The control circuit for DVR compares the load voltage with the reference value to produce the control signal for the PWM generator [6]. This helps to maintain the voltage magnitude at the point of common coupling.

3.3 Voltage Source Inverter (VSI)

The purpose of the Voltage Source Inverter is to convert the DC voltage available from the energy storage device into AC voltage based on the control circuit output.

3.4 Passive Filter Unit

The main purpose of the passive filter circuit is to filter out the harmonics present in the voltage generated from the VSI.

3.5 Series Injection Transformer

The series injection transformer is particularly designed to inject the required compensation voltage to the sensitive load side. The main functions of the series injection transformer are coupling, protection and voltage injection.

4 Controlling Method of DVR

The control circuit in a DVR plays a vital role. It gives a fast response during voltage sags or variation in load [12]. The control of DVR is done by detecting, measuring, synchronizing and performing transformation. This is done to do the voltage compensation during any voltage sag condition. In this paper a feed forward based control with Phase Locked Loop (PLL) is used. The load voltage given to the sensitive load is measured. The three phase *abc* voltage is converted into dq_0 voltage by means of Park transformation. The PLL is used to synchronize the load voltage with the reference voltage and helps to derive the unit vectors $\sin\theta$ and $\cos\theta$. The transformation is given by the equation

$$\begin{bmatrix} V_d \\ V_q \\ V_0 \end{bmatrix} = \begin{bmatrix} \cos\theta & \cos\left(\theta - \frac{2\pi}{3}\right) & 1 \\ -\sin\theta & -\sin\left(\theta - \frac{2\pi}{3}\right) & 1 \\ \frac{1}{2} & \frac{1}{2} & \frac{1}{2} \end{bmatrix} \begin{bmatrix} V_a \\ V_b \\ V_c \end{bmatrix} \tag{3}$$

The reference signal is compared with the load voltage so as to obtain the input signal for the controller. The equation is given by

$$\begin{bmatrix} V_{\mathrm{DVR}a} \\ V_{\mathrm{DVR}b} \\ V_{\mathrm{DVR}c} \end{bmatrix} = \begin{bmatrix} \cos\theta & \sin\theta & 1 \\ \cos\left(\theta - \frac{2\pi}{3}\right) & \sin\left(\theta - \frac{2\pi}{3}\right) & 1 \\ \cos\left(\theta + \frac{2\pi}{3}\right) & \sin\left(\theta + \frac{2\pi}{3}\right) & 1 \end{bmatrix} \begin{bmatrix} V_d \\ V_q \\ V_0 \end{bmatrix} \tag{4}$$

Now the generated three phase voltage is used to produce the PWM modulation signal. This produces the required sinusoidal voltage from the voltage source inverter. This will help in the improvement of the voltage profile into the nominal load voltage.

5 Simulation and Results

The performance of Dynamic Voltage Restorer for the different fault condition is analyzed by the simulink model shown in Fig. 2.

In Fig. 2, 11 kV source is connected to the load via a transformer. The DVR is connected at the point of common coupling. The specifications of the given system are as shown in Table 1.

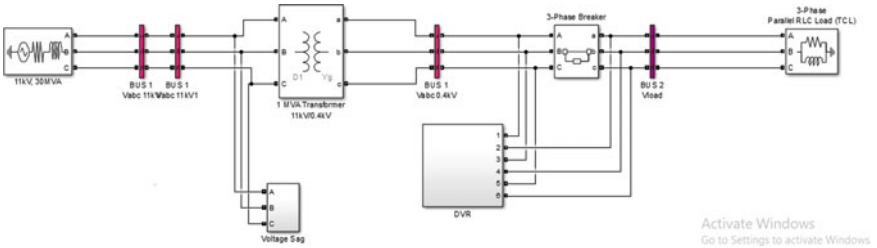

Fig. 2 Matlab simulink model of DVR for protection of sensitive load

Table 1 System parameters

Parameter	Value
Source	11 kV, 30 MVA
Transformer	11 kV/0.4 kV, 1MVA
Parallel RLC Load	400 V, 4.42 kV
DC Supply	500 V
Series injection transformer	10 V/100 V, 1.5 kVA
Line impedance	1 Ω, 1 mH, 20 μF

In this paper, sag for a time period of 100 ms is considered. Analysis and performance of DVR for single line to ground fault, double line to ground fault and three phase fault is done. The results are obtained for both PI based DVR controller and Artificial Neural Network based DVR controller are obtained.

Figure 3 shows the voltage sag from $t = 0.2$ to $t = 0.3$ s. Here the voltage for the different sections in the distribution system is shown. i.e. for the 11 kV line, for 400 V line and the sensitive load. The graph clearly shows that there is voltage sag in the transmission line. But when it reaches the load terminal, the voltage remains

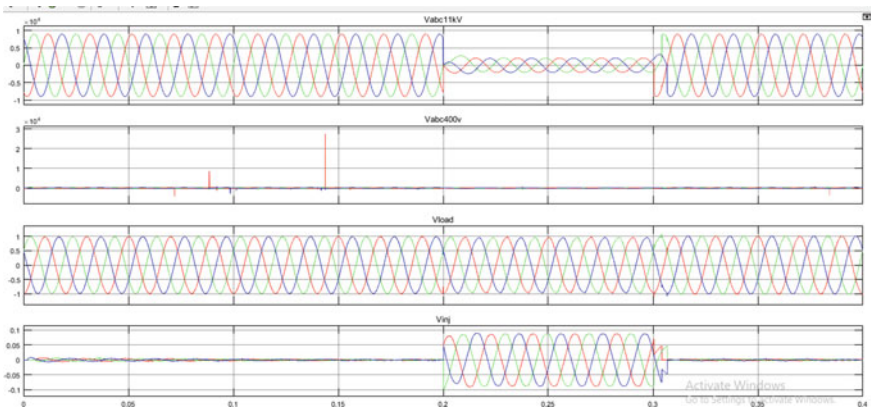

Fig. 3 Voltage sag for 100 ms

Table 2 Single line to ground fault

Sag%	V_{rms} (p.u)			SS	VSLEI	Total Harmonic Distortion (THD)		
	V_A	V_B	V_C			V_{abc} 11 kV	V_{abc} 400 V	V_{abc} load
10	0.94	1.01	0.95	0.972	0.016	2.62	1.68	0.84
25	0.87	1.01	0.90	0.927	0.239	7.10	4.30	0.84
50	0.74	1.01	0.82	0.858	1.959	16.48	9.51	1.02
75	0.61	1.07	0.75	0.804	6.602	29.19	15.7	1.16
85	0.57	1.04	0.73	0.777	8.917	35.53	18.6	1.25
90	0.95	1.03	0.71	0.759	10.89	39.01	30.1	1.21

Table 3 Double line to ground fault

Sag%	V_{rms} (p.u)			SS	VSLEI	Total Harmonic Distortion (THD)		
	V_A	V_B	V_C			V_{abc} 11 kV	V_{abc} 400 V	V_{abc} load
10	0.91	0.96	0.97	0.943	0.063	3.24	3.38	0.89
25	0.77	0.9	0.92	0.862	1.084	8.93	9.27	1.03
50	0.55	0.79	0.85	0.730	9.198	21.42	22.2	1.40
75	0.35	0.69	0.80	0.614	28.60	39.3	41.6	2.16
85	0.29	0.65	0.79	0.575	39.22	48.43	52.1	2.4

Table 4 Three phase to Ground Fault

Sag%	V_{rms} (p.u)			SS	VSLEI	Total harmonic distortion (THD)		
	V_A	V_B	V_C			V_{abc} 11 kV	V_{abc} 400 V	V_{abc} load
10	0.91	0.91	0.91	0.91	0.156	2.9	3.38	0.84
25	0.77	0.77	0.77	0.77	3.012	8.00	9.31	1.03
50	0.56	0.56	0.56	0.56	23.27	19.25	22.2	1.82
75	0.34	0.34	0.34	0.34	79.83	35.99	41.6	2.75
85	0.28	0.28	0.28	0.28	107.4	45.14	52.1	3.10

constant. This is due to the presence of DVR which injects the voltage required by the load.

During the voltage sag from time $t = 0.2$ s to $t = 0.3$ s, the THD analysis is done and the results show that the THD value is 13.66% for the source voltage but it reduces to 1.94% for the load voltage due to the presence of DVR.

5.1 For PI Based DVR Controller

Tables 2, 3 and 4 show the RMS value of voltage for the three different phases for different percentage of voltage sag. The THD value at the load side clearly indicates that with the presence of Dynamic Voltage Restorer the harmonics has been greatly reduced.

5.2 For ANN Based DVR Controller

The artificial neural network works on the three steps i.e. training, validation and testing. The output obtained from the PI based controller is used to train the artificial neural network and the output is obtained for the three above mentioned faults.

Tables 5, 6 and 7 give the RMS voltage for single phase to ground fault, double line to ground fault and three phase to ground fault. The THD for load voltage is measured. The results show that the THD is reduced greatly at the load side with the help of DVR.

Table 5 Single line to ground fault

Sag%	V_{rms} (p.u)			SS	VSLEI	Total harmonic distortion (THD)		
	V_A	V_B	V_C			V_{abc} 11 kV	V_{abc} 400 V	V_{abc} load
10	0.95	1	0.97	0.974	0.009	2.7	1.53	0.8
25	0.88	1	0.93	0.936	0.149	7.32	4.02	0.81
50	0.78	1	0.89	0.89	1.019	14.8	7.78	1.01
75	0.64	1	0.84	0.826	4.449	29.8	14.6	1.08
85	0.57	1	0.82	0.8	7.103	30.49	16.0	1.14

Table 6 Double line to ground fault

Sag%	V_{rms} (p.u)			SS	VSLEI	Total harmonic distortion (THD)		
	V_A	V_B	V_C			V_{abc} 11 kV	V_{abc} 400 V	V_{abc} load
10	0.92	0.96	0.97	0.947	0.052	3.23	3.37	0.96
25	0.76	0.89	0.92	0.853	1.202	8.92	9.27	1.13
50	0.55	0.79	0.85	0.732	9.144	21.4	22.3	1.35
75	0.35	0.69	0.81	0.616	28.91	39.26	41.6	2.05
85	0.29	0.65	0.78	0.572	39.29	48.37	52.2	2.12

Table 7 Three phase to ground fault

Sag%	V_{rms} (p.u)			SS	VSLEI	Total harmonic distortion (THD)		
	V_A	V_B	V_C			V_{abc} 11 kV	V_{abc} 400 V	V_{abc} load
10	0.91	0.91	0.91	0.91	0.140	2.9	3.37	0.85
25	0.76	0.76	0.76	0.76	3.221	7.99	9.27	1.42
50	0.54	0.54	0.54	0.54	26.01	19.23	22.3	1.72
75	0.34	0.34	0.34	0.34	81.76	35.98	41.6	2.50
85	0.29	0.29	0.29	0.29	104.1	45.10	52.2	2.77

6 Conclusion

The working of Dynamic Voltage Restorer for the mitigation of voltage sag in the load side is analyzed in this paper. Here, the DVR is controlled by PI based controller and ANN based controller. The results show that when the voltage sag is very low (i.e. less than 50%) then the performance of PI based controller and ANN based controller remains the same. But when the voltage sag is very high (i.e. greater than 50%) then the performance of ANN is better when compared with PI based controller.

References

1. Wang ZQ, Zhou SZ, Guo YJ (2002) Comparisons on ways of magnitude characterization of power quality disturbances. In: Proceedings of the 2002 large engineering systems conference on power engineering. IEEE, 0-7803-7.520-3
2. Safdarian A, Fotuhi-Firuzabad M, Lehtonen M (2019) A general framework for voltage sag performance analysis of distribution networks. Energies 12:2824
3. Wang B, Ye J, Manandhar U, Ukil A, Gooi HB (2017) A DC microgrid integrated dynamic voltage restorer with model predictive control. 978-1-5386-0971-2/17 IEEE
4. Gayatri M, Parimi AM, Pavan Kumar AV (2015) Application of dynamic voltage restorer in micro grid for voltage sag/swell mitigation. In: 2015 IEEE power, communication and information technology conference (PCITC). https://doi.org/10.1109/PCITC.2015.7438096, October 2015
5. Benachaiba C, Ferdi B (2008) Voltage quality improvement using DVR. Electr Power Qual Utilisation J XIV(1)
6. Raut PA, Kalgunde MN (2015) An overview and design of dynamic voltage restorer to improve power quality in microgrid. In: 2015 international conference on energy systems and applications (ICESA 2015). 978-1-4673-6817-9/15, 2015 IEEE
7. Babu BP, Indragandhi V (2019) A review on dynamic voltage restorer in power systems concerned to the issues of power quality. IOP Conf Ser Mater Sci Eng. https://doi.org/10.1088/1757-899X/623/1/012015, VCADPCA 2019
8. Hamoud F, Doumbia ML, Cherit A (2017) Voltage sag and swell mitigation using DSTATCOM in renewable energy based distributed generation systems. In: 2017 twelfth international conference on ecological vehicles and renewable energies (EVER). 978-1-5386-1692-5117, 2017

Design of Quadratic Boost Converter for Renewable Applications

B. Abinayalakshmi, S. Muralidharan, and J. Gnanavadivel

Abstract This project work aims in exploring a quadratic boost converter which has low voltage ripple achieved using extreme duty cycles and PWM strategy. Normal quadratic boost converter topologies require a higher amount of stored energy by available in the capacitors used. The energy stored capability is directly proportional to the size of the capacitors. By using the minimum stored energy method, the converter size reduces. Also this transformer less proposed topology is suitable for renewable energy applications.

Keywords Pulse Width Modulation (PWM) · Direct current (DC) · Quadratic boost converter (QBC) · Switching time (TS)

1 Introduction

In this paper, the non isolated power converter topology is used [2]. Low storing energy capacitors cause reduced switching losses and increased efficiency [3]. The non isolated power converter is a single circuit having the current flow between the input and the output. Compared to the boost converter, the quadratic boost converters provide double the level of the output voltage at the same duty ratio [5]. This converter use the smaller size capacitor for the particular output voltage ripple specifications [1–10]. Reduced voltage ripples content and improved power quality DC-DC QBC converters [11–13].

B. Abinayalakshmi (✉) · S. Muralidharan · J. Gnanavadivel
Mepco Schlenk Engineering College, Sivakasi, India
e-mail: janusakthi2000@gmail.com

S. Muralidharan
e-mail: smurali@mepcoeng.ac.in

C. Subramani et al. (eds.), *Proceedings of International Conference on Power Electronics and Renewable Energy Systems*, Lecture Notes in Electrical Engineering 795,
https://doi.org/10.1007/978-981-16-4943-1_31

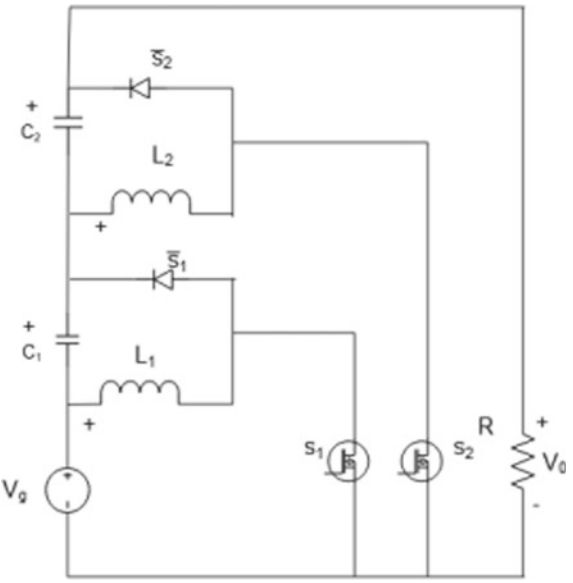

Fig. 1 Proposed QBC circuit diagram

2 Proposed QBC Circuit Diagram

At constant frequency, both the two transistors are commutating with the same duty cycle ratio. The 180° phase shift occurs between both of them (Fig. 1).

3 Dynamic Model of Quadratic Boost Converter

The traditional state averaging technique applies to express the dynamic model of this converter topology. This converter topology can be expressed as,

$L_1\left(\mathrm{d}i_{L_1}/dt\right) = \mathrm{d}V_g - (1-d)V_{c_1}$ (i)
$L_2\left(\mathrm{d}i_{L_2}/\mathrm{d}t\right) = d\left(V_g + V_{c_1}\right) - (1-d)V_{c_2}$ (ii)
$C_1\left(\mathrm{d}V_{c_1}/\mathrm{d}t\right) = (1-d)i_{L_1} - \mathrm{d}i_{L_2} - i_0$ (iii)
$C_2\left(\mathrm{d}V_{c_2}/\mathrm{d}t\right) = (1-d)i_{L_2} - i_0$ (iv)

Vg, V_{C_1}, V_{C_2}—input voltage, voltage across the capacitors C_1, C_2 respectively.
i_{L_1}, i_{L_2}—current flows through the $L1$ and the $L2$ inductors respectively.
i_0, R—converter output current, load resistance respectively.

The output voltage and the output current can be express as,

$$V_0 = V_g + V_{c_1} + V_{c_2} \tag{1}$$

$$i_0 = V_0/R \tag{2}$$

$$V_{c_1} = \frac{Dv_g}{1-D} \tag{3}$$

$$V_{c_2} = Dv_g/(1-D) \tag{4}$$

$$I_{L_1} = I_0/(1-D) \tag{5}$$

$$I_{L_2} = I_0/(1-D) \tag{6}$$

$$V_{c_2} = DV_g/(1-D)^2 \tag{7}$$

4 Modes of Operation

MODE I
During this operation, the capacitor C_1 is discharging and the C_2 is charging. The S_1 switch is on and S_2 switch is off (Fig. 2).

MODE II
During this operation, both the C_1 and the C_2 are discharging. Both S_1 and S_2 switches are on.

MODE III
During this operation, both the C_1 and the C_2 are charging. Both S_1 and S_2 switches are off.

MODE IV During this operation, the C_1 is charging and the C_2 is discharging. The S_1 switch is off and S_2 switch is on.

4.1 Selections of Inductors

(1) **L1 Inductor** The L_1 voltage is equal to the input voltage, when the S_1 switch is closed. During the time period of the DTs, the current rises with the Vg/L_1 slope and also total ripple increases twice of the ΔL_1.

$$L_1 = \left(V_g/2\Delta i_{L_1}\right)\text{DTs}$$

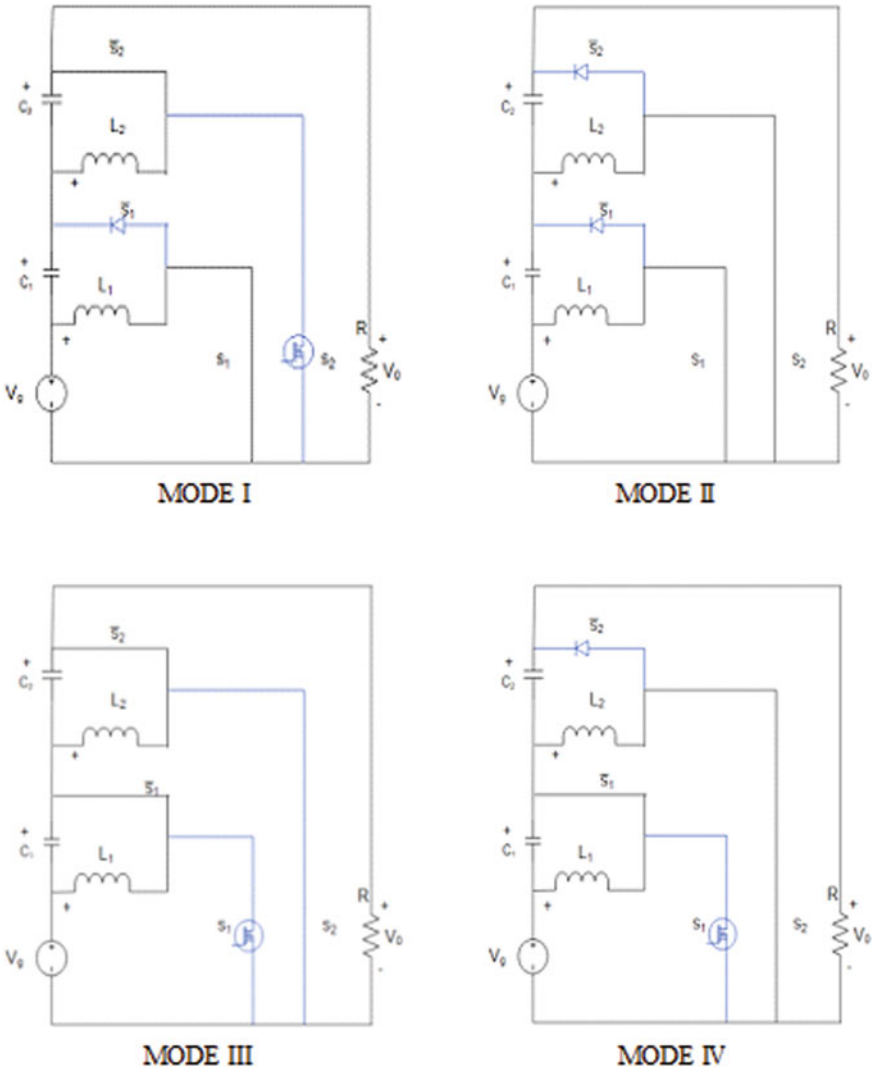

Fig. 2 Modes of operations

(2) L_2 Inductor The L_2 voltage is equal to the $V_{C1} + Vg$, When the switch S_2 is closed. During the period of DTs, the current rises with the $(V_{C1} + Vg)/L_2$ slope.

$$L_2 = \left(V_g/2\Delta i_{L_2}\right)(1/1 - D)\text{DTs}$$

4.2 Selection of Capacitors

In this converter, the four possible switching states are occur at particular duty cycle. During the switching period three switching states are involved. For our convenient consider as ($C_1 = C_2$). 1. $D > 0.5$, 2. $D < 0.5$, 3. $D = 0.5$.

(a) During t_2, the converter operation

$$\Delta V_0/\Delta t| \quad t_2 = -((I_{L_2} - I_0)/c_2) - (I_0/c) = -((I_{L_2} - 2I_0)/c)$$

During $t_2 = (1 - D)\, T_s$, Due to switching in t_2, the output voltage can be express as,

$$\Delta V_0/\Delta t| \quad t_2 = -((I_{L_2} - I_0)/c_2) - (I_0/c)(1 - D)T_S = -((I_{L_2} - 2I_0)/c)(1 - D)T_S$$

(b) During t_1 and t_3, the converter operation

$$\Delta V_0/\Delta t| \quad t_1, t_3 = -((I_{L_2} + I_0/c_1) - (I_0/c_2) = -((I_{L_2} + 2I_0/c)$$

Therefore, t_1 and $t_3 = \mathrm{DTs} - (1 - D)\, T_s = (2D - 1)T_s$, when 180° phase shift occurs

$$\Delta V_0/\Delta t| \quad t_1, t_3 = -((I_{L_2} + 2I_0/c)((2D - 1)T_S/2$$

(c) During t_4, the converter operation

$$\Delta V_0/\Delta t| \quad t_4 = -((I_{L_1} - I_{L_2} - I_0/c_1) - (I_0/c_2)) = -(I_{L_1} - I_{L_1} - 2I_0)/c$$

$$\begin{aligned}\Delta V_0| \quad t_4 &= -(I_{L_1} - I_{L_2} - I_0/c_1) - (I_0/c_2)(1 - D)T_S \\ &= -((I_{L_1} - I_{L_1} - 2I_0)/c)(1 - D)T_S\end{aligned}$$

(d) During t_1 and t_3, the converter operation

$$V_0/\Delta t| \quad t_1, t_3 = ((I_{L_1} - I_0/c_1) + (I_{L_2} - I_0/c_2)) = (I_{L_1} + I_{L_1} - 2I_0)/c$$

$$\Delta V_0| \quad t_1, t_3 = ((\mathrm{I}_{L_1} + \mathrm{I}_{L_2} - 2I_0/c)(1 - 2D)T_s/2$$

5 Specifications

See Table 1.

Table 1 Design values of proposed converters

Duty cycle	I_S (A)
Output power (P_o)	100 W
Duty cycle (d)	0.553
Output voltage (V_o)	100 V
Input voltage (V_s)	20 V
Proportional gain constant (K_p)	0.00001
Integral gain constant (K_i)	0.25
Resistance (Ω)	100
Line frequency	50 Hz
Switching frequency (f_s)	50 kHz
Inductor L_1 (μH)	368
Inductor L_2 (μH)	824
Inductor1 Current (IL_1)	5
Inductor2 Current (IL_2)	2.23
Capacitor C (μF)	10

6 Open Loop Analysis of QBC

See Fig. 3 and Tables 2, 3.

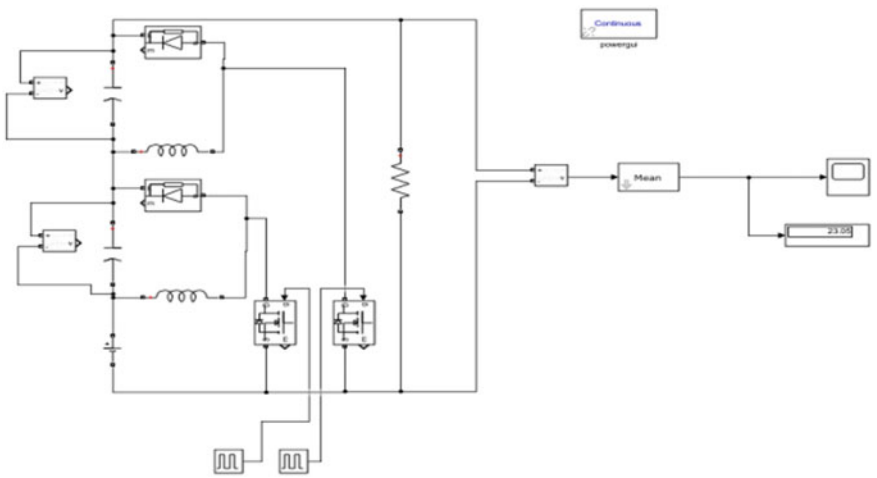

Fig. 3 Simulink diagram of open loop analysis of QBC

Table 2 Various duty cycle for open loop analysis of QBC

Duty cycle	I_S (A)	V_s (V)	I_0 (A)	V_0 (V)	Efficiency
0.1	0.2940	20	0.2299	22.99	89.88
0.2	0.4851	20	0.2941	29.41	89.15
0.3	0.8429	20	0.3878	38.78	89.20
0.4	1.577	20	0.5318	53.18	89.66
0.5	3.271	20	0.7680	76.80	90.15

Table 3 % of load for open loop analysis of QBC

% of load	Resistance	I_S (A)	V_s (V)	I_0 (A)	V_0 (V)	Efficiency
25	400	1.567	20	0.2479	99.15	78.42
50	200	2.717	20	0.4834	96.68	86.00
75	133	3.920	20	0.7239	96.27	88.89
100	100	5.096	20	0.9587	95.87	90.17

7 Simulations of Closed Loop Analysis of QBC

Figure 4 shows the simulation of closed loop analysis of quadratic boost converter.

Tables 4 and 5 shows the efficiency for various input voltage and various % of load.

7.1 Output Voltage Waveform of Quadratic Boost Converter

See Fig. 5.

7.2 Output Current Waveform of Quadratic Boost Converter

See Fig. 6.

8 Conclusion

This project work was started with an objective of designing QBC with high power factor and low voltage ripples. Reduction in output voltage ripple is obtained by using the voltage ripple cancellation technique. The smaller capacitors help in achieving the same voltage ripple specifications by using this converter. In quadratic boost

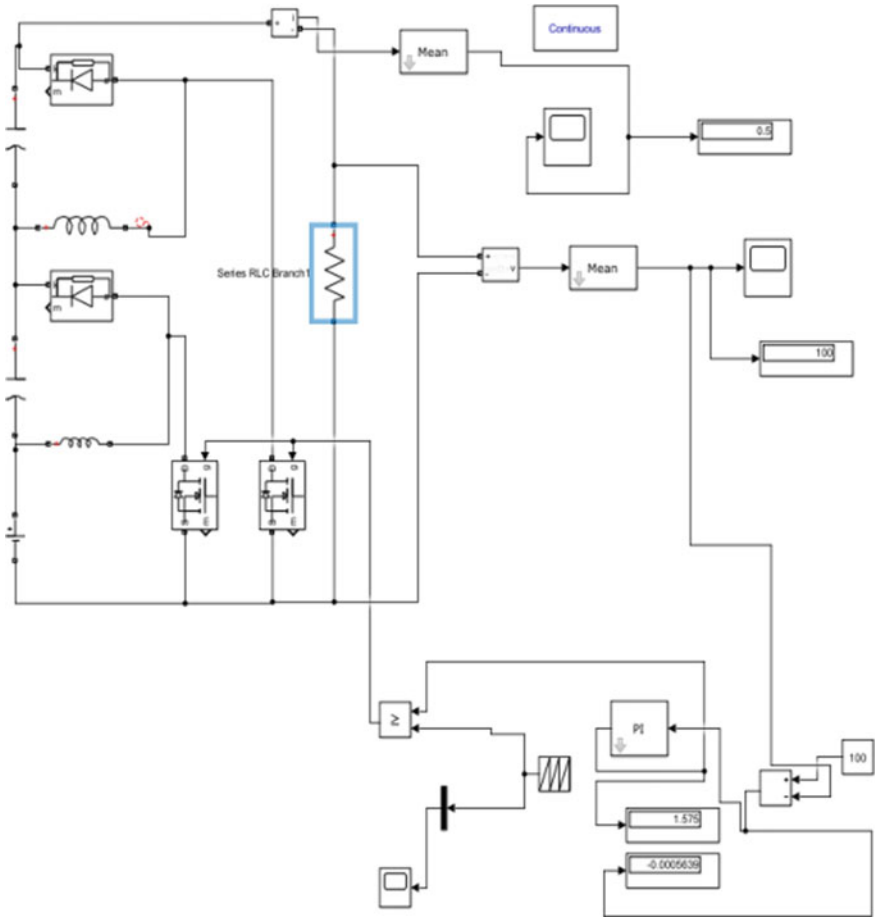

Fig. 4 Simulink diagram of closed loop analysis of QBC

Table 4 Various input voltage for closed loop analysis of QBC

I_S (A)	V_s (V)	I_0 (A)	V_0 (V)	Efficiency
14.60	10	1.008	100	68.49
8.064	15	1.008	100	83.33
5.943	20	1.008	100	84.80
4.674	25	1.008	100	86.26
3.856	30	1.008	100	87.13

Table 5 % of load for closed loop analysis of QBC

% of load	Resistance	I_S(A)	V_s (V)	I_0 (A)	V_0 (V)	Efficiency
25	400	1.854	20	0.2501	100	70.76
50	200	3.241	20	0.4997	100	77.09
75	133	4.593	20	0.7508	100	81.73
100	100	5.943	20	0.9981	100	83.97

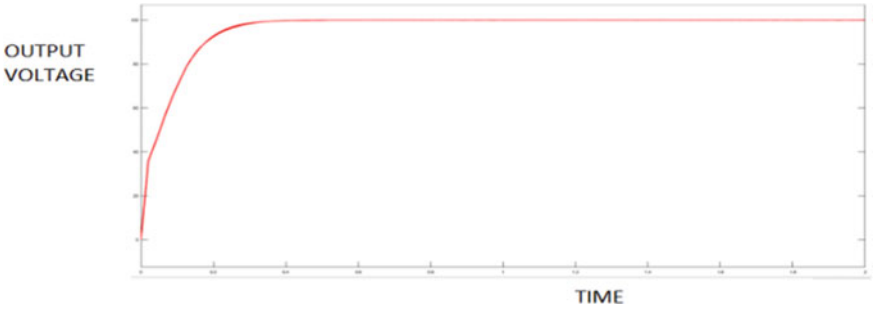

Fig. 5 QBC output voltage waveform

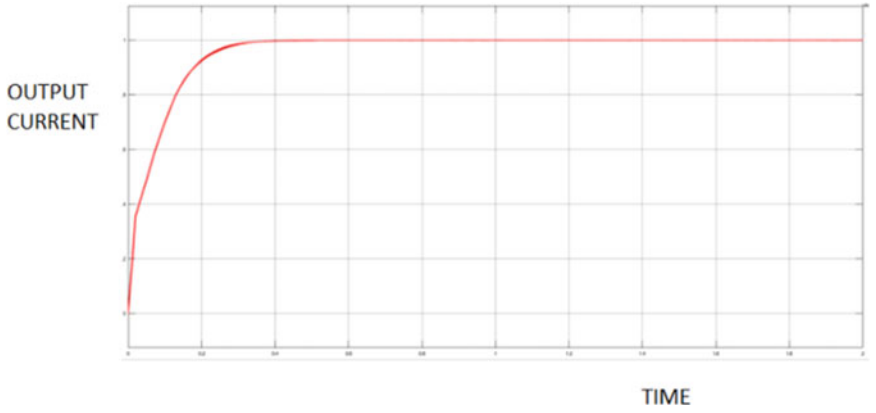

Fig. 6 Output current waveform of QBC

converter, single switch with high voltage rating and the high current rating is preferred. Thus the proposed QBC converter achieved the decreased output voltage ripples and the increased efficiency.

References

1. Hwu KI, Peng TJ (2012) A novel buck–boost converter combining KY and buck converters. IEEE Trans Power Electron 27(5)
2. Tofoli FL, de Castro Pereira D, de Paula WJ, de Sousa Oliveira D (2015) Survey on non-isolated high-voltage step-up dc–dc topologies based on the boost converter. IET Inst Eng Technol Power Electron 8(10)
3. Jiang W, Chincholkar SH, Chan C-Y, Peng TJ (2018) Modified voltage-mode controller for the quadratic boost converter with improved output performance. IET Power Electron Inst Eng Technol 11(14):11–27
4. Weng X, Xiao X, He W, Zhou Y, Shen Y, Zhao W, Zhao Z (2019) Comprehensive comparison and analysis of non-inverting buck boost and conventional buck boost converters. IET Inst Eng Technol Power Electron 2019(16):3030–3034
5. Chen Z, Yang P, Zhou G, Xu J, Chen ZY (2016) Variable duty cycle control for quadratic boost PFC converter. Trans Ind Electron 63(7)
6. Morales-Saldana JA, Galarza-Quirino R, Leyva-Ramos J, Carbajal-Gutierrez EE, Ortiz-Lopez MG, Xu D (2007) Multi loop controllers design for quadratic boost converter. IEEE Trans Ind Electron 1(3)
7. Andrade AMSS, Hey HL, Schuch L, da Silva Martins ML (2018) Comparative evaluation of single switch high-voltage step-up topologies based on boost and zeta PWM cells. IEEE Trans Ind Electron 65(3)
8. Hanisah N, Baharudin, Mansur TMNT, Hamid FA, Ali R, Misrun MI (2017) Topologies of dc-dc converter in solar PV applications, Indonesian J Electr Eng Comput Sci 8(2):368–374
9. Taghvaee MH, Radzi MAM, Moosavain SM, Hizam H, Hamiruce Marhaban M (2013) A current and future study on non-isolated dc-dc converters for photovoltaic applications. Renew Sustain Energ Rev 17(c):216–227
10. Ghamrawi A, Gaubert J, Mehdi D (2016) New control strategy for a quadratic boost converter used in solar energy system. In: 2016 IEEE international energy conference (ENERGYCON), Leuven, Belgium, pp 1-6.https://doi.org/10.1109/ENERGYCON.2016.7514125
11. Selvaperumal S, Muralidharan S, Nedumal Pugazhenthi P, Prabhakar G, Bastin Solai Nazaren J, Parthiban PG, Karuppasamy P (2017) Performance investigation of SHE PWM implementation of GA based LCL resonant inverter in marine applications. Indian J Geo Marine Sci 46(09):1889–1898
12. Gnanavadivel J, Senthil Kumar N, Jaya Christa ST, Muralidharan S (2019) Design and Implementation of FPGA based high power LED lighting system for ships. Indian J Geo Marine Sci 48(05):724–729
13. Menaka S, Muralidharan S (2017) Novel symmetric and asymmetric multilevel inverter topologies with minimum number of switches for high voltage of electric ship propulsion system. Indian J Geo Marine Sci 46(09):1920–1930

Recognition of Partial Discharge Signal Using Deep Learning Algorithm

J. Ashmin Sugaji, M. Ravindran, and R. V. Maheswari

Abstract In transmission frameworks, insulators have a huge impact on the better presentation of the devices. The outside insulators are introduced to an environment that has a high temperature, clamminess similar to pollution from the beachfront and industries. On deposition of contaminants, pollution builds gradually, and spillage current starts to stream on a surface level. Partial Discharge (PD) deteriorates the insulation and leads to the breakdown of the device. The effect of conductive pollution on PD is seen through tests performed on both earthenware and non-ceramic protectors at different pollution levels. To achieve complete information about PD, it is gotten through a PD acknowledgment system that records the PD waveforms close to the regular PD. A couple of sorts of PD signals are difficult to recognize at a starting stage. To crush the test, a Convolutional Neural Network (CNN) based profound learning procedure for PD plan affirmation is presented in this paper. The acquired PD signal is changed into a 3-D (ϕ-q-n) picture. To anticipate such a PD the 3-D (ϕ-q-n) picture is feed as a input to Deep Learning Algorithm. It uses Convolutional Neural Networks (CNN) for picture gathering. In this, Alex Net is used for perceiving the unmistakable PD.

Keywords Partial discharge · Deep learning · Pattern recognition · Spillage current · Spark over voltage

1 Introduction

As indicated by IEC (International Electro-technical Commission) Standard 60,270, partial discharge (PD) is an electrical discharge that does not completely bridge the space between two conducting electrodes. Insulators are protective devices that are utilized in transmission and distribution lines for protection between two conductors. The fundamental driver of the disappointment of overhead line encasing is flashover which happens in the middle of the line and earth during overvoltage in the framework

J. Ashmin Sugaji (✉) · M. Ravindran · R. V. Maheswari
Department of Electrical and Electronics Engineering, National Engineering College, Kovilpatti, India

C. Subramani et al. (eds.), *Proceedings of International Conference on Power Electronics and Renewable Energy Systems*, Lecture Notes in Electrical Engineering 795,
https://doi.org/10.1007/978-981-16-4943-1_32

[2]. During this flashover, the gigantic warmth created by arcing causes penetrates in the insulator body. In transmission frameworks, high voltage gear, covers assume a significant part in the presentation of the hardware. It is a lot important to keep up the protection in the electrical gear for the working activity during high voltage power transmission [3].

Near mountain locality, farming, or beachfront territory, particles are kept on encasing and contamination develops progressively [9]. This decreases the protection strength when the protectors are dry [12]. In any case, when mist or light downpour wets the dirtied protector, a conductive layer is framed on the defiled cover surface, which starts spillage current [1, 10]. Spillage current begins to stream along the surface and there are arcing releases [4]. The bend expansion causes the flashover on the separator [2]. Such electrical releases show up to a span of substantially less than 1 s. PD estimations have arisen as an incredible demonstrative device for protection framework condition observing [7]. Utilizing PD signal investigation the PD action can be classified. The greater parts of the protectors are in the polluted structure [11]. Because of the presence of air, pollutant bubbles (void) are made inside the protecting material. PD consistently happens in a void. Because of the event of release disappointment happens in the protection framework [6, 8]. Because of the above reason, PD identification and estimation are fundamental for the expectation of protection life for HV power hardware [5]. PD ordinarily occurs at imperfection destinations like voids, depressions, breaks, joints, and delamination.

2 Experimental Setup

2.1 Test Specimen

Test specimens used are ceramic and non-ceramic 11 kV insulators shown in Fig. 1. The dimensions of the test specimens are tabulated in Table 1.

1. TYPE A—Porcelain Disc Type Insulator
2. TYPE B—Glass Disc Type Insulator
3. TYPE C—Composite Disc Type Insulator.

2.2 Experimental Setup

The artificial contamination execution test with uniform contamination dissemination is done in a fake chamber. The supply is given as demonstrated in Fig. 2. It shows the test arrangement that having coupling capacitance, high voltage test transformer, and fake chamber to hold the example.

The transformer evaluated voltage is 2*0.22/100/0.22 kV, appraised current 2*22.8/0.1A, the evaluated yield is 10kVA. The testing transformer is utilized to

Fig. 1 Types of ceramic and non-ceramic insulators

Table 1 Dimensions of specimen

Type	Creepage Length (cm)	Height (cm)	Diameter (cm)
A	29.7	5.3	24
B	27.3	3.8	23
C	32	11	10

Fig. 2 Experimental setup and control panel

deliver AC, DC, and impulse voltage. AC supply is given to the example through the transformer. The test arrangement is controlled utilizing a control work area shown in Fig. 2. The flashover voltage and spillage current are estimated from the control work area.

3 Methodology

Before the tests, all the samples are thoroughly washed with refined water to remove any signs of dirt or grease. To prevent dust or other contaminants, the samples are allowed to dry naturally inside. After normal drying, at first, the samples are uncovered for flashover test in unpolluted condition. At that point, the separators are covered with quantitative contamination utilizing the brushing method. Figure 3 shows the insulators polluted with NaCl and Fig. 4 shows the industrial polluted insulators. Kaolin is a non-dissolvable substance. Following 24 h of common drying of the samples, the samples are suspended in the chamber. The sample utilized for testing is suspended vertically on the test arrangement. Then the high voltage is applied gradually from zero voltage until a total flashover happens on the insulator surface. At flashover, the voltage is recorded.

The dissolvable contamination material utilized in this work is NaCl. Kaolin is utilized to address the non-dissolvable toxin. The method utilized for artificial contamination is a strong layer technique. The brushing strategy is done, before the beginning of the contamination test, using a weighing machine, the volume of NaCl (Sodium Chloride), cement, and kaolin is measured. Contamination should be washed and cleaned with refined water and a cloth after each use.

Fig. 3 Coastal polluted ceramic and non-ceramic insulators

Fig. 4 Industrial polluted ceramic and non-ceramic insulators

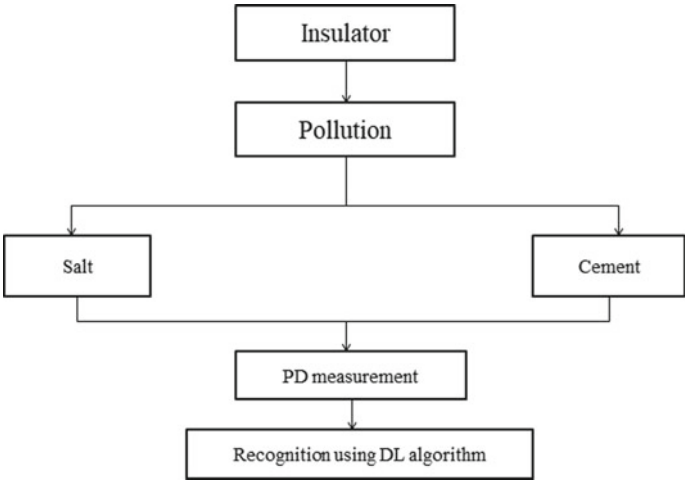

Fig. 5 Block diagram

Figure 5 addresses the block diagram of the process, where the insulators are polluted using salt and cement. After the contamination PD is measured and finally it is recognized using a deep learning algorithm.

3.1 Measurement of Pollution Severity

The degree of seriousness of the pollution has been indicated in two essential manners. For industrial pollution, they are:

(1) The salt deposit density, SDD, the measure of salt pollutant on the insulator surface in units of mg of salt per $cm^2$of protector surface.
(2) To normalize, for industrial pollution, the equivalent salt deposit density or ESDD is utilized, which is characterized as the measure of NaCl that would yield a similar conductivity at complete weakening as the non-NaCl salt.

4 Experimental Results

The flashover voltage decreases with the increase in pollution levels. Table 2 shows the breakdown voltage and leakage current of the test specimens in unpolluted conditions.

Table 2 Flashover test in unpolluted condition

Type	Breakdown Voltage(kV)	Leakage current(mA)
A	110.93	57.21
B	85.27	40.56
C	97.38	41.75

4.1 Partial Discharge Analysis

At first, the test examples were tried without applying any contamination, with an applied voltage and under dry condition. Figure 6 shows the partial discharge at unpolluted condition.

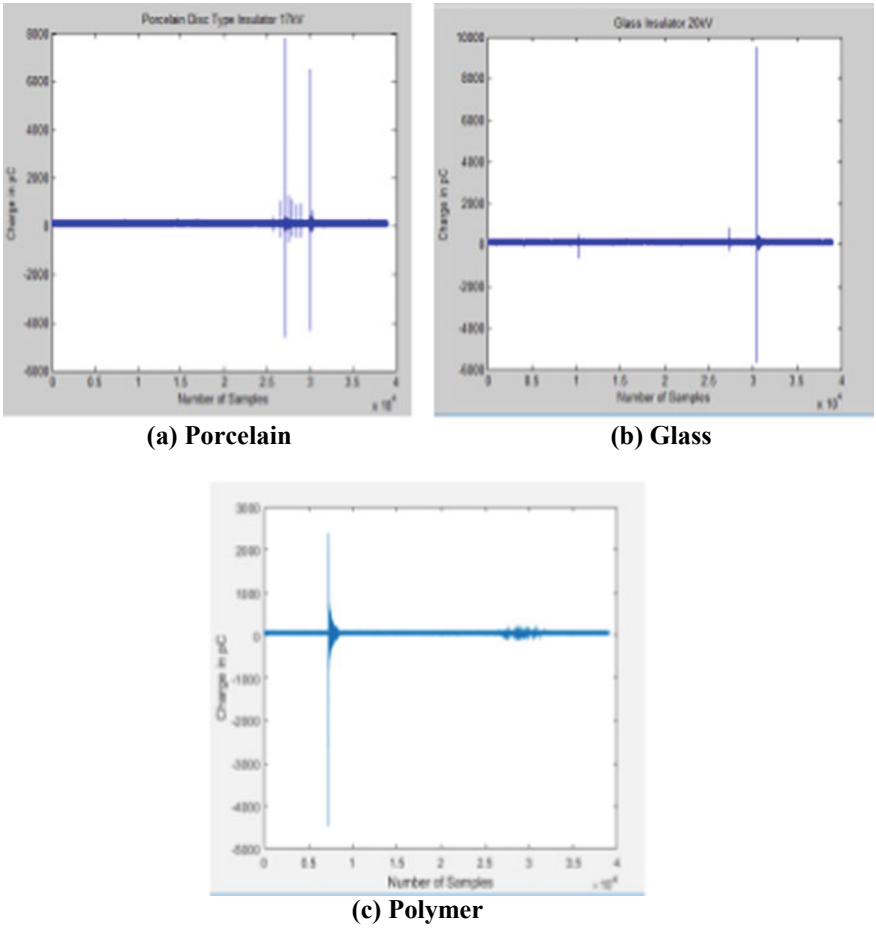

(a) Porcelain **(b) Glass**

(c) Polymer

Fig. 6 PD Waveform at unpolluted condition

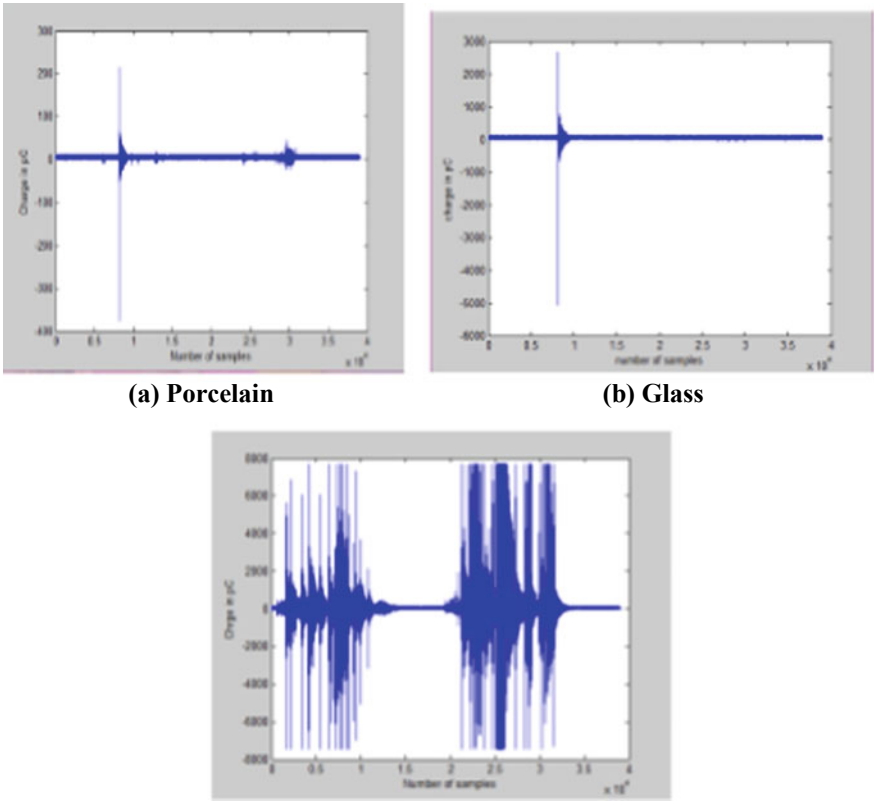

(a) Porcelain **(b) Glass**

(c) Polymer

Fig. 7 PD Waveform at 1:1 ratio condition

Partial discharge test with 1:1 proportion condition: The ceramic and non-ceramic insulator samples were tried by applying the contamination at 1:1 proportion condition. Figure 7 shows the PD at 1:1 proportion dirtied condition.

4.2 3D Plot

The PD signals are changed into 3-D (ϕ-q-n) pictures for design purpose. The PD information comprise of Charge (q), Number of Discharge (n), and Phase angle (ϕ). This gives a phase-resolved PD (PRPD) pattern 3D (ϕ-q-n) plot shown in Fig. 8 and is changed over into a picture.

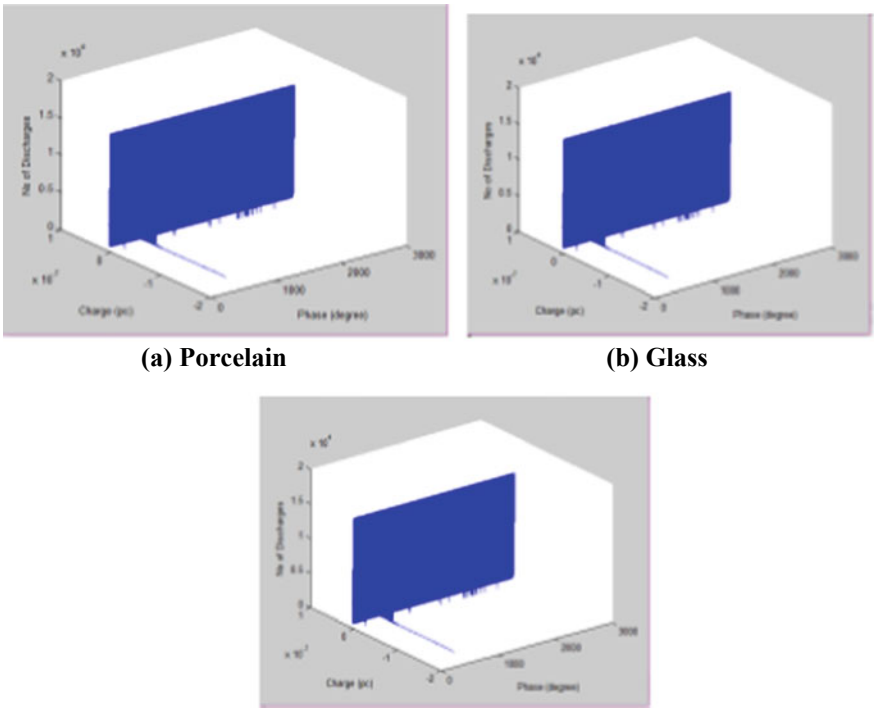

(a) Porcelain **(b) Glass**

(c) Polymer

Fig. 8 3D plot for polluted insulators

The breakdown voltage for 11 kV porcelain insulator with coastal pollution is shown in Table 3. The breakdown voltage diminishes with the increment in contamination levels. Figure 9 shows the relation between salt ratio and breakdown voltage for porcelain insulators.

The breakdown voltage for 11 kV glass insulator with coastal pollution is shown in Table 4. The breakdown voltage diminishes with the increment in contamination levels. Figure 10 shows the relation between salt ratio and breakdown voltage for glass insulators.

Table 3 Breakdown voltage for 11 kV porcelain insulator with coastal pollution

Ratio	Weight of NaCl (g)	Weight of Kaolin (g)	Amount of Water (ml)	ESSD (g/cm^2)	Breakdown voltage (kV)
0:0	0	0	0	0	110.93
1:1	10	10	15	0.011	75.136
2:2	20	10	15	0.016	67.42

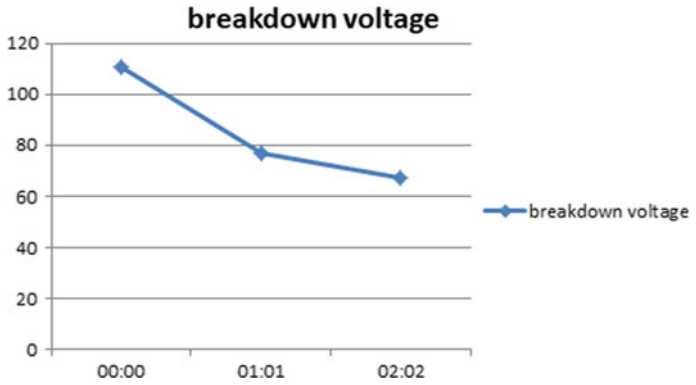

Fig. 9 Relation between ratio of salt and voltage failure for disc type insulator

Table 4 Breakdown voltage for 11 kV glass insulator with coastal pollution

Ratio	Weight of NaCl (g)	Weight of Kaolin (g)	Amount of water (ml)	ESSD (g/cm^2)	Break down voltage (kV)
0:0	0	0	0	0	85.27
1:1	10	10	15	0.016	73.64
2:2	20	10	15	0.018	67.83

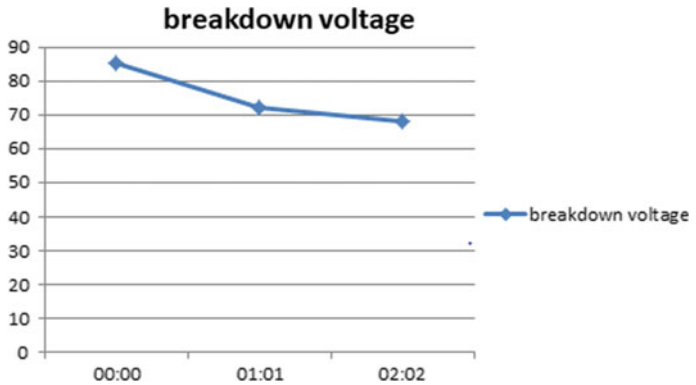

Fig. 10 Relation between ratio of salt and voltage failure for Glass insulator

Breakdown voltage for 11 kV polymer insulator with coastal pollution is shown in Table 5. Figure 11 shows the relation between salt ratio and breakdown voltage for polymer insulator.

Table 5 Breakdown voltage for 11 kV polymer insulator with coastal pollution

Ratio	Weight of NaCl (g)	Weight of Kaolin (g)	Amount of water (g)	ESSD (g/cm^2)	Breakdown voltage (kV)
0:0	0	0	0	0	97.38
1:1	10	10	15	0.0156	96.41
2:2	20	10	15	0.017	95.84

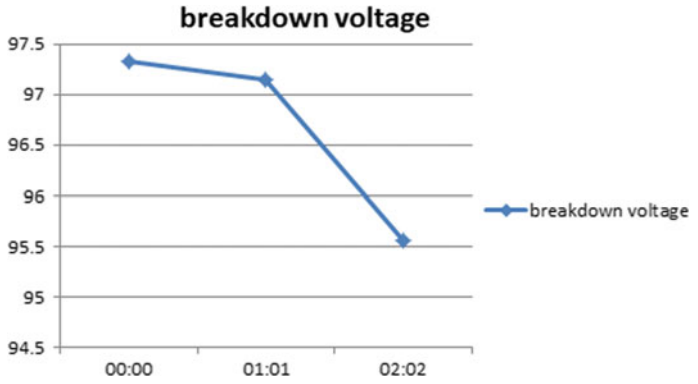

Fig. 11 Relation between ratio of salt and voltage failure for polymer insulator

5 Results and Discussion

In this paper, three cases are tried. The insulators are covered with a quantitative brushing strategy. AC artificial contamination tests for ceramic and non-ceramic insulators under different contamination levels with an alternate proportion and PD are estimated. When the salt deposit density grows for each extent the breakdown was reduced. Under such conditions, these are the inference from the acquired outcomes.

- The breakdown voltage of clean insulators is higher than the polluted insulators.
- Spark over-voltage diminishes with an increment in contamination level.
- The breakdown voltage of the insulators is caused by an increase in the ESDD levels.

References

1. Chandrasekar S, Kalaivanan C, Cavallini A, Montanari GC (2009) Investigations on leakage current and phase angle characteristics of porcelain and polymeric insulator under contaminated conditions. IEEE Trans Dielectr Electr Insul 16(2):574–583

2. Boudissa R, Djafri S, Haddad A, Belaicha R, Bearsch R (2005) Effect of insulator shape on surface discharges and flashover under polluted conditions. IEEE Trans Dielectr Electr Insul 12(3):429–437
3. Cavallini A, Chandrasekar S, Montanari GC, Puletti F (2007) Inferring ceramic insulator pollution by an innovative approach resorting to PD detection. IEEE Trans Dielectr Electr Insul 14(1):23–29
4. Chandrasekar S, Kalaivanan C, Montanari GC, Cavallini A (2010) Partial discharge detection as a tool to infer pollution severity of polymeric insulators. IEEE Trans Dielectr Electr Insul 17(1):181–188
5. Simonyan K, Zisserman A (2014) Very deep convolutional networks for large-scale image recognition. arXiv preprint arXiv: 1409.1556
6. Liao R, Fernandess Y, Tavernier K, Taylor GA, Irving MR (2012) Recognition of partial discharge patterns. In: Power and energy society general meeting, pp 1–8
7. Lewin PL, Petrov LA, Hao L (2012) A feature based method for partial discharge source classification. In: Conference record of the 2012 IEEE international symposium on electrical insulation (ISEI), pp 443–448
8. Schroder P, Neubauer Y, Arumugam S, Schoenemann T (2014) Dielectric and partial discharge investigations on ceramic insulator contaminated with condensable hydrocarbons. IEEE Trans Dielectr Electr Insul 21(6):2512–2524
9. Duan L, Hu J, Zhao G, Chen K, Wang SX, He J (2019) Identification of partial discharge defects based on deep learning algorithm. IEEE Trans Power Deliv 34(4):1557–1568
10. Othman NA, Piah MAM, Adzis Z (2017) Space charge distribution and leakage current pulses for contaminated glass insulator strings in power transmission lines. IET Gener Transm Distrib 11(4):876–882
11. Maadjoudj D, Mekhaldi A, Teguar M (2018) Flashover process and leakage current characteristics of insulator model under desert pollution. IEEE Trans Dielectr Electr Insul 25(6):2296–2304
12. Douar MA, Beroual A, Souche X (2016) Assessment of the resistance to tracking of polymers in clean and salt fogs due to flashover arcs and partial discharges degrading conditions on one insulator model. IET Gener Transm Distrib 10(4):986–994

Design and Analysis of LK Model Based FEFET Memories

S. S. Vijayavelu, K. Mariammal, M. Adhitya Narayan, and P. Subash Rathinam

Abstract Industries scaled down the size but the supply voltage was still in the 1 V range for a decade. Reducing power consumption needs supply voltage to be reduced especially for Dynamic Random-Access Memory (DRAM) which is a storage device whose dynamic power consumption is proportional to the square of the power supply. In this work, design of low power consuming DRAM and Static Random-Access Memory (SRAM) with Ferro Electric Field Effect Transistor (FEFET) as transistor nodes which has higher subthreshold swing due to negative capacitance, hence a lower power supply can be applied and changing process parameter to find Static Noise Margin (SNM) of SRAM and characteristics of DRAM. The simulations are carried out with cadence for 32 nm Verilog-a model and are analyzed with Python.

Keywords FEFET · Subthreshold swing · Verilog-a · DRAM · SRAM

1 Introduction

In view of present-day smartphones which have more use than computers that are plugged into power sockets, smartphones need to have a good mechanism of consuming low power. Smartphone's operating frequency diversely shifting towards higher operating frequency and larger bandwidth. It drastically increases the rate of consumption of power stored in the battery as dynamic power consumption is proportional to the frequency. In order to reduce the power consumption, we need to reduce the other factor that is the power supply but the conventional Metal Oxide Semiconductor Field Effect (MOSFET)s or FinFETs have a lower subthreshold swing, i.e., higher S value of above 60 mV/decade. This higher value of S makes the conventional FETS unusable for lower power supply because of lower I_{ON}/I_{OFF}. Hence lower power consuming nodes are needed for today's high-frequency application. One approach of reducing the power supply without increasing Off current (I_{OFF}) is decreasing the S (inverse of the subthreshold slope) which is ideally can't be lower than 60 mV for conventional FETS. S parameter can be given by the expression,

S. S. Vijayavelu (✉) · K. Mariammal · M. A. Narayan · P. S. Rathinam
Department of Electronics Engineering, Madras Institute of Technology, Chennai, India

C. Subramani et al. (eds.), *Proceedings of International Conference on Power Electronics and Renewable Energy Systems*, Lecture Notes in Electrical Engineering 795,
https://doi.org/10.1007/978-981-16-4943-1_33

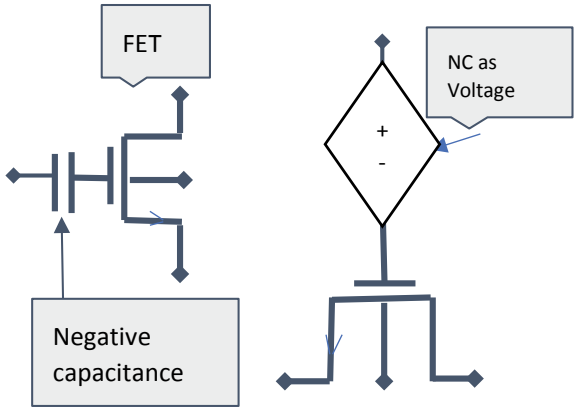

Fig. 1 FE on MOSFET model

$S = \left(1 + \frac{C_D}{C_{ox}}\right) * 60\,\text{mV}$. One way of reducing the S values is reducing depletion capacitance but that only reduces up to 60 mV. In this paper, DRAM and SRAM are simulated from Ferro Electric FET (FEFET) which is designed with the idea of Ferro Electric (FE) on MOSFET model [9] as shown in Fig. 1. Ferro electric materials have the effect of hysteresis and need careful layout in order to reduce the hysteresis. One way is to match the capacitance of MOSFET and Ferro electric material to stable injection of charge carriers over a gate-controlled energy barrier. The subthreshold slope S associated with the FET cannot be reduced below the Boltzmann limit which is of 60 mV/decade, thus leading to enable low voltage and low power operation [2]. Negative Capacitor Field Effect Transistors (NC-FETs) are certain to sustain Moore's law by reducing the supply voltage. The reduction in voltage is achieved by integrating a negative capacitor in the gate, the internal voltage amplification turns a transistor on and off at voltages lower [3]. Negative capacitance field effect transistors (NC-FET) are low voltage and low power field effect transistors (FET) which have the same structure as MOSFET except that ferro electric thin film is used as a gate insulator. It can help us to reduce the leakage and to increase the on-state current of the transistor. It can maintain a reasonable operating speed at very low voltage (0.5 V or less) [4]. NC-FETs include ferro electric-FET that uses a ferro electric material as the gate insulator. In this, the gate insulator behaves like a negative capacitor. In this NC region, however, the gate insulator is thermodynamically unstable unless stabilized using a positive series capacitor. Interestingly, this stabilization provides the necessary voltage amplification to reduce S below Boltzmann limit [5]. Charge conserved capacitor model (CLK) is considered for the simulation as a precaution over if the spice simulator is faulty [6]. FEFET based FDSOI leading edge CMOS is designed and it showed endurance cycles up to 10^5 cycles can be obtained and it is shown that endurance can be increased [7]. A simple 1Transistor process with 10^{12} on/off endurance cycle is achieved by ZrHfO on the p-MOSFET. This shows good results in FEFET based memories [8]. HfO_2 is better than ZrHfO in endurance and ferro electricity. By applying the simple idea of mounting a FE with parameters obtained from HfO_2 experiments on standard Berkley Short channel Insulated Gate

Model (BSIM4) [9]. The Landau Khalatnikov (LK) Equation is used to find Electric field and polarization of Ferro Electric materials (FE). The model for negative capacitance is obtained by the time dependent LK equation which is mounted as an external capacitor [10] given in equation number (1) value [1]. The Current–Voltage characteristics of the field effect transistors FET is obtained by the thermal.

$$E - \rho \frac{dP}{dt} = \alpha P + \beta P^3 + \gamma P^5 \tag{1}$$

Static Parameters (α, β, γ), Kinetic Coefficient (ρ). Considered Values [9] are as follows,

α_{FE} = -8.65e10 (cm/F).
β_{FE} = 1.92e20 ($cm^5/F/C^2$).
gamma = 0 ($cm^9/F/C^4$).
rho = 9 (Ω cm).

This paper is organized as follows,

Section I consists of Introduction and literature survey. Section II presents the design of SRAM and DRAM. Section III discusses the simulation results of SRAM and DRAM and section IV Concludes the work.

2 SRAM and DRAM Design

This section presents the design of SRAM and DRAM. N-channel and P-Channel Transistors are utilized for the design of these memories. Incorporation of FEFETS enables the complete SRAM and DRAM design attractive in terms of power as it requires minimal power consumption when examining with the other transistor-based designs (Fig. 2).

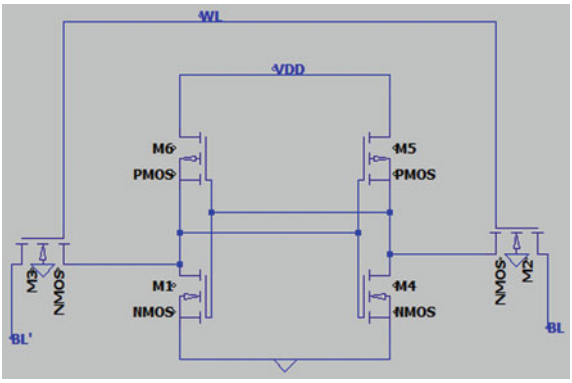

Fig. 2 6 T SRAM

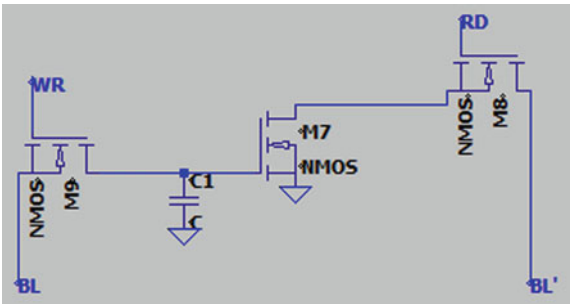

Fig. 3 DRAM circuit design

SRAM is two crossly coupled inverters with access transistors to write and read the data. The cross coupled inverters act as a flipflop to store data as long as power supply is applied and mostly used in caches (Fig. 3).

DRAMs are used in Main memory which uses a capacitor to store charge dynamically. Power consumptions by DRAMs are proportional to supplied Voltage.

3 Results and Discussion

Simulations are done with FEFET which is obtained by connecting Negative Capacitance Verilog-a model and Verilog-a model for 32 nm FET by changing the parameters in Generic BSIM-4 model with those of 32 nm FET [9].

From (1), We can derive for ferro electric Voltage which is modeled for NC model given by Eq. (2)

$$VFE = \rho\left(\frac{TFE}{AFE}\right)\left(\frac{dQp}{dt}\right) + \left(TFE\left\{\frac{\alpha Qp}{AFE} + \frac{\beta Qp^3}{AFE^3} + \frac{\gamma Qp^5}{AFE^5}\right\}\right) \quad (2)$$

First 32 nm modified BSIM4 is obtained (Fig. 4) and NC is obtained (Fig. 5) to get FENMOS and FEPMOS by connecting together.

As from (2) Gate charge information is needed to find VFE. So extra node is created which transfers information about the Gate Charge (Fig. 6 and 7).

A simple Inverter Circuit is first shown which works at 0.3 V power supply. Shown in Fig. 8 and results are shown in Fig. 9.

One thing that changes the characteristics of Ferro Electric Material is thickness (t_{FE}). Depending upon the thickness, Ferro Electric materials may show increased hysteresis and needs to be carefully developed that gives good SNM characteristics and good transfer characteristics.

6 T SRAM Cell with FEFET as transistor nodes is designed in cadence as shown in Fig. 10, and its one inverter output is shown for different thicknesses of the Ferro Electric Material shown in Fig. 11and12.

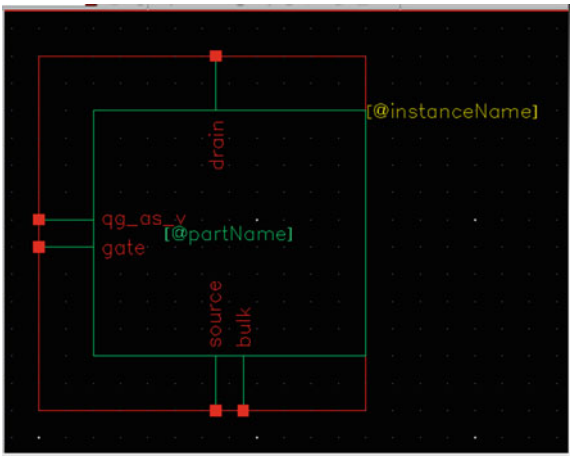

Fig. 4 NMOS simulation layout

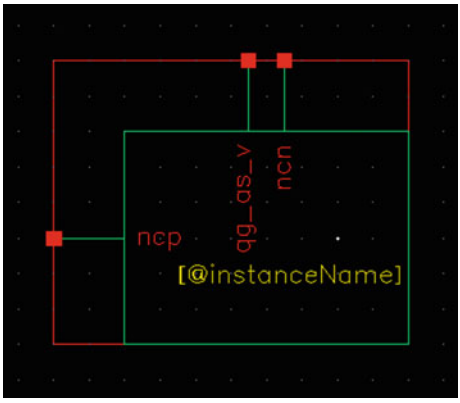

Fig. 5 Negative capacitance (NC) from LK equation

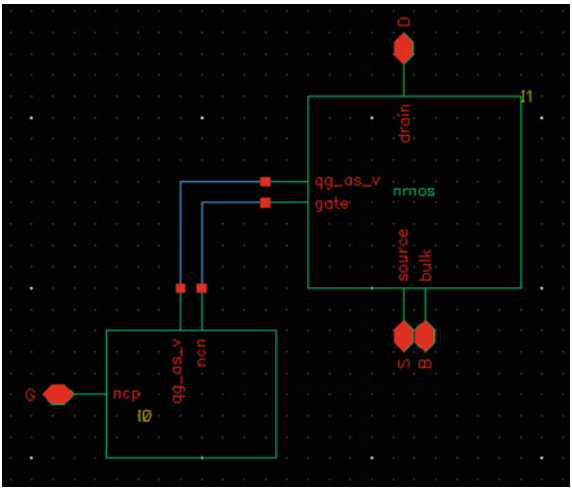

Fig. 6 NMOS and NC connected to form FENMOS

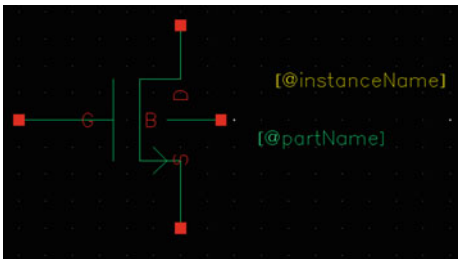

Fig. 7 Modified simulation layout for FENMOS

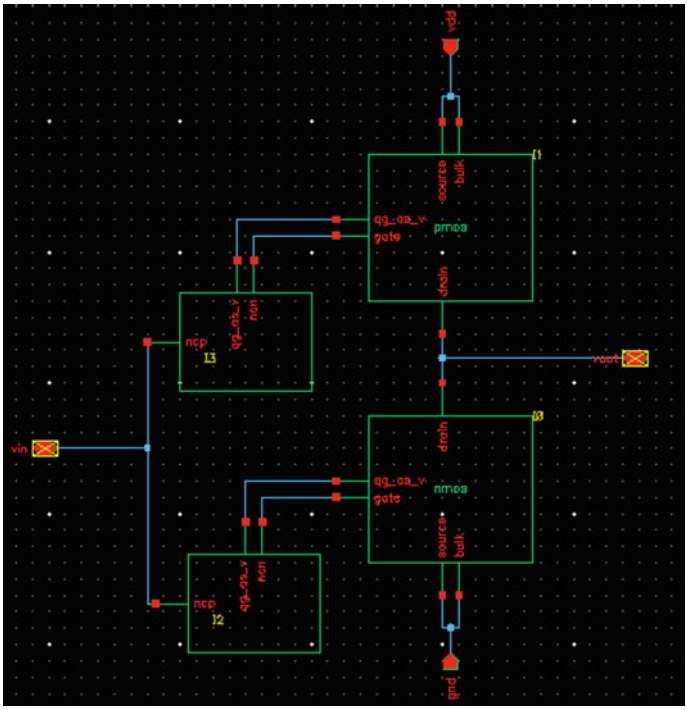

Fig. 8 Simple inverter circuit with 0.3 V supply

In Cadence, SNM calculation for various thicknesses in SRAM is tedious and time consuming, So, we use Python (Fig. 11) to find SNM with data from Cadence for Various Thickness (Figs. 13,14, 15, 16, 17, 18, 19 nad 20).

From the plots, we can find that Static Noise Margin is good and butterfly is wide open for little value of thickness of the Ferro Electric materials which is because, As the thickness increases hysteresis will play a role in one dimensional LK model of the FE. To get good SNM, we have to take narrow FE.

With the plot available, READ and WRITE SNM is obtained for different thicknesses of the material, (Figs. 21, 22)

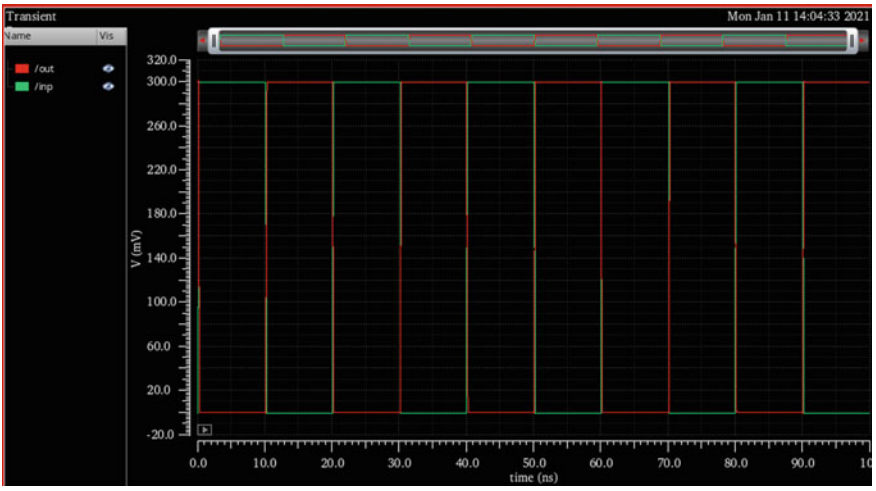

Fig. 9 inverter input, output voltage characteristics

Fig. 10 Cadence design of 6 T SRAM

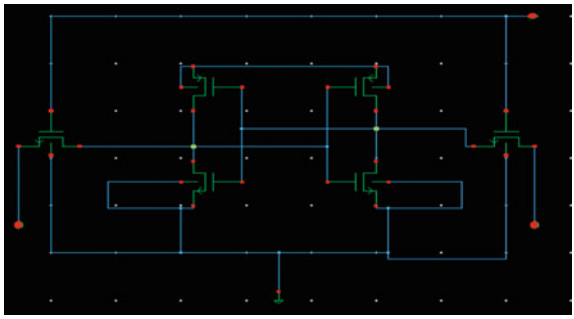

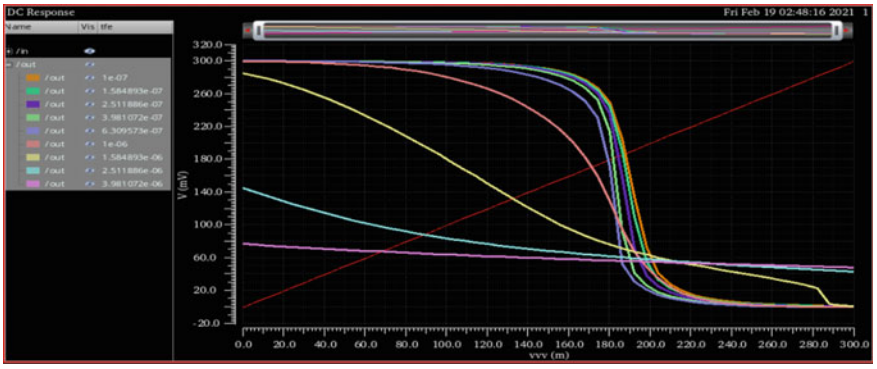

Fig. 11 VTC of one inverter output of SRAM

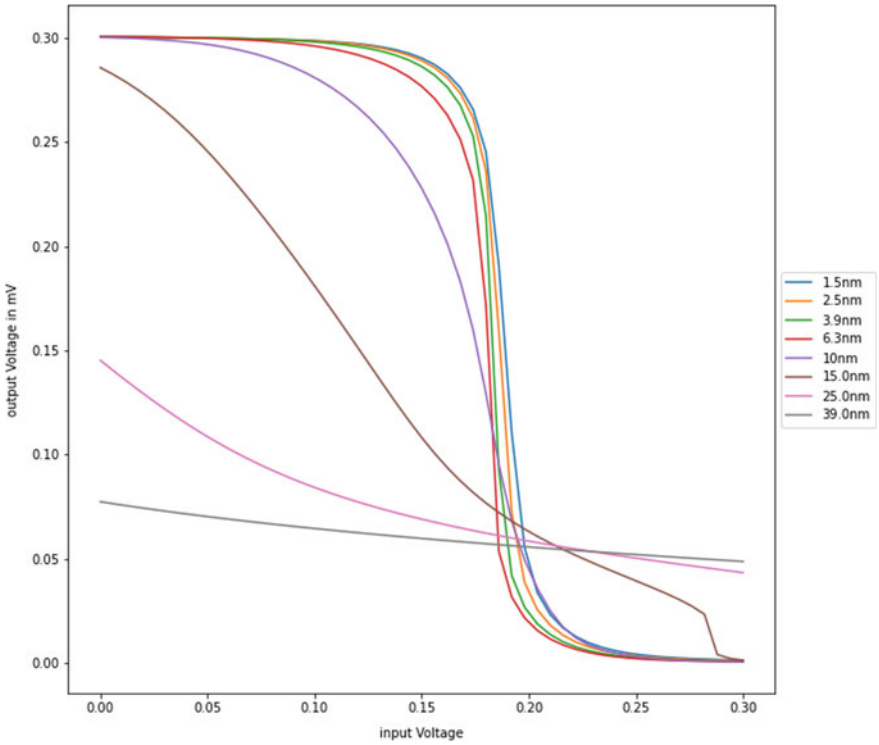

Fig. 12 (equivalent python plot of VTC)

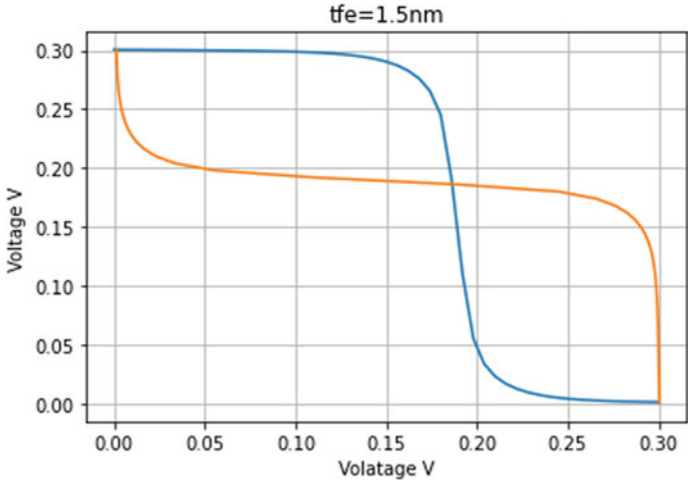

Fig. 13 SNM plot for 1.5 nm tFE

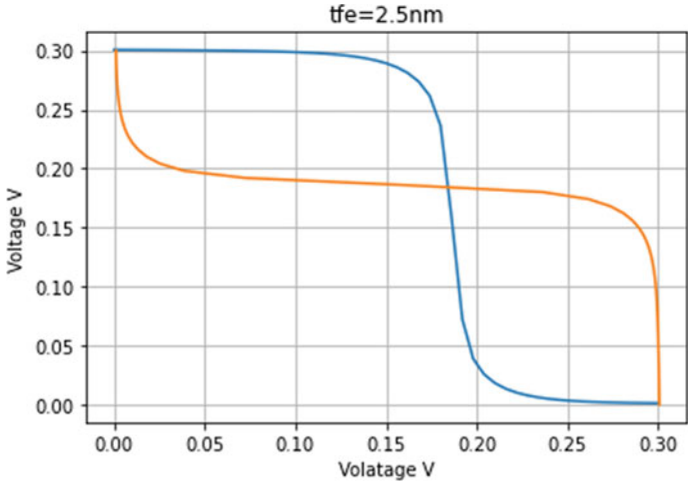

Fig. 14 SNM plot for 2.5 nm tFE

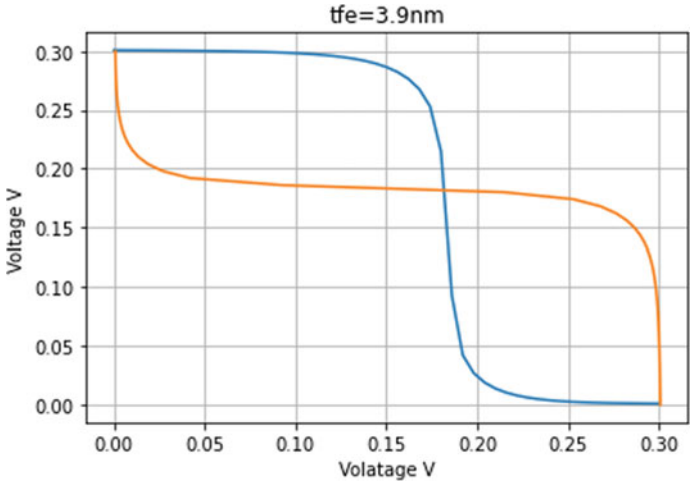

Fig. 15 SNM plot for 3.9 nm

With the Figures of read and write SNM (Figs. 20 and 21), we can find optimum value to get good SNM is around 8 nm. 3T1C DRAM Circuit is simulated with same FEFET as transistor Nodes (Fig. 23) and corresponding simulations are obtained (Fig. 24).

Volatile DRAM is simulated with FEFET with FE @10 nm which doesn't give hysteresis, If FE is at thickness higher than 10 nm, hysteresis will occur and can be used as non-Volatile DRAM as shown in Fig. 25.

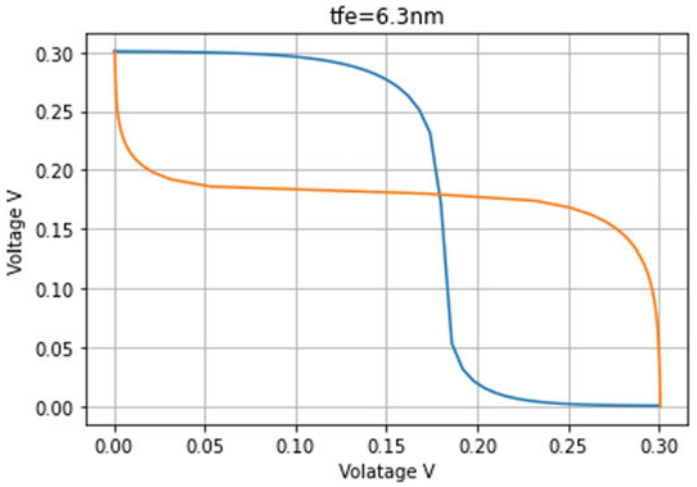

Fig. 16 SNM plot for 6.3 nm

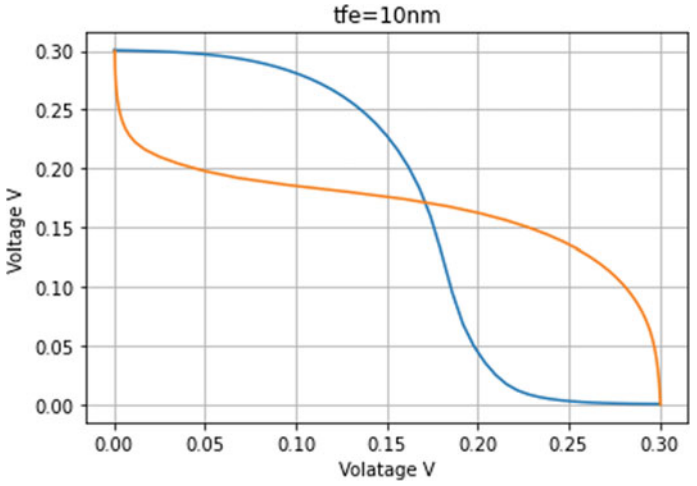

Fig. 17 SNM plot for tFE 10 nm

One another difficulty is to sense the bit. In order to Sense the output and Refresh, we need a sense amplifier to work upon 0.3 V which can be obtained with FEFET with FE thickness less than 10 nm.

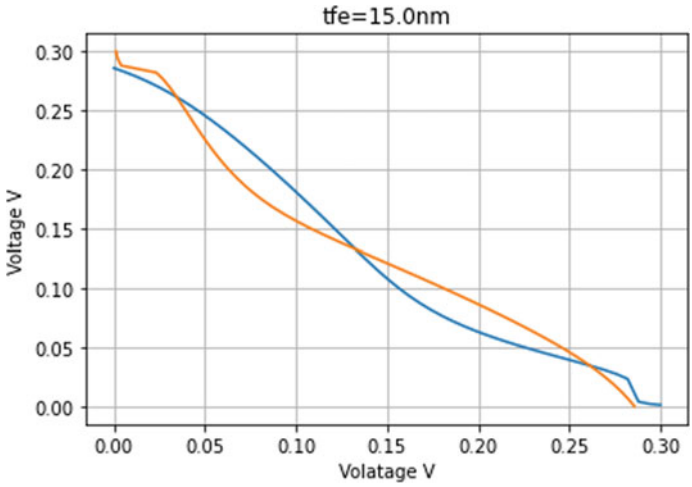

Fig. 18 SNM plot for tFE 15 nm

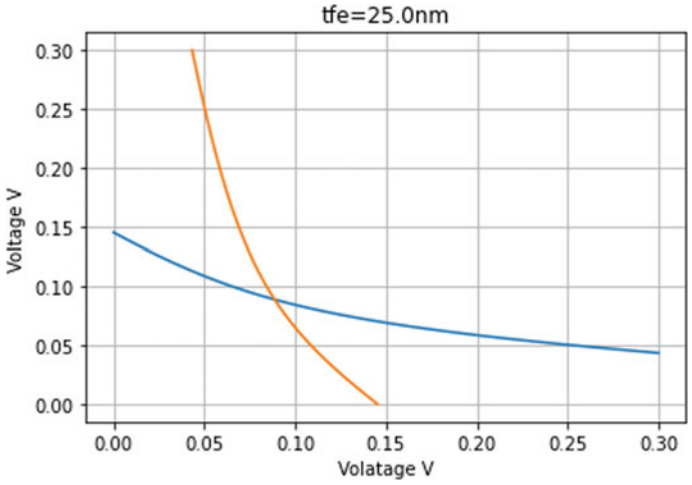

Fig. 19 SNM plot for tFE 25 nm

4 Conclusion

SRAM and DRAM design using FEFET is suggested in this work. The simulations are carried for the suggested designs with FEFET as transistor nodes. For different thicknesses of the Ferro Electric Material, SRAM and DRAM are Characterized and for SRAM, Butterfly plots are plotted to get Static Noise Margin of the SRAM found out optimum thickness of FE to work upon is around 8 nm to get better SNM because of wide opening in butterfly plot such that we can detect higher or lower state of stored

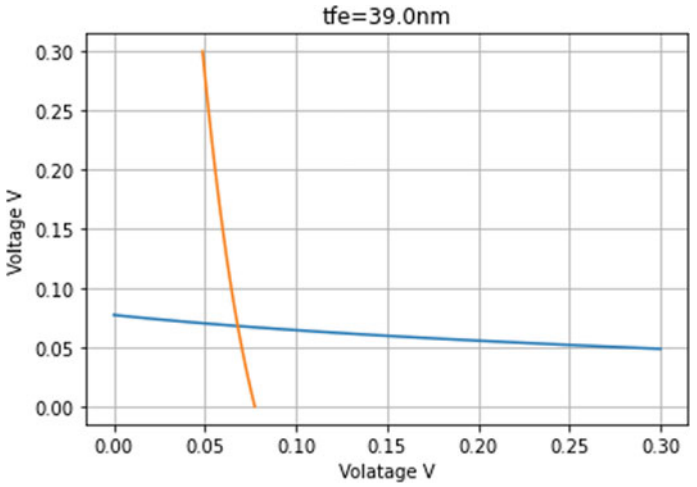

Fig. 20 SNM plot for tFE 39 nm

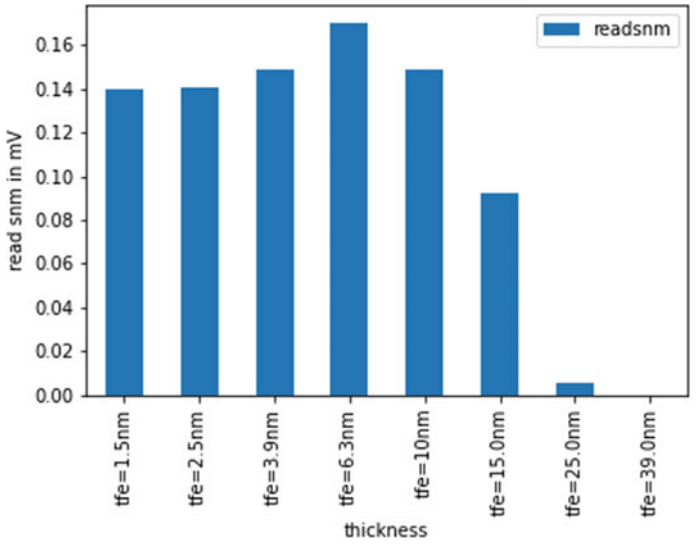

Fig. 21 Read SNM

data precisely and also get good volatile DRAM, thickness of the FE is found to be below 10 nm. As shown in Fig. 25, to get good Non-Volatile memories with the help of hysteresis, $t_{FE} > 10$ nm is a region of interest for non-volatile operations**.**

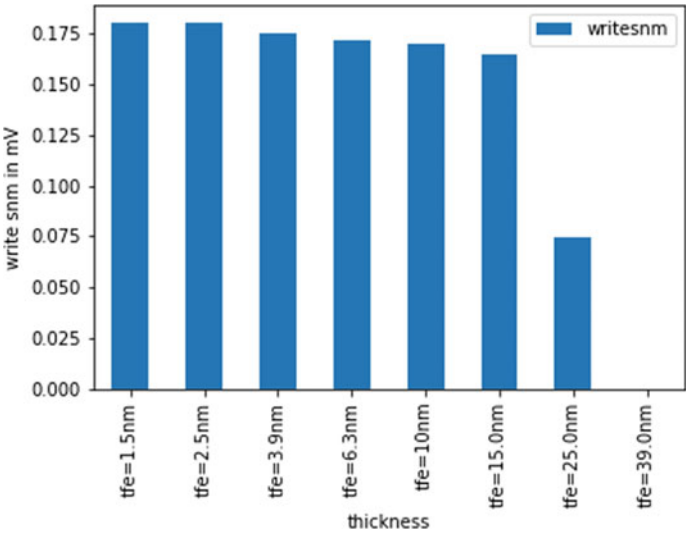

Fig. 22 Write SNM

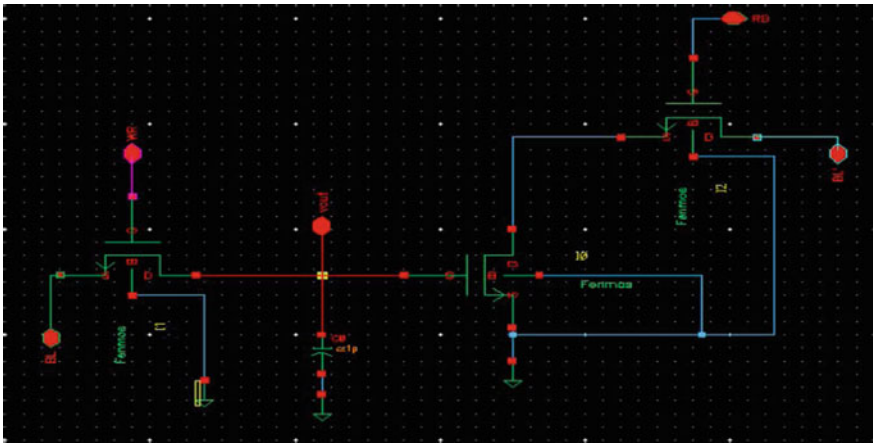

Fig. 23 Cadence simulation design

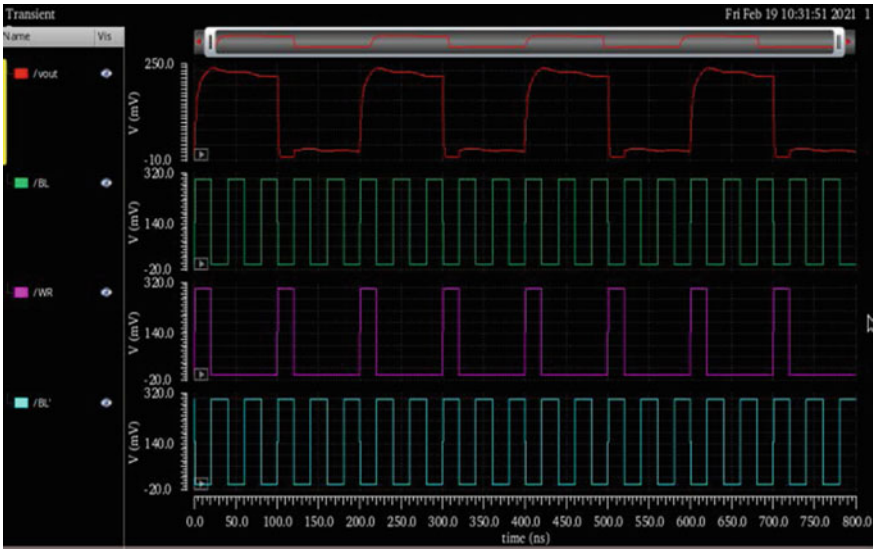

Fig. 24 DRAM transient plot

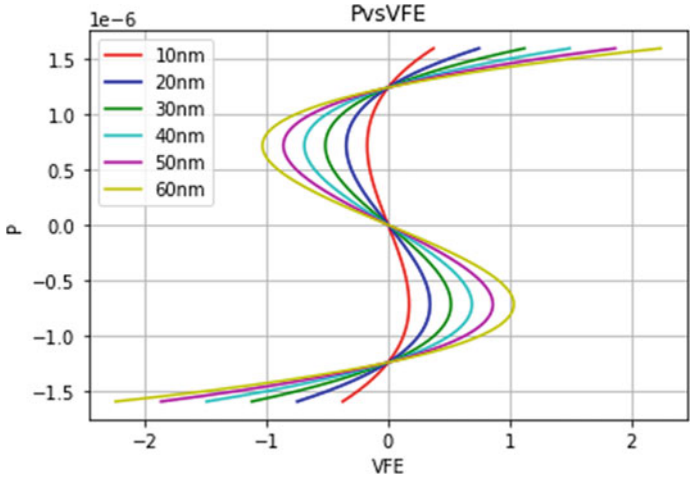

Fig. 25 Hysteresis plot

References

1. Li Y, Lian Y, Yao K, Samudra GS (2015) Evaluation and optimization of short channel ferroelectric MOSFET for low power circuit application with BSIM4 and Landau theory. Solid State Electron 114:17–22
2. Salahuddin S, Datta S (2008) Use of negative capacitance to provide voltage amplification for low power nanoscale devices. Nano Lett 8(2):405–410

3. Jain A, Alam MA (2014) Stability constraints define the minimum subthreshold swing of a negative capacitance field-effect transistor. IEEE Trans Electron Devices 61(7):2235–2242
4. Kobayashi M, Hiramoto T (2015) Device design guideline for steep slope ferroelectric FET using negative capacitance in sub-0.2 V operation: operation speed, material requirement and energy efficiency. In: Proceedings symposium VLSI technology, June 2015, pp T212–T213
5. Sivasubramanian S, Widom A, Srivastava Y (2003) Equivalent circuit and simulations for the Landau Khalatnikov model of ferroelectric hysteresis. IEEE Trans Ultrason Ferroelectr Freq Control 50(8):950–957
6. Cirit MA (1989) The Meyer model revisited: Why is charge not conserved? [MOS transistor]. IEEE Trans Comput-Aided Design Integr Circuits Syst 8(10):1033–1037
7. Dünkel S et al. (2017) A FeFET based super-low-power ultra-fast embedded NVM technology for 22nm FDSOI and beyond. In: IEDM Technology Dignostics, pp 19.7.1–19.7.4
8. Cheng C-H, Chin A (2014) Low-leakage-current DRAM-like memory using a one-transistor ferroelectric MOSFET with a Hf-based gate dielectric. IEEE Electron Device Lett 35(1):138–140
9. A Verilog-A Compact Model for Negative Capacitance FET "Muhammad Abdul Wahab and Muhammad Ashraful Alam, Purdue University
10. Aziz A, Ghosh S, Datta S, Gupta SK (2016) Physics-based circuit-compatible SPICE model for ferroelectric transistors. IEEE Electron Device Lett 37(6):805–808. https://doi.org/10.1109/LED.2016.2558149

Convolutional Encoder–Decoder Architecture for Speech Enhancement

Utkarsh Maheshwari, Piyush Goel, R Annie Uthra, Vinay Vasanth Patage, Sourabh Tiwari, and Saksham Goyal

Abstract Signal processing faces the quandary of not being able to separate non-stationary noise from speech signal. Traditional methodologies relied on spectral subtraction for the same; however, such techniques relied on approximation of spectral mask of the noise. This paper proposes an effective and novel convolutional encoder–decoder architecture to effectuate clean speech from the input audio through denoising the audio input. The architecture uses skip connections to increase information flow from encoder to decoder, which helped the authors bolster the performance of the network. The generated output is evaluated on objective and subjective metrics like signal-to-noise ratio (SDR), perceptual evaluation of speech quality (PESQ) and short time objective intelligibility (STOI). The proposed system outperforms the state-of-the-art systems with respect to SDR, PESQ and STOI. The architecture finds applications in various fields such as speech recognition, machine translation and telecommunication.

Keywords Speech denoising · Neural networks · Speech enhancement · Babble noise · Encoder–decoder networks

U. Maheshwari · P. Goel (✉) · R. A. Uthra
Department of Computer Science Engineering, SRM Institute of Science and Technology, Kattankulathur, India
e-mail: pg1608@srmist.edu.in

U. Maheshwari
e-mail: un7993@srmist.edu.in

R. A. Uthra
e-mail: annieu@srmist.edu.in

V. V. Patage · S. Tiwari · S. Goyal
Samsung Research Institute, Bangalore, India
e-mail: vinay.pv@samsung.com

S. Tiwari
e-mail: sourabh.t@samsung.com

S. Goyal
e-mail: s.goyal@samsung.com

C. Subramani et al. (eds.), *Proceedings of International Conference on Power Electronics and Renewable Energy Systems*, Lecture Notes in Electrical Engineering 795,
https://doi.org/10.1007/978-981-16-4943-1_34

1 Introduction

Speech denoising can be defined as the process of removing unwanted audio signals from the speech that affects the intelligibility of the original message. The aim is to enhance the cognitive quality of speech signals, especially by removing background noise. Noise can be broadly classified into stationary and non-stationary noise. Stationary noises are the ones with single-tone sine waves and constant frequency. Based on the energy levels of the noise, stationary noises can be further classified as white, pink, brown and black noises. Various techniques such as spectral gating, MMCA and MRCA have been used in the past to reduce them. These methods rely on calculating the spectrum of clean speech and blocking off any frequency higher than the spectrum. While such methods perform well for stationary noises, they still have difficulty coping with normal sounds such as the unstoppable noise or the whirling sound found in the crowd at the same time. Most real-world scenarios contain what is described as non-stationary noises. Non-stationary noises have varying frequencies, thus making techniques such as spectral gating impractical. Babble noises like street noise, barking dogs and background chatter make the speech incomprehensible for the listener. However, recent advancements in deep learning have made it possible to reduce such noises as well. Models based on neural networks work much better than traditional methods for all kinds of noises. This could be attributed to the ability of neural networks to generate more complex and nonlinear decision boundaries. Furthermore, in-depth learning methods outperform the traditional methods in both quantitative and qualitative metrics.

Inspired by these recent developments, the authors of this paper propose one such novel architecture aimed to improve the speech quality. A symmetric convolutional encoder–decoder architecture with sequence remodelling network is proposed. The network takes a monophonic sound signal as an input and separates clean and noisy signals. The network also consists of U-Net-type skip connections from encoder to decoder. In addition, our network also performs voice activity detection (VAD), to find silences in between. Many metrics have been shown to be inconsistent with human judgements, we use the benchmark techniques like short time objective intelligibility (STOI) and perceptual evaluation of speech quality (PESQ) to compare our model with the state of the art. Speech enhancement finds applications in hearing aids, robust speech recognition algorithms, mobile communication, etc. This paper aims to propose one such deep learning algorithm to solve the problem of speech denoising. Instead of focusing on the noise, we consider the task of denoising as essentially to learn a mapping from noisy audio to clean audio.

The paper is organised as follows. In Sect. 2, we briefly describe prior work done in the field. In Sect. 3, we propose our encoder–decoder-based architecture with overall design. In Sect. 4, results of experiments are discussed, and finally in Sect. 5, we conclude our study.

2 Literature Review

Prior to the use of deep learning architectures, spectral gating techniques were used for speech enhancement. Such techniques primarily relied on the use of approximation of noise masks which were then removed from speech signals. The authors of the [1] used various minimum mean-squared estimator (MMSE) methods to first approximate spectra of the noise from non-speech parts and then subtracting the noise from the input signal. However, MMSE-based methods were not suitable for non-stationary noises. Additionally, such methods were inadequate for non-acoustic noises. Another approach was proposed by the authors of [2] based on minima-controlled recursive averaging (MCRA). As the name suggests, hypothetical gains related to the presence of speech were recursively averaged to arrive at optimal spectral gain function. Improved versions of MCRA were then proposed which instead of relying on static smoothing parameter was time and frequency dependent, thus providing better results for non-stationary noises with a low signal to noise ratio.

However, both MMSE and MCRA-based methods were not suitable for non-stationary noises, and hence a nonlinear algorithm was required to develop a more dynamic mask. Neural networks overcome this problem as they are capable of developing more intricate decision boundaries. Such networks instead of approximating a noise mask considered the task of denoising as a mapping from noisy input to clean output. One such architecture was proposed by the authors of [3]. A deep neural network architecture trained on Aurora2 data set used pairs of clean and noisy signals. The authors used global variance (GV) and dropout layers. Since speech is a sequential signal, long short-term memory was used by authors of [4]. LSTM approximates masks using differential function between two subsequent time instances. U-Net-based architecture was used by [5]. U-Net initially developed for medical imaging tasks was augmented with long-range skip connections and trained on instrumental sounds to develop spectrogram masks. All the papers mentioned above used signal distortion ratio (SDR) as an objective function. Authors of [6] proposed three architectures to finally meet the objective of universal sound separation. Three architectures, CLDNN based on ConvTasNet [7], TDCN++ with skip connections and normalisation layers and iTDCN++, a two stage iterative TDCN network was proposed.

3 Proposed System

The proposed system achieves speech enhancement through two steps, data preprocessing followed by audio denoising as shown in Fig. 1. Data preprocessing converts the audio signal to MFCC that is fed to the audio denoising module. The audio denoising module separates the speech and noise through symmetric encoder and decoder.

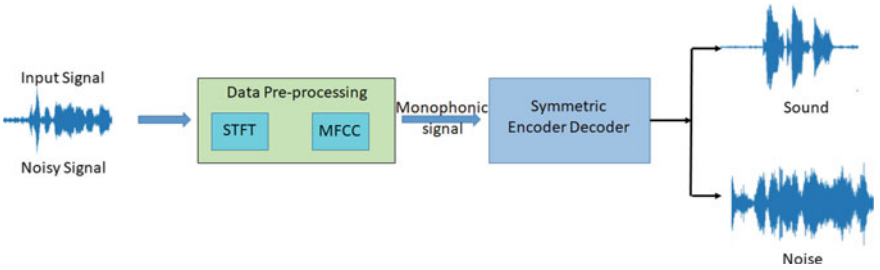

Fig. 1 Proposed system architecture

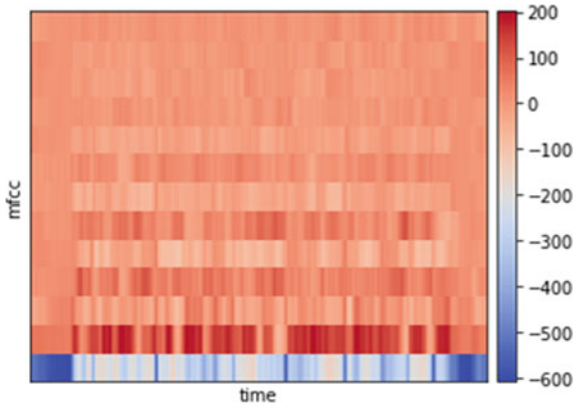

Fig. 2 MFCC features represented on the MEL scale with amplitude versus frequency

3.1 Data Preprocessing

In the proposed system, the sound signals were first converted into monophonic signals each of sample rate 16000 kHz. The signals are then converted into STFT giving values of amplitude change in accordance with time. Next MFCCs of the sound signals were extracted, where the hop length is taken to be 512, the number of coefficients to be extracted is taken as 13, and the number of segments is taken as 1. MFCC accounts for the human perception for sensitivity at particular frequencies by converting the theoretical values into a MEL scale, thus they are suitable for speech recognition. Figure 2 depicts a sample preprocessed noise signal with the various MFCC coefficients on MEL scale.

3.2 Audio Denoising

The proposed denoising network is capable of enhancing monophonic input signal and separating the input signal into its speech and noise constituents. The network

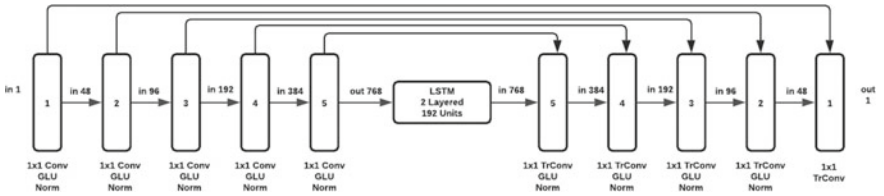

Fig. 3 Symmetric encoder–decoder architecture

consists of a symmetric encoder–decoder architecture along with a two-layered LSTM network in between as shown in Fig. 3. Before feeding the audio to the encoder, the signal is upsampled by a factor of two and then the output of the decoder is downsampled by the same rate. The encoder contains five layers numbered one to five with increasing number of output channels as we go deeper. In order to separate non-stationary noise, nonlinearity needs to be introduced. 1×1 convolution is effective for the same. Therefore, each layer of encoder consists of ReLu followed by 1×1 convolution, normalisation layers and GLU activation. A two-layered LSTM network each with 128 hidden units takes the input from the fifth layer of the encoder, and the output is then fed to the decoder. The architecture of the decoder is symmetrical to the encoder with five layers numbered five to one. Each layer of decoder performs 1×1 transpose convolution followed by a GLU activation. Number of output channels decreases symmetrically along the decoder except in the last layer. The last layer consists of a single channel as the output. Skip connections as proposed by Ronneberger et al. [8] connect the output of the kth layer of the encoder to the kth layer of the decoder.

The network is trained for 300 epochs on Valentini data set with Adam optimiser. The objective function is a ratio between distortion and clean signal.

4 Results and Discussions

Three metrics were used to evaluate the performance of the model on different data sets. Signal to distortion ratio (SDR) is an objective metric that measures the l2 errors present between the model output and ground truth audio. Two additional subjective metrics were evaluated. These were perceptual evaluation of speech quality (PESQ) and short time objective intelligibility (STOI). These metrics measure the intelligibility of speech. The network was trained on Valentini data set. The data set consists of 400 sentences read out by 109 speakers added with babble noise from CSTR corpus.

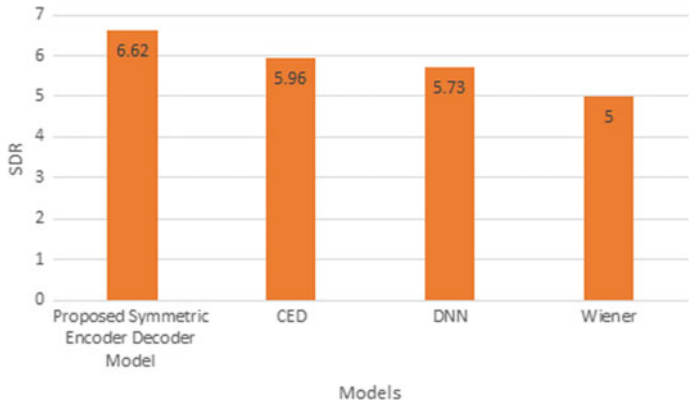

Fig. 4 SDR comparison between the proposed and state-of-the-art models

4.1 SDR Comparison

SDR was compared with convolutional encoder–decoder (CED) network proposed by Park and Lee [9], deep neural network (DNN) proposed by Xu et al. [3] and Wiener filter. SDR performance of wiener filter was least as the algorithm relies on MMSE-based approach. Both CED and DNN showed improvements over traditional approaches as they are capable of nonlinear decision boundaries. The proposed algorithm because of skip connections performed better than CED and DNN, and the results are depicted in Fig. 4.

4.2 PESQ Comparison

The PESQ result was compared with SEGAN [10], Wave U-Net [11] and MMSE-GAN [12]. The proposed architecture performed better than GAN-based architectures. The results are summarised in Table 1.

Table 1 PESQ comparison

Model	PESQ value
Proposed symmetric encoder–decoder model	2.63
SEGAN	2.16
Wave U-Net	2.4
MMSE-GAN	2.53

Table 2 Data set comparison

Data set	PESQ	STOI	SDR
DNS	2.48	0.86	6.19
MCV + UrbanSound	2.34	0.84	6.98
Valentini	2.63	0.87	6.62

4.3 Data set Comparison

The results were compared between three data sets: DNS, Valentini and Urban Sound8K augmented with Mozilla Common Voice to generate clean and noisy speech pairs. The results for the same are summarised in Table 2**.**

4.4 Waveforms

Figure 5 displays the waveforms of noisy input and the clean output of the model. The figure also consists of a waveform of the noise present in the input audio. These waveforms can be used to estimate the performance of the model.

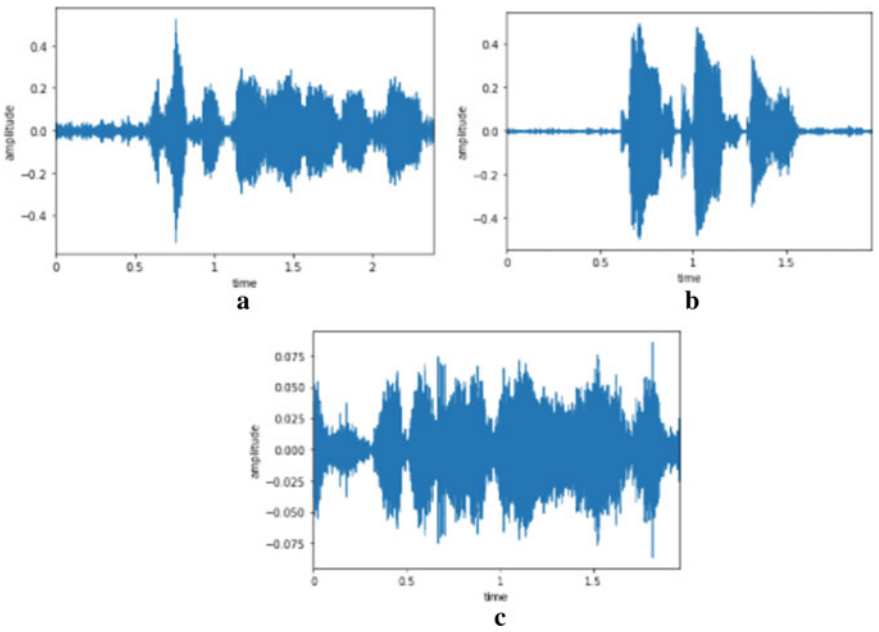

Fig. 5 From left to right: **a** noisy input **b** cleaned output **c** separated noise

5 Conclusion

This paper proposes an idea for an encoder–decoder-based speech enhancement model. The technique is to train a network to learn the mapping between noisy and clean training samples and then use the trained weights to enhance audio signals that are not seen before in the data set. The model is evaluated on three different subjective and objective metrics and three data sets to validate the performance. The idea is to use the proposed algorithm for speech recognition, machine translation and telecommunication.

References

1. Boll S (1979) Suppression of acoustic noise in speech using spectral subtraction. IEEE Trans Acoust Speech Signal Process 27(2):113–120. https://doi.org/10.1109/TASSP.1979.1163209
2. Cohen I, Berdugo B (2009) Speech enhancement for non-stationary noise environments. Signal Process 81:2403–2418. https://doi.org/10.1016/S0165-1684(01)00128-1
3. Xu Y, Du J, Dai L, Lee C (2015) A regression approach to speech enhancement based on deep neural networks. IEEEACM Trans. Audio Speech Lang. Process. 23(1):7–19. https://doi.org/10.1109/TASLP.2014.2364452
4. Weninger F, Hershey JR, Roux JL, Schuller B (2014) Discriminatively trained recurrent neural networks for single-channel speech separation. In: 2014 IEEE global conference on signal and information processing (GlobalSIP), December 2014, pp 577–581. https://doi.org/10.1109/GlobalSIP.2014.7032183
5. Jansson A, Humphrey E, Montecchio N, Bittner R, Kumar A, Weyde T (2017) Singing voice separation with deep U-Net convolutional networks, pp 7
6. Kavalerov I et al. (2019) Universal sound separation. ArXiv190503330 Cs Eess Stat, August 2019, Accessed 28 Jan 2021. [Online]. Available http://arxiv.org/abs/1905.03330
7. Luo Y, Mesgarani N (2019) Conv-TasNet: surpassing ideal time-frequency magnitude masking for speech separation. IEEEACM Trans Audio Speech Lang Process 27(8):1256–1266. https://doi.org/10.1109/TASLP.2019.2915167
8. Ronneberger O, Fischer P, Brox T (2015) U-Net: convolutional networks for biomedical image segmentation. ArXiv150504597 Cs, May 2015, Accessed 09 Mar 2021. [Online] Available http://arxiv.org/abs/1505.04597
9. Park SR, Lee J (2016) A fully convolutional neural network for speech enhancement. ArXiv160907132 Cs, September 2016, Accessed 27 Jan 2021. [Online]. Available http://arxiv.org/abs/1609.07132
10. Pascual S, Bonafonte A, Serrà J (2017) SEGAN: speech enhancement generative adversarial network. ArXiv170309452 Cs, 2017 Jun, Accessed 09 Mar 2021. [Online]. Available http://arxiv.org/abs/1703.09452
11. Macartney C, Weyde T (2021) Improved speech enhancement with the wave-U-Net. ArXiv181111307 Cs Eess, Nov. 2018, Accessed 09 Mar 2021. [Online]. Available http://arxiv.org/abs/1811.11307
12. Phan H et al (2020) Improving GANs for speech enhancement. IEEE Signal Process Lett 27:1700–1704. https://doi.org/10.1109/LSP.2020.3025020

Tuning of MIMO PID Controller Using HCLPSO Algorithm

T. Jeyaraman, D. Joelpraveenkumar, M. Kaliraj, M. Krishna Chandar, and M. Willjuice Iruthayarajan

Abstract In this paper, the heterogeneous comprehensive learning particle swarm optimization is proposed for the tuning of multivariable proportional integral derivative (PID) for Wood and Berry system. This simulation work is done for both the decentralized and centralized PID controller. For comparison, results from the tuning of multivariable PID controller by particle swarm optimization (PSO) algorithm is considered. Here, our objective is to minimize the integral absolute error (IAE) value of the system. For the simulation of the system and algorithm, MATLAB/SIMULINK software is used. Statistical performance of evolutionary algorithms such as best value, mean value, and standard deviation are going to be evaluated based on ten independent initial conditions. In this work, it is observed that HCLPSO give more consistent performance compared to PSO algorithm.

Keywords MIMO · PID · Centralized · Decentralized · HCLPSO · Tuning

1 Introduction

In this modern world, most of the industries are having multiple inputs and multiple outputs systems. These systems are very complicated to get the desired output so that a suitable controller and tuning methods are needed. Most of the MIMO system is controlled by using a PID controller [1]. PID controller [2] is the most popular controller due to its advantages over others. It is most widely used in industrial applications. It uses a control loop feedback mechanism to control the variables. PID stands for the mathematical term proportional, integral, and derivative. Proportional means constant or right value. Integral means the summation of a function over a given interval and derivative is the rate of change of value for a given interval. In this work, decentralized and centralized PID controllers for the tuning of the MIMO system. In decentralized controller [3], there are n PID controllers and in centralized controller [4] $n*n$ PID controllers. In various engineering applications, the tuning of

T. Jeyaraman · D. Joelpraveenkumar · M. Kaliraj · M. K. Chandar · M. W. Iruthayarajan (✉)
Department of EEE, National Engineering College, Kovilpatti 628503, India
e-mail: hodeee@nec.edu.in

C. Subramani et al. (eds.), *Proceedings of International Conference on Power Electronics and Renewable Energy Systems*, Lecture Notes in Electrical Engineering 795,
https://doi.org/10.1007/978-981-16-4943-1_35

the PID controller for various algorithm is mentioned in [5]. In recent times, heterogeneous comprehensive learning particle swarm optimization (HCLPSO) algorithm [6] performs very well. The tuning of PID controller for SISO system for HCLPSO algorithm was explained in the paper [7]. In this paper, we are going to tune the PID controller for MIMO system by using HCLPSO algorithm. Among population-based tuning algorithms, HCLPSO has the learning capability to become the output of the system as consistent, converged, and has better performance. In HCLPSO, the total population is grouped into two subpopulations such as exploration and exploitation. For the optimal results, we have to balance between these two subpopulations. This paper mainly focuses on minimizing the error value such as integral absolute error (IAE) and the performance analysis of the PID controller for the binary distillation column plant that was described by Wood and Berry [8]. The PID controller continuously calculates the error value which is the difference between the desired set point and the measured process variable and applies the correction by changing the proportional, integral, and derivative value. For the performance analysis, we compare the output results of HCLPSO to the output results of PSO.

2 MIMO System

The MIMO system is the multiple inputs and multiple outputs system which requires control techniques for improving the performance of the system. The MIMO system is more difficult to exploit than a SISO system. We have used a 2×2 Binary distillation column plant described by Wood and Berry.

The generalized transfer function for the MIMO system is given below,

$$\mathrm{G(s)} = \begin{bmatrix} \mathrm{g}_{11}(s) & \cdots & \mathrm{g}_{1n}(\mathrm{s}) \\ \vdots & \ddots & \vdots \\ \mathrm{g}_{n1}(\mathrm{s}) & \cdots & \mathrm{g}_{11}(\mathrm{s}) \end{bmatrix} \tag{1}$$

2.1 Wood and Berry System

Wood and Berry have derived the mathematical model for binary distillation column plant. The typical column plant consists of a vertical column, re-boiler, condenser, reflux drum, and it contains a feed stream and two product streams. The column plant requires a minimum four number of feedback control loops. These control loops are used to control the distillate concentration, bottom concentration, level of re-boiler, and level of reflux rate. Each controller loop requires a minimum of one input and output so that the system is considered as a MIMO system.

The derived transfer function for the column plant is given by

$$G(s) = \begin{bmatrix} \frac{12.8e^{-s}}{1+16.7s} & \frac{-18.9e^{-3s}}{1+21s} \\ \frac{6.6e^{-7s}}{1+10.9s} & \frac{19.4e^{-3s}}{1+14.4s} \end{bmatrix} \tag{2}$$

2.2 Decentralized Controller

In a decentralized controller, there are n controllers are used. We used the Wood and Berry system with 2 PID controllers. The decentralized controller system is most frequently used in industries. The computational time is less for a decentralized controller system compared to a centralized controller system. Simulink model for the decentralized controller is shown below (Fig. 1). The general transfer function for the decentralized controller is given by,

$$K(s) = \begin{bmatrix} k_1(s) & \cdots & 0 \\ \vdots & \ddots & \vdots \\ 0 & \cdots & k_n(s) \end{bmatrix} \tag{3}$$

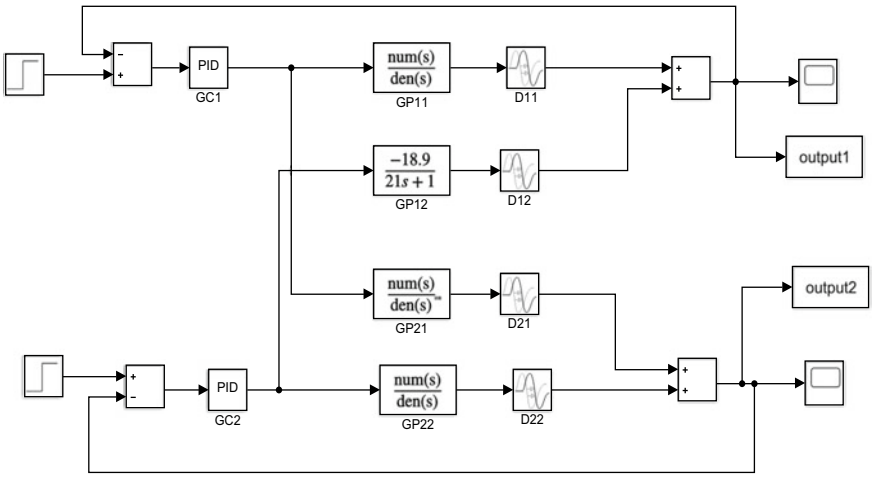

Fig. 1 Simulink model for decentralized controller

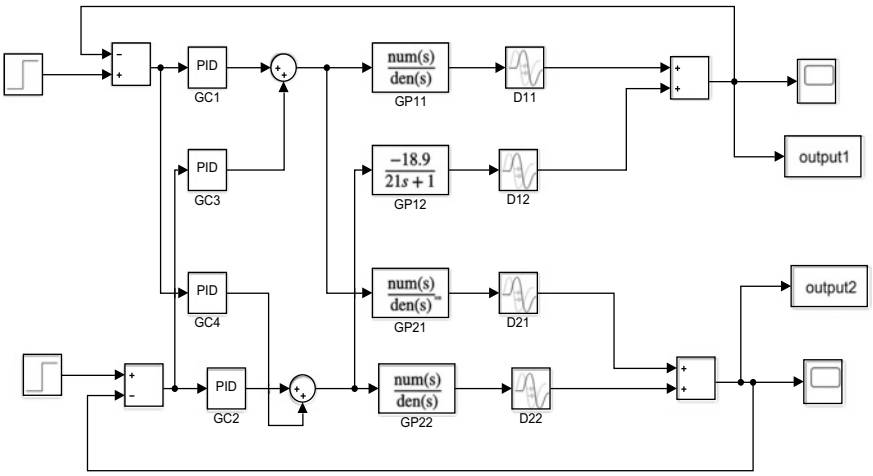

Fig. 2 Simulink model for centralized controller

2.3 Centralized Controller

For a MIMO system, a full multivariable controller is used, such a controller is called a centralized controller. This controller will give satisfactory responses for the desired system. The centralized controller requires *n*n* controllers, whereas the decentralized controller requires only n controllers. In this controller, two PIDs are coupled to each other to obtain the desired output for the system. We can design a full matrix for a centralized controller system and find out the controller parameter values by suitable tuning methods. Simulink model for the centralized controller is shown below (Fig. 2).

The general form of *n* n* multivariable PID controller is given by,

$$K(s) = \begin{bmatrix} k_{11}(s) & \cdots & k_{1n}(s) \\ \vdots & \ddots & \vdots \\ k_{n1}(s) & \cdots & k_{nn}(s) \end{bmatrix} \tag{4}$$

3 HCLPSO Algorithm

In HCLPSO, the swarm is divided into two heterogeneous subpopulations. The first subpopulation is enhanced for exploration and the second subpopulation is enhanced for exploitation. In both exploration and exploitation subpopulations, the exemplar

is generated using comprehensive learning (CL) strategy with the learning probability. Each subpopulation is assigned to focus only on either exploration or exploitation. To generate exemplars, in exploration subpopulation exemplars, the personal best experience of the same subpopulation is used and in the exploitation subpopulation, the personal best experience of the entire swarm population is used. As exploration subpopulation learns only from the same population, the diversity can be retained. The velocity of an exploitation-enhanced subpopulation is updated using the following equation:

$$V_i^d = \omega_* V_i^d + c_{1*}\text{rand}_{1*}^d\left(p\,\text{best}_{fi(d)}^d - X_i^d\right) + c_{2*}\,\text{rand}_{2*}\left(g\,\text{best}^d - X_i^d\right)$$

d	dimension
$V_i{}^d$	updated velocity of an ith particle
ω	inertia weight
c_1, c_2	acceleration factor
$\text{rand}_1{}^{\text{d}}$, rand_2	uniform random between 0 and 1
$X_i{}^d$	dth value of ith particle in the population
$\text{Pbest}^d{}_{fi(\text{d})}$	best position of the ith particle
Gbest^{d}	best position of the whole swarm population

$$V_i^d = wV_i^d + c^*\text{rand}_i^d * \left(p\text{best}_{fi(d)}^d - X_i^d\right)$$

where $f_i(\text{d}) = [f_i(1), f_i(2), \ldots, f_i(D)]$ indicates the ith particle follows its own or other pbest for each dimensions. The particle is specified according to the learning probability values($p_c{}^i$) .

4 Parameter Analysis

For the decentralized controller, we made the performance analysis. In HCLPSO, there are several tuning parameters such as learning probability, grouping, and the velocity of the particle. The output result was analyzed by changing these parameters, keeping the two parameters as constant. So that one parameter is kept as constant and change the other parameter and analyze the output. In order to find the effect of learning probability to the performance of HCLPSO, the velocity of the particle is kept as constant. The obtained statistical performance such as best value, mean value, and optimal value among ten independent runs for the velocity = 0.15, learning probability = 0.25 and velocity = 0.15, learning probability = 0.15 are represented in Table 1.

From Table 1, we infer that

Table 1 Performance of HCLPSO algorithm based on learning probability

Parameters	Functional count	Best value	Mean value	Std deviation value
Velocity = 0.15 and learning probability y = 0.25	9000	8.1462	8.2849	0.1714
	3000	8.6521	9.5202	0.7022
Velocity = 0.15 and learning probability y = 0.15	9000	8.1129	8.5659	0.3783
	3000	8.6511	10.2654	1.9256

Table 2 Performance of HCLPSO algorithm based on velocity of the particles

Parameters	Functional count	Best value	Mean value	Std deviation value
Velocity (V_{max}) = 0.25 Learning probability (Pc) = 0.2	3000	9.7702	10.3743	0.5655
	9000	9.6836	9.7862	0.2620
Velocity (V_{max}) = 0.2 Learning Probability (Pc) = 0.2	3000	9.8895	10.5557	0.5392
	9000	9.6824	9.8263	0.3014

- If we decrease the learning probability value, the standard optimal value will increase and output will not converge.
- If we increase the learning probability value, the standard optimal value will decrease and output will converge, and it will give the consistent performance.

The obtained statistical performance such as best value, mean value, and standard deviation value for the velocity = 0.25, learning probability = 0.2 and velocity = 0.2, learning probability = 0.2 are represented in Table 2. In order to find the effect of maximum velocity of the performance of the HCLPSO algorithm, the learning probability is kept as constant.

From the above Table 2, we infer that

1. If we decrease the velocity of the particle, it will give the best optimal solution.
2. From the above analysis, we conclude that the best optimal solution and system consistent

5 Results

From this paper, we analyze the parameter changes and finally conclude that the best optimal solutions will get for the particular parameters. We made several trials and runs and obtained the suitable parameters for the design of centralized and decentralized PID controllers for HCLPSO algorithm.

For decentralized controller, the parameters are learning probability (pc) = 0.25, grouping ratio (g1) = 0.3, and velocity (Vmax) = 0.2. The overall obtained results for

Table 3 Comparison of HCLPSO algorithm with PSO algorithm for decentralized controller

PSO obtained results	Max_FES	Best optimal	Mean optimal	Standard deviation value
	3000	9.6824	10.2209	0.5433
	6000	9.6824	10.104	0.4444
	9000	9.6824	10.0822	0.5468
Learning probability(pc) = 0.25, Grouping ratio(g1) = 0.3, Velocity(Vmax) = 0.2				
HCLPSO obtained results	3000	9.9101	10.5299	0.4284
	6000	9.6826	9.7301	0.0666
	9000	9.6825	9.6851	0.0018

Table 4 Comparison of HCLPSO algorithm with PSO algorithm for centralized controller

PSO obtained results	Max_FES	Best optimal	Mean optimal	Standard deviation value
	3000	8.3255	9.0636	0.7900
	6000	8.1245	10.0422	2.7854
	9000	8.0189	9.0186	1.5178
	12,000	8.0273	10.9396	4.4975
Learning probability(pc) = 0.25, Grouping ratio(g1) = 0.3, Velocity(vmax) = 0.15				
HCLPSO obtained results	3000	8.6521	9.5202	0.7022
	6000	8.2661	8.8084	1.1179
	9000	8.1462	8.2849	0.1749
	12,000	8.0945	8.2580	0.1289

the decentralized controller using HCLPSO algorithm for various function evolutions are reported in Table 3.

For centralized controller, the parameters are learning probability (pc) = 0.25, grouping ratio (g1) = 0.3, and velocity (vmax) = 0.1. The overall obtained results for the centralized controller using HCLPSO algorithm are represented in Table 4.

From the Tables 3 and 4, the obtained best performance of both the HCLPSO and PSO algorithms are similar, but the performance of HCLPSO algorithm gives more consistent performance compared to PSO algorithm when the number of function evaluations are higher due to their learning ability. Convergence characteristics of both the algorithms are reported in Figs. 3 and 4 which shows both the algorithms have converged their optimal values.

6 Conclusions

- From the Table 1, we conclude that by increasing the learning probability value, the output results are more consistent and the deviation is minimum.

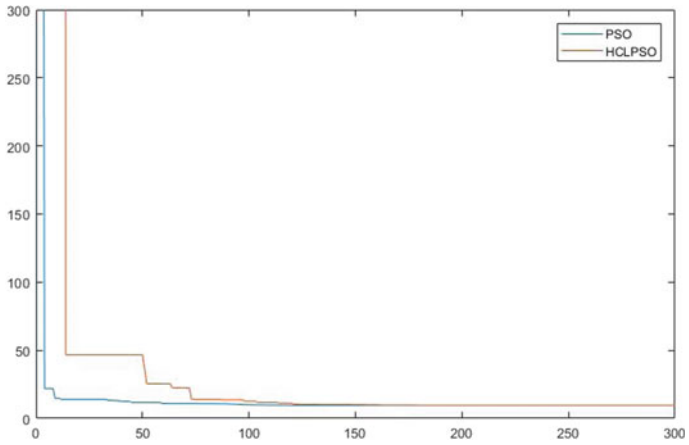

Fig. 3 Convergence graph for decentralized controller

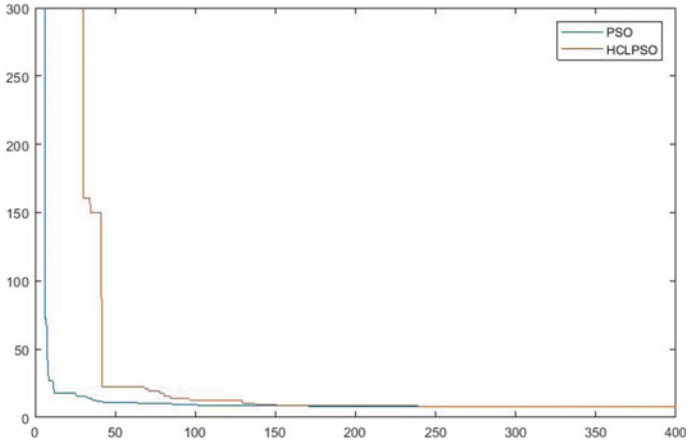

Fig. 4 Convergence graph for centralized controller

- From the Tables 3 and 4, we conclude that PSO and HCLPSO have moreover give same optimal solution, but HCLPSO gives lesser value of standard deviation value for increasing the function evaluation of the particle. Since the HCLPSO has learning probability, it gives more consistent solution for greater value of function evaluation.
- From the Tables 3 and 4, we conclude that centralized controller has better optimal solution compared to the decentralized controller.

Acknowledgements We thank the college management for providing the lab facility to do the project work.

References

1. Juang JG, Huang MT, Liu WK (2008) PID Control using presearched genetic algorithms for a MIMO system. IEEE Trans Syst Man Cybern Part C (Appl Rev) 38(5):716–727
2. Ochi Y, Yokoyama N (2012) PID controller design for MIMO systems by applying balanced truncation to integral- type optimal servomechanism. IFAC Proceed Volumes 45(3):364–369
3. Harjare VD, Patre BM (2015) Decentralized PID controller for TITO systems using characteristic ratio assignment with an experimental application. ISA Trans **59**(385–397)
4. Dhanya Ram V, Chidambaram M (2015) Simple method of designing centralized PI controllers for multivariable systems based on SSGM. ISA Trans 56: 252–260
5. Willjuice Iruthyarajan M, Baskar S (2009) Evolutionary algorithms based design of multivariable PID controller. Expert Syst Appl 36(5):9159–9167
6. Lynn N, NagaratnamSuganthan P (2015) Heterogeneous comprehensive learning particle swarm optimization with enhanced exploration and exploitation. Swarm Evol Comput 24:11–24
7. Muniraj R, Willjuice Iruthayarajan M (2018) Tuning of robust PID controller with filter for PLL system using HCLPSO algorithm. Int J Pure Appl Math 118(16):181–197
8. Wood R, Berry M (1973) Terminal Composition control of a binary distillatillation column. Chem Eng Sci 28(9):1707–1717

Design Guide for Small-Scale Grid-Connected PV System Using PVsyst Software

A. Lavanya, Kushagra Bhatia, J. Divya Navamani, A. Geetha, and K. Vijayakumar

Abstract Recently, small-scale grid-connected PV systems are acquiring familiarity in institutions and industries mainly due to their clean and climate-friendly attribute. A 104 kW grid-connected PV system at Kattankulathur, Tamil Nadu, is discussed in this paper. A software tool is essential to estimate and predict solar energy power generation for a particular location. This paper mainly deliberates the design aspects using a suitable software tool for the grid-connected PV system. The best approach for designing and evaluating energy production in PV systems is PVsyst software. Therefore, this paper demonstrates the step-by-step procedure followed for creating the 104 kW PV system. The approach towards loss distribution and performance ratio analysis is also presented. This paper is proposed as a guide for the researchers working in this field of designing a PV system based on the load requirement.

Keywords PVsyst · Grid connected · Loss distribution · Performance ratio · Case study

1 Introduction

India has a solar potential of about 748 GW, assuming three per cent of the wasteland area covered by PV modules as evaluated by National Institute of Solar Energy. National Solar Mission (NSM) plays a most important role in endorsing the solar energy to the central place in the country's National Action Plan on climate change [1]. NSM was launched on 11 January 2010. NSM is a noteworthy initiative of India's Government with dynamic contribution from states to encourage environmentally sustainable development while addressing India's energy safety trials. It will also establish a substantial involvement by India to the global effort to encounter climate change challenges [2–5]. The mission's objective is to build India as a universal front

A. Lavanya (✉) · K. Bhatia · J. Divya Navamani · A. Geetha · K. Vijayakumar
SRM Institute of Science and Technology, Kattankulathur, TamilNadu 603203, India
e-mail: lavanyaa@srmist.edu.in

K. Bhatia
e-mail: kb1607@srmist.edu.in

C. Subramani et al. (eds.), *Proceedings of International Conference on Power Electronics and Renewable Energy Systems*, Lecture Notes in Electrical Engineering 795,
https://doi.org/10.1007/978-981-16-4943-1_36

Fig. 1 Popular design software for PV system

runner in solar energy by making the strategy circumstances for solar technology dissemination across the country as rapidly as likely. The mission's goal is to install 100 GW grid-connected solar PV plants by the year 2022 is the motivation for this paper. India's total installed generating power capacity is 375.323 GW. As of December 2020, from this coal share is 55.4%, renewable energy is 23.5%, nuclear 1.8%, and hydro energy involvement is 12.3%. The comprehension of a photovoltaic (PV) case study is to complete the step-by-step procedure for sizing, which permits the assumed data confined in the practical manual, as topographical localization of the location and the energy requirements, to assess predominantly the size of the PV array and the volume of the batteries. To achieve this operation, sizing tool is required. An evaluation between the fixed-tilt plane and seasonal tilt adjustment of PV system is finished, built on their efficiency using PVSYST, was proposed in [6, 7]. Based on the statement acquiesced by the Ministry of New and Renewable Energy (MNRE) and TERI an institute for energy and resources, some of the world's most commonly used PV simulation software for PV system design is shown in Fig. 1.

2 Step-by-Step Guild to Simulate a Grid-Connected PV System

In this guild, the objective is to simulate, study and analyse a grid-tied PV system. To start, the basic data collected in order to build and design the system is utilized. All the information will be given in each and every step along the way. PVsyst V6.88 is employed to demonstrate the considered PV plant simulation.

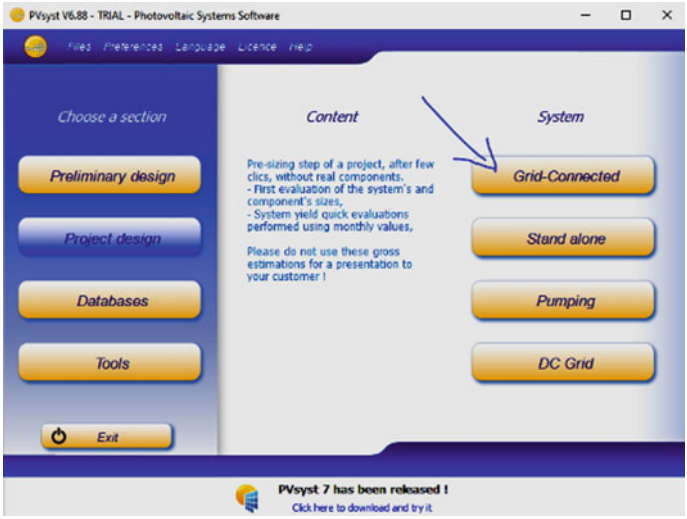

Fig. 2 Start window PVsyst

Step 1: **Start and select the initial in the software**

Start-up PVsyst software; select 'Grid-Connected' under 'Project design' to start the project as shown in Fig. 2.

Step 2: **New project and site file**

As shown in Fig. 3, this is what the work space looks like, two subheadings, namely 'Project's Designation' and 'System Variant'. To start, first thing needed is a 'Site file'. Site data consists of location details such as latitude, longitude, sea level and time zone. Upload 'Site file' of the correct format if in hand or create a new file. PVsyst allows us to generate our custom 'Site file' and 'Meteo file'. Click the highlight icon in Fig. 3. A new window will open as shown in Fig. 4, 'Geographical Site Parameter', three sub-tabs: 'Geographical Coordinates', 'Monthly Meteo' and 'Interactive Map'.

Step 3: **Creating our own Site and Meteo File**

Enter the 'Site Name', 'Country' and the 'Region'. To get the Meteo data, enter 'location coordinates'; Click on the 'Get from Coordinates' to finish. The software will automatically get the 'Altitude' and the 'Time Zone' through the site coordinates. Import Meteo Data. The 'import' option is open under 'Meteo data Import' and select from the data. Use 'Meteonorm 7.2'. Click 'import'. A new window tab 'Monthly Meteo' will be opened which will show all the data parameters that will be applied to our system. Refer Fig. 5 for all the parameters. Select the 'Irradiance units' as 'kWh/m2, day' as shown in Fig. 5.

Step 4: ***System variant configuration, calculation***

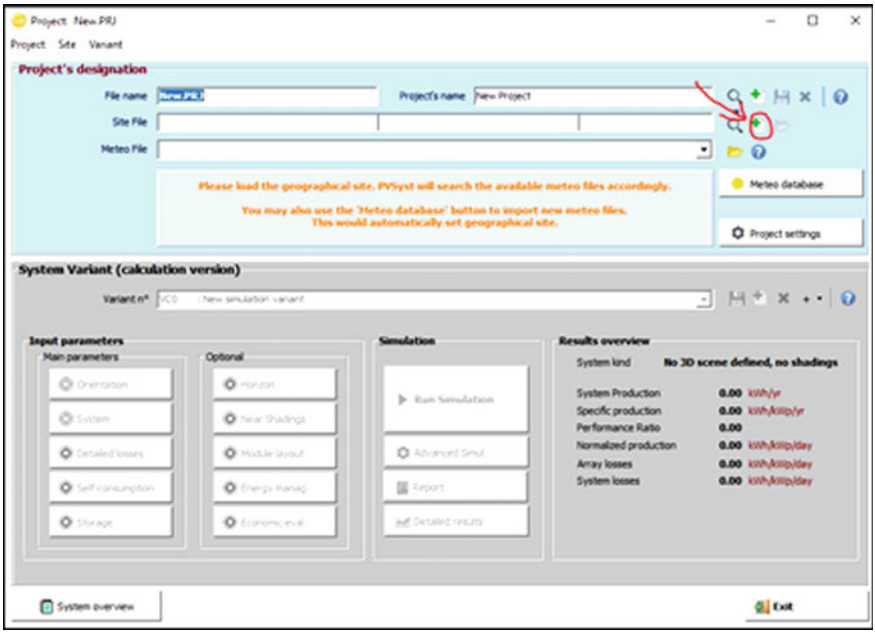

Fig. 3 New project window

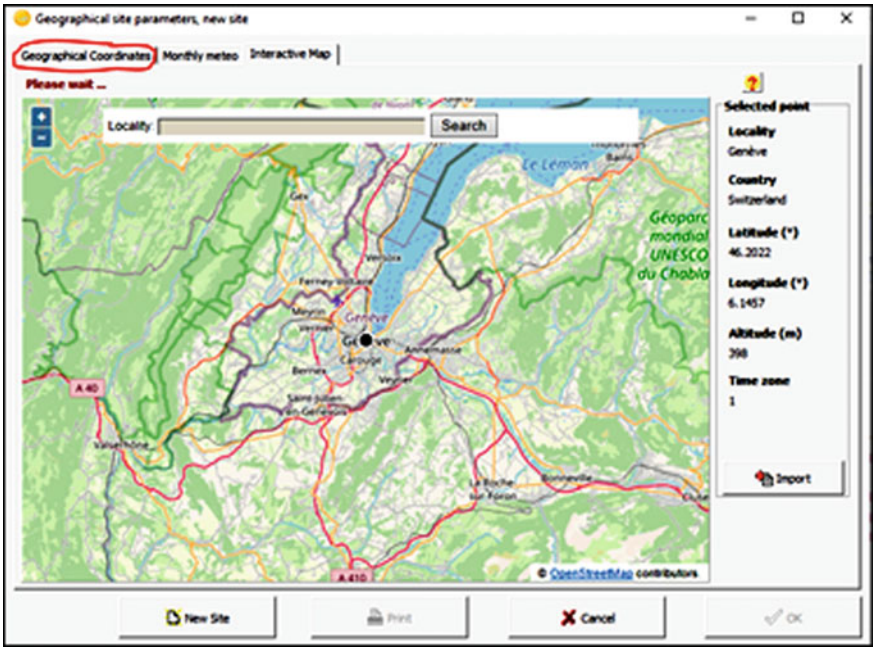

Fig. 4 Geographical site parameters

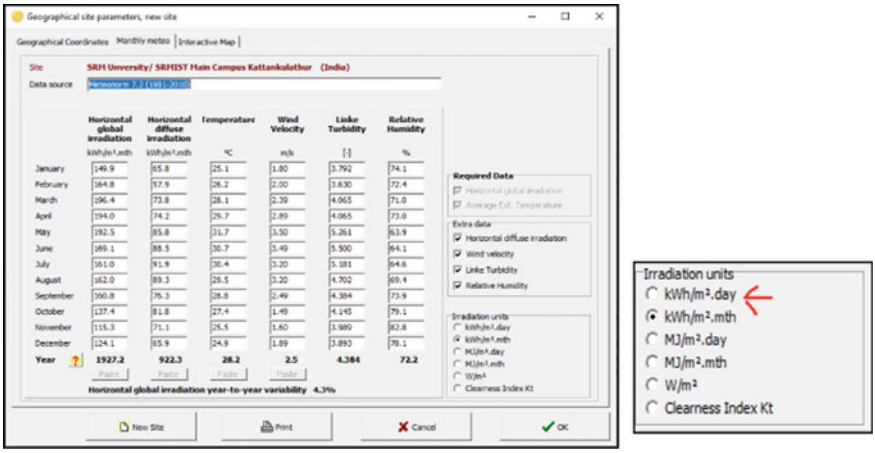

Fig. 5 Data parameters

In Fig. 6, under 'Main parameters', there are two options: 'Orientation' and 'System'.

Click on 'Orientation', a new window pops as shown in Fig. 7. Enter the 'Plane tilt' (in degrees) and 'Azimuth' (in degrees) under 'Field Parameters', as shown in Fig. 7 highlighted. Click 'Ok' when done.

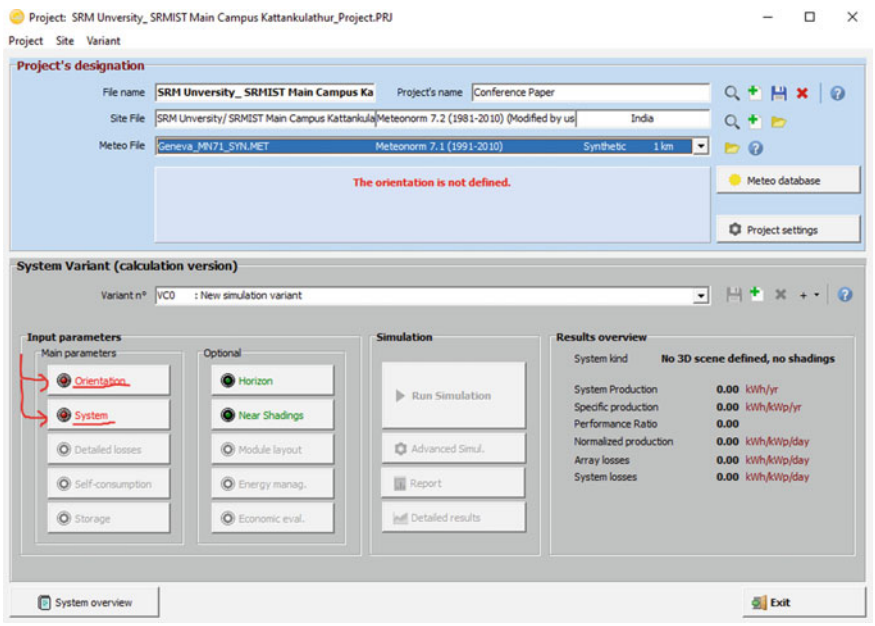

Fig. 6 Main project window, updated

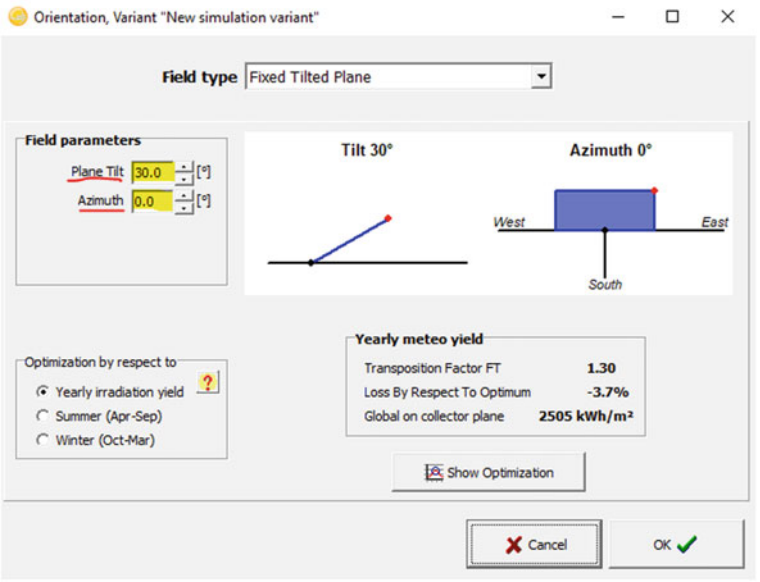

Fig. 7 Orientation tab

Click on 'System', here all the necessary data parameter that is to be entered such as 'Presizing', 'PV modules', 'Inverter'. Under 'Presizing', option is there to either use the 'Planned Power' or 'Available Area'. Use either of the two for presizing. Under 'Select the PV modules', access a large database of existing PV module configurations by manufacturer. Estimate the inverter size using the load side data, or use the inverter configuration present on-site if known. All the selection will be shown in Fig. 8. Click 'Ok' once the configuration is complete.

Step 5: ***Getting things ready for simulation***

Things are almost ready for simulation. There are a few additional parameters that can be explore, such as 'Detailed losses' and 'Self consumption'; refer Fig. 9. After a successful run, results via a report format are obtained, which can be downloaded as a PDF, or click 'Detailed result' to view Figs. 11, 12 and 13 for the result.

3 Results and Discussion

As a result of this study, it is determined that the PVsyst software considered proposes the configuration based on the initial steps as given below in Fig. 10 (Table 1)

Horizontal global irradiation, diffuse irradiation, ambient temperature, global incident and effective radiation, effective energy at the output of the array, energy injected into grid and performance ratio details are given in Table 2.

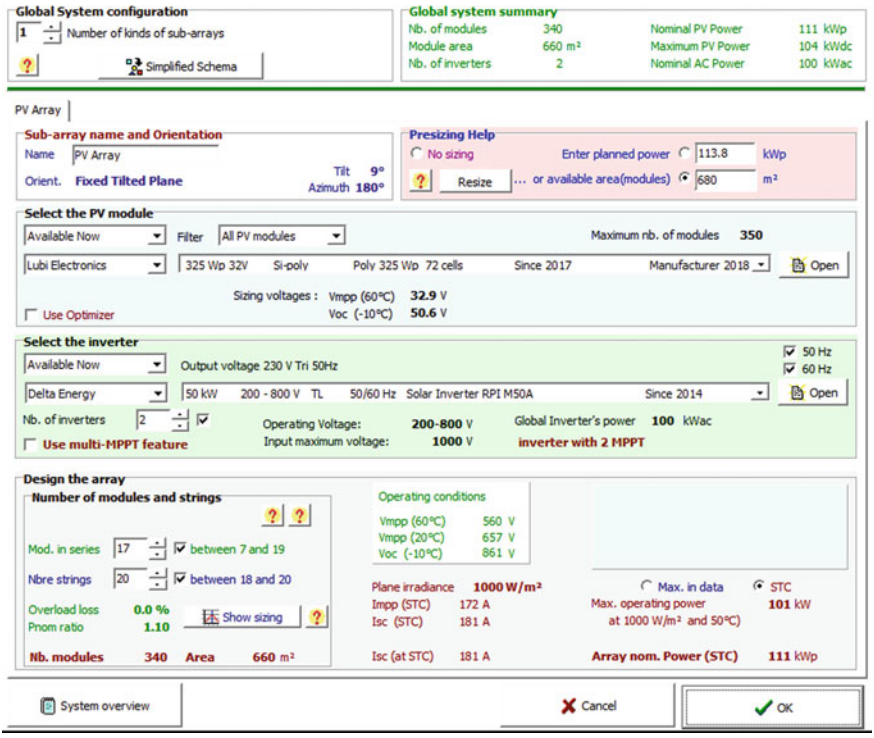

Fig. 8 Complete configuration details

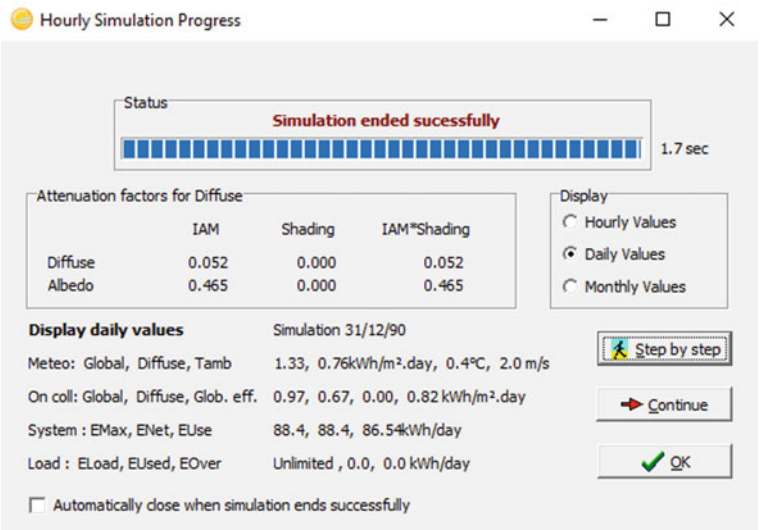

Fig. 9 Simulation run

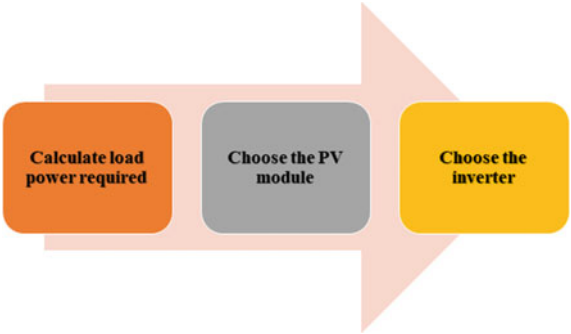

Fig. 10 System design procedure

Table 1 PV array characteristics

PV array characteristics	
PV module Si-poly model poly 325 Wp 72 cells	Manufacturer lubi electronics
Number of PV modules in series 17 modules in parallel 20 strings	Total number of PV modules Nb. modules 340
Unit nom. power 325 Wp	Array global power nominal (STC) 111 kWp
At operating cond. 101 kWp (50 °C) array operating characteristics (50 °C) U mpp 585 V I mpp 172 A	Total area nodule area 660 m^2 Cell area 596 m^2
Inverter model solar inverter RPI M50A	Manufacturer delta energy
Characteristics operating voltage 200–800 V	Unit nom. power 50.0 kWac Max. power (= > 35 °C) 55.0 kWac

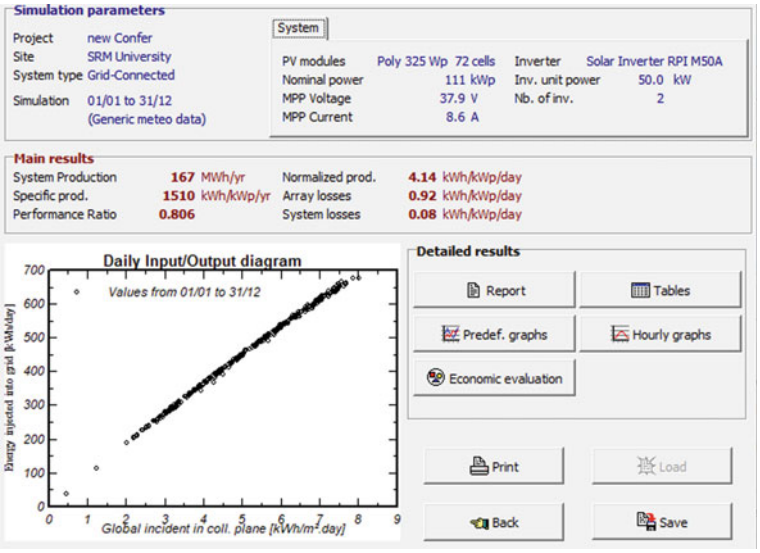

Fig. 11 PVsyst results

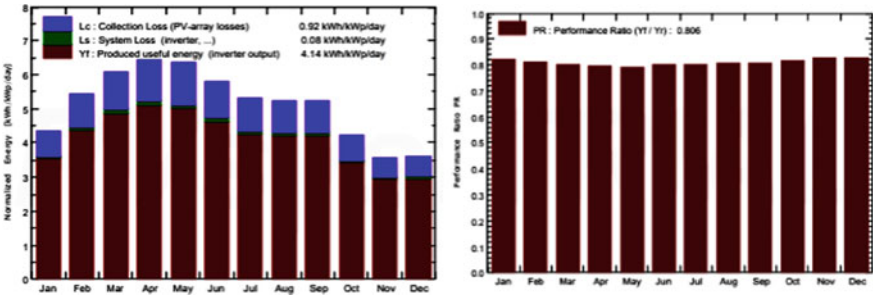

Normalized productions (per installed kWp): Nominal power 111 kWp

Fig. 12 Performance ratio PR. Normalized productions (per installed kWp): Nominal power 111 kWp

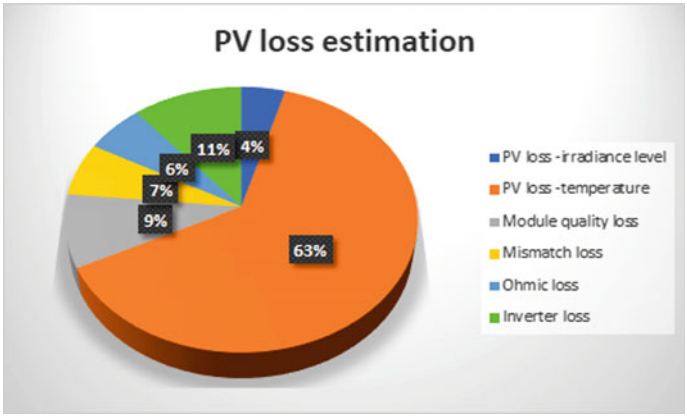

Fig. 13 PV loss estimation

4 Conclusion

The small-scale grid-connected PV system intended for the desired load using the PVsyst software is investigated. PVsyst software analyses the PV system power generation and also the system losses. The entire study is focused to design a grid-connected photovoltaic system for the load assumed in Kattankulathur location, Tamil Nadu, India. 340 PV modules of 325 Wp are estimated for the desired load. From the system considered for design, the energy production is 166.9 MWh/year, with a specific prod. 1510 kWh/ kWp/year and the performance ratio PR is 80.59%. Horizontal global radiation obtained will be 1927 kWh/m^2, and efficiency at STC is estimated as 16.77%.

Table 2 Performance of designed small-scale grid-connected PV system

	GlobHor kWh/m^2	DiffHor kWh/m^2	T_Amb °C	Globlnc kWh/m^2	GlobEff kWh/m^2	EArray MWh	E_Grid MWh	PR
January	149.9	65.83	25.10	135.0	128.0	12.45	12.24	0.820
February	164.8	57.87	26.19	152.0	145.4	13.87	13.62	0.811
March	196.4	73.77	28.06	188.8	181.8	17.06	16.73	0.802
April	194.0	74.16	29.68	193.0	186.6	17.30	16.94	0.794
May	192.5	85.75	31.74	197.1	190.4	17.57	17.21	0.790
June	169.1	88.48	30.72	174.0	168.0	15.69	15.38	0.800
July	161.0	91.88	30.43	164.5	158.4	14.86	14.57	0.801
August	162.0	89.33	29.48	162.8	156.8	14.75	14.47	0.805
September	160.8	76.35	28.80	157.1	151.2	14.21	13.94	0.803
October	137.3	81.81	27.43	130.5	124.7	12.01	11.80	0.818
November	115.3	71.14	25.55	107.2	102.0	9.95	9.78	0.826
December	124.1	65.91	24.90	112.3	106.4	10.41	10.24	0.825
Year	1927.2	922.28	28.18	1874.4	1799.7	170.11	166.91	0.806

References

1. Shalwala RA, Bleijs JAM (2009) Impact of grid-connected PV systems in residential areas in Saudi Arabia. In: Proceedings of the 44th international universities power engineering conference (UPEC) (IEEE 2009), pp 1–5
2. Tallab R, Malek A (2015) Predict system efficiency of 1 MWc photovoltaic power plant interconnected to the distribution network using PVSYST software. In: 2015 3rd international renewable and sustainable energy conference (IRSEC), Marrakech, Morocco, pp. 1–4. https://doi.org/10.1109/IRSEC.2015.7454973
3. Yadav P, Kumar N, Chandel SS (2015) Simulation and performance analysis of a 1KWp Photovoltaic system using PVSYST. In: International conference on computation of power, energy, information and communication
4. Sharma V, Chandel SS (2013) Performance analysis of a 190 kWp grid interactive solar photovoltaic power plant in India. Energy 55:476–485
5. Lavanya A, Divya Navamani J, Vijaya Kumar K, Suman PD, Mishra S (2021) Selection of renewable energy materials for dual input DC–DC converter based hybrid energy system. Materials Today: Proceedings 34:379–385
6. Yadav AK, Chandel SS (2013) Tilt angle optimization to maximize incident solar radiation: a review. Renew Sustain Energy Rev 23:503–513
7. Mazuera MA, Posada J, Manrique P (2016) Analysis and emulation of a photovoltaic solar system using a MATLAB/simulink model and the DS1104 Unit. IEEE, October 2016

Evaluation of Various Machine Learning Algorithms for Detection of Attacks in 5G

C. Arul Stephen, R. Mathesh, L. Venkat, B. Ebenezer Abishek, and A. Vijayalakshmi

Abstract Security plays an essential role in IoT as there are several components connected to the network. An effective intrusion detection system is required to detect all vulnerabilities in wireless networks using machine learning and also to reduce the false alarm rate. The various machine learning algorithms were analyzed in terms of various performance metrics and finally evaluated the best classifier in terms of prediction time, training time, and accuracy. Using confusion matrix, various classes of attacks were analyzed, and results revealed that various machine learning algorithms were compared, And our proposed work was able to predict all the five types of attacks effectively with an accuracy of 94% achieved using extra tree classifier.

Keywords Machine learning · Security · Wireless attack detection · IoT · 5G networks

1 Introduction

This introduction about the wireless attack and discussing IoT data with machine learning is better security.

1.1 Wireless Attacks in Wireless Networks

Wireless networks are Internet-connected networks encompassed by dealing with radio waves. A wireless network enables pursuits to bypass the expensive process of offering cables into buildings or connecting different equipment locations. However, one drawback of a wireless network [1] is a security issue. In a wireless network the information can be hacked. Hence, the research worker moves to a

C. Arul Stephen (✉) · R. Mathesh · L. Venkat · B. Ebenezer Abishek · A. Vijayalakshmi
Vistas, Ch-117, Pallavaram, Chennai, India

C. Subramani et al. (eds.), *Proceedings of International Conference on Power Electronics and Renewable Energy Systems*, Lecture Notes in Electrical Engineering 795,
https://doi.org/10.1007/978-981-16-4943-1_37

sophisticated level like encrypting and decrypting the communications. Still, sometimes hackers may be viable to hack our data. If significant top-level companies lose their information, this leads to millions of dollars which may be defeated. Therefore, we required a secondary shield diagnosis system before black hat hack the data. We can create more advanced when wireless attacks start in contact with a computer device to suddenly identify by detecting system and automatically off the computer before diminishing security. Accordingly, researchers investigate and develop more detecting strategies.

1.2 Reason for IoT is the Need for Machine Learning for Wireless Detection

With the increasing wireless attacks all day, people lose their security from smartphones and laptops, so hackers easily misuse our information. Other side increases demand for the Internet of Things (IoT) automation system for detecting attacks day by day, but technology is improving, IoT models are detectable, and the attacks are more arduous. Progressively, this leads to researchers investigating, moreover, machine learning-based applications besides IoT. Here the machine learning technique is to help the security additionally more robust detectable vulnerability. The machine learning techniques advantage is that it works faster than other methodologies. The regular IoT intrusion detection system inside the data includes an unrelated data signal, so performs it wrongly detecting some attacks [2]. Still, in machine learning, we collected the information directly from the IoT source, analyzed the data, discarded unwanted data, and used the best features to secure the detection of attacks more strongly. Making more robust data in the machine learning and predicting styles that can overcome the problem raised from IoT cannot recognize threats. This machine learning is able to identify the past threads and future unknown threads. Hence, this paper is using machine learning to analyze the IoT data and then preprocessing the data to make it more robust with the help of a machine learning algorithm and to increase the detection rate. Thus improving the efficiency of detection.

2 Proposed Methodology

2.1 Dataset Collection and Description

The open-source dataset is collected from the Kaggle, and the dataset's title is IoT device [3] design of a WSN platform for long-term environmental monitoring for IoT applications network logs. In these datasets, there are 477,426 samples, 13 input features, and one target output name is normality.

Feature Names

Frame_number, Frame_time, Frame_len,eth_src,eth_dst,ip_src,ip_dst,ip_proto,ip_len,tcp_len,tcp_srcport,tcp_dstport, Value.

Target Six Class Names

Normal, man in the middle attack (MITM), distributed denial-of-service (DDos), data-type probing, scan attack and wrong setup.

53,769 is normal data, 81,250 samples are the wrong setup, 17,507 samples are DDOS, 78,958 samples are data-type probing, 73,087 samples are scan attack, 58,703 are MITM attack, remaining 73,790 samples are duplicate data, and 40,362 are outliers.

One of this dataset's benefits is that each attack becomes more numerous weightage samples, so machine learning algorithms accumulate extensive data, so prediction performs very strongly.

2.2 Preprocessing the Data

Preprocessing data means removing noisy data like empty records, duplicates rows and extreme values. If we do not remove it, our machine learning algorithms read this unwanted data and predict it wrong, so accuracy decreases.

2.2.1 Statistical Test

Utilizing the statistical test, we recognize any relationship between input and output data. This step is imperative because these will decide to train the data to an algorithm or not. If in an input there is no relationship, we must eliminate that input features.

Univariant Test

The univariant test is used to check if each feature has a relationship or not. If it is below 0.05 of the p-value for each attribute, the association is genuine. If the p-value is above 0.05, the relationship is worst. In numerical input feature, we use a t-test, and categorical feature uses one proportion test.

Bivariant Test

The bivariant test is utilized to check feature and target having a relationship or not. If numerical input (normal distribution) and output are numerical, use Pearson's correlation coefficient. Numerical input (non-normal distribution) and numerical output use the Spearman rank correlation test. Input numerical (normal distribution) and categorical output use ANOVA test. Input numerical (non-normal distribution) and category target use Kendall's rank correlation test. Input categorical (relationship) and numerical output use ANOVA test. Input categorical (relationship) and

numerical output use Spearman rank correlation. When this bivariant analysis occupies below 0.05 of the p-value, use that features for preprocessing. If above 0.05, do not use that feature for preprocessing because there is no relationship.

Result Of Statistical Test For This Dataset

In the univariant test, we identify our input features numerical, and we perform a t-test. Hence, all features are non-normal distribution that means above 0.05 of the p-value. After that, we have numerical (non-normal distribution) input and categorical output of bivariant test, so we use Kendall's test, and all features of p-value have below 0.05, which indicates a relationship. So we do not remove anything.

2.2.2 Identify the Same Feature

High correlation intends the same features of data repeated various times. In our datasets, we discovered ip_proto, ip_len and frame_len having high correlation features. Hence, we eliminated two feature parts and used only the frame_len feature because the same information occupies all three feature parts. When we neglect two-column data, it does not affect the accuracy, but if we do not remove it, our machine learning algorithm learned this unwanted data and predicted it wrong.

2.2.3 Drop Duplicate Rows

Identical rows exist on another row place. Suppose we do not discard these duplicate rows, our machine learning algorithm mug up. This mug is called overfitting. If our machine mugs up the training data, it predicts well in training, but it does not predict correctly testing, so obligation removes these repeated records. Our dataset consists of 73,790 which is a duplicate sample, so we removed that.

2.2.4 Outlier Removal

Outlier removal is an extreme value. It is not always in a specific range. However, it did not cast off outliers. The detection is predicted wrong. In our dataset observed, the 40,362 outliers are then eliminated.

2.2.5 Standard Scalar

Standard scalar converted the data from 0 to 1. Many algorithms do not perform well based on the higher values of data, so standard scalar is fundamental to transform data from 0 to 1.

2.2.6 Split the Data

We split the data toward training and testing. Training is 70%, and testing is 30% out of 100% of data. Here training data do not constitute any data in testing, so both are different.

3 Algorithm Explanation

3.1 Extra Tree Classifier

Extra tree classifier is a classification tree method. It is an advance than a decision tree [4]. The decision tree splits only two nodes in each feature, but the extra tree classifier splits the best nodes based on the feature columns. Let us consider output as a two target. Based on the condition, if extra tree splits with classifying one target output in one leaf side node and second target in second leaf side correctly for one feature, that type of feature column is most beneficial. By splitting the features which is the root node into a number of trees. When both targets form both leaf nodes, then that is the worst feature.

3.2 Logistic Regression

Logistic regression performs both binary and multiclass classifiers. Using the x-axis, it predicts the y_axis. Let us consider two targets: logistic regression converts the input data 0 to 1. Here, assume two targets in the y-axis and one input x-axis, so data split two sides. If more number of one target is transferred to another side, the model is defective. Above 0.5 refers to the first target, and below 0.5 refers to the second target.

3.3 Gaussian Naive Bayes

Gaussian Naive Bayes is a probability measurements algorithm. It is mainly used for input text classification and also works in numerical input problems. Many Naive Bayes algorithms are available, like Gaussian Naive Bayes, multinomial Naive Bayes and categorical Naive Bayes.

4 Performance Metrics

4.1 Accuracy

Accuracy is one metric for evaluating the classification models. It forms accuracy for all the class that correctly predicted data from the total data. If the actual output and algorithm expect the result are equivalent, the accuracy was rising.

4.2 Confusion Matrix

Confusion matrix is a specific table layout that allows visualization of an algorithm's performance to show the value count for how much data are correctly predicted and not predicted for all output classes. TP and FN indicate correctly predicted data, and FP and TN indicate wrongly predicted data.

4.3 Precision

Precision is a model evaluation metric. The accuracy is formed by how much correctly predicted data are occupying from the actual results.

4.4 Recall

The recall is a model evaluation metric. This accuracy is formed by how precisely the predicted data occupied by the machine's expected results.

4.5 F1-Score

F1-score measures the performance of the model. F1-score accuracy has formed a combination of both precision and recall.

5 Results and Discussion

see Table 1.

Comparative Analysis for all Classifiers:

Table 1 Comparison of various performance metrics

	Trained accuracy	Tested accuracy	Training Time (Sec)	Precision	Recall	F1-Score
Logistic regression	0.90	0.90	13.71	0.91	0.91	0.91
Extra tree classifier	0.94	0.94	0.09	0.95	0.95	0.95
Neural network	0.88	0.88	152.23	0.93	0.83	0.85
Gaussian Naive Bayes	0.64	0.64	2.25	0.62	0.63	0.60
SGD classifier	0.90	0.90	2.55	0.91	0.91	0.91
Ridge classifier	0.91	0.91	0.21	0.92	0.92	0.92

As the tested accuracy outcome, extra tree classifier is the Best classifier because it scored 94% when corresponded to other classifiers. And Gaussian Naive Bayes is the worst classifier because its score is 64% compared to all the classifiers.

As the analysis result of the training time, the extra tree classifier and ridge classifier catch 1 s for training to compare all the classifiers. And neural network is the worst classifier in training time because it exerts 152 s. In final research analysis of this table, we determined that the extra tree classier is the most trustworthy classifier to distinguish all the classifier precision, recall and F1-score concerning 91,91,91 scores. The Gaussian Naive Bayes is the worst classifier than all classifiers for precision, recall and F1-score.

5.1 Confusion Matrix

In the confusion matrix, extra tree classifier is a good algorithm rival to all the algorithms. Because it has low wrong predicted other attacks. Out of 16,248 test data of normal class, machine's 140 samples incorrectly predicted the wrong setup. One sample wrongly predicted to data-type probing, ten classes wrongly expected as scan attack, and 77 samples wrongly predicted to a MITM attack. Out of 24,420 sample test data for the wrong setup, the machine perfectly founded all. Out of 5179 test data of DDoS, the machine learning algorithm was all correctly established (Fig. 1).

Out of 21,775, machines wrongly predicted 3047 samples. Out of 17,650 test samples of MITM attack, machine wrongly predicted 5683 samples of scan attack.

Compared to all the confusion matrix classifiers, the extra tree classifiers help less wrongly predicted samples and more correctly predicted samples.

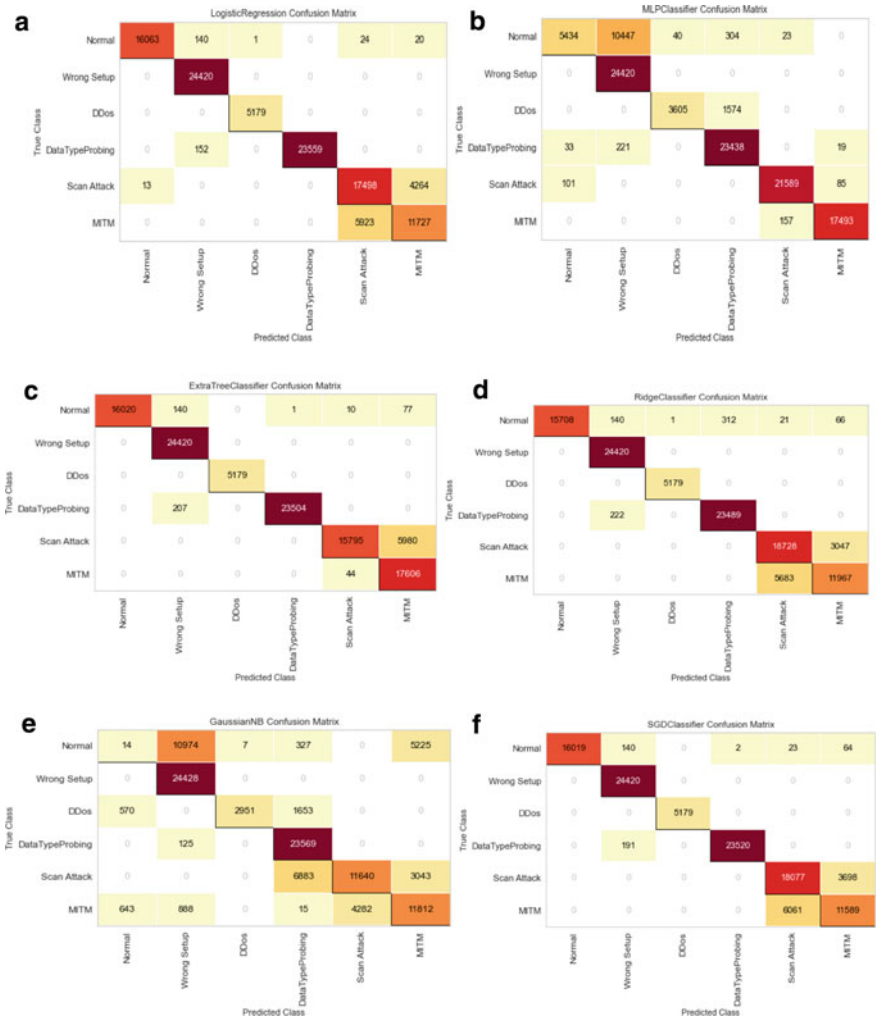

Fig. 1 **a** Logistic regression, **b** multilayer perceptron, **c** extra tree classifier, **d** ridge classifier, **e** Gaussian Naive Bayes, **f** stochastic classifier

6 Conclusion

The dataset, which we have analyzed in multiclass attacks hence on evaluating the various machine learning algorithms, extra tree classifier was able to exactly predict the various attacks. Since extra tree classifier is much suitable for multiclass attacks with an accuracy of 94%, with training time it is 1 s based on various parameter analyses. At the complete analysis, finally we conclude that extra tree classifier is best suited for IoT network log dataset.

7 Future Scope

In the future viable for interpolating machine learning in the hardware of analysis signal after detecting the attack, the alarm is working. It is the secondary purposes when the hacker hacks the encrypted data.

References

1. Pahl M-O, Aubet F-X (2018) All eyes are on you: distributed multi-purpose microservice acquisition. In: At fourteen procedures international conference on network and performance management (CNSM) (CNSM 2018), Rome, Italy
2. Liu X, Liu Y, Liu A, Yang L (2018) Protecting unwanted attacks using simple test messages on smart sensors of industrial communication systems, IEEE
3. Lazarescu MT (2013) Design of a WSN platform for long-term environmental monitoring for IoT applications, IEEE, pp 1–14
4. Deo RC (2015) Mechanical learning in medicine. Distribution 132(20):1920–1930

Performance Analysis of Slope-Compensated Current Controlled Universal PV Battery Charger for Electric Vehicle Applications

S. Ramprasath, R. Abarna, G. Anjuka, K. Deva Priya, S. Iswarya, and C. Krishnakumar

Abstract The main purpose of the proposed system is to design a low-cost universal PV battery charger for electric vehicle application. The proposed system is integrated with a slope-compensated current controller which controls the charging current that corresponds to maximum power point of the PV module. As an interface converter, the proposed system consists of a buck converter to control the flow of the charging current and to find out the reference current Iref from the PV array at MPP. The battery control circuit is implemented by measuring the state of charge (SOC) of the battery, and an LCD display has been used to monitor the battery parameters. This proposed system acts as a smart and efficient PV battery charger for e-vehicles.

Keywords Electric vehicle · Battery charger · State of charge · Slope compensated

1 Introduction

The current and future of energy options were renewable energies. This major change toward green energy resources has culminated noticeable emission losses to numerous environmental habitats due to the widespread use of fossil fuels as an energy supply. From charging a Tesla vehicle to recharging a basic street lamp, the energy generated from a PV panel can be used in numerous ways. Study in the field of solar energy has shed light on its integration methods with different electronic power converters. While the different energy sources are known, it is still a mandate to store them in batteries for potential and effective use. What we call a renewable energy reservoir is a PV panel combined with a power converter topology and lithium-ion batteries.

A universal battery charger for lithium ion and lead acid is proposed. Figure 1 shows overall all block diagram of proposed battery charger, centered on a single

S. Ramprasath (✉) · R. Abarna · G. Anjuka · K. Deva Priya · S. Iswarya · C. Krishnakumar
Saranathan College of Engineering, Trichy, Tamilnadu, India
e-mail: ramprasath-eee@saranathan.ac.in

C. Subramani et al. (eds.), *Proceedings of International Conference on Power Electronics and Renewable Energy Systems*, Lecture Notes in Electrical Engineering 795,
https://doi.org/10.1007/978-981-16-4943-1_38

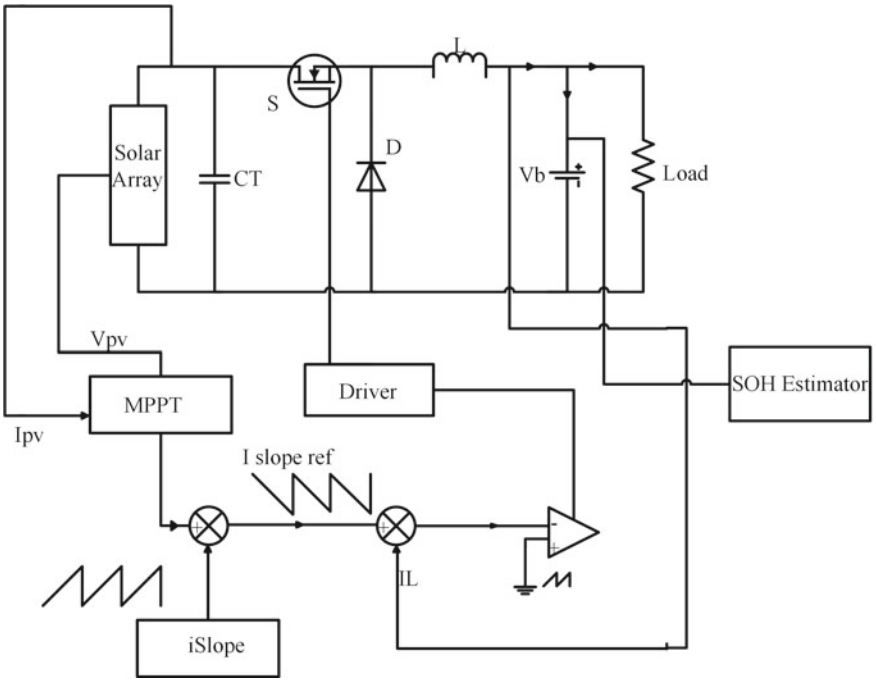

Fig. 1 Overall block diagram

control loop, the slope-compensated current mode control systems with a single-stage buck DC–DC converter. The proposed system has a SOC measuring module to avoid overcharge and isolate the battery if needed.

1.1 Methodology of Proposed System

A DC–DC converter is attached to the PV array and the power converter output is connected to a battery that needs to be charged. It has a control input D to control the operating point around MPP. As the batteries are the source, the voltage around the battery terminals is fixed by the battery, then what the charge current would be, so let's say we need to put the maximum power from the panel into the battery; hence, an MPPT that gives a current reference of the PV module is proposed [1, 2].

Generally, a PV panel and a battery cannot be connected directly for a battery voltage of greater than 12v. So a charge controller is used in between the PV panel and battery to steer the power flow from PV module between the battery and load. The charge controller used here is a DC–DC converter (Buck converter). PV panel are supposed to operate at maximum power point. In order to obtain the maximum power output of the solar panel, MPPT (maximum power point tracking) technique is

used. MPPT technique increases the efficiency of the solar panel, it compensates for changing the V–I characteristics of the solar panel, and also maximum solar energy is being utilized from the panel. For duty cycle ($d < 0.5$), the system is stable. But for ($d > 0.5$), the system is unstable, so we need to provide slope compensation [6]. Current control with slope compensation will give best results, and even if there are errors, the errors will be removed within a cycle itself. Hence, this slope compensation method is highly efficient. The battery is efficiently charged with the help of PV array and Buck converter, and thus, the energy is stored and fed to the load. The charging level can be sensed and displayed with the help of Arduino. Therefore, this methodology seems to be more reliable and of low cost for implementation.

The control part of our proposed model will be done by programming the Arduino for sensing the charging level of the battery. Once the battery has reached its charging level, it cuts off from the PV array automatically. This can be achieved by coupling the battery with Arduino also the charging level of the battery can also be displayed with the help of LCD display.

1.2 Need for Slope Compensated Current Controller

The main purpose of a conventional battery charger is to charge the battery at an ideal rate and break-off the charging at an appropriate time. On overcharging a battery, stress is produced in the chemicals inside the battery. Thus, recombination of chemicals takes place faster than they can. Undercharging a battery can lead to problems like sulfation. Therefore, both overcharging and undercharging reduce the lifetime of the battery [4, 5]. Hence, our project aims to design a current controlled battery charger with an optimum charge profile.

When the duty cycle of the pulse width modulation (PWM) signal is more than 50%, then the current mode design may experience instability (sub-harmonic oscillation). In order to overcome this instability, a technique called slope compensation is employed to bring back the stable operation across the entire PWM duty cycle range. Figure 2 shows slope compensated current waveform [8–10].

2 Design Specification

The proposed system is designed to charge a 12 V, 40 AH lead acid battery. The charging system consists of three modules—battery module, converter module and PV module.

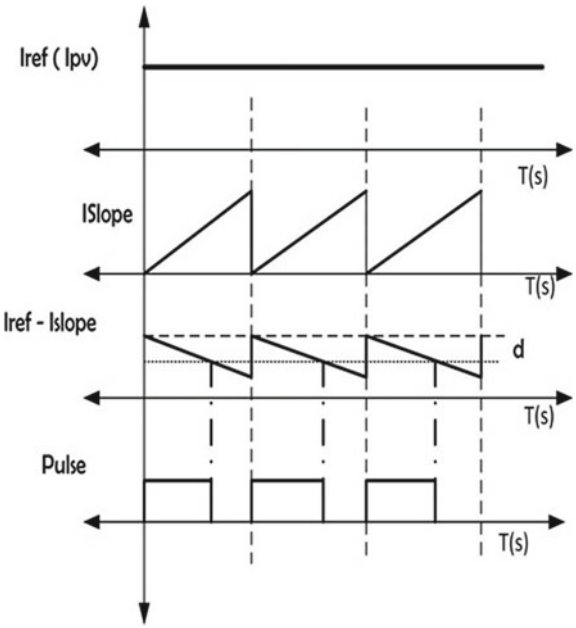

Fig. 2 I-slope-compensated current reference

2.1 Module 1: Battery

Table 1 shows the battery specification, the charging current required to charge the battery is derived from C-rate as.

C-rate (From datasheet) is C10

Max charging current = 40 / 10 = 4A

Charging time = 10 h

Table 1 Lead acid battery specifications

Battery parameters	Value
Type	Lead-acid (Solar Tubular Battery)
Nominal voltage	12 V
Capacity	40Ah
Internal resistance	0.5Ω
Fully−charged voltage	14.5 V
C rate	C10

2.2 Module 2: DC-DC Buck Converter

The conventional non-isolated Buck converter is used as power modulator for charging system. The converter was designed for 80 W, with charging voltage as 13 V. From the converter design equations in [3, 7] for the specification show in Table 2, we design the DC–DC converter parameters [11, 12].

Load current (I_o)

$$I_o = \frac{P_o}{V_o} = \frac{80}{13} = 6.153\ A$$

Duty cycle (D)

$$\frac{V_o}{V_{\text{in}}} = \frac{22.7}{13} = 0.572$$

Inductor (L)

$$\frac{V_o * (1 - D)}{\text{del}_{IL} * f} = 0.009H$$

Capacitor (C)

$$\frac{I_L}{8 * f * \text{del}_{vo}} = 1.183\mu f$$

Input Capacitor (C_{in})

$$\frac{10}{V_{\text{in}} * f}(D - D^2) = 10.6\mu f$$

Table 2 Converter specifications

Input voltage (V_{in})	22.7 V
Output voltage (V_o)	13 V
Power (P)	80 W
Del IL	5% of IL_{avg}
Del V_o	5% of V_o
Frequency	5000 Hz

Table 3 PV Parameters

S.no	Parameters	Values
1	Rated max power(P_{max})	100 W
2	Current at P_{max}(I_{MP})	5.34A
3	Voltage at P_{max}(V_{MP})	18.78 V
4	Short-circuit current(SC)	5.71A
5	Open-circuit voltage(V_{oc})	22.64 V
6	Operating temperature	−40 to 85 °C
7	Weight	8.0 kg
8	Max system voltage	DC1000

2.3 Module 3: PV Module

100 W PV panel is used for the proposed system, and Table 3 shows the parameters.

3 Simulation Results of Proposed Universal Charger

The proposed system is simulated in MATLAB for the design specification. Figure 3 shows the Simulink block of proposed system.

Figure 4 shows the simulation output for step change in reference current from 3 to 5A at 2 s. The change in battery voltage, output power, load current and duty cycle was plotted.

Figure 5 shows the variation in charging current for variation in irradiance at 1 s from 500 to 1000 W/m2.

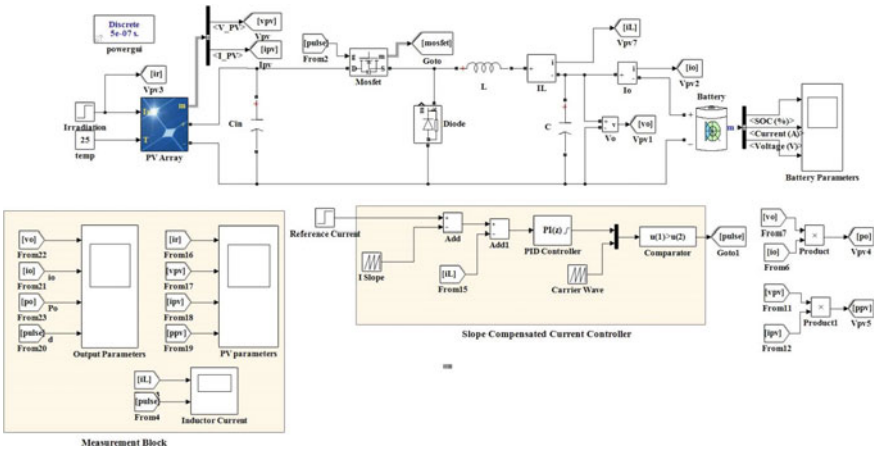

Fig. 3 Simulink block for proposed system

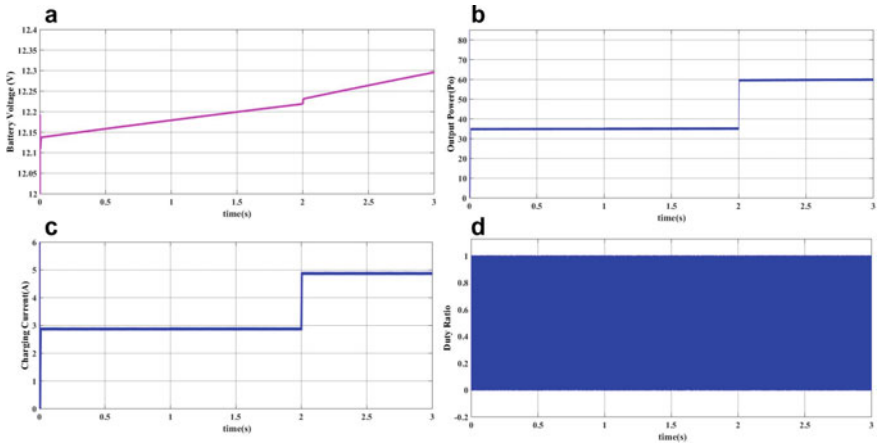

Fig. 4 **a** Battery voltage (V), **b** Output power (W), **c** Charging current (A), **d** Duty cycle

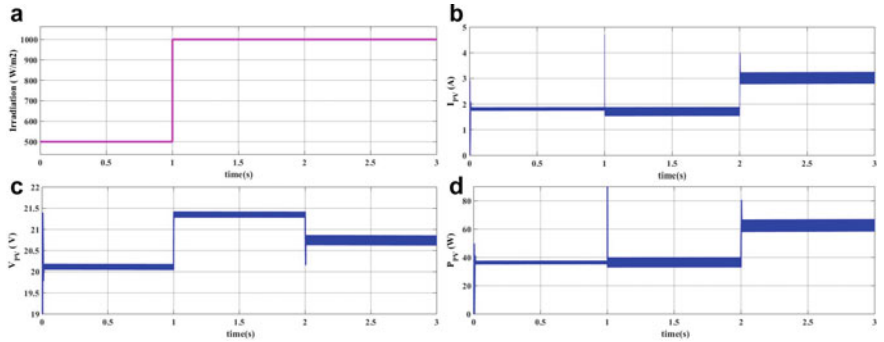

Fig. 5 **a** Irradiation W/m2, **b** PV current (A), **c** PV voltage (V), **d** Power Ppv (W)

The current from PV module is maintained at MPP and the charging current varies accordingly. Figure 6 shows the battery parameters for step change in irradiance and charging current. The initial state of charge of the battery is assumed at 70% and the variation is plotted.

The battery SOC and battery voltage increase as battery charges with constant current. The battery charging current is shown as negative because the current enters the battery is termed as negative and vice versa.

4 Conclusion

In this article, the slope-compensated current control technique is extended to the universal constant current battery charger. The various building blocks of the

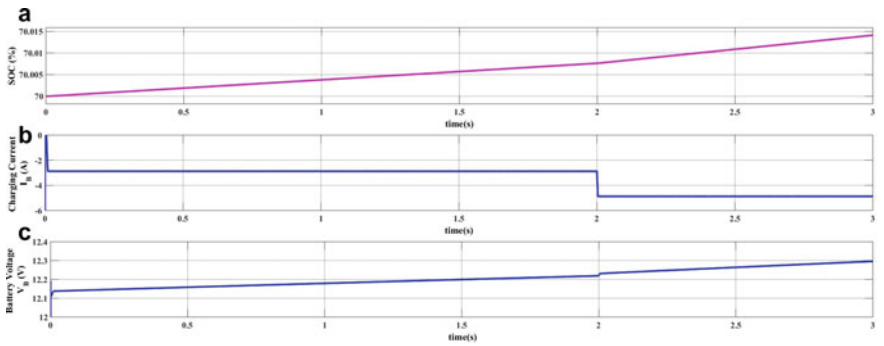

Fig. 6 **a** SOC (%), **b** Charging current (A), **c** Battery voltage (V)

proposed system were designed and simulated in MATLAB/Simulink environment. For a step-change in irradiation and charging current, the converter and battery parameters are plotted and satisfactory results were found. The work carried out here is adequate for practical implementations. The proposed universal battery charger would be manufactured with the requisite battery management scheme, and a charging station for electric vehicles would be introduced in the future.

References

1. Biswas S, Huang L, Vaidya V, Ravichandran K, Mohan N, Dhople SV (2016) Universal current-mode control schemes to charge Li-Ion batteries under DC/PV source. In: IEEE transactions on circuits and systems I: regular papers, Sept. 2016, vol 63(9), pp 15311542. https://doi.org/10.1109/TCSI.2016.2571218
2. Singh HK, Kumar N (2020) Current controlled charging scheme for off board electric vehicle batteries from solar PV array. In: 2020 7th International conference on signal processing and integrated networks (SPIN), Noida, India, pp 935–940. https://doi.org/10.1109/SPIN48934.2020.9071160
3. Maity A, Patra A, Yamamura N, Knight J (2011) Design of a 20 MHz DC-DC buck converter with 84 percent efficiency for portable applications. In: 2011 24th international conference on VLSIdesign, Chennai, India, pp 316–321. https://doi.org/10.1109/VLSID.2011.37
4. Achaibou N, Haddadi M, Malek A (2012) Modeling of lead acid batteries in PV systems. Energy Proc 18:538–544. ISSN 1876–6102. https://doi.org/10.1016/j.egypro.2012.05.065
5. Sant'Ana WC et al (2019) Implementation of automatic battery charging temperature compensation on a peak-shaving energy storage equipment. In: 2019 IEEE 15th Brazilian power electronics conference and 5th IEEE Southern power electronics conference (COBEP/SPEC), Santos, Brazil, pp 1−7. https://doi.org/10.1109/COBEP/SPEC44138.2019.9065670
6. Kondrath N, Kazimierczuk MK (2013) Slope compensation and relative stability of peak current-mode controlled PWM dc-dc converters in CCM. In: 2013 IEEE 56th international midwest symposium on circuits and systems (MWSCAS), Columbus, OH, USA, pp 477−480.https://doi.org/10.1109/MWSCAS.2013.6674689R
7. Sivakumar R, Ramprasath S, Babu PR (2015) Efficency and power packing density improvement for DC-DC boost converter by soft switching techniques. In: 2015 International conference on circuits, power and computing technologies [ICCPCT-2015], Nagercoil, India, pp 1–7. https://doi.org/10.1109/ICCPCT.2015.7159504

8. Wiesner, Diez R, Perilla G (2013) Design and implementation of a buck converter with MPPT for battery charge from solar module. In: 2013 Workshop on power electronics and power quality applications (PEPQA),Bogota, pp 1–6. https://doi.org/10.1109/PEPQA.2013.6614938
9. Zhong J, Liu S (2011) Design of slope compensation circuit in peak-current controlled mode converters. In: 2011 International conference on electric information and control engineering, ICEICE 2011—Proceedings. IEEE, pp 1310–1313. https://doi.org/10.1109/ICEICE.2011.5778040
10. Hu Y, Wei Y, Wang J, Sun M (2016) Design of slope compensation for a high-efficiency high-current DC-DC converter. In: Proceedings 13th IEEE international conference solid-state integration circuit technology (ICSICT), October 2016, pp 1306–1308
11. Matwankar CS, Alam A (2019) Solar powered closed-loop current controlled DC-DC buck converter for battery charging application. In: 2019 International conference on vision towards emerging trends in communication and networking (ViTECoN), Vellore, India, pp 1–5. https://doi.org/10.1109/ViTECoN.2019.8899645
12. Radianto D, Dousoky GM, Shoyama M (2015) Design and implementation of fast PWM boost converter based on low cost microcontroller for photovoltaic systems. IECON 2015–41st annual conference of the IEEE industrial electronics society, Yokohama, Japan, pp 002324–002328. https://doi.org/10.1109/IECON.2015.7392449

Comparative Analysis of Solar PV Production in Durban to Other Cities in South Africa

Sanjeeth Sewchurran, Innocent E. Davidson, and Elutunji Buraimoh

Abstract Solar irradiation levels in South Africa compare favourably with the rest of the world. However, developers and installers in South Africa must know how the irradiation levels affect solar PV production within different cities. An investigation was carried out to compare the PV generation production in nine cities situated in each of the nine provinces in South Africa to understand how solar PV generation varies in each city. The city of Durban was used for the base case with its solar production compared to that of other cities. Technical and non-technical factors affecting solar PV generation production/installations in Durban were then investigated, and a case study of simulated vs. actual plant production in Durban was compared.

Keywords Solar PV · Specific yield · PV generation production

1 Introduction

Solar PV projects are becoming a common sight in Durban and across South Africa (SA). This has been driven by rising energy costs and reducing solar PV costs, leading to very lucrative payback periods. Similarly, there is a need to reduce carbon emissions in the face of impending carbon tax implementation, changes in regulations, feed-in tariffs, energy shortage, etc. [1]. Studies have shown that SA and Africa have some of the best Global Horizontal Irradiation (GHI) globally and is well suited for solar PV projects [2]. Figure 1 shows the map of GHI across SA, which indicates that the GHI levels vary across the different provinces indicating solar energy production will vary across provinces. Thus, the best irradiation levels

S. Sewchurran (✉)
eThekwini Electricity, eThekwini Municipality, Durban, South Africa
e-mail: sanjeeth.sewchurran@durban.gov.za

I. E. Davidson · E. Buraimoh
Department of Electrical Engineering, Durban University of Technology, Durban, South Africa
e-mail: InnocentD@dut.ac.za

E. Buraimoh
e-mail: ElutunjiB@dut.ac.za

C. Subramani et al. (eds.), *Proceedings of International Conference on Power Electronics and Renewable Energy Systems*, Lecture Notes in Electrical Engineering 795,
https://doi.org/10.1007/978-981-16-4943-1_39

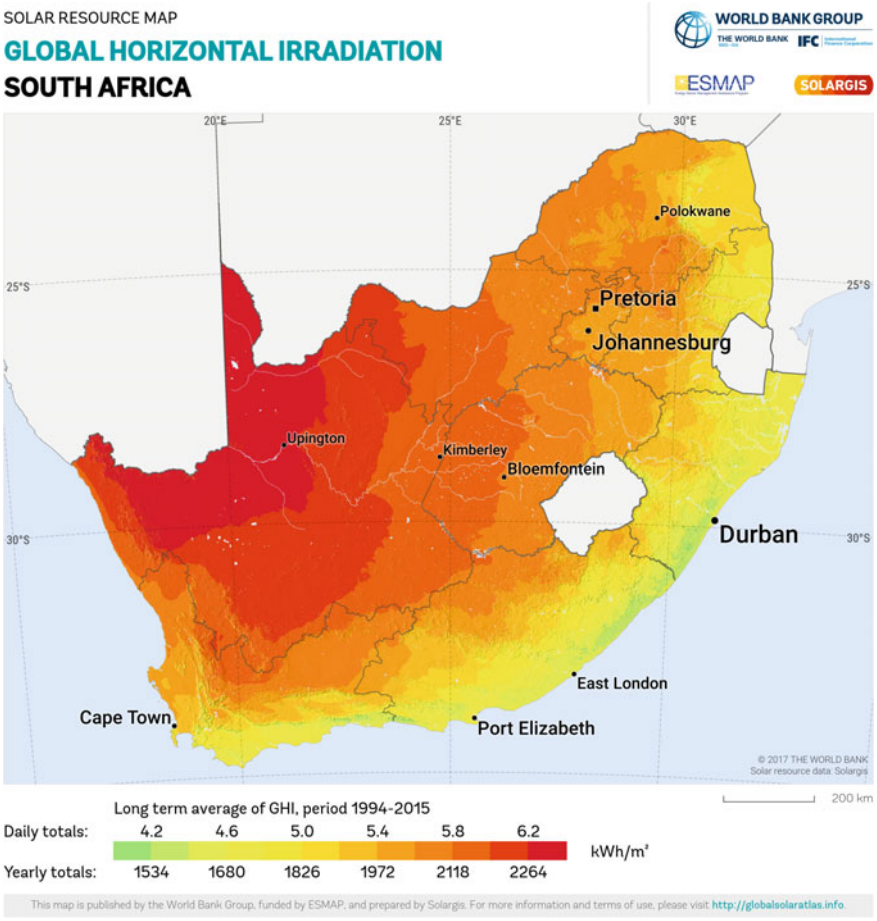

Fig. 1 Global horizontal irradiation across South Africa [4]

can be found in the Northern Cape, while Durban has the lowest irradiation levels. Durban's climate is humid, subtropical, with hot summers and mild winters. There is an average of 2343 h of sunlight a year, with an average of 6.4 h of sunlight a day [3]. This paper investigates the generation from a PV system in Durban compared to the production from similar system in different cities. Also, the impacts of technical and non-technical factors affecting PV are investigated, and a comparative analysis is presented.

2 Investigation and Analysis

The PV production is simulated for a 1 MW rooftop solar PV system installed in nine selected cities of Bloemfontein (BFN), Cape Town (CPT), Durban (DUR), Johannesburg (JHB), Nelspruit (NLP), Polokwane (PLW), Port Elizabeth (PEZ), Rustenburg (RSB), and Springbok (SGK) in Provinces of Free State, Western Cape, KwaZulu-Natal, Gauteng, Mpumalanga, Limpopo, Eastern Cape, North West, Northern Cape, Free State, and Western Cape, respectively. The PV system consists of 2500 Canadian Solar 400 W solar panels and 20 Huawei 50 kW inverters. The PV production simulations were carried out for a flat roof, meaning zero degrees' inclination angle. In most PV installations, the panels are often installed to take the existing building roof structure's inclination and orientation angle. The panels were installed on the profile of the existing flat roof of the building. The results from the simulations are shown in Table 1 showing the monthly PV production for the cities.

Table 1 summarises the PV production for the cities, and it can be seen from the case study that Durban has the lowest annual PV production, whilst Springbok has the highest annual PV production. This ties up with Fig. 1, which shows that Springbok has the highest irradiation levels and Durban the lowest. Subsequently, a comparative analysis is carried out to indicate percentage annual production excess of Springbok with respect to other cities. Table 1 also shows that the annual PV production in Springbok is 36.01% more than Durban, 22.63% more than Port Elizabeth, 22.63% more than Nelspruit, 14.09% more than Cape Town, 10.7% more than Johannesburg, 10.42% more than Rustenburg, 6.86% more than Polokwane, and 4.99% more than Bloemfontein. Lower annual PV generation production will ultimately affect the solar PV system's payback period together with the city's electricity tariff.

3 Factors Influencing PV Production

3.1 Inclination and Orientation Angle on PV Production

Most roof-mounted PV systems are installed at the angle of the roof inclination and orientation, except mostly in the case of a solid decked flat concrete roof. In the case of the flat concrete roof, the designer has flexibility with the PV panel inclination and orientation; however, factors such as wind loading, parapet walls, shading from adjacent buildings, trees, air conditioners, chimneys, etc. have to be taken into account. A study was then carried out to understand how the inclination and orientation angle of a PV panel affects the annual PV production in Durban. Several simulations were carried out for the annual PV production at different panel inclination angles and orientations to compile Table 2. From the simulations carried out, the highest annual PV production was then taken as 100%, or maximum generation output which was for a PV system that was north-facing at an inclination angle of 30 degrees. After

Table 1 Monthly and annual PV production results for cities

City	BFN	CPT	DUR	JHB	NLP	PLW	PEZ	RSB	SGK
January	177,510	194,940	139,330	158,430	127,580	164,020	169,710	158,490	202,500
February	147,110	157,550	121,130	135,050	113,170	136,700	138,190	135,080	166,070
March	142,290	146,460	121,010	136,940	128,090	141,360	125,480	138,070	157,280
April	118,580	102,100	96,995	113,500	124,130	121,060	96,726	114,090	121,590
May	104,130	74,229	83,106	106,850	123,330	116,140	77,552	107,750	101,610
June	91,310	60,517	73,820	95,042	123,730	103,070	65,318	95,248	84,760
July	102,480	68,312	80,184	105,460	129,430	111,230	73,406	105,600	94,723
August	124,310	88,792	94,405	124,760	128,480	132,080	92,630	124,910	117,130
September	143,570	118,580	101,850	139,900	127,960	144,140	111,480	140,990	141,120
October	166,630	154,970	118,540	153,870	132,650	153,960	145,240	153,620	175,780
November	172,190	180,490	124,400	155,370	127,200	161,870	162,060	155,760	193,640
December	189,000	198,180	141,410	167,160	126,160	163,990	179,760	166,860	206,570
Total	1,679,110	1,545,120	1,296,180	1,592,332	1,511,910	1,649,620	1,437,552	1,596,468	1,762,773

Table 2 Percentage of annual generation production for a rooftop PV system in Durban [5]

		Orientation																											
		South		South East			East			North East			North			North West			West			South West				South			
		-180	-165	-150	-135	-120	-105	-90	-75	-60	-45	-30	-15	0	15	30	45	60	75	90	105	120	135	150	165	180			
Inclination	90°	22	24	28	33	40	46	52	57	60	62	64	64	64	64	64	62	60	57	52	46	40	33	28	24	22	90°	Inclination	
	80°	26	28	32	39	46	53	59	64	68	71	73	74	75	74	73	71	68	64	59	53	46	39	32	28	26	80°		
	70°	32	33	37	44	51	59	66	71	76	79	82	83	84	83	82	79	76	71	66	59	51	44	37	33	32	70°		
	60°	38	39	43	50	57	65	71	77	82	86	89	91	91	91	89	86	82	77	71	65	57	50	43	39	38	60°		
	50°	45	46	50	56	63	70	76	82	87	91	94	96	96	96	94	91	87	82	76	70	63	56	50	46	45	50°		
	40°	53	54	57	63	69	75	80	86	90	94	97	99	99	99	97	94	90	86	80	75	69	63	57	54	53	40°		
	32°	60	61	64	68	73	78	83	88	92	95	98	99	100	99	98	95	92	88	83	78	73	68	64	61	60	32°		
	30°	62	63	66	69	74	79	84	88	92	95	98	99	100	99	98	95	92	88	84	79	74	69	66	63	62	30°		
	20°	72	72	74	76	79	83	86	89	92	95	97	98	98	98	97	95	92	89	86	83	79	76	74	72	72	20°		
	10°	80	81	81	82	84	86	87	89	91	92	93	94	94	94	93	92	91	89	87	86	84	82	81	81	80	10°		
	0°	87	87	87	87	87	87	87	87	87	87	87	87	87	87	87	87	87	87	87	87	87	87	87	87	87	0°		

that, all other simulation results were then expressed as a percentage of the maximum production.

In order to then understand how the annual PV production for the simulations done in Table 1 for Durban change by changing the inclination angles and orientation of the PV panels, we derived Table 3 and annual PV production at 0° inclination angle versus 30° north-facing inclination. In Durban, 1296.2 MWh and 1491 MWh of power are generated at 0° and 30° inclination angle, respectively. Based on the inclination and orientation angle of the actual PV panels installed on a roof, we then select the corresponding factor from the table and multiple it by the annual production from Table 1 for the actual inclination angle and orientation of the system installed in Durban. Table 3 shows the annual PV production when the solar system is inclined at 30° north facing will give us the best overall annual PV production from a fixed mounted solar system. This increases the annual PV production by 15%.

3.2 DC:AC Ratio of the Solar PV System

To further increase the annual production from an installed PV system, one can increase the size of PV system DC rating compared to the system AC rating. This typically means that we can add more panels, the sum of which will give us the system DC rating. In comparison, the sum of the inverter ratings will give us the AC rating. The ratio of the two will give us the DC:AC ratio. Table 4 shows the simulation results from several installed rooftop solar PV systems in Durban, showing the DC rating, AC rating, annual production, and the calculated specific yield. It must be noted that these systems were installed to take the inclination angle and orientation of the existing building roof structures, while many of the PV systems faced a number of different orientations to avoid the effects of shading and take the shape of the building roof. Specific yield is the ratio of the total annual energy generated from a PV system divided by the DC installed plant's size. Annual production is the total amount of electricity generated from the PV system over a year. Installed capacity is the sum of the number of solar panels installed for the PV system.

The production can be increased substantially by increasing the DC:AC ratio. Thus, new PV panels are also designed to allow for higher inverter voltage input of up to 1500 V, and newer inverters are also designed to allow for a DC/AC ratio of up to 1.5. This means that for 1.5 MWp of PV panels, 1 MW of inverters can be installed and the system will operate safely. However, it must be noted that factors such as the panels' inclination angle, orientation, shading effects from the building, cleanliness of the panels, annual production degradation of the panels, etc. will influence the DC/AC ratio when designing the rooftop solar PV system.

Table 3 Factor for annual generation production for a rooftop PV system in Durban (North–South)

		Orientation																								
		South		South East				East		North East				North		North West			West		South West					South
		-180	-165	-150	-135	-120	-105	-90	-75	-60	-45	-30	-15	0	15	30	45	60	75	90	105	120	135	150	165	180
Inclination	90°	0.25	0.28	0.32	0.38	0.46	0.53	0.60	0.66	0.69	0.71	0.74	0.74	0.74	0.74	0.74	0.71	0.69	0.66	0.60	0.53	0.46	0.38	0.32	0.28	0.25
	80°	0.30	0.32	0.37	0.45	0.53	0.61	0.68	0.74	0.78	0.82	0.84	0.85	0.86	0.85	0.84	0.82	0.78	0.74	0.68	0.61	0.53	0.45	0.37	0.32	0.30
	70°	0.37	0.38	0.43	0.51	0.59	0.68	0.76	0.82	0.87	0.91	0.94	0.95	0.97	0.95	0.94	0.91	0.87	0.82	0.76	0.68	0.59	0.51	0.43	0.38	0.37
	60°	0.44	0.45	0.49	0.57	0.66	0.75	0.82	0.89	0.94	0.99	1.02	1.05	1.05	1.05	1.02	0.99	0.94	0.89	0.82	0.75	0.66	0.57	0.49	0.45	0.44
	50°	0.52	0.53	0.57	0.64	0.72	0.80	0.87	0.94	1.00	1.05	1.08	1.10	1.10	1.10	1.08	1.05	1.00	0.94	0.87	0.80	0.72	0.64	0.57	0.53	0.52
	40°	0.61	0.62	0.66	0.72	0.79	0.86	0.92	0.99	1.03	1.08	1.11	1.14	1.14	1.14	1.11	1.08	1.03	0.99	0.92	0.86	0.79	0.72	0.66	0.62	0.61
	30°	0.71	0.72	0.76	0.79	0.85	0.91	0.97	1.01	1.06	1.09	1.13	1.14	1.15	1.14	1.13	1.09	1.06	1.01	0.97	0.91	0.85	0.79	0.76	0.72	0.71
	20°	0.83	0.83	0.85	0.87	0.91	0.95	0.99	1.02	1.06	1.09	1.11	1.13	1.13	1.13	1.11	1.09	1.06	1.02	0.99	0.95	0.91	0.87	0.85	0.83	0.83
	10°	0.92	0.93	0.93	0.94	0.97	0.99	1.00	1.02	1.05	1.06	1.07	1.08	1.08	1.08	1.07	1.06	1.05	1.02	1.00	0.99	0.97	0.94	0.93	0.93	0.92
	0°	1.00	1.00	1.00	1.00	1.00	1.00	1.00	1.00	1.00	1.00	1.00	1.00	1.00	1.00	1.00	1.00	1.00	1.00	1.00	1.00	1.00	1.00	1.00	1.00	1.00

Table 4 Simulation results of various projects in Durban

kWp DC	kW AC	Annual production (MWh)	Specific yield (kWh/kWp)
1041.15	948	1,344,200	1291.1
1199.55	1000	1,494,778	1246.1
1201.2	960	1,500,521	1249.2
1155	966	1,524,466	1319.9
1149.75	986	1,550,117	1348.2
1227.6	988	1,580,295	1287.3
1211.76	1000	1,622,300	1338.8
1313.4	1000	1,699,563	1294.0
1344	1000	1,788,460	1330.7
1368	1000	1,808,797	1322.2
1428.48	1000	1,900,000	1330.1

3.3 PV Panel Performance Degradation

A solar panel performance degrades every year, and an example of a manufacturer performance warranty for Longi LR4-60GBD solar panel is explained. As per the performance warranty offered by Longi, a 98% performance is guaranteed in year 1, 93.95% in year 10, 91.7% in year 15, 89.45% in year 20, 87.2% in year 25, and 84.95% in year 30. For an actual solar PV installation, this will be the maximum degradation that can be expected using these panels.

3.4 Shading of Panels

When installing solar panels, an assessment needs to be taken to avoid the shading of panels. Shading can be either temporary, such as the case of trees that may grow and cast shadows on the panels. Trees and their branches can periodically be trimmed to prevent shading, or permanent such as high-rise buildings where the effects cannot be amended. Shading of the panels results in a reduction in the annual generation production. If one panel on a string is shaded, it reduces generation on the entire string. Solar panels come with built-in bypass diodes that can assist with bypassing partial shading on a panel. The methods to deal with shading will be to use an inverter with multiple maximum power point trackers (MPPT) where strings which may be shaded can be installed on a separate MPPT or the use of an inverter which uses power optimisers installed per panel such as solar edge. In this case, only the shaded panel production will be affected and not the rest of the panels on the string.

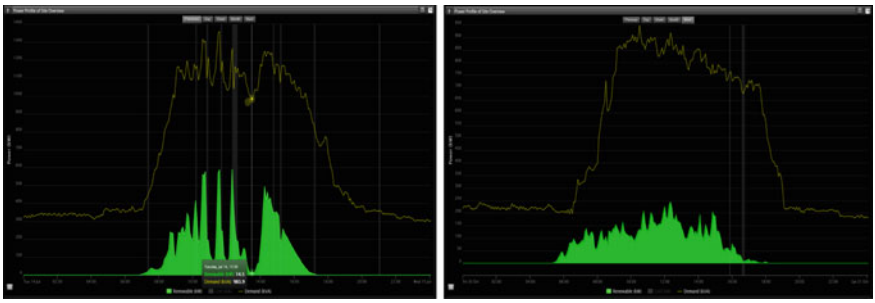

(a) (b)

Fig. 2 **a** Effect of cloud cover on a 1 MW PV generation system **b** Effect of rain on a PV generation profile

3.5 Site Climatic Conditions

Several climatic conditions will affect the PV generation; such as cloud cover in the area. When clouds cover the sky, they reduce the amount of the sun's irradiation reaching the solar panel resulting in a reduction in the generation. An example of the effects of cloud cover on PV production is shown in Fig. 2a for an installed 1 MW PV system in Durban, which shows how cloud covers affect solar system generation. This results in rapid decreases and increases in generation production. The PV production on a rainy day is also drastically reduced since it will be cloudy when it is rainy. An example of the PV production from a 1 MW PV system performance on a rainy day in Durban is shown in Fig. 2b.

The operating temperature of the solar cell also affects its power output. Solar panels are rated at standard test conditions, which is 25 °C and 1000 W/m^2. The effects of temperature on the panel operating voltage and current has been shown in the literature; thus, the panel power output is equal to the sum of the voltage and current. Hence, the reduction of the panel voltage results in a reduction of the panel power output. Similarly, the effects of irradiation levels on the panel power output; as the irradiation levels reduce, so does the PV panel power output. The irradiation levels are affected by several factors, including clouds, dust, shading, etc. Figure 3a shows how the irradiance vs. PV generation production for a 1 MW solar PV installation in Durban on a clear day whilst Fig. 3b shows the irradiance versus PV generation for the same system on a cloudy day in Durban.

3.6 Cleanliness of Panels

The cleanliness of the PV panels affects the generation production from the panel. The amount of PV production produced by the PV cell depends on the amount of irradiance that reaches the PV cell. Like the dirt, soil, dust, leaves, salt sprays (in

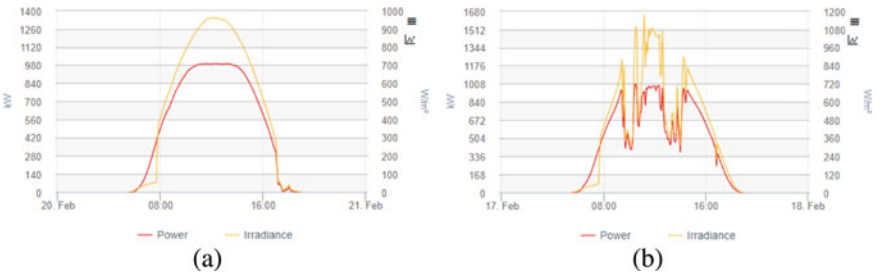

Fig. 3 **a** Clear day irradiance vs. generation output for a 1 MW PV plant **b** Cloudy day irradiance vs. generation output for a 1 MW PV plant in Durban

coastal installations) builds upon the PV panel's glass surface, the panels' production starts to reduce due to lower irradiance levels reaching the PV cell. In the case of panels mounted on an inclined roof, rain assists with washing away dirt and dust from the panels. Most inverters have software that monitors the strings' PV production or even some at the individual panel level, which then allows the owner to see when the panel production starts reducing and the panels are in need of washing.

3.7 System Losses

In a PV system, there a number of losses that are experienced which includes the following:

1. **DC cable losses**: depending on the length of the DC cable run to the inverter will affect the losses that incur.
2. **Inverter losses:** Most inverters are highly efficient and generally exceed 98% efficiency under STC, but the efficiency reduces when the inverter temperature increases. This can be mitigated by placing the inverter in a substation that is cooled by an air conditioner. Figure 4 shows the efficiency curve for an SMA Sunny Tripower Core 1 STP 50–40 inverter. Figure 4a indicates that the efficiency is also a function of the power output, with lower efficiency at below 20% power output compared to greater than 20%.

3. **Clipping losses:** This occurs in systems with much larger DC:AC ratios and occurs when the DC power fed into the inverter is greater than the inverter's AC rating. Figure 4b shows an example of a larger DC panel installation compared to the 1 MW inverter rating and the result of clipping of generation due to the inverter rating. Most PV systems will generate maximum energy during the summer months, and depending on the DC:AC ratio, and clipping may most likely only occur during the summer months. Installers also need to consider that the production from the PV system degrades over time coupled with the cleanliness of the panels, etc. Therefore, clipping may only occur in the first

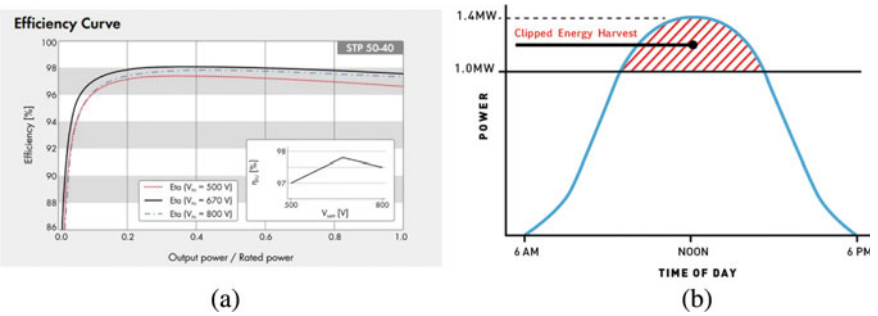

Fig. 4 **a** Efficiency curve for a SMA Sunny Tri Power STP 50–40 inverter **b** Graph of clipped energy for a 1 MW PV system [6]

few years after installation. Most modern inverters can allow up to 1.5:1 DC:AC ratio and will clip off the energy exceeding its rating safely with no damage to the inverter.

4. **PV panel mismatch:** This is the difference in performance between panels on the string. This results in mismatch losses on the string.
5. **Reflection:** Solar radiation reflected by the surface/collector/module will not hit the cell and therefore cannot contribute to the generation of electricity.
6. **Efficiency of the PV panel:** The efficiency of a solar panel refers to the amount of energy it produces from the maximum produced from the amount of irradiance that strikes the panel. There have been numerous solar PV technology developments in recent years, such as bi-facial solar panels, passivated emitter and rear contact cells, half-cut cells, and multi-junction concentrator solar cells. This has improved solar panels' efficiency currently on the market, offering efficiencies of up to 23.81%, such as Trina Solar panels, whilst labs such as the National Renewable Energy Lab have obtained higher efficiency up to 47.1% using multi-junction concentrator solar cells. However, these are not currently commercially available.

3.8 Grid Availability

Grid-tied solar PV systems need the grid as a reference in order to generate electricity. However, network faults, outages, and load shedding all negatively affect the availability of the grid. This then in turn, results in no PV generation production when the grid is not available, resulting in loss of production. Figure 5 shows the effect of 2-h load shedding on a grid-tied solar PV system in Durban. The effects of grid unavailability for pure grid-tied PV can be mitigated with the addition of battery storage or configuring the PV system to operate in parallel with a suitably sized standby generator.

Fig. 5 Loss in PV production during 2 h' load shedding

4 Simulation versus Practical Examples of Solar PV Generation

Table 1 shows the simulation results from a 1:1 DC:AC ratio flat roof solar PV installation. The monthly generation varies and is dependent on the seasons, with the highest generation in summer and the lowest generation in winter. Subsequently, a practical example of a 1 MW PV system installed in Durban was examined and compare the simulation results of Table 1 to the actual installed solar PV system monthly production. The DC size of the system was 1,199,550 kW. The AC system size was 1000 kW. This resulted in a 1.2:1 DC:AC ratio. The panels were inclined at 3° to take the roof profile, which is very close to the flat roof used in the simulation.

Figure 6 shows that the simulation results versus the actual 1 MW installed solar PV system percentage of the total monthly production. The results reflect the simulation, and the actual results are very close to each other. The largest difference is 1. 53%, which occurred in March 2020. Since the actual plant installed on site is 20% bigger on the DC side than the simulated plant, we see a 20% higher production in the installed plant compared to the simulated plant.

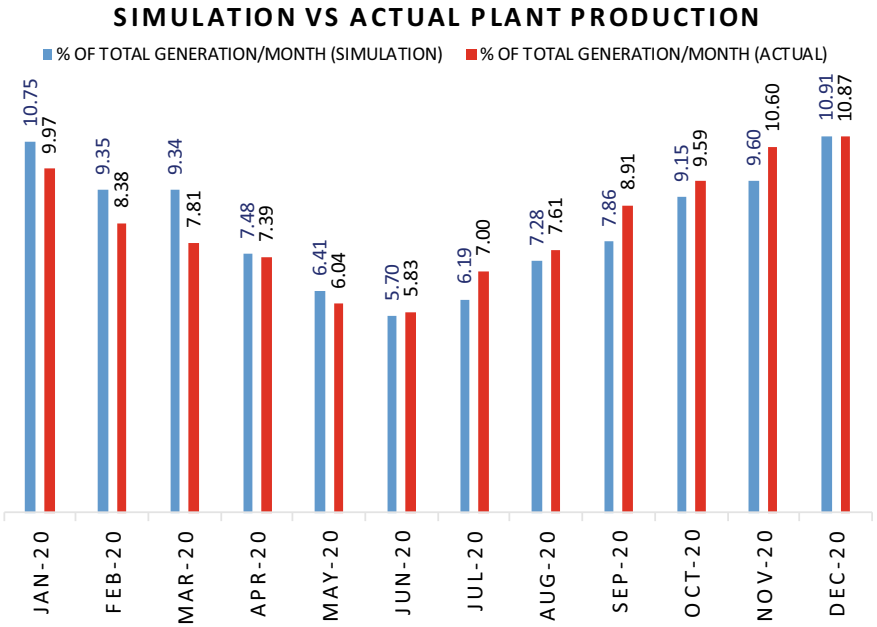

Fig. 6 Monthly PV Production from a 1 MW PV System

5 Conclusion

The studies have shown that Durban's PV production is the worst compared to the other provinces in South Africa. This, however, still compares well with other countries in the world, such as Germany. A higher DC:AC ratio of the PV system can be utilised to compensate for additional energy production. When designing and installing a PV system, it is crucial to consider numerous sources' potential for losses. Some could be avoided whilst others were permanent and cannot be avoided. The effects of panels' inclination angles and orientation, shading, etc. can be taken into account, and these have major impacts on the amount of energy produced from the PV system. Many additional factors need to be considered when deciding to install a PV system, including technical and financial analysis. A comparative analysis between the software simulation results and an existing plant in Durban reveals similar results. This provides us with confidence in the use of software simulation to provide accurate PV production data.

References

1. National Energy Regulator of South Africa (2015) Small-scale embedded generation: regulatory rules consultation paper, 25 February 2015

2. Pegels A, (2010) Renewable energy in South Africa: Potentials, barriers and options for support. Energy Policy 38(9):4945–4954. ISSN 0301–4215
3. Zawilska E, Brooks MJ (2011) An assessment of the solar resource for Durban, South Africa. Renew Energy 36(12):3433–3438
4. http://solargis.info/doc/free-solar-radiation-maps-GHI. Last Accessed 28 February 2021
5. Sewchurran S (2016) Modelling and performance analysis of the ethekwini electricity distribution grid with increased embedded generation sources. PhD Thesis, UKZN 2016
6. Serdio Fernández F, Muñoz-García MA, Saminger-Platz S (2016) Detecting clipping in photovoltaic solar plants using fuzzy systems on the feature space. Solar Energy 132:345–356. ISSN 0038–092X

An Experimental Analysis of the Impact of a Grid-Tied Photovoltaic System on Harmonic Distortion

Abayomi A. Adebiyi, Ian J. Lazarus, Akshay K. Saha, and Evans E. Ojo

Abstract This study presents analyses of the results of selected experimental power quality (PQ) data obtained on a grid-tied photovoltaic (PV) system composed of different PV modules technologies and four PV inverters integrating the grid at the point of common coupling. A PQ analyzer is utilized to collect the data from the 110 kW PV system for two weeks. The measured PQ data was obtained by following South Africa and international power quality measurement standards. The data measured were RMS voltage, RMS current, voltage unbalance, frequency, voltage total harmonic distortion (THD_V), current total harmonic distortion (THD_I), active and reactive power. Voltage unbalance, frequency, voltage total harmonic distortion (THD_V), current total harmonic distortion (THD_I) have been appraised and juxtaposed with the requirements of the South Africa Renewable Energy Grid Code. These parameters were all found within the regulated limits, except for the current total harmonic distortion (THD_I) that exceeded the grid code limit due to sudden voltage variations. This occurrence is observed primarily at dawn and dusk when the PV inverter output active power is at the lowest level. This study's performance analysis contributes to evaluating large-scale PV systems inverters' behaviour and their impact on the distribution grid power quality at different power generation levels.

A. A. Adebiyi (✉)
Department of Electrical Power Engineering, Durban University of Technology, Durban, South Africa
e-mail: abayomia@dut.ac.za

I. J. Lazarus
Department. of Physics, Durban University of Technology, Durban, South Africa
e-mail: lazarusi@dut.ac.za

A. K. Saha
School of Engineering, Howard College, University of KwaZulu-Natal, Durban, South Africa
e-mail: saha@ukzn.ac.za

E. E. Ojo
Department of Electrical Power Engineering, Durban University of Technology, Durban, South Africa
e-mail: evanso@dut.ac.za

C. Subramani et al. (eds.), *Proceedings of International Conference on Power Electronics and Renewable Energy Systems*, Lecture Notes in Electrical Engineering 795,
https://doi.org/10.1007/978-981-16-4943-1_40

Keywords Photovoltaic system · Total harmonic distortion · Voltage unbalance

1 Introduction

Electricity generation from photovoltaics (PV) systems, a climate-friendly and clean energy source, has evolved significantly over the years. It is projected that the PV technology will provide a significant proportion of energy demand as time goes on [1]. The Photovoltaic Power System Program of the International Energy Agency indicated that 75 gigawatts of PV power plants were installed globally in 2016, therefore taking the total global PV installed capacity to about 305.5 gigawatts (GW). As shown in Fig. 1, the global cumulative installed capacity stands at 627.2 GW at the end of 2019, 82% over the previous year [2]. The rapid increase in this technology's deployment is motivated by increasing global warming, implementing renewable energy standards, government incentives and cost reduction of PV systems. The intermittency of the power injected by the grid-tied PV system due to the variation of solar irradiation and temperature on the distribution system could result in major power quality issues. Thus, power utilities are concerned about these systems' impacts on the power system [3, 4]. Different research studies have been conducted to evaluate PV systems' impact on the low-voltage distribution grid, particularly their impact on distortions in power quality, voltage control and system security [5].

Conventionally, in the event of a disturbance in the distribution network, distributed generation must disconnect within 1 s [6, 7]. But with the high-level penetration of the local generation on the distribution grid, a sudden disconnection of a large portion of the grid will trigger transient disturbances in the network, therefore degrade the grid stability. Consequently, different countries have come up with new

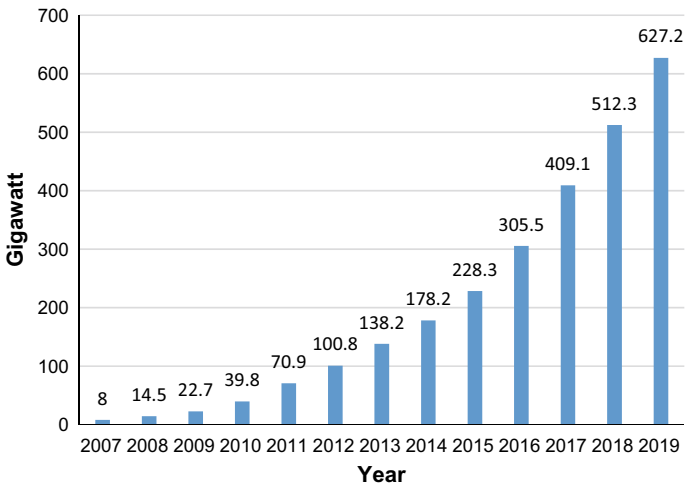

Fig. 1 PV power global cumulative installed capacity

standards to address this issue, like the South Africa Renewable Energy Grid Code (SAREGC), which provides that the local generation must remain connected to the grid under specific variations in voltage and frequency [8–10]. The grid code provided for the concept of Low-Voltage Ride-Through (LVRT) or Fault Ride-Through (FRT) capability for the PV inverters to ride-through voltage dip up to 0 pu at the point of common coupling (PCC) for a maximum period of 0.15 s in the event of grid disturbance with a variation within the upper and lower limits of 1.1–0.9 pu as depicted in Fig. 2.

Significant attention has been drawn to voltage and current harmonics' contribution by PV systems in the distribution grid's power quality in many studies [11–14]. It is established from the literature that the inverter technology, solar irradiation level, temperature and loads determine the harmonic generation of a PV system [14]. The PV system harmonics have intrinsic and extrinsic effects in that the distortions are inherently attributable to nonlinearities of the inverter control loop and limited resolution of Pulse Width Modulation. The external impact of the harmonic distortion is due to PV penetration on an unbalanced and weak grid. In this case, the inverter control system senses the distorted voltage as a disturbance, distorting the current waveform curve that the inverter generates [14, 15]. Thus, since South Africa has abundant solar energy resources, this paper analyzes the power quality impact of the low-voltage grid-tied 110 kW PV power plant in Durban. The results are compared to the South Africa Renewable Energy Grid Code required limits.

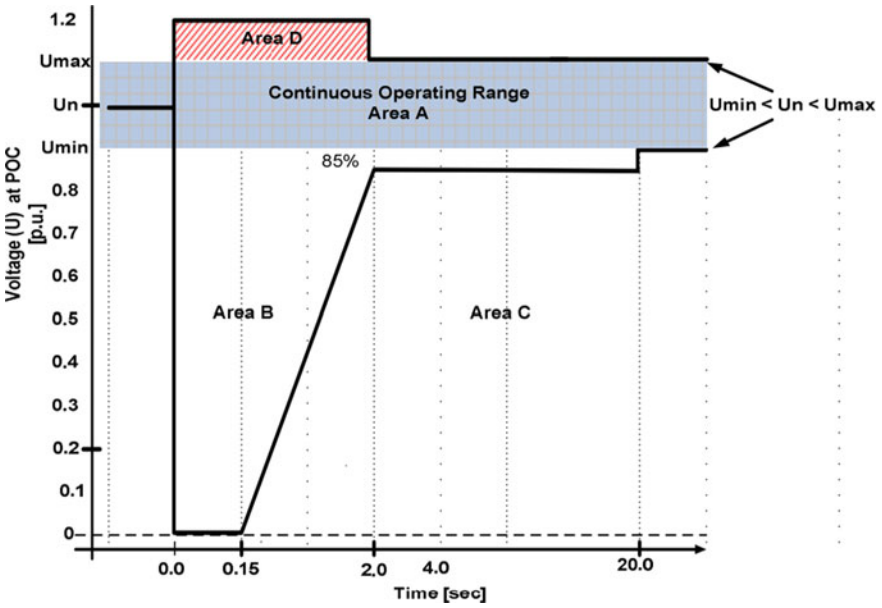

Fig. 2 The SAREGC voltage ride-through capacity

2 Methodology

2.1 The PV Power Plant Layout

The photovoltaic system analyzed in this work is a 110 kW PV power plant with different PV panels and inverters. The plant was installed by the Durban University of Technology energy research centre called the KZN Industrial Energy Efficient Training and Resource Centre at the university's Steve Biko campus. It is the highest installed PV system capacity currently in operation in the university power system. The average solar irradiation on the campus is 4.6 kWh/m^2/day; the average ambient temperature is 26 °C. The wind speed generally varies between 0.83 m/s and 1.4 m/s. Figure 3 depicts the layout of the grid-tied PV system. The PV array is installed on a flat roof with a tilt angle of 30° and oriented towards the South. The panels' correct tilt helps the PV array generate maximum energy when the solar irradiation hits it directly to receive the Global Horizontal Irradiance (GHI) [16, 17]. The system has 328 polycrystalline silicon (330 and 340 watts) PV panels connected in series into eleven strings to form the PV array that is, in turn, connected in parallel into four different DC-AC inverters. The PV system penetrates the grid via the transformerless inverters. The PV panel's electrical characteristic is presented in Table 1, while Table 2 presents the inverter specification.

Fig. 3 The grid-tied PV array

Table 1 Characteristics of the PV panels

Description	Value
(ARTsolar 330–72)	
Maximum power (P_{max})	330 W
Maximum voltage at peak power (V_{max})	37.4 V
Maximum current at peak power (I_{max})	8.83 A
Open circuit voltage (V_{oc})	46.1 V
Short-circuit current (I_{SC})	9.3 A
(ARTsolar 340–72)	
Maximum power (P_{max})	340 W
Maximum voltage at peak power (V_{max})	37.8 V
Maximum current at peak power (I_{max})	9.0 A
Open circuit voltage (V_{oc})	46.3 V
Short-circuit current (I_{SC})	9.41 A

Table 2 Solar Edge three-phase inverter SE-27.6 K specification

Description	Value
Output	
Rated AC power output	27 600 VA
Maximum power output	27 600 VA
Nominal output voltage: line to line/line to neutral	400/230 V_{ac}
Maximum output current (per phase)	40 A
Frequency	50 ± 5 Hz
Three-phase grid support	WYE with neutral
Input	
Maximum DC power (STC)	37 250 W
Maximum input voltage	900 V_{dc}
Nominal DC input voltage	750 V_{dc}
Maximum input current	40 A_{dc}
Transformerless	Yes

3 Methodology

3.1 The PV Power Plant Layout

The photovoltaic system analyzed in this work is a 110 kW PV power plant with different PV panels and inverters. The plant was installed by the Durban University of Technology energy research centre called the KZN Industrial Energy Efficient Training and Resource Centre at the university's Steve Biko campus. It is the

highest installed PV system capacity currently in operation in the university power system. The average solar irradiation on the campus is 4.6 kWh/m^2/day; the average ambient temperature is 26 °C. The wind speed generally varies between 0.83 m/s and 1.4 m/s. Figure 3 depicts the layout of the grid-tied PV system. The PV array is installed on a flat roof with a tilt angle of 30° and oriented towards the South. The panels' correct tilt helps the PV array generate maximum energy when the solar irradiation hits it directly to receive the Global Horizontal Irradiance (GHI) [16]. The system has 328 polycrystalline silicon (330 and 340 watts) PV panels connected in series into eleven strings to form the PV array that is, in turn, connected in parallel into four different DC-AC inverters. The PV system penetrates the grid via the transformerless inverters. The PV panel's electrical characteristic is presented in Table 1, while Table 2 presents the inverter specification.

3.2 Standards and Measurement of the Selected Power Quality Indicators

This study considered the requirement of the standards IEC 61000-4-30, IEC 61000-3-6:2.0, IEEE 519: 2014, Eskom quality of supply NRS 048-2:2003 and the South African Renewable Energy Grid Code. The different parameters to identify for quality of supply analysis include RMS Voltage, RMS current, voltage unbalance, flickers, voltage total harmonic distortion (THD_V), current total harmonic distortion (THD_I), frequency, power factor, active and reactive power. The power quality data of the PV installation was measured with the ELSPEC Blackbox PQ analyzer, in line with the IEC 61000-4-30 standard; it measures and calculates all the power quality indicators at the point of common coupling (PCC), as illustrated in Fig. 4. The measured PQ data was downloaded and extracted using ELSPEC Sapphire software on a computer. The software was used for data analysis. The technical requirements for power quality by the South Africa grid code for renewable energy are presented in Table 3 are juxtaposed with this study's results.

Total harmonic distortion, the ratio of the sum of all harmonic components' powers to the fundamental frequency, measures the harmonic distortion contained in a voltage or current signal. Equations (1) and (2) express the voltage and current THD.

$$\mathrm{THD} = \frac{V_{n\_\mathrm{RMS}}}{V_{\mathrm{Fundamental\_\ RMS}}} \tag{1}$$

$$I_{\mathrm{THD}} = \frac{\sqrt{\sum_{h=2}^{N} I_{n\_\mathrm{RMS}}^2}}{I_{1,\mathrm{RMS}}} \times 100\% \tag{2}$$

where: V_{n_RMS} is the summation of harmonic signal frequencies from the 2nd harmonic and the $V_{\mathrm{Fundamental\_RMS}}$ is the RMS voltage of the fundamental frequency.

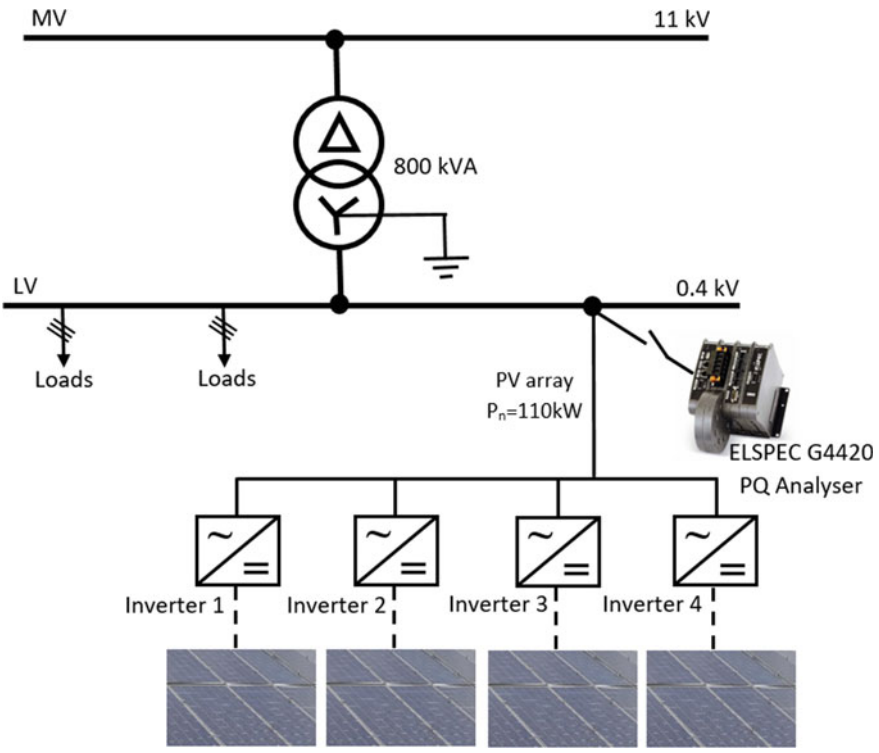

Fig. 4 The schematic diagram of the installation

Table 3 Selected grid code limits for power quality indicators

Description	Value
Voltage THD	8%
Current THD	5%
Voltage unbalance	2%
Frequency	50 ± 5 Hz

Voltage unbalance in a three-phase system is one of the major concerns of distribution system operators. It is a state in which a poly-phase voltage magnitude fluctuates or is not within the standard 120° phase angle or both. The extent of this unbalance is generally expressed as the ratio of the voltage negative sequence component to the positive sequence component. This measured disparity in phase voltages degrades the performance and significantly reduces loads' lifespan on the distribution network. All the power quality standards reviewed for this study set 2% [18, 19] as the allowable limit for poly-phase system voltage unbalance, calculated as expressed in Eq. (3).

$$\begin{aligned} \text{VU} &= \frac{\text{Maximum Voltage Deviation}}{\text{Average Voltage}} \times 100 \\ \text{Voltage Unbalance } (\%) &= \frac{V_2}{V_1} \times 100\% \end{aligned} \tag{3}$$

4 Measured PQ Data Analysis

As measured on the DUT Low-Voltage switchboard in steady-state on different operating days, the power quality data is presented in this section. This study choice to evaluate the PV system impact on the grid power quality using the following dataset:

- Total Voltage Harmonics (THD_V [%])
- Total Current Harmonics (THD_I [%])
- Voltage unbalance (U_2/U_1 [%])
- Frequency (F [Hz])

The data analyzed in Table 4 indicates that the three-phase system voltage total harmonic distortion content, voltage unbalance and frequency did not violate the grid code required maximum limit, also depicted in Figs. 5, 6 and 7. On the other hand, there were unusual values beyond the required limits measured for the current total harmonic distortion on Phase B and C, as depicted in Figs. 9 and 10, indicating that some loads draw current with total harmonic distortion above the limit. This occurs during the PQ event of voltage dip during load shedding and when the PV system was starting up, this causes the current harmonic distortion to increase exponentially [20].

Likewise, another factor that could cause the unusual current THD is the level of active power generated by the PV system, depending on the solar irradiation levels. During cloudy days, sunrise and sunset, current THD values tend to increase significantly at low solar irradiation levels since the PV inverter's active output power

Table 4 Analysis of measured PQ data

Parameter	Maximum	Minimum
THD_{Va} (%)	2.04	1.48
THD_{Vb} (%)	1.88	1.35
THD_{Vc} (%)	2.15	1.55
THD_{Ia} (%)	2.74	1.48
THD_{Ib} (%)	17.61	1.43
THD_{Ic} (%)	22.14	2.85
Voltage unbalance (%)	1.1	0.16
Frequency (Hz)	50.24	49.77

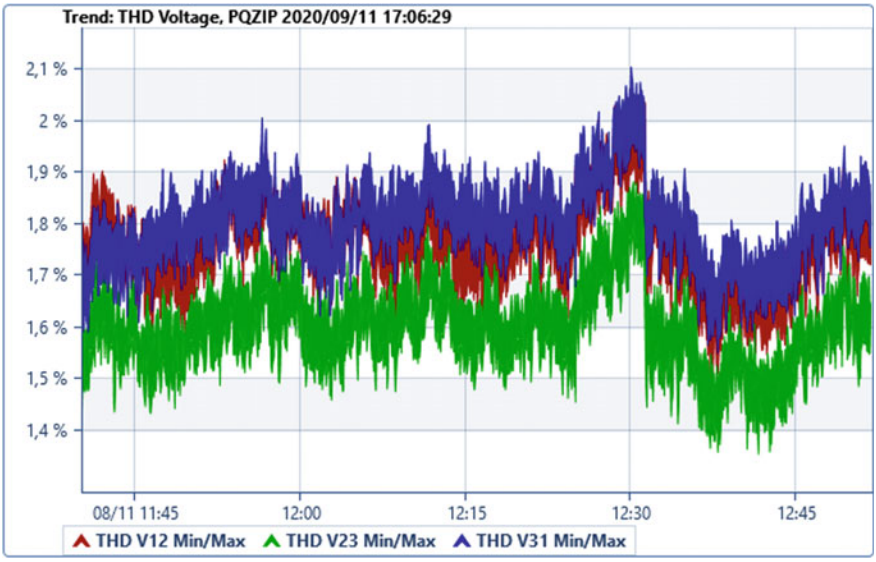

Fig. 5 Voltage total harmonic distortion content

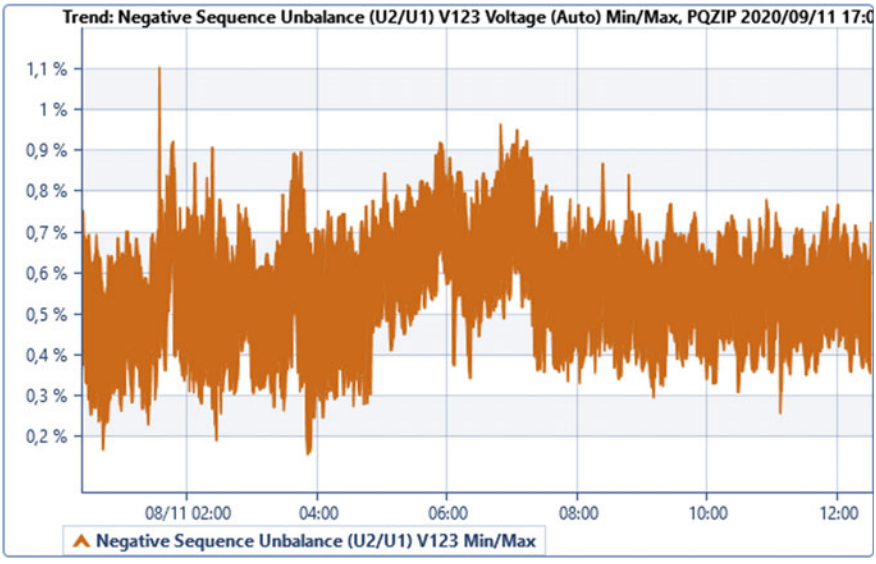

Fig. 6 Measured voltage unbalance

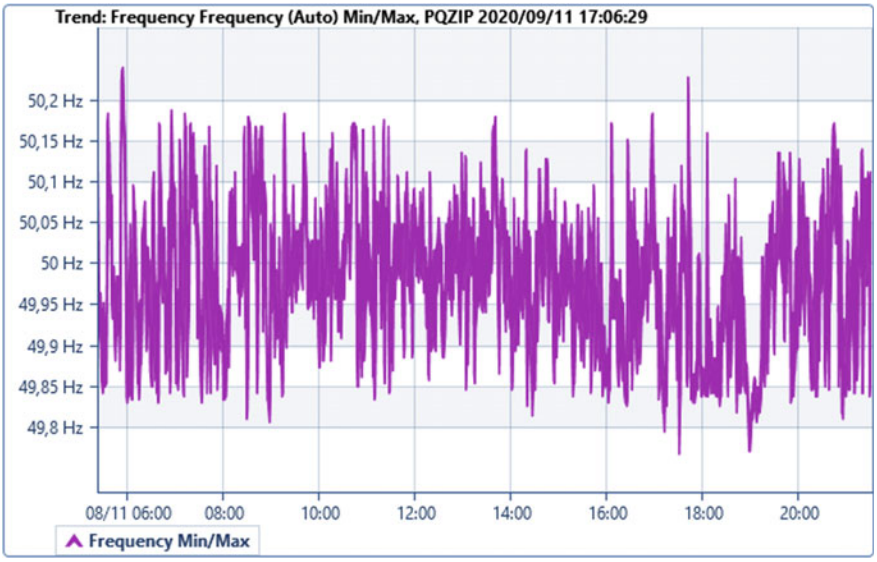

Fig. 7 Measured frequency

is proportional to the inverse of the total harmonic distortion factor. The curves depicted in Figs. 8 and 9 characterize the RMS current and current THD generated by the PV inverter as a function of solar irradiation behaviour [20]. However, the

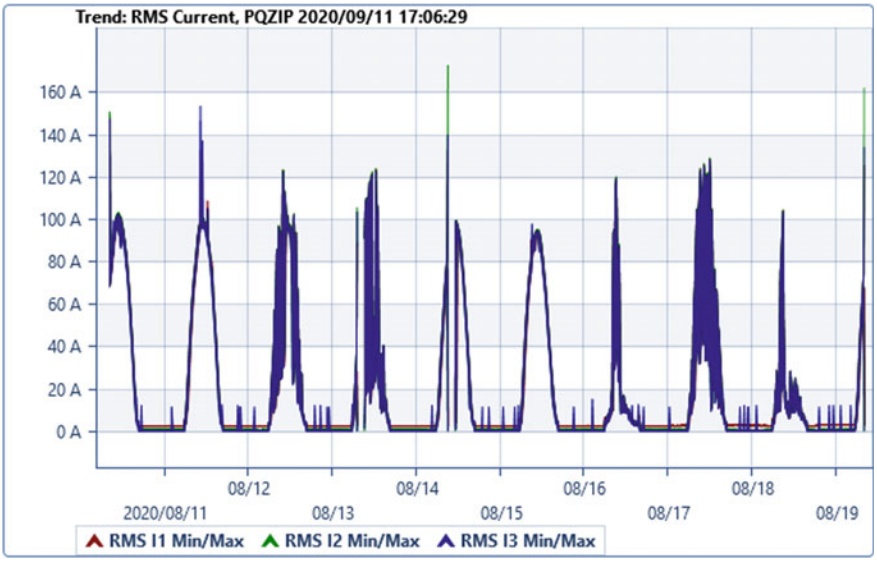

Fig. 8 RMS current on a sunny and cloudy day

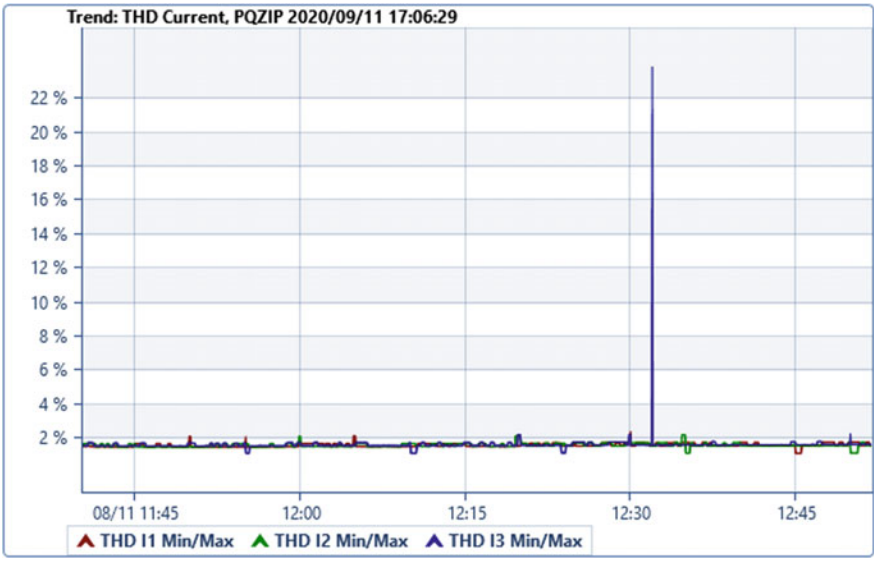

Fig. 9 Measure three-phase current total harmonic distortion

current THD significantly decreased towards regulatory limit value with increased PV system active power output, as shown in Fig. 10.

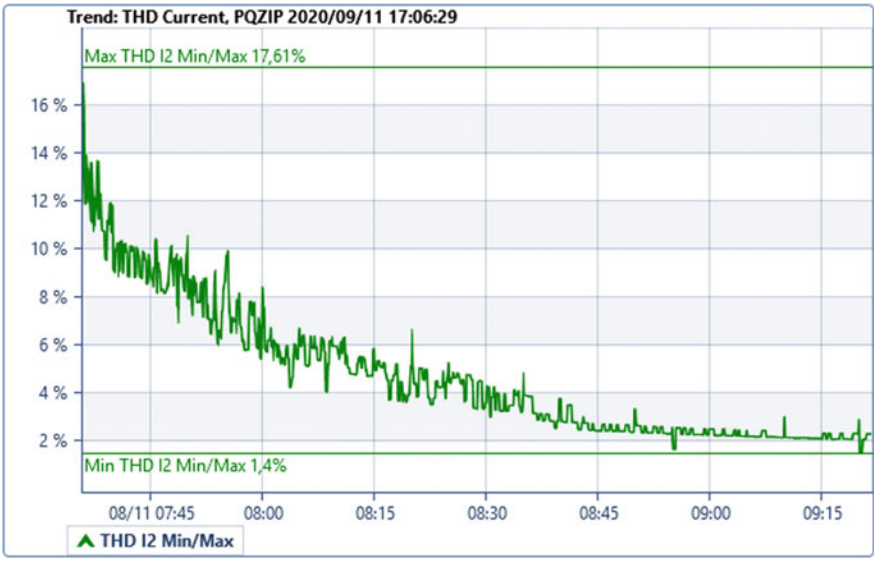

Fig. 10 Sharp decay of current THD during increased solar irradiation

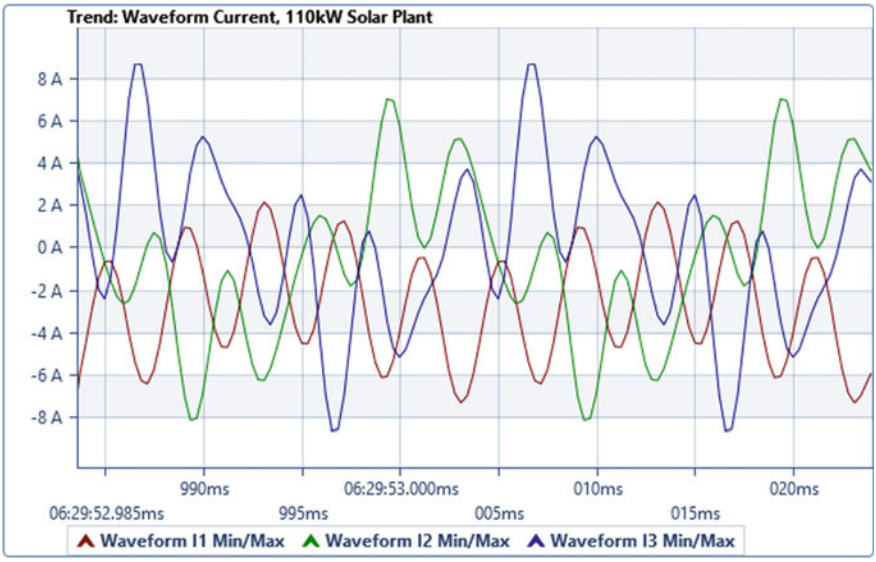

Fig. 11 The current waveform distortion at dawn

5 Discussion

Figure 10 presents the sharp decay of the current THD obtained after the PV inverter has tracked the PV output power as the solar irradiation level rises towards the midday. The distortion level decreased to 1.4% to maintain the required limit. Remarkably, the harmonic current is higher for low power values. It is visible that the high content of current THD is obtained during the periods that the current generated is low, as shown in Fig. 11.

Figure 11 depicts the three-phase current waveform distortion during the period that the current THD rose above the limit at dawn when the PV inverter begins to track power generation under low solar irradiation.

6 Conclusion

This study presented the power quality measurement results obtained on a 110 kW PV system, which contributes extensively to evaluating PV systems' impact on the distribution network. For two weeks, under different generation conditions, the PV inverter's performance and impact on power quality (PQ) were measured and evaluated. For the analysis, four PQ indicators were selected and juxtaposed with the South Africa Renewable Energy Grid Code requirements. The voltage total harmonic distortion, voltage unbalance and frequency was found to be within the required limits.

The current total harmonic distortion (THD_I) measured data was observed to have exceeded the grid code limits. This occurrence is observed primarily at dawn and dusk when the PV inverter output active power is at the lowest level when the PV system does not generate power. Although the current THD obtained was significantly higher than the standard limits during low power generation, the value does not pose a problem to the grid due to the grid robustness as the PV output power is less than the rated output at that period. It is essential to study further the impact of a large-scale PV system on a weak distribution grid that reflects new inverter technology with improved response during low power generation.

Acknowledgements The authors are grateful to PQ Flow Solutions, a power quality risk manager, for providing the ELSPEC power quality analyser used for this study.

References

1. IEA (2019) Solar energy mapping the road ahead, France
2. Kaizuka I, Jäger-Waldau A, Donoso J, Detollenaere A, Wetter JV, Masson G (2019) Trends in photovoltaic (PV) applications. International Energy Agency
3. Adebiyi AA, Saha AK, Lazarus IJ, Ojo EE (2019) Investigation to determine the impacts of SPV penetration on an unbalanced distribution grid. In: IEEE PES/IAS PowerAfrica. IEEE, pp 116–120
4. Adebiyi AA, Lazaru I, Saha AK, Ojo EE (2019) High PV penetration impact on an unbalanced distribution network. In: IEEE PES/IAS PowerAfrica. pp 706–710
5. Mahela OP, Shaik AG, Gupta N (2015) A critical review of detection and classification of power quality events. Renew Sustain Energy Rev 41:495–505
6. Antonova G, Nardi M, Scott A, Pesin M (2012) Distributed generation and its impact on power grids and microgrids protection. In: 65th Annual Conference for Protective Relay Engineers. pp 152–161
7. Seyedi Y, Karimi H, Grijalva S (2016) Distributed generation monitoring for hierarchical control applications in smart microgrids. IEEE Trans Power Syst 32:2305–2314
8. Eskom (2014) Grid connection code for renewable power plants (RPPs) connected to the electricity transmission system (TS) or the distribution system (DS) in South Africa. In: Grid Code Version 2.8 ed. National Energy Regulator of South Africa (NERSA), South Africa, p 64
9. Marinopoulos A, Papandrea F, Reza M, Norrga S, Spertino F, Napoli R (2011)Grid integration aspects of large solar PV installations: LVRT capability and reactive power/voltage support requirements. In: 2011 IEEE Trondheim PowerTech. Trondheim, Norway, pp 1–8
10. Sewchurran S, Davidson IE (2016) Guiding principles for grid code compliance of large utility scale renewable power plant intergration onto South Africa's transmission/distribution networks. In: IEEE international conference on renewable energy research and applications (ICRERA). pp 528–537
11. Barbu V, Chicco G, Corona F, Golovanov N, Spertino F (2013) Impact of a photovoltaic plant connected to the MV network on harmonic distortion: an experimental assessment. Univer Bucharest Electr Eng Comput Sci Ser C 75:179–194
12. Etier I, Abderrazzaq M, Al Tarabsheh A, Saraereh O, Albdour M (2016) The impact of large scale photovoltaic systems on the harmonic increase in distribution networks. Jordan J Mech Ind Eng 10:239–244
13. Granja AV, De Souza TM, Sobrinho PM, Santos DFA (2018) Study of power quality at the point of common coupling of a low voltage grid and a distributed generation system of 7.8 kWp in a tropical region. Energies 11:1–19

14. Block PA, Salamanca HL, Teixeira MD, Dahlke DB, Shiono OM, Donadon AR et al (2014) Power quality analyses of a large scale photovoltaic system. In: 5th international renewable energy congress (IREC). pp 1–6
15. Abeyasekera T, Johnson CM, Atkinson DJ, Armstrong M (2005) Suppression of line voltage related distortion in current controlled grid connected inverters. IEEE Trans Power Electron 20:1393–1401
16. Adebiyi A, Lazarus I, Saha A, Ojo E (2018) Performance analysis of PV panels connected in various orientations under different climatic conditions. In: Proceedings of the 5th Southern African Solar Energy Conference (SASEC 2018). pp 46–51
17. Adebiyi AA, Lazarus IJ, Saha AK, Ojo EE (2021) Performance analysis of grid-tied photovoltaic system under varying weather condition and load. Int J Electr Comput Eng 2088–8708(11):94–106
18. Zolkifri NI, Gan CK, Khamis A, Baharin KA, Lada MY (2017) Impacts of residential solar photovoltaic systems on voltage unbalance and network losses. In: TENCON 2017–2017 IEEE Region 10 Conference. pp 2150–2155
19. Liao H, Milanović JV (2017) Methodology for the analysis of voltage unbalance in networks with single-phase distributed generation. IET Gener Transm Distrib 11:550–559
20. Niitsoo J, Jarkovoi M, Taklaja P, Klüss J, Palu I (2015) Power quality issues concerning photovoltaic generation in distribution grids. Smart Grid Renew Energy 6:148–164

Genetic Algorithm Based Energy Management in Microgrid

M. Sadees, Aishwarya Raju, Utsahan Mukherjee, and K. Vijayakumar

Abstract Microgrid gives a viable way to advance sustainable power source use through conveying multiple distributed generators (DGs) with energy storage systems (ESSs), loads, control gadgets, and ensure gadgets, which can work in either islanded mode or lattice associated mode. So as to organize the yield of various DGs and understand the capability of sustainable power source, vitality of the executives, and financial dispatch of the microgrid is required. Both distributed energy resources (DERs) and client stacks in microgrids have vulnerability qualities; so, the irregularity of the breeze speed and sunlight based radiation force is displayed by interim science, and the interim yield of the breeze turbine and photovoltaic (PV) age framework are obtained. At that point, a microgrid monetary enhancement model dependent on an interim advancement technique is proposed.

Keywords Microgrid · DG placement · DG sizing · Genetic algorithm · Cost reduction

1 Introduction

The lattice associates homes, organizations, and different structures to focal force sources, which permit us to utilize machines, warming/cooling frameworks, and gadgets. In any case, this interconnectedness implies that when part of the matrix should be fixed, everybody is influenced. This is the place a microgrid can help. A microgrid by and large works while associated with the matrix, yet critically, it can serve and work on its own utilizing neighborhood vitality age in the midst of emergency like tempests or force blackouts, or for different reasons. A microgrid can be fueled by circulated generators, batteries, as well as sustainable assets like

M. Sadees (✉) · A. Raju · U. Mukherjee · K. Vijayakumar
Department of Electrical and Electronics Engineering, SRM Institute of Science and Technology, Kattankulathur, Chengalpattu, India

A. Raju
e-mail: aishwaryaraju_raju@srmuniv.edu.in

C. Subramani et al. (eds.), *Proceedings of International Conference on Power Electronics and Renewable Energy Systems*, Lecture Notes in Electrical Engineering 795,
https://doi.org/10.1007/978-981-16-4943-1_41

sun powered boards. In [1, 7] the model for calculating the optimal size and placement of DGs in a distribution network is investigated. The modeling of the wind and solar DGs has been mainly done as illustrated by Kutaiba et al. *in* [2]. Load flow in distributed networks by distributed generators as elaborated in [3, 4]. In [5] there has been explained, a way to integrate solar generators into the planned hybrid network model efficiently. The increasing penetration of wind energy in the network in [6] has helped to improve the wind generator model. The methods of improvement of distributed networks are discussed in [8]. Crucial information on placing multiple DGs is obtained from [9]. Maximization of benefits from DG placements in distribution as modeled in [10] has been used. The placement of DGs in a radial distribution system is elaborated in [11] which helped us in choosing a 33-bus radial system.

1.1 Checking Problems of Dg Fixing

The progress towards microgrid prompts new necessities and difficulties for assurance that should be versatile for varieties in the system topology along with the association of dynamic assets. The assurance challenges, related to microgrids, develop from adding DG sources to the matrix. The impacts of including DG assets to systems are abundant, including changing force stream and expanded or diminished shortly out levels among other harmful impacts. The impacts of DG on the insurance additionally depend on the sort of DG source utilized. The simultaneous generator can continue higher deficiency current for longer time frames while the deficiency current created by an acceptance generator rots quickly. Converter-interfaced DG sources have short-circuited current creating abilities restricted to roughly 2—multiple times their appraised current.

2 Proposed Objectives

(a) To design using MATLAB a functional microgrid, powered by solar and wind power,
(b) To transform a standard IEEE 33 bus system into a microgrid and run load flow analysis,
(c) To integrate into the microgrid, equations for reduction of losses and emission reduction.

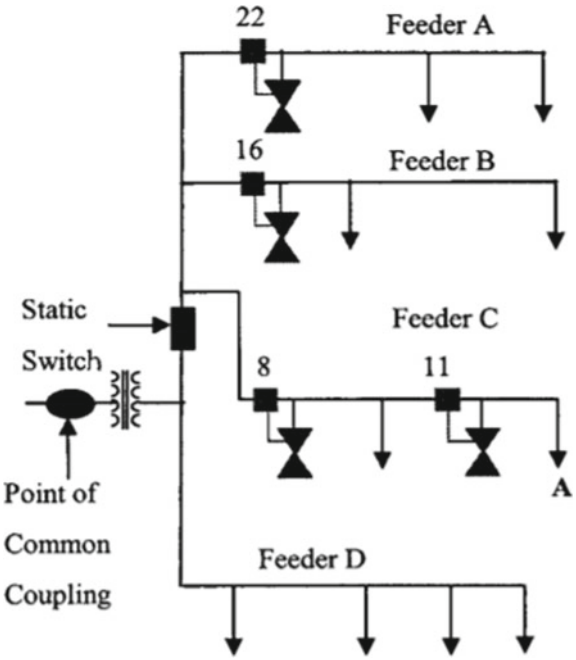

Fig. 1 Basic layout of Microgrid

3 Mathematical Design of Distributed Generators

3.1 System Architecture Modeling and Simulation

The two DG frameworks are connected in AC settings. Separately, every DG produces its own excellent AC power. The DG units are then associated together to shape a neighborhood AC miniaturized scale framework.

This is a secluded structure is shown in Fig. 1 Pretty much DG units could be added to fulfill the nearby need. The interest is constantly provided through the built smaller scale lattice. Such design needs subordinate help, especially VAR prerequisites. Exact coordination between the DG units is basic for the coherence of the force stream into the network. Force trade with existing utility is conceivable. In the following subsections, the mathematical modeling of the micro grid's DG systems is presented.

3.2 Photovoltaic (PV) System Mathematical Modeling

In the glassy silicon PV module of Fig. 2, the intricate material science of the PV cell can be spoken to through the comparable electrical circuit that appeared in the diagram. For the given specific comparable circuit, many conditions have already

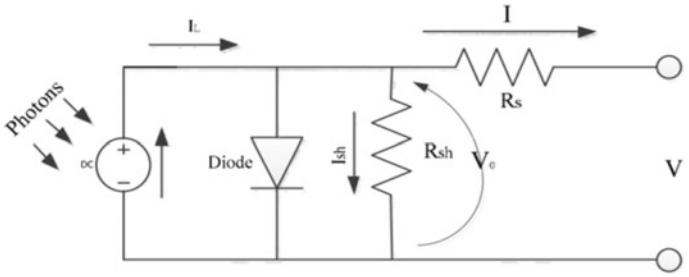

Fig. 2 Equivalent electrical circuit of a PV module

Table 1 Parameters and specifications of solar panel used

Parameters used	Value
Short circuit current	3.92 A
Open circuit voltage (at 25C)	0.585 V
Maximum power (at 25C)	60 W

been inferred, in light of standard hypothesis which permits the activity of one sun oriented cell which was to be recreated utilizing information from producers or field tests. The proportional circuit of the diagram, the present conveyed to the outer weight approaches the present I_l produced by the light, lessen the semiconductor diode current Id as well as the ground thrust present I_{sh}.

The expression is given by:

$$I = I_l - I_d - V_o/R_{\text{sh}} \tag{1}$$

The cell can be represented by a voltage current formula as follows:

$$V = V_o - R_s I \tag{2}$$

$Vo =$ Voltage on the semiconductor diode and the thrust struggle (V);
$I_d =$ DiodeCurrent(A), $V =$ Cell yield voltage (V),
$I =$ Weight (cell) output current (A), $I_L =$ Photocurrent(A) (Table 1);

3.3 Modeling of Wind Turbine

The FSWECS is separated into two sections; the electrical part speaking to the acceptance generator, and the mechanical part speaking to the breeze turbine activity. The electrical portion of the machine is spoken to by a fourth-request state-space model and the mechanical part by a second-request framework. Every single electrical variable and parameter has alluded to the stator. This is demonstrated by the prime

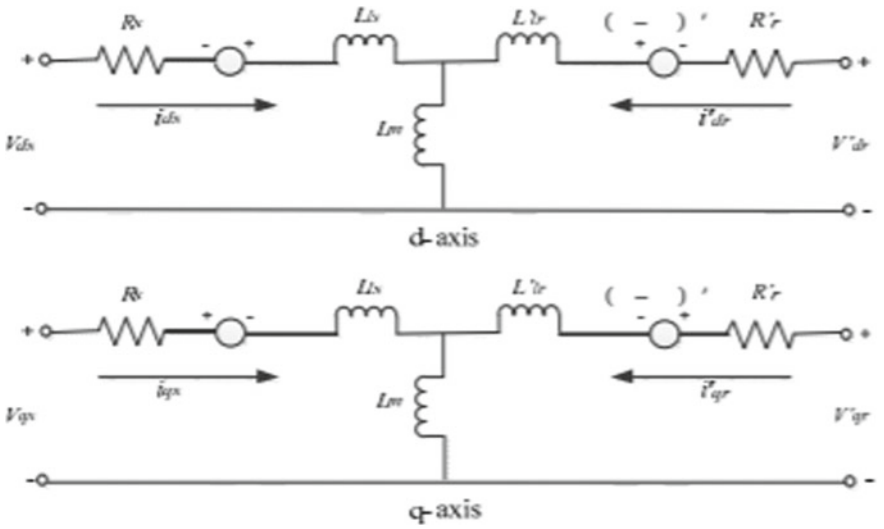

Fig. 3 Induction generator dq equivalent circuit referred to the stator

signs in the machine conditions given underneath. All stator and rotor amounts in the subjective two-hub reference outline (dq-outline) have appeared and are shown in the following Fig. 3.

The electrical mathematical model of the presented circuits from the above Fig. 3 is as follows and given as per the satisfying conditions (Table 2):

$$V_{qs} = R_s i_{qs} + d\varphi_{qs}/dt + \omega\varphi_{ds} \tag{3}$$

$$V_{ds} = R_s i_{ds} + d\varphi ds/dt - \omega\varphi_{qs} \tag{4}$$

Table 2 Parameters and specifications used

Parameters used	Specific value
Rotor diameter	6 m
Rated output	5KW
Cut in speed	4 m/s
Rated wind velocity	15 m/s
Cut out velocity	37 m/s

4 Problem Formulation

Consideration ought to stay assumed to fixing and measuring distributed generator assets when arranging a dissemination framework as well as its effect. The improper area and scope of DG can bring about high genuine force misfortune as well as diminished dependability. It isn't prudent to introduce exceptionally high-limit DG in the system. In choosing the ideal size of DG for least framework misfortune, the system design and the heaps on the conveyance framework assume a significant job. So as to satisfy the previously mentioned objectives, the issue is planned to meet two targets. In the first place, to choose a proper area at which the framework misfortune gets least; second, to register the ideal DG size for least framework misfortune. We will be using an IEEE 33 bus Radial Distribution system to perform the tests.

4.1 Selection of Location

The ideal amount of areas is the amount of transports that give the greatest advantages (reserve funds) for ideal size DGs set at chosen areas. The adjustment in a functioning control loss of the organization because of the adjustment in dynamic power infusion at a hub is communicated as:

$$\partial P_L / \partial P_i = 2\left(\sum_{j=1}^{n} \alpha_{ij} P_i - \beta_{ij} Q_i\right) \tag{5}$$

$$P_L = \sum_{i=1}^{n}\sum_{j=1}^{n} \alpha_{ij}\left(P_i P_j + Q_i Q_j\right) + \beta_{ij}\left(Q_i P_j - P_i Q_j\right) \tag{6}$$

$$\text{To maximize, } \mathrm{F} = C_e P_L^{\text{without}} - \left(\sum_{k=1}^{LN} Ce P_{\mathrm{LK}} T_k + \sum_{i}^{\mathrm{Ng}} C_{\mathrm{dg}} \mathrm{P}_{\mathrm{DGi}}\right) \tag{7}$$

$$V_i^{\min} \le V_i \le V_i^{\max}, \tag{8}$$

$$\left|I_{ij}\right| \le \left|I_{ij}\right|_{\text{sheduled}} \tag{9}$$

At lowest possible losses, energy lessening cost and fixing, procedure, and preservation costs of DGs are used for assessment of investments.

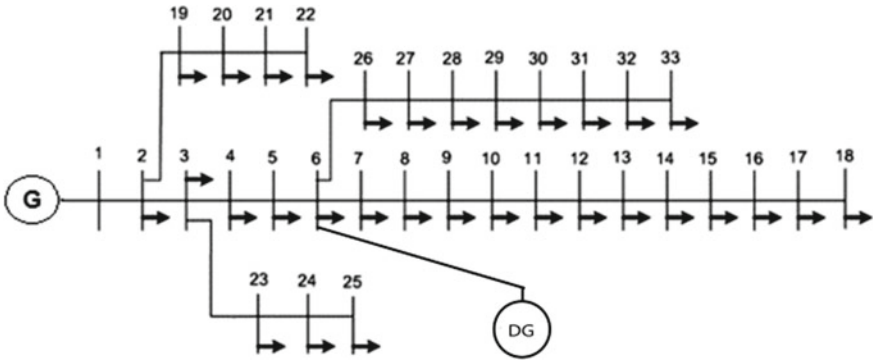

Fig. 4 Position of Dg In 33 bus radial distribution system after placement of Dg

4.2 Optimal Sizing of Distributed Generators Using Genetic Algorithm

The GA recreates the organic procedures that permit sequential ages trendy a populace to adjust to their condition. GAs are unrestrained enhancement techniques that are typical the developmental adjustment in nature. The benefits of utilizing GAs are that they want no evidence on angle data around the reaction superficial, they are impervious to getting caught in neighborhood goals, and they could be utilized for a varied assortment of enhancement issues (Fig. 4).

4.3 Genetic Algorithm Implementation

Step 1: Decide competitor areas. Position the buses in downward order of their PLS, and choose the bus with maximum PLS after running the load flow algorithm to calculate the entire actual control loss and loss compassion factors of different buses.
Step 2: Input GA control parameter data.
Step 3: Initialize population with random strings and copy into mating pool.
Step 4: Do while generation number is not exactly the most extreme number of generations picked. Do while populace number is not as much as populace size.
Step 5: Get key for ideal DG extent, least system damage, and reserves.
Step 6: Recurrence Step 1 to Step 5 with DG at the bus found former.
Step 7: Quit.

4.4 After Placement of Dg

The proposed methodology is tested on two widely used 33-bus–32- branches at different loading conditions. The active power (sum of total connected load and base system losses) at the source node at the beginning of the period is about 3936 kW. The base case loss sensitivity results of the six most sensitive buses arranged in descending order are shown in the following Table 3.

As bus 6, is the most sensitive node, it is selected as the candidate location for DG placement in the 33-bus system. The optimal DG size of 2380 kW was obtained by the above mentioned method. A distributed generator combining the solar and wind output was brought to 2380 kW. A combination of solar panels and wind turbines gave us the output required to be integrated. On integration of said output at bus 6, the power loss was found to be 132.64 kW. The power loss was reduced from 216 kW to 132.64 which is a reduction of 83.36 kW.

5 Energy Output of the Matlab Code

In the Fig. 5. we have obtained two graphs, namely the I-V characteristics graph and the PV characteristics graph for solar energy power at an ideal temperature of 25 °C. From the I-V graph, we can say that at 3.9 Amperes when there was an ideal temperature of 25 °C the voltage obtained was approximately around 22 V. When different temperature data were fit into the system then at the same current of 3.9 A the different data corresponding to the different temperatures showed a gradual and drastic decrease in the amount of voltage that was generated.

From this graph, we can conclude that the maximum voltage for solar power was obtained at 25C when the current was around 3.9 Amperes and for the rest of the data is kept on decreasing gradually as obtained. From the PV graph we can say that the maximum power of 60 Watts was obtained at around 18 V approximately and then as the voltage increased, the power decreased gradually to zero. The maximum power output was obtained for 25C, whereas for other data corresponding to the required temperatures we got less power outputs and there was a gradual decrease of power as the voltage increased as shown.

Table 3 Sensitivity values

Systems bus no	Sensitivity values
6	0.06779
2	0.0670792
5	0.0664193
20	0.0573545
8	0.0537697
7	0.0476795

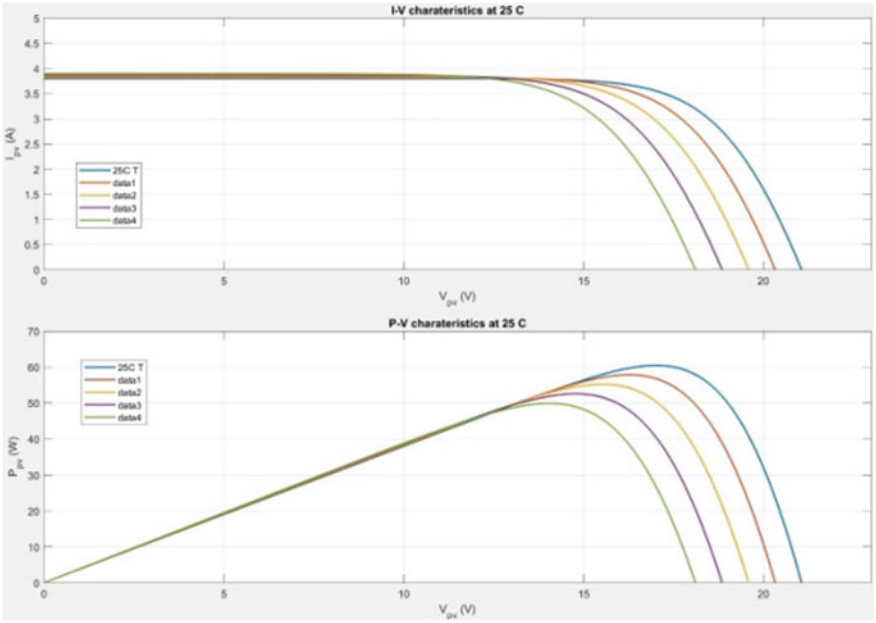

Fig. 5 Output of the code representing solar energy power

5.1 Wind Turbine Output of the Matlab Code

The above obtained graph Fig. 6 is a Power (kW) vs Speed (ms) graph where the pink line represents the power in an ideal wind machine whereas the light blue line represents the typical characteristics of a wind generator. The respective starting points are called cut in wind while the end points are called as cut out wind speed points. For both the cases as we can see the cut in wind speed is 0 m/s while the cut out wind speed for ideal case is 40 m/s and that for the typical case is around 37 m/s approximately. The rated wind speed is between 20—30 m/s. For the ideal case, the maximum power obtained is 55,000 Watts and that for the typical wind machine case it is coming around to be 4000 Watts. In both cases, after reaching the maximum power output the graph flattens as shown and then after a particular point they start decreasing to their respective cut out wind speeds as shown. The area under the blue line is called idealized power output. The area between the pink and the blue line is the area of inefficiencies.

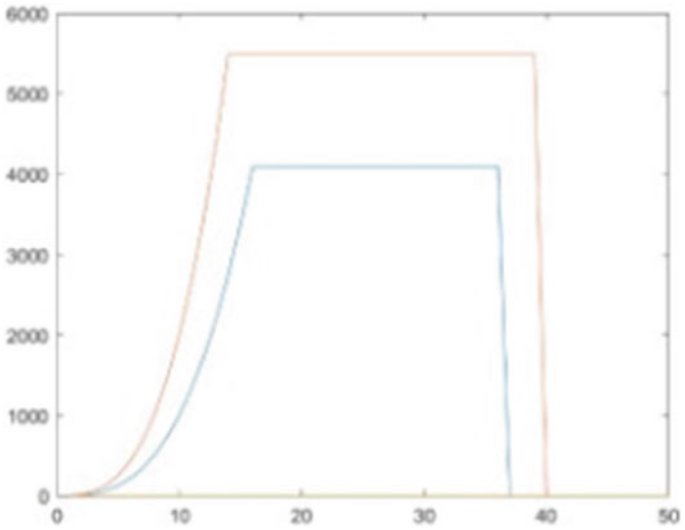

Fig. 6 Output of the code representing wind energy power

6 Conclusion

In this paper, we aimed to reduce the costs and emissions of a microgrid by using intensive programming techniques. As node 6, is the most sensitive bus, it is chosen as the optimal area for DG arrangement in the 33-transport RDS. The ideal DG size of 2380 kW was acquired by the previously mentioned technique. A disseminated generator joining the sunlight based and wind yield was brought to 2380 kW. A blend of sunlight based boards and wind turbines gave us the yield required to be incorporated. On the coordination of said yield at transport 6, the power misfortune was seen as 132.64 kW. The power misfortune was diminished from 216 kW to 132.64 which is a decrease of 83.36 kW. This spares energy and along these lines energy cost is advanced. As we have utilized the ideal size of DG we have utilized sustainable assets to the most extreme potential in the microgrid. In this manner, emanation costs have likewise been advanced. If we assume 83.36 kW of energy is saved per hour per day, by integrating DGs into the microgrid and the cost of one unit is Rs. 5/unit

$$\text{Energy consumed in one day} = 83.36 * 24 = 2000.64 \text{ kWh}$$

$$\text{Energy consumed in a year } = 2000.64 * 365 = 7, 30, 233.6 \text{ kWh}$$

$$\text{Cost of 7,30,233.6kWh} = 5 * 7, 30, 233.6 = 36.5 \text{ Lakhs}$$

References

1. Hung DQ, Mithulananthan N, Bansal RC (2013) Multiple distributed generators placement in primary distribution networks for loss reduction. IEEE Trans Ind Electr
2. Kutaiba S, El-Bidairia, Nguyena HD, Jayasinghe SDG, Mahmoud TSB, Penesis I (2005) A hybrid energy management and battery size optimization for standalone microgrids: a case study for Flinders Island, Australia. IEEE Trans Power Syst 20:856–791
3. Ackermann T, Anderson G, Soder L (2001) Distributed generation: definition. Elect Power Syst Res. 57(3):195–204
4. Jóos G, McGillis BT, Ga D, Liana FD, Marceau R (2000) The potential of distributed generation to provide ancillary services. In: Proceedings of the IEEE power engineering society summer meeting, seattle. WA
5. Hoff T, Wenger HJ, Farmer BK (1995) The value of grid-support photovoltaic in providing distribution system voltage support. In: Clean power research conference. Napa, CA, 1995.
6. Rau NS, Wan YH (1994) Optimum location of resources in distributed planning. IEEE Trans Power Syst 9(4):2014–2020
7. El-Khattam W, Hegazy YG, Salama MMA (2006) Investigating distributed generation systems performance using Monte Carlo simulation. IEEE Trans Power Syst 21(2):524–532
8. Wang C, Nehrir MH (2004) Analytical approaches for optimal placement of distributed generation sources in power systems. IEEE Trans Power Syst 19:2068–2076
9. Naik SNG, Khatod DK, Sharma MP (2015) Analytical approach for optimal siting and sizing of distributed generation in radial distribution networks. IET Gener, Trans Distrib
10. Shukla TN, Singh SP, Srinivas Rao V, Naik KB (2010) Optimal sizing of distributed generation placed on radial distribution systems. Electr Power Comp Syst
11. Shaaban MF, Atwa YM, El-Saadany EF (2013) DG Allocation for benefit maximization in distribution networks. IEEE Trans Power Syst

Improvement of Voltage Stability in Micro Grid System Using Hybrid Power Flow Controller

R. Suganya and M. Anitha

Abstract Hybrid Power Flow Controller (HPFC) discovers habitation amongst weak buses in multi-bus systems to condense the properties of voltage sag. This effort deals with power quality improvement of Four Bus System (FBS) using HPFC. This effort mainly deals with the simulation of FBS with and without HPFC (Hybrid Power Flow Controller). The outcomes are assessed in terms of real power, reactive power, and voltage. The simulation consequences characterize the aptitude of the HPFC in enlightening the power quality.

Keywords Hybrid Power Flow Controller (HPFC) · FACTS controller · Unified Power Flow Controller (UPFC) · Four Bus System (FBS) · Transient stability

1 Introduction

Simulation readings for HPFC-based controller for SMIB system were presented by Swati Bhasin [1]. This effort covered the reviews of HPFC for developing the accomplishment of power system. Here we used one topology of HPFC which results in by- 2VSC's in shunt and series passive component between the tie-lines.

Optimal placement of UPFC and HPFC using optimization technique was presented by Anjali Atul Bhandakkar [2]. Optimal placement of UPFC and HPFC was obtained using Genetic Algorithm (GA) based approach. A power flow model of UPFC and HPFC was developed using constraint equations and objective functions.

A hybrid power flow controller for flexible operation of multi-terminal DC grids was presented by Kumars Rouzbehi [3]. The idea for proposing HPFC was inspired by the successful operation of FACTS devices, the FACTS includes static power electronics-based elements to provide voltage regulation, power control, and load flow control in the multi-terminal DC (MTDC) grids.

R. Suganya · M. Anitha
Department of Electrical Engineering, Annamalai University, Chidambaram, India

R. Suganya (✉)
Department of Electrical and Electronics Engineering, IFET College of Engineering, Villupuram, India

C. Subramani et al. (eds.), *Proceedings of International Conference on Power Electronics and Renewable Energy Systems*, Lecture Notes in Electrical Engineering 795,
https://doi.org/10.1007/978-981-16-4943-1_42

Displaying and use of HPFC in distribution frameworks was introduced by Behnam Tamimi [4]. A nitty gritty unique model of the HPFC was created and actualized in PSCAD, portraying and proposing control techniques to appropriately work this regulator in dispersion framework applications, for example, a compelling and basic method for firing up the gadget.

Demonstrating and simulation of HPFC actualized on Multi-Machine framework was introduced by Lini Mathew [5]. Novel and financially savvy converter based FACTS geographies had been proposed which utilize probably existing aloof parts likewise and in this manner viewed as cross breed in nature. The distinctive HPFC setups concocted by the examiner had been actualized on a Multi-machine framework.

Commonsense utilization of the HPFC was introduced by Behnam Tamimi [6]. An outline of the HPFC and its controls was familiarized, and its solicitation to the Ontario-Canada network was examined. The outcomes indicated the achievability of utilizing this regulator for blockage alleviation in commonsense lattices, at lower costs than those of a UPFC.

HPFC consistent state demonstrating, control, and viable application was introduced by Behnam Tamimi [7]. A procedure for control mode exchanging and limit dealing with in power stream computations was proposed. The OPF model of the HPFC spoke to all the gadget control and actual cutoff points as limitations in the numerical definition, so the HPFC can be ideally dispatched as a piece of the transmission framework control resources.

Near Simulation reads for HPFC and UPFC based regulator for SMIB-framework was introduced by Swati Bhasin [8]. This exertion characterized the investigation of execution act of spontaneity in the force framework by looking at the HPFC and UPFC. Here we utilized 1topology of HPFC which was shaped by 2VSC's were associated in arrangement and SVC is associated in shunt through the tie-lines.

Demonstrating and simulation of HPFC actualized on SMIB framework was introduced by Lini Mathew [9]. Novel and financially savvy FACTS geographies had been proposed which were based on existing gear which utilized static converters. The diverse HPFC designs concocted by the examiner had been executed on a SMIB framework and mimicked utilizing MATLAB/SIMULINK.

Examination of HPFC utilizing static burden model under possibility screening was introduced by Sai Ram Seshapalli [10]. This exertion introduced a correlation of HPFC utilizing static burden displaying on the transmission framework. Burden stream was brought out on each chose strategy for the base case-load and pre-possibility conditions. The detailing of a question was set to be poorly adapted whenever assessed values were entirely helpless to minute changes in info conditions.

MATLAB/Simulink based simulation of an HPFC was introduced by Garima Aggarwal [11]. Here, HPFC model was planned utilizing programming and investigation of the force framework security upgrade by executing the HPFC in SMIB System power framework. The framework likewise had the arrangement of a similar investigation of the exhibitions of UPFC and HPFC with respect to control framework security improvement of the framework.

Transformer-less UPFC utilizing the course MLI was recommended by Liu. Consistent state models of the HPFC for power stream and OPF studies were introduced, considering the various control methods of the gadget. A system for control mode exchanging and limit dealing with in force stream estimations was proposed. The OPF model of the HPFC spoke to all the gadget control and actual cutoff points as requirements in the numerical detailing, with the goal that the HPFC can be ideally dispatched as a piece of the transmission framework control assets [12]

With the expanding significance of BESS in miniature frameworks, exact demonstrating assumes a vital part in understanding their conduct. This work researched and thought about the exhibition of BESS models with various profundities of detail. In particular, a few models were analyzed: a normal model spoke to by voltage sources.

2 Research Gap

The above literature does not deal with the comparison of performance of 4 bus-MG systems with and without HPFC. This work proposes HPFC to augment PQ in 4 bus microgrid system. The above exertions don't deal with voltage stability enhancement of 4 bus systems using FOPID/PR/SM controllers.

3 System Description

The single line-diagram of the 4 bus MGS with HPFC is revealed in Fig. 1. The HPFC is sited amongst buses 3 and 4. The Single line-diagram of the 4 bus MGS without HPFC is revealed in Fig. 2.

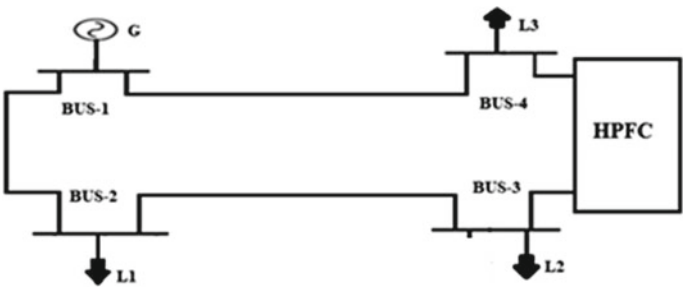

Fig. 1 Single line-diagram of the 4 bus MGS

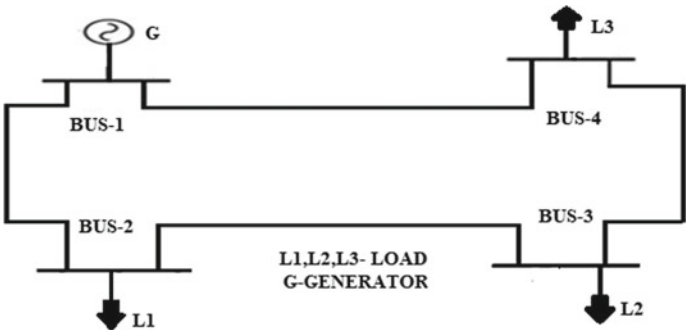

Fig. 2 Single line-diagram of the 4 bus MGS with HPFC without HPFC

4 Simulation Results

Figure 3 outlines the simulink diagram of 4 bus systems without HPFC. Figure 4 outlines the circuit model of 4 bus system. Figure 5 outlines the -Voltage at bus3 without HPFC and its significance is $0.75*10^4$ V. Figure 6 outlines the current at-bus-3 without HPFC and its significance is 70A. Figure 7 outlines the Real power at bus3 without HPFC and its significance is $2.3*10^5$ MW. Figure 8 outlines the reactive power at bus3 without HPFC and its significance is $5.6*10^4$ MVAR.

Figure 9 outlines the simulink diagram of 4 bus systems with HPFC. Figure 10 outlines the Circuit model of 4 bus system with HPFC. Figure 11 outlines the Voltage

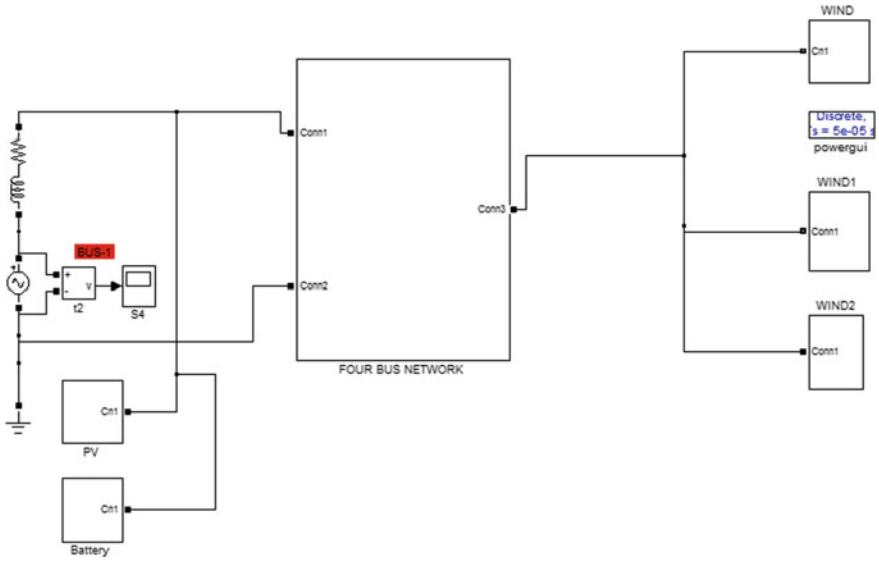

Fig. 3 Simulink diagram of 4 bus systems without HPFC

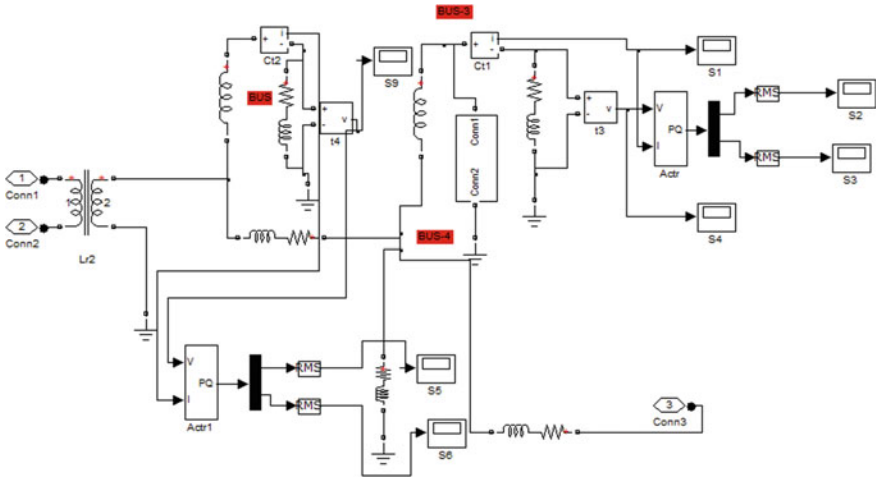

Fig. 4 Circuit model of 4 bus system

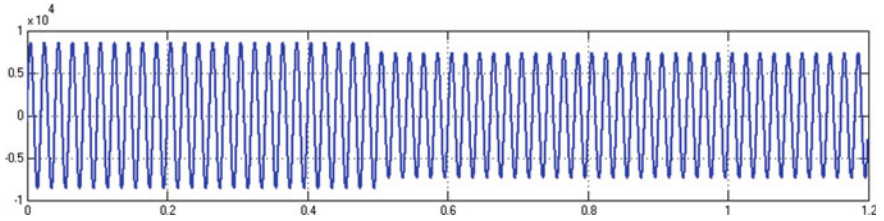

Fig. 5 -Voltage at-bus-3 without HPFC

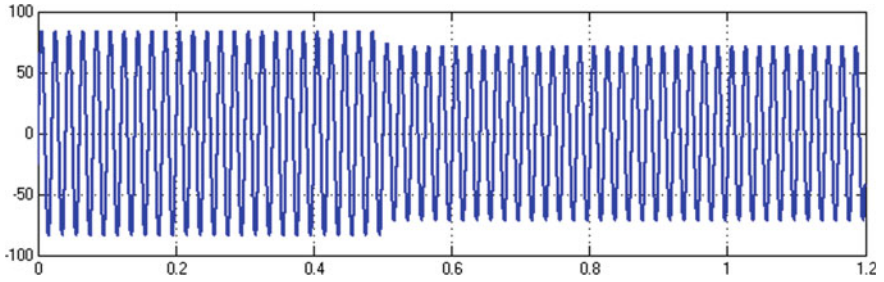

Fig. 6 -Current at-bus3 without HPFC

at bus3 without HPFC and its significance is $0.8*10^4$ V. Figure 12 outlines the Current at-bus-3 without HPFC and its significance is 80A. Figure 13outlines the Real power at bus3 without HPFC and its significance is $3.4*10^5$ MW. Figure 14 outlines the Reactive power at bus3 without HPFC and its significance is $7.9*10^4$ MVAR.

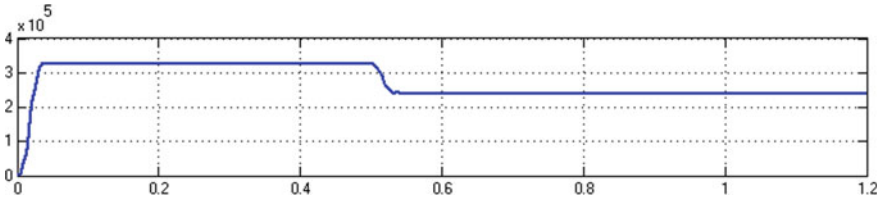

Fig. 7 Real power at-bus-3 without HPFC

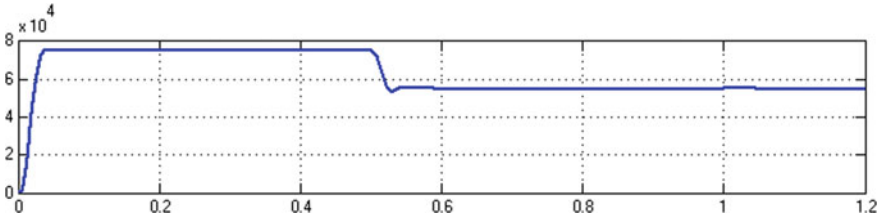

Fig. 8 Reactive-power at bus3 without HPFC

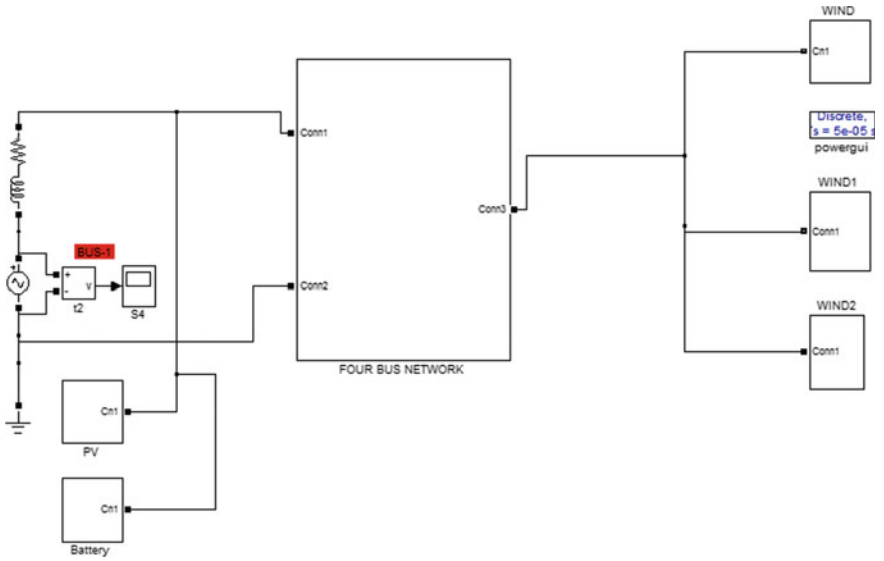

Fig. 9 Circuit diagram of 4 bus system with HPFC

Assessment of voltage, real power, and reactive power with and without HPFC is outlined in Table 1. By using HPFC, Real power is enhanced from 0.240 to 0.336 MW. Reactive power is enhanced from 0.055 MVAR to 0.076 MVAR; Voltage is enhanced from 7500 to 8700 V. Hence, the outcome represents that the 4 bus system with HPFC is superior to 4 bus system without HPFC.

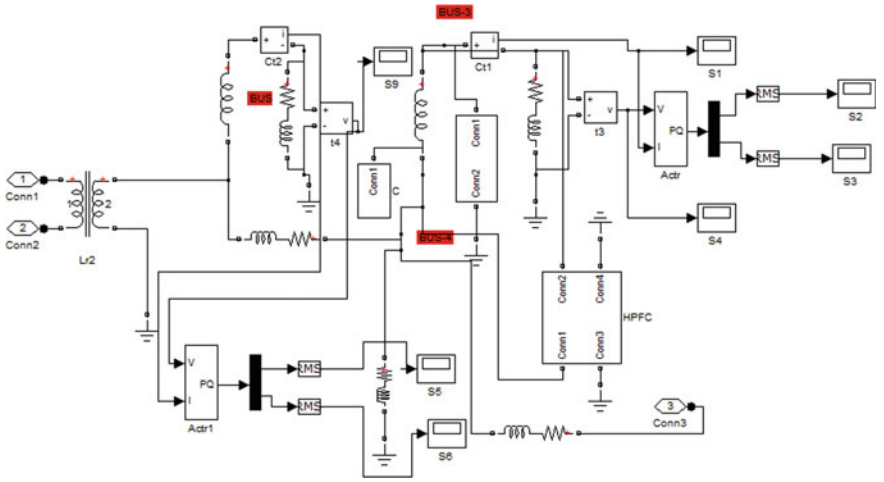

Fig. 10 Simulink diagram of 4 bus system with HPFC

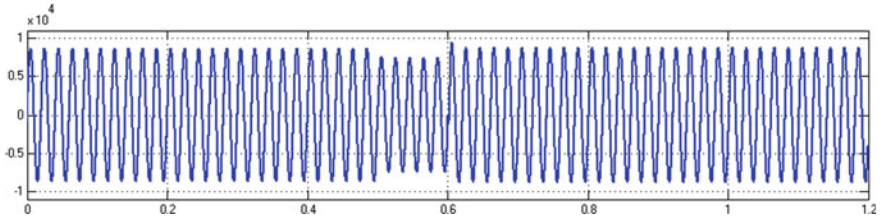

Fig. 11 Voltage at bus3 with HPFC

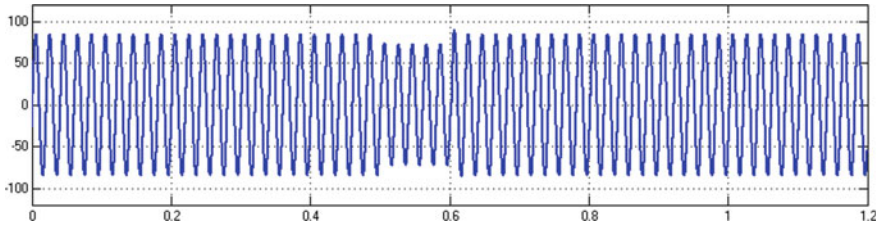

Fig. 12 Current at bus3 with HPFC

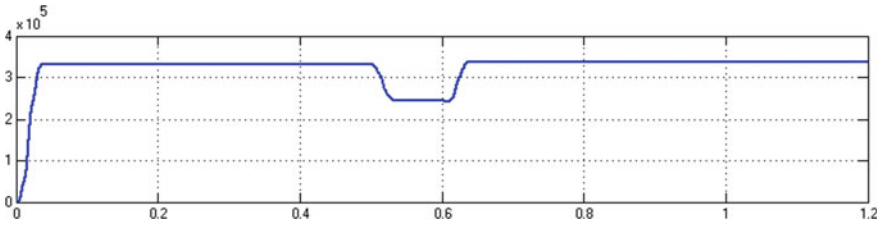

Fig. 13 Real power at bus3 with HPFC

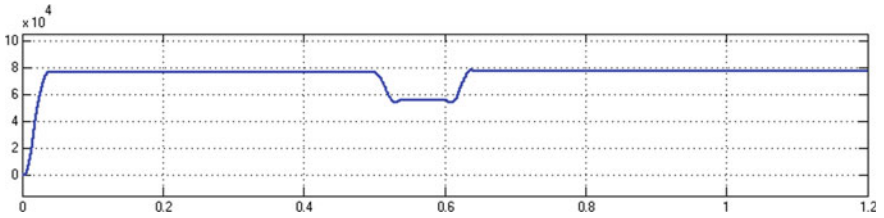

Fig. 14 Reactive power at bus3 with HPFC

Table 1 Assessment of voltage, real power, and reactive power with and without HPFC

Case	Voltage	Real power	Reactive power
Without HPFC	7500	0.240	0.055
With HPFC	8700	0.336	0.076

5 Conclusion

The 4 bus systems with and without HPFC (Hybrid Power Flow Controller) are modeled, analyzed, and simulated. The outcomes are assessed in terms of voltage, real power, and reactive power. By using HPFC, Real power is enhanced from 0.240 to 0.336 MW. Reactive power is enhanced from 0.055 to 0.076 MVAR. Voltage is enhanced from 7500 to 8700 V. Hence, the outcome represents that the 4 bus system with HPFC is superior to 4 bus system without HPFC. The present work deals with the simulation of four bus systems with and without HPFC. The closed loop HPFC 4 bus system with FOPI can be done in Future.

References

1. Bhasin S, Bhargava A, Chaudhary V, Verma S (2019) Simulation studies for hybrid power flow controller based controller for SMIB system. In: 2019–2nd international conference on power energy, environment and intelligent control (PE-EIC)
2. Bhandakkar AA, Mathew L (2018) Optimal placement of unified power flow controller and hybrid power flow controller using optimization technique. In: 2018 IEEE/IAS 54th industrial and commercial power systems technical conference (I&-CPS)
3. Rouzbehi K, Miranian A, Candela JI, Luna A, Rodriguez P (2014) A hybrid power flow controller for flexible operation of multi-terminal DC grids. In: 2014 international conference on renewable energy research and application (IC-RERA)
4. Tamimi B, Cañizares CA (2018) Modeling and application of hybrid power flow controller in distribution systems. IEEE Trans Power Delivery 33(6)
5. Mathew L, Chatterji S (2015) Modeling and simulation of hybrid power flow controller implemented on Multi-Machine system. In: 2015 2nd international conference on recent advances in engineering & computational sciences (RA-ECS).
6. Tamimi B, Cănizares C (2016) Practical application of the hybrid power flow controller. In: 2016 IEEE conference on power and energy society general meeting

7. Bhasin S, Bhargava A, Verma S, Chaudhary V (2019) Simulation studies for hybrid power flow controller and UPFC based controller for SMIB system. In: 2019 2nd international conference on power energy, environment and intelligent control (PE-EIC).
8. Mathew L, Chatterji S (2014) Modeling and simulation of hybrid power flow controller implemented on SMIB system. In: 2014 North American power symposium (N-APS). Year2014 |-ConferPaper
9. Seshapalli SR (2019) Analysis of hybrid power flow controller using Static load model under Contingency Screening. In: 2019 IEEE international conference on clean energy and energy efficient electronics circuit for sustainable development (IN-CCES)
10. Aggarwal G, Mathew L, Chatterji S (2014) MATLAB/-simulink based simulation of a hybrid power flow controller. In: 2014 fourth international conference on advanced computing & communication technologies
11. Peng FZ, Liu Y, Yang S, Zhang S, Gunasekaran D, Karki U (2016) Transformer-less unified power flow controller using the cascade multi-level inverter. IEEE Trans Power Electron 31(8):1077–1084
12. Tamimi CA, Canizares, Battistelli C (2017) Hybrid power flow controller steady state modeling control and practical application. IEEE Trans Power Syst 32(2):1483–1492

An Intelligent Fuzzy Controlled Microgrid Fed by Distribution Generation Sources

Md. Aijaz, T. Muthamizhan, and T. Venkateswarlu

Abstract In this paper, intelligent fuzzy based microgrid fed distribution generating sources are presented. Optimal power electronic converters (PEC) are employed to produce and control the performance of PV-wind power. Double fed IG is employed as wind generator to obtain maximum power wind. Peak power is absorbed from solar with help of proposed fuzzy MPPT algorithm. The simulation results for steady state variation of wind speed and dynamic behavior of load variations are presented. Real/reactive power energy management is managed efficiently with fuzzy control algorithm. The proposed fuzzy controller scheme provided improved performance results and solved power quality issues at load side**.**

Keywords Micro grid · Fuzzy controller · MPPT · PV-Wind system · DFIG

1 Introduction

For rapid growth of population providing electricity to the society is the biggest challenge in front of electrical engineering. Electricity is acts as a backbone to run any industry, so implementation of generations growing very fast in every ware. Now the absorption of power assets has multiplied, so efforts were made to production of power from RES sources that include wind, solar. Wind strength has emerged as certainly one of the most important and promising assets of renewable strength. This needs extra transmission capability and a better approach to preserving system reliability. Non-conventional energy sources (NCES) are greener and ecofriendly nature, Production of power throughout the year is possible. It doesn't need any fossil fuels to generate power. CES is hydro and thermal. In thermal power generation, raw material used is a fossil fuel is almost ended by next two decades. For hydro Power plants, the source is available seasonally so power generation is not throughout the year. These two power generations inject various fuel gases into the environment

Md. Aijaz · T. Venkateswarlu
Kodada Institute of Technology and Science for Women, Nalgonda, India

T. Muthamizhan (✉)
Sri Sai Ram Institute of Technology, Chennai, 44, India

C. Subramani et al. (eds.), *Proceedings of International Conference on Power Electronics and Renewable Energy Systems*, Lecture Notes in Electrical Engineering 795,
https://doi.org/10.1007/978-981-16-4943-1_43

and pollute the atmosphere. These problems are overcome by using RES, which is greener and ecofriendly nature, and power can be generated throughout the year.

In this paper a Hybrid PV-wind energy power generation with grid connected converters topology and various control schemes [1–3], to enhance the power quality is discussed. Basically, the presence of nonlinear loads always prohibits disturbances and uncertainties in the PS network [4, 5]. If these nonlinear loads are available longer time period in the PS network, it is very difficult to provide smooth power supply to the load. When power feeds to this nonlinear load (PEC converters, laptop/mobile chargers, etc.) it creates harmonics into the power system network, fault conditions, sudden insertion or removal of load also create disturbance [6, 7] in the power system network very severe extent. If duration these unstable issues are many that may lead to damage the load. The major objective of this article is (i) to implement more groups of hybrid power generating systems in various locations and all of them are connected to main AC bus/grid through Fuzzy decision-making control system, (ii) Enhance power quality and reliability with fuzzy control-based demand management systems to meet the desired power demand, (iii) Extract maximum power from solar [8, 9], wind and utilized with optimum pricing and (iv) Solve PQ issues of micro grid when it is fed with nonlinear loads.

2 System Configuration

The system configuration of isolated microgrid fed by RES sources is shown in Fig. 1. Different topologies are available to get maximum/lower power from PV [10–12] such as Ripple Correlation Technique (RCT), Perturb & Observe (P&O),

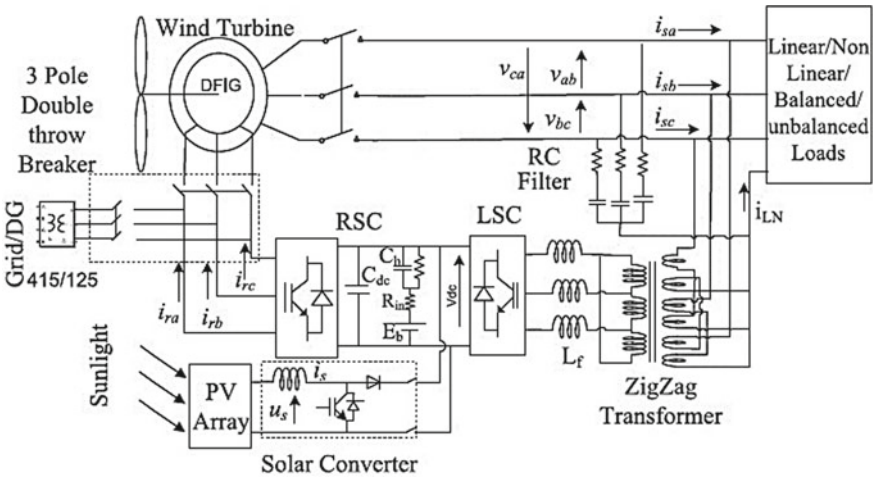

Fig. 1 Structure of microgrid fed by RES sources

and incremental conductance (IC). These techniques sense the amplitude of the load current and make changes in input current quickly. The main drawback of this MPPT technique is its transient response of variation in current is sluggish. This is overcome by fuzzy MPPT intelligent control algorithm. To maintain constant voltage across capacitor (Cdc) and maximum utility DC-DC converters are operated with fuzzy controller.

2.1 Design of PV Cell

Generally, the design of solar cell is characterized by a current source in shunt with a diode, and two resistors are connected anti parallel to each other. These resistors control the power generation of solar cells. To get desired output voltage and output current from PV panel, N number of PV panels are interfaced in series-parallel combinations, the voltage and current is expressed in terms of mathematically as given below

$$V_{\text{series}} = \sum_{j=1}^{n} + V_j = V_1 + V_2 + \cdots + V_n f \tag{1}$$

$$V_{\text{seriesoc}} = \sum_{j=1}^{n} V_j = V_{\text{oc1}} + V_{\text{oc2}} + \cdots + V_{\text{ocn}} + \text{for} I = 0 \tag{2}$$

$$I_{\text{parallel}} = \sum_{j=1}^{n} I_j = I_1 + I_2 + \cdots + I_n \tag{3}$$

$$V_{\text{parallel}} = V_1 = V_2 = \cdots = V_n \tag{4}$$

By default, we are placing the bypass diodes in solar panels to diminish the over voltages in the system. But it causes an increase in the system cost (Fig. 2).

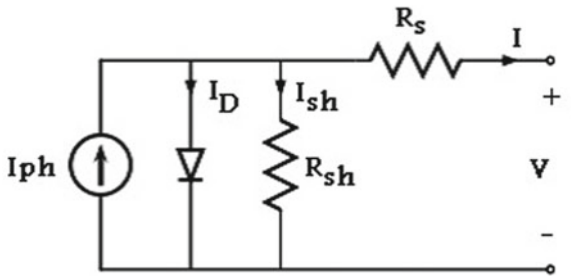

Fig. 2 Schematic diagram of a PV Cell

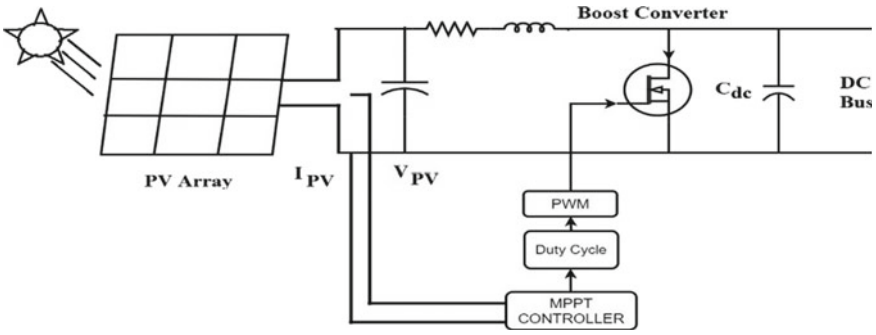

Fig. 3 Structure of fuzzy logic based boost converter

2.2 DC-DC Converters

In generally controlling and switching of series VSC converters by duty ratio this will expose for satisfactory performance, switches with some delay this causes stress on the switches as well as life time of the converters in dc-dc converter and getting the lower power from PV panels. Nowadays controlled switching pattern is done by fuzzy MPPT algorithm to extract the peak power from the PV module. Fuzzy based operated DC-DC converters provide This fuzzy based DC converter provides less oscillatory voltage to the series VSCs improves dynamic performance and overall efficiency of the PS network. The structure of fuzzy based DC-DC converter is shown in Fig. 3.

2.3 Modeling of DFIG Based WECS:

In WECS systems, Wind turbine (WT) converts the movement wind speed (kinetic energy) into mechanical energy, WT coupled With DFIG generator converts mechanical energy into electrical energy. Produced electrical energy from generators is transmitted to a power station (grid). Wind power is abundant in some states, with the largest wind farms located in Texas. Wind is unique because it carries incentives for farmers to give parcels of land for building wind turbines, and has the most potential as far as widespread adoption due to the large areas of land with consistent wind available to harness. The stator of the DFIG is directly associated with the grid or load, and rotor is connected to the VSC based converters via a slip rings. Power converters (A.C to D.C and D.C to A.C) are effectively control rotor speed and frequency of rotor. The rotor linked converter is compensating the torque ripple as well as compensating the reactive power. Rotor side converter and stator side converter are connected via dc link. It controls the real and reactive power of WECS system, by varying the terminal voltages of rotor circuit of DFIG. Hence it controls the power factor of whole WECS. The DFIG is a wound rotor induction generator

Table 1 Fuzzy ruleset

Error (e) Change in error (Δe)	NB	NS	Z	PS	PB
NB	NB	NB	NS	NS	Z
NS	NB	NS	NS	Z	PS
Z	NS	NS	Z	PS	PS
PS	NS	Z	PS	PS	PB
PB	Z	PS	PS	PB	PB

so it is simple and robust construction. Low cost compared to PMSG generator. This feature may leads higher advantages such as lower switching losses, harmonics inserted in grid are less, reduced power rating means is volume of power converters is less so it more economical and require filtering section also less. By controlling this dc link to enhance the converter performance, the dc link voltage may be done by considering handiest percent voltage. In V_{ab} is line voltage at CPI: m is modulation index is selected as 1 for linearity.

3 Control Scheme

Fuzzy based VSI controller implementation is similar to the fuzzy MPPT algorithm. In this error is treats as a set of fuzzy rules. These fuzzy sets are provide PI control parameters by selecting rules, shape of membership, and de-fuzzification. The fuzzy rules set mentioned in Table 1. The fuzzy logic rationale contrasts with both idea and substance from conventional multi = valve legitime frame works such as negative big (NB), negative small (NS), zero (Z), positive big (PB), and positive small (PS).

The actual value of voltage across (Vdcact) CPI point is in contrast with reference DC voltage (Vdc) that error is optimized with fuzzification then error is rectified send to the system after de-fuzzification. The structure DFIG control scheme is shown in Fig. 4.

4 Simulation Results

4.1 Performance of the System with Wind Energy Variation

A 10 KW and 5.5 KVAR constant load is considered as output solar providing fixed power and wind energy production is varying. Where wind at $t = 0.6$ s, the speed is 7 m/sec and at $t = 0.6$ s as to t=1 s WT speed is varied from 7 m/sec to 8 m/sec that observed in Fig. 5. WT power variations occurred in between 0.6 to 1 s. The variation of performance characteristics of simulation results is represented in Fig. 6,

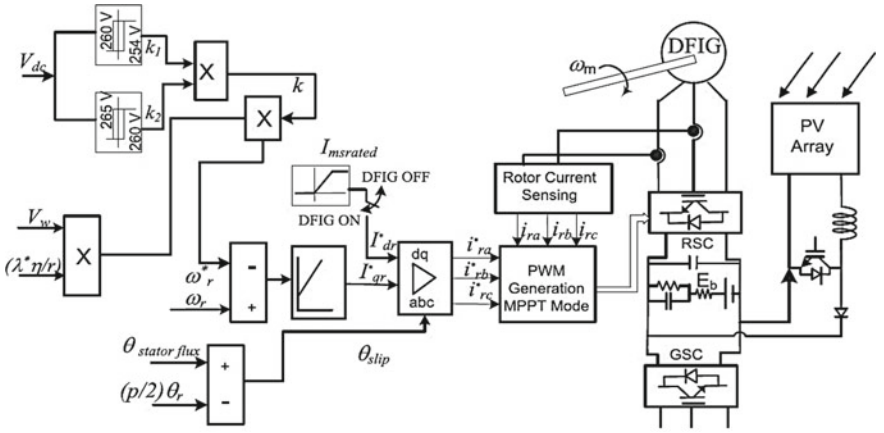

Fig. 4 Control scheme for DFIG connected to wind turbine

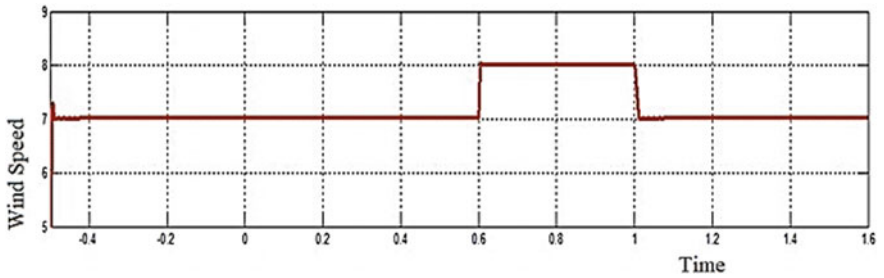

Fig. 5 Wind speed profile of the wind turbine

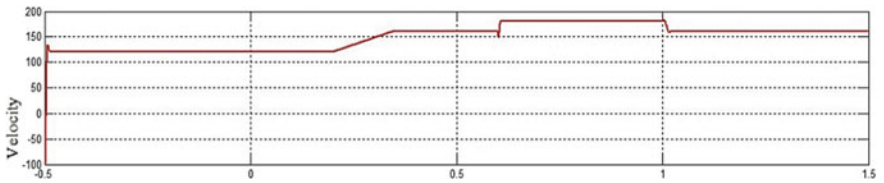

Fig. 6 Wind turbine velocity

7, 8 and 9 respectively. Those are WT velocity, performance of WT, load voltage, voltage across DC link capacitor, and load power.

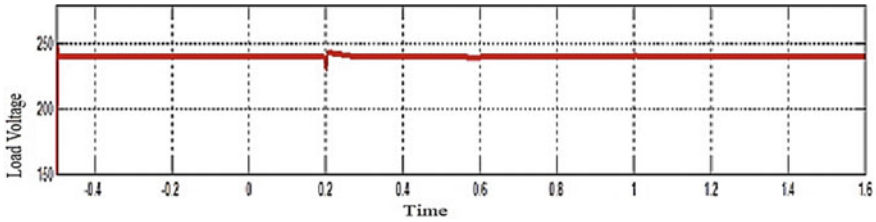

Fig. 7 Voltage generated by the DFIG

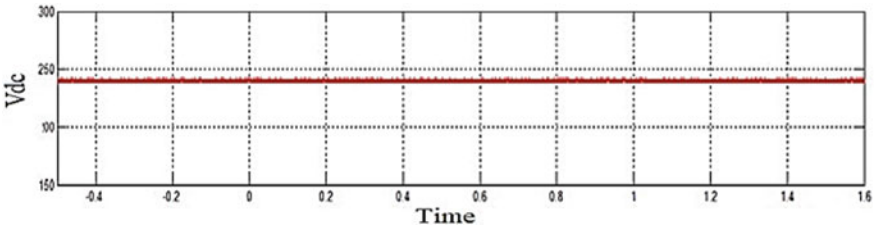

Fig. 8 Voltage available at the DC link

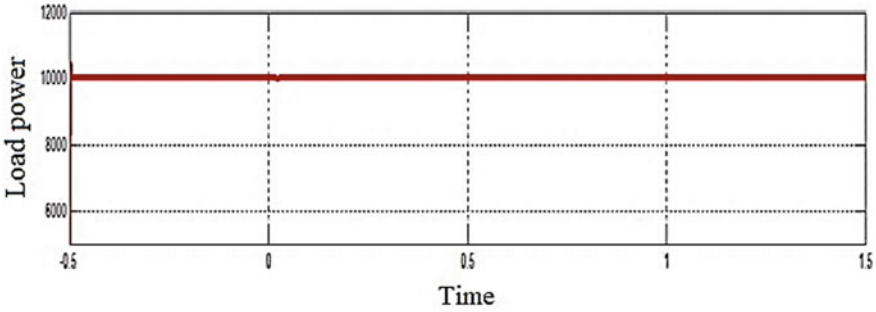

Fig. 9 Power measured at the load

4.2 Performance of the System with Solar Energy Variation

A 10 KW and 5.5 KVAR constant load is considered as where WE CS system providing fixed power and PV energy production is varying. Where At $t = 0.4$ s, the irradiance of PV cell is 0.8 Kw/m2, and at $t = 0.4$secas to $t = 0.6$secs irradiance is consider is 0.9 Kw/m2, illustrate in Fig. 10. The variation of performance characteristics simulation results is represented in Fig. 11, 12 and 13 respectively. Those are irradiance level, power production in PV array, load voltage, and load power.

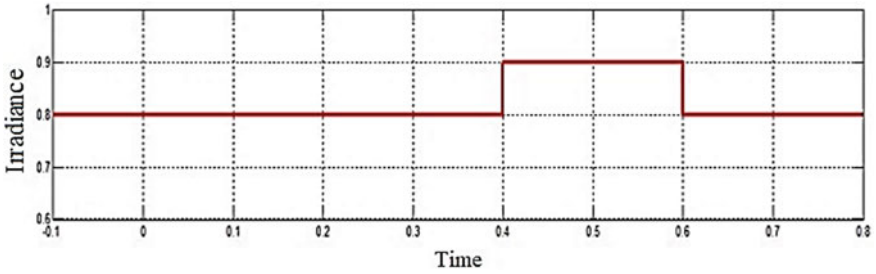

Fig. 10 Irradiance level to the PV array

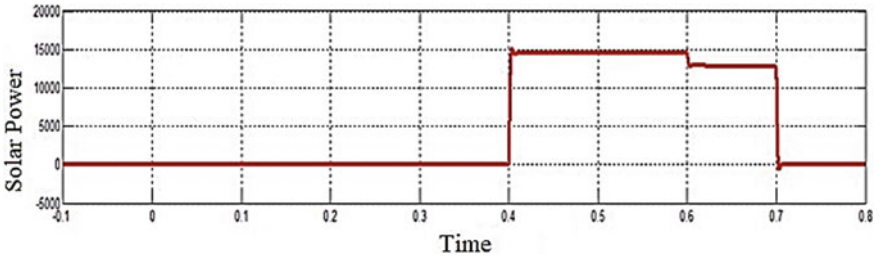

Fig. 11 Power generated using solar PV array

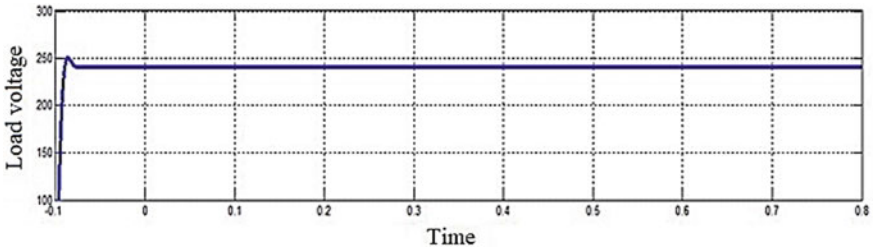

Fig. 12 Voltage available at the load

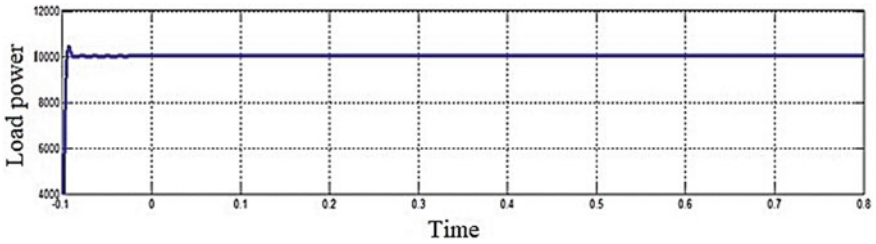

Fig. 13 Power available at the load

4.3 Performance of System with Unbalanced Loads

The performance characteristics of the PV—Wind battery based microgrid system with nonlinear loads is mentioned below Fig. 14, 15, 16, 17 and 18 respectively. Those are load voltage, unbalanced phase current (ABC), and load power. The connected load consists of 2 kW linear load and 8 kW nonlinear load. At $t = 3.25$ S, the load of a-phase is disconnected from the network followed by b-phase load at $t = 3.46$ S. Even unbalanced loads also by employing proposed technique energy management is done by solar and wind.

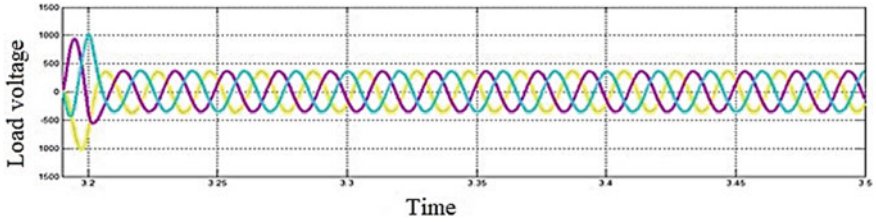

Fig. 14 Three phase load voltage (for unbalanced load condition)

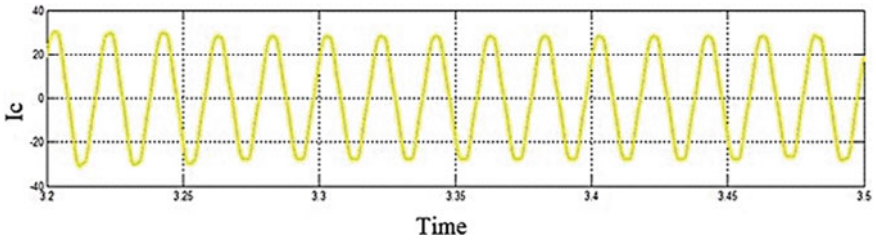

Fig. 15 Phase current-C (measured with unbalanced load condition)

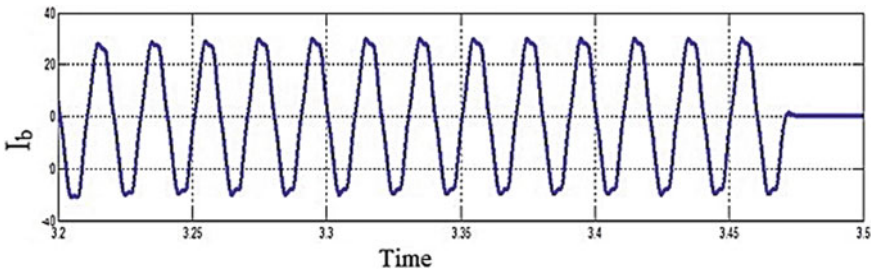

Fig. 16 Phase current-B (measured with unbalanced load condition)

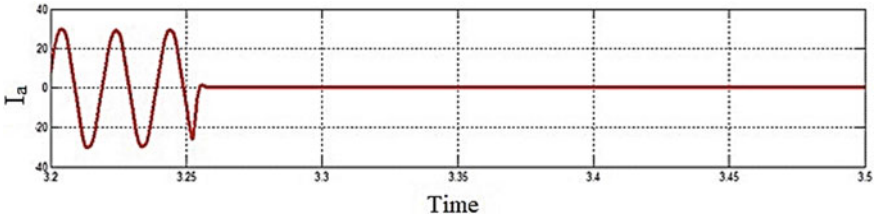

Fig. 17 Phase current-A (measured with unbalanced load condition)

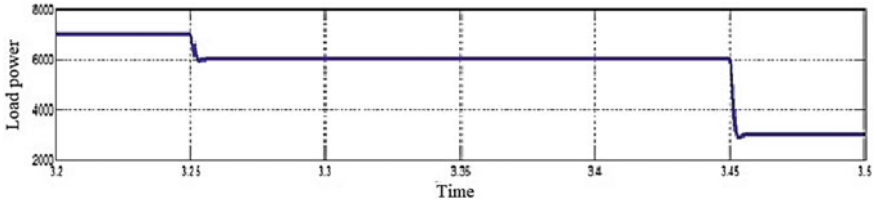

Fig. 18 Power measured at the load side (P_L)

5 Conclusion

The three phase PV-wind-battery integrated hybrid power generation with enhanced reliability and continuity power is modeled with fuzzy logic controllers. The simulation results are more evident that the proposed control schemes work well with less number of Power Electronic converters and optimal cost. Proposed fuzzy logic control scheme, proves best management of active and reactive power to load demand over conventional control approaches. Satisfied performance is obtained, when the microgrid is operated with constant load and solar/wind energy generation, and microgrid is connected to the nonlinear loads.

References

1. Muthamizhan T, Ramesh R (2014) Experimental investigations on PV powered SVM-DTC induction motor without AC phase current sensor. Int J Eng Technol 6(2):842–857
2. Basaran K, Cetin NS, Borekci S (2017) Energy management for on-grid and off-grid wind/PV and battery hybrid systems. IET Renew Power Gener 11(5):642–649
3. Chen YM, Cheng CS, Wu HC (2006) Grid-connected hybrid PV/wind power generation system with improved DC bus voltage regulation strategy. In: Twenty-first annual IEEE applied power electronics conference and exposition, 2006. APEC '06., Dallas, TX
4. IEEE guide for selecting, charging, testing, and evaluating lead-acid batteries used in stand-alone photovoltaic (PV) systems. IEEE P1361/D5, February 2014
5. Javed K, Ashfaq H, Singh R (2019)Application of supercapacitor as hybrid energy storage device in stand-alone PV system. In: International conference on power electronics, control and automation (ICPECA). New Delhi, India, pp 1–4

6. Mohanty S, Subudhi B, Ray PK (2016) A new MPPT design using grey wolf optimization technique for photovoltaic system under partial shading conditions. IEEE Trans Sustain Energy 7(1):181–188
7. Abinaya I, Sundarsingh Jebaseelan SD, Ravi CN (2016) Reactive power compensation in grid system using STATCOM with closed loop control. Indian J Sci Technol 9(6):1–4
8. Marlin S, Sundarsingh Jebaseelan SD, Padmanabhan B, Nagarajan G (2014) Power quality improvement for thirty bus system using UPFC and TCSC. Indian J Sci Technol 7(9):1316–1320
9. Muthamizhan T, Ramesh R (2014) PV powered fuzzy based direct torque controlled induction motor without AC phase current sensor. Int Rev Electr Eng 9(2):307–314
10. Kollimalla SK, Mishra MK, Narasamma NL (2014) Design and analysis of novel control strategy for battery and supercapacitor storage system. IEEE Trans Sustain Energy 5(4):1137–1144
11. Merabet A, Tawfique Ahmed K, Ibrahim H, Beguenane R, Ghias AMYM (2017) Energy management and control system for laboratory scale microgrid based wind-PV-battery. IEEE Trans Sustain Ener 8(1):145–154
12. Ramyar A, Iman-Eini H, Farhangi S (2017) Global maximum power point tracking method for photovoltaic arrays under partial shading conditions. IEEE Trans Ind Elect 64(4):2855–2864

Multiresolution Representation of SONAR Pipeline Image Using Pyramidal Transforms

R. Kumudham, P. Sathish Kumar, V. Rajendran, M. S. Jagan Mugesh, and U. Charan Raj

Abstract This research work is anxious with the issues of identification of objects placed on seabed captured on underwater sonar images. Image segmentation methods play a very important responsibility in partitioning dividing the image into segments. In this paper, we are applying watershed segmentation algorithm for detecting pipelines in underwater seabed using sonar images. Initially, we applied Gaussian and Laplacian pyramid for image resolution enhancement, fixing threshold automatically using Otsu threshold determination. Also, morphological operations were performed for identifying the foreground and background of the image. Followed by that for marking the regions on the image, we used watershed segmentation algorithm to detect the pipeline in underwater acoustic images.

Keywords Image processing · Gaussian pyramid · Laplacian pyramid · Otsu threshold · Watershed algorithm

1 Introduction

Side Scan sonar image analysis is utilized in several underwater applications, including object localization and also object identification to seabed categorization and 3-D reconstruction. There are two main approaches in side scan image analysis: categorization using consistency features and supervised learning and unsupervised classification and segmentation. Many of the researchers analyzed object detection in underwater sea and classifying objects into rocks or mines specifies that rocks are abnormal whereas mines are normal. But the proposed work insists that identifying pipelines [1, 2] which is buried in underwater sea level that has to be taken out and replaced by some others pipeline if any cracks or damages were available. The main objective of this work is

R. Kumudham (✉) · P. Sathish Kumar · V. Rajendran · M. S. Jagan Mugesh · U. Charan Raj
Vels Institute of Science, Technology & Advanced Studies (VISTAS), Chennai, India
e-mail: kumudham.se@velsuniv.ac.in

P. Sathish Kumar
e-mail: sathish.se@velsuniv.ac.in

C. Subramani et al. (eds.), *Proceedings of International Conference on Power Electronics and Renewable Energy Systems*, Lecture Notes in Electrical Engineering 795,
https://doi.org/10.1007/978-981-16-4943-1_44

- To gather sonar underwater images from specified sources.
- To find the Gaussian pyramid and Laplacian pyramid for image resolution enhancement.
- To perform Otsu threshold determination method that fixes the threshold value automatically to detect the regions of sonar images.
- To apply segmentation technique [3, 4] namely, watershed algorithm partitions the images into foreground and background portions to mark the regions of sonar images.
- To detect the pipeline in underwater acoustics using sonar images.

Anastasios Stamoulakatos et al. [1] presented an automatic image marginal note construction that classifies key events of interest on video footage. Here, the investigator applied transfer learning with Deep Convolutional Neural Network (ResNet-50), fine-tuned on real-life data from challenging sub-sea environment, with low lighting conditions, sea-life, vegetation, and sand agitation. The CNN is configured to execute multi-label image classifications for critical events. The marginal note performance fluctuates between 95.1 and 99.7% by means of accuracy as 90.4 and 99.4% for F1-Score depending on types of events. Synthetic Aperture Sonar segmentation method by Imen Mandhouj et al. [5] is based on statistical attributes of the sonar images, decorated by the Mean-Standard deviation (MSD) plane. This segmentation method is automated by using an entropy criterion by Maussang et al. [6]. Huo et al. [7] found that categorization of objects in underwater on side scan sonar images using deep learning based transfer algorithm. Here several CNN models were tried for better performance in finding objects as well as perform classification too.

2 Methodology

In this section, our research work describes how we are segmenting the sonar images as pipeline using image processing techniques. The proposed workflow is mentioned in Fig. 1.

2.1 Image Acquisition

The sonar images were collected from some specified resources as Indomer coastal hydraulics ltd and Edgetech websites to detect the pipeline in underwater submarine system. From those images, we used only two images to perform pipeline identification using image processing techniques. Initially, we have taken the images with size along with their dimensions as (1131, 693).

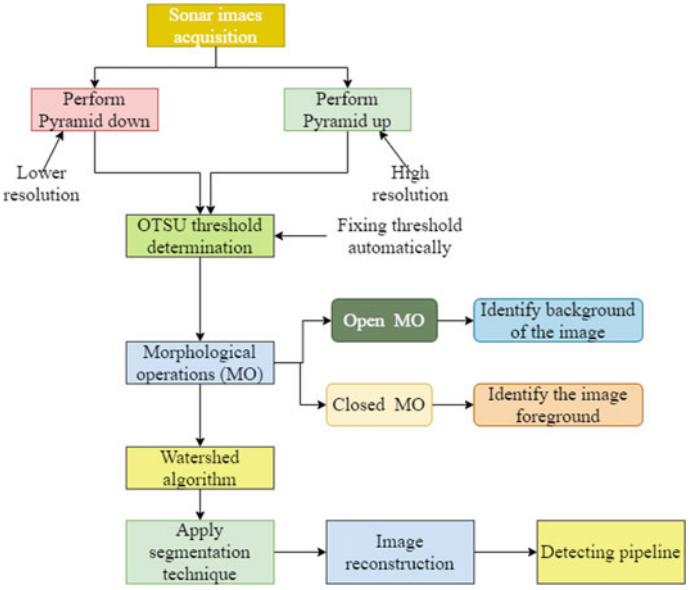

Fig. 1 Proposed framework for pipeline detection

2.2 Pyramid Technique

Then we apply pyramid technique which is a kind of multi scale signal representation enlarged by image processing as well as signal processing society in that the images are repeatedly smoothening and sub-sampling. This representation mainly focused on two categories namely down sampling of images and pyramid up especially to enhance the images for high resolution.

2.2.1 Down Sampling

The down sampling is otherwise called Pyramid down in which the succession of low-pass, down-sampled images, $[l_0, l_1 \ldots l_N]$. Typically assemble with a discrete 1 dimensional kernel $h = [h1; h2; h3; h4; h5]$, (Fig. 2) and a down sampling feature of two.

The main impetuses of image pyramids are redundancy diminution as well as image modeling for

- Efficient and effective coding.
- Image enhancement/restoration.
- Image analysis/synthesis.

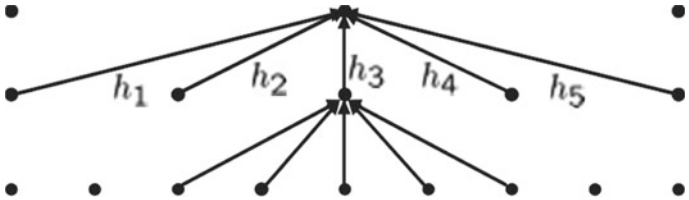

Fig. 2 Representation of features as down sampling

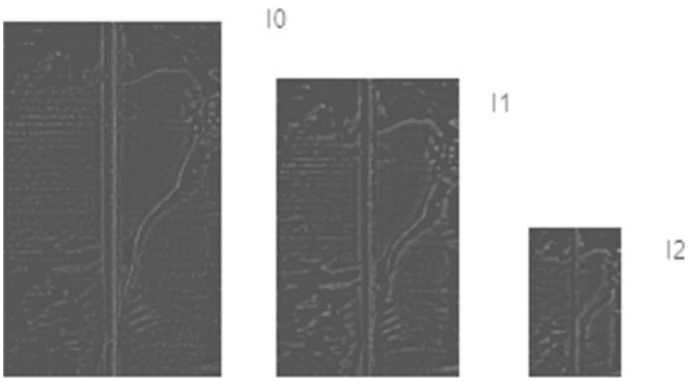

Fig. 3 Level of Gaussian pyramid represented as down sample procedure

The sonar images were sampled using down sampling procedure with three iterations for enhancing the property of the image. The levels of Gaussian pyramid expanded to the size of the original image as shown in Fig. 3.

2.2.2 Up Sampling

Similar to down sampling procedure, here the images are decomposing into low pass as well as high pass bands recursively. Each band of the Laplacian pyramid is the divergence among 2-adjacent low-pass images of Gaussian pyramid, $[I_0, I_1, \ldots I_N]$.

The constructions of Laplacian pyramid along with two levels are illustrated in Fig. 4.

The Laplacian pyramid with two levels is shown in Fig. 5.

2.3 OTSU Threshold Determination

Otsu is an automatic threshold selection region based segmentation method applied on images. This approach is a form of global thresholding which depends only on

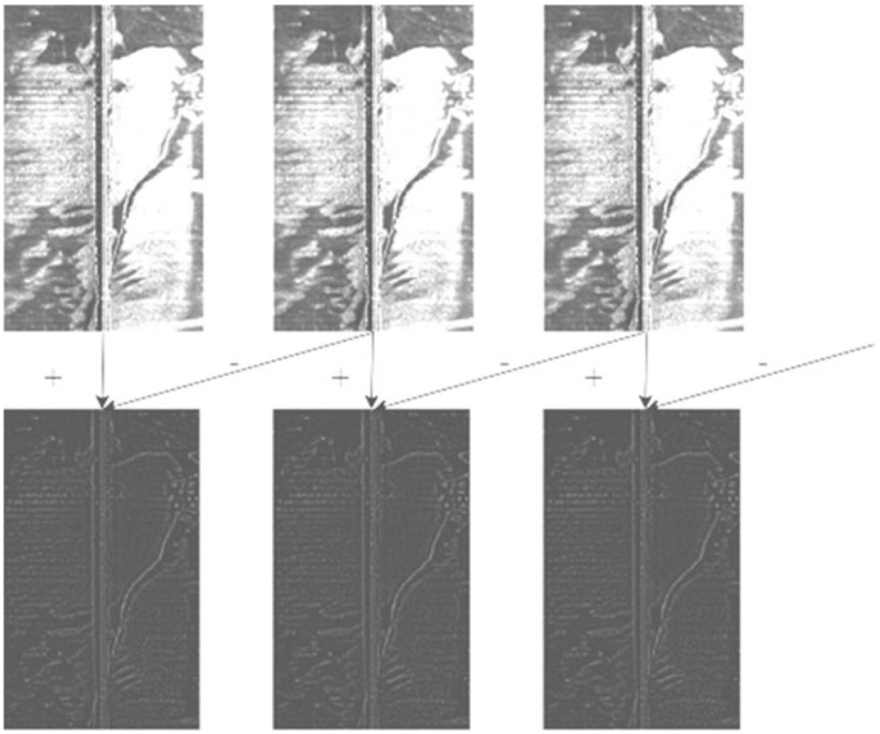

Fig. 4 Representation of Laplacian pyramid

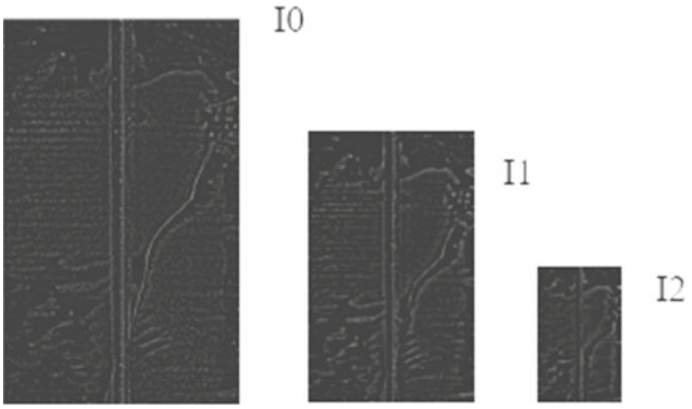

Fig. 5 Laplacian pyramid with two levels

gray scale value of the image. In 1979 Scholar Otsu proposed Otsu method which is broadly utilized since it is trouble-free and efficient. Hence, we applied this Otsu method on sonar images intended to mark the regions for identifying the pipelines by fixing the threshold automatically.

2.4 Morphological Operations

The word morphology refers to the study of the outward appearance of images including the composition of objects. The morphological functions can be utilized to perform some activities in image processing like image enhancement, noise removal, smoothening the images, thinning, and segmentation. Therefore, we are utilizing these morphological operations such as open and closed to find the background and foreground of the image to find the pipeline underwater as a parameter. The foreground method is intended to identify the deviations if any occurs in image sequences whereas the background technique that consents foreground image to be mined for object detection on images especially pipeline detection.

2.5 Watershed Algorithm

The intention of morphological watershed segmentation [8] technique being envisioned input gray level image into its contour depiction sort it out into minimum intensity of image, catchment basin and watershed boundaries. Therefore, in our research work, we utilized this algorithm to segment the input sonar image, dense region of image specified as fewer altitudes also transparent regions have to be taken as greater altitudes which seems to be contour façade. Hence, this algorithm is well suited for image segmentation which recognizes affected areas very easily.

2.6 Segmentation Technique

Ivan Aleksi et al. [9] proposed a novel Robust A-Search Image Segmentation (RASIS) scheme. RASIS scheme signifies a hybrid combination of both region based and contour based image segmentation methods. Priyadharshini et al. [10] edge based segmentation method so as to utilizes the morphological operations for categorizing the edges followed by an object tracing algorithm is proposed. Here they utilized real time images which were captured through Edgetech 4125 SSS device. The segmentation technique is a process of partitioning the given input image into several regions which are called segments. An image is a combination of different pixels. We cluster the pixels together that have similar attributes using image segmentation.

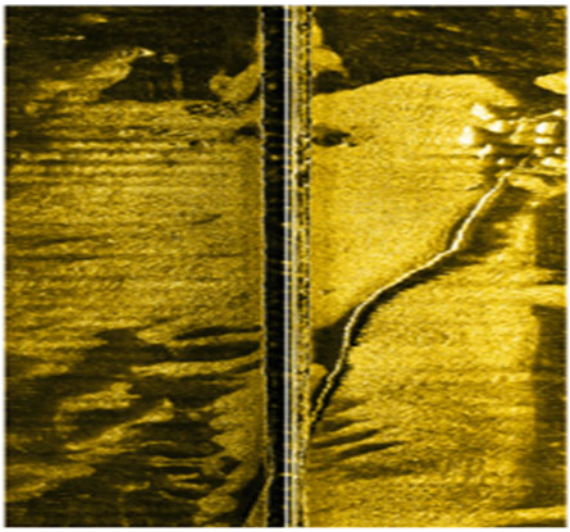

Fig. 6 Input images for pipeline recognition in underwater

Using this technique, we can identify the pipeline in underwater sonar images via region based segmentation to detect the specified regions on images.

3 Results and Discussion

3.1 Input Images

The original images shapes are specified in dimensions as (1131, 693). These images were utilized for performing underwater pipeline detection are depicted in Fig. 6.

3.2 Original Image Representation in Matrix Form

Primarily the images are represented in pixels since large number of pixels together formed a digital image. To process the image, we necessitate to represents it in pixels. Hence, the pipeline input images are mentioned in matrix resolution to make familiar about image pixels as well as resolution. The input images are specified in a matrix format which is depicted in Table 1.

Table 1 Input image represented in matrix resolution

255	255	255	255	255	255	255	255	255	255
255	255	255	255	255	255	255	255	255	255
255	255	255	255	255	255	255	255	255	255
255	255	255	255	255	255	255	255	255	255
255	255	255	255	255	255	255	255	255	255
255	255	255	255	255	255	255	255	255	255
255	255	255	255	255	255	255	255	255	255
255	255	255	255	255	255	255	255	255	255

Table 2 Output image representation

1	0	0
1	0	0
1	0	0
1	0	0
1	0	0
1	0	0
1	0	0
1	0	0
1	0	0
1	0	0

3.3 Output Image Representation in Matrix Form

Here we are representing the pipeline image output as matrix resolution as 1 and 0. Note that "1" mentioned that the pipeline is detected in underwater seabed whereas "0" represents the pipeline is not found in underwater aquatic environment. The output image resolution is depicted in Table 2.

3.4 Resolution Enhancement and Segmentation Process

Generally, SONAR images are affected by ambient noise, hence pixels carrying valued data are missing in image. Hence the image is implemented with Resolution enhancement Pyramidal Transform techniques. First Lower Pyramid Image shape dimensions as (566, 347). The restored images having only slight variations while comparing with original images. The dimension of resorted image with high resolution is specified as (1132, 694). Here, we are identifying the pipeline [11] which is buried in underwater seabed using segmentation techniques [12] from images

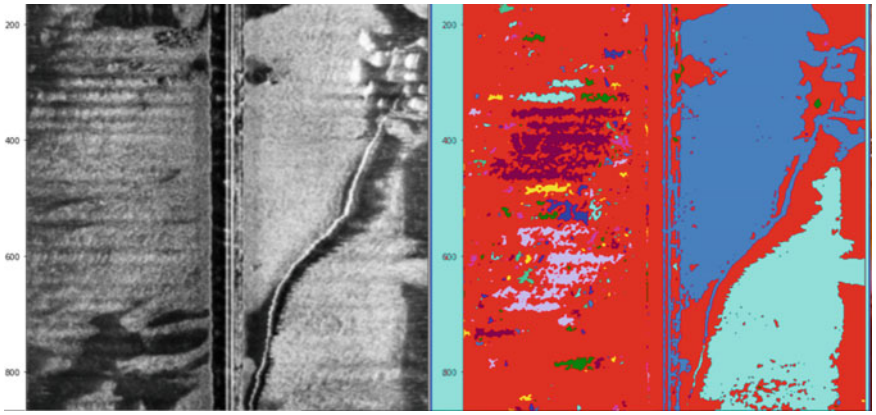

Fig. 7 Finding pipeline after segmentation process

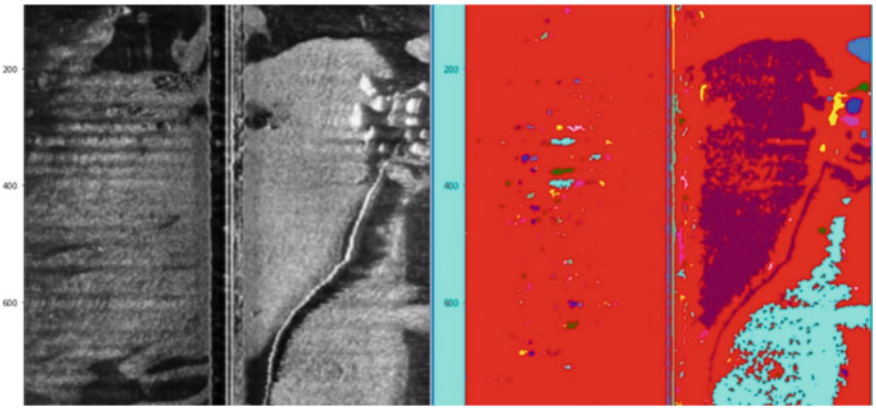

Fig. 8 Marking pipeline after Watershed Technique

which will be helpful in finding the cracks and replacing if any damages are available. After segmentation process using morphology, the pipeline edges are marked utilizing Watershed Technique illustrated in Figs. 7 and 8 respectively.

3.5 Restored Image Representation in Matrix Resolution

Image restoration is the process on the way to recover an image from corrupted version frequently vague impression image or unclear or noisy image. After performing segmentation procedure the pipeline which was buried underwater is

Table 3 Restored image representation in matrix resolution

92	73	43	29	24	22	22	92	73	43
91	73	43	28	23	21	21	91	73	43
91	73	43	28	22	20	20	91	73	43
92	74	44	29	24	22	23	92	74	44
94	75	45	31	26	25	26	94	75	45
95	77	47	32	27	26	27	95	77	47
96	78	48	34	29	27	26	96	78	48
97	79	51	37	30	26	23	97	79	51
97	80	53	38	30	24	20	97	80	53
95	78	49	35	28	23	20	95	78	49
94	75	45	30	25	21	19	94	75	45
92	73	42	27	22	19	18	92	73	42

identified to remove the cracks that make helpful in avoiding eroded underwater soil (Table 3).

4 Conclusions

In this paper, we detect the pipelines in underwater seabed using image processing techniques. We applied Gaussian and Laplacian pyramid which performed down sampling and up sampling procedures to sample the images by different pyramid levels for enhancing sonar image. Next, we utilized Otsu threshold determination for marking the regions based on fixing threshold automatically. In addition to that, we found foreground and background of the image by performing morphological operations. Finally, we applied segmentation procedure to segment the images to detect the pipeline in underwater sonar images. In future, based on features we will detect the buried pipeline on underwater images.

References

1. Stamoulakatos A, Cardona J, McCaig C, Murray D, Filius H, Atkinson R, Bellekens X, Michie C, Andonovic I, Lazaridis P, Andrew Hamilton Md, Hossain M, Di Caterina G, Tachtatzis C (2019) Automatic annotation of subsea pipelines using deep learning. Sensors 20:674. https://doi.org/10.3390/s20030674
2. Peng X-L, Hao H (2012) A numerical study of damage detection of underwater pipeline using vibration-based method. Int J Struct Stab Dyn 12(03):1250021. https://doi.org/10.1142/s0219455412500216
3. Tian Y, Lan L, Guo H (2020) A review on the wavelet methods for sonar image segmentation. Int J Adv Rob Syst 17(4):172988142093609. https://doi.org/10.1177/1729881420936091

4. Wang X, Guo L, Yin J, Liu Z, Han X (2016) Narrowband Chan-Vese model of sonar image segmentation: a adaptive ladder initialization approach. Appl Acoust 113:238–254. https://doi.org/10.1016/j.apacoust.2016.06.028
5. Mandhouj I, Amiri H, Maussang F, Solaiman B (2012) Sonar image processing for underwater object detection based on high resolution system. In: Signal and document processing
6. Maussang F, Chanussot J, Hetet A (2003) Automated segmentation of SAS images using the mean—standard deviation plane for the detection of underwater mines. In: Oceans 2003. Celebrating the Past ... teaming toward the future (IEEE Cat. No.03CH37492). https://doi.org/10.1109/oceans.2003.178236
7. Huo G, Wu Z, Li J (2020) Underwater object classification in sidescan sonar images using deep transfer learning and semisynthetic training data. IEEE Access 8:47407–47418. https://doi.org/10.1109/access.2020.2978880
8. Liu F, Fang M (2020) Semantic segmentation of underwater images based on improved deeplab. J Mar Sci Eng 8:188. https://doi.org/10.3390/jmse8030188
9. Aleksi I, Matić T, Lehmann B, Kraus D (2020) Robust A*-search image segmentation algorithm for mine-like objects segmentation in SONAR images 11(2). https://doi.org/10.32985/ijeces.11.2.1
10. Priyadharsini R, Sree Sharmila T (2019) Object Detection in underwater acoustics images using edge based segmentation method. In: International conference on recent trends in advanced computing 2019, ICRTAC 2019
11. Jacobi M, Karimanzira D (2014) Multi sensor underwater pipeline tracking with AUVs. In: 2014 Oceans—St. John's. https://doi.org/10.1109/oceans.2014.7003013
12. Burguera A, Bonin-Fon F (2020) On-line multi-class segmentation of side-scan sonar imagery using an autonomous underwater vehicle. J Mar Sci Eng

Dual Motor Power Management Strategy for Plug-in Hybrid Electric Vehicle

Vinoth Kumar Balan and P. Avirajamanjula

Abstract In order to increase the driving range of plug-in hybrid electric vehicle, dual motor control strategy was proposed. This method will offer various mode of control and less energy consumption. This dynamic performance of system improved by using the rule-based algorithm of fuzzy logic. Power demand for vehicle propulsion and energy storage system parameter is estimated. The effect of this value based on the torque requirement for vehicle propulsion is calculated. Based on the total torque requirement and SoC of the battery, the corresponding mode of operation is identified by using the rule-based algorithm. The main controller will monitor the propulsion control and dynamic performance of the system. The power train configuration for dual motor with engine control is designed using Simulink. Most of period of control, torque requirement for the vehicle propulsion met by the single electric motor, i.e., vehicle operating in electric mode. The result shows the extension of driving range and reduced energy consumption.

Keywords Motor · Fuzzy · Plug-in hybrid vehicle · Power management · Driving cycle · Power split hybrid vehicle

1 Introduction

Rising oil prices is causing a setback in the transport sector. Further increase in fossil fuel consumption causes air pollution such as global warming and fuel shortages, etc. Increasing the use of electric vehicles is the best solution for solving these problems [1–3]. Traveling long distances, refilling fuel is still a problem in fully battery-operated vehicle. Using more battery to increase battery capacity also increases the capital cost of the electric vehicle. That is why people are reluctant to buy electric vehicles.

To address these issues, the electric motor and engine combination propulsion hybrid architecture was explored. In hybrid electric vehicle, improved control method enables multi-mode operation and high performance. Based on the condition, this

V. K. Balan (✉) · P. Avirajamanjula
Department of Electrical and Electronics Engineering, PRIST University, Thanjavur, India

C. Subramani et al. (eds.), *Proceedings of International Conference on Power Electronics and Renewable Energy Systems*, Lecture Notes in Electrical Engineering 795,
https://doi.org/10.1007/978-981-16-4943-1_45

system will operate in both electric and conventional mode, i.e., engine mode. So, through this, extended range of driving and high efficiency can be obtained [4–7]. The hybrid vehicle not having option of battery charging using grid. This limits the electric mode of operation for long driving condition. The plug-in hybrid vehicle has attractive feature of grid charging, and also, charging period can be reduced by fast charging method. The advanced power electronics technology, high performance electric motors, and better control technology are main key for developing power train configuration of PHEV.

2 Power Train Configuration

This system comprises dual motor, engine, generator, and CVT-based power train which was designed for plug-in hybrid vehicle as shown in Fig. 1. The main objective is to achieve best drive ability and extended driving range. The sizing of the components for the power train configuration, control strategy will play major role for controlling vehicle dynamic and improving the overall performance of the PHEV [7–9]. The various type of electric traction motor is reviewed for electric vehicle such as induction motor, brushless DC motor, permanent magnet synchronous motor and switched reluctance motor, etc. The high rated motors is preferred as permanent magnet synchronous motor for this system. These motor drive has feature of high-power density, small size, low weight, and high performance [10–12].

$$P_t = P_{\text{ice}} + P_{\text{em1}} + P_{\text{em2}} \tag{1}$$

$$P_{\text{em1}}^{\min} \leq P_{\text{em1}} \leq P_{\text{em1}}^{\max} \tag{2}$$

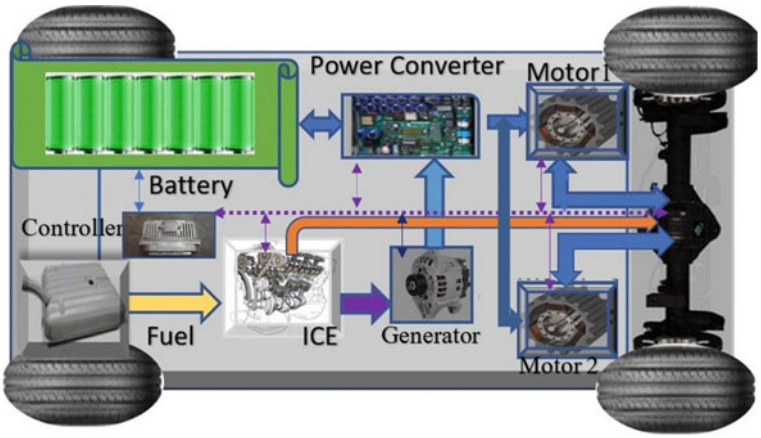

Fig. 1 Powertrain configurations for plug-in hybrid electric vehicle

Table 1 Specification of power train element

Name	Value
Electric motor A power	89 KW
Electric motor B power	60 KW
Engine	160 KW
Battery capacity	180 Ah
Nominal voltage	380 V
Vehicle loaded mass	1400 kg
Gear box	3.52,2.04,1.40,1
Air resistance coefficient	0.01
Rolling resistance coefficient	0.012
Frontal area, A*f*	2.33 m^2
Drag coefficient, C*d*	0.26
Air density, ρ_{air}	1.22 kg/ m^3
Wheel radius, R*wh*	0.32 m

$$P_{\text{em2}}^{\min} \leq P_{\text{em2}} \leq P_{\text{em2}}^{\max} \tag{3}$$

$$P_{\text{ice}}^{\min} \leq P_{\text{ice}} \leq P_{\text{ice}}^{\max} \tag{4}$$

$$\text{SoCmin} \leq \text{SoC}(t) \leq \text{SoCmax} \tag{5}$$

$$P_{\text{dem}}^{\min} \leq P_t \leq P_{\text{dem}}^{\max} \tag{6}$$

where the P_{dem} is the power demand of the vehicle, P_t is the total traction power, andP_{ice} is the power produced by the ICE engine. P_{em1} is the power produced the Motor A, P_{em2} is the maximum power of the Motor B, $P_{\text{em1}}^{\min}$ is the minimum power of the Motor A, $P_{\text{em1}}^{\max}$ is the maximum power of the Motor A, $P_{\text{em2}}^{\min}$ is the minimum power of the Motor B, and $P_{\text{em2}}^{\max}$ is the maximum power of the Motor B. SoCmin is minimum state of the charge of the battery. SoCmax is maximum state of the charge of the battery. Here the specification of power train elements mention in Table 1.

3 Modes of Hybrid Drive System

The goal of the control strategies is operating vehicle maximum in electric mode and extending the driving range of the vehicle. Based on the enviroment condition and vehicle operator control, the vehicle power demand will change. The environmental condition includes the wind speed, road slope, traffic condition, etc.

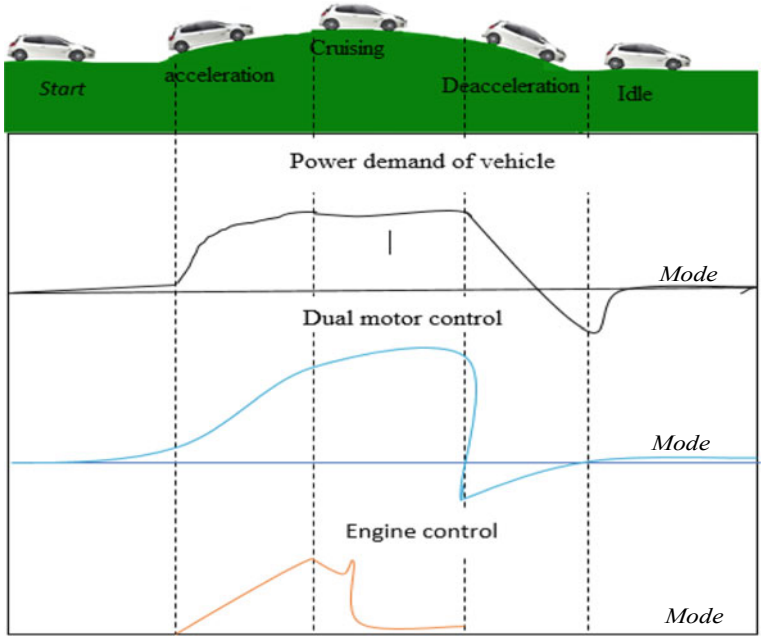

Fig. 2 Driving modes of plug-in hybrid electric vehicle

Based on the torque requirement, vehicle operation mode generally classified as start/stop, acceleration, cruising, de-acceleration, and Idle are shown in Fig. 2 so the power requirement of each mode will various accordingly [13–15]. Mode of operation initialized based on the SoC value of the battery and traveling distance of the vehicle. If SoC $\geq$ D, the electric mode of operation is decided by the fuzzy controller. The dual motor power train configuration has the different transmission pattern based on power demand of the vehicle. The acceleration condition power demand is so high. In this mode, based on the SoC of the battery and power demand, vehicle power train will be configured either series or parallel hybrid mode. Acceleration mode further classified in to three type. In case of heavy load (A), the Medium SoC level and high-power demand parameter estimated by the controller, so hybrid dual power transmission is configured; i.e., in this case, motor A and engine work. In heavy load (C) case, the high SoC and medium power demand required, So Motor A and Motor B will meet the power demand of the vehicle. The cruising mode further classified into two types such as Medium Load (A) and Medium Load (B). In the case of Medium Load (A) SoC is high and power demand less the dual motor power, then the power train is configured in dual motor operation. When motor operate in Medium Load (B), the power demand is greater than dual motor power, so the Motor A and engine operating togeather to meet the power demand. For Start/stop mode, the vehicle power demand of the vehicle is very low, so the motor A exclusive power the vehicle. The fuzzy controller will decide the Motor B and Engine rating

Table 2 Operating mode of PHEV

Load condition	Motor A	Motor B	Engine	Vehicle mode
Start/stop	Off	On	Off	Parking mode
Heavy load (A)	On	Off	On	Acceleration
Heavy load (B)	On	On	On	Acceleration
Heavy load (C)	On	On	Off	Acceleration
Breaking (A)	On	On	Off	Regenerative mode
Breaking (B)	On	Off	Off	Regenerative mode
Medium load (A)	On	On	Off	Cruising
Medium load (A)	On	Off	On	Cruising
Light load	Off	Off	On	Idle or traffic mode

Table 3 Fuzzy control tables

ESS	P dem	Engine	Motor B
H	VL	VL	VL
H	L	L	L
H	M	M	M
H	H	H	H
M	VL	VL	VL
M	L	L	L
M	M	M	M
M	H	H	H
L	VL	L	VL
L	L	M	VL
L	M	H	VL
L	H	H	VL

of operation. In de-acceleration mode, regenerative power is stored in battery. When vehicle in idle mode, the Motor B will be engaged (Tables 2 and 3).

4 Simulation

The rule-based system using fuzzy logic controller is designed for various mode of operation. The input of the controller is vehicle power demand, and SoC of the battery using this parameter desired mode of operation is identified, and propulsion element will be controlled for desired power train configuration. The fuzzy control membership function as shown in Fig. 3.

The variable speed control of the vehicle condition is simulated using Simulink software. Figure 4a shows vehicle body response for controller dynamic response of

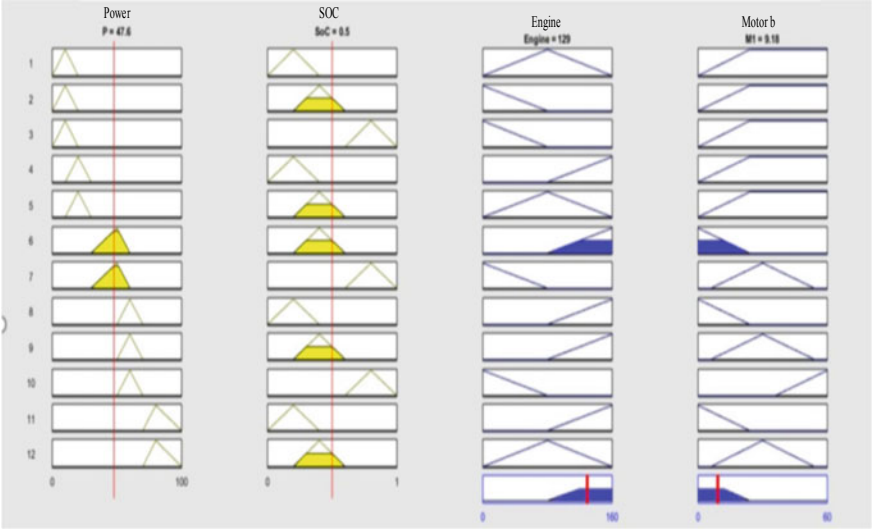

Fig. 3 Fuzzy logic for various of driving modes

various load. Figure 4b Engine, Motor A and B shaft rpm response. Figure 4c, d is the battery loss and temperature result for the various load. The Fig. 4e shows the result of load power supply by both battery and engine. This pattern of the power train drive system is decided by the fuzzy rule controller. The time period of 0–5, light load demand is occurring, the power demand is met by motor B drive system, and the fuzzy controller enables the dual motor power train after 5 s of the time period, so battery loss also increasing certain level. Due to high acceleration, the power demand of the vehicle was increased. So the power split mode was activated and this mode power train configuration meet the maximum power demand of vehicle. The battery losses are comparing to conventional vehicle 20% optimally reduced in this power train configuration. The de-acceleration starts at 11 ms time period. So, the power demand, i.e., required power of the vehicle for propulsion is calculated, and based on the fuzzy rule, the controller is optimizing the motor drive. Here engine operate at minimum torque. So, this vehicle mostly operating linear mode of control. The result of this optimizing control the SoC of the battery is varying linearly.

5 Conclusion

In both acceleration mode and cruising mode, better dynamic control was achieved with dual motor power train. This configuration is supporting maximum electric mode of operation. This system was designed through Simulink and tested for various dynamic condition. The optimized method of rule-based fuzzy logic controller is effectively control the power train at various dynamic condition. The dual motor

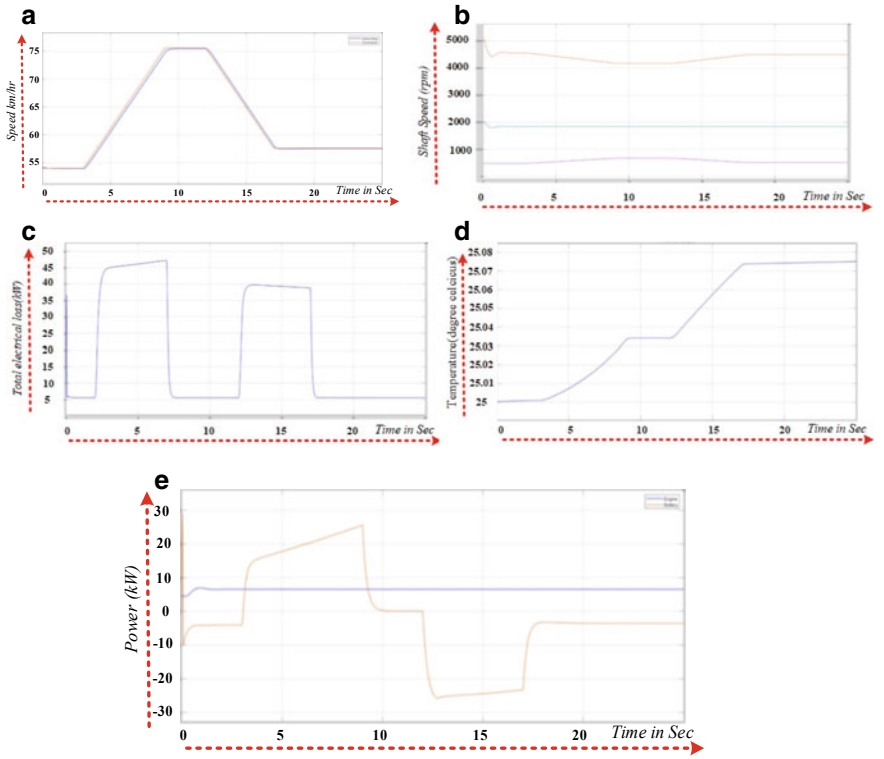

Fig. 4 **a** Vehicle command. **b** Shaft speed of power train elements. **c** Battery loss for different load. **d** Battery temperature condition. **e** Load sharing of battery and engine

configured hybrid plug-in vehicle satisfies the main objective of extended driving range and better drivability.

References

1. Urbina Coronado PD, Ahuett-Garza H (2015) Control strategy for power distribution in dual motor propulsion system for electric vehicles, vol 2015. Hindawi Publishing Corporation
2. Wang Y, Sun D (2014) Powertrain matching and optimization of dual-motor hybrid driving system for electric vehicle based on quantum genetic intelligent algorithm, vol 2014. Hindawi Publishing Corporation
3. Nguyen CT, Walker PD, Zhang N, Ruan J (2020) Efficiency improvement of a novel dual motor powertrain for plug-in hybrid electric buses. Proc Instit Mech Eng, Part D: J Automobile Eng 234(7):1869–1882
4. Zhang L, Liu W, Qi BN (2020) Energy optimization of multi-mode coupling drive plug-in hybrid electric vehicles based on speed prediction. Energy 206:118126
5. Wang Y, Zeng X, Song D (2020) Hierarchical optimal intelligent energy management strategy for a power-split hybrid electric bus based on driving information. Energy 199:117499

6. Jin-Hua X, Guo JF, Peng B, Nie H, Kemp R (2020) Energy growth sources and future energy-saving potentials in passenger transportation sector in China. Energy 206:118142
7. Goetz M (2005) Integrated.: powertrain control for twin clutch transmissions (Leeds, U.K.: Univ. Leeds)
8. Wang W, Li Y, Shi J, Lin C (2018) Vibration control method for an electric city bus driven by a dual motor coaxial series drive system based on model predictive control. IEEE Access 6:4118841200
9. Wang W, Zhang Z, Shi J, Lin C, Gao Y (2018) Optimization of a dual-motor coupled powertrain energy management strategy for a battery electric bus based on dynamic programming method. IEEE Access 6:3289932909
10. Ruan J, Walker PD, Zhang N, Wu J (2017) An investigation of hybrid energy storage system in multi-speed electric vehicle. Energy 140:291306
11. Morozov A, Humphries K, Zou T, Martins S, Angeles J (2014) Design and optimization of a drivetrain with two-speed transmission for electric delivery step van.In: Proceeding IEEE international electric vehicle conference (IEVC). Florence, Italy, pp 18
12. Kim H, Kim J, Lee H (2011) Mode transition control using disturbance compensation for a parallel hybrid electric vehicle. Proc IMechE, Part D: J Automobile Eng 225:150–166
13. Enang W, Bannister C (2017) Modelling and control of hybrid electric vehicles (A comprehensive review). Renew Sust Energ Rev 74:1210–1239
14. Naunheimer H, Bertsche B, Ryborz J et al (2010) Automotive transmissions: fundamentals, selection, design and application. Springer Science & Business Media, Dordrecht
15. Enang W, Bannister C (2016) Robust proportional ECMS control of a parallel hybrid electric vehicle. Proc IMechE, Part D: J Automobile Eng 231:99–119

Investigation on Power System Stability Improvement Using Facts Controllers

Gajana Penchalaiah and R. Ramya

Abstract Due to rising demand and constraints on the construction of new lines, modern power transmission networks are becoming more complex. Following a disruption, the loss of stability is one of the key issues with such a modern power system. Transient stability control is a vital principle that ensures the power system's stable operation during faults and significant instabilities. FACTS tools have proven to be very effective in improving controllability and increasing power transfer capability while retaining the necessary stability margin in a power system transmission network. The improvement of transient stability of a three-machine, nine-bus power system using FACTS controllers (SSSC, SVC, and UPFC) is investigated in this paper. In the MATLAB/SIMULINK environment, the simulation results demonstrate the effectiveness and solidity of the FACTS devices in improving system transient stability.

Keywords SVC · SSSC · UPFC · FACTS · Transient stability

1 Introduction

The combination of numerous generators, transmission lines, and different types of loads makes the power system network complex. As demand for power increases, some of the transmission lines are overloaded. If a failure occurs during overloading of a transmission line, the issue of transient stability arises [1]. Transient stability in the system, even after disruptions, should be managed to keep the system in stable service. The switching operations and faults in the transmission line are considered to be disturbances [2]. Due to heavy deviations between the stator and rotor, FACTS controllers are the latest developed power electronic controllers that are used in the

G. Penchalaiah (✉) · R. Ramya
Department of Electrical and Electronics Engineering, SRM Institute of Science and Technology, Kattankulathur 603203, India
e-mail: pg1113@srmist.edu.in

R. Ramya
e-mail: ramyar4@srmist.edu.in

C. Subramani et al. (eds.), *Proceedings of International Conference on Power Electronics and Renewable Energy Systems*, Lecture Notes in Electrical Engineering 795,
https://doi.org/10.1007/978-981-16-4943-1_46

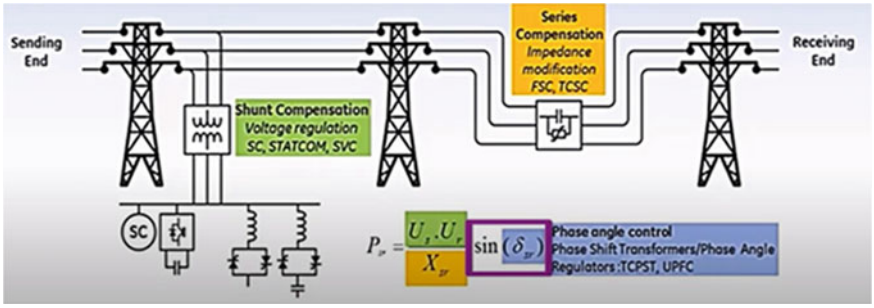

Fig. 1 Present day solutions for improving power system stability [7]

power system to improve voltage profile, compensation of reactive power thereby controlling, transient and steady-state stability of the desired power system. Static VAR compensator (SVC), series compensators (SSSC), combination of series and shunt controller (UPFC), and others are examples of FACTS controllers [3–8]. Static VAR Compensator is a FACTS system that flattens the voltage profile by controlling the voltage at the desired end. This is possible through the compensation of reactive power [9]. SVSs are preferred over traditional shunt compensators for improving the performance during transient and steady-state conditions, and it is also used to damp out the oscillations in power, reducing losses thereof improving transient stability. SSSC is a FACTS device, which plays a vital role in controlling the power systems. The role of SSSC includes controlling the load flow, reducing system losses, and providing good voltage regulation [10]. It also helps in limiting short-circuit currents, damping the power swings, and thereby regulating transient stability [11].

Unified power flow controller is the most effective one among all the controllers. It improves the control attributes such as transient, dynamic, and steady-state stability of the electrical system. It is the product of combining SSSC and STATCOM. It can control many parameters like phase angle, voltage magnitude, etc. [12]. A MATLAB/Simulink model is created for a three-machine, nine-bus power system with a UPFC. The UPFC exhibition is contrasted, and various FACTS devices such as SVC and SSSC are used individually. According to the simulation results, UPFC is a strong FACTS device for transient stability studies (Fig. 1).

2 Test System-WSCC Three-Machine Nine-Bus Power Systems

For transient stability studies, the WSCC system is widely used. The synchronous machines have voltage regulators, an exciter, and a detailed model of a steam turbine and governors. A hydraulic turbine and governor (HTG), an excitation mechanism, and a power system stabilizer are mounted on each of the three devices (PSS). As

shown in Figs. 2 and 3, a single-circuit long transmission line connects a WSCC three-machine nine-bus power system with series and shunt FACTS units.

Here are the data for the nine buses, three generator systems. The system depicted in a single line diagram in Table 1 include information about the actual values of the transmission line parameters. We must assume the system ratings of MVA BASE 100 MVA, $f = 60$ Hz, bus nominal voltage = 230 kV, maximum voltage = 1.1pu, minimum voltage = 0.9 p.u, transformer 1 rating 16.5/230 kV, transformer 2 rating 18/230 kV, and transformer 3 rating 13.8/230 kV [4]. When measuring the actual

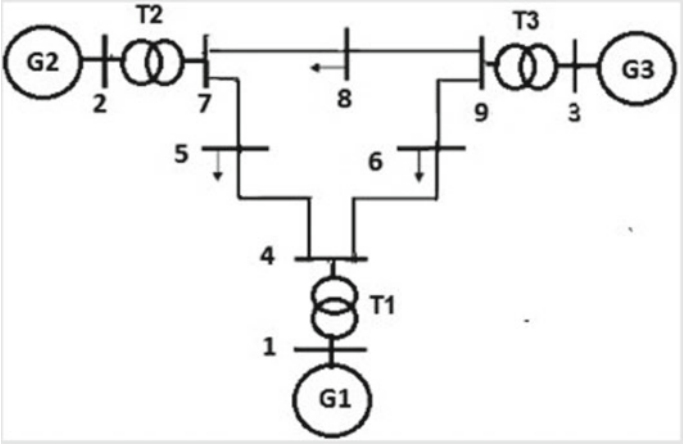

Fig. 2 WSCC three-machine nine-bus power system

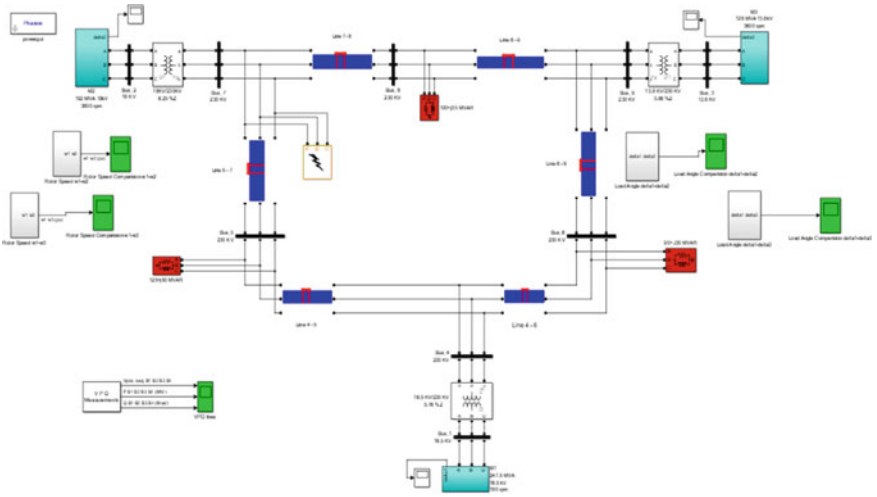

Fig. 3 WSCC's three-machine nine-bus power system simulation diagram

Table 1 Three-machine nine-bus power system at WSCC: data from the transmission line parameters

Line	Length(km)	$R1(\Omega/km)$	$R0(\Omega/km)$	$L1$(H/km)	$L0$(H/km)	$C1$(F/km)	$C0$(F/km)
1–4	–	–	–	–	–	–	–
2–7	–	–	–	–	–	–	–
3–9	–	–	–	–	–	–	–
4–5	97.38	0.054	0.162	0.0012	0.0036	9.06×10^{-9}	2.72×10^{-8}
4–6	95.99	0.093	0.281	0.0013	0.004	8.257×10^{-9}	2.477×10^{-8}
7–5	176.71	0.095	0.287	0.0012	0.0038	8.687×10^{-9}	2.606×10^{-8}
9–8	115.56	0.054	0.163	0.0012	0.0036	9.073×10^{-9}	2.721×10^{-8}
9–6	196.41	0.105	0.315	0.0012	0.0036	9.144×10^{-9}	2.743×10^{-8}
7–8	82.5	0.054	0.163	0.0012	0.0036	9.073×10^{-9}	2.721×10^{-8}

values of transmission system using per unit parameters, these equations can be used to measure transmission length as well as positive, zero sequence resistance, inductance, and capacitance.

$$\text{Length} = \left(\frac{\sqrt{X \times B}}{2 \times 3.14 \times f}\right) \times \text{Velocity of Light in Km per Sec,}$$

$$\text{Where} v = 3 \times 10^8 \text{m/Sec}$$

$$\text{Transmission line} \frac{R1}{R0} \text{Calculations}$$

$$R_{\text{actual}} = R_{\text{p.u}} \times R_{\text{base}}$$

$$R_{\text{base}} = X_{\text{base}} = \frac{(V_{\text{base}})^2}{S_{\text{base}}}$$

$R1$is a Positive Sequence and

$$R0 = R1 \times 3 \, is \, a \, Zero \, Sequence \, Component$$

Similarly$L1$and$L0$&$C1$and$C0$should be calculated.

As shown in Fig. 3, the simulation focuses on 230 kV, three-machine nine-bus power systems which are made up of three generators linked together in a transmission line network. The $G1$ generator has a limit of 247.5 MVA, the $G2$ generator has a limit of 192 MVA, and the $G3$ generator has a limit of 128 MVA. The corresponding wave forms for the system without FACTS controllers are shown below.

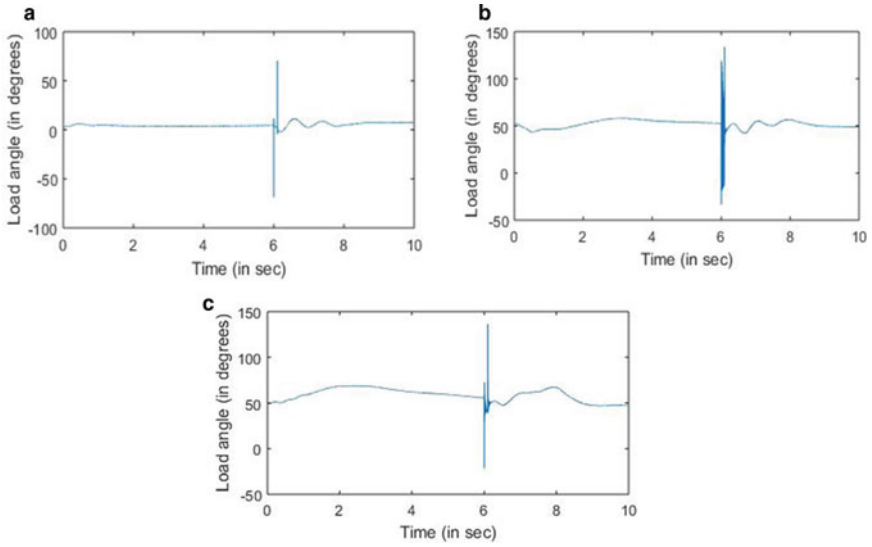

Fig. 4 **a** WSCC three-machine nine-bus power system load angle of Generator 1. **b** WSCC three-machine nine-bus power system load angle of Generator 2. **c** WSCC three-machine nine-bus power system load angle of Generator 3

Table 2 Settling time for load angle in sec for three machines

Machines	Settling time for load angle in sec
247.5 MVA Generator	8.8
192 MVA Generator	7.8
128 MVA Generator	9.2

A three-phase fault is created at $t = 6$ s for a duration of 100 ms. Fig. 4a–c reveals a transient behaviour of system at the time of fault created.

As shown in Table 2, a relation is established between the above systems for improving the stability of the three-machine nine-bus system, based on simulation results shown in Fig. 4a–c.

3 Performance Analysis of WSCC System with FACTS Controller

To control the power flow in the lines and to maintain the voltage levels at buses, the SVC, SSSC, and UPFC are installed separately in the centre of bus 4 and bus 5. The WSCC three-machine nine-bus systems making use of series and shunt FACTS devices. Here, UPFC which is the combination of (STATCOM and SSSC); SVC is

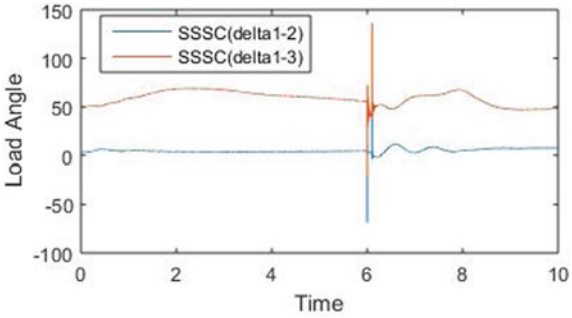

Fig. 5 SSSC delta1-2 and delta1-3 load angle comparison

equipped with 4 bus and SSSC and UPFC which are equipped with 4 and 5 bus system.

- **Case-i: Inclusion of SSSC**
- **Case-ii: Inclusion of SVC**
- **Case-iii: Inclusion of UPFC**

Case-i: Inclusion of SSSC

The 'SSSC' is a FACTS unit that is used in conjunction with VSI and a transformer on the transmission line. The SSSC unit, on the other hand, injects voltage into the line in sequence. Inductive or capacitive reactance may also be used with the voltage injected. The electric power in the line can be changed by using variable reactance in series with the line. As a result, the SSSC system is used to dampen the oscillations that occur after a three-phase fault (Fig. 5).

The above simulation results for synchronous machine of three-machine nine-bus system shows the response of load angle. At the time of 6.1 s, Fig. 5 reveals a symmetric three-phase fault for 100 ms. As compared to earlier traditional types that did not employ a controller, the 'SSSC' system is used to suppress power oscillations in the system.

Case-ii: Inclusion of SVC

As SVC is used to stabilize the network, the value of SVC in fixed susceptance mode Bref = 0 is used to observe the extreme contingency conditions. Open the simulation phase and select voltage regulation mode from the SVC block menu. When the voltage drops below the reference voltage, the SVC will try to compensate by combining open force on the line (1.0 p.u). If the SVC is unavailable, the selected SVC reference voltage is equal to the system voltage. The SVC will now be 'flick through' and keeping the voltage together for voltage compensation as it departs from its reference set point in steady express (Fig. 6).

The load angle plot for synchronized machines in a three-machine nine-bus system is shown in the diagram above. At a rate of 6.1 s, a three-phase symmetric 100 ms problem is applied. The power curve exhibits oscillations after a deficiency occurrence, which evolves into a stable state. As compared to when the device does not have a regulator, oscillations are damping prior to applying SVC.

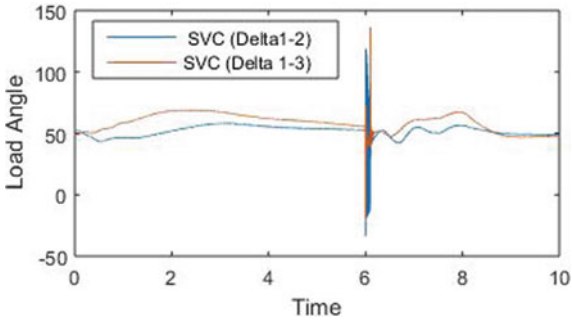

Fig. 6 SVC delta1-2 and delta1-3 load angle comparison

Case-iii: Inclusion of UPFC

In a three-machine nine-bus configuration, the simulation results for load angles are shown in the diagram above. A three-phase 100-ms short-circuit fault is introduced at a rate of 6.1 s. The power curve shows an oscillation after the issue occurs, which settle to a stable state. When comparing movements with and without a regulator in the system, it is observed that oscillations are damping prior to the application of UPFC. In order to improve the stability of the nine-bus system, a relationship is established between the above FACTS devices, as shown in Table 3. Since the UPFC post-fault time is less than that of the SSSC and SVC, it is presumed that UPFC is the superior FACT devices for stability improvement over the SSSC and SVC (Fig. 7).

The system without FACTS controller takes 2.8 s to settle to normal operating conditions after fault occurrence. Whereas, the system installed with FACTS controllers settles to steady state operating conditions within 1.4 s. This shows the

Table3 Comparison between FACTS devices

FACTS devices	Time for delta1_2 to settle (in sec.)	Time for delta1_3 to settle (in sec.)
SSSC	7.4	7.8
SVC	7.6	7.9
UPFC	6.8	7.2

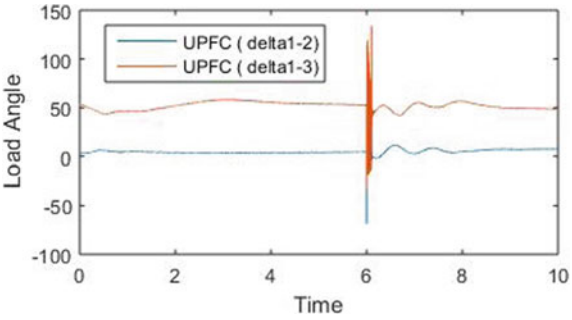

Fig. 7 UPFC delta1-2 and delta1-3 load angle comparison

effectiveness of installing FACTS controllers at the appropriate place in the test system.

4 Conclusion

The power system stability of a WSCC three-machine nine-bus system with SSSC, SVC, and UPFC has been explored for the test system of a WSCC three-machine nine-bus system. The comparative study is made among the SSSC, SVC, and UPFC controllers to test the dynamic behaviour of the power system in the event of a major disturbance such as three phase fault. The simulation results show that using the UPFC device, which has a shorter settling time in post-fault conditions than the other controllers and it, improves system efficiency significantly.

References

1. Yu S, Chau TK, Fernando T, Savkin AV, Iu HH-C (June 2019) Novel Quasi-decentralized SMC-based frequency and voltage stability enhancement strategies using valve position control and FACTS device. IEEE Access
2. Liu T, Liu Y, Liu J, Yang Y, Taylor GA, Huang Z (Sept 2016) Multi- indicator Inference Scheme for fuzzy assessment of power system transient stability. IEEE 2(3)
3. Liu Y, Wu QH, Kang H, Zhou X (June 2016) Switching power system stabilizer and its coordination for enhancement of multi-machine power system stability. IEEE 2(2)
4. Chen B-S, Hsu Y-Y (Jan 2007) An analytical approach to harmonic analysis and controller design of a STATCOM. IEEE 22(1)
5. Liu S, Li G, Zhou M (June 2016) Power system transient stability analysis with integration of DFIGs based on center of inertia. IEEE 2(2)
6. Hingorani NG, Gyugyi L (2000) Understanding FACTS: concepts and technology of flexible AC transmission systems. In: El-Hawary M (ed) vol 1. IEEE press, New York
7. Sharma B, Sharma A (May 2015) Power system stability enhancement using FACTS. IJARCSSE 5(5)
8. Prakash D, Tripathi EVK Enhancing stability of multi-machine IEEE 9 bus power system network using PSS. IJAREEIE 4(5)
9. Kundar P (1994) Power system stability and control. McGraw-Hill, NewYork
10. Nallagalva SK, Kirar MK, Agnihotri G (July 2012) Transient stability analysis of the IEEE 9-bus electric power system. IJSET 1(3)
11. Sethy SK, Moharana JK (Nov 2012) Design, analysis and simulation of linear model of a STATCOM for reactive power compensation with variation of DC-link voltage. IJEIT 2(5)
12. Murthy PSR (2007) Power system analysis. BS Publications, Hyderabad

Power Quality Enhancement Using Interline Dynamic Voltage Restorer in Renewable Energy System

T. Ahilan, P. Suresh, S. Elam Cheren, and G. Ramya

Abstract Nowadays, renewable energy is attractive due to the depletion of fossil fuels. The energy requirement in most developed countries is met by solar and wind energies. In this paper, solar and wind energies are used in a safer way for power utilization and power quality improvement. Solar energy and wind energies are utilized by employing custom power devices (CPD). Interline dynamic voltage restorer (IDVR) is the most advanced CPD device for wind and solar energy utilization. IDVR is the combination of two DVRs which protect the sensitive loads in various distribution feeders. The solar energy source is connected with feeder 1 and wind energy is connected with feeder 2. If the power requirement in feeder 1 is more, the feeder 2 aid feeder 1 by compensating reactive power using IDVR and it is vice versa. IDVR helps to maintain the power continuity and power quality in both feeder 1 and 2. Simulation of two bus system using solar and wind energy with and without IDVR is simulated using MATLAB/Simulink and analyzed in terms of real and reactive power.

Keywords Interline dynamic voltage restorer · Power quality · Photovoltaic · Renewable energy

T. Ahilan (✉)
Department of Mechanical Engineering, St. Joseph College of Engineering, Sriperumbudur, India

P. Suresh
Department of Electrical and Electronics Engineering, St. Joseph College of Engineering, Sriperumbudur, India
e-mail: suresh@stjoseph.ac.in

S. E. Cheren
Department of Electrical and Electronics Engineering, Sri Krishna College of Engineering and Technology, Coimbatore, India

G. Ramya
Department of Electrical and Electronics Engineering, SRM Institute of Science and Technology, Ramapuram, India
e-mail: ramyag@srmist.edu.in

C. Subramani et al. (eds.), *Proceedings of International Conference on Power Electronics and Renewable Energy Systems*, Lecture Notes in Electrical Engineering 795,
https://doi.org/10.1007/978-981-16-4943-1_47

1 Introduction

Recently, a renewable source of energy plays a vital role in compensating the depleting of conventional fuel resources. One of the renewable sources of energy is the photovoltaic system. Using this technique, PV arrays convert solar energy into electrical energy. Based on the development of PV systems, PV arrays efficiencies have been increased. So, the PV system studies have been at the forefront [1–3]. In remote areas, standalone PV generation is an attractive essential source of energy. The PV system has two disadvantages 1. Weather conditions vary the PV power generation and 2. The energy conversion range is minimal during low irradiation conditions. Though the PV system has demerits, two different techniques can be employed for effective utilization. Firstly, through space heating applications, solar thermal energy is obtained using captured heat. Secondly, incident solar radiation is converted into useful electrical energy [4–6]. MPPT technique is employed in all power inverters to extract maximum power. Incremental conductance (INC), perturbation and observation (P&O) and fuzzy logic controller are the different techniques of MPPT [7–9]. P&O algorithm-based MPPT technique has modest structure and limited parameters. It measures PV voltage using a voltage sensor, and the cost of the sensor is very less, so it is easy to implement [10]. The power from the PV panel determines the efficiency of the PV system. The position of the panel determines the maximum extraction of power from the panel. MPPT algorithm includes software coding at a reasonable price to supplement the energy throughout. The algorithm ensures that the PV panel works at full efficiency with PV characteristics. P&O and INC are the different MPPT techniques applied to extract maximum power. The phase angle jump in the voltage can initiate transient current in the capacitors, transformers and motors. It can also disturb the operation of converters and may lead to glitch in the performance of thyristor-based loads. In order to protect sensitive loads from grid voltage sags, custom power devices (such as, SVC, D-STAT COM, DVR and UPQC) are being widely used. Among these devices, IDVR has most cost effective and comprehensive solution. The above literature survey does not deal with a comparison of with and without IDVR in renewable energy system for the power quality enhancement. Integrating two renewable sources in a grid with compensating the power quality was not done in the above papers. In this paper, the main objectives are to improve the power quality, and fully utilize the wind and solar energy was mainly considered. In Sect. 2, the conventional method of solar and wind energy system connects to the grid were given. The proposed method of integrating the solar and wind energy system is connected in a grid with compensation using IDVR were described. The operation of IDVR, flow chart of IDVR control system was explained. In Sect. 3, the simulation results of the proposed system with and without IDVR were presented. In Sect. 4, the conclusion of this work.

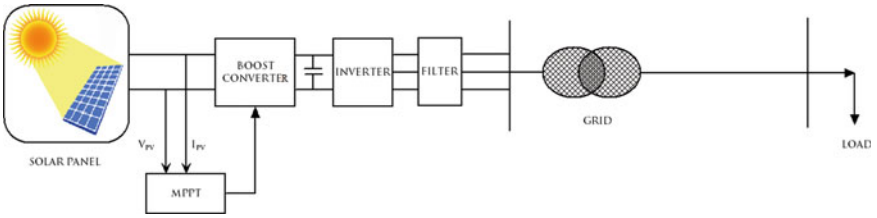

Fig. 1 Block diagram of solar power generation system

2 Proposed Research Method

In this section, described the proposed method of power quality enhancement using IDVR in renewable energy system.

2.1 Solar Energy Source

PV system is used to convert the incident sunlight on the PV panel into electrical energy. Maximum PV output is extracted from the PV system automatically by using the MPPT concept which varies the load conditions of PV array. The utilization factor of the existing PV inverter is very less, as all PV arrays are provided with MPPT, which is an inefficient method for tracking maximum power. In recent times, MPPT is applied to the individual PV array since radiation is weak during night time. Figure 1 represents the block diagram of an existing solar power generation system. It consists of a boost converter, DC energy storage device, injecting boost transformer and PWM control strategy. Three phase AC voltage is obtained from DC voltage using VSI in synchronization with the line voltage. Performance of 6.6 kV 3 phase 2 bus system is analyzed using Sinusoidal Stepped Pulse Width Modulation (SSPWM).

2.2 Wind Energy Source

The wind energy conversion system (WECS) is used to convert mechanical energy into electrical energy. Generally in WECS, two types of generators are used to produce electricity. One of the generators is PMSG and another one is DFIG. Both the generators offer an AC voltage at a frequency of 50 Hz. The converters are needed to interface the power flow from turbine to grid. Figure 2 represents the block diagram of an existing wind power generation system. It consists of a permanent magnet synchronous generator (PMSG), boost converter, DC energy storage device, injecting boost transformer and PWM control strategy. Three phase AC voltage is obtained from DC voltage using VSI in synchronization with the line voltage. Performance

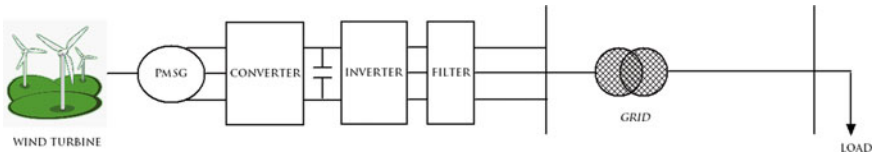

Fig. 2 Block diagram of wind power generation system

of 6.6 kV 3 phase 2 bus system is analyzed using Sinusoidal Stepped Pulse Width Modulation (SSPWM).

2.3 Integrating of Solar and Wind Energy Using IDVR

Figure 3 depicts the block diagram representation of the proposed system. The interconnection of the utility grid with a renewable source of energy creates power quality issues. IDVR system consists of two DVR connected back to back with a common DC link. Two DVRs of IDVR are connected to two various feeders which are fed from two grids with solar and wind sources. These two feeder voltage levels could be equal or different.

Whenever the power quality issues occur in any one of the load, one of the DVR mitigates the voltage quality, the other DVR in IDVR system is operated in power flow control mode to restore the DC link capacitor. The poor voltage quality in the power system occurs due to a fault, which depends on many factors like fault current, different voltage level and transformer connecting arrangement. To overcome the above factors, the IDVR system should be connected in two feeders and each feeder is connected to two different grid sources. Figure 4 shows the flowchart of IDVR

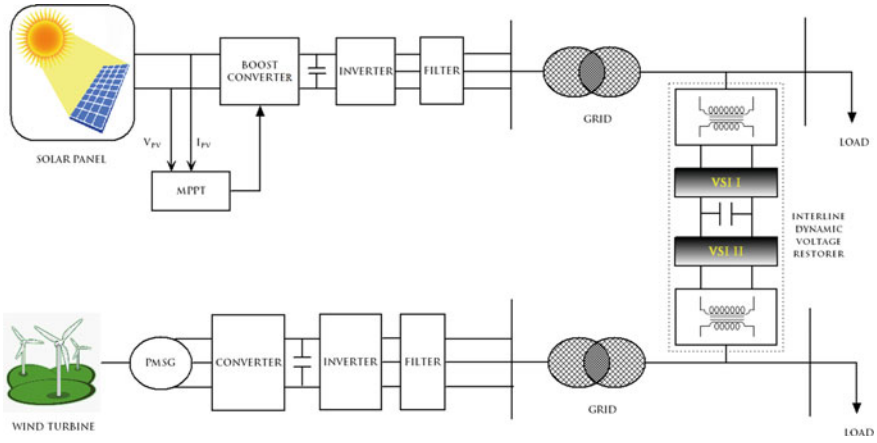

Fig. 3 Block diagram representation of proposed system

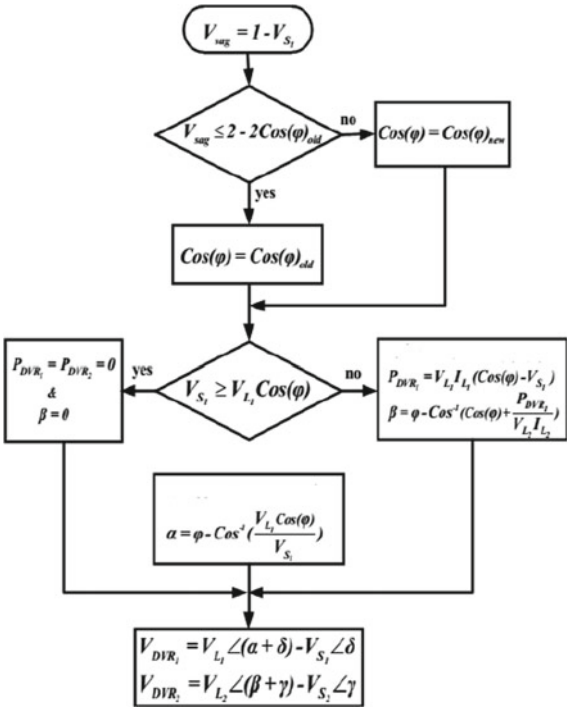

Fig. 4 Flowchart of the IDVR control system

control system. In this control strategy, first the amplitude of voltage sag is calculated and compared with $2 - 2(\varphi)$. If the voltage sag amplitude is greater than this value, then the shunt reactance are similar to the loads to decrease the load power factor. Next, with respect to equivalent power factor which is seen by the source voltage, the DVR voltages are resolved. This control system needs a quick and exact estimation framework for figuring of magnitude and phase of relating waveform.

3 Simulation Results and Discussion

To investigate the system performance in voltage compensation, several simulations have been done in the MATLAB/Simulink software on a single-phase IDVR.

Single line diagram of the proposed model with IDVR that is simulated is shown in Fig. 5. Figure 5: Simulink diagram of two bus system is connected in solar and wind energy source with IDVR. The output voltage of solar and wind generating stations are depicted in Figs. 6 and 7, and their values are 2000 V and 4000 V, respectively. Figure 8 shows the real and reactive power.

Figure 9 shows the voltage across the load in feeder 2 without compensation. Figure 10 shows the injecting voltage from IDVR in feeder 2. Voltage across the load in feeder 2 with compensation using IDVR is shown in Fig. 11. Frequency

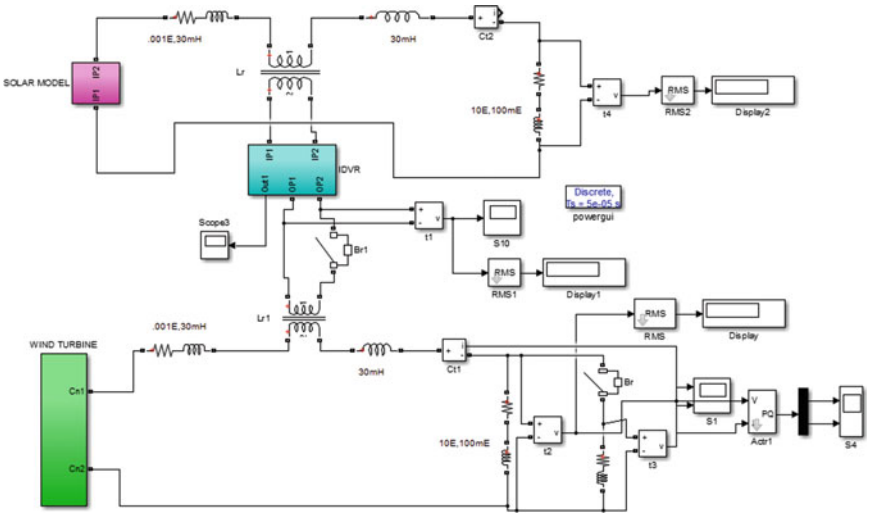

Fig. 5 Simulink diagram of two bus system is connected in solar and wind energy source with IDVR

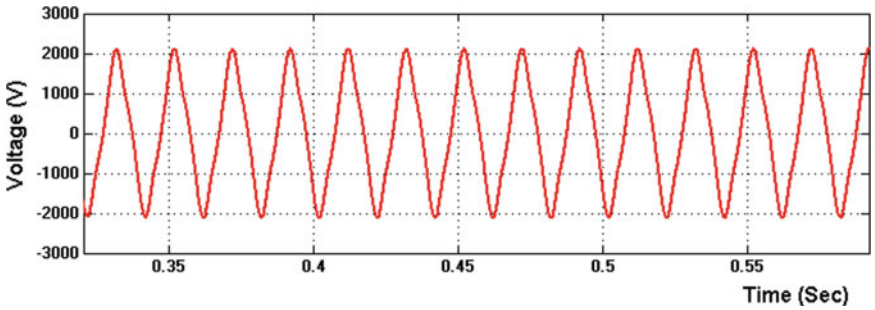

Fig. 6 Output voltage of solar generating station

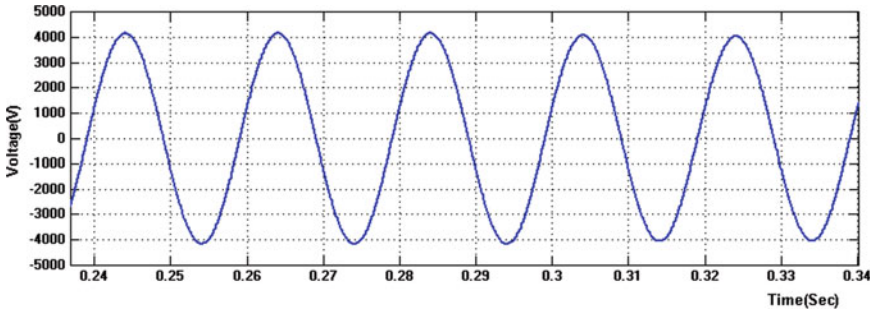

Fig. 7 Output voltage of wind generator

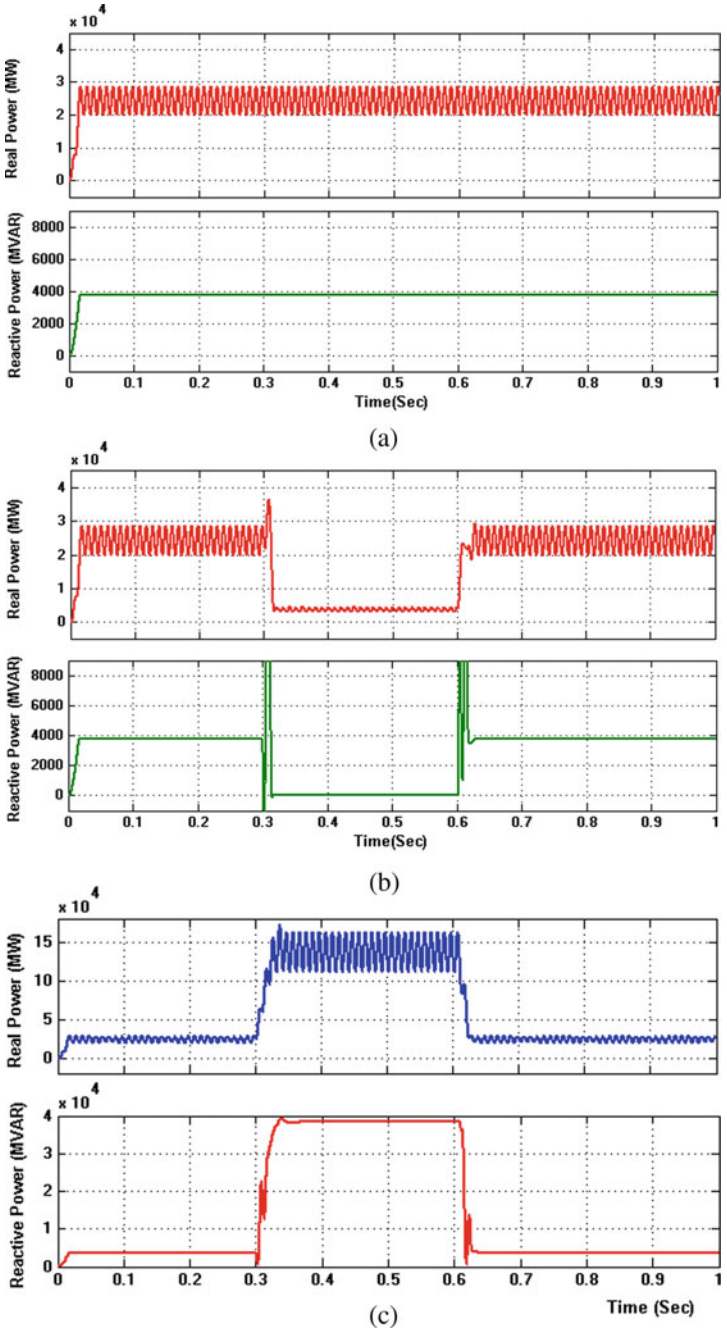

Fig. 8 Real and reactive power across the load in feeder 2. **a** Linear condition. **b** Nonlinear condition. **c** Nonlinear with compensation using IDVR

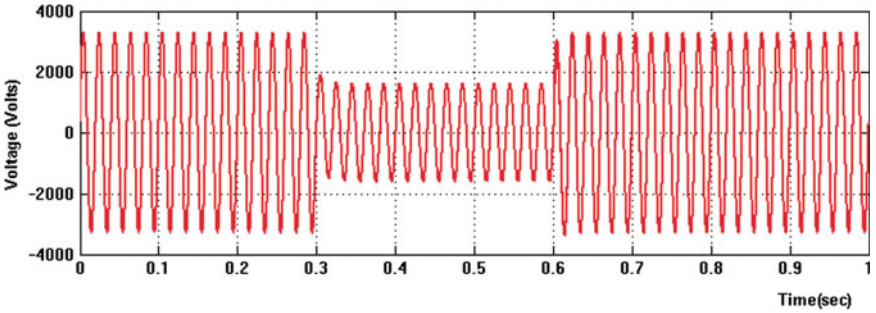

Fig. 9 Voltage across the load in feeder 2 without compensation

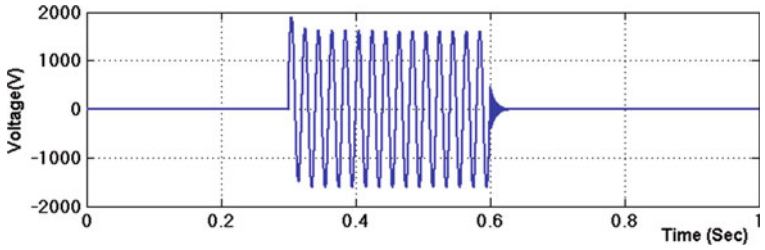

Fig. 10 Injecting voltage from IDVR in feeder 2

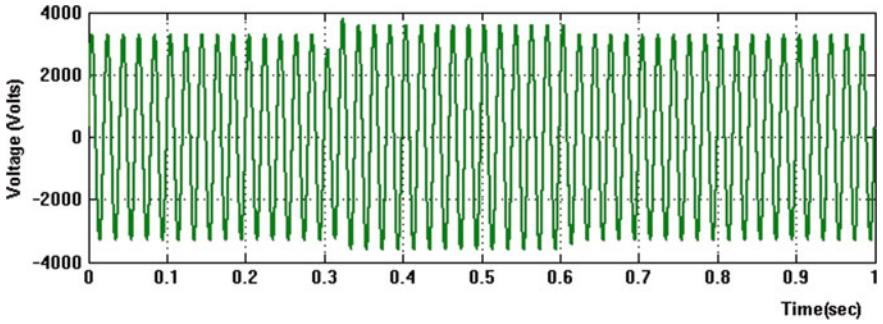

Fig. 11 Voltage across the load in feeder 2 with compensation using IDVR

spectrum analysis with IDVR system is 4.85% and it is Fig. 12. Table 1 shows the summary of real and reactive power loss with DVR and without DVR. Summary of real and reactive power across the load is shown in Table 2, and their values with nonlinear load using IDVR are 0.992 MW and 0.05043 MVAR.

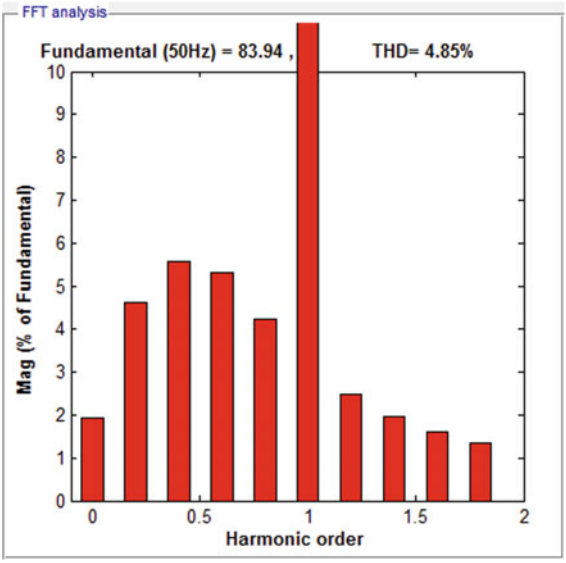

Fig. 12 Frequency spectrum analysis with IDVR system

Table 1 Summary of real and reactive power loss with DVR and without DVR

Feeder	Real power loss Without IDVR (MW)	Real power loss With IDVR (MW)	Reactive power loss Without IDVR (MVAR)	Reactive power loss With IDVR (MVAR)
Feeder 1 (solar energy source)	0.0754	0.0521	0.0351	0.0278
Feeder 2 (Wind energy source)	0.3671	0.2184	0.3210	0.2047
Total loss	0.4425	0.2705	0.3561	0.2325
% loss reduced using IDVR	35%		25%	

Table 2 Summary of real and reactive power across the load

Feeder 2	Real power (MW)	Reactive power (MVAR)
Normal condition	0.564	0.03753
Voltage sag without IDVR	0.394	0.01750
Voltage sag with IDVR	0.992	0.05043

4 Conclusion

IDVR is the advanced CPD device used for wind and solar energies utilization. Simulation of two bus system using solar and wind energy with and without IDVR is simulated using MATLAB/SIMULINK and analyzed in terms of real and reactive power. The real power and reactive power of feeder 1 (solar energy source) is improved with IDVR when compared without IDVR and its values are found to be 0.0521 MW and 0.0278 MVAR, respectively. Feeder 2 (wind energy source) has improved real power and reactive power with IDVR and its values are 0.992 MW and 0.05043, respectively. The total real power and reactive power losses are found to be decreased by 17% and 12%, respectively, by employing IDVR.

References

1. Ghiasi M, Esmaeilnamazi S, Ghiasi R, Fathi M (2020) Role of renewable energy sources in evaluating technical and economic efficiency of power quality. Technol Econom Smart Grids Sustain Energy 5(1):1
2. Jain SK, Soni A (2020) Mitigation of power quality for wind energy using transmission line based on D-STATCOM. In: Intelligent computing techniques for smart energy systems, Springer, Singapore, pp 927–935
3. Ola SR, Saraswat A, Goyal SK, Sharma V, Khan B, Mahela OP, Alhelou HH, Siano P (2020) Alienation coefficient and wigner distribution function based protection scheme for hybrid power system network with renewable energy penetration. Energies 13(5):1–25
4. Khadem SK, Basu M, Conlon M (2010) Power quality in grid connected renewable energy systems: role of custom power devices
5. Gowrishankar A, Ramasamy M (2020) Experimental validation of solar photovoltaic-based unified power quality conditioner with modified power angle control scheme. J Test Eval 48(1)
6. Mallesham G, Kumar CS (2020) Power quality improvement of weak hybrid PEMFC and SCIG grid using UPQC. In: Advances in decision sciences, image processing, security and computer vision, Springer, Cham, pp 406–413
7. Sarker K, Chatterjee D, Goswami SK (2020) A modified PV-wind-PEMFCS-based hybrid UPQC system with combined DVR/STATCOM operation by harmonic compensation. In: Int J Model Simul pp 1–13
8. Suresh P, Baskaran B (2017) Power quality improvement of nine bus system during line interruption using IVDFC. Int J Appl Eng Res 12(10):2527–2537
9. Suresh P, Baskaran B (2017) Voltage sag compensation in multiline distribution system using closed loop controlled IDVR. Int J Appl Eng Res 12(8):1576–1583
10. Suresh MP, Ramya MG, Vijayalakshmi MK, Babu KS, Nithya MS (2018) Performance of DVR and IDVR For voltage sag compensation in power distribution network. Int J Pure Appl Math 119(16):4225–4239

Enhanced Hybrid Touch Screen Display for Industrial Applications

A. Vignesh Babu, J. Ajay Daniel, V. N. Ganesh, S. Balaji, and G. Ramya

Abstract A Hybrid model with resistive touch and laser grid system is the solution proposed to rectify the problems faced by the existing industrial touch screen displays. Placing laser grid above the touch screen has improved the touch recognition and also reduces the possibility of erroneous inputs. Lasers and phototransistors are placed above the bezel of the display to form the laser grid. Laser grid forms a 2-dimensional co-ordinate system for navigation of input location on the display. In order to avoid unnecessary inputs caused by non-human entities like dust, flies, etc., inputs should be taken by both laser grid and resistive touch panel simultaneously. Touch input is taken into account only when the co-ordinates from both resistive touch screen and laser grid are the same. If not, co-ordinates from laser grid alone are taken to calibrate the resistive touch screen. If the calibration is not successful, then the touch functionality is fully taken over by laser grid system.

Keywords Resistive touch screen · Laser grid system · Hybrid touch screen

1 Introduction

Nowadays, touch screen display plays a major role in every industry, and they are widely implemented to enable features that allow complex touch inputs. Touch

Present Address:
A. Vignesh Babu (✉) · J. Ajay Daniel · V. N. Ganesh · S. Balaji · G. Ramya
Department of Electrical and Electronics Engineering, SRM Institute of Science and Technology, Ramapuram, India

J. Ajay Daniel
e-mail: ajaydanj@srmist.edu.in

V. N. Ganesh
e-mail: ganeshv1@srmist.edu.in

S. Balaji
e-mail: balajis2@srmist.edu.in

G. Ramya
e-mail: ramyag@srmist.edu.in

C. Subramani et al. (eds.), *Proceedings of International Conference on Power Electronics and Renewable Energy Systems*, Lecture Notes in Electrical Engineering 795,
https://doi.org/10.1007/978-981-16-4943-1_48

display gives many features such as multi-touch operations, gesture control. Devices with touch screen displays also have a longer lifetime than the older devices with mechanical keys.

The equipment in an industry is controlled from small computers called Human Machine Interfaces (HMI). These HMIs are equipped with resistive touch screens which results in reduced clarity and they are also easily prone to scratches/cracks. Since any malfunction of HMI directly affects the production, it is necessary to provide a reliable solution to improve durability and precision of touch sensing in HMI touch screens.

Finger touch can be recognized by various methods such as measurement of pressure, variation in electrical characteristics and optical sensing [6]. Resistive touch panel depends on both pressure and variation in electrical characteristics. Touch panels which depend only on electrical characteristics are capacitive touch panels. Optical touch panels include infrared touch screens which detects touch inputs with photodetectors.

For industrial applications, resistive touch screens are mostly preferred over capacitive touch screens. The touch screen devices are placed near manufacturing lines on-field where the operators are supposed to always wear protective gloves and capacitive touch screens won't respond when used with a glove which makes resistive touch screen the obvious choice in industrial applications. Since resistive touch screens are used, features such as multi-touch and gesture controls cannot be implemented in industrial displays.

Another such technology which can be implemented to improve precision and durability is optical touch screen [1]. Optical touch screens also have the ability to incorporate features such as multi-touch, gestures controls and sensitivity but implementing optical touch screens alone will not be a proper solution as the optical sensing could misidentify any dust particle or insects as a touch input.

The proposed solution is a hybrid that brings together the features of resistive and optical touch screen technologies and also compliments each other to eradicate their individual disadvantages.

2 Existing Technologies

Currently, most industries use resistive touch screens for almost all Human Machine Interfaces. The few applications that use capacitive touch screens are located in places like control rooms where there is no need for usage of gloves. Surface Acoustic touch screen is another new technology which is sparsely implemented.

The major disadvantage of resistive touch screens is that multi-touch cannot be implemented and it is easily affected by temperature changes. Since touch sensing in resistive touch screen depends on resistance measurement, the display might take erroneous inputs under non-ideal temperatures and such conditions require frequent calibration of the touch screen. Implementation of resistive touch screen also reduces the clarity of the display because of a thin resistive layer present on top of the display.

It is more prone to scratches and cracks. If there are any cracks, it might stop working or take improper inputs. Since these resistive touch screens are under repeated stress because every touch is done with a small amount of pressure to make the two resistive layers within it to meet resulting in a change in electrical characteristics. On the other hand, capacitive touch screens are more sensitive than resistive touch screens, it enables multi-touch capabilities which in turn provides multiple gesture controls. Unlike resistive touch screen, capacitive touch screen does not reduce the clarity of the display. It works even with small crack or scratches. Hardened glasses can be placed above the capacitive touch layer in order to prevent cracks or scratches. These displays cannot be used while wearing gloves. Since it does not need any pressure for sensing, its lifetime is comparatively higher than the resistive touch screen.

The optical touch screens include infrared and laser-based touch screens. This technology is not as reliable as the previous technologies as it can easily misjudge any kind of dust particle/flying insect to be a touch input.

Surface Acoustical Wave is another similar technology which makes use of sound wave reflectors to detect touch input. The major issue with this technology is its vulnerability to external interferences and very low lifetime.

3 Proposed Solution

The proposed solution is a combination of both resistive touch screen and optical touch screen technologies. The optical touch screen based on laser grid system has the major advantage of being precise and resistant to damages done by repeated usage but it can misread any kind of interruption between laser diodes and phototransistors as an input which can lead to unintended operations. The resistive touch screens are already widely used in industries but they lack features like multi-touch and gesture control. These resistive touch screens are also vulnerable to damages like cracks due to repeated stress on its surface. This technology also has the drawback of being defective under non-ideal heat conditions. These drawbacks of optical and resistive touch screens can be overcome by combining them both and making a hybrid system with them. This solution is feasible as this can be implemented on existing HMIs with minimal cost and labor. When a touch input is given, Both the laser grid system and resistive touch screen system recognizes the input and the co-ordinates from both these systems are taken in by microcontroller unit and it processes the data to give out the corresponding output on the display (refer Fig. 1).

4 Simulation

The simulation for the proposed solution is done using proteus simulation software. The model of laser grid is created using switches which represent the sensing points on the touch screen (refer Fig. 2). Each time these switches are turned on, it simulates

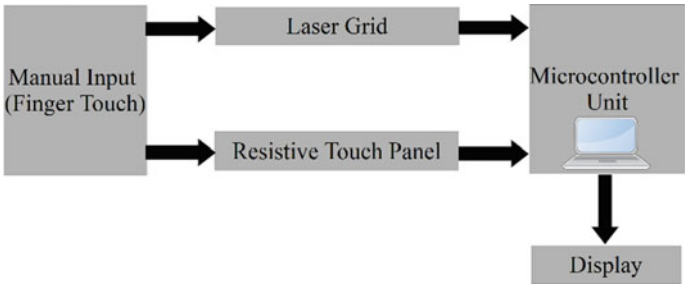

Fig. 1 Block diagram of proposed hybrid solution

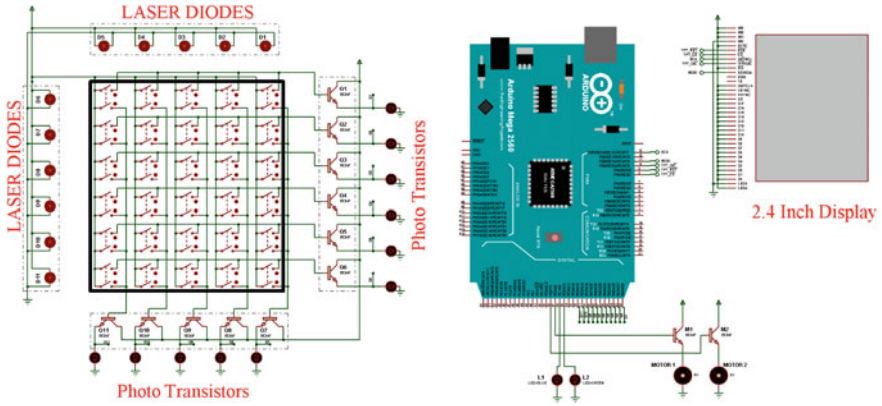

Fig. 2 Proteus simulation model

the process done when a touch input is given at that point on the touch screen. The inputs from this laser grid model are taken to the Arduino mega microcontroller unit for processing. The display is shown separately in the model but in reality, the laser grid will be placed above the screen itself.

The simulations show that the touch response from the laser grid is properly recognized by the microcontroller unit and being displayed on the display.

5 Construction

The simulation for the proposed solution is done using proteus simulation software. The model of laser grid is created using switches which represent the sensing points on the touch screen (refer Fig. 2). Each time these switches are turned on, it simulates the process done when a touch input is given at that point on the touch screen. The inputs from this laser grid model are taken to the Arduino mega microcontroller unit

for processing. The display is shown separately in the model but in reality, the laser grid will be placed above the screen itself.

5.1 Laser Grid Formation

Optical touch system is created by forming a laser grid array using laser diodes and phototransistors. Laser diodes are placed on one horizontal and one vertical side serially and phototransistors are placed on opposite sides to the laser diodes. Figure 3 shows the arrangement of laser diodes and phototransistors.

These laser diodes and phototransistors are placed in a custom designed 3-*d* model which houses these components and is capable of being placed above the resistive touch screen.

Each intersection point represents laser light intersections. Touch is recognized only on these intersections when a finger blocks the laser beam from hitting its corresponding phototransistor. This prototype model has lower resolution because there are only 11 phototransistors and 11 laser diodes which are arranged as 5 in horizontal and 6 in vertical positions. To increase the resolution, number of laser diodes and number of phototransistors should be increased which will result in increase in the number of touch points.

This laser grid structure is placed above the resistive touch screen display and they are both connected to an Arduino mega for processing the operations.

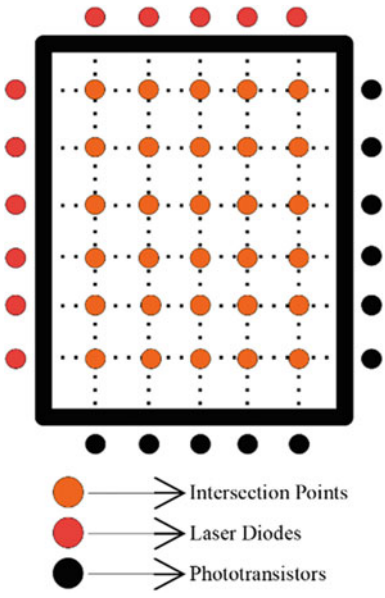

Fig. 3 Laser grid arrangement

5.2 Resistive Touch Panel

The prototype is made with a 2.4-inch TFT LCD resistive touch display module which is compatible with Arduino. It is a 4-wire resistive touch screen with a display resolution of 240×320 pixels. A 4-wire resistive touch screen has two conductive layers which are placed one on top of the other spaced in-between by spacer dots to prevent sagging. The 4 wires are on the 4 edges of the screen and they are responsible to detect the co-ordinates. Whenever a pressure (touch) is given on a point on the screen, the top layer comes in contact with the bottom layer. To obtain the X co-ordinate, a voltage is applied from left wire to right wire and the voltage drop at the sensing point is captured. To obtain the Y co-ordinate, a voltage is applied from top wire to bottom wire and the voltage drop at the sensing point is captured. These captured voltages drop values are processed by the processing unit to identify the point of touch on the screen.

5.3 Design Considerations

Laser grid is placed slightly above the display (around 5 mm above the surface) to avoid any foreign particles such as dust or insects to disrupt the laser beam. Figure 4 shows the arrangement. This positioning is extremely necessary for displays which are placed horizontally, due to gravity some foreign particles might fall on the display which could interrupt the laser grid. Such foreign particles would normally lie well below the laser beams or they might not have enough pressure to be recognized by resistive touch screen, and since the hybrid system needs both inputs, there erroneous inputs can be prevented. 5 mm is the threshold height of laser beam above screen surface that has been implemented in the prototype. This height is more than enough to overcome the issues which will be faced by these foreign particles.

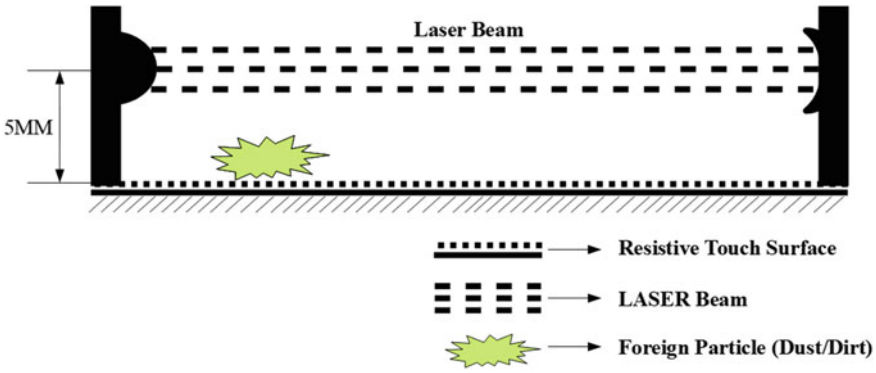

Fig. 4 Design consideration (Height)

5.4 Processing Unit

A program is written on Arduino to integrate both the resistive and laser grid system to get input co-ordinates. Additionally, multi-touch feature is also coded. The Arduino mega is used as the processing unit. The inputs from both the systems are taken and compared by the Arduino. When both the systems show same co-ordinates, the Arduino does a corresponding processing to perform intended operation. When the co-ordinates from the two systems are not same, then the Arduino tries to calibrate the resistive screen with the laser grid inputs as reference. If the resistive screen is not calibrated properly, then the input sensing is totally taken over by laser grid alone.

5.5 CAD Model

A 3-*D* printing model had to be created for housing the laser diodes, phototransistors and resistive touch screen together. The 3-*D* model was designed using Autodesk 360 Fusion (as shown in Fig. 5). The number of lasers and phototransistors used in the

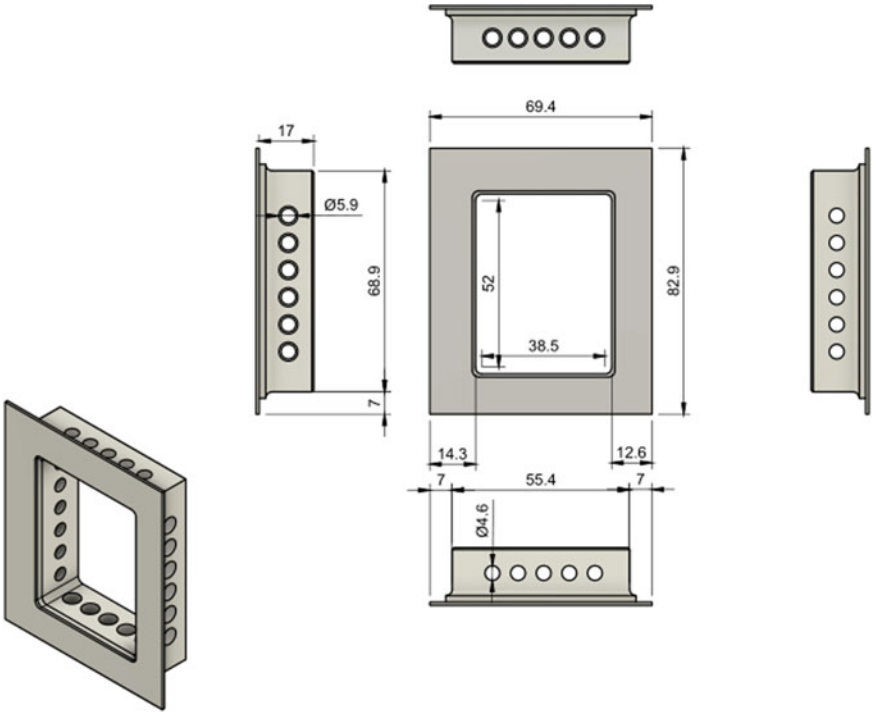

Fig. 5 CAD model for prototype housing

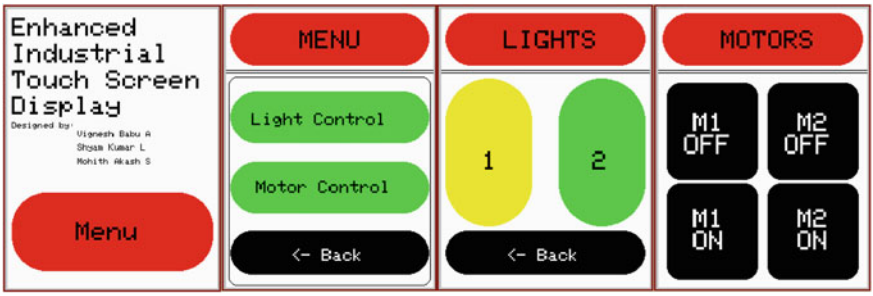

Fig. 6 Main screen, menu screen, lights and motors control page

prototype are few due to size and budget constraints but with custom manufactured components, this solution could be easily implemented with lesser size and also at a reduced cost (Fig. 5).

6 Working

The flow chart in Fig. 7 shows the actual algorithmic workflow when a touch is sensed in this system. The system is actively waiting to sense any kind of touch input. When it identifies any input that blocks laser beam and also provides pressure on resistive touch screen, it is validated as a proper touch. The co-ordinates are obtained from both resistive panel and laser grid and compared to check if they are equal. The corresponding operation is carried on when both the co-ordinates are equal. If they are not equal, the system tries to calibrate the resistive touch screen with laser co-ordinates as reference. The values are compared again to check whether the calibration removed the error. If they are still not same, the calibration and checking process happens again for a maximum of three trials. After three trials, the resistive panel is totally removed off the loop and only the co-ordinates of laser grid are considered for operation.

6.1 Operations with Proposed Model

For demonstration purpose, the prototype is built to operate lights and motors. The prototype is supposed to be an HMI in an industry which is connected to 4 loads which are two lights and two motors. The demonstration is to showcase the multi-touch feature of this system. Figure 6 shows the main screen and the menu screen of the prototype. The light control screen is shown in Fig. 6. The light control screen helps to control lighting loads. The motor control screen has motor switching buttons (refer Fig. 6). This screen allows the user to simultaneously operate both the motors.

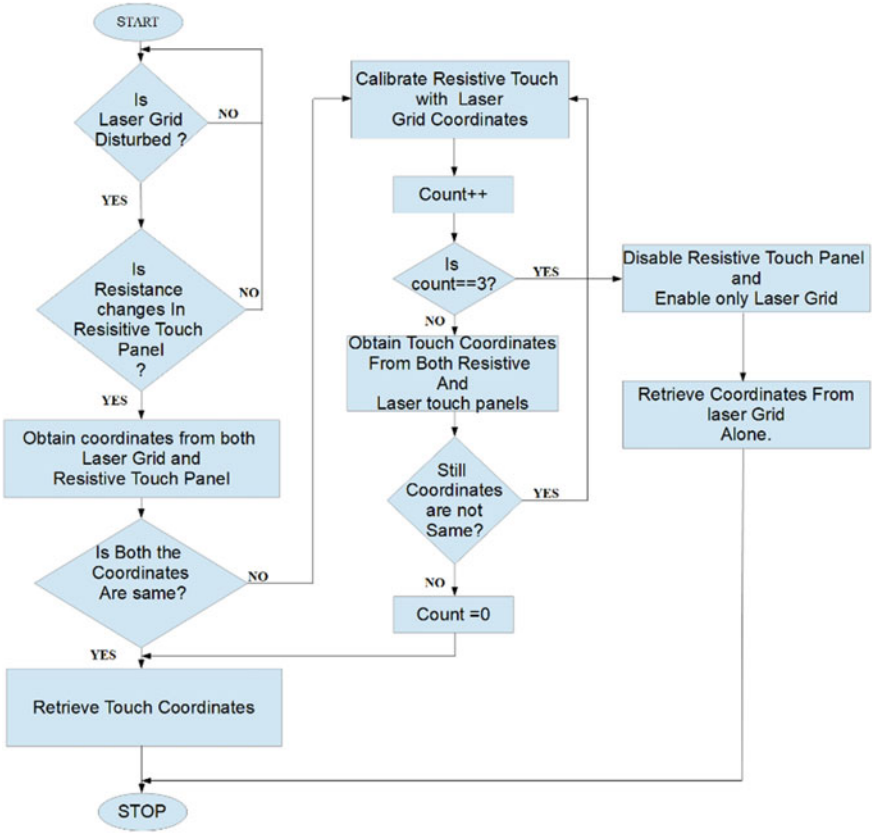

Fig. 7 Flow chart

The proposed model also has the ability to self-calibrate its resistive touch screen when it gets erroneous due to temperature changes. The working model that was created proved to overcome the challenges faced by the older isolated technologies.

7 Result

The simulation and prototype were developed and tested. The working prototype has been satisfactory in operation. Multi-touch functionality was tested by taking a case where 4 loads are operated simultaneously by turning on/off on the display by multi-touch. To perform multi-touch 4 loads such as 2 DC motors and 2 LEDs are connected to the Microcontroller, in which two motors can be turned on or off by simultaneously touching on/off button for the corresponding motor in the display. Similarly, 2 LEDs can be controlled simultaneously by providing 2 touch points.

The hybrid solution is working as intended and also overcomes the drawbacks of previous technologies.

References

1. Liang J, Lin K, Wang W (2018) Turn any display into a touch screen using infrared optical technique. vol 6, pp 13033–13040

Reliability Study on the Distribution System Integrated with Wind Generator

S. B. Aruna and D. Suchitra

Abstract Electricity should be provided to the customers with good quality and continuity of power supply. To predict the future of distribution system performance, reliability assessment is one of the major factors that have to be considered. Reliability assessment helps in designing and planning of distribution system and also helps in analyzing the severity of the system failures. The system performance indices for reliability help in analyzing the severity of the system failures and thereby help in predicting the reliability of the system in future. In this paper, the system performance analysis has been simulated in ETAP on the Bus 2 of Roybillinton Test system (RBTS) for Feeder 1, 3 and 4. The system performance indices such as SAIFI, SAIDI, CAIFI, ASAI, ASUI, AENS and EENS under different scenarios of operations with and without distributed generator have also been analyzed.

Keywords Reliability Assessment · Distribution generation · Load oriented indices · RBTS

1 Introduction

Power systems are subjected to random faults due to component failures, transmission faults, climatic conditions, etc. Regarding the modeling and operation of the power network, maintaining a reliable power supply becomes a crucial factor that needs to be addressed first for the better operation of the system. The concept of power system reliableness is extraordinarily broad and covers all the aspects associated with the flexibility of the power system to produce adequate supply of electricity thereby satisfying the user's necessities. Electric power utilities also face increasing uncertainty due to the political, economic, societal and environmental constraints, as they have to effectively operate the existing system and also should plan for the

S. B. Aruna (✉) · D. Suchitra
Department of Electrical and Electronics Engineering, SRM Institute of Science and Technology, Kattankulathur, India

D. Suchitra
e-mail: suchitrd@srmist.edu.in

C. Subramani et al. (eds.), *Proceedings of International Conference on Power Electronics and Renewable Energy Systems*, Lecture Notes in Electrical Engineering 795,
https://doi.org/10.1007/978-981-16-4943-1_49

enhancement to manage the ever increasing demands. All these conditions have created an environment for the utility to plan for the new facilities, optimal use of the existing system configuration for the improvement in system reliability and reduced operation costs [1]. The Distributed Generators (DG) are connected near to the load centers in the distribution network for obtaining a better reliability of the system. By connecting DG at the appropriate locations in the distribution system, the power demand of the system can be satisfied which in turn improves the reliability. When properly designed, a regional power grid that combines both large central plants and distributed generator can provide higher capacity factor on all the assets and reliability enhancement.

Many research has been carried out until now, considering the various aspects of reliability with respect to power system. More number of techniques for reliability evaluation of distribution system and significance of reliability indices were summarized in [2]. The impact of distributed generators with respect to the reliability was described and analyzed with various ratings at different locations on distribution system [3]. The significance of integration of distribution generation with the various reliability indices was analyzed, with the different case studies [4]. Reliability analysis of distribution system under the impact of different operating configurations were presented in [5]. Reliability Index for the distribution system with distribution generation and its effect on the power losses were explained in [6]. Reliability assessment of the medium voltage network with respect to automation, aging and load growth were presented in [7]. Reliability assessment of the overall power system with various hierarchical levels and analysis of reliability indices with actual customer levels of service was explained in [8]. Hence, this work analyzes the impact of DG on the reliability, based on the various indices, by varying the locations of the DG. Also, it brings out the best location of the DG for the considered feeder.

2 Reliability Indices of Distribution System

Providing an uninterrupted and quality power supply to its consumers becomes the main objective of the distribution system. Normally distribution networks are radially configured, so failure of single section may lead to whole supply interruption. Hence, reliability of the system has a major impact on such system, and therefore, system performance has to be completely analyzed. Failure rate, repair time and annual unavailability of the system are the primary reliability indices used to envisage the reliability of a distribution system. The overall System performance indices such as SAIDI, SAIFI, CAIDI, ASAI, ASUI, EENS and AENS were also evaluated to assess the operating conditions of the distribution systems. The system performance indices of the utility with respect to distribution level are as follows:

System Average Interruption Frequency Index (SAIFI) [int/yr]

$$= \frac{\text{Total Number of customer interruptions}}{\text{Total number of customers served}} = \frac{\sum \lambda i Ni}{Ni} \tag{1}$$

where N_i represents the number of customers at load point 'i', λ_i represents failure rate.

System Average Interruption Duration Index (SAIDI) [hr/yr]

$$= \frac{\text{Total Number of customer interruption duration}}{\text{Total number of customers served}} = \frac{\sum \text{U}i\,Ni}{Ni} \tag{2}$$

Customer Average Interruption Duration Index (CAIDI)[hr/int]

$$= \frac{\text{Total Number of customer interruption Durations}}{\text{Total number of customers interruptions}} = \frac{\sum \text{U}i\,Ni}{\sum \lambda i\,Ni} \tag{3}$$

Average Service Availability Index (ASAI)

$$= \frac{\text{Customer hours available in service}}{\text{Customer hours demanded}} = \frac{\sum 8760Ni - \sum \text{U}i\,Ni}{\sum 8760Ni} \tag{4}$$

where U_i represents annual unavailability.

Average System Unavailability Index (ASUI)

$$= \frac{\text{Customer hours not available in service}}{\text{Customer hours demanded}} = \frac{\sum \text{U}i\,Ni}{\sum 8760Ni} = 1 - \text{ASAI} \tag{5}$$

Expected Energy Not Supplied (EENS) [hr/yr] $= \sum_{i=1}^{n} E_i$ (6)where E_i represents the average of interruption energy per load point.

Average Energy Not Supplied (AENS) [kWh/yr] $= \frac{\sum_{i=1}^{n} E_i}{N_i}$ (7)

3 Test System Description

Roy Billinton Test System (RBTS) is a benchmark system, which is considered for the reliability study to estimate the overall reliability indices. RBTS was developed by university of Saskatewan, Canada for carrying research activities in 1996. RBTS is a system with five load buses and eleven-generator bus. The installed capacity is 240 MW and peak load of the system is 185 MW. This system has five voltage levels 230 kV, 138 kV, 33 kV, 11 kV, 415 V. Figure 1 depicts the RBTS Bus-2 system that is considered for the reliability analysis in this work [9, 10].

This system has 22 load points with four feeders at a working voltage of 11 kV. A Breaker is positioned at the source end of the 11 kV main feeder. It is calculable that the operation of the breaker is 100% and the breaker is opened if any fault happens within the system. Also, it separates the faulty load area in order that the service is sustained for the remaining customers with the healthy load points. A

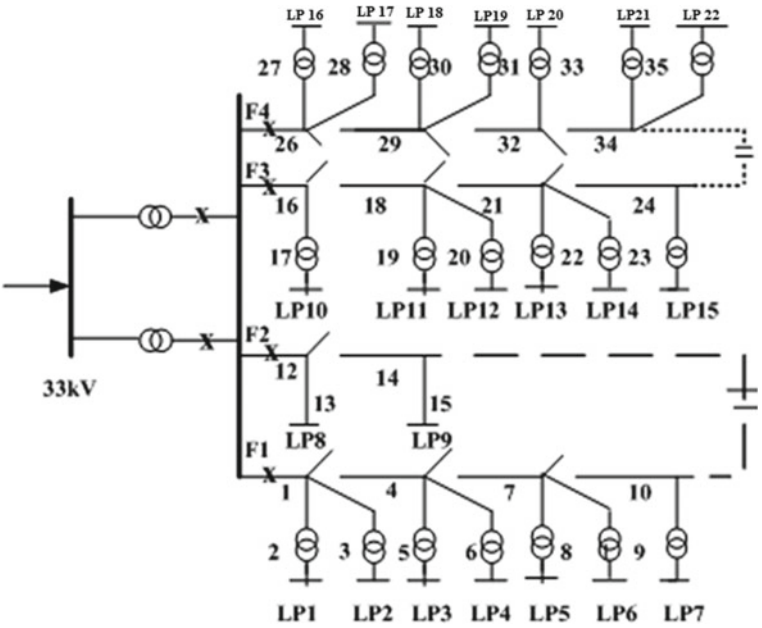

Fig. 1 Roybillinton bus-2 test system

radial distribution feeder along with main and lateral feeder sections are considered. Load points are connected to the main feeder through lateral distributors. Fuses are used in distributors to eliminate failures on the lateral section from the main feeder. Disconnects or isolators are used in main feeder section to detach faulted sections. Furthermore, an alternate power supply is provided to the healthy load points with the aim continuing the service throughout the failure. Table 1 is listed with the input data of main feeder and lateral distributors. The reliability parameters for the different components connected to the system is given in Table 2. The input data related to peak load with respect to load point connected is specified in Table 3.

Table 1 Main feeder and lateral distributor load point and distance data

Length in km	Load points in feeders
0.60	4, 6, 9, 14, 15, 18, 24, 29, 31, 32
0.75	1, 2, 3, 5, 7, 10, 12, 13, 20, 25, 27, 30, 35
0.80	8, 11, 16, 17, 19.21, 22, 23, 26, 28, 33, 34, 36

Table 2 Reliability parameters of components connected to the system

Components connected	Failure rate (f/hrs)	Repair rate (hrs)	Switching time (hrs)
Transformers			
33 kV/11 kV	0.015	15	1
11 kV/0.415 V	0.015	10	1
Breakers			
33	0.002	4	1
11	0.006	4	1
Bus bars			
33	0.001	2	1
11	0.001	2	1
Feeder			
11	0.065	5	1

Table 3 Peak load data of load points

Load points connected to feeders	Type of customer connected	Load point customers	Peak load (MW)
1, 2, 3, 10, 11	Residential	210	0.8668
12, 17, 18, 19	Residential	200	0.4500
4, 5, 13, 14, 20, 21	Government and industrial	1	0.566
8	Industrial	1	1
9	Industrial	1	1.15
6, 7, 15, 16, 22	Commercial	10	0.454

4 Reliability Evaluation of RBTS Bus-2 System Integrated with Distributed Generation

A wind turbine generator is taken as DG source and integrated into feeders 1, 3 and 4 of RBTS Bus-2. Feeder-2 consists of only two load points so integrating wind turbine will not have more impact on the system performance so remaining feeders are taken for reliability analysis. A Wind turbine with a rating of 1 MW has been integrated for feeder 1 of RBTS Bus 2. The failure rate and average repair time of wind turbine are 0.25 f/yr and 20 h respectively. The wind turbine integrated with feeder is considered to operate with the average wind velocity $V_{avg} = 4.05$ m/sec, rated velocity $V_r = 10$ m/sec, cut in velocity $V_{ci} = 2.0$ m/sec, cut off velocity $V_{co} = 22$ m/sec. The Test system RBTS Bus 2 Feeders 1, 3 and 4 have been simulated in ETAP (Electrical Transients Analysis Program) environment [11, 12]. The reliability indices were calculated at various distances from supply terminal of the Feeders. The wind turbine generator has been placed at four distant locations and indices were calculated for Feeders -1, 3 and 4 (Fig. 2).

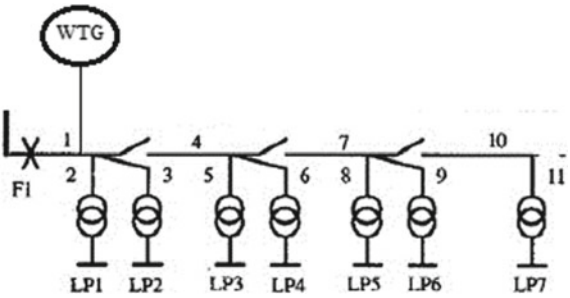

Fig. 2 RBTS Bus-2 system feeder-1 connected with DG

Case study-1:

Feeder-1 of RBTS consists of seven load points, i.e., LP-1 to LP-7 with different categories of customers. The reliability indices were calculated for the following scenarios by placing wind turbine generator at various distant points from supply terminal of feeder-1.

Scenario -1: RBTS Bus -2 Feeder 1 without Distributed Generator (DG).

Scenario -2: RBTS Bus -2 Feeder 1 with DG at 1.35 km away from supply point.

Scenario -3: RBTS Bus -2 Feeder 1 with DG at 2.3 km away from supply point.

Scenario -4: RBTS Bus -2 Feeder 1 with DG at 3.05 km away from supply point.

Scenario -5: RBTS Bus -2 Feeder 1 with DG at 3.65 km away from supply point.

Case study-2:

Feeder-3 of RBTS consists of six load points, i.e., LP-10 to LP-15 with different categories of customers. The reliability indices were calculated for the following scenarios by placing wind turbine generator at various distant points from supply terminal of feeder- 3 (Fig. 3).

Scenario -1: RBTS Bus -2 Feeder 3 without Distributed Generator (DG).

Scenario -2: RBTS Bus -2 Feeder 3 with DG at 1.55 km away from supply point.

Scenario -3: RBTS Bus -2 Feeder 3 with DG at 2.15 km away from supply point.

Scenario - 4: RBTS Bus -2 Feeder 3 with DG at 2.9 km away from supply point.

Scenario - 5: RBTS Bus -2 Feeder 3 with DG at 3.5 km away from supply point.

Case Study-3:

Feeder-4 of RBTS consists of seven load points, i.e., LP-16 to LP-22 with different categories of customers. The reliability indices were calculated for the following

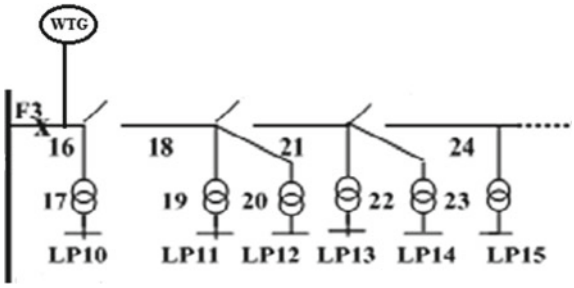

Fig. 3 RBTS Bus -2 system feeder -3 connected with DG

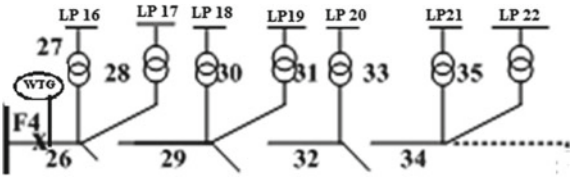

Fig. 4 RBTS Bus -2 system Feeder -4 connected with DG

scenarios by placing wind turbine generator at various distant points from supply terminal of feeder- 4 (Fig. 4).

Scenario -1: RBTS Bus -2 Feeder 4 without Distributed Generator (DG).

Scenario -2: RBTS Bus -2 Feeder 4 with DG at 1.35 km away from supply point.

Scenario -3: RBTS Bus -2 Feeder 4 with DG at 2.3 km away from supply point.

Scenario - 4: RBTS Bus -2 Feeder 4 with DG at 3.1 km away from supply point.

Scenario - 5: RBTS Bus -2 Feeder 4 with DG at 3.65 km away from supply point.

By using ETAP RBTS bus-2 feeder 1, 3 and 4 has been simulated and overall indices are listed in the following Table 4, Table 5 and Table 6.

Table 4 Reliability indices of bus-2, feeder-1 connected with DG at various distant points

Reliability indices of feeder-1	Scenario 1	Scenario 2	Scenario 3	Scenario 4	Scenario 5
SAIDI (hr/customer.yr)	6.5794	6.8617	5.6899	5.1305	5.0982
SAIFI (f/customer.yr)	1.2429	0.6538	0.5839	0.5549	0.5527
CAIDI (hr/customer.yr)	6.579	6.862	5.690	5.130	5.098
ASAI(pu)	0.9992	0.9992	0.9994	0.9994	0.9994
ASUI(pu)	0.00075	0.00078	0.00065	0.00059	0.00058
AENS (MW hr/customer.yr)	0.0394	0.0395	0.0364	0.0336	0.0317
EENS (MW hr/yr)	75.160	75.431	69.433	64.122	60.400

Table 5 Reliability indices of bus-2, feeder-3 connected with DG at various distant points

Reliability Indices of Feeder- 3	Scenario 1	Scenario 2	Scenario 3	Scenario 4	Scenario 5
SAIDI (hr/customer.yr)	6.5294	6.8130	6.1349	5.0570	5.0490
SAIFI (f/customer.yr)	1.2129	0.6520	0.5980	0.5435	0.5427
CAIDI (hr/customer.yr)	6.519	6.813	6.135	5.057	5.049
ASAI(pu)	0.9992	0.9992	0.9993	0.9994	0.9994
ASUI(pu)	0.00075	0.00078	0.00070	0.9994	0.00058
AENS(MW hr/customer.yr)	0.0394	0.0387	0.0369	0.0341	0.0317
EENS (MW hr/yr)	75.226	73.844	70.322	65.082	60.544

Table 6 Reliability indices of bus-2, feeder-4 connected with DG at various at various distant points

Reliability indices of feeder-4	Scenario 1	Scenario 2	Scenario 3	Scenario 4	Scenario 5
SAIDI (hr/customer.yr)	6.5294	6.7834	6.1032	5.0513	5.0457
SAIFI (f/customer.yr)	1.2129	0.6500	0.5954	0.5422	0.5414
CAIDI (hr/customer.yr)	6.519	6.783	6.103	5.051	5.046
ASAI(pu)	0.9992	0.9992	0.9993	0.9994	0.9994
ASUI(pu)	0.00075	0.00077	0.00070	0.00058	0.00058
AENS (MW hr/customer.yr)	0.0394	0.0393	0.0366	0.0342	0.0327
EENS(MW hr/yr)	75.226	75.029	69.915	65.301	62.451

5 Discussions

It is analyzed from Fig. 5 that, the interruption duration is more in the base case, i.e., without DG in three feeders. If any fault occurs in the feeder end or in lateral section, breaker disconnection will result in unsupplied energy for the customers in all the load points. Integration of 1 MW wind turbine generator at various distant points reduces the interruption duration especially at the ends of feeder.

It is observed from Fig. 6 that the failure rate of three feeders is high for the base case. Connecting DG of 1 MW at various distant points has reduced the failure rate considerably, when placed at 3.65 km away from supply point for feeder-1, 3.5 km away from the supply point for feeder-3 and 3.65 km away from supply point for feeder-4 hence increased the continuity of power supply to the feeder.

From Fig. 7, it is explored that, the Expected energy not supplied for the three feeders has reduced after the placement of DG of 1Mw and helps in providing the quality power to the consumers.

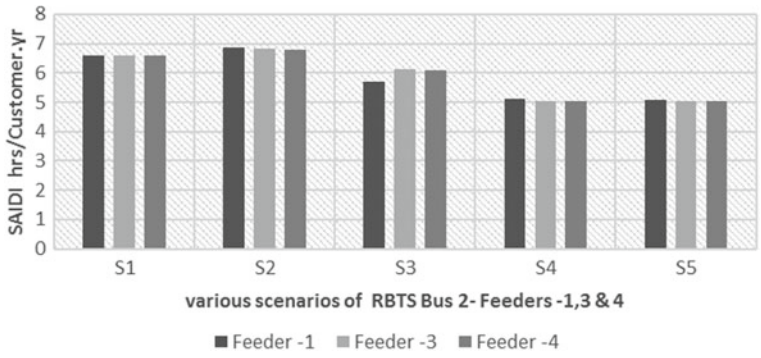

Fig. 5 SAIDI for RBTS bus-2- feeders-1, 3 and 4

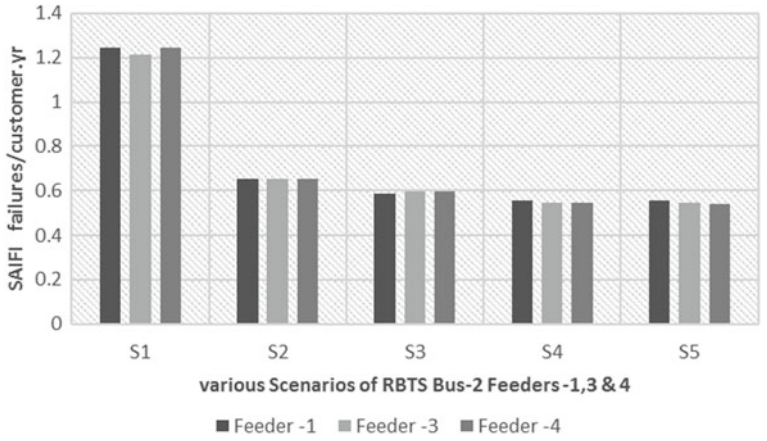

Fig. 6 SAIFI for RBTS bus-2 feeders-1, 3 and 4

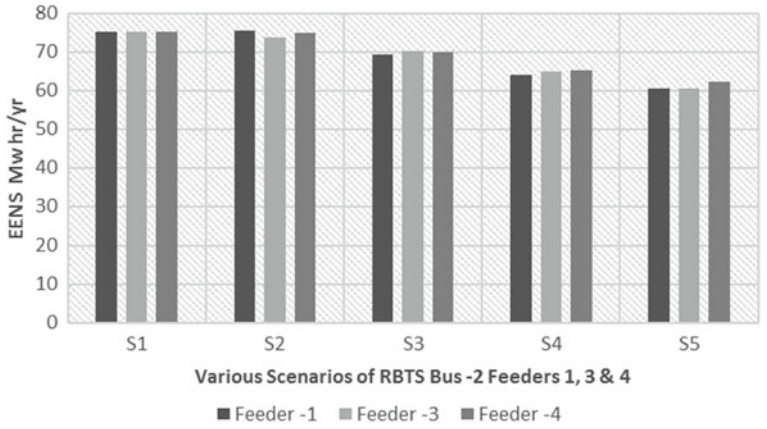

Fig. 7 Expected energy not supplied for RBTS bus-2 feeders-1, 3 and 4

6 Conclusion

The significances of reliability indices of Roybillinton Test system bus-2 feeders-1, 3 and 4 with the inclusion of the distributor generator at various distant points are analyzed. Five different scenarios are considered for the three feeders of bus-2 and the system performance indices are obtained by using ETAP simulation Tool. Associating the results of all the five scenarios of three feeders shows that the reliability indices SAIDI, SAIFI and EENS have been improved for all the load points due to the presence of DG. Injecting the Wind turbine generator as distribution generation source into feeder configuration has provided positive impact on distribution system reliability. Reliability analysis of distribution system provides an outline for

the performance assessment of distribution system and supports in progress of future load operations.

References

1. Chandhra Sekhar P, Deshpande RA, Sankar V (2016) Evaluation and improvement of reliability indices of electrical power distribution system. 2016 Natl Power Syst Conf NPSC, no 4. Nov 2017
2. Divakar V, Raviprakash MS, Keshavan BK (2016) A survey on methods of evaluation of reliability of distribution systems with distributed generation. Int J Eng Res V5(08):220–226
3. Sailaja CVSS, Prasad PVN (2016) Reliability and cost benefit analysis of DG integrated distribution system. Bull Electr Eng Informatics 5(4)
4. Subramanya Sarma S, Madhusudhan V, Ganesh V (2018) Reliability constrained planning of distribution system under high penetration of stochastic DG units. Int J Eng Sci Res Technol 7(3):538–548
5. Kirubarani K, Peer Fathima A (2019) Distribution system reliability assessment for improved feeder configuration. Int J Eng Adv Technol 8(6):4416–4421
6. Al-Maghalseh MMA (2018) Evaluating the reliability worth indices of electrical medium voltage network: case study. Procedia Comput Sci 130:744–752
7. Chiradeja P, Pothisarn C, Ngaopitakkul A (2020) The study of reliability indices, power losses, and economic effects when distributed generators (DG) connected to a distribution system. Int J Smart Grid Clean Energy 9(2):338–345
8. Sonwane PM, Kushare BE (2015) Distribution system reliability: an overview. 5(3):148–153
9. Billinton R (1996) A test system for teaching overall power system reliability assessment. IEEE transactions on power systems 11(4):1670–1676
10. Shiwen Y, Hui H, Chengzhi W (2017) Review of risk assessment of power system. Sci Direct Proceedia Comput Sci WTISG 2017 1200–1205
11. Ahmad S et al (2017) Reliability analysis of distribution system using ETAP. Int J Computer Sci Inf Secure 15(3):197–201
12. Ahmad S, Sardar S, Noor B, Ul A (2016) Analyzing distributed generation impact on the reliability of electric distribution network. Int J Adv Comput Sci Appl 7(10):217–221

Retrofitting of Internal Combustion Engine Vehicles with DC Motor

Femi Robert, Muskan Puri, Ashay Kumar Thakur, and Gajendran Marimuthu

Abstract This article gives a detailed report on the retrofitting of an IC engine vehicle with a specially designed DC motor. The emission losses of an old ICE vehicle increase and saturates to its highest value at around this time. The load and rpm analysis of ICE shows that the available usable torque to produce the desired RPM is in a very small range and thus replacing such engines with electric engines which have high torque to speed ratio will increase the performance of the vehicle greatly. The DC motor used in this application has been specially designed for the vehicle. The Total Tractive Effort (TTE) is calculated considering the curb weight of the chassis and then eliminating the components which are specific to the ICE such as engine and fuel tank. Other factors such as the static and dynamic friction, rolling resistances and other constants have been considered taking into account the road safety, road transportation and NHAI standards. The retrofitted vehicle has a curb weight less than that of the ICE counterpart. The high torque DC motor gives better acceleration and the high RPM provides better maximum speeds. The main goal is to have a used ICE vehicle and to completely renew it with a DC motor. This would eliminate the use of non-renewable fuels while also extending the life of the vehicle.

Keywords Electric Vehicle · ICE vehicles · DC motor · Sensors

F. Robert (✉) · M. Puri · A. K. Thakur
Department of EEE, SRM Institute of Science and Technology, Kattankullathur 603 203, India
e-mail: femir@srmist.edu.in

M. Puri
e-mail: mp8401@srmist.edu.in

A. K. Thakur
e-mail: at4206@srmist.edu.in

G. Marimuthu
Department of EIE, RMK Engineering College, Kavaraipettai 601 206, India

C. Subramani et al. (eds.), *Proceedings of International Conference on Power Electronics and Renewable Energy Systems*, Lecture Notes in Electrical Engineering 795,
https://doi.org/10.1007/978-981-16-4943-1_50

1 Introduction

Electrical vehicles are green traction drives that are currently used to replace the conventional type of vehicle such as internal combustion engine [1]. Electrical vehicles are very easy to operate, quite energy efficient while being very effective and better than LPG engines on all grounds such as cost, impact on environment. The development of electrical vehicles is increasing very rapidly, due to the environmental issues and fossil fuel shortages [2]. Electrical vehicles consist of a fuel cell electric vehicle (FCEV) and battery electric vehicle (BEV). EVs basically are generally considered to be consisting of different sub-systems. Each of the subsystems needs to work in tandem with each other to make an EV work [3]. There are many technologies used to develop coordination in between the systems. The heart of the EV is a motor. Normally for such applications, a DC series motor drive with armature control is used, which provides a very good high starting torque and a good speed regulation. The maximum speed of EV is equivalent to the speed of the motor [4]. A major sub-system for the EV is the drive circuit of the motor and its necessary sensor circuitry. Sensors are used for continuously reading the output of the battery in terms of the voltage and current delivered to the motor drive circuit. It also continuously monitors the temperature of the battery [5]. In this paper both the subsystems are used to make a setup for the EV. All the sensors used in the system are custom made.

2 Sensor Simulation Profile

The simulation is done on the MATLAB/Simulink and Proteus 8 Professional with some pre-defined and measured initial conditions.

2.1 Voltage Senor

It continuously senses the output voltage of the battery [6] and displays the output in digital form by the voltage division rule using the microcontroller. Equation for calculating the Voltage in the circuitry is shown below in Fig. 1

$$V = 24.0 - (0.4x) \tag{1}$$

$x =$ range of the voltage increase to the Arduino.

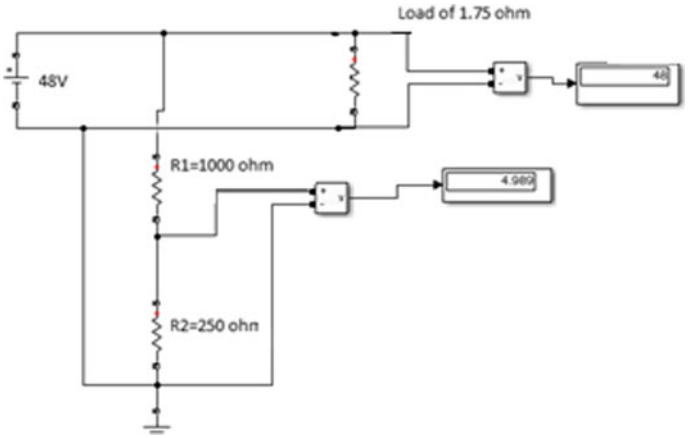

Fig. 1 Voltage Senor

2.2 Position Sensor (Hall Effect)

This sensor is used to control the speed of the DC motor by determining the position of the rotor magnet [7]. There are three sensors which are used for analyzing the rotor position as shown in the given Fig. 2. Each senor will give output in volt as the magnet passes it. By using the comparator and voltage division rule having value of two resistors ($R1 = 1000\ \Omega$ and $R2 = 250\ \Omega$), the sensor is then interfaced with the microcontroller to get the readable output. The output sent by the sensor can be varied by the PWM signal for varying the speed of the motor.

Fig. 2 Position sensor

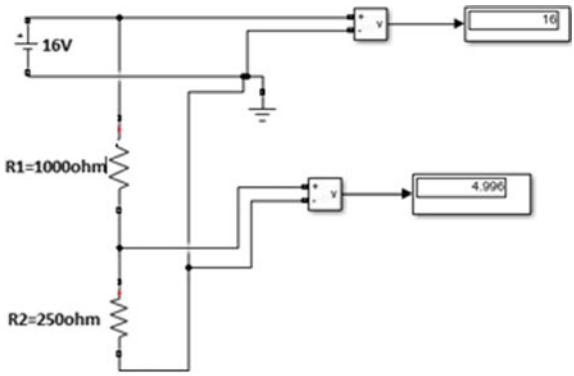

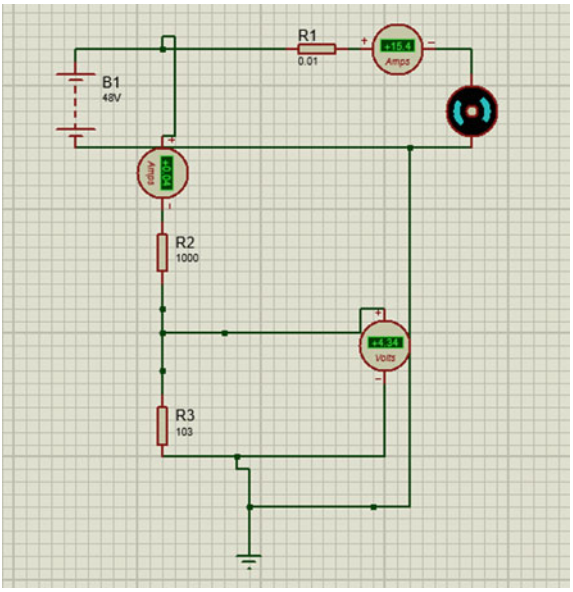

Fig. 3 Current sensor

2.3 Current Sensor Simulations

It is used to continuously monitor the current drawn from the battery to the motor [8]. The output of the sensor is in volts, that is derived from the voltage division law, the relation between the voltage and current is of difference $0.15x$. The maximum current drawn from the battery is 15.4 A as shown in Fig. 3 and with that reference the input voltage to Arduino is 4.34 V as shown in Fig. 4.

Equation for calculation of the current in the circuitry is shown below

$$I = 13.4 - (0.2x) \tag{2}$$

$x =$ range of the voltage increase to the Arduino.

2.4 Temperature Sensor

It continuously senses the temperature of the battery at the time of charging as well as at discharging. The range of the temperature measurement is between −40 C and 125 C. The output of the senor is 10 V thus it is stepped down by voltage divider rule for feeding the output to the microcontroller [9] which as a input limit of 5 V as shown in Fig. 5. By interfacing it with the microcontroller, the digital values are obtained as output.

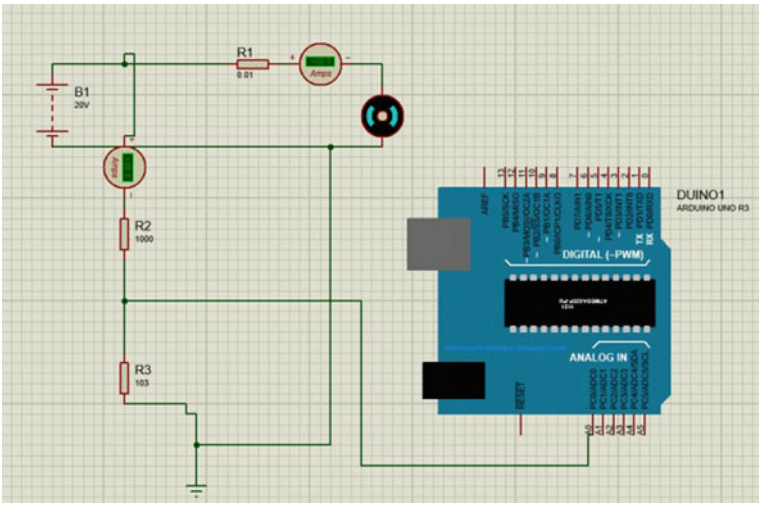

Fig. 4 Current sensor interface with Arduino

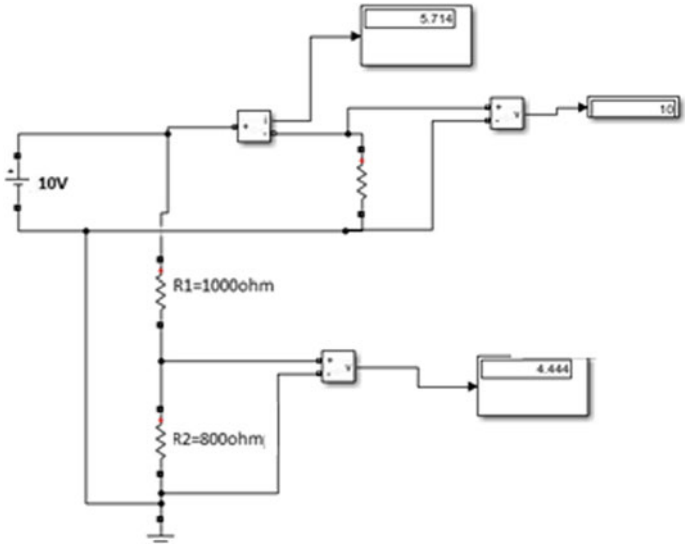

Fig. 5 Temperature sensor circuitry

3 Drive Circuit Simulation Profile

Now for the retrofitting of the concerned electrical vehicle, the concerned article covers two kinds of driver circuits for PWM generation and speed cum direction control of the concerned DC motor for the speed control. The first circuit depicts

an analog-based circuit for speed control while the second circuit depicts a microprocessor-based method for the overall speed control cum direction control.

3.1 Analog Circuitry

As shown in Fig. 6, it is a basic analog-based controller that controls the speed of the motor with a fixed analog input. The output is controlled with the help of a 500Ω potentiometer. The potentiometer varies the motor armature current of the motor [10] and accordingly the RPM of the motor. For ensuring constant speed of the motor, a throttle switch is provided to ensure the supply of rated current to the motor whenever required [11]. In the above circuit, a 24 V DC input is connected to drive the control circuit.

A Schottky diode is connected anti-parallel to the motor to protect the circuitry against reversal of high magnitude currents. Since the DC motor [12] has an inductive load, when driver desires to switch off the motor and reduces the voltage across the motor terminal to zero, the residual current in the motor winding will generate a high back emf if there is no discharge of current. So, the Schottky diode acts as a short circuit for discharge and has a low power drop. The battery supplies 24 V but the main op-amp of the circuit requires a maximum of 12 V across its terminal.

This is achieved by the use of LM7812 voltage regulator. It bucks the 24 V to a 12 V signal and contains a capacitor in parallel in order to filter out the ac components. This signal is then passed to the comparator IC which helps in triggering the transistor. When the comparator output is high, the gate of the transistor is turned ON and vice versa when the comparator output is LOW. The output of the comparator changes each time the pulse changes its polarity. The output of the transistors serves as the gate

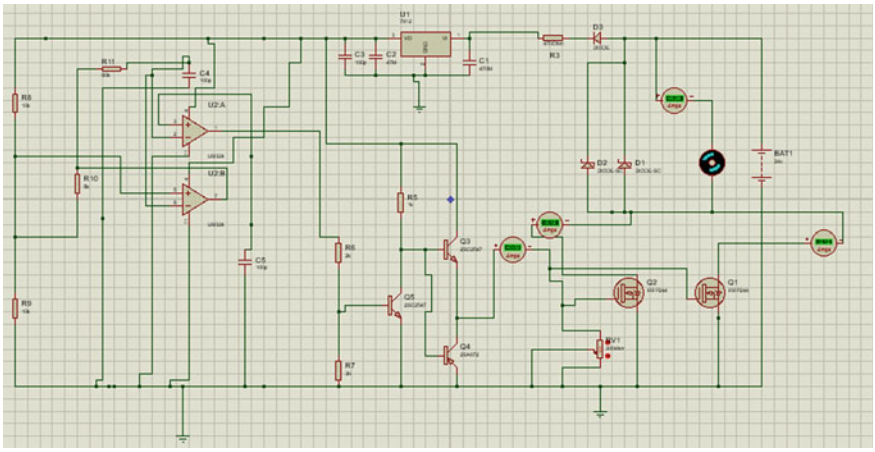

Fig. 6 Analog motor drive circuit

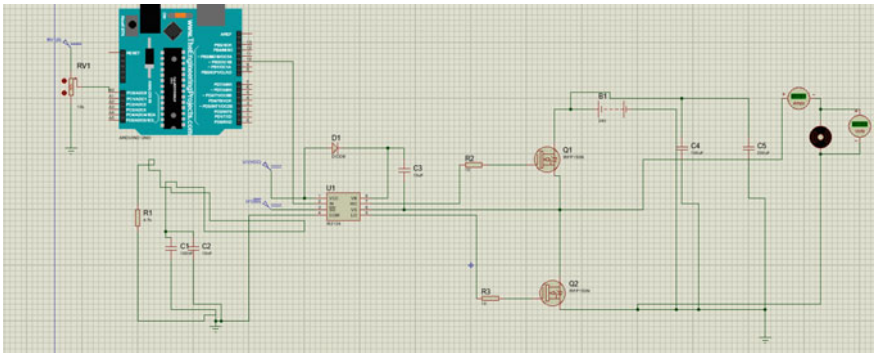

Fig. 7 Microcontroller-based drive circuit

pulses for the two MOSFETs (Metal Oxide Semiconductor Field Effect Transistor) which generates an electric field when voltage is applied at the gate) [13]. This helps to control the current flow through the channel between drain and source. The potentiometer mentioned earlier is used at the gate of the MOSFET to change the duty cycle of switching of the MOSFET [14]. This helps in controlling the output current of the MOSFET which further controls the current through the motor and thus ensuring a uniform control of speed as far as the motor is concerned [15].

3.2 Microcontroller-Based Circuitry

Figure 7 shown above shows the circuit design and simulation of another alternative motor control circuit which is purely microcontroller-based as shown in the simulation diagram. In this diagram, an external potentiometer connected to a 5 V supply is read by the microcontroller which then maps into the corresponding gate pulse with the corresponding duty cycle [16]. A single MOSFET driver IR2104 is used to run at the same time two high power MOSFETs thereby controlling the speed of the DC Motor on a voltage basis and ensuring uniform open loop control of the DC Motor. The circuit is enabled with the help of decoupling capacitors and gate resistors and input filter circuit. The concerned micro- controller used for this operation is the Arduino Uno or the AtMega 328P IC [17]. It reads the analog input of the driver from the variable rheostat connected to one of its analog pins. The IC accordingly generates the PWM Signal from one of its PWM pins and feeds it to the high power IR2104 MOSFET Driver [18]. This driver with the help of an external 12 V Vcc generates a reference signal higher than the 5 V PWM output of the AtMega 328P IC for proper conducting and switching of the two concerned high power MOSFETs IRFP120N. Capacitors of various values are connected in parallel to filter out the unnecessary AC components. In this method of speed control, contrary to the previously mentioned analog method, the speed of the motor is varied by varying the

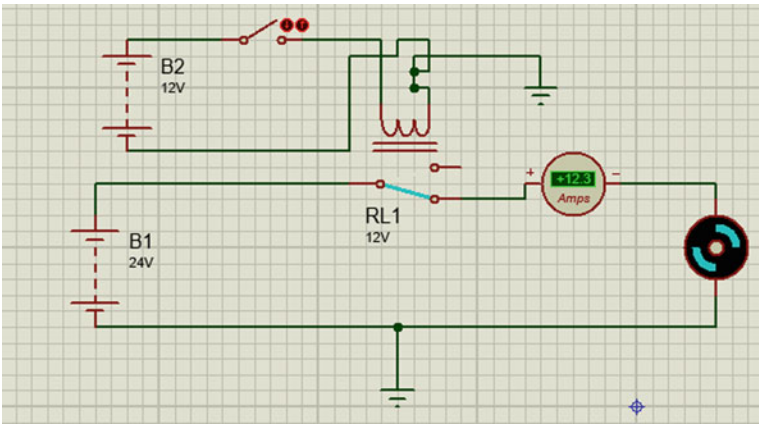

Fig. 8 Open state

net supply voltage across the motor input terminals. Thus the microcontroller-based method of controlling speed is based on voltage control method of speed control as against the current control-based method of speed control of the aforementioned analog controller in Fig. 6.

4 Kill Switch Mechanism

The kill switch mechanism [19] is used to ensure the over-current protection of the motor. In case there is any anomaly in the operation of the motor, the kill switch is switched on which in turn shorts the relay with its 12 V actuation voltage thereby cutting off the motor with its supply voltage. Vice versa, when normalcy is restored, the kill switch is turned off to restore normal running of the motor [20] as shown in Figs. 8 and 9.

5 Results and Observations

The results and the corresponding variations in the speed of the motor with respect to various parameters like the net armature current and the rheostat resistance connected in series with the gates of the MOSFETs are graphically represented. Figure 10 shows a variation of speed vs the net armature current of the motor, we observe different stages of variation. While initially, the speed rises steeply with increase in the current, after a certain point, we observe that beyond a certain point of saturation the rise in speed with current becomes less steep and more or less uniform giving the resultant curve the shape of an Ogive curve. The second curve which is shown in Fig. 11

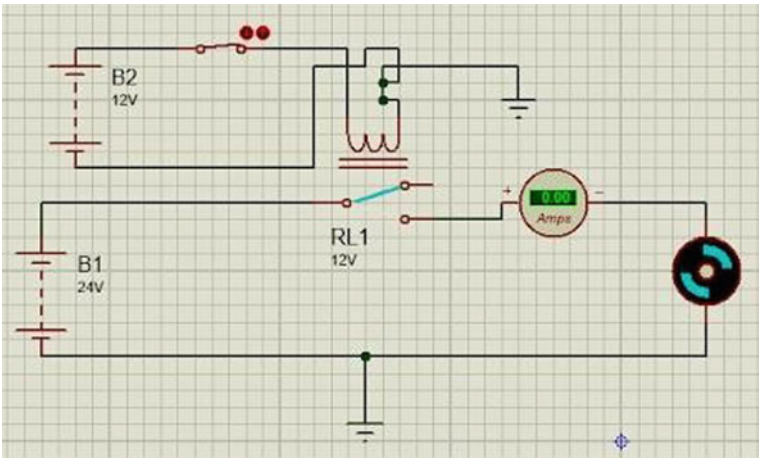

Fig. 9 Close state

Fig. 10 Speed versus current for the DC motor

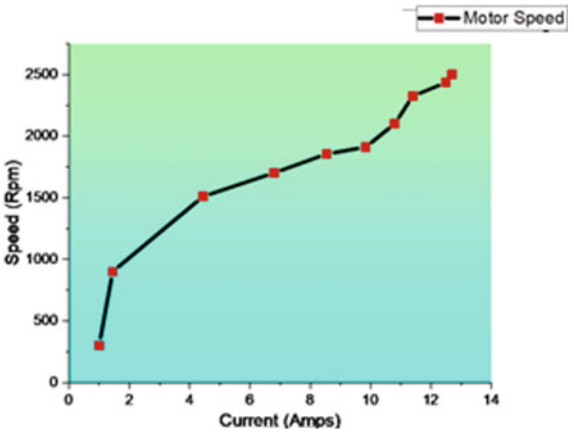

shows that the rheostat or the potentiometer is directly responsible for controlling or limiting the speed of the motor. The curve shown in Fig. 11 is that of a uniform curve showing decrease in speed with increase in value of net resistance on the rheostat which is varied by varying the knob on the potentiometer.

Although the rheostat offers a maximum resistance of 500 ohms, we can observe that the concerned motor's rpm comes to a standstill zero at a value of around 300 ohms from the graph shown in Fig. 11.

Figure 12 shows a screenshot of the drive circuit when the rheostat resistance in series with the gate is minimum, and thus the current flowing through the motor is maximum as is donated by the denoted ammeter reading, and thus the concerned rpm of the motor is also maximum. Figure 13 shows a screenshot of the drive circuit when the rheostat resistance in series with the gate is maximum, and thus the current

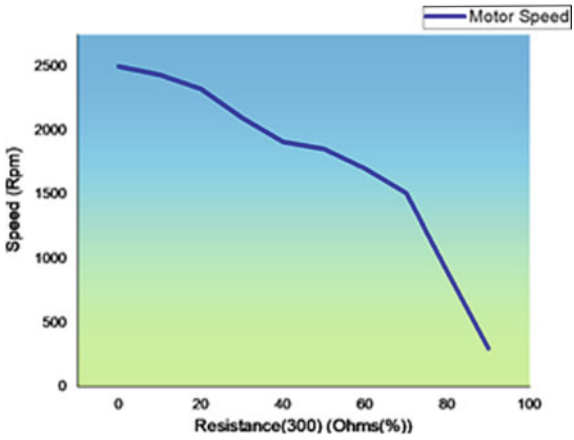

Fig. 11 Speed versus rheostat resistance for the DC motor

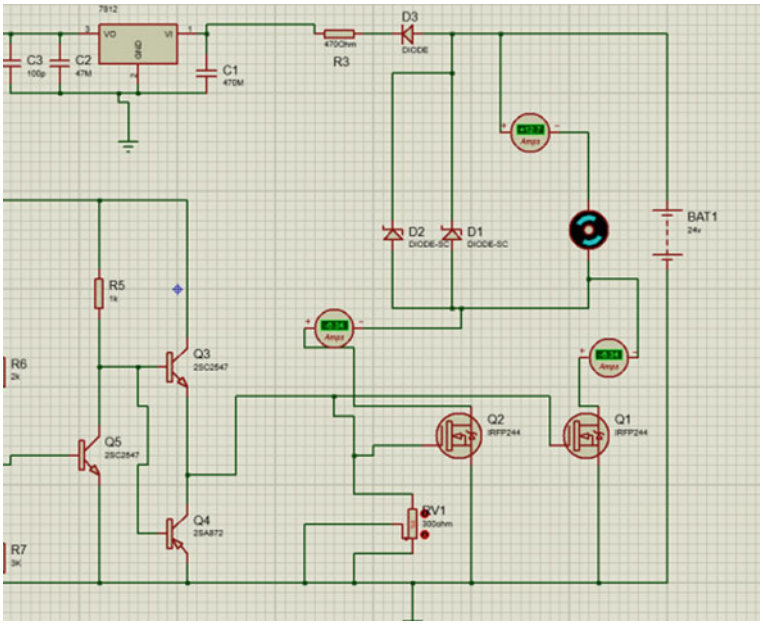

Fig. 12 Maximum current to the motor

flowing through the motor is minimum and thus denotes the standstill or rest position of the concerned DC motor. It is to be noted that all the concerned simulations in the article have been performed using the software Proteus 8 Professional.

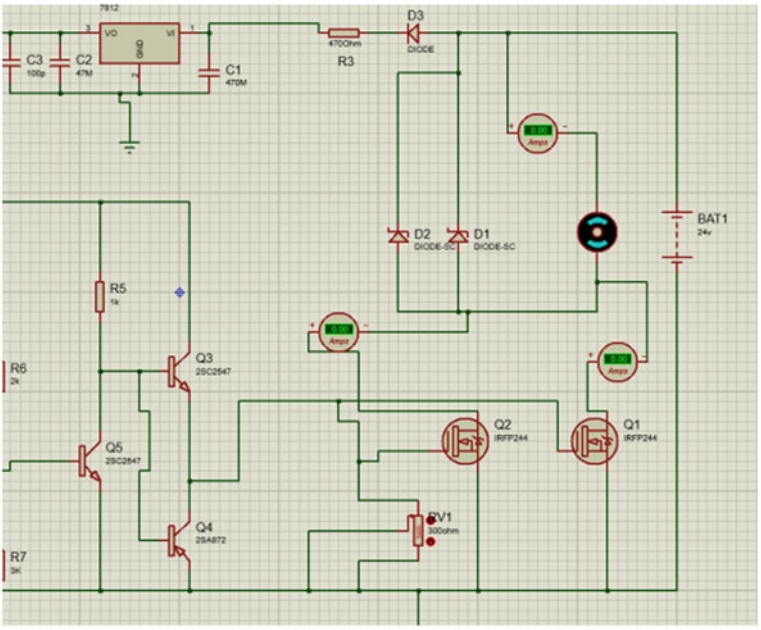

Fig. 13 Minimum current to the motor

6 Conclusion

This article gives a detailed view on the retrofitting of ICE-based vehicles with corresponding electrical vehicle designs which helps in providing effective alternatives to the generic fossil fuel run vehicular transmission systems sometimes using both fossil fuels and natural gas. By using the proposed simulation profile which implements the use of real-time and active simulations of various vehicle running and sensing operations, the overall energy and power efficiency for the accustomed power electrical vehicular transmission system can be calculated and further implementations can be executed accordingly. Along with the promised performance efficiency, which is more or less equivalent to its corresponding ICE-based vehicle design, the motor transmission is comparatively way less polluting and offers less losses due to noise and other external physical disturbances. However the shortcoming of this article, it provides detailed calculations and simulations for very low HP vehicles, and the net electrical output can be compared to that of those clean energy tow-tow vans. This design can be further used as reference for high energy electrical output vehicle designs like ICE-based sedans offering a HP rating of as high as 75 HP. The fossil fuels levels are declining rapidly, and with this, the need for alternative energy sources has risen. Over one-third of fossil fuels are used to power the transportation industry and thus it is important to limit the use of these fuels in vehicles. Electric Vehicles have begun to capture the market slowly but the industry is still in its budding stages

and thus catering to the complete needs of the people is far from a reality. Even if EVs take over the industry completely then we would face the issue of excess road traffic with the already existing ICE vehicles and the new EV. Thus, eliminating ICE vehicles is just as important as introducing EVs.

References

1. Abas N, Kalair A, Khan N (2015) Review of fossil fuels and future energy technologies. Futures 69:31–49
2. Hasnira H, Didi I (2014) Energy estimation on BLDC electric vehicle using MATLAB. IPTEK J Proc Series 1:485–489
3. Sundriyal P, Shantanu B (2019) Sensors for automotive and aerospace applications. Springer, Singapore pp 1–6
4. Bimal K, Robert L (1978) A DC motor control system for electric vehicle drive. IEEE Trans Ind Appl IA-14(6):56572
5. Rowlette MR (1994) Temperature sensor. U. S. Patent
6. Jose S (2001) Rechargeable battery pack and the battery pack charger with safety mechanism. United States Patent. 1(12)
7. Murray A (1998) Position and speed sensors. United States Patent.19
8. Patel A, Ferdowsi M (2009) Current sensing for automotive electronics—a survey. IEEE Trans Veh Technol 58:4108–4119
9. Carkhuff BG (2019) Battery internal temperature sensing battery management system. US10461374
10. White KE (1980) Control system and method for operating a DC motor. US4240015
11. Morisset MR (2019) Throttle control system and method. US10479200
12. Thattil A, Vachhani S, Raval D, Patel P, Sharma P (2008) Comparative study of using different electric motor for EV. Int Res J Eng Technol 9001:4601–4604
13. Zhou Q, Gao F, Jiang T (2015) A gate driver of SiC MOSFET with passive triggered auxiliary transistor in a phase-leg configuration. IEEE Energy Convers Congr Exposition 7023–7030
14. Smith TA, Dimitrijev S, Barry Harrison H (2000) Controlling a DC-DC converter by using the power MOSFET as a voltage controlled resistor. IEEE Trans Circ Syst I: Fundam Theory Appl 47:357–362
15. Silvestre J (2008) Half-bridge bidirectional DC-DC converter for small electric vehicle. In: SPEEDAM 2008—international symposium on power electronics, electrical drives, automation and motion, pp 884–888
16. Ali YSE, Noor SBM, Bashi SM, Hassan MK (2003) Microcontroller performance for DC motor speed control system. In: Proceedings national power engineering conference, pp 104–109
17. Gavran M, Fruk M, Vujisi G (2017) PI controller for DC motor speed realized with Arduino and Simulink, pp 1557–1561
18. Shetti PR, Mangave AG (2014) DC motor speed control with feedback monitor based on C# application. Int J Res Eng Technol 03:398–401
19. Pedersen BB, Reese DA, Joyce J (2013) Method and apparatus for securing a programmable device using a kill switch. U.S. Patent 8,461,863
20. Gadade JB, Bharane GR, Rupanwar TP, Kale RU (2018) DC motor protection, Control and Monitoring. pp 3458–3460

Analysis of Cascaded Multilevel Inverters for Smart Grid Connected PV Systems

R. L. Josephine, M. Yoogesh Kumar, and S. Harishankar

Abstract With the increasing need for renewable energy systems to reduce the dependence on conventional resources and fossil fuels and to counter the impact of their usage, more efficient and robust power generation, management and storage systems are required. To best augment the capabilities of such systems, it is imperative that a smart grid-based control strategy is adopted. This will improve the efficiency of such a system and will lead to better integration of the system with the grid. With increased penetration of such smart grid connected systems, the need for securing them from cyberattacks, having the potential to cripple strategic assets of nations, becomes quite necessary. In this paper, a Cascaded *H*-bridge-based Multilevel Inverter topology is proposed, for integration of PV systems in smart grid. A possible cloud control strategy using blackboard architecture and protection has also been discussed.

Keywords Multilevel inverter · Smart grids · Renewable energy · Cloud · Blackboard architecture

1 Introduction

Global warming is a phenomenon not new to us. Emission of greenhouse gases primarily from the usage of fossil fuels, is an extensive global problem, with many nations pledging to reduce their emissions by fixing targets [1]. The emission of CO2 related to energy production and consumption will increase 6% in between 2015 and 2050, considering ongoing and future policies. Share from non-conventional energy sources in the supply of primary energy would rise by 14% in the same period. Non-conventional energy sources and efficient energy usage, along with end-use electrification, will account for around 94% of the world's emissions reductions [2]. Electric mobility and *E*-vehicles also play an important role in these goals.

R. L. Josephine (✉) · M. Y. Kumar · S. Harishankar
National Institute of Technology, Tiruchirappalli, India
e-mail: josephinerl@nitt.edu

C. Subramani et al. (eds.), *Proceedings of International Conference on Power Electronics and Renewable Energy Systems*, Lecture Notes in Electrical Engineering 795,
https://doi.org/10.1007/978-981-16-4943-1_51

For the purposes of this paper, we've implemented a PV RES system. To best analyze the effect of adopting RES with integration into Smart Grids, the project can be broadly divided into three distinct levels; namely the Power Generation and Distribution (PGD) level, Commercial level, and the Domestic level. In the PGD level, the major generation of PV power takes place, followed by the industries and services level where the presence of heavy loads and a degree of self-sufficiency distinguishes it from the domestic level, where a typical smart home system, with solar power production capability is present (Fig. 1).

Energy storage systems are present at both the PGD and the domestic levels, to divert excess power and to tap into the reserves, when sudden spikes in demand are observed. Cascaded *H*-bridge Multilevel Inverter was the major converter device adopted for this model, since it allows a scalable, modularized circuit layout and packaging, and also requires a lesser number of components for the same output

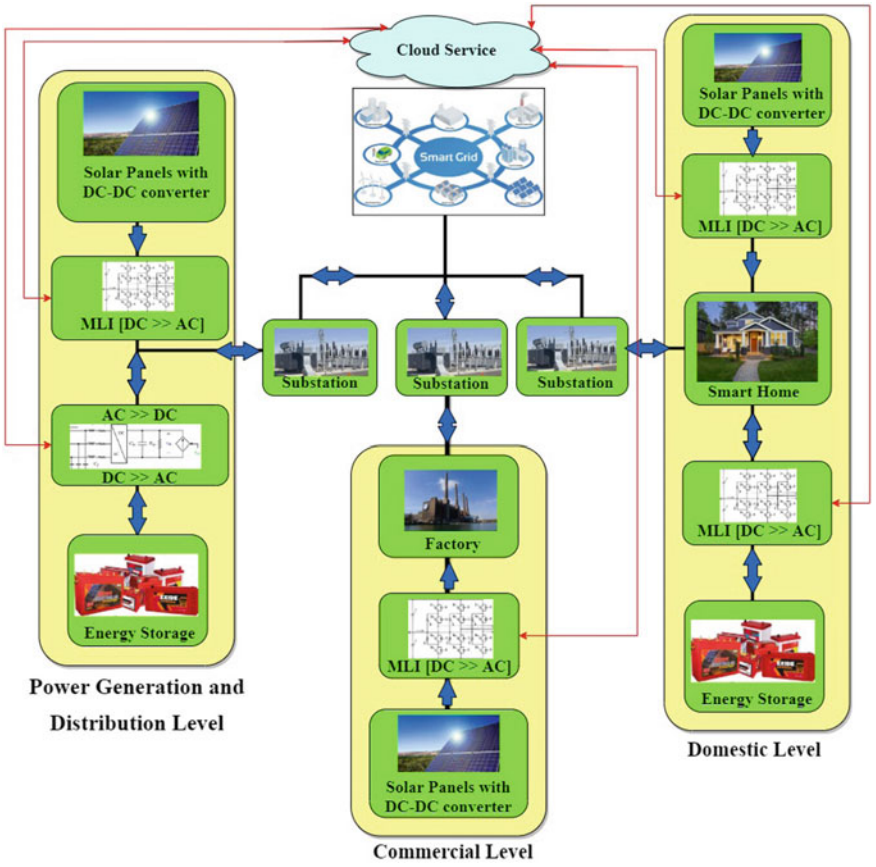

Fig. 1 Overview of CHBMLI-based smart grid system with cloud control strategy

voltage levels. MPPT algorithm was used for controlling the intermediate DC-DC boost converter, before feeding the output into the inverter.

An increasingly popular mode for computation and control for demand and response facilities, is cloud computing [3], employing huge storage and computing facilities at remote locations, which can be shared between a host of different users. To effectively control the system, and to protect it from a host of different cyberattacks and other sabotage, the need for a novel cloud control strategy has also been discussed.

2 PV System Integration with Smart Grid

Smart Grids are a form of advanced digital bidirectional power flow system that is flexible, robust, and sustainable, with the ability to forecast outcomes under a variety of conditions, and is designed with current and future requirements of cyber-secured components, computers, and systems [4]. In [5], a novel Multilevel Converter for on-grid interface of RES in Smart Grids is discussed, where a front-end multilevel power electronic converter is employed for the three levels of the electric power system, namely the power distribution, industrial and services, and the residential levels.

Composition and description of each of the levels mentioned above in this system will be discussed below:

2.1 Power Generation and Distribution Level

In the power generation and distribution level, we have RES in the form of a PV array, an intermediate DC-to-DC boost converter, connected to 3-ph, 5-level Cascaded H-bridge Multilevel Inverter (CHBMLI). It is in turn connected to the grid. An energy storage system along with a converter is also present, connected to the grid. The generated voltage from the PV array is stabilized using the DC-to-DC converter. MLI converts the DC input into a 3-ph AC output, before feeding it into the grid via the substation. Whenever excess power is generated, the Energy Storage System (ESS) would be charged through the AC-DC converter, which then helps in meeting sudden spikes in demand. Here, integration of solar energy as a source, and energy storage with batteries can be done, and its QoS and control nature ensured by both distribution and transmission system operators [5].

2.2 Commercial Level

At the Commercial Level, we have a very similar setup as that of the PGD level, with the notable absence of an ESS. The power flow in this particular level is unidirectional. Commercial level represents heavy industrial loads, with a high demand for power throughout the day. To reduce the carbon footprint and harmful emissions from this level, and to lower the dependence of the level on the grid, RES can be integrated into this level. It also helps in lowering the consumption of energy, thereby reducing costs. As mentioned earlier, the I&S level also has a CHBMLI as intermediate between the PV arrays and the industrial loads.

2.3 Domestic Level

The objective of the domestic level is to represent the growing number of smart home communities and individuals. Smart home technology is a key component and a live dynamic communication between the power grid and consumers that enables intelligent and interactive electricity use while also enhancing the power grid's operating mode and users' consumption habits to boost energy efficiency. It employs cutting edge technology like IoT, smart sensors and control technologies to link multiple facilities via the network to automate the entire system [6]. Solar power and energy storage devices can be integrated in a smaller scale to minimize the energy costs for the end-user, and also to improve the strategies for managing demand response, thereby establishing a renewable energy source system which is highly distributed.

The need for a cloud-based control interface and communication strategy arises here, for linking the three levels described above effectively. This defines the status of the deployed inverters and other power electronic equipment, and also reports issues in power quality, defining reference points for operation and details regarding the transactions of power. With such specialized technology employed, the need arises to secure the system from external actors with malicious intent. Hence, the strategy adopted should also be well resistant to such attacks from the cyberspace.

3 Components of the Proposed System

3.1 PV Array

The solar module used for the simulation of the PV array is 1Soltech 1STH-215-P, with 47 strings in parallel, and 10 modules per string. The maximum power of the PV array is 213.5 W, and the open circuit voltage (V_{oc}) is 36.3 V, short circuit current (I_{sc}) is 7.84 A. The number of cells per module ($N_{cell}I$) is 60. For an irradiance of

1000 kW/m^2, at a temperature of 25° C, the power output is 100.2 kW and the output voltage 290 V, with an output current of 345.4 A.

3.2 DC-DC Converter and MPPT Algorithm

A DC-DC boost converter is employed for boosting the output of the PV array. The design of the converter capacitor and inductor was done to boost the array output to a steady 700 V.

To track the peak power output of the array at all times, MPPT algorithm was used to control the converter output. This ensures a steady output voltage even when changes in irradiance or temperature happen. The working of the MPPT algorithm is shown in Fig. 2.

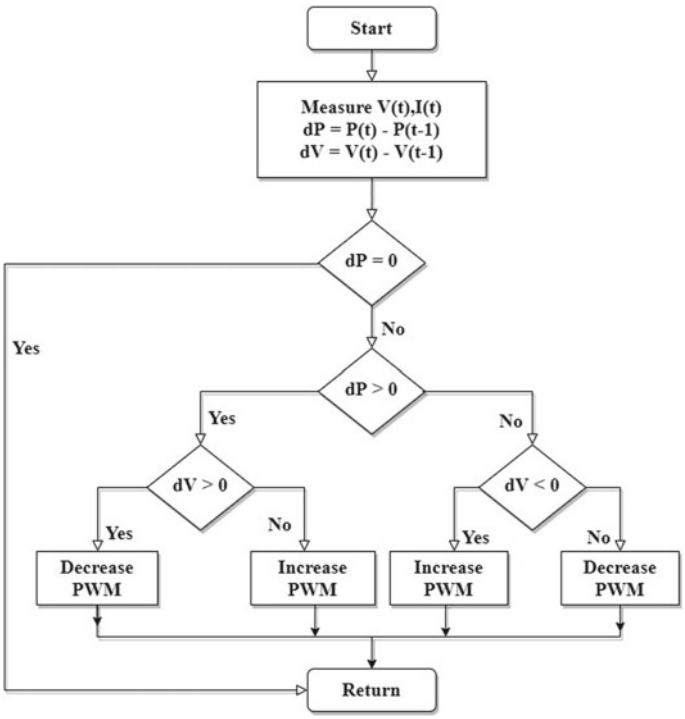

Fig. 2 MPPT algorithm

3.3 Inverter

Inverter topologies suitable for on-grid solar power systems is discussed in [7]. In this system, a CHBMLI is adopted for all DC-AC conversions. The advantages of CHBMLI are many, as discussed in [8, 9]. A higher peak voltage can be obtained, reducing the voltage load on the switches. Multilevel inverters have also proven to be an efficient and cost-effective way to reduce switching errors in applications demanding high voltage and power. When number of DC voltage levels increases, the obtained output increases in stages and generates an output that resembles a sinusoidal wave with minimal THD (Total Harmonic Distortion), eliminating the need for an output filter.

3.4 LCL Filter

A comparative study of L, LC and LCL filters for grid connected inverters is discussed in [10]. The advantages of LCL filter over others, and a design methodology for an LCL filter for a 3-phase grid connected inverter, is discussed in [11].

4 Results

Power output from the solar array, and output voltage of the boost converter can be seen in Fig. 3. These correspond to the PV array parameters specified in Sect. 3. We observe a steady DC voltage output from the converter, which is controlled by the MPPT algorithm, also discussed in Sect. 3. In Fig. 4, the grid voltage and current of the commercial level is shown. The values correspond to a grid voltage of $V_{L\text{-}L} =$ 415 V, and a frequency of 50 Hz. The peak solar array output for an irradiance of 0.5 kW/m^2 at 25° C is 49.78 kW. We observe that the grid current and voltage is in phase, with harmonics removed using the LCL filter described earlier.

5 Need for a Cloud-Based Control Strategy

The conceptual analysis of a grid system with and without a cloud communication system is discussed in [3]. For a smart grid system that doesn't utilize cloud computing, all the components can interact with the utility providers directly over the network. But the absence of a robust cloud-based control architecture, has a host of disadvantages as discussed below:

- The master–slave architecture leads to a high exposure to cyberattacks. These cyberattacks can be crippling to the energy infrastructure of a nation. India recently

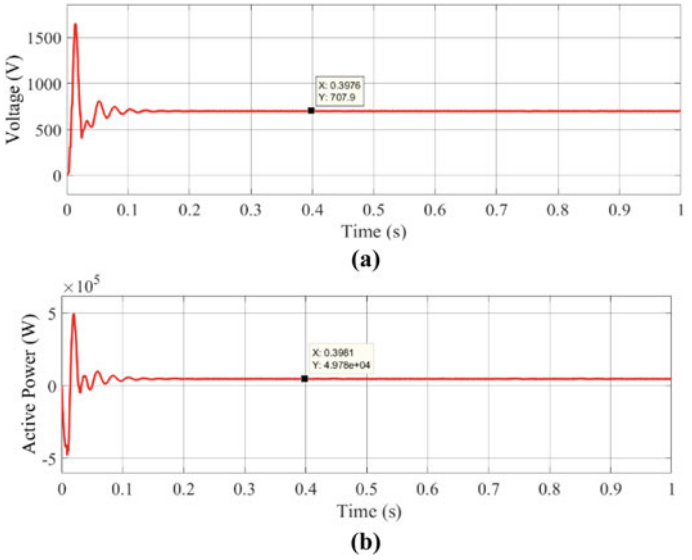

Fig. 3 **a** DC-DC converter—voltage waveform and **b** Output power of PV array

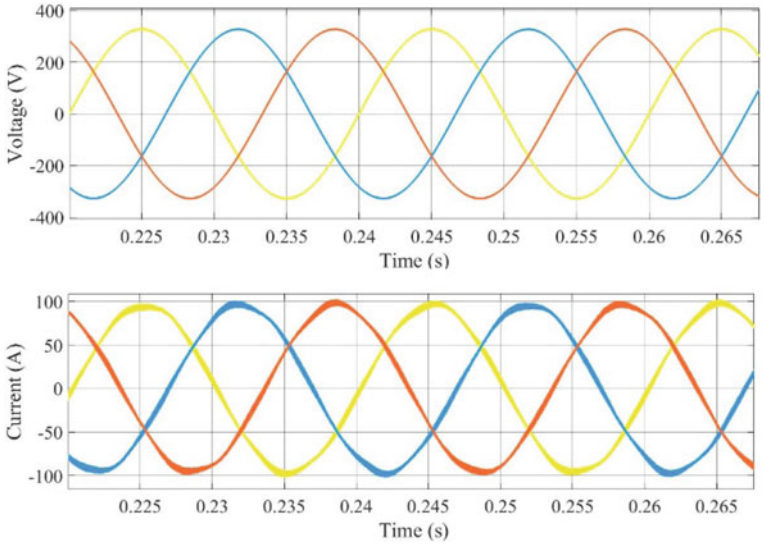

Fig. 4 Grid voltage and current in the I&S level

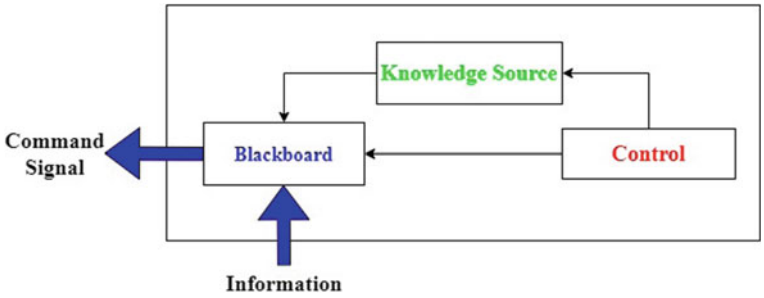

Fig. 5 Blackboard architecture

witnessed this, when reportedly state backed actors were responsible behind an attack which led to widespread outages in the grid of Mumbai.

- When a grid provides services in islanded mode, adequate management and control are necessary. This gained prominence recently, when a historic cold wave swept the entire Midwest and southern regions of the USA and Texas.

The blackboard architectural pattern is a popular method to solve problems characterized by their uncertain and non-deterministic nature. No solutions, which are direct and algorithmic, exist for these problems. Often, the best effort to approximate the solution would suffice [12]. Since a smart grid would also be required to handle uncertain load variation over a large area, this architecture would be suited for the job.

As seen in Fig. 5, the architecture can be divided into three major subdivisions, namely blackboard, knowledge sources and control. Blackboard acts as a global database, and it helps in storing all the data which are collected and produced over the period. There can be more than one knowledge source, and each source will be assigned to take care of a particular problem. The knowledge source would get the data from the blackboard, process that data and store the output in the blackboard. Control acts as a manager for the whole architecture, by taking the runtime decisions and making sure that the right knowledge sources are active at right time.

6 Conclusion

To meet the growing need for clean energy. Renewable Energy Sources and Smart Grids are currently leading the way for future power transmissions. This paper deals with certain aspects through which the smart grid could become more efficient. Using the AC module-based CHBMLI gives several advantages such as easier failure detection of the solar modules, flexible and expandable design and so on. When smart grid grows on a large scale, communicating and coordinating becomes a key requirement for its management. Cloud control strategies can cover large area in real time over the Internet, making it easy for communication, and also improves

the security of critical infrastructure. On implementing blackboard architecture over the cloud, it becomes easier to manage the smart grid as this architecture is flexible as well as expandable. The paper also highlights the advantages of implementing cloud-based strategy over classical solutions.

References

1. Bose BK (2010) Global warming—energy, environmental pollution, and the impact of power electronics. IEEE Ind Electron Mag 4(1):6–17
2. Gielen D, Boshell F, Saygin D, Bazilian MD, Wagner N, Gorini R (2019) The role of renewable energy in the global energy transformation. Energ Strat Rev 24:38–50
3. Bera S, Misra S, Rodrigues JJ (2014) Cloud computing applications for smart grid: a survey. IEEE Trans Parallel Distrib Syst 26(5):1477–1494
4. Dileep G (2020) A survey on smart grid technologies and applications. Renew Energy 146:2589–2625
5. Monteiro V, Sousa TJ, Sepulveda MJ, Couto C, Martins JS, Afonso JL (Sept 2019) A novel multilevel converter for on-grid interface of renewable energy sources in smart grids. In: 2019 international conference on smart energy systems and technologies (SEST), IEEE, pp 1–6
6. Li M, Gu W, Chen W, He Y, Wu Y, Zhang Y (2018) Smart home: architecture, technologies and systems. Procedia comput sci 131:393–400
7. Deshpande S, Bhasme NR (Apr 2017) A review of topologies of inverter for grid connected PV systems. In: 2017 Innovations in power and advanced computing technologies (i-PACT), IEEE, pp 1–6
8. Noman AM, A Al-Shamma'a A, Addoweesh KE, Alabduljabbar AA, Alolah AI (2018) Cascaded multilevel inverter topology based on cascaded H-bridge multilevel inverter. Energies 11(4):895
9. Azli NA, Choong YC (Nov 2006) Analysis on the performance of a three-phase cascaded H-bridge multilevel inverter. In: 2006 IEEE international power and energy conference, IEEE, pp 405–410
10. Yagnik UP, Solanki MD (2017) Comparison of L, LC and LCL filter for grid connected converter. In: 2017 international conference on trends in electronics and informatics (ICEI), Tirunelveli, India, pp 455–458. https://doi.org/10.1109/ICOEI.2017.8300968
11. Dursun M, DÖŞOĞLU MK (2018) LCL filter design for grid connected three-phase inverter. In: 2018 2nd international symposium on multidisciplinary studies and innovative technologies (ISMSIT), Ankara, Turkey, pp 1–4. https://doi.org/10.1109/ISMSIT.2018.8567054
12. Dong J, Chen S, Jeng JJ (Apr 2005) Event-based blackboard architecture for multi- agent systems. In: International conference on information technology: coding and computing (ITCC'05)-Volume II, vol 2, IEEE, pp 379–384

Voltage Stability Improvement of PV and Battery-Based Sliding Mode-Controlled Microgrid System

V. N. Ganesh and S. Manivannan

Abstract This work points on improving the unique time reaction of a PV and battery energy change framework in shut circle flying capacitor support converter-controlled force methodologies with SMC. This work manages displaying and recreation of SM-controlled current impediment of framework-associated inverter. Force procedures are a famous gadget inside the group of force framework gadget. The voltage security is carried out with voltage source inverter (VSI), and the exchanging beats are created utilizing sliding mode regulator. The dynamic channel is utilized for weakening of burden voltage and current sounds. The reenactment results are introduced to discover the impact of dynamic and responsive channel utilizing SMC. The reproduction results with PID and sliding mode (SM) controller-based voltage soundness are looked at, and the steady time–space restrictions are introduced. The outcomes show that sliding mode regulator framework has improved reaction than PID-controlled framework.

Keywords Flying capacitor boost converter · Solar panel · PWM inverter · PWM pulse · MOSFET battery · Inverter · PI · SMC

1 Introduction

Before, power quality signified the capacity of electric utilities to give electric force without interference. In any case, with higher infiltration of non-straight loads, computerized gadgets and other progressed power electronic gear, power quality at present incorporates any deviation from an ideal sinusoidal waveform which incorporates electromagnetic interference (EMI), radio-frequency interference (RFI) commotion, drifters, floods, lists, earthy colored outs, power outages and some other mutilations to the sinusoidal waveform. Symphonious twists, a genuine force quality issue can cause overheating of transformers, breaking down of hardware and even

V. N. Ganesh (✉) · S. Manivannan
Dr. MGR Educational and Research Institute, Maduravoyal, Chennai, India

S. Manivannan
e-mail: manivannan.s@drmgrdu.ac.in

C. Subramani et al. (eds.), *Proceedings of International Conference on Power Electronics and Renewable Energy Systems*, Lecture Notes in Electrical Engineering 795,
https://doi.org/10.1007/978-981-16-4943-1_52

reason harm to the computerized electronic control frameworks in activity. With expanding thickness of delicate gear on the electric matrix, there is expanding tension on the controllers to lay severe principles in regards to control quality issues. In a microgrid network framework, brilliant meters introduced at end client areas have the ability to decide the total harmonic distortion (THD) of the stockpile voltage. Such data will permit the utilities to decide the wellspring of symphonious mutilations fast. Industrialization, urbanization and unremitting foundation improvements have prompted a change in perspective in the manner power is produced, communicated and devoured, and it has brought about massive weight on the deep-rooted electrical lattice framework. Furthermore, challenges because of expanding energy interest with better caliber of force and dependability are mounting. The quick expansion in entrance of nonlinear loads, for example, server farms, huge variable-speed drives and other force electronic gadgets across the framework, has brought about expanded dependability and force quality concerns.

The idea of brilliant matrix gives a large group of answers for a considerable lot of the issues looked by the flow electric lattice by exploiting cutting edge advances like disseminated age, circulation mechanization, energy the executives frameworks, progressed metering foundation (AMI), environmentally friendly power age advances, module mixture electric vehicles, two-way remote correspondence and web, to give some examples. Expanded familiarity with the exhaustion of energy utilization and climate, need for protected and consistent activity of the force matrix to give top caliber and solid force supply to buyers in the advanced age have pushed exercises in the domain of brilliant network to the front line all through the world.

The fundamental idea of a microgrid is to add checking, examination, control, and correspondence abilities to the public electrical conveyance framework to expand the throughput of the framework while decreasing the energy utilization. The brilliant matrix will permit utilities to move power around the framework as proficiently and financially as could be expected. The keen network can be characterized as a framework that utilizes computerized data and control innovations to encourage the arrangement and coordination of conveyed and inexhaustible assets, brilliant buyer gadgets, mechanized frameworks, power stockpiling and pinnacle shaving advances.

With higher infiltration levels, the electrical network would require all the quicker beginning and quick inclining assets to compensate for the age deficiencies when such assets are not working at their normal yield levels. Significant measure of exploration is going on in this field, and proposed framework like the future renewable electric energy delivery and management (FREEDM) guarantees a considerable lot of the issues. The goal is to have an effective electric force network coordinating profoundly stochastic, dispersed and versatile elective age sources and fuel stockpiling with existing force frameworks to encourage a green and feasible energy-based society, alleviate the developing energy emergency and the effect of fossil fuel byproducts on the climate. In this way, the presentation of shrewd matrices will not just decrease ozone depleting substance discharges yet additionally empower expanded incorporation of sustainable sources and fuel stockpiling resources with the electric force network.

2 System Description

PV array and flying capacitor boost converter with inverter in closed loop grid-connected system with PID and SMC controller are shown in Fig. 1. Closed loop circuit diagram of flying capacitor boost converter with grid-connected inverter PID and SMC controller is shown in Figs. 2 and 3.

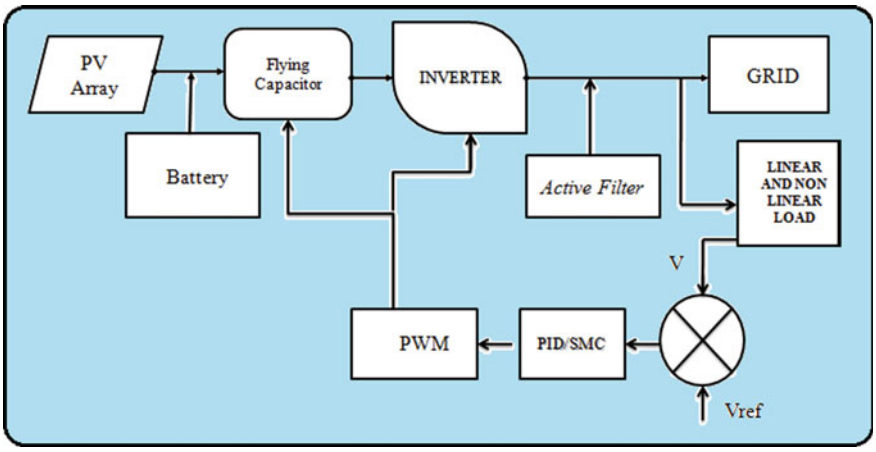

Fig. 1 Block diagram of PV, battery and flying capacitor boost converter with inverter in closed loop grid-connected system with PID and SMC controller

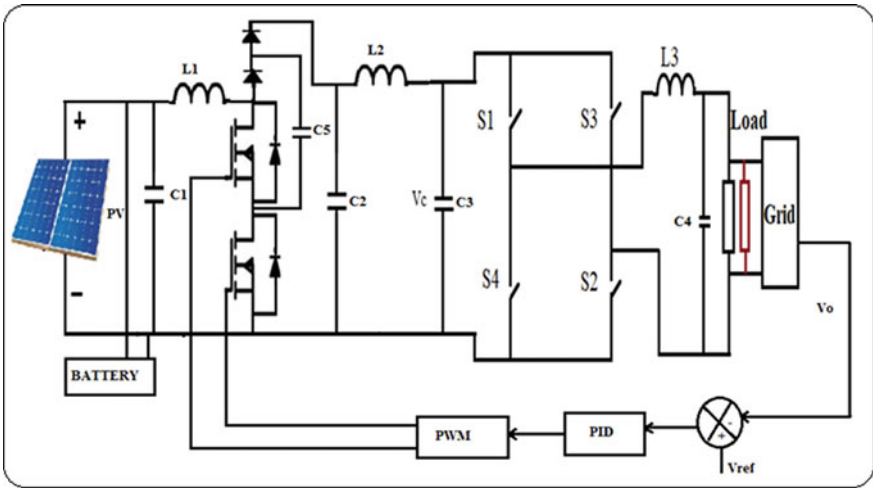

Fig. 2 Circuit diagram of closed loop PID-controlled PV and battery-based microgrid-connected system

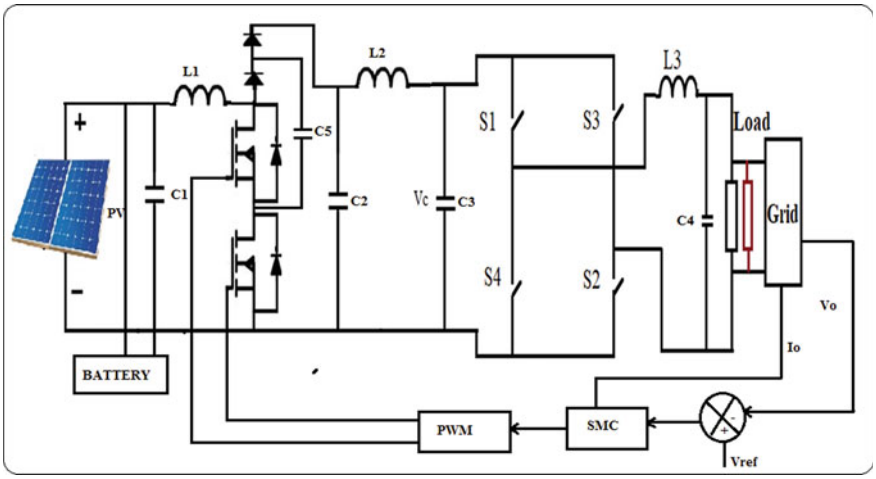

Fig. 3 Circuit diagram of closed loop SM-controlled PV and battery-based microgrid-connected system

3 Simulation Results

The bar outline examination of voltage THD and current THD on PV with inverter and PV and battery of lift converter based inverter is appeared in Fig. 4. Circuit chart of PV and battery based on microgrid-associated inverter with shut circle PID regulator is addressed in Fig. 5 Voltage across PV and battery based on microgrid-associated inverter framework is appeared in Fig. 6, and its worth is 22 V. Voltage across PV and battery based on microgrid-associated inverter framework is appeared in Fig. 7,

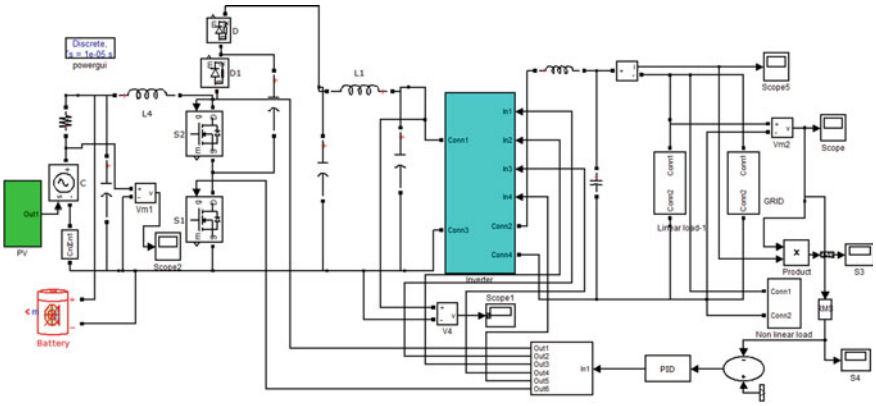

Fig. 4 Circuit diagram of PV and battery based on microgrid-connected inverter with closed loop PID controller

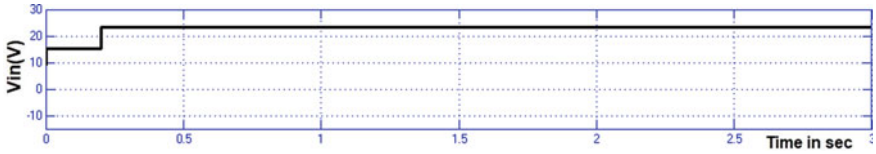

Fig. 5 Input voltage

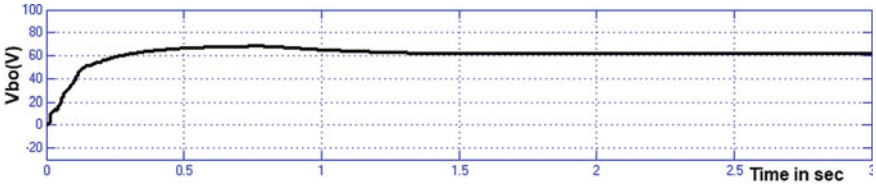

Fig. 6 Voltage across flying capacitor boost converter

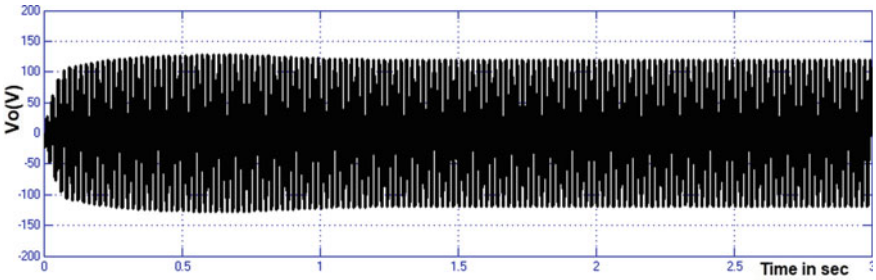

Fig. 7 Voltage across RL load

and its worth is 22 V. Voltage across RL heap of PV and battery based on microgrid-associated inverter framework is appeared in Fig. 8, and its worth is 120 V. RMS voltage across RL heap of PV and battery based on microgrid-associated inverter framework is appeared in Fig. 9, and its worth is 80 V. The voltage THD esteem is fundamental 50 Hz = 100, and THD esteem is 2.12% is appeared in Fig. 10. The current THD esteem is fundamental 50 Hz = 7.07, and THD esteem is 2.04% and is

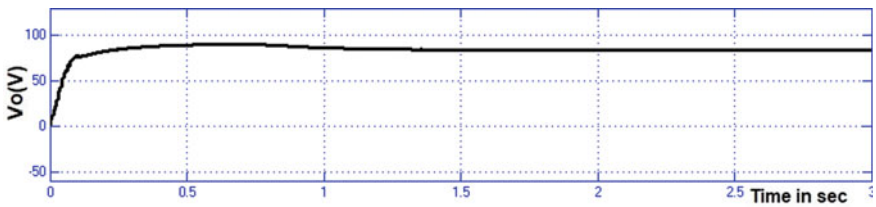

Fig. 8 RMS voltage across RL load

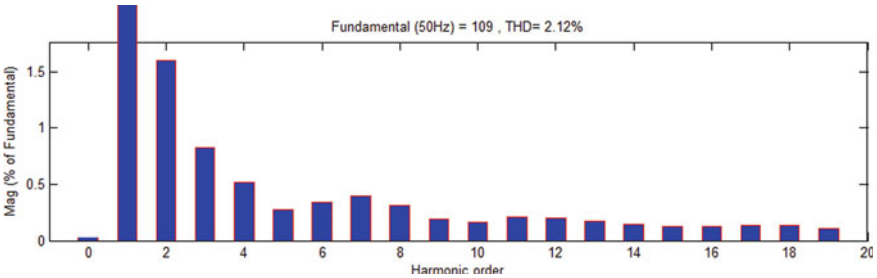

Fig. 9 Voltage THD

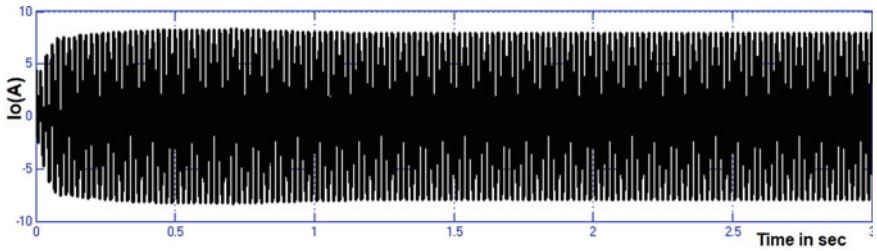

Fig. 10 Current through RL load

appeared in Fig. 11. Output force of PV and battery based on microgrid-associated inverter framework is appeared in Fig. 12, and its worth is 320 W.

Circuit outline of PV and battery based on microgrid-associated inverter with closed loop SM controller is addressed in Fig. 13. Voltage across PV and battery based on microgrid inverter framework is appeared in Fig. 14, and its worth is 22 V. Voltage across flying capacitor support converter of PV and battery based on microgrid network-associated inverter framework is appeared in Fig. 15, and its worth is 60 V. Voltage across RL heap of PV and battery based on microgrid-associated inverter framework is appeared in Fig. 16, and its worth is 120 V. RMS voltage across RL heap of PV and battery based on microgrid-associated inverter framework

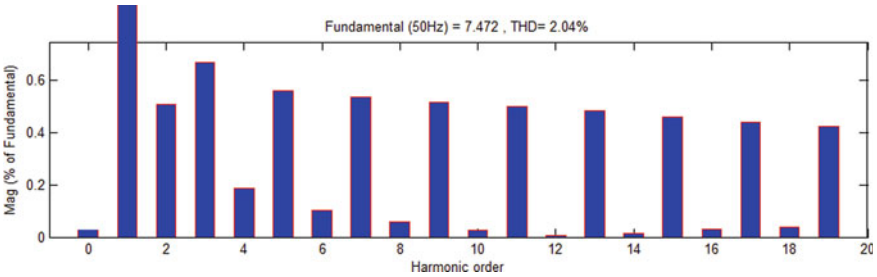

Fig. 11 Current THD

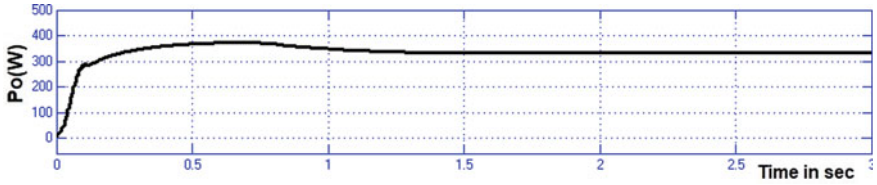

Fig. 12 Output power

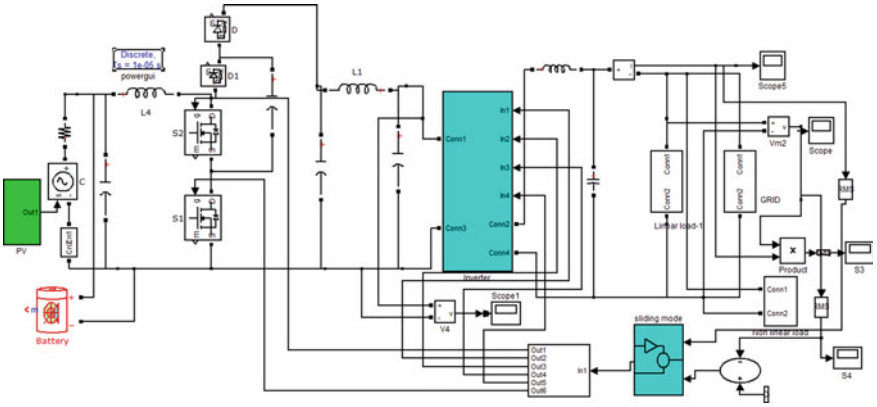

Fig. 13 Circuit diagram of PV and battery based on microgrid-connected inverter with closed loop SM controller

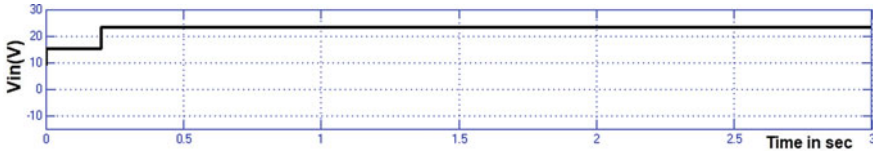

Fig. 14 Input voltage

Fig. 15 Voltage across flying capacitor boost converter

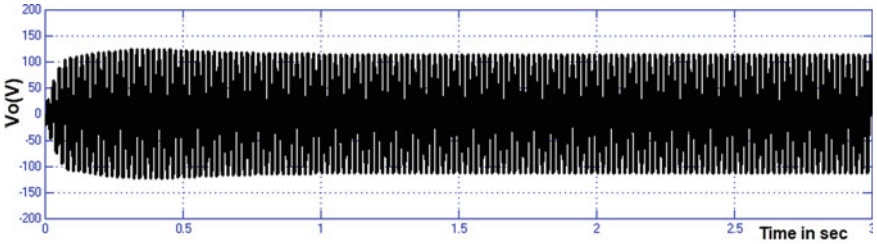

Fig. 16 Voltage across RL load

is appeared in Fig. 17, and its worth is 80 V. The voltage THD esteem is fundamental 50 Hz = 108.5, and THD esteem is 1.61% and is appeared in Fig. 18. Current through RL heap of PV and battery based on microgrid-associated inverter framework is appeared in Fig. 19, and its worth is 8 A. The current THD esteem is fundamental 50 Hz = 8.116, and THD esteem is 1.36% and is appeared in Fig. 20. The current THD esteem is fundamental 50 Hz = 100, and THD esteem is 1.36% and is appeared in Fig. 21. Yield force of PV and battery based on microgrid framework-associated inverter framework is appeared in Fig. 22, and its worth is 300 W.

Table 1 gives the correlation of time-domain boundaries with PID and SMC controller of PV and battery based on microgrid network-associated inverter framework. Utilizing SMC regulator, the ascent time is decreased from 0.38 to 0.33 s, the settling time is diminished to 0.84 from 1.10 s, the rush hour is diminished from 0.73 to 0.42 s, and the consistent state mistake is diminished to 0.43–1.33 V.

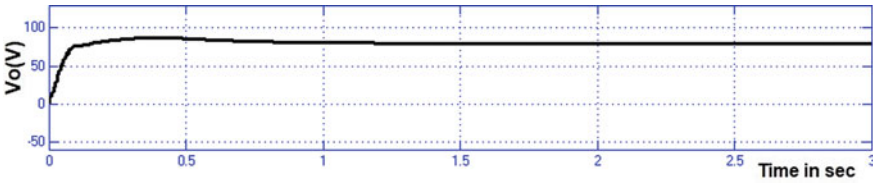

Fig. 17 RMS voltage across RL load

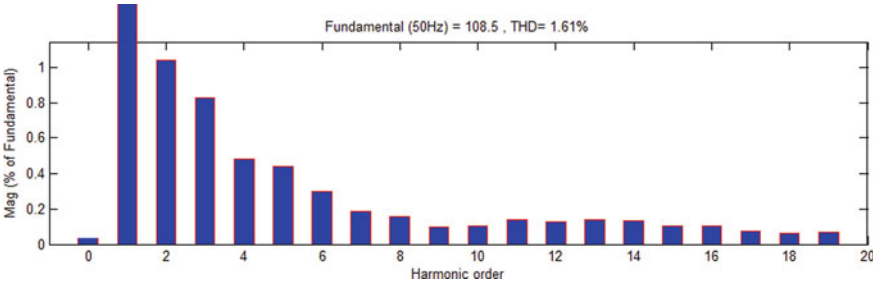

Fig. 18 Voltage THD

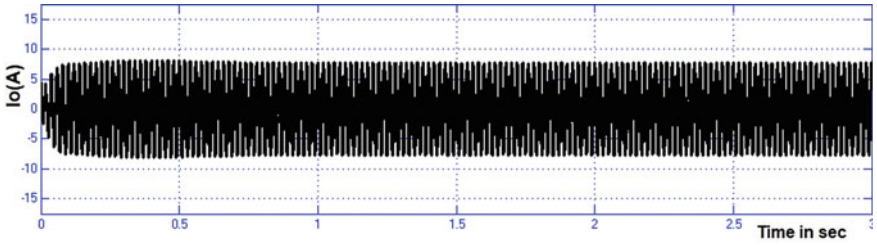

Fig. 19 Current through RL load

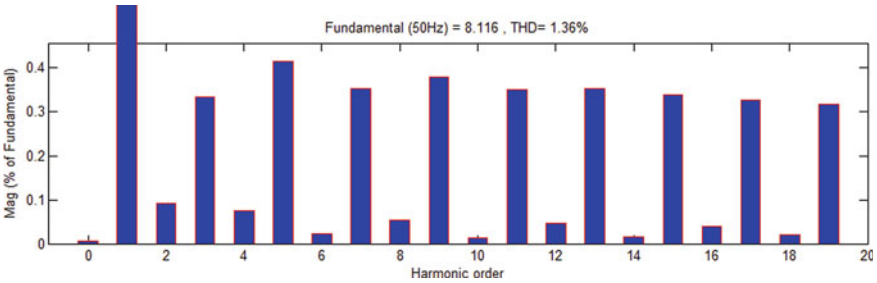

Fig. 20 Current THD

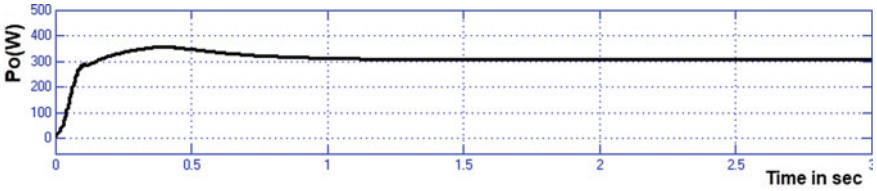

Fig. 21 Output power

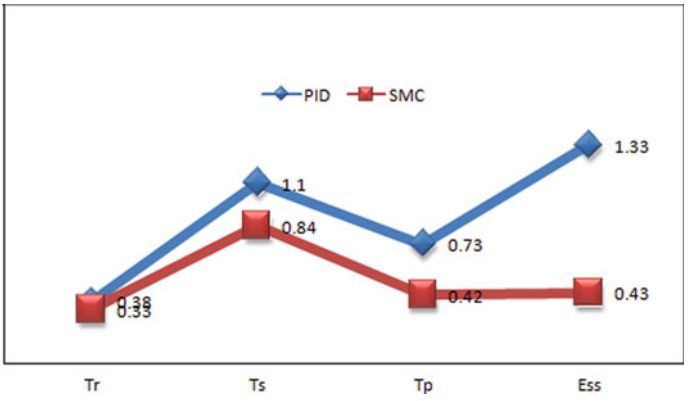

Fig. 22 Bar chart comparison of time-domain parameters for PID and SMC controller

Table 1 Comparison of time-domain parameters

Controller	Tr	Ts	Tp	Ess
PID	0.38	1.10	0.73	1.33
SMC	0.33	0.84	0.42	0.43

Table 2 Comparison of voltage and current THD

Controller	Voltage THD (%)	Current THD (%)
PID	2.12	2.04
SMC	1.61	1.36

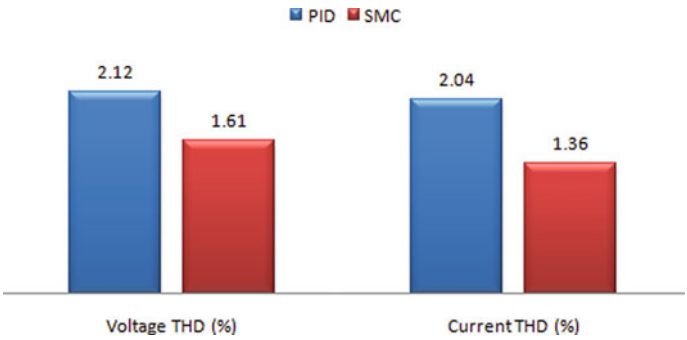

Fig. 23 Bar chart comparison of voltage and current THD of PID and SMC controller

Figure 22 shows the bar graph correlation of time-domain boundaries for PID and SMC controller. Table 2 gives the examination of voltage and current THD of PID and SMC controller of PV and battery based on microgrid framework-associated inverter system. Fig. 23 gives the bar graph examination of voltage and current THD of PID and SMC controller.

4 Conclusion

The flying capacitor support converter-based dynamic and receptive channel utilized for framework-associated voltage source inverter in shut circle is reproduced, and the outcomes with PID and SMC are introduced. By utilizing SMC, the ascent time is lessened from 0.38 to 0.33 s; the rush hour is reduced from 0.73 to 0.42 s; the settling time is decreased from 1.10 to 0.84 s; the consistent state blunder is reduced from 1.33 to 0.43 V. Thusly, SM-based dynamic and responsive channel might be a feasible option in contrast to the current framework. The decrease in settling time and the consistent state mistake Reponses is better on account of SMC framework. The benefits of the proposed framework are the decrease in voltage THD and current

THD, line drop, consistent state blunder and settling time. The impediment is that it requires an enormous inductor and a capacitor.

The present work deals with the investigation PID- and SMC-controlled grid-connected inverter system. The improvement with HC will be done in future.

References

1. Blaabjerg F, Chen Z, Kjaer SB (2004) Power electronics as efficient interface in dispersed power generation systems. IEEE Trans Power Electron 19(5):1184–1194
2. Wang F, Duarte JL, Hendrix MAM, Ribeiro PF (2011) Modeling and analysis of grid harmonic distortion impact of aggregated DG inverters. IEEE Trans Power Electron 26(3):786–797
3. Asiminoaei L, Blaabjerg F, Hansen S, Thogersen P (2008) Adaptive compensation of reactive power with shunt active power filters. IEEE Trans Ind Appl 44(3):867–877
4. Asiminoaei L, Blaabjerg F, Hansen S (2007) Detection is key—Harmonic detection methods for active power filter applications. IEEE Ind Appl Mag 13(4):22–33
5. Chakroborty S, Weiss MD, Simoes MG (2007) Distributed intelligent energy management system for a single-phase high-frequency ac microgrid. IEEE Trans Ind Electron 54(1):97–109
6. Brahma SM, Girgis AA (2004) Development of adaptive protection scheme for distribution systems with high penetration of distributed generation. IEEE Trans Power Del 19(1):56–63
7. Hossain MR, Maung Than Oo A, Shawkat Ali ABM (2010) Evolution of smart grid and some pertinent issues. In: 2010 20th Australasian universities power engineering conference (AUPEC), pp 1–6, 5-8 December 2010

Electric Propulsion System with Dual-Motor Power Management Strategy

Vinoth Kumar Balan, P. Avirajamanjula, and A. Dominic Savio

Abstract Dual-motor electric powertrain offers the independent control and less energy consumption in plug in hybrid electric vehicle model. The component sizing and control strategy are play the important role in dynamic control, power management and energy saving. The proposed system vehicle architecture comprises the dual motor, downsized engine and synchronizer. For optimizing the dynamic load sharing with the dual-motor powertrain configuration, rule-based fuzzy logic control strategy is implemented. The variable load will be managed by the way of selecting different transmission topologies using fuzzy logic control strategy. This dual-motor architecture configuration is simulated using Simulink software. Single motor propulsion drive control is engaged for all driving pattern except the peak load condition. In peak load, such as acceleration mode and high-speed mode, the dual-motor power transmission is engaged. The powertrain configuration is test at different dynamic and load conditions. As a result, it shows the better drivability, high efficiency and extended driving range.

Keywords Motor · Fuzzy · Plug in hybrid vehicle · Power management · Driving cycle · Series hybrid electric vehicle

1 Introduction

The day-by-day usage fossil fuel rapidly increasing, due to this rising oil prices, makes more impact on transport sector and economic. On other hand, the usage of oil causes the air pollution, global warming, acid raining, etc. So, most of the governments are encouraging the people to use electric vehicle [1–3]. The pure

V. K. Balan (✉) · P. Avirajamanjula
Department of Electrical and Electronics Engineering, PRIST University, Thanjavur, India

P. Avirajamanjula
e-mail: avmanju17@gmail.com

A. D. Savio
Department of Electrical and Electronics Engineering, SRM Institute of Science and Technology, Chennai, India

C. Subramani et al. (eds.), *Proceedings of International Conference on Power Electronics and Renewable Energy Systems*, Lecture Notes in Electrical Engineering 795,
https://doi.org/10.1007/978-981-16-4943-1_53

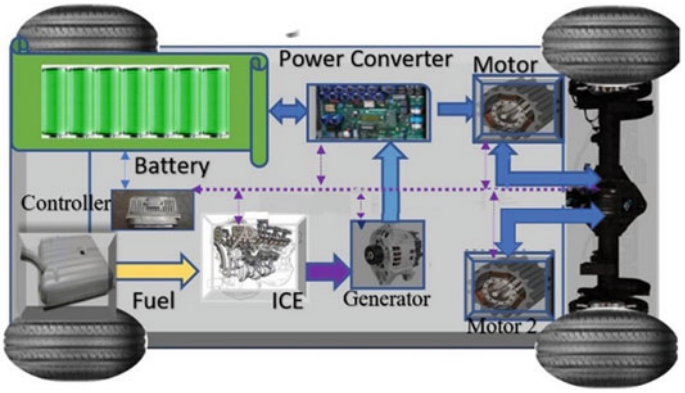

Fig. 1 Powertrain configurations for plug-in hybrid electric vehicle

electric vehicle has features of zero emission, economic operation, less maintenance, etc. Even though pure electric vehicle has problem of long-range driving problem due to limited energy storage, long charging periods, the people are reluctant to buy the electric vehicle [5–9]. So, auto industries and many researchers are finding feasible solution for electric vehicle. Plug-in hybrid electric vehicles have features of extended driving range, grid charging, multi-mode of operation the powertrain configuration of PHEV as shown in Fig. 1.

$$\text{Hybridization factor} = \frac{P_{\text{em}}}{\left(P_{\text{em}} + P_{\text{eng}}\right)} \tag{1}$$

$$\text{Hybridization factor} = \frac{P_{\text{em}}}{P_{\text{hve}}} \tag{2}$$

$$F_{\text{Total}} = F_I + F_s + F_r + F_a \tag{3}$$

$$F_I = ma \tag{4}$$

$$F_s = m.g.\sin\theta \tag{5}$$

$$F_r = m.g.Crr.\cos\theta \tag{6}$$

$$F_a = \frac{1}{2}\rho C_d A V^2 \tag{7}$$

$$P_{\text{Total}} = F_{\text{Total}}.V \tag{8}$$

Table 1 Value of parameters for the simulation of the powertrain

Name	Value
Electric motor *A* power	59 KW
Electric motor *B* power	40 KW
Engine	50KW
Battery capacity	110 Ah
Vehicle loaded mass	1400 kg
Air resistance coefficient	0.01
Number of batteries	25
Rolling resistance coefficient	0.012
Frontal area, A_f	2.33 m^2
Drag coefficient, C_d	0.26
Air density, ρ_{air}	1.22 kg/m^3
Wheel radius, R_{wh}	0.32 m

$$E_{\text{Total}} = \int P_{\text{Total}} .\mathrm{d}t \tag{9}$$

$$E_{\text{Total}} = \frac{1}{3600}[m.g(f\cos\theta + \sin\theta) + 0.386(\rho C_d A V^2) + \left(m + m_f \frac{\mathrm{d}v}{\mathrm{d}t}\right)]D \tag{10}$$

$$\text{SOC}_{\text{min}} \leq \text{SOC}(t) \leq \text{SOC}_{\text{max}} \tag{11}$$

$$P_{\text{min}} \leq P(t) \leq P_{\text{max}} \tag{12}$$

where the P_{em} is the power produced by the electric motor, P_{eng} is the power produced by the ICE engine, P_{hve} is the total power the hybrid power propulsion system, F_r is aerodynamic drag, F_I is inertial force, F_s is the road slope force, F_a is the aerodynamic drag force, P_{Total} is the total traction power, F_{Total} is the traction force, V is the vehicle speed, E_{Total} is vehicle energy required, road load coefficient, Crr is the road load coefficient, g is the gravitational acceleration, m is the mass of the vehicle, θ is the road slope angle, ρ is the air density, C_d is the air drag coefficient, A is the vehicle frontal area, D is the distance of travelling (Table 1).

2 Modes of Hybrid Drive System

The plug-in hybrid vehicle, powertrain, comprises the dual motor, downsized engine and synchronizer. The rule-based fuzzy logic controller is developed for various

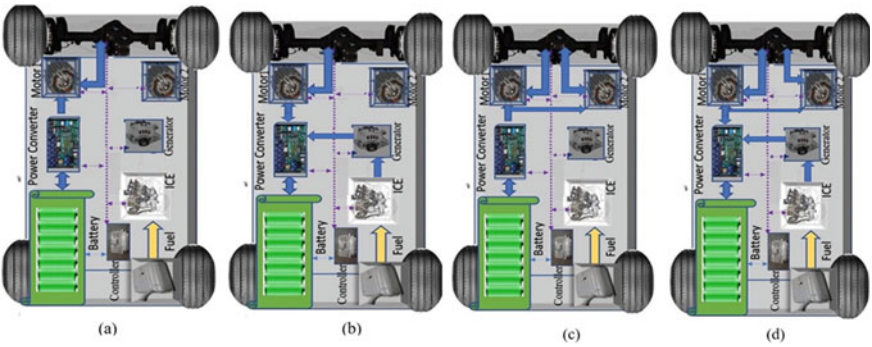

Fig. 2 **a** Single motor drive control, **b** series hybrid powertrain, **c** dual-motor drive control, **d** dual-motor series hybrid powertrain

load conditions of transmission pattern [10–12]. The different powertrain patterns are shown in Fig. 2. The SoC of the battery and power demand of vehicle are the two main controlling parameters. Based these values rule-based controller will decide the configuation of powertrain elements. The operating mode of the vehicle is mainly classified as start/stop, acceleration, cruising, de-acceleration, idle. The power demand of the vehicle is very high, when its operating either in cruising mode or acceleration mode. The acceleration and high-speed mode, i.e., cruising mode the power demand of the vehicle is so high [13–15]. In this peak power demand condition, the torque requirement of the vehicle is met by the dual-motor powertrain. The remaining mode of operation is managed by the single motor powertrain. The result of single motor power configuration, extended driving range, fuel economy, extended battery life can be obtained. The result of single motor driving, this system can obtain fuel economy, battery saving, extended driving range.

3 Operation Mode Transition

The powertrain driving propulsion pattern condition is explained through flow chart as shown in Fig. 2. Fuzzy controller evaluated the SoC of the battery and vehicle travelling distance (D). If energy storage system parameter is in acceptable range, i.e., (SoC > *D*), the driving pattern will be identified either dual-motor drive or single-motor drive condition. In case, SoC < *D,* the engine turns to on condition for charging the battery. The transient condition is periodically evaluated and improved by the rule-based fuzzy logic controller. If SoC is 0.6 < SoC < 0.8 and the power demand is P_dem ≤ P_em1, condition results the motor *A* met the torque requirement of the vehicle. Even SoC of the battery in the range of 0.6 to 0.8 and power demand is high (P_dem ≥ P_em1), the dual-motor powertrain configuration will met the torque requirement of the electric vehicle (Fig. 3).

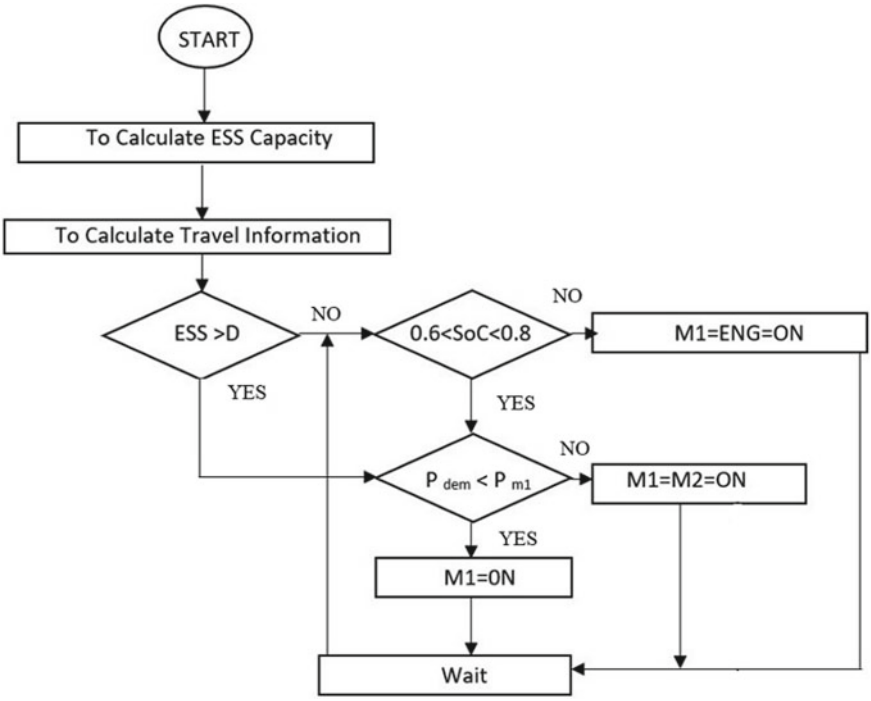

Fig. 3 Flow diagram of the control strategy

4 Simulation

In this proposed method, rule-based fuzzy controller was designed for the plug-in electrical vehicle to enhance the fuel economy and battery energy savings. The control strategy of fuzzy membership is created based on the power demand and SoC of the battery as shown in Fig. 4. The fuzzy membership for load control is shown in Fig. 4. For the different load condition, the controller will meet the power demand of the vehicle, based the load sharing in propulsion system (Figs. 5 and 6).

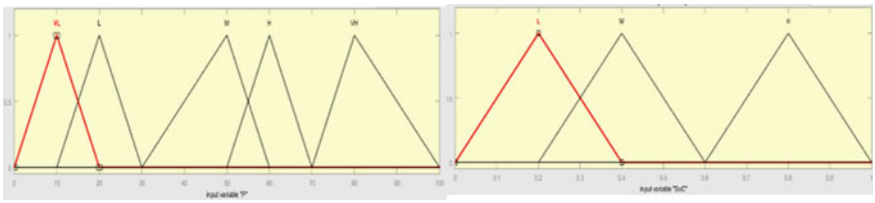

Fig. 4 Fuzzy membership for input

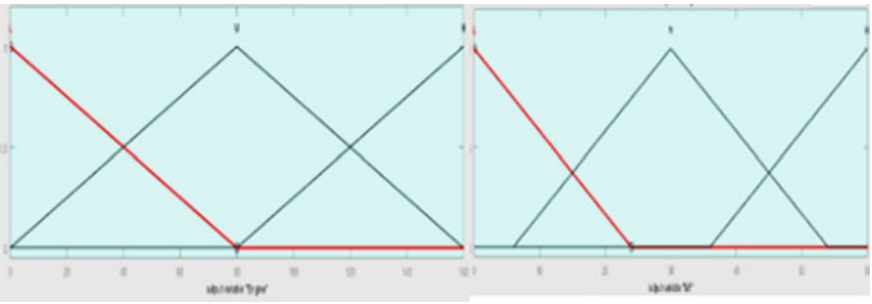

Fig. 5 Fuzzy membership for output

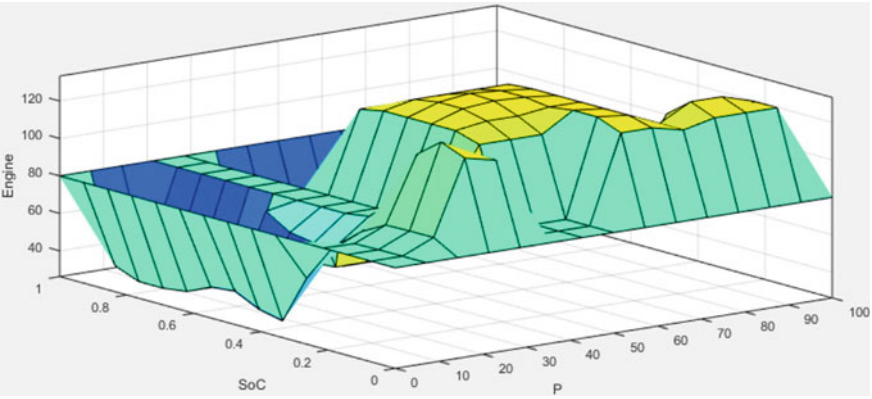

Fig. 6 3D Fuzzy control rule

In order to verify the energy consumption of the powertrain, the proposed system is simulated for various driving conditions. Dual-motor powertrain power output is shown in Fig. 7a. Low SoC condition was initiated for operating engine and generated in charging mode. The powertrain element shaft output is shown in Fig. (b). In start mode, the single motor driving pattern will meet the torque requirement of the vehicle from 0 to 2 s time period. The battery power loss is minimum in starting condition, and SoC of the battery is improved in this mode as shown in Fig. 7c, d.

When vehicle moves to the accelerating mode during the time interval of 2–5 s, the high-power demand occurs and the controller will optimize the load sharing of propulsion elements. In this mode, the dual-motor powertrain is configured. So, the powertrain requires consume more charge for the propulsions of the vehicle; due to this, the battery power loss increases rapidly and SoC decreases linearly. The vehicle was entering into cruising operation after the acceleration mode, so the controller will estimate the power demand and identifies feasible control strategy for this mode. In this cruising mode, vehicle operates by single motor powertrain to provide constant speed. So, the battery power loss is constant and SoC is linearly decreasing. The

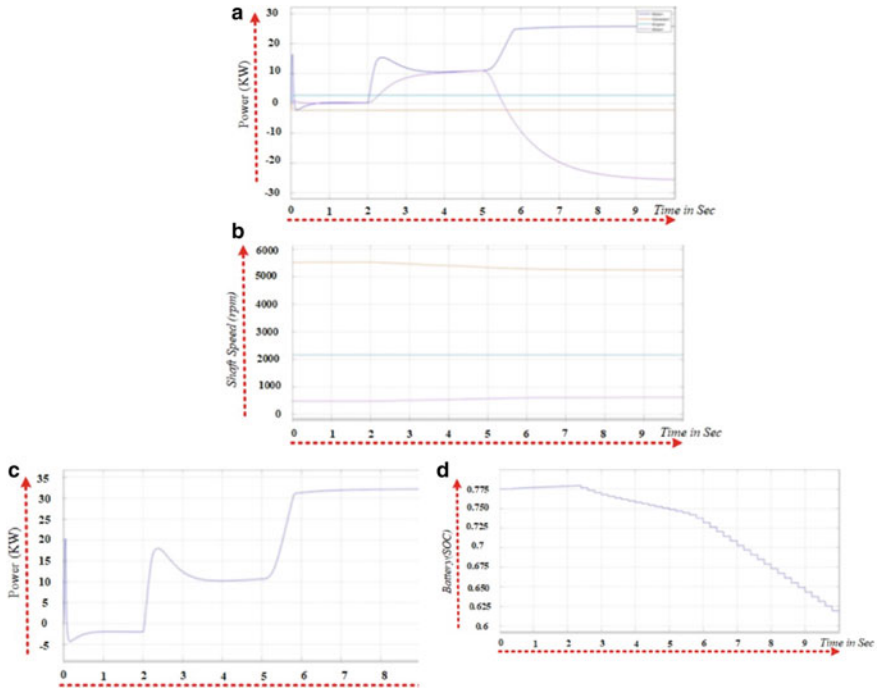

Fig. 7 **a** Dual-motor powertrain output. **b** Powertrain element shaft output. **c** Battery power loss. **d** Battery SoC at various load conditions

effect of the control strategy results, better dynamic control and extend driving range was obtained.

5 Conclusion

In this work, extending driving range of vehicle dual-motor propulsion powertrain is configured. By using the rule-based fuzzy logic controller, the control strategy is developed for different driving patterns. This system is design using Simulink software and tested for various load dynamic conditions. Peak load condition in dual-motor powertrain met the power demand of the load. All other load conditions are managed with single motor powertrain configuration. Compared to the conventional hybrid model, dual-motor powertrain offers the extended electric mode of operation. The result shows the better drivability and improved overall performance.

References

1. Wang F, Fang Z, Zhu X (2011) Matching, simulation and optimization of the new power transmission device for an electric vehicle. Autom Eng 33(9):805–808
2. Wang Y, Sun D (2014) Powertrain matching and optimization of dual-motor hybrid driving system for electric vehicle based on quantum genetic intelligent algorithm, vol 2014. Hindawi Publishing Corporation
3. Lv C, Zhang J, Li Y, Yuan Y (2015) Mechanism analysis and evaluation methodology of regenerative braking contribution to energy efficiency improvement of electrified vehicles. Energ Convers Manag 92:469–482
4. Zhang L, LiuW, Qi BN (2020) Energy optimization of multi-mode coupling drive plug-in hybrid electric vehicles based on speed prediction. Energy 206
5. Wang Y, Zeng X, Song D (2020) Hierarchical optimal intelligent energy management strategy for a power-split hybrid electric bus based on driving information. Energy 199
6. Xu J-H, Guo J-F, Peng B, Nie H, Kemp R (2020) Energy growth sources and future energy-saving potentials in passenger transportation sector in China. Energy 206
7. Goetz M (2005) Integrated: powertrain control for twin clutch transmissions. Univ. Leeds, Leeds, U.K
8. Wang W, Li Y, Shi J, Lin C (2018) Vibration control method for an electric city bus driven by a dual motor coaxial series drive system based on model predictive control.IEEE Access 6:41188–41200
9. Wang W, Zhang Z, Shi J, Lin C, Gao Y (2018) Optimization of a dual-motor coupled power-train energy management strategy for a battery electric bus based on dynamic programming method.IEEE Access 6:32899–32909
10. Ruan J, Walker PD, Zhang N, Wu J (2017) An investigation of hybrid energy storage system in multi-speed electric vehicle.Energy 140:291–306
11. Morozov A, Humphries K, Zou T, Martins S, Angeles J (2014) Design and optimization of a drivetrain with two-speed transmission for electric delivery step van.In: Proceedings of IEEE international electric vehicle conference (IEVC), Florence, Italy, December 2014, p 18
12. Kim H, Kim J, Lee H (2011) Mode transition control using disturbance compensation for a parallel hybrid electric vehicle. Proc IMechE Part D J Autom Eng 225:150–166
13. Enang W, Bannister C (2017) Modelling and control of hybrid electric vehicles (A comprehensive review). Renew Sust Energ Rev 74:1210–1239
14. Naunheimer H, Bertsche B, Ryborz J et al (2010) Automotive transmissions: fundamentals, selection, design and application. Springer Science & Business Media, Dordrecht
15. Enang W, Bannister C (2016) Robust proportional ECMS control of a parallel hybrid electric vehicle. Proc IMechE Part D J Autom Eng 231:99–119

Realization and Implementation of Peak Energy Management

P. Kanakaraj and L. Ramesh

Abstract Peak energy management (PEM) is an important tool in energy audit, which will manage and reduce the excess power demand required during peak hours. The role of PEM is to reduce the peak demand with the help of pricing tariffs and incentives for the consumers. The PEM is reviewed with techniques, applications, and ancillary services. Based on that, review new model is proposed. Here, we use a PV panel to charge the battery which is connected to the load through an inverter and switch. The grid is connected to the load through a switch as well. Hence, using this model enables us to supply power to the load with the help of a battery during peak hours, and the PV panel charges the battery during off-peak hours. Thus, it enables us to reduce the peak hour consumption and the bill cost as well.

Keywords Peak energy management · Demand response program · Renewable energy system · Battery energy storage system · Thermal energy storage · Diesel generator · Time of use · Multi-agent systems

1 Introduction

In the power system, the balancing of power demand is the major task [1]. In recent years, energy management is playing a vital role in balancing of power demand. It is a perfect solution for the reduction of energy consumption with the help of solar, wind, biomass, battery storage, and demand-side management (DSM) techniques. It is the skill and knowledge of optimal use of energy to maximize profits (minimize costs) and thereby increase the financial competitiveness. It can save up to 70% of the energy consumption in a typical building or plant, which is achieved with the help of required investment in transmission and distribution system, and also require proper monitoring system. It has forecast and development of energy production and

P. Kanakaraj · L. Ramesh (✉)
Dr.M.G.R. Educational and Research Institute, Maduravoyal, Chennai, India
e-mail: prof.lramesh@theigen.org

P. Kanakaraj
e-mail: kanakaraj.restu@drmgrdu.ac.in

C. Subramani et al. (eds.), *Proceedings of International Conference on Power Electronics and Renewable Energy Systems*, Lecture Notes in Electrical Engineering 795,
https://doi.org/10.1007/978-981-16-4943-1_54

energy consumption units. It is used by industries, residences, commercial buildings, and islanded systems. It is the procedure of monitoring, controlling, and preserving energy in a building or an industry. Energy management program has the major elements like setting your goal (size of energy reduction), know your numbers (size of requiring consumption), reduction in consumption (major consumption units to be reduced), and continuous review and management.

The energy should be used economically, efficiently, and optimally which can be identified with the help of energy efficiency [2]. Energy efficiency is very important for managers of commercial buildings. Commercial buildings are utilizing the energy in the form of heating, cooling, lighting, and hot water. The major aim of energy managements is resource preservation, climate protection, and cost savings. The population is increasing day by day, and due to this, electricity demand also increased with a higher number of electrical appliances which is affecting the reliability and efficiency of the utility grid.

Peak electricity demand was creating the constraints and congestion for transmission, which also increases the electricity cost for all the end-use consumers. Distribution and transmission infrastructure should be upgraded for providing power during the peak demand period. Normally, service providers charge a higher price at peak time and normal price during the off-peak time [4].

DSM helps to maximize the energy efficiency of all consumers and reduces the peak load and total power utilization [3]. The different DSM techniques are peak shaving (peak clipping), load shifting, flexible load pattern, and reduction of energy consumption. These techniques have the following benefits like reduction in electricity bills, managing the ancillary services, reduction requirement of new power plants, and upgradation of requiring transmission and distribution networks. The integration of storage devices into renewable energy systems requires novel load management techniques to manage more complex energy systems. This complex renewable energy system creates full of uncertainties like renewable energy sources, errors in renewable energy forecast, electricity demand, and electricity prices.

The structure of this paper is as follows: Sect. 2 explained the different existing peak energy management articles in the view of different techniques, different applications, and different ancillary services. Open issues and research directions are discussed in Sect. 3. Section 4 is deliberated the proposed work and its results. Finally, this paper is concluded in Sect. 5.

2 Recent Research on Peak Energy Management

Peak energy management articles were discussed based on the techniques to reduce the peak demand, applications where peak energy management was proposed, and ancillary services which were helpful to reduce the peak demand. Some of the abovementioned topics are discussed further in this section.

2.1 Techniques

Peak energy management techniques are implemented to reduce the peak demand during peak time. These techniques are classified into the time of use (TOU), peak shaving, peak shaving and valley filling, multi-agent program, peak strategies based decision-making process, real-time pricing, variable peak pricing, critical peak pricing, interruptible/curtailable service, capacity market program, and direct load control. The few of the above techniques are implemented recently, and in this, some of them are discussed below based on the results obtained.

(i) Time of Use

Ali Mehdizadeh et al. proposed an information gap decision theory (IGDT) for obtaining the bidding strategy of micro-grid (MG) [6]. MG considered the two different uncertainty environments like robustness decision (risk-averse) and opportunity decision (risk-taking). The main purpose of the demand response program (DRP) in MG was a reduction in energy procurement cost.

Ilze Laicane et al. investigated a study of demand-side management, which reduces the peak load of residential houses [7]. This article considered a household with four members and focused on two dissimilar appliances like a washing machine and dishwasher for load shifting. DRP was used to identify the pattern of household appliances. It was noted with the help of a smart meter installed in the houses. TOU or load shifting algorithm was implemented in the DRP. Figure 1 shows the impact of optimization on peak-time demand.

(ii) Peak Shaving

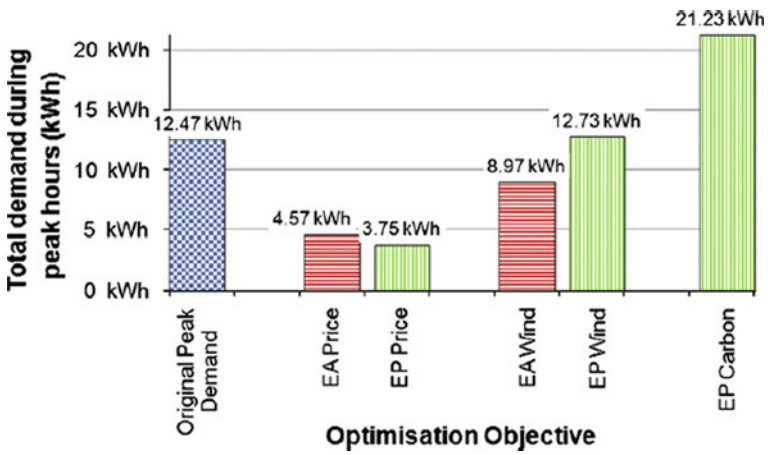

Fig. 1 Impact of optimization on peak-time demand

Sanjeev et al. designed a real-time simulation of different practical scenarios in the residential houses like peak, off-peak, and isolated modes of operations in RSCAD/RTDS software platform to bring the comprehensive power flow control strategy (PFCS) [9]. These modes were operated based on the RES, BESS, and ultracapacitor.

Fakeha Sehar et al. proposed an ice storage technology to shift the air-conditioning (AC) load of the medium-sized office building to off-peak periods, which reduced the total electricity consumption to 17.8% [5]. This study was performed during the summer season with a different combination of DRP, solar power generation, and cold storage systems.

(iii) Multi-Agent System

Hantao Huang et al. proposed a multi-agent minority game-based energy management system (MG-EMS) to reduce the peak electricity demand on the main grid [13]. The static and centralized energy management system (SC-EMS) was considered a traditional energy management system, which was taken as a base case. Experimental results of MG-EMS and uncertainty-aware minority game-based energy management systems (UAMG-EMS) were compared with the SC-EMS method. MG-EMS was mainly framed for reducing the peak demand of the grid and also providing additional support to the grid with solar energy. Figure 2 shows the summer and winder energy cost savings comparison with different energy management systems.

(iv) Peak Strategies (Decision Making)

Cristina Azcarate et al. planned a new management policy named Peaking Strategies. In this peaking strategy, electricity was converted into hydrogen at the off-peak price

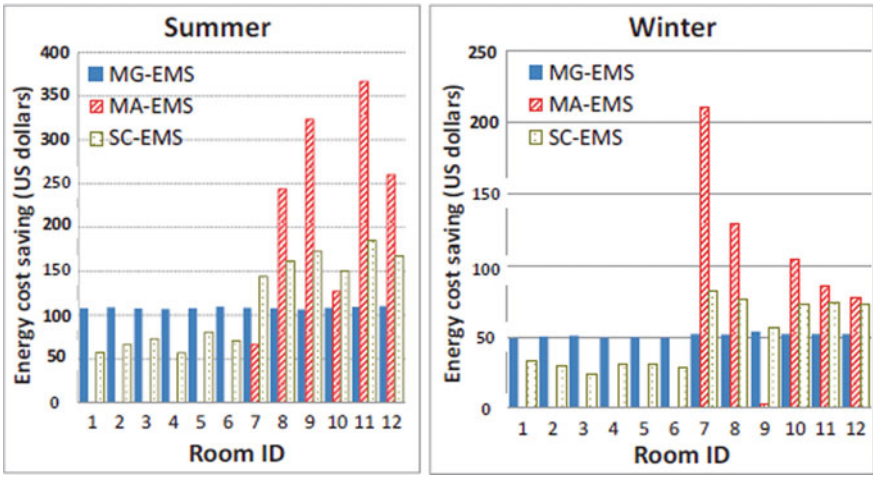

Fig. 2 Summer and winter energy cost savings comparison with different energy management systems

period and similarly, hydrogen was converted into electricity at peak price periods [14]. Also, stored hydrogen was used to convert as electricity during the high peak demand in the daytime when the grid reinforcement was high.

2.2 *Applications*

Peak energy management is a very important tool to reduce peak demand during peak time and is implemented in many applications like rural areas/islanded power systems, residential consumer, industrial consumers, and smart buildings (medium-sized office building/high-rise residential building). In this section, some of the applications are discussed as follows.

(i) Islanded Power Systems/Rural Areas

Spyridon Chapaloglou et al. proposed a new algorithm of EMS for an islanded power system [12]. In this algorithm, we combined diesel generators, a PV farm, and a battery energy storage system (BESS) with the help of load forecasting methodology and pattern recognition procedure. Figure 3 shows the developed neural network for load forecasting.

Michael T. Wishart et al. proposed a novel peak load management for the rural areas with diesel generator (DG) [10]. In order to avoid peak demand during peak time, some parts of the residential consumers were supplied with the help of DG.

(ii) Residential Consumer

Jagruti Thakur et al. designed the load balancing and load shifting for effective management of the power grids with the help of DSM mechanisms [1]. The main objective of this paper was to control the monthly bills as well as to discover the dynamics of demand response-based tariff mechanisms on consumer load profiles. DSM program was applied to obtain the economic savings for the residential consumer and classified into price-based technique and incentive-based technique.

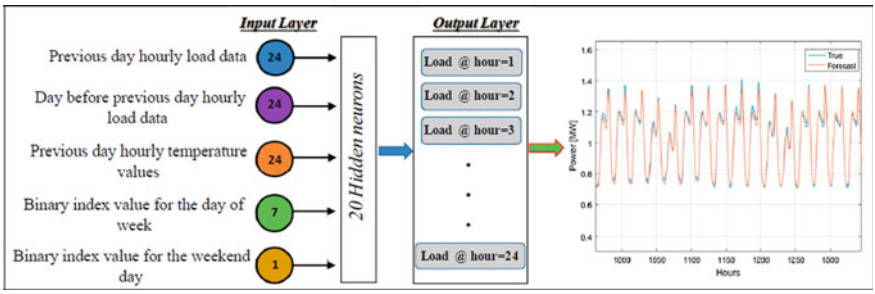

Fig. 3 Developed neural network for load forecasting

Krystian X. Perez et al. designed a centralized model predictive control (MPC) scheme for residential consumer to minimize the peak demand [15]. The scheduling operation was formulated to minimize peak demand with a mixed-integer linear program (MILP) for time-shiftable individual appliances like dishwashers, washing machines, and dryers in each house.

K. Keerthi Jain et al. discussed the saving of energy with the help of effective energy audits [18]. In this paper, the energy audit was conducted for a double bedroom house in Chennai. After the critical energy audit, the author recommended the few implementations in that house with and without investments to achieve more energy savings.

(iii) Industrial Consumer

C. A. Babu et al. presented optimized load management for electrolytic process industries [8]. Load management was implemented with the help of mixed-integer nonlinear programming (MINLP) technique to minimize the electricity cost and reduce the peak demand by rescheduling the loads and satisfying the industrial constraints.

S. Ashok presented a common load model for any type of process industry, which was based on the characteristics of batch-type loads [16]. The main objective is minimizing the total electricity cost with an optimal response for any industry under time-varying tariff. The case study of a steel plant was considered and obtained the significant reduction in peak-period demand around 50% and total electricity cost around 5.7% with an optimal load schedule.

Dongmin Yu et al. implemented the TOU method in the DRP to the industrial consumers [2]. The total electricity cost of the industry was compared between deterministic method and the proposed method with and without considering DRP. Finally, the total electricity cost was reduced by 8.2% for the optimization method and 6.5% for the deterministic method with the help of DRP.

(iv) Smart Buildings

Fakeha Sehar et al. simulated a medium-sized office building to reduce the peak load and energy utilization, which was located in Virginia, USA [5]. The building's peak electricity demand and energy consumption were reduced with the help of solar power generation, DR, and cold storage systems. In Table 1, savings in peak load, energy utilization with partial, and full ice storage are displayed. Figure 4 shows the power consumption profiles of the simulated building with combinations of PV generation, full ice storage, and DR.

Yu Wang et al. investigated the peak shaving and valley filling potential of the energy management system (EMS) in a high-rise residential building with the help of multi-agent system (MAS) framework with equipped PV storage system [17]. The simulation was done with the help of EMS, which flattened the HRB electricity demand profiles, and also, the peak-to-valley ratio of demand profiles was reduced much.

Table 1 Savings in peak load, energy utilization with partial and full ice storage

	Peak load at 4:10 pm (kW)		Energy consumption for the simulation day (GJ)	
	Building	HVAC	Building	HVAC
Without ice storage (conventional DX unit)	223.40	107.34	10.42	4.52
With full ice storage	128.37	12.31	16.88	10.98
With partial ice storage	190.22	74.15	14.52	8.63

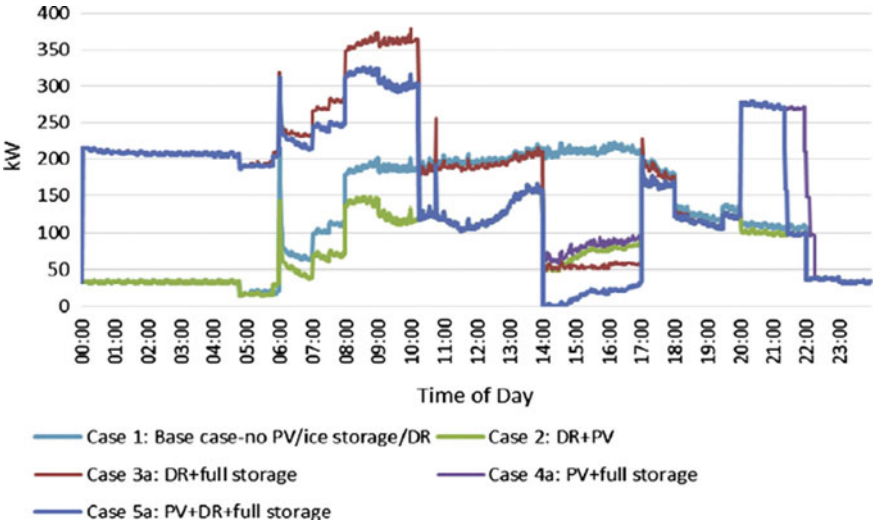

Fig. 4 Power consumption profiles of the simulated building with combinations of PV generation, full ice storage, and DR

2.3 Ancillary Services

Ancillary services helped to compensate the peak demand during peak time. It is classified into renewable energy sources (RES), battery energy storage system (BESS), thermal energy storage (TES)/ice storage, diesel generator (DG), and ultracapacitor. The following ancillary services are discussed in the recent peak energy management articles.

(i) Renewable Energy Sources (RES)

Surekha Dudhani et al. proposed the optimal allocation of various renewable energy sources (RES) to meet the peak load demand at various places in India [11]. This proposed algorithm was implemented by using a linear programming algorithm with various constraints. Different RESs were small hydel power, solar PV, wind power, co-generation, and biomass energy which was varied depending upon the places.

Table 2 Cost savings of combined TES and PV power generation

	Cost savings (€)			Cost savings (%)		
	Demand	Energy	Total	Demand	Energy	Total
Denver	6167	12,636	18,803	12.7%	8.8%	9.8%
Nebraska	5697	12,526	18,223	11.7%	8.8%	9.5%
Syracuse	5580	10,834	16,414	11.5%	7.6%	8.6%

(ii) Battery Energy Storage System (BESS)

Dongmin Yu et al. proposed a novel optimization technique for modeling of uncertainty in the electricity market [2]. The industrial customer was taken energy from the electricity market, reciprocal agreements, small-scale turbines, energy storage devices (ESD), wind generation, and solar panel generation with DRP. The newly proposed optimization technique was implemented with the help of the risk-averse method, which was also recommended to compare with the risk-neutral method.

(iii) TES/Ice Storage

Mohammad Saffari et al. proposed the optimized DSM techniques with TES and PV power generation for peak load reduction in commercial and industrial power sectors [3]. The proposed DSM technique results confirmed the effectiveness of the peak demand reduction when compared with TES and PV individually. These techniques were implemented in the dairy factory which is located in the three different places like Denver, Nebraska, and Syracuse in Spain. Table 2 displays the cost savings of combined TES and PV power generation system.

(iv) Diesel Generator (DG)

Michael T. Wishart et al. presented a new peak load management for the rural areas with the help of diesel generator (DG) [10]. In this peak load management, some customer's power demand was shifted to the local non-embedded generators at peak time. This paper considered a case study in Central Queensland, Australia.

(v) Ultracapacitor

P. Sanjeev et al. proposed the reduction of the peak demand shortage available in the grid-connected system and also reliable power supply provided even in case of blackout or grid failure [9]. A comprehensive PFCS was designed as a real-time simulation of different practical scenarios in the residential houses like peak, off-peak, and isolated modes of operations in RSCAD/RTDS software platform with the help of RES, BESS, and ultracapacitor.

3 Open Issues and Research Directions

The following inferences are identified from the peak energy management articles which are discussed above.

- One of the major issues is creating an awareness among the public about peak, off-peak, and mid-peak hours in peak energy management [1].
- The requirement of customized tools of demand-side management is important for flexible loads in smart buildings [5].
- The proposed method (combined TES and solar PV) in the dairy factory should be applied to all other food processing factories, supermarkets, and any other industries which required significant cooling demand [3].
- The renewable generation's uncertainty modeling should be designed with the help of combined stochastic programming, information gap decision theory, and robust optimization approach [6].
- The home energy management systems (HEMS) would be designed for the individual residential consumer with the help of energy storage systems and the influence of distributed generation systems [15].
- The development of solar PV storage technique would be made with higher efficiency and lower investment cost to promise larger peak shaving and valley filling [17].
- Real problems in industrial and healthcare contexts would be addressed with the combination of simulation as well as optimization techniques [14].
- In the future, the fuel consumption of the diesel generators and detailed power inverter configuration would be considered [12].
- The DCMG will be implemented only where the conventional grid does not exist such as low power domestic consumers, remote villages, data-centers, and telecommunication systems [9].
- The latest optimization technique would be extended to industries where the controllable loads are running continuously. Here, peak demand would be reduced with the help of rescheduling of their process [16].

4 Proposed Work with Results

This proposed work consists of buck/boost converters, a load (bulb), a battery for storage of energy, and a solar panel. Figure 5 shows the block diagram of the proposed work. The switch S_2 connects the grid and load. The switch S_3 connects the battery and load. Figure 6 shows the hardware model of the proposed system.

During the off-peak hours, the power is directly supplied to the load from grid as no excess load is demanded at that time. During the daytime, the battery is directly charged with the help of the solar panel as ample amount of sunlight is available. If the SOC of the battery is low then the battery is charged when the off-peak period

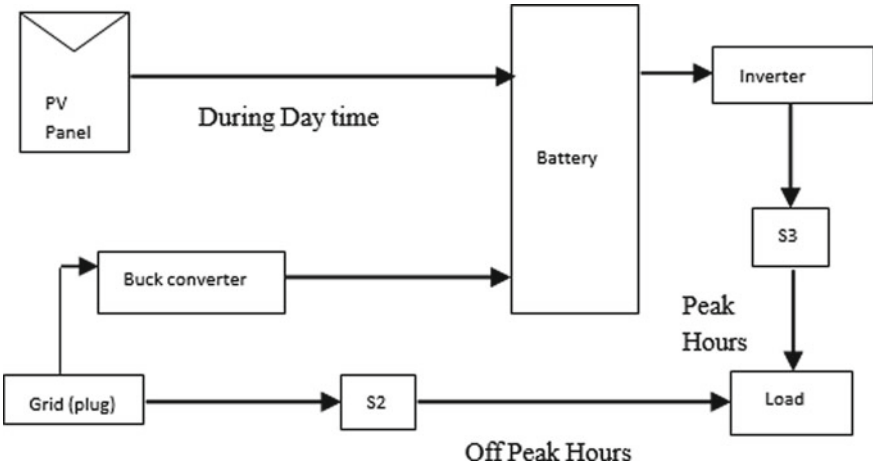

Fig. 5 Proposed block diagram

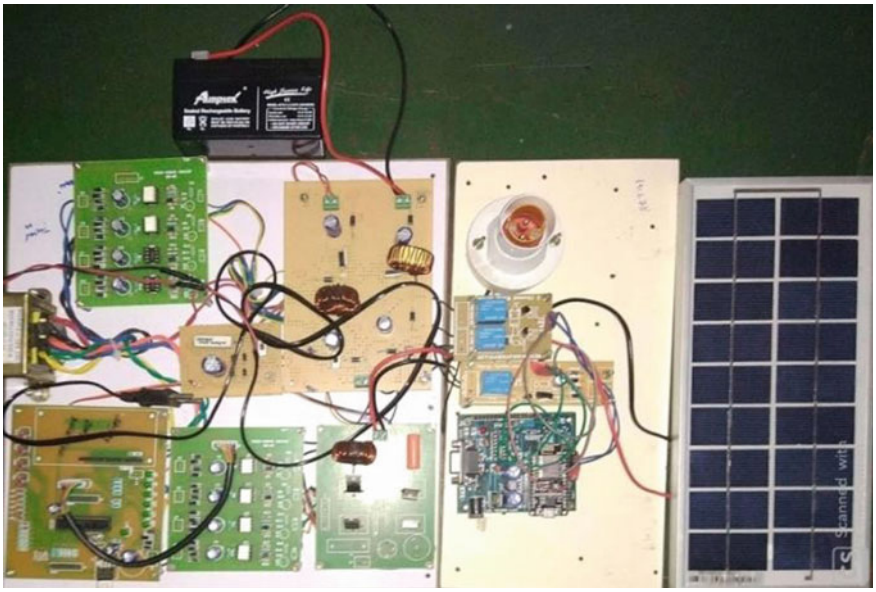

Fig. 6 Proposed system hardware model

starts (after 12 am). And during the peak hours, the grid is disconnected from the load, and the battery is connected to the load for supplying power.

The battery can be connected directly to the solar panel for charging as the system deals with a power of 5 W and 12 V, and no charge controller is required. However, a proper and standard charge controller will be required for a higher rating system.

From Fig. 7, it is shown that the model is in OFF condition and no supply is given to the bulb of 0.5 watts, neither from the grid nor from the battery.

From Fig. 8, it can be depicted that the system is working. However, it is not possible to distinguish from the picture whether the supply is given by grid or battery. When Switch 2 is turned on, the supply to bulb is given by the grid. When Switch

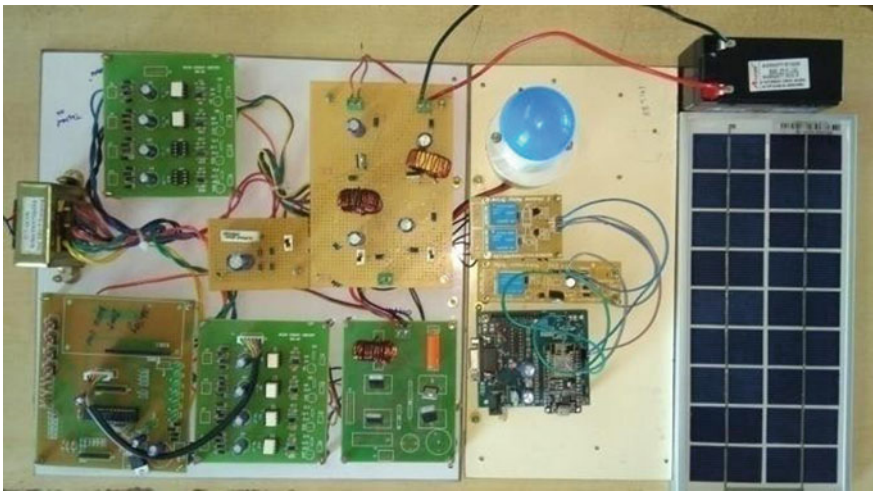

Fig. 7 System at OFF condition

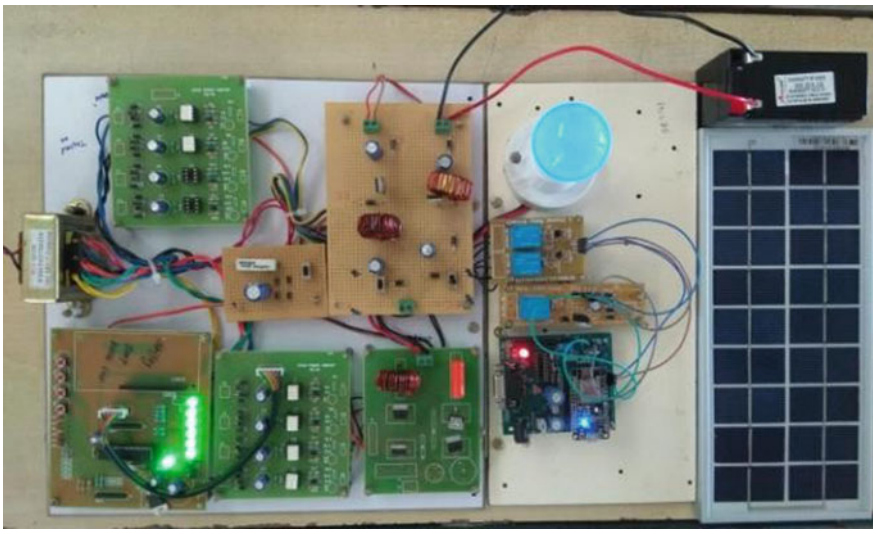

Fig. 8 System at ON condition

2 is turned off and Switch 3 is turned on then the supply to the bulb is given by the battery.

5 Conclusion and Future Scope

In this paper, a review of PEM is discussed with some inference. Based on that inference, new hardware model is proposed with an objective of reduction in peak load and reduction in consumer's electricity consumption cost. This proposed system can also be implemented on a larger scale. Some of the future scopes for improvements in the proposed systems are listed below.

- As the above process requires collection of readings and detailed analysis of load during night time, another renewable source such as wind can be utilized to charge the battery during the night time instead of the grid.
- Further, our system at present plans to deal with the load of a single house. With proper implementation and planning and strategy, this system might be utilized for an apartment and later a community with about 40–50 houses.
- This system can also be modified into one where the battery will be used to supply power during the peak hours to the lighter loads in a household like fans and tube lights.
- Also, the system that we have proposed is improvised into an automated one using intelligent controller unit.

References

1. Thakur J, Chakraborty B (2016) Demand side management in developing nations: a mitigating tool for energy imbalance and peak load management. Energy 114:895–912
2. Yu D, Liu H, Bresser C (2018) Peak load management based on hybrid power generation and demand response. Energy 163:969–985
3. Saffari M, de Gracia A, Fernández C, Belusko M, Boer D, Cabeza LF (2018) Optimized demand side management (DSM) of peak electricity demand by coupling low temperature thermal energy storage (TES) and solar PV. Appl Energ 211:604–616
4. Yao L, Yang B, Cui H, Zhuang J, Ye J, Xue J (2016) Challenges and progresses of energy storage technology and its application in power systems. J Mod Power Syst Clean Energ 4(4):519–528
5. Sehar F, Pipattanasomporn M, Rahman S (2016) An energy management model to study energy and peak power savings from PV and storage in demand responsive buildings. Appl Energ 173:406–417
6. Mehdizadeh A, Taghizadegan N, Salehi J (2018) Risk-based energy management of renewable-based microgrid using information gap decision theory in the presence of peak load management. Appl Energ 211:pp. 617–630
7. Laicane I, Blumberga D, Blumberga A, Rosa M (2015) Reducing household electricity consumption through demand side management: the role of home appliance scheduling and peak load reduction. Energ Procedia 72:222–229

8. Babu CA, Ashok S (2008) Peak load management in electrolytic process industries. IEEE Trans Power Syst 23(2):399–405
9. Sanjeev P, Padhy NP, Agarwal P (2018) Peak energy management using renewable integrated DC microgrid. IEEE Trans Smart Grid 9(5):4906–4917
10. Wishart MT, Turner J, Perera LB, Ghosh A, Ledwich G (2011) A novel load transfer scheme for peak load management in rural areas. IEEE Trans Power Deliv 26(2):1203–1211
11. Dudhani S, Sinha AK, Inamdar SS (2006) Renewable energy sources for peak load demand management in India. Int J Electr Power Energ Syst 28(6):396–400
12. Chapaloglou S et al (2019) Smart energy management algorithm for load smoothing and peak shaving based on load forecasting of an island's power system. Appl Energ 238:627–642
13. Huang H, Cai Y, Xu H, Yu H (2017) A multiagent minority-game-based demand-response management of smart buildings toward peak load reduction. IEEE Trans Comput Des Integr Circ Syst 36(4):573–585
14. Azcárate C, Blanco R, Mallor F, Garde R, Aguado M (2012) Peaking strategies for the management of wind-H 2 energy systems. Renew Energ 47:103–111
15. Perez KX, Baldea M, Edgar TF (2016) Integrated HVAC management and optimal scheduling of smart appliances for community peak load reduction. Energ Build 123:34–40
16. Ashok S (2006) Peak-load management in steel plants. Appl Energ 83(5):413–424
17. Wang Y, Liu L, Wennersten R, Sun Q (2019) Peak shaving and valley filling potential of energy management system in high-rise residential building. Energ Procedia 158:6201–6207
18. Jain KK, Kumar NK, Ramesh L, Raju MM (2014) An analysis to save electrical energy in a residential house. Int J Eng Sci 6(2):59–66

Novel Template Protection Scheme for Multimodal Data

C. Hari Akhilesh, M. Gayathri, and C. Malathy

Abstract A popular form of technology used for securing data is 'biometrics'. Biometrics are stored as templates, which are nothing but a digital reference of the unique characteristics extracted from the biometric, usually stored in a database which are used for authorizations and encryption. The concern for security of storage of templates is mainly due to the fact that the templates may not always be securely stored, and if a hacker does manage to crack the database, the attacker may find all the data stored in the template use it pilfer other important data or obtain access to confidential secrets. This paper suggests a novel scheme where in the fingerprint are stored safely using multi-modal biometric, namely iris, salting and chunking. It also proposes an efficient way to detect presentation attacks which using salt.

Keywords Biometric templates · Fingerprint template protection · Multimodal biometrics · Distributed template storage · Detection of presentation attack using salting

1 Introduction

To understand about template protection, we need to understand first what the biometrics are and why are the biometrics needed or have to be protected.

C. Hari Akhilesh (✉) · M. Gayathri · C. Malathy
Department of Computer Science and Engineering, SRM Institute of Science and Technology, SRM Nagar, Kattankulathur, Chengalpattu District, Tamil Nadu 603203, India
e-mail: cr3487@srmist.edu.in

M. Gayathri
e-mail: gayathrm2@srmist.edu.in

C. Malathy
e-mail: malathyc@srmist.edu.in

C. Subramani et al. (eds.), *Proceedings of International Conference on Power Electronics and Renewable Energy Systems*, Lecture Notes in Electrical Engineering 795,
https://doi.org/10.1007/978-981-16-4943-1_55

1.1 Biometrics

Biometrics are physical attributes or characteristics that help us identify a person uniquely. The world progressing towards a digital era has made the biometrics turn digital as well. There are multiple parameters that have to be taken in for considering a characteristic as a biometric. A few of them that are generally considered are universality which means majority of the people should have that particular trait or characteristic, another parameter is uniqueness which means that the characteristic should be vary from person to person, and a more common parameter used is permanence meaning the time before which the characteristic may change. An ideal biometric would one which is universal, unique and has less permanence.

These biometrics cannot be directly stored in the digital mode and hence are generally stored in the form of a template. These templates are generated from characteristics that are unique to that biometric, and there are many methods to generate the templates for different biometrics.

1.2 Need for Biometrics

Biometrics have begun to replace traditional passwords and pins as an authentication method; the main reason for this is because these types of authentication methods have become easy to break over the period of time due to increase in computation power. The shortcomings of traditional authentication methods are overcome by biometrics as it is very hard to crack or imitate a biometric.

Apart from authentication, biometrics are used to encrypt data and other day-to-day activities such as logging attendance of staff and students and solving crimes. This is mainly because a biometric cannot be forged and the person can be traced down easily using the biometric. All these have led to a huge prominence in the usage of biometrics in day-to-day life in the digital world.

1.3 Importance of Protection of Biometrics

Biometrics now being a key part of day-to-day routines is now being targeted by hackers who want the same for their personal benefits. The exposure can lead to data leaks by decrypting data that had been encrypted by a biometric or can lead to digital impersonation and hence access secure data. During impersonation, one can even defame the person who's biometric has been leaked, leading to trauma or false accusation.

When a person is able to get access to the biometric template, through impersonation, there can be a lot of other dependent services which are breached. There exist services that are linked using a biometric ID such as banks and other government

sectors, and if such an ID is accessed by a hacker with the help of the biometric template of the person, then it will be giving the hacker almost all details of the person right from his phone number to his physical address.

With all this being said, the need of protecting the biometric templates has increased and has provided a huge scope of research. Researchers have been trying to find and implement better biometric template protection schemes and hence fortify our privacy and security.

2 Proposed System

The proposed system aims to protect the biometric against multiple attacks using other biometrics. It also aims to detect presentation attack when the template is stolen and fed to the biometric system in a faster way. This detection is achieved by detection of salt. The enrolment steps of the proposed system in a brief manner are combining of biometrics, addition of salt, chunking, encryption and then random distributed storage. The main point to note here is that the main biometric is used for matching (first given one); the rest are used to protect this biometric. The verification process is of a similar manner where in the given biometrics are combining of given biometrics, fetching and rebuilding template from database, checking of salt in given template, then sending the given main template and defused template to matcher. The process is demonstrated using the physiological biometrics, namely fingerprints and iris. The processes of enrolment and verification are as shown in the Figs. 1 and 2, after which the system is elaborated based on its modules in the following sections.

2.1 Enhancement, Combining and Decombining

In this module, the system takes care of enhancing the received iris and fingerprints and then combines them or recombines them as required. This is done using the XOR method as this enables removal of the biometrics later when the same biometrics are given. For combining of the iris and fingerprint, we first normalize the iris and enhance the fingerprint and then we fuse them [1]. Enhancement of the fingerprint is done using a loosely followed method as proposed in the paper [2] wherein the fingerprint is enhanced using oriented Gabor filters and made into binary images. After enhancement, the fingerprint is skeletonized to enable combination. The iris is enhanced using canny edge detection followed by Hough circular transform after which we normalize it to a rectangular block with the help of 1D Gabor filters and phase quantization as suggested in [3] following which again canny edge detection is taken place to obtain the iris edges. Before combining, data can be resized to match a standard format to enable ease of combining. For decombining, the same process of enhancement and resizing is done after which the main biometric is skipped and

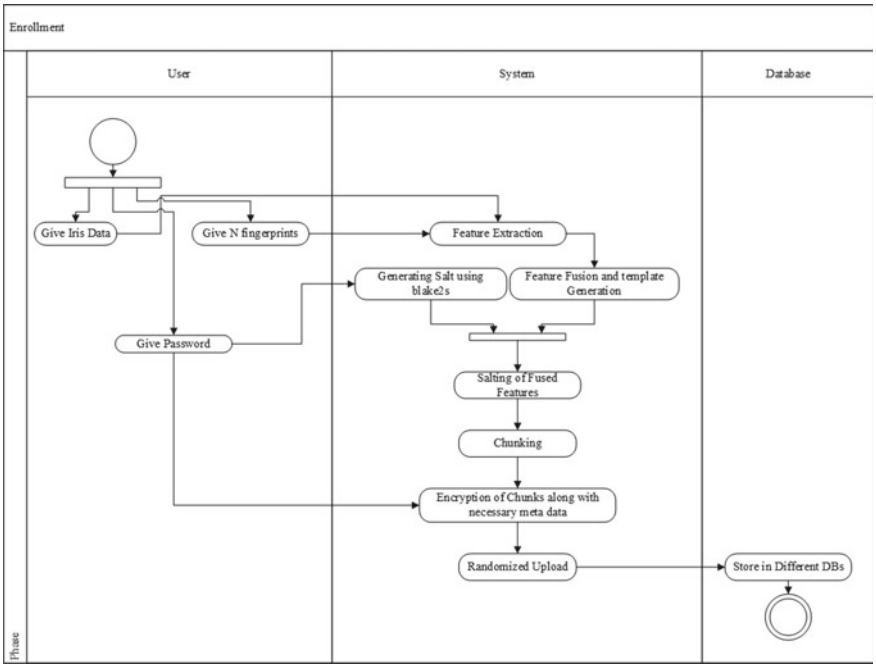

Fig. 1 Enrolment activity diagram

rest of the given biometrics are xored with the stored template to obtain the main biometric.

2.2 Salt

In the salt module, three major functions are achieved, namely salting, desalting and salt check. While the first two do what they imply, the third salt check function is for checking of salt existence in the given template for verification. To generate salt, we use password in conjunction with blake2s (which is a secure, lightweight and fast hash function) [4], wherein the key for blake2 is hardcoded in the machine and can only be accessed by direct access alone. Now, we convert this hash to a binary format which in turn is coded into a different number to avoid collision with image. Then, it is added or removed from template as required. For checking of salt, we first compare the given template directly with the assembled template from database. In the case it is the same the main, admin is notified for breach and the user is denied access. If it turns out to be negative, then we create a temporary unsalted template from the assembled template which is used to subtract data from the given template.

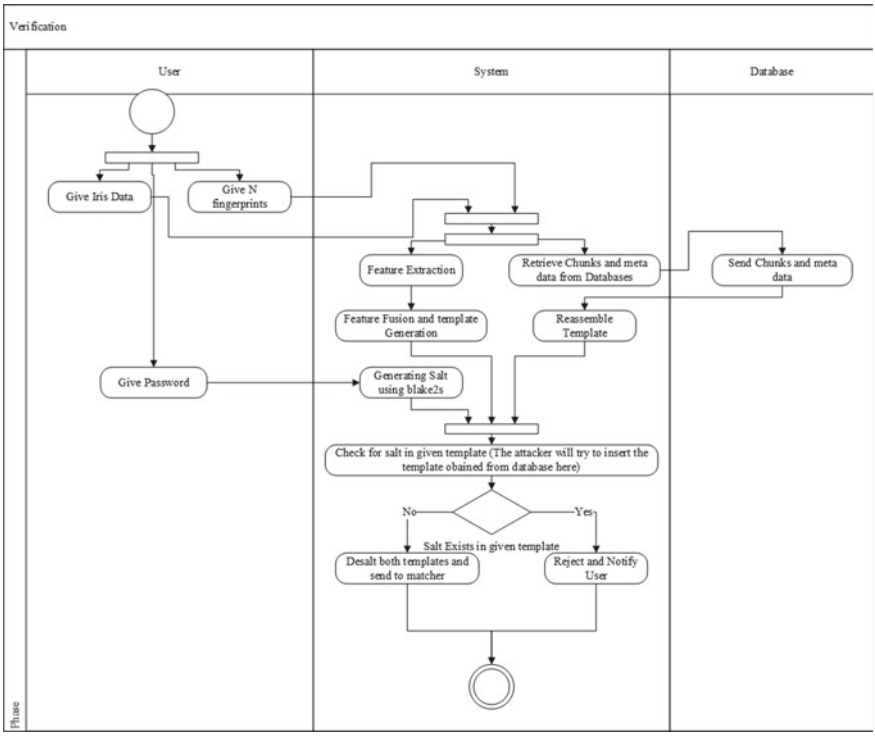

Fig. 2 Verification activity diagram

Now, we check the modified given template for remnants of the salt. If remnants exists, then we again notify the main admin and deny access.

2.3 Chunking, Encryption and Decryption, Assembly

This module takes care of chunking, assembling, encryption and decryption of the template. The chunking is done using array splitting as the images are nothing but data. For encryption, we obtain the password, which in turn is used to generate a key. Key generation is done using scrypt which is a strong key generator which may prove to be memory intensive for attackers [5]. For key generation, we generate a salt to be used using the SHA256 algorithm which is a strong hash function used to generate 256 bits of hash [6]. The key given to SHA256 is nothing but the password concatenated with a hardcoded string which is ideally different from the one used for salting module of template. Thus, making the salt a very strong one and hence making the key to be stronger. Now this generated key from scrypt algorithm is used in conjunction with AES. AES is chosen because it is a strong symmetric

cipher compared to other symmetric cipher algorithms [7]. Now, the chunks and the required meta data such as the shape of the chunk, chunk position are encrypted kept ready for uploading. For decryption and assembly, the process of key generation is repeated, and then, the chunks and meta data are decrypted using the key and assembled.

2.4 Database

The database module will handle the part where the chunks are randomly uploaded to different databases across the world, and this is done to ensure that all chunks are not available in the same database, which might enable the attacker to actually reassemble the salted template. Though the data can be stored in relational database, it is recommended to put in non-relational database (NoSQL) as it is optimized for key value storage and has better query times [8, 9]. This comes in handy, especially when there are multiple data to be stored, which will be the case due to chunking. For retrieval and storage, a username will be used, so therefore ensuring that the password is not stored in any form in any database.

3 Evaluation

3.1 Template Protection Scheme Analysis

A good template protection is one said to be one with good revocability, performance, security, unlinkability and diversity.

Revocability of the proposed system is achieved because of salting, encryption and combination of different biometrics, and the stored template chunks can be modified by simply modifying the password; in case that feels to be inadequate, a different combination of biometrics can be used to secure the template, hence making it different from the previous template. Diversity is attained as the combination of multiple biometrics along with salting, and in turn, encryption with AES will result in a different chunk of template even if biometrics given are same. Security is also achieved since visually the attacker will not be able to figure out the chunks due to encryption and their randomized upload order.

Performance of the template matching scheme actually depends on the matcher since the proposed system brings back the original main biometric and gives it to the matcher along with the given main biometric, so therefore no major performance hinderance is given by the proposed system. The time consumed for processes apart from enhancement is almost constant as shown in Fig. 3 (Table 1). Thus, we can say that the performance is unhindered in the proposed template protection scheme.

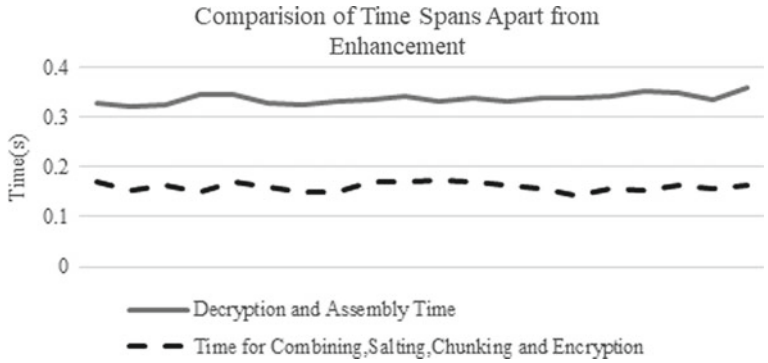

Fig. 3 Comparison of time spans apart from enhancement

Table 1 Time spans apart from enhancement

S. No.	Time for combining, salting, chunking and encryption (s)	Decryption and assembly time (s)
1	0.171608925	0.329058409
2	0.152110367	0.321273565
3	0.162323952	0.325931311
4	0.149440494	0.344387054
5	0.171329737	0.345149041
6	0.160823584	0.329431295
7	0.150390158	0.324714899
8	0.148513556	0.332785131
9	0.171221849	0.333497763
10	0.169684069	0.341736059
11	0.172198019	0.330428123
12	0.171744553	0.337514412
13	0.164268494	0.332345486
14	0.156521332	0.337944508
15	0.142908838	0.339892511
16	0.156084385	0.341259861
17	0.153265476	0.352910995
18	0.162986685	0.348599911
19	0.157442571	0.333347082
20	0.162786774	0.357174873

Also, due to the combination of multiple fingerprints and Iris, the proposed system manages to achieve unlinkability due to its complex combination possibility. Therefore, the proposed system gives a good balance of revocability, performance, security, unlinkability and diversity which are desired for a template protection scheme.

3.2 Salt Detection Analysis

The proposed system to detect salt and use against presentation attacks was trailed using custom-made template samples which resulted with the FAR and FRR as 0% and 1.6%, respectively, which is better than the results obtained by the proposed system in [1] even though it is a custom matching module versus an attack detection module, the FAR being better can reduce unnecessary time used up.

4 Conclusion

The proposed system uses a combination of salting, encryption and chunking using various modules to secure the template while ensuring revocability, performance, security, unlinkability and diversity apart from which a presentation attack either direct or using tampered templates is also detected with ease using the proposed salt detection method, hence ensuring further safety. Since this acts as a middle man between feature obtaining and matching, it can be used by a system for its betterment. The proposed system can also be extended to other biometrics such as finger knuckle print and finger vein. The system can be made better by using better enhancement techniques and using other better salt generation or key generation functions that are created in the future. Future works can be targeted for the same.

References

1. Conti V, Militello C, Sorbello F, Vitabile S (2010) A Frequency-based approach for features fusion in fingerprint and iris multimodal biometric identification systems. IEEE Trans Syst Man Cybern Part C (Applications and Reviews) 40(4):384–395. https://doi.org/10.1109/TSMCC.2010.2045374
2. Hong L, Wan Y, Jain A (1998) Fingerprint image enhancement: algorithm and performance evaluation. IEEE Trans Pattern Anal Mach Intell 20(8):777–789. https://doi.org/10.1109/34.709565
3. Masek L (2003) Recognition of human iris patterns for biometric identification. Doctoral dissertation, Master's thesis, University of Western Australia
4. Aumasson JP, Neves S, Wilcox-O'Hearn Z, Winnerlein C (2013) BLAKE2: simpler, smaller, fast as MD5. In: Jacobson M, Locasto M, Mohassel P, Safavi-Naini R (eds) Applied cryptography and network security. ACNS 2013. Lecture notes in computer science, vol 7954. Springer, Berlin, Heidelberg. https://doi.org/10.1007/978-3-642-38980-1_8

5. Alwen J, Chen B, Pietrzak K, Reyzin L, Tessaro S (2017) Scrypt is maximally memory-hard. In: Coron JS, Nielsen J (eds) Advances in cryptology—EUROCRYPT 2017. EUROCRYPT 2017. Lecture notes in computer science, vol 10212. Springer, Cham. https://doi.org/10.1007/978-3-319-56617-7_2
6. Gilbert H, Handschuh H (2004) Security analysis of SHA-256 and sisters. In: Matsui M, Zuccherato RJ (eds) Selected areas in cryptography. SAC 2003. Lecture notes in computer science, vol 3006. Springer, Berlin, Heidelberg. https://doi.org/10.1007/978-3-540-24654-1_13
7. Advani N, Rathod C, Gonsai AM (2019) Comparative study of various cryptographic algorithms used for text, image, and video. In: Rathore V, Worring M, Mishra D, Joshi A, Maheshwari S (eds) Emerging trends in expert applications and security. Advances in intelligent systems and computing, vol 841. Springer, Singapore. https://doi.org/10.1007/978-981-13-2285-3_46
8. Li Y, Manoharan S (2013) A performance comparison of SQL and NoSQL databases. In: 2013 IEEE pacific rim conference on communications, computers and signal processing (PACRIM), Victoria, BC, Canada, pp 15–19. https://doi.org/10.1109/PACRIM.2013.6625441
9. Čerešňák R, Kvet M (2019) Comparison of query performance in relational a non-relation database. Transp Res Procedia 40:170–177. ISSN 2352-1465. https://doi.org/10.1016/j.trpro.2019.07.027

Performance Optimization of Stepper Motor Using MATLAB

R. Gopalakrishnan, A. Dominic Savio, K. Dhayalini, and Nithya Rani Navaneethan

Abstract The importance of special machines has become an utmost necessity in the current scenario. The implementation of the different types of special machines in various types of applications has become quite challenging, keeping their mechanical and electrical characteristics in mind. In this paper, we have proposed the hybrid stepper motor performance analysis. The performance of the given motor is controlled for user-defined value, and errors are reduced to make the system more reliable. The performance stepper motor analyzed in MATLAB and the corresponding verified through hardware implementation.

Keywords Stepper · MATLAB · Special machines

1 Introduction

The machines have outgrown in numbers more than humans, and the purpose of the machines is so vast that their growth is nonstoppable nor the invention of new techniques, machines for each purpose going to be very normal. The applications of special machines like, switched reluctance, stepper motor, brushless DC have become so common and more advisable these days, because of their competency. For various stepping applications like angled movement, precise rotation, and other angular rotation applications, Le and Jeon [1] explain about the low-speed control of stepper motors with advanced FPGA technology, whereas the [2] paper describes the position control of a sensorless stepper motor. The more the electronic component in the circuitry, the complications and other disturbance in the performances increase.

R. Gopalakrishnan (✉) · K. Dhayalini
K. Ramakrishnan College of Engineering, Tiruchirappalli, India

A. Dominic Savio
School of Electrical Engineering, SRM Institute of Science and Technology (formerly known as SRM University), Kattankulathur Campus, Chennai 603203, India

N. R. Navaneethan
Sri Sairam Engineering College, Chennai, India
e-mail: nithyarani.ei@sairam.edu.in

C. Subramani et al. (eds.), *Proceedings of International Conference on Power Electronics and Renewable Energy Systems*, Lecture Notes in Electrical Engineering 795,
https://doi.org/10.1007/978-981-16-4943-1_56

The sensorless control of machines gives the open loop direct control of any motor. Masi et al. [3] give the sensorless stepper motor drive with extended Kalman filter; [4] studies the overview of the permanent magnet stepper motor for microstepping using a disturbance observer. The controlling of a motor for any nonlinear module is going to be very difficult; [5] explain the microstepping with nonlinear torque modulation for a permanent magnet stepper motor. Unlike other motors, the stepper motor construction is different with the input which is phased sequence, [6] where the phased-compensated microstepping for permanent magnet stepper motor is validated. Butcher et al. [7] it is stated the use of hybrid machines in intelligence drives, where we need go in for control technique algorithms for intelligence. The special machines have also become an important component for an automatic test bench system; [8] gives the complete characterization of vibration energy harvesters in an automated system. Wilcox and Devasia [9] describe the detailed study of stability of velocity control of piezoelectric stepper machines. Wei et al. [10] where the new design technique of 3-D printing technology using stepper motors is discussed, nowadays the printing system has become more advanced with the help of robotic guiding technology which is only possible cause of the new machines, thanks to stepper motors. Shin et al. [11] validate the nonlinear control interconnected system. Druti ranjan in [12] proposes the real-time precision control tracking with stepper motor; here it is controlled with microstepping technique. Lim and Yan [13] work on high-precision motion control for industrial microscopes. Arias [14] proposes the technique for reducing the cogging torque in hybrid stepper machines by using resonant controllers. Tran [15] validates the adaptive current controller for the stepper motor which uses a neural network and double compensators. Although the controlling for speed is quite easy, the rotating angle estimation in hybrid motors is going to be a very difficult task; Wang et al. [16] propose the angle estimation for hybrid stepper motor with fault diagnosis. Also, some of the hybrid motors have the issues of vibration due to their high speed; Pillans [17] proposes a method of reducing positional errors by going in for vibration optimization of the drive. Kim [18] gives a nonlinear gain position control using positional feedback. The control of feedback gain plays an important role in any linear or nonlinear control. Blauch [19] demonstrates the high-speed parameter estimation of stepper motor. In our proposed work, the difficulty in motion control and other stepping errors are neglected. The control technique is easily implemented using the drivers. Both MOSFET and IGBT functions are analyzed. The IGBT control is comparatively faster than precise than the MOSFET, although the current rating makes the IGBT tougher for implementation.

2 Working of Hybrid Motor

The motor is excited by a combination of winding and by permanent magnets in it. The pole in the motor has two excitations. The number of poles or rotor teeth gives the length of each step, which is calculated by

$$\text{steep length} = \frac{90}{P} \tag{1}$$

The hybrid stepper motor has small steep typically 1.8 when compared to reluctance motor. This decides the advantage over the other motors, where the hybrid motor requires limited operating space. Small signal modeling is used to reduce the inductance in the magnetic coupling,

$$\frac{\mathrm{d}i_a}{\mathrm{d}t} = \frac{U_a + K_m\omega\sin(N_\theta) - Ri_a}{L} \tag{2}$$

$$\frac{\mathrm{d}i_b}{\mathrm{d}t} = \frac{U_b + K_m\omega\sin(N_\theta) - Ri_b}{L} \tag{3}$$

$$\frac{\mathrm{d}w}{\mathrm{d}t} = \frac{K_m i_b\cos(N_\theta) - T_i - K_m i_a\sin(N_\theta) - K_v\omega}{J} \tag{4}$$

$$\frac{\mathrm{d}\theta}{\mathrm{d}t} = \omega \tag{5}$$

i_b is the current phase B and i_a is the current phase A; correspondingly, the U_bV, U_aV is the voltage in phase in A and phase B.

3 Simulation Results

The motor phases are fed by two H-MOSFET PWM converters connected to a 12 V DC voltage source. The motor phase currents are independently controlled by two MOSFET drive signals by comparing the measured currents with their references. The initial input signal for driving the phases is given by the step frequency, which is given as gate pulse. Also, the movement of the hybrid stepper motor drive is controlled by the step signal from by user-defined value.

The output of the simulation results is obtained for 0.25 s operation of the stepper motor drive during which the stepper rotates during 0.1 s in the positive direction, stops for 0.05 s and rotates in the reverse direction for 0.05 s and stops.

Figure 1 represents the Simulink block, where the load torque is purposely reduced to study the triggering output of the waveform and as a result, the output by the stepper motor is null with respect to any given input.

During zero torque condition, all the result parameters are measured as zero. When the torque is input, the torque of the system is increased to 1.8. The hybrid motor achieves some critical output without any controlled response. The response of the system, where the voltage waveform, is initially high; the value gets settled to threshold value after 2.5 s is shown in Fig. 2.

In the Simulink, the drive switching has been triggered from both IGBT and MOSFET, which gives the output to a controlled value projected. Figure 3 represents

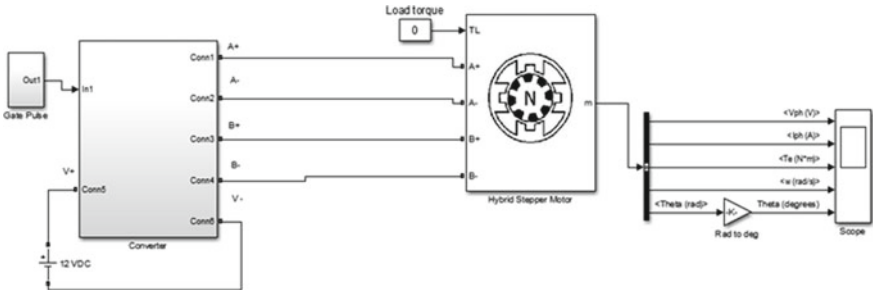

Fig. 1 Simulink module of hybrid stepper motor with zero torque

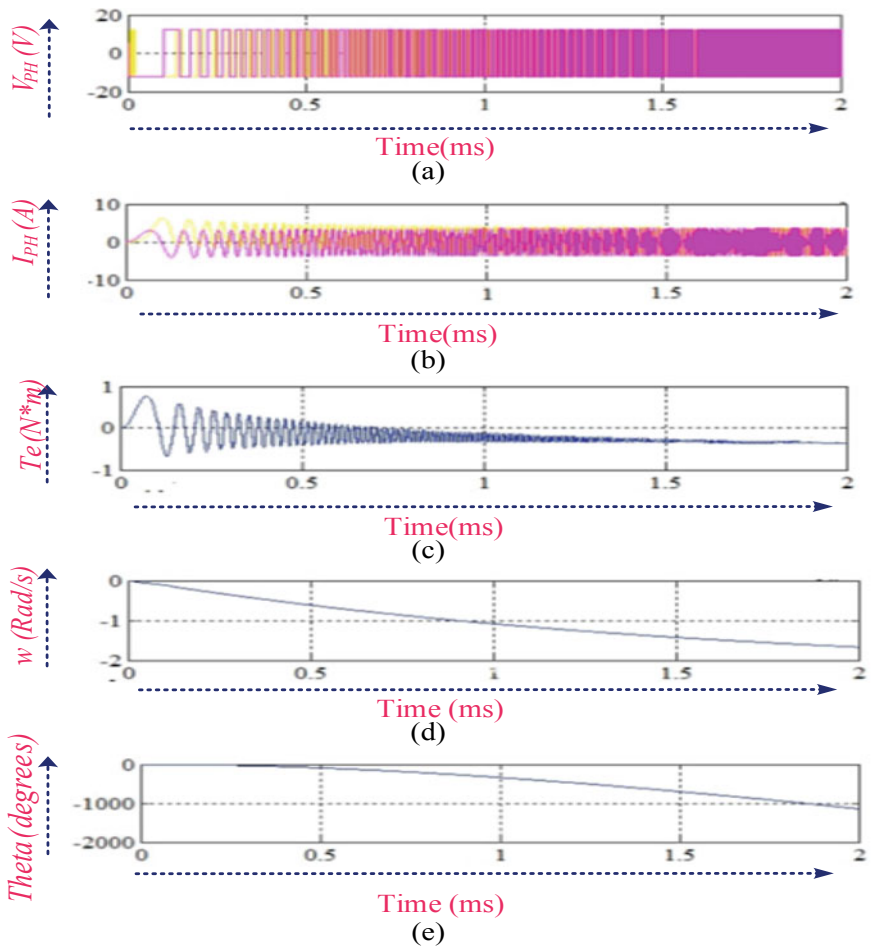

Fig. 2 Different output at the torque value of 1.8 N/M with MOSFET drive

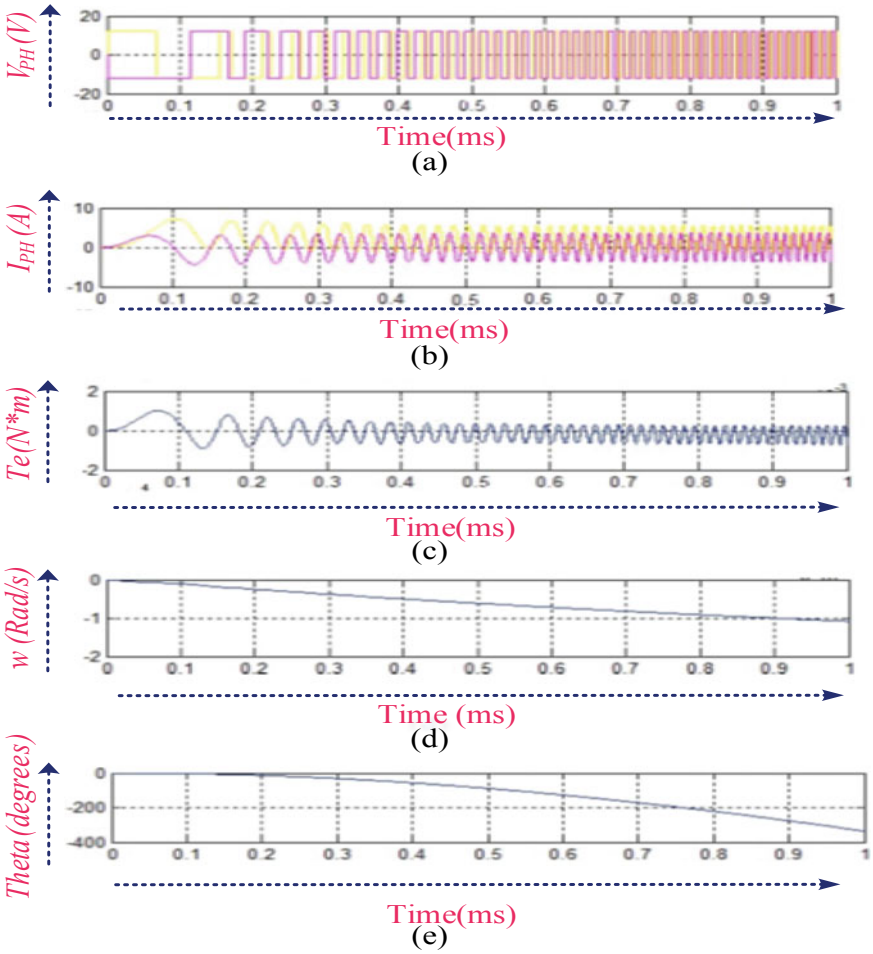

Fig. 3 Different output at the torque value of 1.8 N/M with IGBT drive

the value triggered from an IGBT, the second waveform is much more precise than the former one, which is because of the range of the IGBT. In the above Simulink, the values for voltage, current, torque, speed, operating drive temperature are provided and been analyzed. The value of the waveform is shown for 2 s. Due to the initial torque produced, we could see the starting response which is much distorted and the response gets settled after the time period 0.5 s.

The observations are made from Fig. 4 response value for both current and voltage which is the user-defined input value is gets settled. The value torque is at 1.8, still needed to fine-tune. The value for given rpm is not settling proper value; also, the temperature value is more deviating when compared to the value obtained from

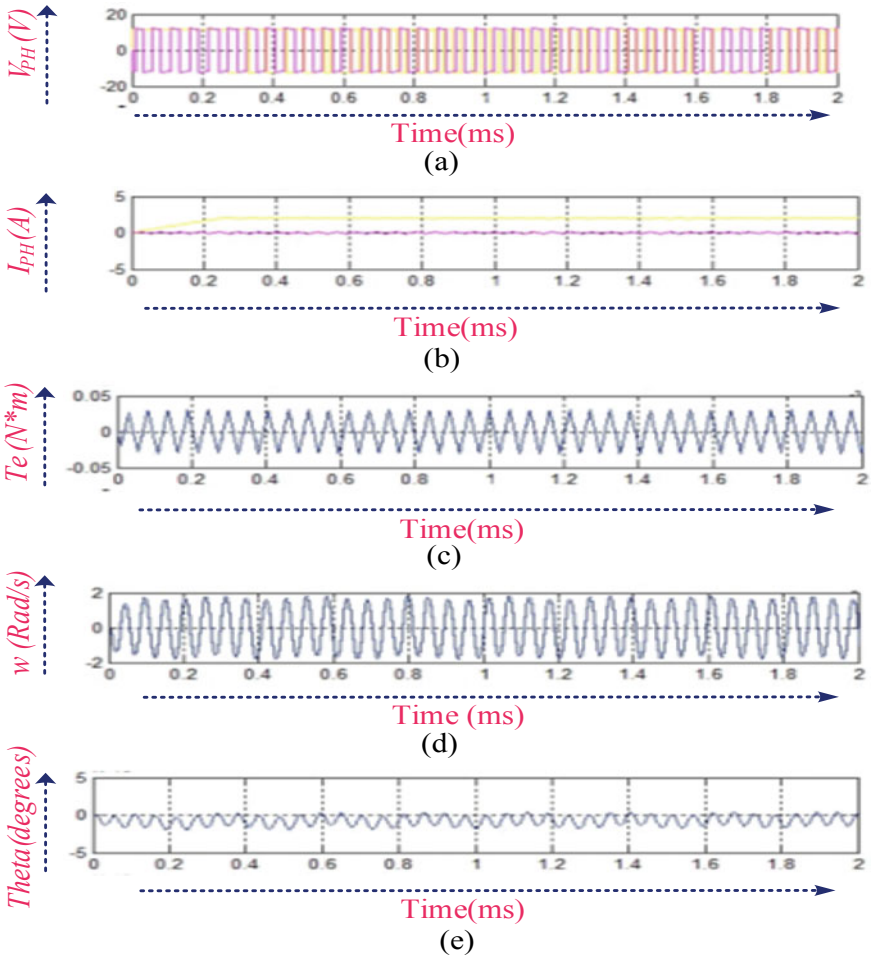

Fig. 4 Different output at tuned condition with 1.8 torque with IGBT drive

MOSFET. Therefore, the shows more precise value, so that the finer value can be obtained.

The values of voltage, current, torque, speed and the system temperature are analyzed and produced at a precision value with use of higher tuning method employed.

In the above Simulink module, the input to the IGBT driver circuit is given after tuning using a comparator, necessary filter networks and gain, which resulted in the output waveform value more tuned than the previous. The current and voltage values are more accurate 12 V and 1.1 A, respectively. The speed and the torque values show significant steady-state response and the value more accurate to the given input. The

temperature value while using IGBT drives is significantly very low compared to the higher value, when the tuning is not employed.

4 Hardware Implementation

The experimental validation of the stepper motor control is done using laboratory prototype shown in Fig. 5. The input to the motor is initially converted from an AC to DC, and with help of switching mode, the current rating to the motor is maintained. The proposed motor is 12 V, DC, 1.1 A and 13 Watts (Fig. 5).

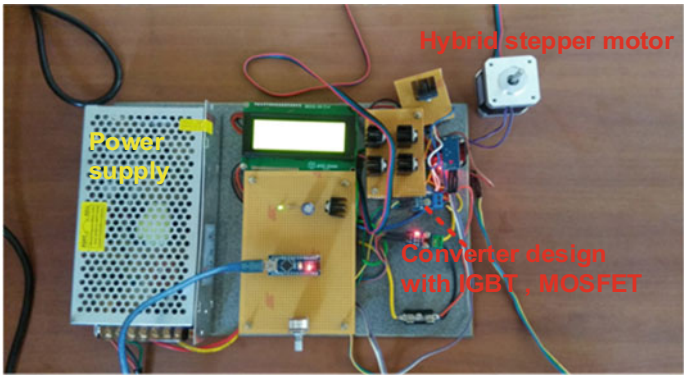

Fig. 5 Experimental setup

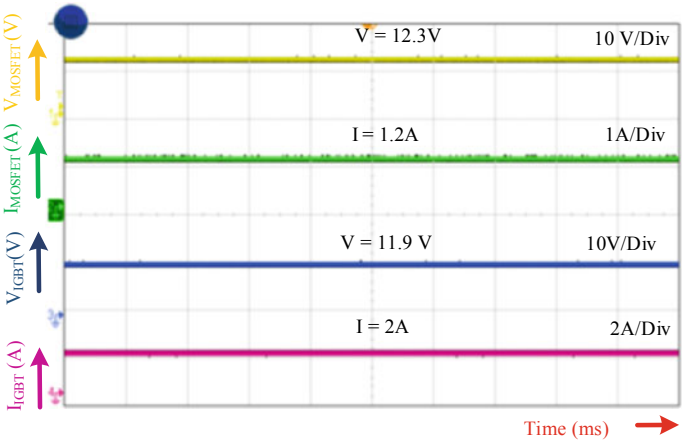

Fig. 6 Experimental result

The experimental results validate the output obtained from the Simulation results. Both the values are analyzed for performance improvement. Initially, the input value given to the converter, both IGBT and MOSFET which, due to the integral design improves the output value. From the analyzed hardware results, it is suggested that the result from IGBT has better faster triggering than MOSFET, but the MOSFET result shows better performance in sequential time period. So, IGBTs can be used for high current ratings, whereas MOSFETs can be used for low speed and better performance optimization.

5 Conclusion

This paper demonstrates the working of stepper motor with converter control technique. Initially, the working and optimization of the motor are simulated using the MATLAB/Simulink software. The performance of the simulated machine improves with the changing the converter technique. A hardware prototype module is developed, and the performance of the motor is improved considerably, with respect to the simulated results. The hybrid stepper motor performance characteristics are determined for various conditions. The different motion directions are also examined with different torque values.

References

1. Le QN, Jeon J-W (2010) Neural-network-based low-speed-damping controller for stepper motor with an FPGA. IEEE Trans Ind Electron 57(9)
2. Bendjedia M, Ait-Amirat Y, Walther B, Berthon A (2012) Position control of a sensorless stepper motor. IEEE Trans Power Electron 27(2)
3. Masi A, Butcher M, Martino M, Picatoste R (2012) An application of the extended Kalman filter for a sensorless stepper motor drive working with long cables. IEEE Trans Ind Electron 59(11)
4. Kim W, Shin D, Chung CC (2012) Microstepping using a disturbance observer and a variable structure controller for permanent-magnet stepper motors. IEEE Trans Ind Electron 60(7)
5. Kim W, Shin D, Chung CC (2013) Microstepping with nonlinear torque modulation for permanent magnet stepper motors. IEEE Trans Control Syst Technol 21(5)
6. Shin D, Kim W, Lee Y, Chung CC (2013) Phase-compensated microstepping for permanent-magnet stepper motors. IEEE Trans Ind Electron 60(12)
7. Butcher M, Masi A, Picatoste R, Giustiniani A (2014) Hybrid stepper motor electrical model extensions for use in intelligent drives. IEEE Trans Ind Electron 61(2)
8. Ruan JJ, Lockhart RA, Janphuang P, Quintero AV, Briand D, de Rooij N (2013) An automatic test bench for complete characterization of vibration-energy harvesters. IEEE Trans Instrum Meas 62(11)
9. Wilcox S, Devasia S (2015) Stability of velocity control for a piezoelectric stepper. IEEE/ASME Trans Mechatron 20(2)
10. Wei Y, Chen Y, Yang Y, Li Y (2018) Novel design and 3-D printing of nonassembly controllable pneumatic robots. IEEE/ASME Trans Mechatron 21(2)

11. Shin D, Kim W, Lee Y, Chung CC (2017) Nonlinear control with state-dependant reset integrator for a class of singularly perturbed interconnected nonlinear systems. IEEE Trans Control Syst Technol 25(4)
12. Gaan DR, Kumar M, Sudhakar S (2018) Real-time precise position tracking with stepper motor using frequency modulation based microstepping. IEEE Trans Ind Appl 54(1)
13. Lim LHI, Yang D (2019) High-precision XY stage motion control of industrial microscope. IEEE Trans Ind Electron 66(3)
14. Arias A, Caum J, Ibarra E, Grino R (2019) Reducing the cogging torque effects in hybrid stepper machines by means of resonant controllers. IEEE Trans Ind Electron 66(4)
15. Tran HN, Le KM, Jeon JW (2019) Adaptive current controller based on neural network and double phase compensator for a stepper motor. IEEE Trans Power Electron 34(8)
16. Wang X, Lu S, Zhang S (2020) Rotating angle estimation for hybrid stepper motors with application to bearing fault diagnosis. IEEE Trans Instrum Meas 69(8)
17. Pillans J (2021) Reducing position errors by vibration optimization of stepper motor drive waveforms. IEEE Trans Ind Electron 68(6)
18. Kim W, Lee Y, Shin D, Chung C (2021) Nonlinear gain position control using only position feedback for permanent magnet stepper motors. IEEE Trans Power Electron 36(7)
19. Blauch AJ, Bodson M, Chiasson J (1993) High-speed parameter estimation of stepper motors. IEEE Trans Control Syst Technol 1(4)

Performance and Analysis of Voltage Compensation in Transmission Line Using SMES-Based IDVR

M. Jagadeesh Kumar, T. Muthamizhan, P. Rathnavel, G. Ezhilarasan, and T. Eswaran

Abstract Rise in the power demand and existence of loss in transmission sector is increasing linearly. This is due to the increase in use of nonlinear load which causes voltage fluctuation in transmission lines. Some of the problems in it are sag, swell, voltage spikes, harmonics, open and short circuit faults. Among the above mentioned power quality issues, sag and swell will be considered as major fault, and it can be resolved and overcome by including the interline dynamic voltage restorer (IDVR). IDVR has enough capability to perform voltage compensation in an appropriate rate, and it maintains stable energy across DC link capacitor. The proposed method can have several DVRs connected to various distribution feeders in power system sharing common energy storage. A superconducting magnetic energy storage system (SMES) is selected to feed DVR, whenever DVR undergoes compensation. Further, fuzzy logic control also took part in it. The Simulink results convey the effectiveness and performance of proposed method.

Keywords Interline dynamic voltage restorer (IDVR) · Sag/swell · DC link capacitor · Fuzzy logic control

M. Jagadeesh Kumar (✉) · T. Muthamizhan · P. Rathnavel · G. Ezhilarasan · T. Eswaran
Department of Electrical and Electronics Engineering, Sri Sairam Institute of Technology, Chennai 44, India
e-mail: jagadeeshkumar.eee@sairamit.edu.in

T. Muthamizhan
e-mail: muthamizhan.eee@sairamit.edu.in

P. Rathnavel
e-mail: rathnavel.eee@sairamit.edu.in

G. Ezhilarasan
e-mail: g.ezhilarasan@jainuniversity.ac.in

T. Eswaran
e-mail: eswaran@aktmcet.in

C. Subramani et al. (eds.), *Proceedings of International Conference on Power Electronics and Renewable Energy Systems*, Lecture Notes in Electrical Engineering 795,
https://doi.org/10.1007/978-981-16-4943-1_57

1 Introduction

Variation in load level will cause failures in electrical devices due to power quality disturbances. Power quality took major part in functioning entire system at desired rate. Most of the distribution systems encounter sag, swell, switching transient, harmonics, etc. The sudden fall in voltage level is said to be as voltage sag, and rise in voltage at a particular portion is described as voltage swell. The existing voltage sag compensation techniques are in-phase, pre-sag and optimized energy. By comparing amplitude of positive sequence component with its reference value, pre-sag method of voltage compensation is studied. Another method [3], implies reduction in injecting voltage of DVR and mitigate nearer to load. To resolve these, lot of power conditioning devices is available. Among that, DVR is preferred to provide effective solution against sag and swell. DVR is said to be as power electronic-based device which is connected in series with feeder of sensitive load. The structure of DVR is comprised of voltage source converter (VSC), an energy storage element, passive filter, injecting transformer and a control topology to deliver controllable voltage in distribution sector such as amplitude and phase angle. DVR is used mostly for low-level and medium-level voltage applications. Simpler structure and fast dynamic response will be the key factors for choosing it. Other than that a short-term energy storage system is mandatory to perform restoration; for that, SMES is chosen. It is responsible to protect consumer from voltage fluctuation. This combination plays a vital role in compensating sag/swell and also concentrates upon power flow control too [1–3]. The concentration upon selection of control topology is unavoidable. In addition, ANFIS controller (Adaptive Neuro Fuzzy Inference System) is proposed to stabilize the functioning of DVR by maximizing the system efficiency. Fuzzy and PI controller analysis predicts the rate of dynamic response in accordance with voltage compensation. Replacement of PI control is carried out through fuzzy logic control in which predecessor method has improper tuning of KP and KI. It leads to rise in settling time and affects speed of response. Due to this, fuzzy logic control is progressed in [4, 5]. To bring this into next stage, IDVR is proposed. It is a combination of several DVR connected in it to split the part of work for each one (i.e., one for performing sag/swell and another one for power conditioning). The SPWM technique in turn makes harmonic reduction by regulating switching action in an appropriate rate [6–10]. The main drawback in DVR is that it receives abundant quantity of power from DC link capacitor. Even it has certain limitations, this FACTS device is unavoidable due to its plenty of advantages, by combining more devices to overcome the limitations of the IDVR. It is evident that IDVR is considerably a perfect solution to raise the dynamic response and performance. With proper selection of control technique, the quality of real and reactive power injection is considerably at a steady state. In Sect. 2, a detailed study upon modelling of DVR is presented. In continuation with compensation method, energy storage system is represented in Sect. 3. Section 4 dealt with structure and operating principles of IDVR. The modelling of IDVR and occurrence of voltage sag/swell is represented in Sect. 5. Further, the level

of compensation achieved through proposed topology is defined in both Sects. 5 and 6.

2 Structure of DVR

The structure of DVR is depicted in Fig. 1. It is more efficient and effective custom power device. DVR is solid state device that supplies voltage which in order to regulate line voltage. Other than sag/well compensation, it focuses on harmonics compensation, fault current reduction and reduction in voltage transient, respectively. The role of injecting transformer is to limit noise and transient from primary winding to secondary. And it connects distribution network with DVR; also, it couples injected compensating voltage with supply voltage. Whenever the isolation of feeder and VSC is needed, it performs that too. If any kind of harmonics is developed by VSC, harmonic filter took care upon it and eliminates as much as possible. VSC is a collection of power semiconducting devices which produce sinusoidal voltage at desired rate. Further, energy required for whole process is delivered through electromagnetic energy storage element. The preliminary tasks need to perform by it are to energize the entire section to perform sag compensation and after that maintain a constant voltage at DC link.

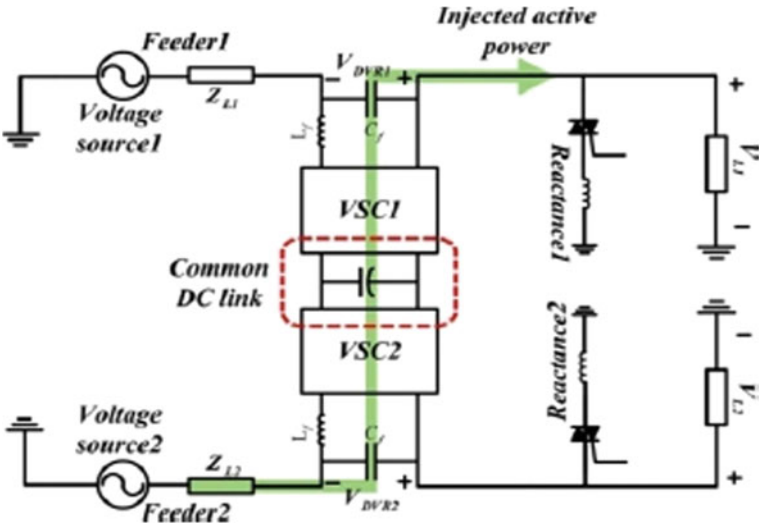

Fig. 1 Structure of IDVR

3 Principle of IDVR

The structure of DVR is shown in Fig. 1 comprising voltage source converters configured at front and back with link capacitor. From this structure, it is evident that IDVR is capable to transfer active power in-between feeder and another one. A common DC link capacitor connected between both would share power whenever DVRs needed.

If one among DVR presented in IDVR continues to absorb active power from DC link capacitor, then another tends to be operating under rectification mode, and it would supply energy towards DC link to maintain a constant voltage across it. This compact structure concentrates upon deducing the components rating. Due to this strategy, reduction in size and cost has been progressed without affecting the performance. Without bypassing normal condition of DVR, the DVR present in proposed method has potential to raise the displacement factor of an individual feeder. The functioning of DVR is said to be exchanging active and reactive power between individual feeders. It utilizes a shunt reactance parallel with load to minimize load power factor during sag condition. When load power factor is small, much deeper voltage sags can also compensated. At higher power factor, the performance of DVR should lag. To resolve these factors, a proposed method adopts some changes in it. It would make DVR to operate at medium power.

4 Superconducting Magnetic Energy Storage System

The superconducting magnetic material stores energy in magnetic field, and it possesses quick charging and discharging time which makes it to supply load whenever the system needs to perform compensation. SMES parts are categorized into three, and they are superconducting coil, power conditioning system and cryogenic cooled refrigerator. Once a coil is charged, the current should not decay, and it retains its magnetic field identically. Power conditioning system does rectification or inverting voltage as it totally depends upon the voltage it may be taken. In comparison with alternative energy storage system, this method lost electrical energy level which is least in nature (Figs. 2 and 3).

The equation represents energy storage in a superconducting coil, $E = 1/2$ LI * I. Most of the industrial sectors face interrupts due to voltage sag. At that condition, improving performance of FACTS controller requires higher performance storage device. From above concern, SMES is said to be a better choice even the system may fall towards sudden interruption consistently.

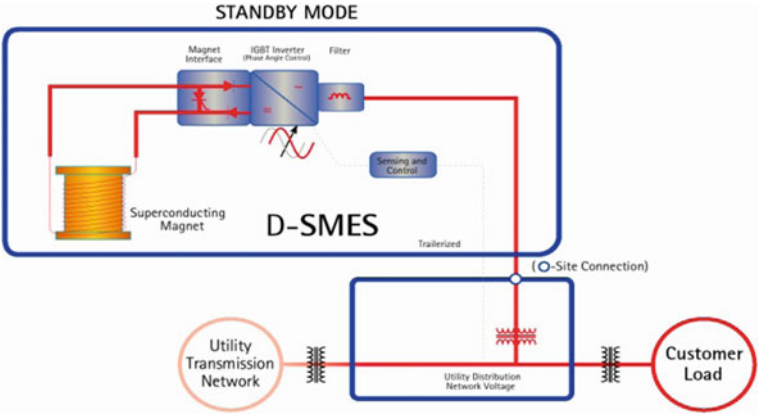

Fig. 2 Layout diagram of a Superconducting Magnetic Energy Storage (SMES) System

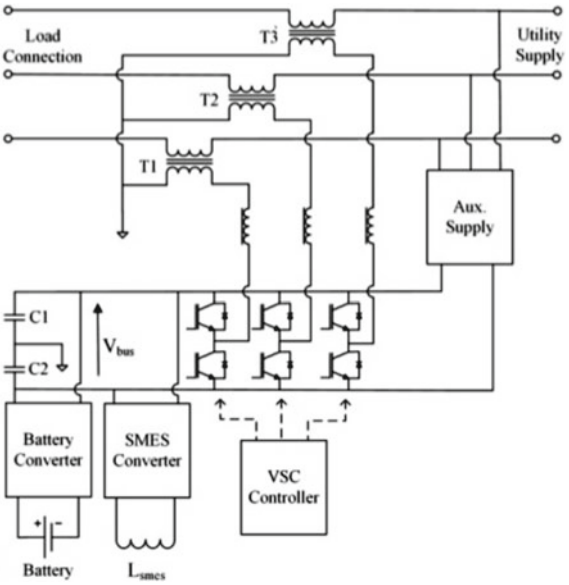

Fig. 3 Schematic diagram of SMES-based DVR

5 Results and Discussion

The proposed system is designed for 3-phase, 415 V, 50 Hz supply simulated using MATLAB/SIMULINK R2014a software. To examine the functioning of IDVR, a fault is applied at resistance of 0.66, and after that, DVVR is connected, and compensation is visualized in below waveform (Figs. 4, 5 and 7, Table 1).

By implementing fuzzy logic control, the generated gate pulse for switches present in VSC is represented in Fig. 6. Normally, a system faces critical voltage fluctuation

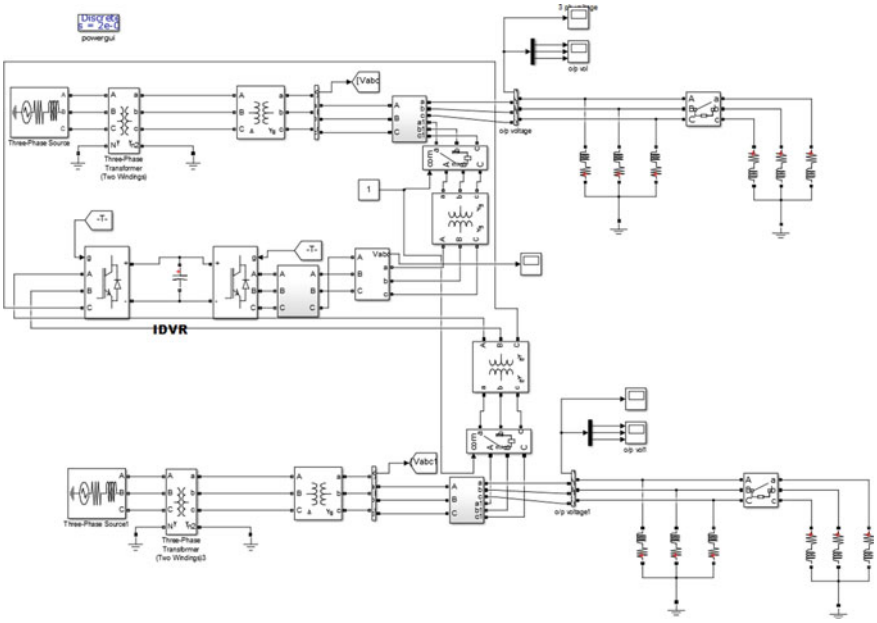

Fig. 4 MATLAB/SIMULINK Model of the proposed method

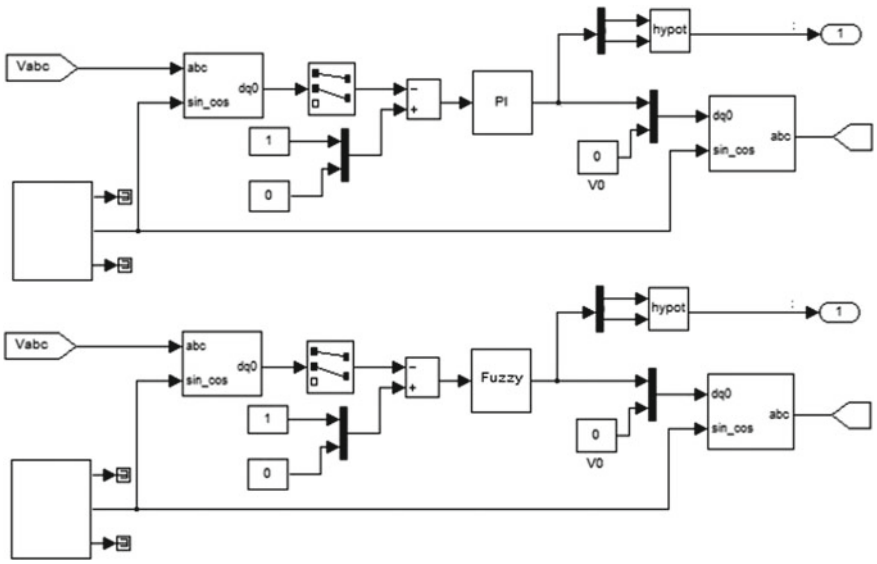

Fig. 5 Combination of conventional battery and SMES-based DVR

Table. 1 Fuzzy rule base (7 x 7 Matrix) for the IDVR control

CE							
E	NB	NM	NS	ZE	PS	PM	PD
NB	NB	NB	NB	NB	NM	NS	ZE
NM	NB	NB	NB	NM	NS	ZE	PS
NS	NB	NB	NM	NS	ZE	PS	PM
ZE	NB	NM	NS	ZE	PS	PM	PB
PS	NM	NS	ZE	PS	PM	PB	PB
PM	NS	ZE	PS	PM	PB	PB	PB
PB	ZE	PS	PM	PB	PB	PB	PB

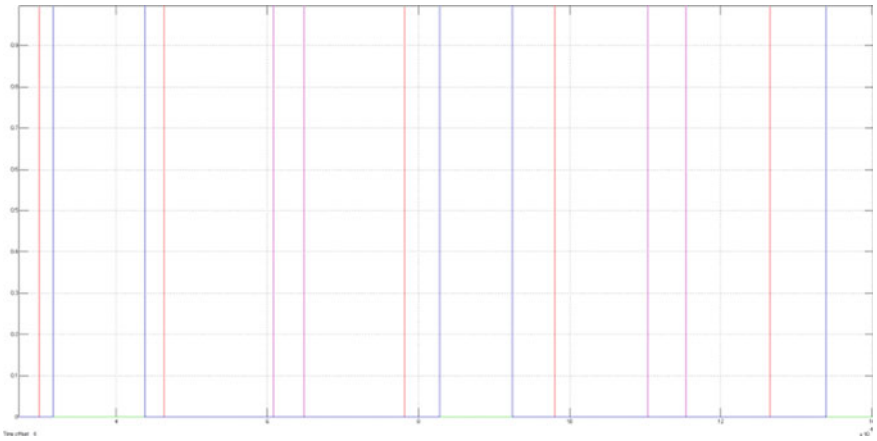

Fig. 6 Gate signal generation for the switches of IDVR

under severe circumstances. It may be voltage sag, swell, oscillation, etc. In transmission, the line struggles with sag and swell. There are various topologies available to it. In upcoming waveforms, how much amount of sag and swell occurred and what are processes undertaken to eliminate it are visualized graphically.

A sudden reduction in voltage flow is said to be voltage sag, and its occurrence is considerably 10% to 90% in manner. In Fig. 8, the level of voltage of sag occurred is represented. It should be 12.4% in below figure. The disturbance in real and reactive power occurred during time range of 0.5–0.25 s. (Figs. 10 and 11).

FFT analysis revealing THD value is high, and it becomes 4.81%. It makes the entire system inefficient. For swell, the value of THD is almost high. From this, it is evident that this range of voltage feed to distribution system may affect the consumers load requirement. The waveform is shown in Fig. 12 witnessing compensated voltage by IDVR with fuzzy controller. From Figs. 9 and 13, the THD of the three phase voltage is found as 4.81% for the voltage sag, 0.12% for the voltage swell and the THD for the total three phase system is found as 0.08%. From the above results the

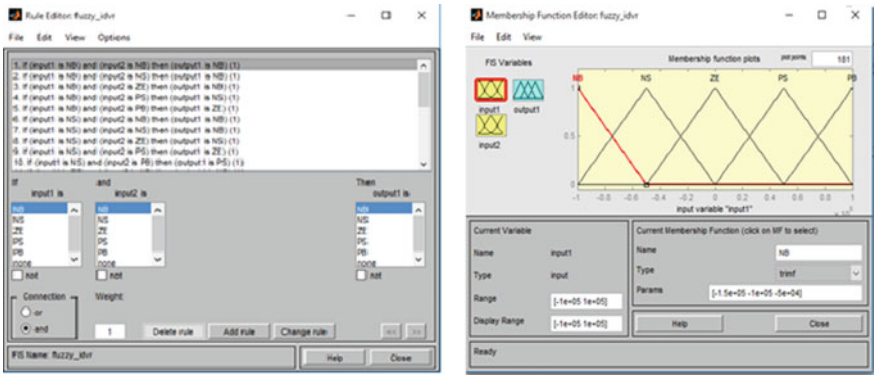

Fig. 7 Rules and membership function presented in fuzzy logic control

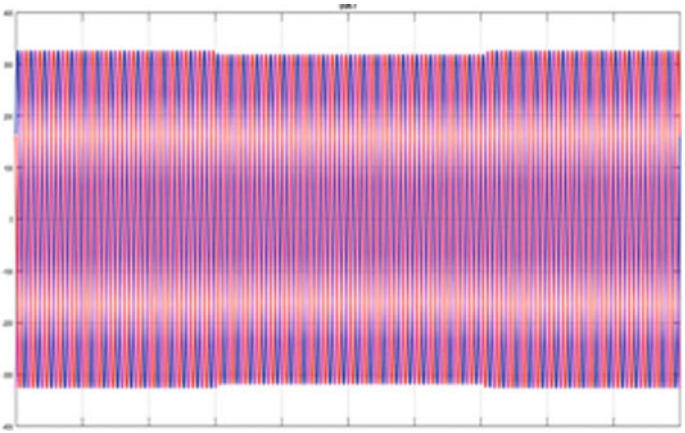

Fig. 8 Occurrence of voltage sag in 3-phase transmission system

compensation of the controller aids the systems to get good results with minimum percentage of THD.

6 Conclusion

The modelling and functioning of IDVR to compensate voltage sag/swell are experimentally verified, and its efficiency is visualized through waveforms. The model of IDVR for 13.08% of voltage swell and 12.4% of voltage sag is compensated in addition to fuzzy logic control method. The results examine that the proposed method

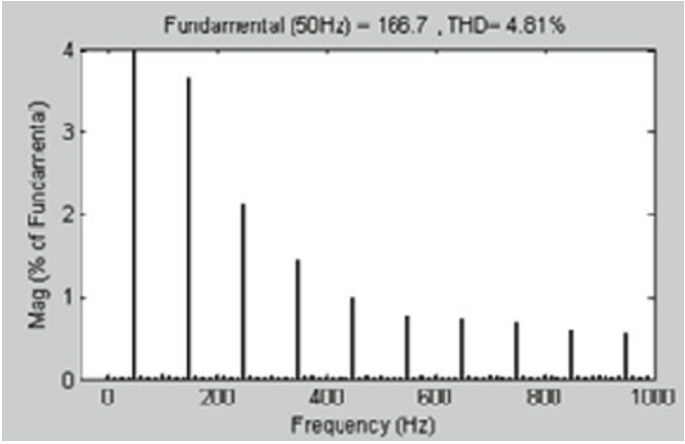

Fig. 9 FFT analysis of voltage sag

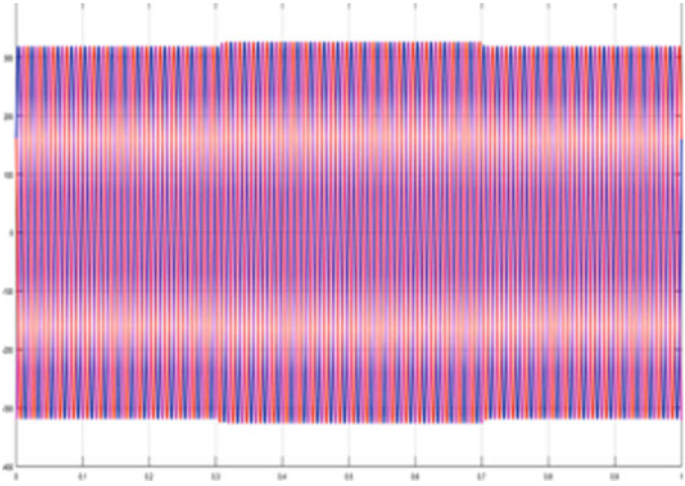

Fig. 10 Occurrence of voltage swell in a 3-phase transmission system

compensated effectively and at high accuracy. Input sources are continuously monitored, and if any sag/swell is noted, the shunt reactance decreases load power factor to maximize the performance of IDVR.

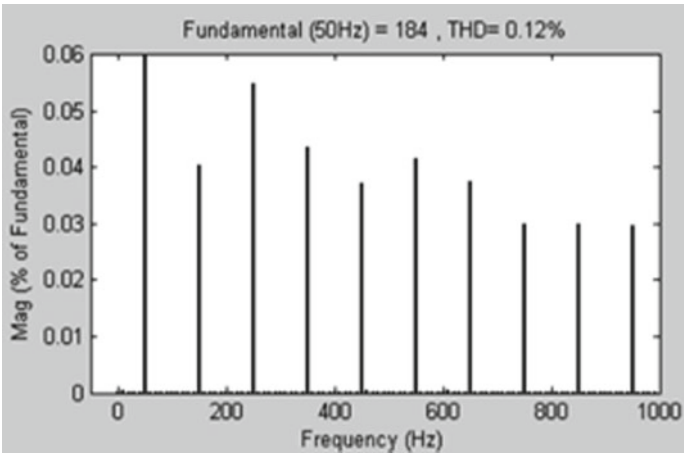

Fig. 11 FFT analysis of swell

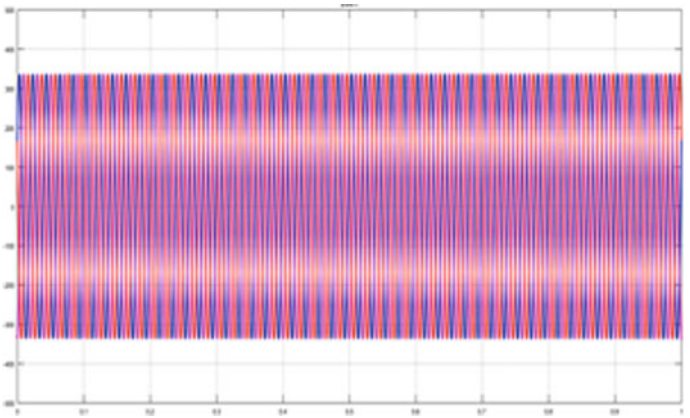

Fig. 12 Compensated voltage of the 3-phase transmission system using SMES-Based IDVR

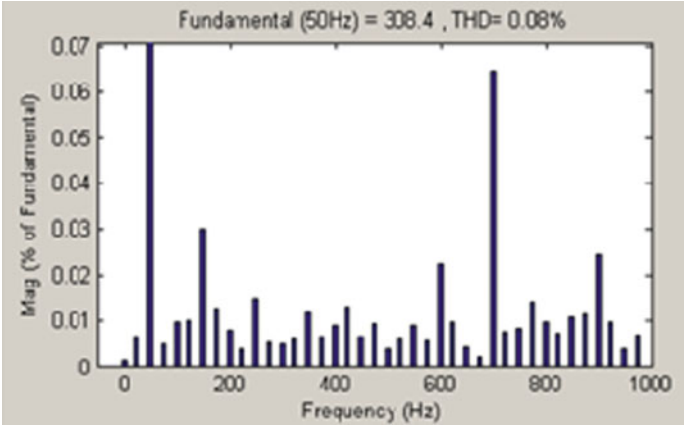

Fig. 13 FFT analysis for three-phase system

References

1. Prema R (2016) SMES based DVR against voltage sag using ANFIS system. Int J Innov Sci Eng Res 3(3):23–32
2. Ravirajan S, Muthamizhan T (2016) Modelling and digital simulation of a standard IEEE—30 bus system to improve power quality of grid with UPQC using MATLAB. Asian J Res Soc Sci Humanities 6(10):830–845
3. Hossain MI, Rahaman I, Rahman MN, Hasan MF, Hasan MM, Sarker RC (2020) Voltage sag compensation in distribution system using dynamic voltage restorer. In: 2nd international conference on advanced information and communication technology 2020, Dhaka, Bangladesh, pp 492–497
4. Thaha HS, Prakash TRD (2020) Use of fuzzy controller based DVR for the reduction of power quality issues in composite micro-grid. In: International conference on renewable energy integration into smart grids: a multidisciplinary approach to technology modelling and simulation (ICREISG), Bhubaneswar, India, pp 131–136
5. Naveen V, Bharat Kumar P (2015) Fuzzy and adaptive control strategies of voltage source converter for correction of power factor. Int Res J Eng Technol 2(6):160–174
6. Karshenas HR, Moradlou M (2011) Design strategy for optimum rating selection in interline DVR. IEEE Trans Power Deliv 26(1):242–249
7. Pal R, Gupta S (2017) Interline dynamic voltage restoration for power quality compensation. Electr Comput Eng Int J (ECIJ) 4(2):79–98
8. Xie Q, Chen XY, Feng J, Lei Y (2020) Feasibility analysis of SMES-based interline DC dynamic voltage restorer. In: IEEE international conference on applied superconductivity and electromagnetic devices (ASEMD), Tianjin, China, pp 1–2
9. Usha RP, Sudha R, Reddy SR (2011) Voltage sag/swell compensation in an interline Dynamic Voltage Restorer. In: International conference on emerging trends in electrical and computer technology, Nagercoil, India, pp 309–314
10. Meenakshi N, Manivel K (2015) Interline DVR with reduced rating control. Int J Eng Res Technol 3(4):1–6

Multiple Regression-Based Adaptive Protection Scheme for Microgrids

Aindrila Dey, Moumita Dhang, Rangit Ray, and C. Vaithilingam

Abstract The dynamic behavior of microgrid on the protection point of views such as modes of operation (grid-connected/islanded) and generation levels of renewable energy sources makes the fault current vary randomly. Subsequently, the relay operating conditions are to be changed based on the above factors so that relay can differentiate between fault condition and normal operating condition. The conventional protection schemes will be unable to differentiate between modes of operations. Further, the fault current is dynamic in nature. Hence, electromechanical or static relays may be replaced with processor-based relays. This paper proposes an adaptive protection scheme for the microgrid using machine learning algorithm. Multiple regression machine learning algorithm is used to develop adaptive protection scheme. The proposed model will be able to differentiate between normal operating condition and fault condition and trip the relay if needed. The hardware prototype developed for the adaptive relaying scheme has been tested successfully.

Keywords Adaptive protection · Microgrids · Machine learning · Multiple regression

1 Introduction

Distributed generations are gaining much importance in today's power system as it solve the perennial prime concerns of the power systems to ensure reliable, stable, and quality power supply [1]. From [2], it is inferred that, with the advent of DGs, the electricity producer–consumer gap has been optimally met and helped in minimizing the transmission losses. Also, with the introduction of PV and wind energy generations, the need for power electronic systems for the reliable supply necessitates the faster operation of protection system [3]. The idea of this paper into this field has been on the fact that this adaptive protection scheme is a developing topic and has a huge potential to be in rigorous usage in the future. As the development of

A. Dey · M. Dhang · R. Ray · C. Vaithilingam (✉)
Vellore Institute of Technology, Chennai, India
e-mail: vaithilingam.c@vit.ac.in

C. Subramani et al. (eds.), *Proceedings of International Conference on Power Electronics and Renewable Energy Systems*, Lecture Notes in Electrical Engineering 795,
https://doi.org/10.1007/978-981-16-4943-1_58

such a scheme requires highly efficient technologies and devices, thorough research has been done on this field of interest [4]. The power system requires major revamp in protection schemes due to the penetration of renewable energy resources in the network [5]. From [6], it has been inferred that traditional protection schemes become inappropriate due to the following reasons:

(1) Dynamic fault current.
(2) Bidirectional power flow.
(3) Randomness associated with renewable energy generation.
(4) Quantum of power and power injection node.

Also, from the literatures, it is observed that new methods for adaptive protection schemes for Microgrids can be divided into two groups as follows,

(i) Fuzzy logic and ANN-based approaches.
(ii) Machine learning-based methods.

The philosophy of adaptive protection is not new. More than three decades ago, the results of an investigation into the possibilities of using digital techniques to adapt the transmission protection to PS changes had been presented in [6]. The growing number of publications on adaptive protection has been observed. Particularly, large no. of a rise in the citation on this topic has been observed in 2007 and the highest number in 2018. One important observation which has been made is that adaptive protection scheme has been divided into three sub-areas: transmission lines, transformer, and DSs/MGs. In [7], a rule-based adaptive protection scheme using a machine learning methodology for microgrids in extensive distribution automation (DA) has been modeled. In this paper, ANN–SVM-based method is used. The paper [8] presents a study of microgrid protection scheme based on Hilbert-Huang transform (HHT) and ML techniques. Three different machine learning models are being tested and compared in this paper: naïve Bayes classifier, SVM, and extreme learning machine. The observations and inferences in the aforementioned survey motivated to develop a model based on the ML technique. An adaptive protection scheme using a multiple regression model is developed and tested. This paper explains the unique essence of adaptive protection scheme and also the demerits of the traditional protection scheme.

2 Design Approach

The microgrids are becoming essential in the energy industry and may become an inevitable part of the power system network for sustainable energy generation. Therefore, to use the full potential of the microgrid, various technical challenges have to be addressed. One of the major challenges is the protection scheme. The two major factors, the randomness of the renewable energy sources and the different modes of operation, results in dynamic fault currents. Thus, designing a suitable protection scheme and coordinating relays would require the understanding of fault current

values. Hence, the conventional protection schemes, for example, a conventional overcurrent protection scheme could not differentiate the fault condition, and normal operating condition, hence, will face selectivity and sensitivity issues. The main objectives are to develop an adaptive protection scheme for the microgrid using ML algorithm and develop a hardware prototype using DC Sources, intelligent electronic devices, and suitable relaying and switching devices.

A MATLAB Simulink model of microgrid with two solar energy sources as DGs and provision for grid connection is developed. The simulation consists of two photovoltaic panels (PV panels) connected to an AC load. The simulation model consists of PV panels, three-phase inverters with RLC filters, and then the load. The effect of fault in microgrid side is chosen in this paper so that the proposed model is validated by ensuring the fault is detected and the microgrid is protected in both grid-connected and islanded modes. The notion behind this model has been that the microgrid should not induce any fault currents into the system, and following a fault in the microgrid, it should be isolated from the main grid. Also, when the microgrid is in islanded mode and fault occurs at the load side, the DGs will be isolated from the fault.

2.1 Dataset Preparation

The normal operating current of the system at different operating conditions was obtained. The generations of DGs (PV sources) are varied by varying the irradiance values. The fault currents of the system under different operating conditions and fault types are obtained. The fault currents when the system is operating in grid-connected mode are also obtained for all operating conditions. The sample data obtained from the fault analysis are given in Table. 1

The above dataset has been scaled down in the range of (0–5) volt. Also, here, the current values are given in terms of voltage in the mentioned range as in real-time setup, all voltage values have been taken from RPSs representing PV1, PV2, current value, and mode of operation. Also, while importing the dataset into the real-time system (machine algorithm), only the LG fault value is chosen as the threshold value among all types of faults because LG fault value is minimum among all the fault values. If the input current is more than the predicted fault current value under a given condition, then the system is under fault and vice versa.

2.2 Machine Learning Algorithm

Linear regression is a prime statistical tool that can be used to estimate the values using the training dataset. Multiple regression is used majorly when there are a one dependent and more than one independent variables. The general form of the multiple regression is given by the equation:

Table 1 Training dataset samples (pre-scale down)

Irradiance (PV1)	Irradiance (PV2)	Type of fault	Mode operation	Fault current (A)	Normal current (A)
100	200	LG	Islanded	628	398
		LL		1860	
		LLG		1820	
		LLL		1375	
400	800	LG	Islanded	1893	492
		LL		6398	
		LLG		6466	
		LLL		5479	
600	1200	LG	Islanded	1433	502
		LL		7350	
		LLG		7500	
		LLL		7307	
100	200	LG	Grid-connected	2216	1478
		LL		3685	
		LLG		3589	
		LLL		3061	

$$Y = B_1 \times X_1 + B_2 \times X_2 + \ldots B_n \times X_n + A$$

$Y =$ dependent variable
$X1, X2 \ldots Xn =$ independent variables.

Scatter plot is used in multiple regression to fit in single line. Multi-dimensional voids of data patterns are used to fit multiple regression. The simplest form of this algorithm has one dependent and two independent variables. The output or the value to be estimated is dependent variable. The variables decide that the values of dependent variable are independent variables.

In this paper, the number of independent variables is two, which are the irradiance values of PV1 and PV2. With the values of the independent variables, the LG fault current value is predicted for the unknown irradiance values.

The algorithm has been implemented using the scikit library in Python. The following steps have been used for the process.

1. After calling all the required libraries, the dataset in CSV extension has been imported to Python with the help of the pandas library.
2. The following step is to divide the data into “attributes” and “labels." Independent variables are attributes, and dependent variables are called as labels. In this paper, the PV values are the attributes, and the fault current value is the label.
3. Next, the 70% of data were used for training the model, and 30% were used for testing the model.

4. After splitting the dataset, the algorithm is trained by importing linear regression class. Linear regression model fundamentally finds the values of slope and intercept; using the values of slope and intercept, the value of dependent variable will be predicted.
5. After training the algorithm, some predictions are used to check how accurately the algorithm can predict the data. To make a prediction on the test case, "regressor.predict" command is used. By this, the actual output values of the test cases can be compared with the predicted values.
6. Next, we can get the desired fault current value for the unknown irradiance value.

2.3 Hardware Implementation

A microgrid model with two PV panels has been designed which will function in grid-connected and islanded modes. In both, the modes LG, LL, LLG, and LLL faults have been analyzed for different values of irradiances. As LG fault current values are minimum, they have been chosen as the threshold value to decide whether the system is in fault condition or normal operating condition. The simulation values obtained are scaled down to suitable values for the microcontroller to handle. For the hardware model, the irradiance values are scaled down and normalized to suitable voltage values. Four voltage inputs are given from RPS representing two PV Sources, modes of operation, and current value. These voltages are given to the microprocessor called Raspberry Pi 3B + with the help of an ADC called Arduino UNO. The real-time inputs received by the Raspberry Pi will be processed by the machine learning algorithm embedded in Raspberry Pi. The algorithm selects the dataset to be compared, based on the four inputs. This processor will then compare the measured current value with the predicted fault current value obtained from the machine learning algorithm. If the predicted fault current value is more than the input current, then the system is not under any fault. If it is lesser than input current value, it reflects a fault condition and the relay will be activated. With the help of the Raspberry Pi processor, a relay has been tripped to glow an LED and turn on a buzzer to indicate the relay trip following a fault condition. The clearance time of the relay is lesser than 15 ms (Fig. 1).

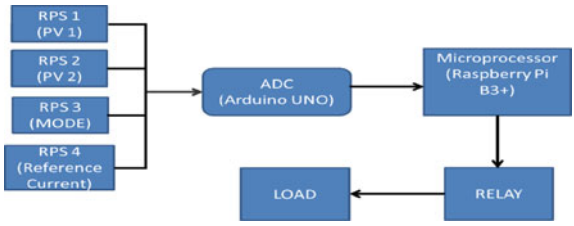

Fig. 1 Block diagram of the hardware model

The developed prototype is tested in the laboratory to validate the effectiveness of machine learning algorithm and the capability of processors.

- In this prototype, the irradiation levels of the PV panels have been varied to determine fault current values, to prepare a dataset that is to be used to train the multiple regression algorithm.
- All irradiation levels and current values are expressed as voltage levels within (0–5)V range.
- Depending upon the mode of operation and the power generation levels of the renewable energy sources, which are random/intermittent, the fault current will vary accordingly.
- The multiple regression algorithm is implemented in the Python platform in Raspberry Pi to predict the fault current value for a specific irradiation level and a given mode of operation.
- The predicted fault current value is then compared with the reference current value (depicted as a voltage value) given as input. If this reference current value is greater, it is a fault condition, else not.
- It has been observed that the relay trips within 15 ms after the occurrence of a fault.

3 Results and Discussions

3.1 Simulation Results

A simulation model of a microgrid has been designed and operated in the modes (grid-connected or islanded mode) using two PV panels, whose irradiation levels were varied to notice the change in fault current value.

3.2 Overview of the Prototype

1. Figure 2 shows the four voltage levels which have been used to represent the four significant inputs in the hardware setup. The four voltage levels represent the following:
    i. **PV1**—Representing the input from one PV panel. Changing of voltage here represents the changing generation level of the PV panel.
    ii. **PV2**—Representing the input from the second PV panel. Changing the voltage value here also represents the changing generation level of the PV panel.
    iii. **Mode of Operation**: Representing the mode of the microgrid, i.e., islanded or grid-connected mode. If this voltage level is higher than “1”,

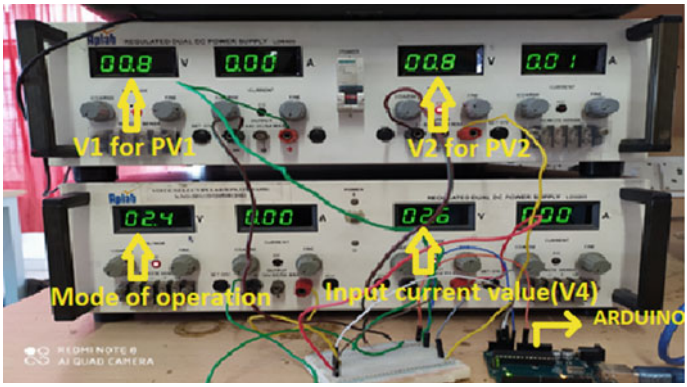

Fig. 2 Four voltage levels are used as demonstrated above

then the microgrid represents grid-connected mode, else the microgrid is in islanded mode.

iv. **Reference Current Value**: This value has been represented by another voltage value from RPS. All values are in the range of (0–5) V as the Arduino has a maximum capacity of 5 V.
The analog inputs are given to Arduino, as shown in Fig. 2, and are converted to digital outputs by Arduino (ADC) and then given to Raspberry Pi.

2. Figure 3 shows the hardware setup of Raspberry Pi 3B + , relay, LED, and buzzer. The Raspberry Pi acts as the brain of this setup. Based on the input from

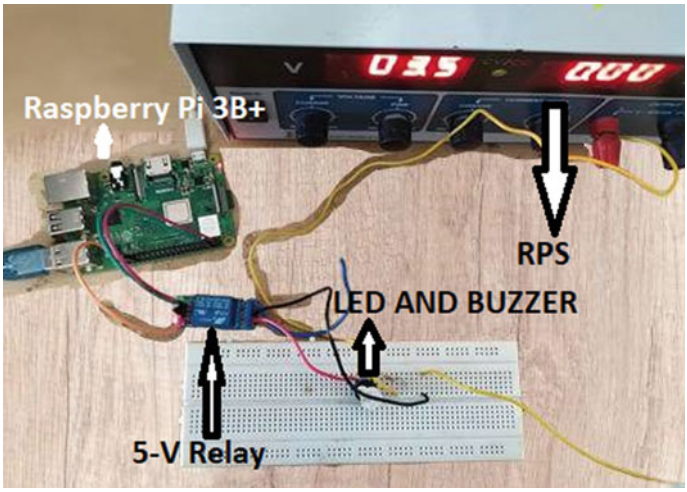

Fig. 3 Hardware setup of Raspberry Pi, LED, and buzzer

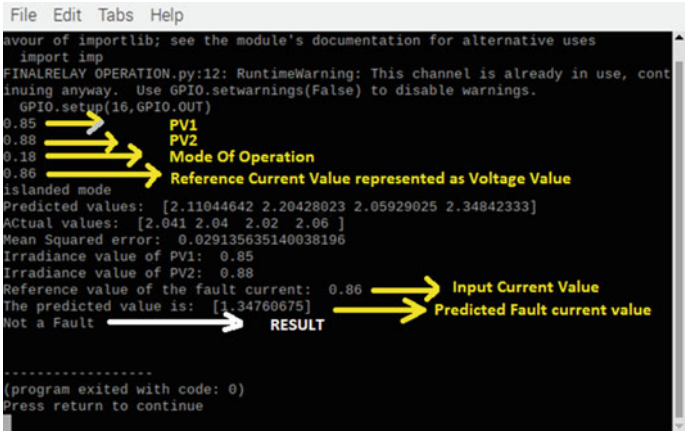

Fig. 4 Console window of the Geany IDE

Arduino and the machine learning algorithm, it predicts the fault current value. If the fault current value is greater than reference current value, then it shows "Fault," else "NO FAULT." If the platform predicts fault, then the relay trips and LED glows and buzzer buzzes simultaneously.

3. Figure 4 shows the console window of the machine learning platform.

The console window in Fig. 4 is the output window of the Geany platform in Raspberry Pi 3B + . Python language has been used to implement the **multiple regression** algorithm by importing libraries like scikit in Python. The status of the code in this console window shows that the mode of operation is in islanded mode as the input from the RPS is less than 1 (as per the given condition in code). The reference current input which is given as voltage input from the RPS is compared, and in this condition, it is less than the predicted value of the fault current from the code implemented in Raspberry Pi platform, and hence, therefore, the result in the console window shows **"Not a Fault."**

Raspberry Pi 3B + has been chosen to make hardware prototype as it has the latest features and advanced technology. The machine learning code has been done in the Geany platform using Python language in Raspberry Pi.

The Arduino Uno is based on ATmega328P. It consists of 14 and 6 digital and analog pins, respectively, and a 16 MHz resonator. This module acts as an analog to digital converter. The analog inputs from the regulated power supplies (RPSs) are taken by Arduino and then the digital output is given to the Raspberry Pi module as this module only accepts digital inputs. The values from RPSs and also the training dataset are in the range of (0–5) Volts as the Arduino Uno has a maximum capacity of 5 V.

The 5-V one-channel relay module has been used to trip the circuit during the fault conditions. The relay remains in normally open (NO) position, and when a fault occurs, it moves to normally open (NO) position, and the fault is cleared within the

maximum fault clearance time. The change of contact of the relay is made possible with the help of trigger voltage (Vin) which is in the range of (0–1.2) Volts, and it is powered through Vcc which is 5 V. The relay is powered through Raspberry Pi 3B +.

The LED glows and buzzer buzzes when the fault condition occurs if the relay is normally open (NO) mode. The relay circuit closes whenever the tripping takes place and LED and buzzer get ON simultaneously.

3.3 Summary.

The adaptive relaying scheme is developed using ML algorithm "**multiple regression**" which has been implemented in the Geany platform in Raspberry Pi using scikit library in Python. The dataset finally imported as "CSV" file to the ML platform which consisted of two independent variables PV1 and PV2 and one dependent variable, i.e., LG fault current value (since LG fault value is the least fault value) under two different modes of operation, namely: grid-connected and islanded. The multiple regression algorithm implemented in the Geany platform in Raspberry Pi would be able to predict the LG fault current value based on the real-time inputs from RPSs and given dataset. The real-time inputs are given through Arduino, which acts as analog to digital converter to the Raspberry Pi, which then commands the relay to trip during fault conditions. The trip condition is indicated when the LED glows and buzzer buzzes.

4 Conclusion

The protection scheme for microgrid developed in this paper is adaptive in nature. A simulation model with two PV sources as DGs has been developed to get the training dataset for two independent variables PV1 and PV2 and one dependent variable LG fault value under two modes of operation. The dataset has been taken in both islanded and grid-connected modes and imported as a "CSV" file to the ML platform in Raspberry Pi. The ML algorithm used here is "multiple regression" for prediction of fault current value in both the modes of operation. This system includes four inputs: PV1, PV2, reference current value (given in terms of voltage), and mode of operation from the RPS. The algorithm has been designed in such a manner that if the value from the mode of operation input is greater than "1", then it is grid-connected mode else islanded mode. The input values from the RPSs are given through Arduino which acts here as an analog to digital converter to Raspberry Pi. The algorithm predicts the LG fault current value and compares it with the input current value. If the LG fault current value is less than the input value, then there is a fault condition, the relay trips, and the LED glows and buzzer buzzes. This system, thus, leads to the development of more stable and reliable power system network

as the incorporation of DGs changes the grid contribution to the fault current and, thus, changes the protection needs of the system. The constant need for change in the current settings and time settings in the relay according to the fault current level and modes of operation makes the adaptive protection scheme an inevitable part of the modern power system network. This research work is, thus, a venture made to make a small but significant contribution in making the modern power system network more durable, reliable, and stable. The adaptive protection scheme developed can have wide range of applications and scope. The scheme developed can be used in the microgrid connected to the conventional power system network as well as for microgrids operates in an islanded mode. The algorithm used can be adopted for the protection of real-time microgrids as the proposed model collected system data as voltage signals and the processor processes those data. The software model developed using machine learning algorithm will process these data and identify the fault condition. This proposed method can be implemented for the protection of real-time microgrids.

References

1. Barra PHA, Coury DV, Fernandes RAS (2019) A survey on adaptive protection of micro grids and distribution system with distributed generators. Published in: Elsevier
2. Lin H, Sun K, Tan Z-H et al (2019) Adaptive protection combined with machine learning for micro grids. IET Gener, Transm Distrib 13:770–779
3. Mishra M, Rout PK (2018) Detection and classification of micro grid faults based on HHT and machine learning techniques. IET Gener Transm Distrib 12(2):388–397
4. Che L, Shahidehpour M, Alabdulwahab A, Al-Turki Y (2015) Hierarchical coordination of a community micro grid with AC and DC Micro grids. In: Published in: IEEE transactions on Smart Grid, vol 6, no 6
5. Anil Kumar P, Shankar J, Nagaraju Y (2013) Protection issues in Micro grid. Int J Appl Control, Electr Electron Eng (IJACEEE) 1(1)
6. Kandukuri S, Vyjayanthi C (2018) Fault level analysis in modern electrical distribution system considering various distributed generations. In: Proceedings of 2018 international conference on power, energy, control and transmission systems, Chennai. 978-1-5386-3817-0/18
7. Kailun Z, Kumar DS, Srinivasan D (2018)An adaptive overcurrent protection Scheme for micro grids based on real-time digital simulation. In: Published in:2018 71st annual conference for protective relay engineers (CPRE). TX, USA. https://doi.org/10.1109/CPRE.2018.8349769
8. Nikkhajoei H, Lasseter RH (2007) Micro grid Protection. In: 2007 IEEE power engineering society general meeting. Tampa, FL, USA. https://doi.org/10.1109/PES.2007.385805

Power Quality Improvement in Distribution Network Using Levenberg–Marquardt (LM) Algorithm-Based Controller for Active Current Harmonic Filter

P. Balamurugan, N. Senthil Kumar, and C. Vaithilingam

Abstract Levenberg—Marquardt (LM) algorithm-based current controller for shunt active harmonic filter (SAHF) is implemented for minimizing harmonic currents in power distribution network. A simple and versatile soft computing algorithm for implementing controller to minimize the current error of SAHF is developed for improving power quality (PQ) in conventional distribution grid. The effectiveness of the control algorithm proposed is analyzed considering group of balanced and unbalanced nonlinear supplied from a balanced sinusoidal AC power supply. The objective is to minimize the tracking error in the output of SAHF compensating current harmonics resulting in distortion-free source current. Simultaneous compensation of reactive power by SAHF results in unity power factor operation at the source. The algorithm is developed and implemented using MATLAB/Simulink environment using discrete solver.

Keywords LM algorithm · Artificial neural network (ANN) · SAHF · Harmonics · THD

1 Introduction

In recent decade, the growth of renewable energy sources emerged as an alternate for the conventional fossil fuels due to the development of high-power converters. Sophisticated and fast-acting controllers enable the interfacing of renewable sources with power grid and interconnection of several types of renewables to operate in integrated manner. Electric mobility has gained attraction as an alternate for the existing

P. Balamurugan (✉)
eVITRC, Vellore Institute of Technology, Chennai, India
e-mail: balamurugan.p@vit.ac.in

N. Senthil Kumar · C. Vaithilingam
School of Electrical Engineering, Vellore Institute of Technology, Chennai, India
e-mail: senthilkumar.nataraj@vit.ac.in

C. Vaithilingam
e-mail: vaithilingam.c@vit.ac.in

C. Subramani et al. (eds.), *Proceedings of International Conference on Power Electronics and Renewable Energy Systems*, Lecture Notes in Electrical Engineering 795,
https://doi.org/10.1007/978-981-16-4943-1_59

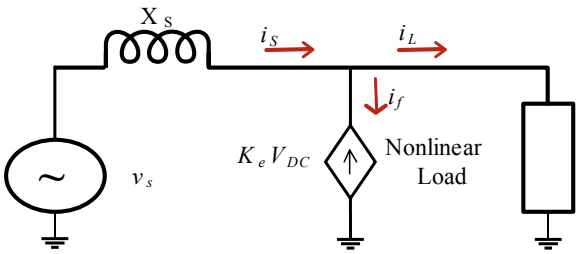

Fig. 1 Illustration of SAHF

transportation system to provide cleaner environment. In all the mentioned applications, power converters bridge the energy conversion from one form to another form. Power converters integrating renewables and power network introduce harmonics into it resulting in harmonic distortion. Conventional grids are designed to operate only at fundamental frequency which cannot withstand the harmonic pollution. This results in proper functioning of sensitive equipment like adjustable speed drives, lifesaving equipment in hospitals, microprocessor/controller-based process control systems in various industries, reduced losses throughout the system [1].

Harmonics are limited by means of installing passive or active power filters at suitable locations in the power system. Active power filters facilitate flexible compensation and advantageous compared to passive filters. SAHF is a controlled current source connected in parallel to the sensitive load to supply the harmonics required by the load as depicted in Fig. 1. Kirchhoff's law at node 'a' yields $i_s = i_L + i_f$. The nonsinusoidal current drawn by nonlinear load is resolved in to sinusoids of integer multiples of supply frequency using Fourier series. The nonlinear load current (i_L) is the sum of current component at line/fundamental frequency (i_{L1}) and currents at integer multiple of fundamental frequency components (i_{Lh}). If SAHF delivers i_{Lh}, then the source current will be at fundamental frequency of i_L [1].

The current injected by SAHF is essential in regulating harmonics in the grid, and hence, the problem is formulated to regulate the current output of SAHF. The harmonic extraction from the distorted current essentially determines the performance. In this work, pq-theory is adopted for its flexibility in compensation.

ANN technique develops self-decisive system enabling the designer the flexibility and adaptive nature for control design. ANNs are significant in the following aspects: The input–output relationships need not to be specified, and the same is established through learning process or adaptive through any learning algorithm. Secondarily, the parallel computation architecture of ANN increases speed and reliability of the system. Adaptive networks estimate the reference compensation currents, and a multilayer perceptron feedforward network-based hysteresis band comparator is developed in [2] which employs backpropagation algorithm to train the feedforward network. Intelligent adaptive power line conditioner based on supervised learning rule to realize optimal adaptive weight vector for filter is realized in [3] with adaptive NN for harmonic computation, and a feedforward network implements PWM control using digital signal processor in [2]. Control efforts to balance the source currents, canceling the neutral currents. Online extraction of fundamental voltage component

using Adaline network is proposed in [4]. It recovers the balanced and equilibrated voltage and different methods for harmonic filtering. Several soft computing techniques like fuzzy logic, neural control and genetic algorithm-based filter control were proposed and compared in [5]. Adaline-based notch filter was implemented to extract fundamental grid frequency estimated based on neural-based PLL employing ADALINE NN, trained by a least square algorithm (LS). This enabled online computation of compensation currents from the values of load current and PCC voltage to work. Dynamic performance improvement of SAHF by utilizing the dynamics of DC link voltage is proposed in [6] using Adaline-based current. NN control strategy for selective harmonic elimination was proposed in [7] to extract the harmonic reference for a medium voltage 6-pulse current source converter by introducing time delay. Feedforward multilayer neural network-based current control is proposed in [8] with step-by-step approach. Echo-state network-based fundamental current extraction technique was implemented. It evaluates weight values to extract the reference currents. Variable leaky least mean square (VLLMS)-based controller for making SAHF self-adaptive to the operating conditions was proposed in [9]. VLLMS-based algorithm replaced the conventional weight updating algorithm, enhancing the execution speed and weight extraction to a greater extent, claiming variable band adaptive current control technique to circumvent auditory noise, and irregular switching frequency in conventional hysteresis regulator.

In this paper, Levenberg–Marquardt algorithm is adopted to control the SAHF. LM algorithm locates the minimum of a multivariate function in a reiterative manner, which is expressed as the sum of squares of nonlinear real-valued functions. Evolving as a standard solution technique, LM algorithm is applied for nonlinear least square problems. This work utilizes LM algorithm to generate duty cycle of PWM signals for SAHF. Discussing the LM algorithm formulation in Sect. 2, this paper covers the harmonic compensation principle in Sect. 3. Section 4 describes the algorithmic implementation of the proposed control in MATLAB/Simulink environment.

2 Levenberg–Marquardt Algorithm

The Levenberg–Marquardt (LM) algorithm is a combination of the Gauss–Newton and steepest descent methods. When the deviation between currently arrived solution and the desired one is more, the algorithm switches to steepest descent method: providing sluggish, but assured convergence. When the deviation between currently arrived solution and the desired solution is minimal, it follows Gauss–Newton method [10].

The update rule of Gauss–Newton method is given by

$$w_{k+1} = w_k - \left(J_k^T J_k\right)^{-1} J_k e_k \tag{1}$$

For convergence, the approximated Hessian matrix $J^T J$ approximation must be invertible. To ensure this condition, another approximation is introduced to Hessian matrix by the Levenberg–Marquardt algorithm expressed as in Eq. (2):

$$H \approx J^T J + \mu I \tag{2}$$

where μ = combination coefficient (positive always) and I = identity matrix.

It may be observed from (2), the principal diagonal elements of the approximated Hessian matrix will be a positive number. The guesstimate in (2) when applied to Eq. (1) ensures matrix H is invertible always. With the approximations applied, the new update law of Levenberg–Marquardt algorithm can be expressed as

$$w_{k+1} = w_k - (J_k^T J_k + \mu I)^{-1} J_k e_k \tag{3}$$

During training process, the Levenberg–Marquardt algorithm switches between the Gauss–Newton algorithm and the steepest descent algorithm in computing the grouping coefficient 'μ'. Gauss–Newton algorithm is employed when negligible values of μ (nearly zero) approximating Eq. (3) to Eq. (1). The steepest descent method is applied for larger values of μ, by approximating Eq. (3) to $w_{k+1} = w_k - \alpha\, g_k$. If the grouping coefficient μ in Eq. (3) is larger, it can be taken as the learning coefficient: $\alpha = 1/\mu$, in the steepest descent method.

Node y is significant and flexible, to define a neuron output. To interpret, $y_{j,\,i}$, is the ith input of jth neuron. To define the output of neuron j, it is represented as y_j. The single index of node 'y' implies an output neuron, whereas two indices (neuron and input) indicate the node as input of a neuron.

The output node of jth neuron is computed as in Eq. (4).

$$y_j = f_j(\text{net}_j) \tag{4}$$

where f_j = the activation function of jth neuron and net_j = the sum of weighted input nodes of neuron j

$$\text{net}_j = \sum_{i=1}^{ni} w_{j,i} y_{j,i} + w_{j,0} \tag{5}$$

where
$Y_{j,\,i}$ = ith input node of neuron j, weighted by $w_{j,\,i}$
$w_{j,\,0}$ = bias weight of neuron j.

The training process for LM algorithm must be framed as follows:

1. Generate random initial weights and compute the total error.
2. Adjust and update weights using Eq. (3).
3. Evaluate total error using updated new weights.

4. After an update, if the present overall error is enlarged, then pull back weight vector to the preceding value and upsurge grouping coefficient μ by a factor 10 or higher. Repeat step-2 and try updating weights.
5. After an update, if the present overall error is diminished, then retain the new weight vector to its present value and lessening the grouping coefficient μ by a factor 10 or by the same factor as in step-4.
6. Return to step-2 with the new weights until the recent total error is smaller than the vital value.

3 Principle of Harmonic Compensation

Utilizing Clarke's transformation, Akagi H [11] formulated a theory to compute instantaneous real and reactive powers with instantaneous voltages (v) and currents (i) as key parameters. Transforming a set of time varying space varying phasors in to two orthogonal components and a zero-sequence component, powers are computed.

$$\begin{bmatrix} v_\alpha \\ v_\beta \\ v_0 \end{bmatrix} = \sqrt{\frac{2}{3}} \begin{bmatrix} 1 & -0.5 & -0.5 \\ 0 & 0.866 & -0.866 \\ 1 & 1 & 1 \end{bmatrix} \begin{bmatrix} v_r \\ v_y \\ v_b \end{bmatrix} \tag{6}$$

$$\begin{bmatrix} i_\alpha \\ i_\beta \\ i_0 \end{bmatrix} = \sqrt{\frac{2}{3}} \begin{bmatrix} 1 & -0.5 & -0.5 \\ 0 & 0.866 & -0.866 \\ 1 & 1 & 1 \end{bmatrix} \begin{bmatrix} i_r \\ i_y \\ i_b \end{bmatrix}$$

The instantaneous real power (p) and reactive power (q) are calculated in the converted domain as in (7).

$$p = v_\alpha i_\alpha + v_\beta i_\beta + v_0 i_0$$

$$q = v_\beta i_\alpha - v_\beta i_\alpha \tag{7}$$

The components of power in (7) are composed of fundamental and nonfundamental components. A higher-order low-pass Butterworth filter is used to segregate the average component of power from the computed total power. The average value corresponds to instantaneous real and reactive powers at the fundamental frequency of the system. The oscillating components of power correspond to the harmonic frequencies.

The compensating reference currents are computed from (7) after extricating the average and oscillating components using (8) for SAHF.

$$\begin{bmatrix} i^*_{c\alpha} \\ i^*_{c\beta} \end{bmatrix} = \frac{1}{\sqrt{v_\alpha^2 + v_\beta^2}} \begin{bmatrix} v_\alpha & v_\beta \\ v_\beta & -v_\alpha \end{bmatrix} \begin{bmatrix} p^*_c \\ q^*_c \end{bmatrix} \tag{8}$$

The inverse Clarke's transformation of Eq. (8) results in real-time current references for the filter controller and is expressed in Eq. (9).

$$\begin{bmatrix} i_{cr}^{*} \\ i_{cy}^{*} \\ i_{cb}^{*} \end{bmatrix} = \sqrt{\frac{2}{3}} \begin{bmatrix} 1 & 0 \\ -0.5 & 0.866 \\ -0.5 & -0.866 \end{bmatrix} \begin{bmatrix} i_{c\alpha}^{*} \\ i_{c\beta}^{*} \end{bmatrix} \tag{9}$$

The SAHF is forced to track the reference currents employing suitable current control algorithms used in practice. The compensation for oscillating components of power results in harmonic free source current and voltage at constant power factor decided by the reactive power drawn from the source. For unity power factor, along with oscillating real power, the compensator must supply total reactive power.

Typical VSC-based SAHF power circuit in [1] is essentially a voltage source converter with capacitor-powered DC link, connected at PCC in distribution network with an interfacing filter. The filter controller is equipped with data acquisition system to compute the harmonic currents by processing the system voltage and load current signals. In addition, the filter controller ensures DC link voltage regulation during its operation. The calculated reference and filter current outputs are related to produce the PWM switching signals for the power switches in VSC and resulting in minimal regulating error. Harmonic currents of any order can be synthesized and injected by appropriate selection of power components and computing the reference current [12].

4 Design of ANN-Based Current Controller

A customized neural network controller was generated using training data obtained from the measured samples of the active filter controlled. The input to the neural network is the current deviation/error from the comparator. The output is the duty ratio for the switches in voltage source converter. The converter duty ratio must be regulated to maintain DC voltage regulation and output current regulation of the voltage source converter. The duty ratio is then converted into PWM signals by comparing the duty ratio output from ANN with a unipolar triangular ramp carrier. The switching frequency of the voltage source converter limits the size of the filter inductor.

In the design of ANN controller, error samples acquired at a sample interval of 1 μs are fed to the neural network. Using *'nntool'* command, the NN is generated and trained. The input samples are parameterized as vector in the workspace and imported to the toolbox. The selection parameters like training function, number of input and output layers and neuron contained in the layers are configured initially. The network type is chosen as feedforward-backpropagation type for better performance and mean square error as the performance parameter for convergence. One such

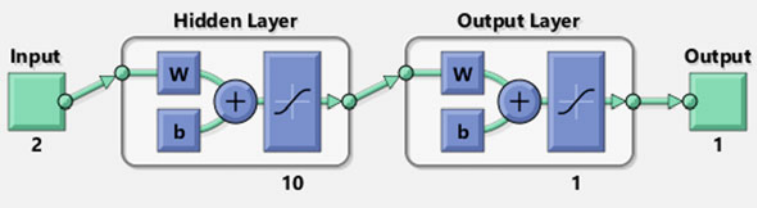

Fig. 2 Customized neural network generated and trained using MATLAB

network as shown in Fig. 2 is created and trained using LM algorithm described in Sect. 2.

5 MATLAB implementation of ANN-based current controller for SAHF

The MATLAB implementation of ANN-based current controller for SAHF was developed in MATLAB as discussed in Sect. 4 and implemented using Simulink tool. The filter configuration for distribution network is shown in Fig. 3. The condition considered for simulation study and implementation and the system parameters taken for study are detailed in Table 1.

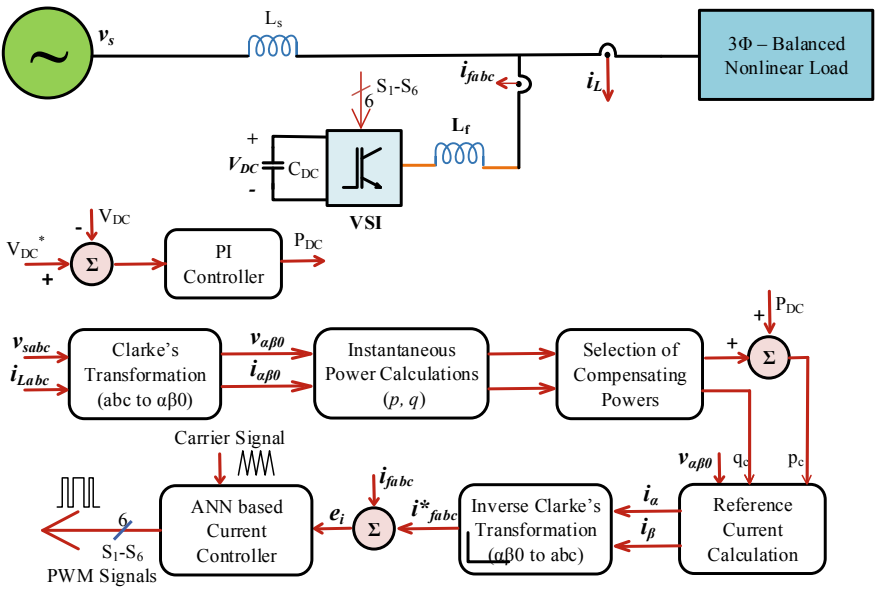

Fig. 3 Simulink implementation block diagram of ANN current controller-based SAHF

Table 1 System configuration and parameters used for the design of ANN current controller

System parameter	Value
Source parameters	
Voltage (V_s)	440 V, 50 Hz, 3-phase AC supply with no transformer
Line resistance (R_s) and inductance (L_s)	0.1 ohms, 5 mH
Load parameters	
Nature of load	Three-phase diode bridge rectifier
Load resistance (R_1) and inductance (L_1)	10 ohms, 15 mH
Filter parameters	
Voltage source converter	IGBT based three-phase three-leg converter with DC capacitor in DC link with floating neutral
Filter inductance (L_f) and resistance (R_f)	5 mH, 0.2 ohms
DC link capacitance (C_{DC})	1000 microfarad
DC link voltage reference (V_{DC}*)	800 V
DC link controller	Output limited PI controller
Filter controller	ANN controller
Filter interface	Direct coupling with L filter

The results of simulation are shown in Fig. 4. The waveforms of source voltage, source current after compensation, load current, harmonic current in phase 'c' and DC link voltage are shown, respectively. Since only one nonlinear load is considered, the source current is same as the load current in the absence of compensation using SAHF. Hence, the pre-compensated source current is similar to the load current (i_L). To analyze the effect of current controller under dynamic conditions, an additional load is added in the DC side of the diode bridge rectifier whose rating is similar to the first load. The transient behavior of SAHF with the proposed current controller for load changes on DC side is studied in this study. The second load is switched 'ON' at the mid-range of simulation, and the transients were observed in the behavior of parameters like filter output current, DC link capacitor voltage and source current compensation.

The effectiveness of compensation is measured in terms of harmonic indices performance. Total harmonic distortion in source current is the important parameter that indicates the quality of the source current waveshape and hence the effectiveness of harmonic compensation. Also, lesser the value of THD, closer the wave shape is sinusoidal and power factor is near unity. Hence, the source current waveform is analyzed using fast Fourier transform (FFT) tool with 50 Hz as the fundamental component. The FFT is expressed as wave spectrum and is shown in Fig. 5a for the uncompensated source current. The distortion level is as high as 28.96% for the measured uncompensated source current. The standard allowable harmonic penetration pertaining to the operating voltage is 5% as governed by IEEE519:2014 guidelines. The dominant harmonics are 250, 350, 550, 650 and 850 Hz for the operating

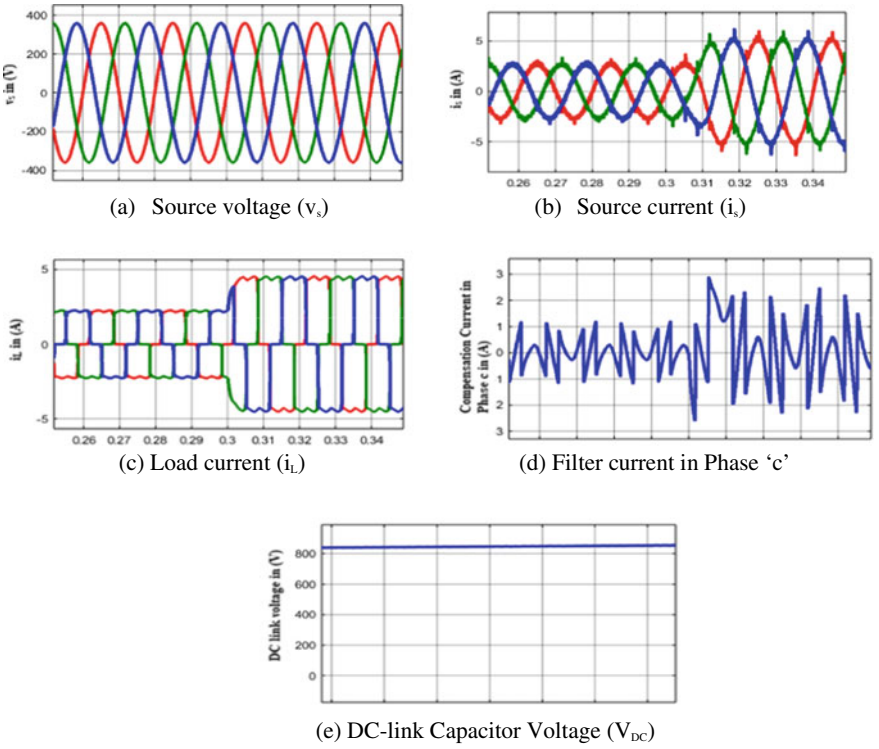

(a) Source voltage (v_s) (b) Source current (i_s)

(c) Load current (i_L) (d) Filter current in Phase 'c'

(e) DC-link Capacitor Voltage (V_{DC})

Fig. 4 Simulink results of ANN current controller-based SAHF

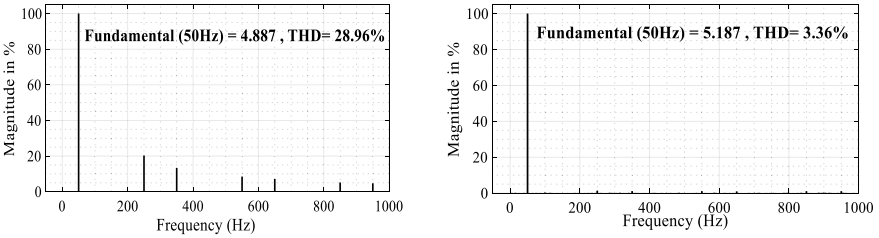

(a) Pre-compensation. (b) Post-compensation.

Fig. 5 Harmonic spectrum of source current in phase—'a'

condition considered. Among these, up to 550 Hz, the harmonic elimination using conventional passive filter fails to be a feasible solution.

In the presence of active power compensation filter, with the proposed current controller, the THD of compensated source current is 3.36% and is better than the results obtained with conventional current controllers in [1, 12]. Moreover, the THD is much within the limits specified by IEEE519:2014 guidelines for the utility grid at

Table 2 Performance analysis of ANN current controller under different operating conditions

System parameter	Balanced load		Unbalanced load		Single phasing	
	I_{RMS} (A)	% THD	I_{RMS} (A)	% THD	I_{RMS} (A)	% THD
Phase—a	3.5	3.36	3.5	2.66	3.8	4.08
Phase—b	3.5	3.36	3.5	2.68	3.8	4.1
Phase—c	3.5	3.36	5	2.09	3.8	4.09

distribution voltage levels. The harmonic spectrum of compensated source current is shown in Fig. 5b. Similar analysis was conducted for different operating conditions like addition of unbalanced nonlinear load and single-phasing of balanced linear load by open circuiting phase 'c' at the source. The results of source currents and the corresponding THD levels are shown in Table 2.

The performance of the proposed LM algorithm-based ANN for shunt active harmonic filter is evident from Table 2 after compensation. The source currents are balanced sinusoids under various operating conditions at the load side. In this work, the proposed current control algorithm is evaluated under balanced sinusoidal supply voltage considerations, and the performance is observed to be satisfactory. Similar studies can be extended under supply voltage nonidealities to deal with optimum and real-time implementation of the proposed current control algorithm.

6 Conclusion

In this paper, a feedforward-backpropagation-based artificial neural network based on LM algorithm was developed, implemented and analyzed for current control of shunt active harmonic filter at distribution level. The results are evidence for the proof of concept in the application of ANN for power control and harmonic regulation at distribution voltages. The objective of reference current tracking at nonfundamental frequency to compensate for harmonic currents is in effect with negligible tracking error. The results of simulation show that the source currents are sinusoids and in-phase with their respective voltage sinusoids achieving near unity power factor operation. Also, the problem of eliminating low-frequency harmonics with traditional passive filters is greatly eliminated by the use of SAHF resulting in cheaper power quality solution.

References

1. Balamurugan P, Senthil Kumar N (2019) Regulation of current harmonics in grid with dead-beat controlled shunt active power filter. Prz. Elektrotechniczny. 95:17–23. https://doi.org/10.15199/48.2019.12.04

2. Salmerón P, Vázquez JR (2005) Practical design of a three-phase active power-line conditioner controlled by artificial neural networks. IEEE Trans Power Deliv 20:1037–1044. https://doi.org/10.1109/TPWRD.2004.838513
3. Lin HC (2004) Intelligent neural-network-based adaptive power-line conditioner for real-time harmonics filtering. In: IEE Proceedings: generation, transmission and distribution. https://doi.org/10.1049/ip-gtd:20040757
4. Abdeslam DO, Wira P, Mercklé J, Flieller D, Chapuis YA (2007) A unified artificial neural network architecture for active power filters. IEEE Trans Ind Electron 54. https://doi.org/10.1109/TIE.2006.888758
5. Kumar P, Mahajan A (2009) Soft computing techniques for the control of an active power filter. IEEE Trans Power Deliv 24:452–461. https://doi.org/10.1109/TPWRD.2008.2005881
6. Bhattacharya A, Chakraborty C (2011) A shunt active power filter with enhanced performance using ANN-based predictive and adaptive controllers. IEEE Trans Ind Electron 58:421–428. https://doi.org/10.1109/TIE.2010.2070770
7. Hamad MS, Gadoue SM, Williams BW (2012) Harmonic compensation of a six-pulse current source controlled converter using neural network-based shunt active power filter. IET Power Electron 5:747–754. https://doi.org/10.1049/iet-pel.2011.0336
8. Qasim M, Khadkikar V (2014) Application of artificial neural networks for shunt active power filter control. IEEE Trans Ind Infor 10:1765–1774. https://doi.org/10.1109/TII.2014.2322580
9. Ray PK (2018) Power quality improvement using VLLMS based adaptive shunt active filter. CPSS Trans Power Electron Appl 3:154–162. https://doi.org/10.24295/cpsstpea.2018.00015
10. Yu H, Wilamowski BM (2011) Levenberg–Marquardt Training. In: Industrial electronics handbook. pp. 12–1 to 12–15. CRC Press. https://doi.org/10.1134/1.1788770
11. Akagi H (1996) New trends in active filters for power conditioning https://ieeexplore.ieee.org/abstract/document/556633. https://doi.org/10.1109/28.556633.
12. Parandhaman B, Nataraj SK, Baladhandautham CB (2020) Optimization of DC-link voltage regulator using Bat algorithm for proportional resonant controller-based current control of shunt active power filter in distribution network. Int Trans Electr Energy Syst 30:1–15. https://doi.org/10.1002/2050-7038.12369

Modified Multiverse Optimization, Perturb and Observer Algorithm-Based MPPT for Grid-Connected Photovoltaic System

N. K. Rayaguru and S. Sekar

Abstract The main objective this work is to analyze the total harmonic distortion for grid-connected photovoltaic system. A novel modified multiverse optimization algorithm (MMVO) is proposed to unravel the issues of the conventional maximum power point tracking (MPPT). The goal of this new methodology is to spice up the PV array efficiency. The proposed modified algorithm has a low convergence time and excessive efficiency compare to perturb and observe (P&O) algorithm.

Keywords Modified MVO · P&O · PV system · Utility grid · Grasshopper optimization

1 Introduction

Many strategies of monitoring the maximum power point of a PV have been established to decide the disadvantage of efficiency without algorithm or suitable controllers [1]. The MPPT governs the DC-to-DC converter that serves as an interface between the PVM and the load. The number of MPPT-based algorithms has been reviewed within the literatures such as standard perturb and observe (SPO), fuzzy logic management (FLM), incremental conductance (INC), golden part search (GPS), gray wolf optimization (GWO) and multiverse optimizer (MVO) [2]. Alternatively, the multiverse optimization (MVO) is analyzed to be an algorithm with benefits like good tuned outcomes of result and quick convergence process as in comparison with many different MPPT algorithms [3]. The new modification MVO approaches the benefits of quick convergence time and the benefit of the high-quality tuned outcomes with a small step measurement to trace the MPP with greater accuracy and really low oscillations [4].

N. K. Rayaguru (✉) · S. Sekar
Department of Electrical and Electronics Engineering, Hindustan Institute of Technology & Science, Chennai, India
e-mail: rp.14772025@student.hindustanuniv.ac.in

S. Sekar
e-mail: ssekar.pt@hindustanuniv.ac.in

C. Subramani et al. (eds.), *Proceedings of International Conference on Power Electronics and Renewable Energy Systems*, Lecture Notes in Electrical Engineering 795,
https://doi.org/10.1007/978-981-16-4943-1_61

1.1 Modified Multiverse Optimization and It's Flowchart

Multiverse optimization [5] is a population-based algorithm. The MVO algorithm is simulated on the basis of the concepts that is present theoretically in astronomy together with white holes which are the key rudiments of the formation of universes and have never been observed in the whole universe; black holes which draw objects toward them by gravity applied to those around them; and worm holes which are tunnels that unite parts in the external space. Here, the three components are mathematically modeled to build up an optimizer, which mimics teleportation and object exchange among universes starting from white holes through wormholes to black holes. The aforesaid algorithm believes on a population of growing individuals (Fig. 1).

Each entity is a candidate solution that encodes the three concepts of black, white and wormholes in its objects. The multicandidate solutions aid and share information with each other to move toward promising area [6].

$$ux_i^j = \begin{Bmatrix} ux_j^i + \mathrm{TD} + (hv_i - lv_i) * r^d + qb_j \\ ux_j^j \end{Bmatrix}$$
$$r^c < \mathrm{EPW}, r^c \geq \mathrm{EPW}, r^b < \mathrm{EPW}, r^b \geq \mathrm{EPW} \quad (1)$$

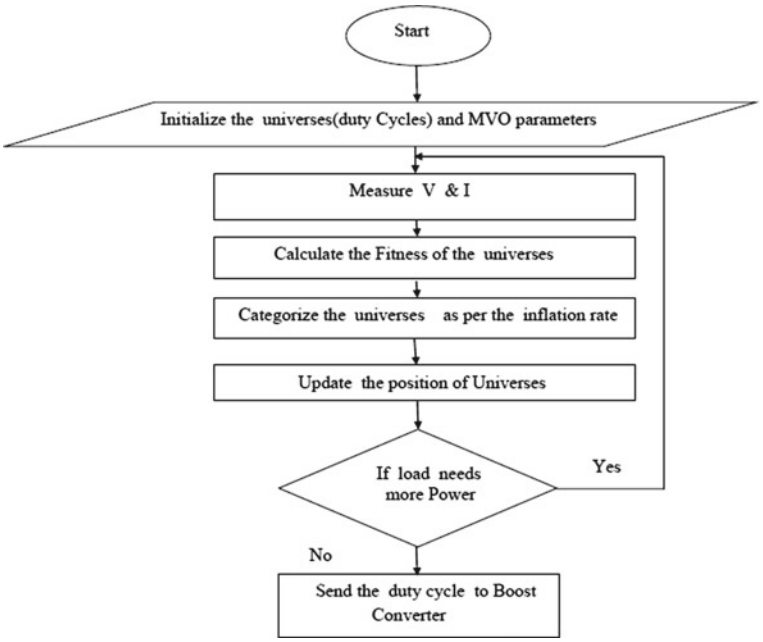

Fig. 1 Flowchart of modified multiverse optimization

where ux_j^i—j_{th} variable in ith universe; ux_j^j—the jth formed universe; TD stands for distance traveling rate; EPW—represents existence probability of wormhole; lv represents lower variable; hv represents highest variable; qb_j—represents lowest jth variable; r^b, r^c, r^d, re represents the variable with random numbers between [0, 1].

For the two coefficients, the formulas are as follows:

$$\text{EPW} = \text{low value} - q\left(\frac{\text{low value} - \text{high value}}{J}\right) \tag{2}$$

where q indicates the current iteration and J indicates the iterations with maximum number.

$$\text{TD} = 1 - \left(\frac{q^{\frac{1}{g}}}{J^{\frac{1}{g}}}\right) \tag{3}$$

$g \neq 0$, range from[0, 10]

1.2 The P&O Algorithm and It's Flowchart

Here voltage is perturbed by a minute increment ΔV. The resulting alteration in power is ΔP. It is analyzed that if P is positive, the next perturbance is in this direction. If P is in negative, the system operation has moved away from the maximum power point (MPP). The selection of duty cycle will affect the system, and the steady-state error will be reached in the system [7]. The complete iteration process has been done as shown in Fig. 2. P&O algorithm procedure is considered as follows.

Step1: Check and read $V(k)$ and $I(k)$, initialize duty cycle D.
Step 2: Calculate $P(k) = V(k)$ *I (k).
Step 3: Calculate $\Delta P = P(k) - P(k\text{-}1)$, $\Delta V = V(k) - V(k-1)$.
Step 4: If $\Delta P > 0$ is yes, then check $\Delta V > 0$. If $\Delta V > 0$ is yes, then $D = D + \Delta D$ otherwise $D = D\text{-}\Delta D$.
Step 5: If $\Delta P > 0$ is no, then check $\Delta V > 0$. If $\Delta V > 0$ is yes, then $D = D\text{-}\Delta D$ otherwise $D = D + \Delta D$.

1.3 Proposed System Description Using Both Algorithms

A PV array of 100 kW is coupled to a 25 kV grid through a DC-DC boost converter followed by a 3-Φ, three-level voltage source converter (VSC). The model consists of (a) PV array that delivers a maximum of 100 kW power at an irradiance of

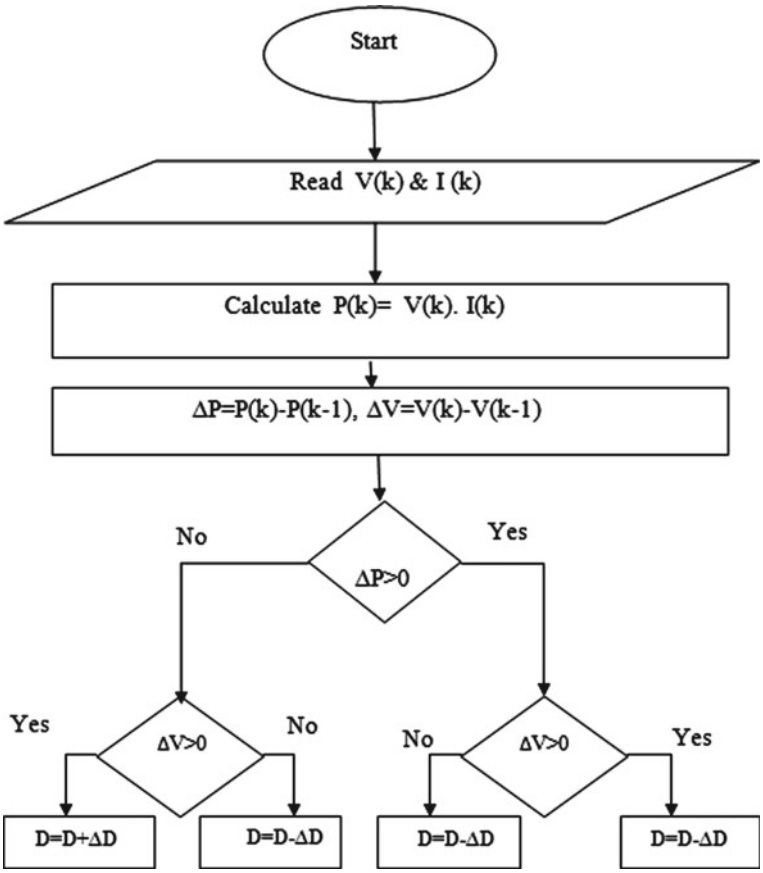

Fig. 2 Perturb and observe optimization flowchart

500 W/m^2 (b) DC-DC step-up converter, (c) three-level three-phase VSC, (d) a three-phase coupling transformer rating of 100 kVA, 260/25 kV and (e) utility grid. This configuration has proposed a boost converter in a grid-tied PV system through voltage source converter, filter and step-down coupling transformer as shown in Fig. 3. The MPPT algorithms are executed through boost converter (DC-to-DC converter) with decoupled control tactic not only supplying generated PV power to the grid but also it satisfied the load requirements of the consumer side [7, 8]. The P&O-based MPPT with the system is depicted in Fig. 3.

Figure 4a, b shows the characteristics between PV voltage and current; PV power and voltage shows the indication of maximum power point using P&O MPPT controller. The simulation waveforms for PV voltage, current and duty cycle variations corresponding to changes in solar irradiance and temperature are shown in Fig. 5. The DC-DC converter of PV system is controlled with P&O MPPT algorithm. With this implementation, they obtained maximum PV current 382.08 A at a

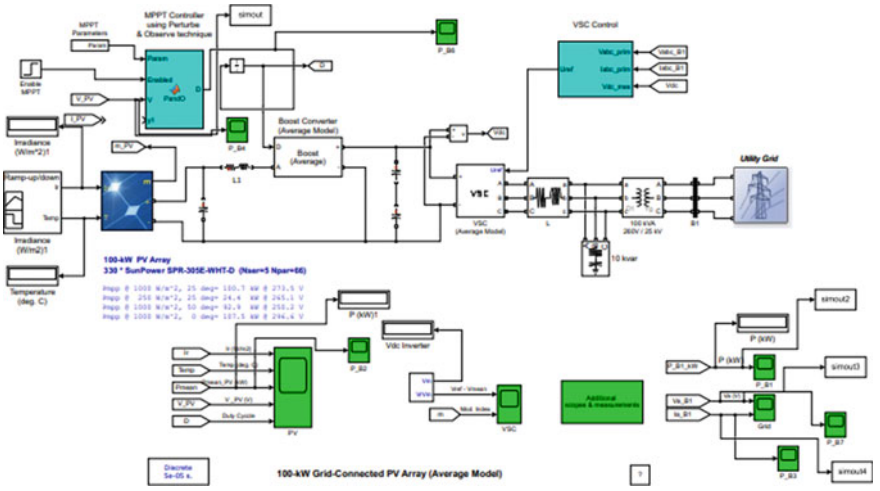

Fig. 3 PV panel with 100 W utility grid system through P&O

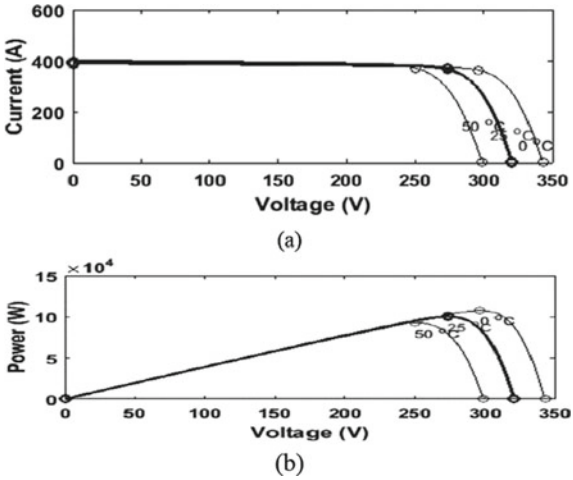

Fig. 4 **a** PV array characteristics of current verses voltage. **b** Power verses voltage in perturb and observe method

duty cycle of 0.7. The maximum power given to grid is approximately 90.2 KW as shown in Fig. 6. The grid voltage and current are shown in Fig. 7.

In Fig. 8, it is observed that the harmonic produced by the photovoltaic inverter system is 1.26%. The multilevel inverter is very much useful for providing preferred AC output voltage. In the MATLAB environment, a bridge inverter has used and is integrated of PV array into the utility grid. Table 2 depicts the harmonically generated current at the output of the Vsc (Table 1).

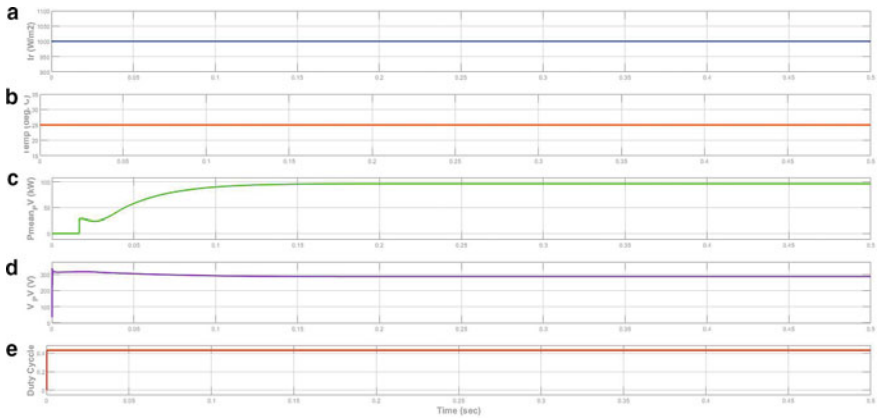

Fig. 5 Waveform for PV system parameters. **a** Irradiance. **b** Temperature. **c** PV power. **d** PV voltage. **e** Duty cycle

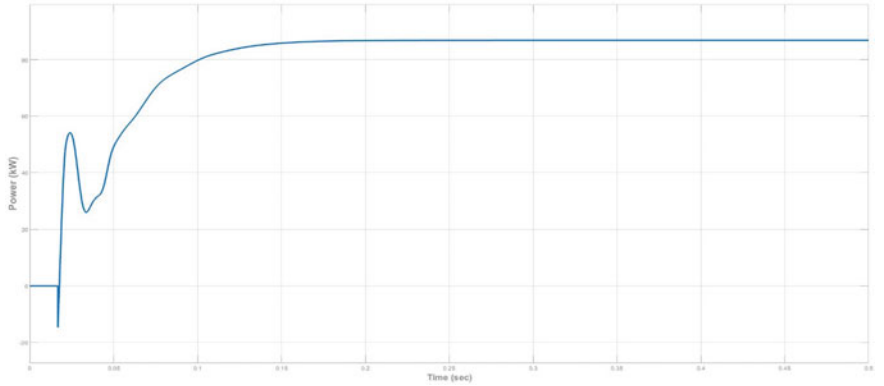

Fig. 6 Waveform for PV—grid power

2 Modified Multiverse Optimization-Based MPPT

The MMVO-based MPPT with the system is shown in Fig. 9. In this case, the proposed grid-connected PV system is implemented with MMVO optimization for generating duty cycle required for DC-DC converter. Table 4 depicts the harmonically generated current at the output of the Vsc [9] (Table 3).

Figure 10a, b shows the characteristics between PV voltage and current. The simulation waveforms for PV voltage, current and duty cycle variations corresponding to changes in solar irradiance and temperature are depicted in Fig. 11. With this implementation, they obtained maximum PV current 394.08 A at a duty cycle of 0.82. The maximum power given to grid is approximately 106.2 KW as revealed in Fig. 12. The grid voltage and current are publicized in Fig. 13.

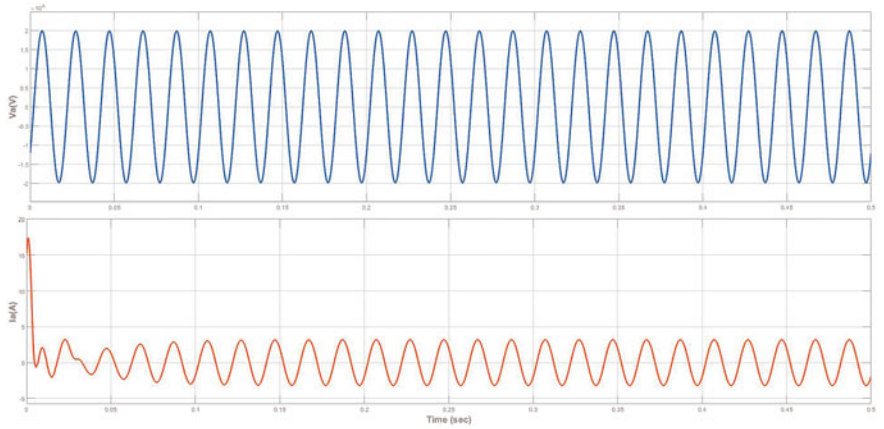

Fig. 7 Waveform for grid voltage and current

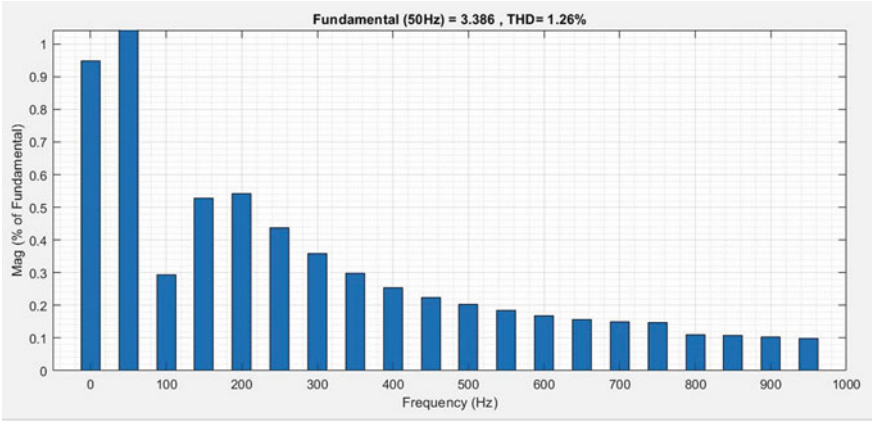

Fig. 8 THD for inverter current

Table 1 System parameters with P&O method

Parameters	Values
Irradiance	1000 W/m^2
Temperature	25°c
PV array's output voltage	273.54 V
PV array's output current	366.98 A
Maximum power extracted from PV panel	90.22 KW

Table 2 Current harmonics from VSC using perturb and observe method

Order No	RMS values (kA)	% of fundamental
1	0.01035	100
3	0.00012	0.145
5	0.00104	1.002
7	0.00090	0.850
9	0.00045	0.390
11	0.00020	0.195
13	0.00070	0.250
15	0.00095	0.455
THD	0.01100	1.26

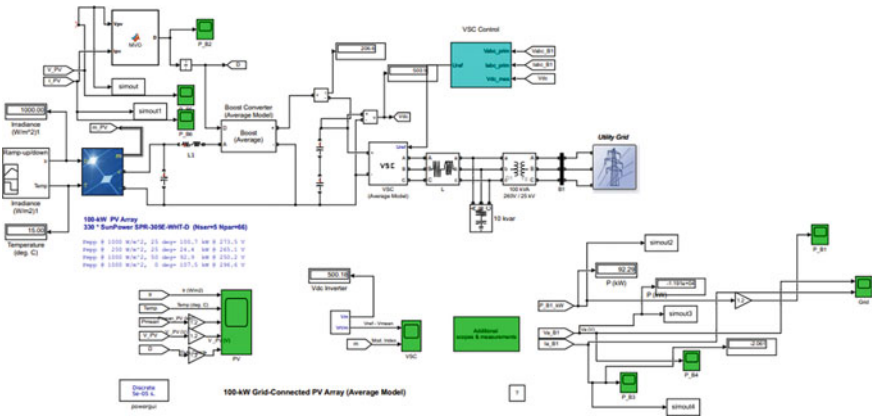

Fig.9 PV array with 100 KW utility grid system through MMVO

Table 3 System parameters with MMVO method

No. parameters	Values
Irradiance	1000 W/m^2
Temperature	25°c
PV array's output voltage	284.45 V
PV array's output current	394.08 A
Maximum power extracted from PV panel	106.20 KW

In Fig. 14, it is observed that the harmonic produced by the photovoltaic inverter system is 0.77%

The peak power extracted from PV panel is maximum in MMVO method when compared to P&O method. It is depicted in Table 5. The constant temperature and power output v/s solar irradiation are shown in Table 6. It is observed that solar

Table 4 Current harmonics from VSC MMVO method

Harmonic number	RMS current (KA)	% of fundamental
1	0.01012	100
3	0.00010	0.125
5	0.00009	1.000
7	0.00070	0.740
9	0.00035	0.320
11	0.00015	0.155
13	0.00055	0.230
15	0.00078	0.405
THD	0.01500	0.77

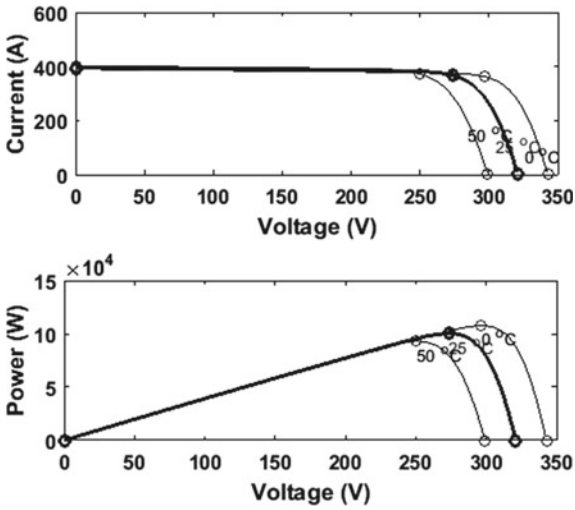

Fig. 10 PV array characteristics of current verses voltage and power verses voltage graph in MMVO method

irradiation decreases and power output decreases. Solar irradiation remains constant; but power increases, and it is shown in Table 7.

3 Conclusion

The modified multiverse optimization method has helped the power extraction and reduced the harmonics level than the P&O method. The peak power of the PV array has been tracked with adjustable duty cycle using both algorithms. The modified MVO method has given good efficiency when compared to other method. The harmonic distortion has reduced to 1% from 1.58%.The future scope of this method has to be done the algorithmic performance in the real panels.

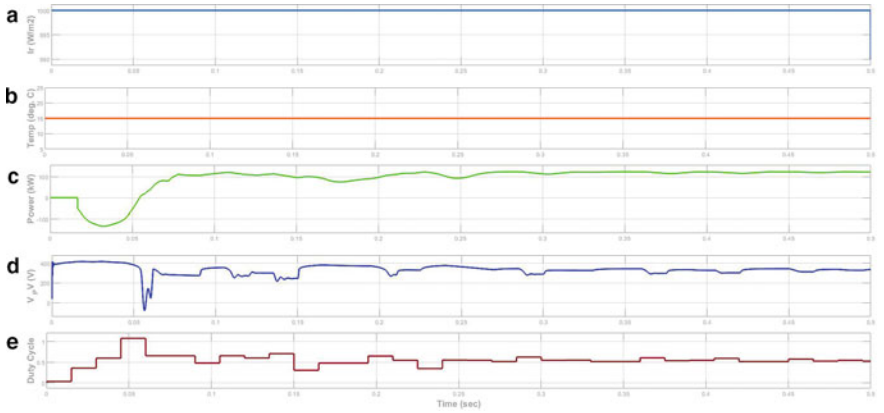

Fig. 11 Waveform for PV system parameters. **a** Irradiance. **b** Temperature. **c** PV power. **d** PV voltage. **e** Duty cycle

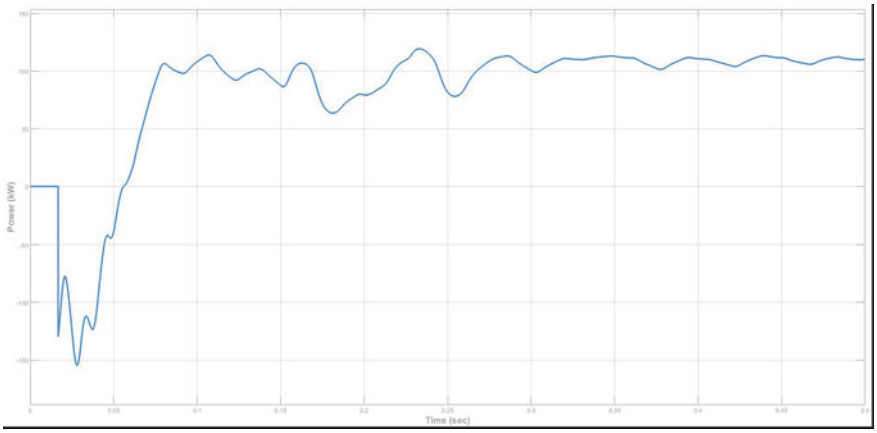

Fig. 12 Waveform for PV—grid power

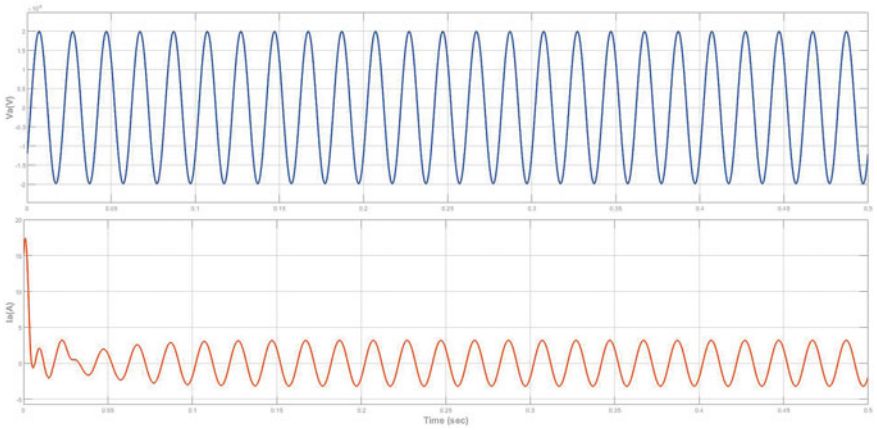

Fig. 13 Waveform for grid voltage and current

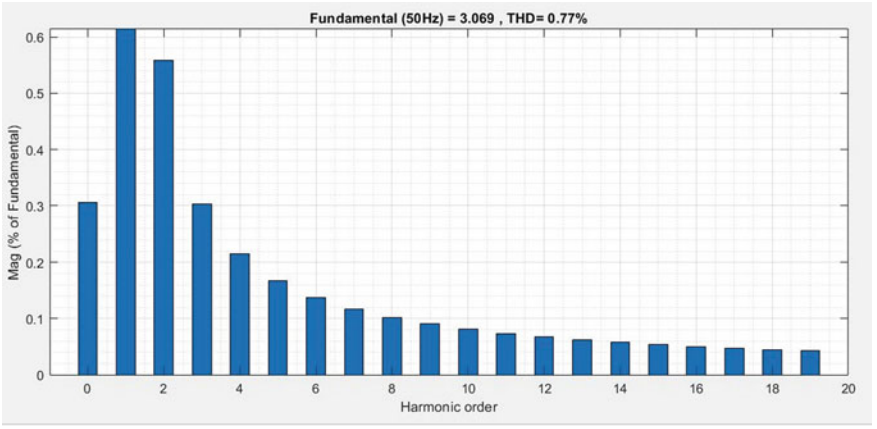

Fig. 14 THD for inverter current with MMVO

Table 5 Maximum power extracted and harmonics levels of the systems

Algorithms	Maximum power extracted (KW)	Harmonics level
MMVO	106.2	0.77%
P&O	90.80	1.26%

Table 6 Constant temperature, power output and solar irradiation

Solar irradiation (W/m^2)	Temperature in degrees	Power output to the grid (kW)
1000	25	106.22
980	25	92.10
960	25	89.37
940	25	86.90
920	25	85.96
900	25	84.43

Table 7 Constant and irradiation, output and temperature

Solar irradiation (W/m^2)	Temperature in degrees	Power output to the grid (kW)
1000	25	106.22
1000	30	91.20
1000	35	87.07
1000	40	85.20
1000	45	83.69
1000	50	82.43

References

1. Physical Progress (Achievements) ministry of new and renewable energy, Government of India. 31 January 2014. Retrieved 21 February 2014
2. Alik R, Jusoh A (2018) An enhanced P&O checking algorithm MPPT for high tracking efficiency of partially shaded PV module. Sol Energy 163:570–580
3. Lakshmi M, Hemamalini S (2019) Coordinated control of MPPT and voltage regulation using single—stage high gain DC–DC converter in a grid-connected PV system. Electr Power Syst Res 169:65–73. https://doi.org/10.1016/j.epsr.2018.12.011
4. SeyedaliMirjalili SM, Mirjalili AL (2014) Grey wolf optimizer. Adv Eng Softw 69:46–61
5. Benmessahel I, Xie K, Chellal M (2018) A new evolutionary neural networks based on intrusion detection systems using multiverse optimization. Appl Intell 48(8):2315–2327
6. Mirjalili S, Mirjalili SM, Hatamlou A (2016) Multi-verse optimizer: a nature-inspired algorithm for global optimization. Neural Comput Appl 27(2):495–513
7. Tobnaghi M (2016) A Review on impacts of grid-connected PV system on distribution network. Int J Electr, Comput, Energ, Electron Commun Eng 10(1):137–152
8. Sreedevi J et al (2016) A study on grid connected PV system. In: IEEE conference
9. Jui JJ, Ashraf Ahmad M, Mohd Rashid MI (2020) Modified multi-verse optimizer for solving numerical optimization problems. In: 2020 IEEE international conference on automatic control and intelligent systems (I2CACIS). Shah Alam, Malaysia, pp 81–86. https://doi.org/10.1109/I2CACIS49202.2020.9140097

IOT-Monitored EV Charging Stations Using DC–DC Converter with Integrated Split Battery Energy System

M. Arun Noyal Doss, R. Brindha, A. Ananthi Christy, and Viswanathan Ganesh

Abstract This paper proposes a multiport converter-based idea of preparing a fully monitored UFEVCS. Different converters are utilized in order to test the achievement of ultrafast charging station. This charging station also seeks a factor of automation in battery management system. This battery management is accomplished by the use of IOT. A worldwide control project being designed to control different varieties of power flowing directions if anything unbalances in the system. The methods are thus simulated and therefore are being implemented on hardware. By the usage of CHB converter, the SOC of a system can balance itself. IOT-based battery management is carried in order to automate the charging station with much less efforts and more efficiency. The parameters calculated from the sensors are current (I), voltage (V) and power (W). These quantities from the sensors are transferred to things peak cloud. Thing speak cloud can be accessed from anywhere at any moment of time. Complete parameters of the battery of an EV can be uploaded to the user's device

Keywords EV · UFEVCS · BMS · Cascaded H-bridge converter (CHB) · State of charge (SOC) · Dual half-bridge converter · Internet of Things (IOT) · NodeMCU

1 Introduction

In today's world, there are many advancements in usual cars and other vehicles, but the most reliable and fit for the environment conditions are electric vehicle. These vehicles have a plethora of merits. These are also suitable for certain load demand. The best part of this technology is that it requires electric charge as fuel to operate. These vehicles are easy to operate for the drivers and also have sufficient power

M. Arun Noyal Doss (✉) · R. Brindha · V. Ganesh
EEE Department, SRM Institute of Science and Technology, Chennai, India
e-mail: arunoyad@srmist.edu.in

R. Brindha
e-mail: brindhar@srmist.edu.in

A. Ananthi Christy
Saveetha School of Engineering, SIMATS, Saveetha University, Chennai, India

C. Subramani et al. (eds.), *Proceedings of International Conference on Power Electronics and Renewable Energy Systems*, Lecture Notes in Electrical Engineering 795,
https://doi.org/10.1007/978-981-16-4943-1_62

[1–3]. This ideology of EV charging station also consists of IOT-based BMS. The data measured from the battery of E are is uploaded to cloud and can be accessed by the owner of the car or by the workers and owner of the station in their respected devices. EVs usually attain power to operate from the grid supply. This involves AEVs and PHEVs. AEVs are driven by usually one or more amount of motors. It receives power from the grid and supplies electric charge to the different types of batteries. These vehicles are pollution-free as there is no consumption of any fuel like diesel, LPG. PHEVs motor usually accepts charging by the batteries which itself takes power from the grid supply. This power of motor is usually utilized to power up the engine of the vehicle. BEVs, battery electric vehicles, also known as EVs, are fully functional electric vehicles which consist batteries as their power source. These vehicles store charge in high-capacity storage packs. This power obtained from the batteries is completely utilized to run the car and its other assets (gadgets). These BEVs absorb power from the external sources. That is why they never emit any unhealthy fumes in the environment [4–6]. The groupings are L1, L2, and L3 or DC quick (fast) charging. L1 EV charging uses a common family (120v) outlet to be plugged into the EVs and consumes approximately 8 h to charge it for roughly 85–90 miles. L1 charging is a basic procedure which can be carried out at home or at any other working place. L1 chargers are capable of powering up most EVs available. L2 charging demands a special charging station which provides power at 240 V. L2 chargers are commonly found at work environments and open charging stations and will consume around 3 to 4 h to power up a battery to 85–90 miles of range. L3 charging, DC fast charging, or just fast charging is currently the fastest charging method in the EV charging system. DC fast chargers are found at respective EV charging stations and power up a battery to 100 miles extending around 35 min. PHEVs can power up the battery via both regenerative braking and supply from the grid, while basic EVs can travel up to 2–3 miles before the motor turns on which is running on fuel [8–10]. These EVs can travel up to the range of 10–50 miles before their fuel motors come into action. HEVs consist of both gas and power. The electric charge is resupplied by the braking mechanism of the vehicle. Due to this method of braking, the battery life is extended. The electric engine kicks in as the speed increases, and fuel motor stops operating [11, 12].

2 Existing System

There are many systems which are used for charging system for certain demands. All of the charging systems usually accepts AC supply from the grid. This AC supply will not provide fast charging or will not meet charging requirements all the time. A basic ideology is about applying a rectifier after receiving the supply from the grid. This converts the AC input and provides DC output. The major part we commonly snub here is the ripples; while converting the supply, this also brings too many unwanted ripples which need to be removed in order to save energy. This is performed by using a filter along with the rectifier. Now, all we want is to minimize the size of

the new gadget and also improve its functionality. This increases the usage of boost converter in order to achieve higher voltage without increasing the number of cells. Boost converters can be of different varieties. Suppose some stations using DC to DC converters with boosting operations. These have some demerits as they cannot have additional battery storage system. CHB converter is one of the options which we have come across in order to come over this demerit. CHB can allow the system to apply another storage system which can store charge while grid connection is lost. The boost converter plays a vital role in order to achieve ultra fast charging. Some other ideas are also in the box as some renewable resources are also used to generate power and to utilize it for the charging of electric vehicle. There exist less reliability with such systems. There are some systems which connects six interleaved groups consisting of two DC–DC converters connected in parallel, performing the charging process of the battery and fed by DC. But limitation is that we need to concentrate in total harmonic distortion and power factors. PV panel optimum-sizing algorithm has been developed. Battery storage system and transformer are connected to the grid for the charging station surrounded by grid constraints. But the limitation is that the optimization of loss of load needs to be concentrated. In huge batteries during charging and discharging rates to avail low charge holding loss, special cathodes made from nano-structures are used which are bi-continuous. The limitation is that the battery compatibility needs to be increased.

3 Proposed System

This paper proposes a multiport converter-based idea of preparing a fully monitored UFEVCS. Different converters are utilized in order to test the achievement of ultrafast charging station. This charging station also seeks a factor of automation in battery management system. This battery management is accomplished by the use of IOT. A worldwide control project being designed to control different varieties of power flowing directions if anything unbalances in the system. The methods are thus simulated and therefore are being implemented on hardware. By the usage of CHB converter, the SOC of a system can balance itself. IOT-based monitoring is performed in order to maintain station (charging) with much less efforts and more efficiency. The constraints registered from the sensors is current (I), voltage (V) and power (W). These constraints registered from the sensors are transferred to ThingSpeak cloud. ThingSpeak cloud can be accessed from anywhere at any moment of time [1]. Complete battery status is uploaded to the user's gadgets so that the vendor gets complete information about the station at any moment of time from any place; it also does fast charging. If grid fails to supply, still the operation can be executed (Fig. 1).

Attaining the supply from the grid which charges the battery, in middle, there is a CHB converter which permits to imply an external battery storage which will store charge and provide it to the battery when grid connection is OFF. IOT is used in our model to measure the parameters of the EV battery. The parameter will be then

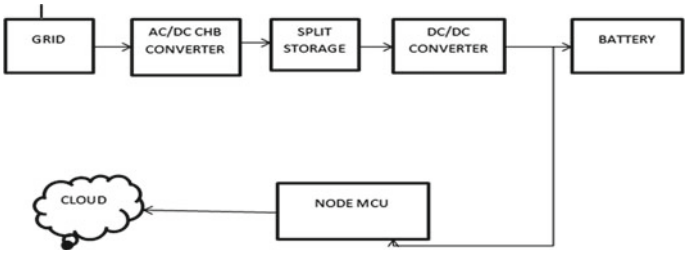

Fig. 1 Block diagram of proposed system

directly uploaded to the cloud. The vendor can access the cloud to get the information about the implanted charging station.

4 Circuit Diagram

Left side of this circuit is CHB converter which permits connections of an additional external storage system, the right side of the circuit is DC–DC converter, and this permits a multiport charging system. The output voltage is attained at the end of the operation of DC–DC converter. DC to DC converter: The output DC is at an another yield level in comparison with the input voltage. They are significant in versatile electronic gadgets like laptops, getting their power from the batteries. They require voltage levels not as quite as same as provided by the battery. They supply different controlled voltages from a solitary variable battery voltage and in this way sparing space as opposed to utilizing various batteries to supply various pieces of the gadget. Rectifier: For the time period $t = 0$ to $T/2$, the diodes D2 and D3 conduct, whereas D1 and D4 are in the state of no operation. For the other input cycle D1 and D4 are in conducting state and vice versa, thus resulting in maintaining the polarity of load. Filter: We are utilizing a LPF to get 0 Hz DC voltage by utilizing capacitor for a capacitive filter circuit associated at rectifier output resulting in DC across filtered waveform and eventually is supplied to the load. When the state of charge of the battery of electrical vehicle is above 80%, the circuit itself performs the buck operation and converse of this; if it is less than 80%, it will perform boost operation (Fig. 2).

5 Simulation

Electrical vehicle gains supply from the grid, and then, a CHB converter is placed in the circuit which gives an option to apply a split storage for battery which can be used as a backup for the charging station. This simulation works on basic operation of buck or boost. When the battery percentage is lower than 80%, the boost operation

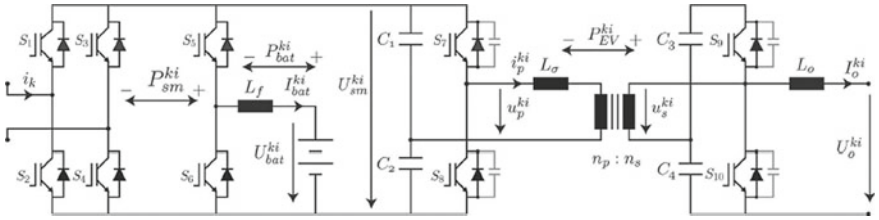

Fig. 2 Proposed circuit diagram

comes in action and starts charging the battery. If the battery percentage is higher than 80%, then operation takes place is buck operation [4, 5]. Voltage as well as current can be measured with the help of different functional blocks and can be visualized by scope. Voltage and current measurement blocks are implemented at different stages of the simulation, and this gives different measurements of the parameters (Figs. 3 and 4).

Final output is visualized in scope connected to the load (Fig. 5).

This is output of the battery of EV, and X-axis denotes time period and Y-axis denotes the output voltage of the EV (Fig. 6).

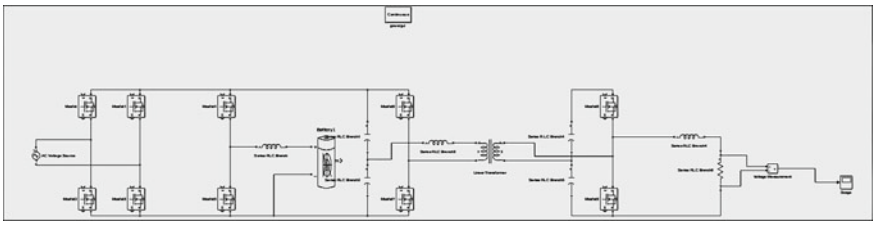

Fig. 3 Simulation diagram of the proposed system

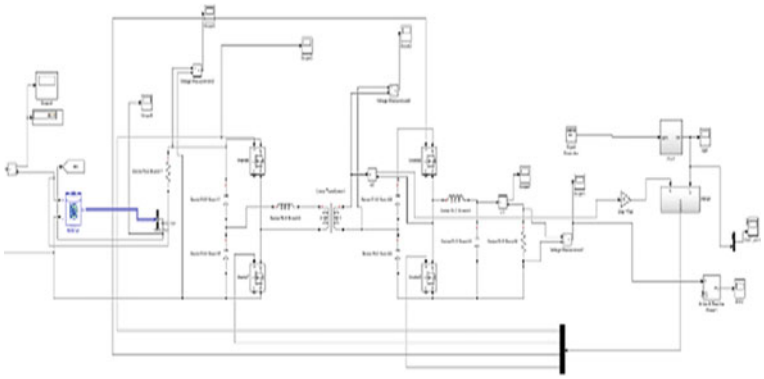

Fig. 4 Simulation of final output part

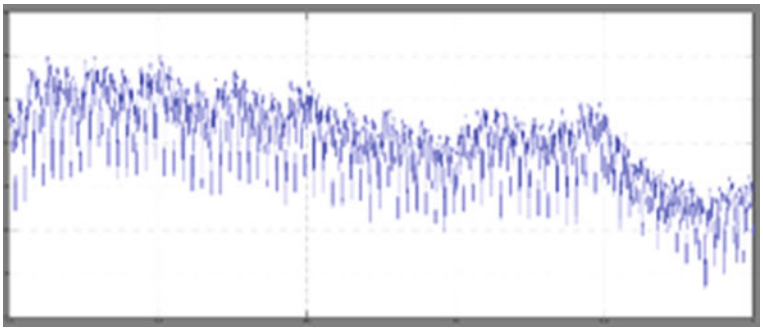

Fig. 5 Output voltage of battery of EV

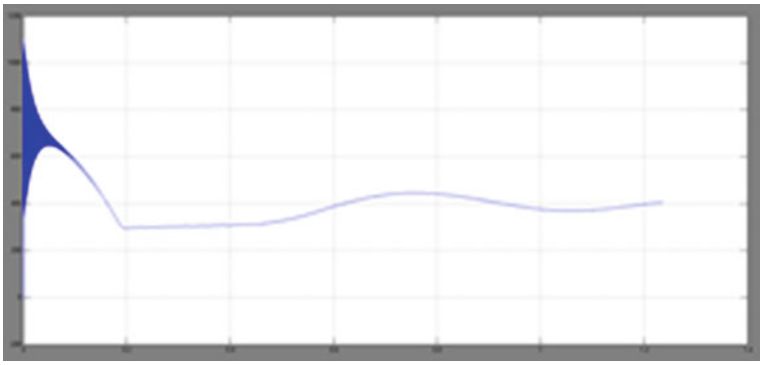

Fig. 6 Output of controlled rectifier

This output is of the controlled rectifier in the circuit which is decrease or increase the output voltage which completely depends on the battery charging operation (Fig. 7).

This is state of charge of battery which depends on buck or boost operation. If battery percentage is below 80%, then it will perform boost operation and above 80% buck operation takes place. In the above figure, battery percentage is 100% (fully charged). *X*-axis of the above graph in Fig. 7 is battery percentage, and *Y*-axis is time taken to charge the battery (Fig. 8).

As we can observe that battery percentage is below 80%, so the operation is boost operation and battery gets charged from grid (Fig. 9).

As there is some loss in the battery, that is why graph is slightly going down. *X*-axis of the overhead graph is battery percentage, and *Y*-axis is time period (Fig. 10).

As we can observe that the battery percentage is above 90% so the operation will be buck operation. The state of charge of the battery is 90% that is why required operation is of low voltage that is to directly give supply to the electrical vehicle battery (Fig. 11).

Fig. 7 State of charge of the battery

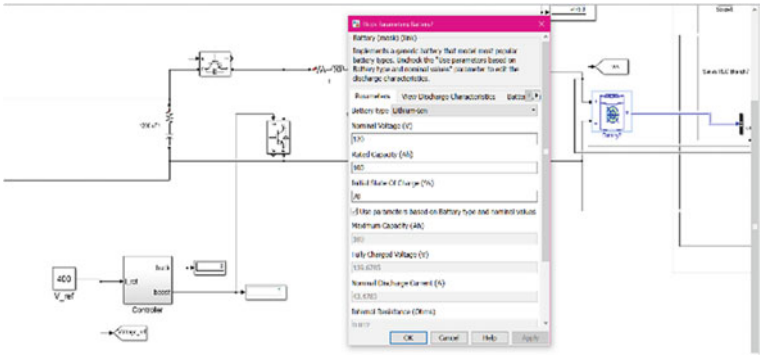

Fig. 8 Simulation settings for boost operation

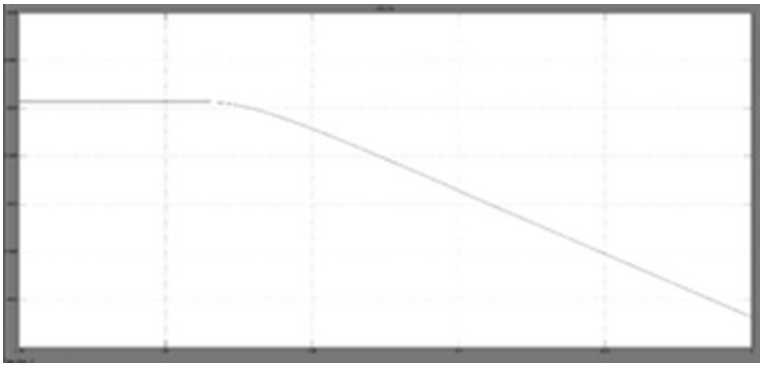

Fig. 9 State of charge of boost operation

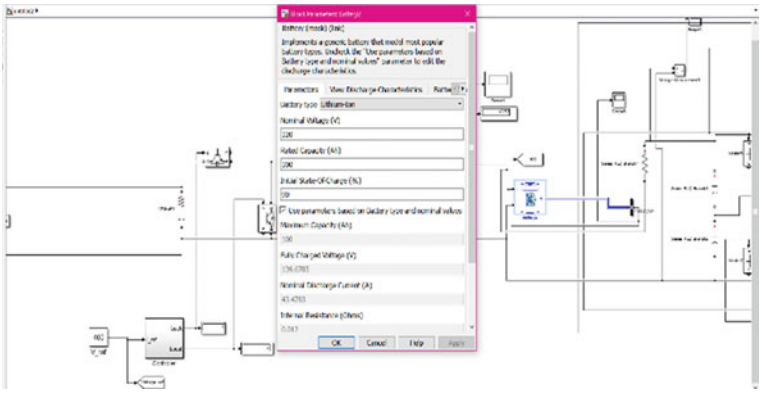

Fig. 10 Simulation settings of buck operation

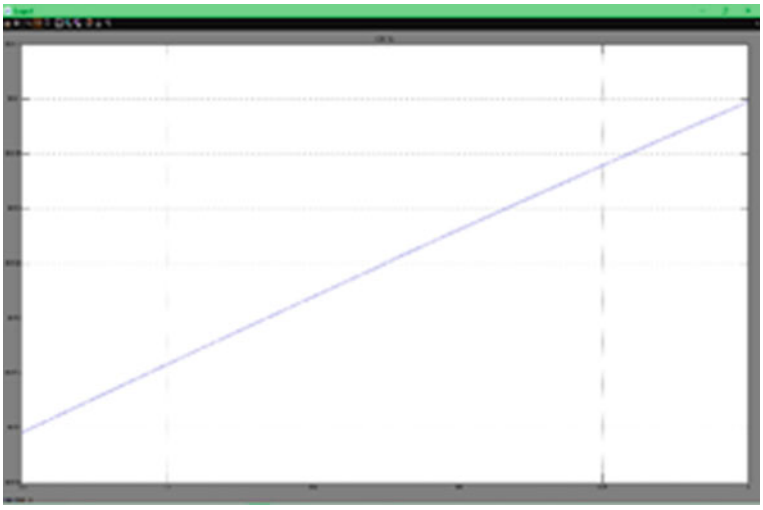

Fig. 11 Output of buck operation

Battery is slowly getting charged toward its full potential. X axis of the above graph is battery percentage and Y-axis is time period.

6 Hardware

We can observe that the battery supply voltage is increased due to the implementation of CHB converter. This also allows integration of split battery storage. Input AC transformer is connected to the power-controlled rectifier converts AC to DC, and

then, we are using capacitor to obtain the pure DC. Based on the duty cycle, it acts as a buck or boost converter. Then, we are connecting the 12 V EV battery which will get charged. Then, the half-bridge inverter will convert the DC to AC and give it to isolation transformer or 1:2 transformers which is connected to the output circuit. The other two are driver circuits being used for isolation and amplifying the input pulses. We are generating the PWM pulses using PIC controller. The PWM pulses are given as input to the driver circuits. Optocoupler IC TL250 is used for isolating the main circuit and control circuit to prevent the main circuit components from burning due to overvoltage. We are using the Darlington pair transistor to amplify the input pulses which is connected to each device. Driver circuit: We are using the driver circuits for impedance matching to provide the main circuit from burning and provide buffer to the input voltage. PWM pulses are sent to driver circuits to open the gates for driver circuits. The battery we are using here is lithium-ion battery. The specialty of this battery is that it is rechargeable. This battery is used in portable electronics and EVs and is also finding its application from military to aerospace fields, etc. In lithium ion batteries the positive electrode is made up of lithium and negative electrode is made up of graphite. During discharging process the ions move from negative to positive electrodes through electrolyte, whereas in charging process it is opposite. These batteries consist of high energy densities and low self-discharge and no memory effect. We are intending of using a 12 V lithium-ion battery for our project. This battery will be charged by our proposed battery charging system (Figs. 12 and 13).

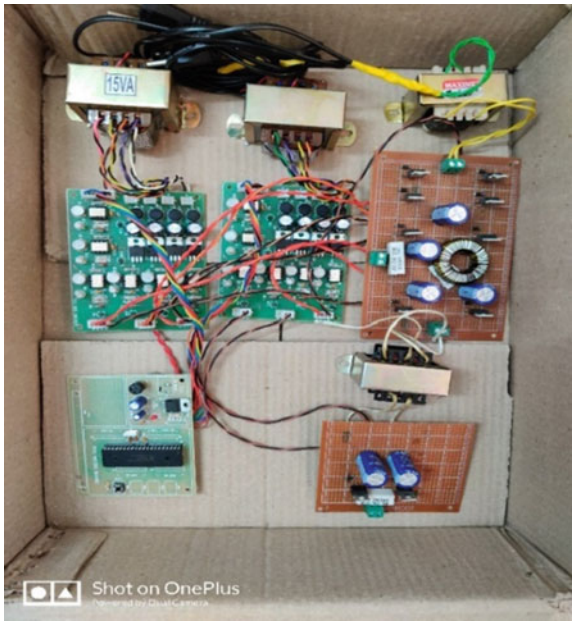

Fig. 12 Hardware connection

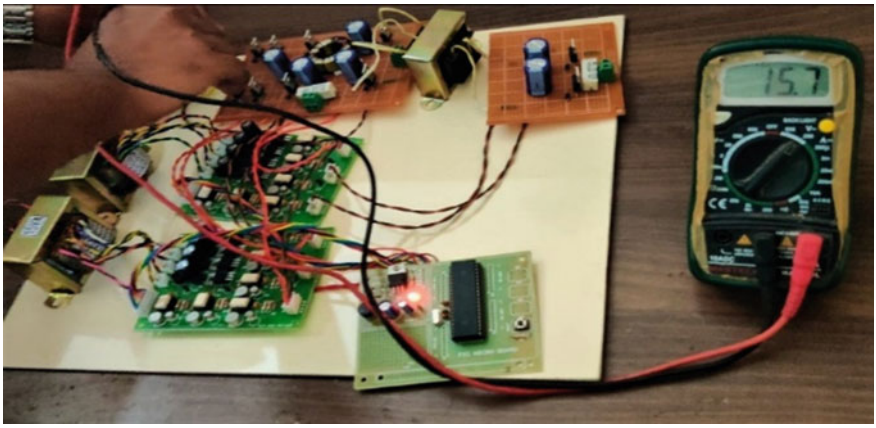

Fig. 13 Hardware input voltage

Hardware input voltage is measured with the help of a multi-meter. We have used four transformers of 15VA rating each. Driver circuits plays an important role in achieving the target to charge the battery (Figs. 14 and 15).

The name nodeMCU is a combined form of "node" and "MCU (microcontroller unit)". It is a prototyping board which can be open sourced. It uses Lua scripting language. Hardware used is a circuit panel working as a DIP adding a USB with a smaller panel consisting of antenna and MCU. This nodeMCU will be connected to the CT and PT which will measure different parameters of the battery [1]. This will be uploaded to ThingSpeak cloud and can be accessed by anyone via Internet (Fig. 16).

The output of the battery is uploaded to the cloud via IOT, and this can be accessed through ThinkSpeak page on your respective browsers. This is accessible worldwide.

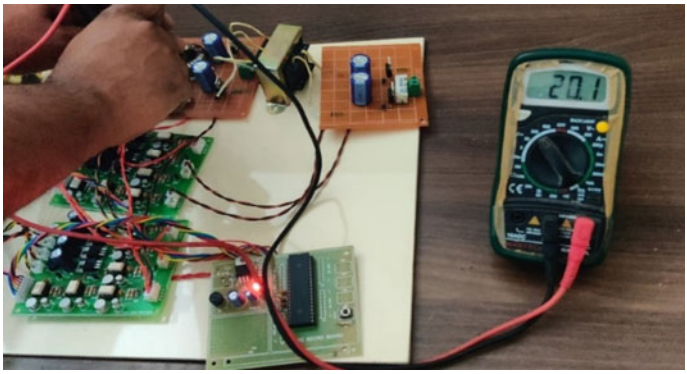

Fig. 14 Hardware battery input voltage

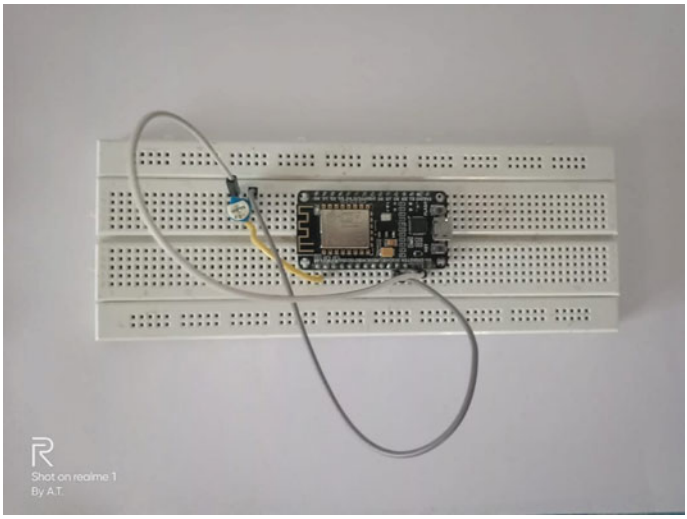

Fig. 15 NodeMCU

Fig. 16 Things peak cloud

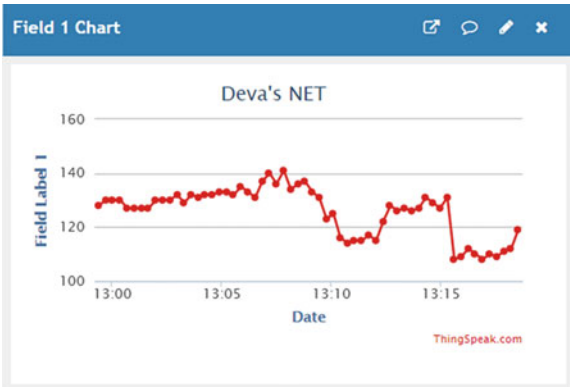

7 Conclusion

Projects consisting battery controlling methods for the operation generally use more amount of cells to attain required voltage. As there is a lot of lack of space, there are restrictions of using such more amount of batteries. By making use of several boost converters, we can decrease the amount of cells required and also attain the high voltage for the application. In today's world, there are plethora of applications which requires the high voltage uses these converters to boost the voltage. Some of the best examples are EVs, and there are plenty of EVs launching in the market nowadays as seeking the brighter and healthier future. There are the results of experiments that showed that using boost converter the appliances would need less cells and still can

attain higher voltage. Implementation of IOT is also a key role to this project which makes it easier to maintain the battery system of the EVs. ThingSpeak cloud gives an excess to the parameters measured by the sensors. The conclusion is that CHB converter not only give the power supply to the battery but also provide a backup to the battery charging. These also improve the fast charging. Implementing this combination with IOT management system provides a complete automated charging station.' Without using high-powered chargers, we can charge several EVs simultaneously. All conceivable charging station working modes among with the planned vital control capacities are investigated. The state-of-charge self-adjusting method of the delta-associated CHB converter is additionally presented.

References

1. Arun Noyal Doss M, Ananthi Christy A, Krishnamoorthy R, Modified hybrid multilevel inverter with reduced number of switches for PV application with smart IoT system. J Ambient Intell Humanized Comput. https://doi.org/10.1007/s12652-018-1151-2
2. Haghbin S, Lundmark S, Alaküla M, Carlson O (2013) Grid-connected integrated battery chargers in vehicle applications: review and new solution. IEEE Trans Ind Electron 60(2):459–473
3. Lee J-Y, Chae H-J (2014) 6.6-kW onboard charger design using DCM PFC converter with harmonic modulation technique and two-stage dc/dc converter. IEEE Trans Ind Electron 61(3):1243–1252
4. Amjadi Z, Williamson SS (2010) Power-electronics-based solutions for plug-in hybrid electric vehicle energy storage and management systems. IEEE Trans Ind Electron 57(2):608–616
5. Yilmaz M, Krein PT (2013) Review of battery charger topologies, charging power levels, infrastructure for plug-in electric and hybrid vehicles. IEEE Trans Power Electron 28(5):2151–2169
6. Zhang H, Yu X, Braun PV (2011) Three-dimensional bicontinuous ultrafast-charge and -discharge bulk battery electrodes. Nature Nanotech 6:277–281. www.nature.com/naturenanotechnology
7. Battapothula G, Yammani C, Maheswarapu S (2019) Multi-objective optimal planning of FCSs and DGs in distribution system with future EV load enhancement. IET Electr. Syst. Transp. 9(3):128–139
8. Zou H, Manzie C, Neˇsi D (2015) PDE battery model simplification for charging strategy evaluation. c 978-1-4799-7862-5/15/$31.00 © 2015 IEEE
9. Chellaswamy C, Nagaraju V, Muthammal R (2018) Solar and wind energy based charging station for electric vehicles. Int J Adv Res Electr Electron Instrum Eng 7(1):313–324
10. Kang B, Gerbrand (2009) Battery materials for ultrafast charging and discharging. Ceder1 Nature 458
11. Rishav M, Maity R, Shiva D (2019) Integration of renewable resources such as wind for electric vehicle and implementation of smart electric vehicle using IOT 8(1s4). ISSN: 2277–3878
12. Vasiladiotis M, Rufer A (2015) A modular multiport power electronic transformer with integrated split battery energy storage for versatile ultrafast EV charging stations. IEEE Trans Ind Electron

Implementation of TLBO Optimised $PI^{\lambda}D^{\mu}$ Controller for LFC of Nonlinear Reheat Thermal Power System

Nimai Charan Patel, Binod Kumar Sahu, and Ramesh Chandra Khamari

Abstract This article explains the load frequency control (LFC) of dual area interlinked reheat type thermal plant including nonlinearities such as generation rate constraint (GRC) and governor dead band (GDB) by employing fractional order proportional integral derivative ($PI^{\lambda}D^{\mu}$) controller. A PID controller is also separately implemented for performance comparison. The parameters corresponding to both the controllers are fine-tuned by application of a teaching learning based optimisation (TLBO) algorithm using integral time absolute error (ITAE) as the fitness function. A comparative performance analysis is accomplished between the two types of controllers by injecting an instantaneous load of 10% in area-1. It is seen that the TLBO optimised $PI^{\lambda}D^{\mu}$ controller yields better transient response when compared with the other controller. Lastly, the robustness of the TLBO optimised $PI^{\lambda}D^{\mu}$ controller is verified by applying a randomly varying step load in area-1.

Keywords Load frequency control · Area control error · $PI^{\lambda}D^{\mu}$ controller · Objective function · Teaching learning based optimisation · Transient response

1 Introduction

Frequency control is a key aspect in interconnected power systems. It is imperative to uphold the system frequency within the prescribed limits so as to preserve the stability of the power system as well as to maintain the power quality at the consumers' premises. The frequency of the system is basically a function of the real power demand on the system [1–3]. Practically, the real power demand is random and dynamic in nature. Therefore, a suitable secondary controller is used to regulate the generation of power according to the active power demand so as to uphold the frequency within a tolerable band and this method of achieving the balance between demand and generation is known as LFC.

N. C. Patel (✉) · R. C. Khamari
Government College of Engineering, Keonjhar, Odisha, India

B. K. Sahu
Siksha 'O' Anusandhan University, Bhubaneswar, Odisha, India

C. Subramani et al. (eds.), *Proceedings of International Conference on Power Electronics and Renewable Energy Systems*, Lecture Notes in Electrical Engineering 795,
https://doi.org/10.1007/978-981-16-4943-1_63

The first ever work on LFC was carried out by Cohn in 1956 [4]. Since then, various research works on LFC have been carried out. Elgerd and Fosha proposed an optimum LFC method for multi area power system in 1970 [5]. Many control strategies for LFC including the application of various artificial intelligence techniques along with the conventional controllers have been reported in the literature. Design of PI controller with fuzzy gain scheduling approach is described for LFC of four area interlinked system [6]. Performance comparison of various classical controllers for LFC has been outlined in [7]. Implementation of differential evolutionary (DE) algorithm tuned 2-DOFPID controller has been illustrated for LFC of dual area interlinked thermal plant taking the effect of GDB into account [8]. LFC of two area solar-thermal system by invasive weed optimisation (IWO) algorithm tuned multi staged PID controller is explained in [9]. LFC analysis of power systems having different generation sources has been carried out by implementing whale optimisation algorithm (WOA) tuned fuzzy integrated PI (FIPI) controller [10]. Ant lion optimiser (ALO) designed fractional order fuzzy PID (FOFPID) controller is presented for controlling the frequency of two area interlinked power systems having different generation sources [11]. PD and FOPI controller are combined together and optimised by salp swarm algorithm (SSA) for LFC of dual area multi-unit system [12]. LFC analysis of thermal plant with electric vehicle (EV) aggregators having time varying delay has been explained in [13]. Cascading of fractional order controller for LFC study has been illustrated in [14].

In this study, a dual area interlinked nonlinear thermal plant having reheat turbine is considered for LFC analysis with $PI^{\lambda}D^{\mu}$ and PID controller. In the first step, the PID controller is fine-tuned separately by the application of TLBO algorithm to study the dynamic response of the considered system. In the next step, a TLBO optimised $PI^{\lambda}D^{\mu}$ controller is employed for further improvement of system performance and stability. In all the cases, a step disturbance of 10% is imparted in area-1 to analyse the transient response of the system. Finally, the robustness of the recommended TLBO optimised $PI^{\lambda}D^{\mu}$ (TLBO–$PI^{\lambda}D^{\mu}$) controller is verified by the application of a random load.

2 System Modelling

The model of the power system is sketched in Fig. 1. It has two control areas that are interlinked via the tieline. The tieline facilitates the power interchange among the two control areas. Each control area consists of a thermal unit with reheat turbine. Effect of generation rate constraint (GRC) and governor dead band (GDB) is also considered in designing the power system model to make the system more practical and realistic. In the present work, limiting value of GDB has been taken as 0.036 and the GRC has been taken as 3%/minute. Inclusion of GDB and GRC makes the power system highly nonlinear and therefore, selection and design of appropriate controllers are vital to maintain the power system stability.

Area control error (ACE) of every area is given by the following equations.

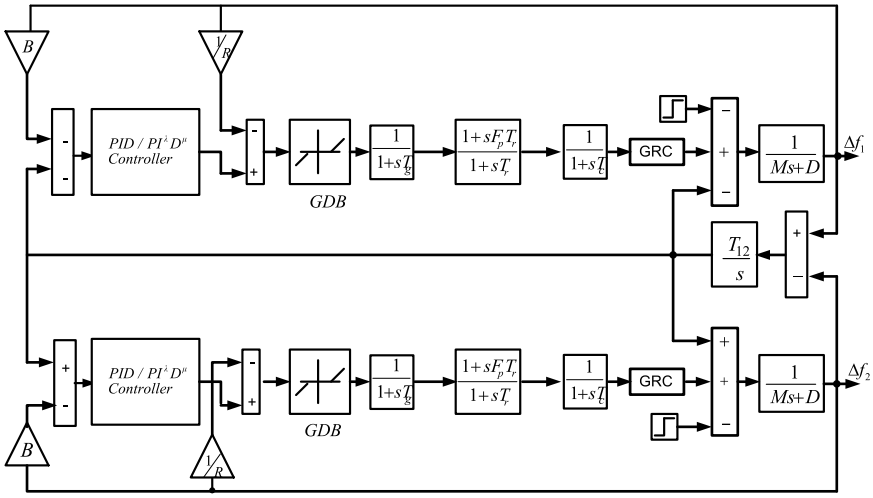

Fig. 1 Power system model under investigation

$$\mathrm{ACE}_1 = B\Delta f_1 + \Delta P_{\mathrm{tie}} \tag{1}$$

$$\mathrm{ACE}_2 = B\Delta f_2 + \Delta P_{\mathrm{tie}} \tag{2}$$

where, ACE_1 and ACE_2 denote the area control errors in area-1 and area-2 respectively. B is the frequency bias factor, Δf_1 and Δf_2 represent the frequency changes in area-1 and area-2 respectively and ΔP_{tie} denotes the tieline power change. ACEs of every area serve as the inputs to the controller of the respective areas. Parameters of the model shown in Fig. 1 are depicted in Appendix-1 [13].

3 Proposed Control Approach

The various controllers used in this work are the PID and PI$^{\lambda}$D$^{\mu}$ controller. The description of these controllers is outlined below.

3.1 PID Controller

PID controllers are very popular controllers due to their simple design and robustness. Also, it delivers better dynamic response and therefore, PID controller has always been the 1st choice of engineers for many decades. Schematic arrangement of PID controller is sketched in Fig. 2.

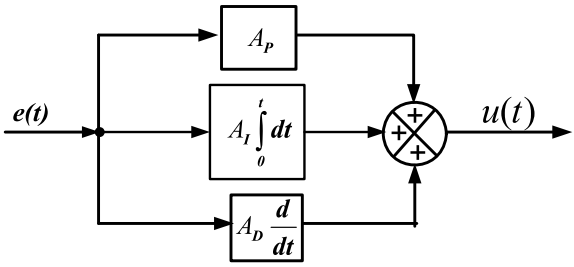

Fig. 2 Configuration of PID controller

The time-domain output and the transfer function (TF) of a PID controller are expressed as given below.

$$u(t) = A_P e(t) + A_I \int_0^t e(t)\mathrm{d}t + A_D \frac{\mathrm{d}}{\mathrm{d}t} e(t) \tag{3}$$

$$G(s) = A_P + \frac{A_I}{s} + A_D s \tag{4}$$

where, A_P, A_D and A_I are the proportionality gain, derivative gain and integral gain respectively.

3.2 $PI^{\lambda}D^{\mu}$ Controller

In PID controllers, the order of the derivative and integral (μ and λ) are integers and often taken as 1. But the order of the derivative and integral (μ and λ) in a $PI^{\lambda}D^{\mu}$ controller may take the value of any positive real number. Thus, there are two extra parameters μ and λ in a $PI^{\lambda}D^{\mu}$ controller which provides additional flexibility in adjusting the system dynamics and hence the $PI^{\lambda}D^{\mu}$ controller delivers enriched performance than the PID controller. A specific instance of $PI^{\lambda}D^{\mu}$ controller is the PID controller, where $\mu = \lambda = 1$. Configuration of the controller is sketched in Fig. 3.

The output for this controller is expressed by the Eq. (5) and its transfer function is given by the Eq. (6).

$$u(t) = A_P e(t) + A_I \frac{\mathrm{d}^{-\lambda}}{\mathrm{d}t^{-\lambda}} e(t) + A_D \frac{\mathrm{d}^{\mu}}{\mathrm{d}t^{\mu}} e(t) \tag{5}$$

$$G(s) = A_P + \frac{A_I}{s^{\lambda}} + A_D s^{\mu} \tag{6}$$

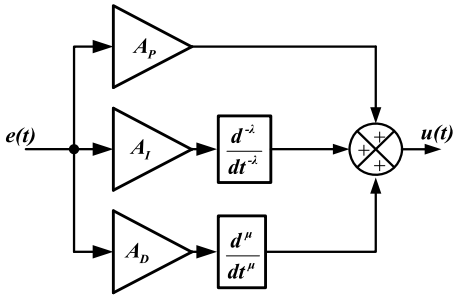

Fig. 3 Configuration of FOPID controller

3.3 Optimal Design of Controllers

The time response of the power system is greatly dependent on the parameters of the controller and hence the parameters of the controller must be properly selected by using suitable optimisation techniques. Optimisation technique employs a function known as the objective function or fitness function denoted by J and then the optimisation problem is formulated by minimisation of this objective function under the constraints of lower and upper limits of the parameters to be optimised. Various objective/fitness functions for LFC analysis of the power system are mentioned in the literature. In the present work, ITAE is selected as the objective/fitness function. ITAE is expressed by the Eq. (7) and the optimisation problem is structured as minimisation of J under the restrictions described by the Eqs. (8–10).

$$J = \text{ITAE} = \int_0^{t_s} (|\Delta f_1| + |\Delta f_2| + |\Delta P_{\text{tie}}|) t \, \text{d}t \tag{7}$$

$$A_{P,D,I\,\min} \leq A_{P,D,I} \leq A_{P,D,I\,\max} \tag{8}$$

$$\lambda_{\min} \leq \lambda \leq \lambda_{\max} \tag{9}$$

$$\mu_{\min} \leq \mu \leq \mu_{\max} \tag{10}$$

where, $A_{P,D,I\,\max}$ and $A_{P,D,I\,\min}$ are respectively the upper and lower values of the proportional, derivative and integral coefficients of the PID and PI$^{\lambda}$D$^{\mu}$ controller and taken as 5 and 0.01, $\lambda_{\max}$ and $\lambda_{\min}$ are respectively the upper and lower values of the order of the integral in PI$^{\lambda}$D$^{\mu}$ controller and taken as 1 and 0.01, $\mu_{\max}$ and μ_{mim} are respectively the upper and lower values of the order of the derivative in PI$^{\lambda}$D$^{\mu}$ controller and taken as 1 and 0.01. Various optimisation techniques have been mentioned in the literature for solution to different optimisation problems in engineering and appropriate selection of the optimisation technique is vital for a given problem otherwise it may lead to unsatisfactory results. After a careful examination

of the literature, TLBO is chosen in this work to solve the optimisation problem so as to get the optimum parameters of the controllers.

3.3.1 Teaching Learning Based Optimisation (TLBO):

TLBO was developed by Rao et al. in the year 2011 [15]. It is a metaheuristic population oriented search algorithm stimulated by the teaching and learning procedure. This algorithm simulates the effect of teacher's impact on the outcome of students in a particular class. The outcome of a student is assessed by the result or grades secured by the student. The teacher is considered to be highly educated person than the students as he shares his experience and knowledge with the students and the quality of the teacher considerably influences the output of the students. A quality teacher imparts training on the students in such a way that the outcome of the students is improved. The students can further enhance their knowledge and produce good results by interaction among themselves. The working method of TLBO is split into two phases. The first phase is the teacher phase which comprises of learning from the teacher and the second phase is the learner phase which consists of learning by interactions between the learners or students. Various steps of TLBO algorithm are described below.

(i) Initialisation: Initially a population with size [NP $\times$ D] is generated randomly, where NP represents the number of all learners and D represents dimension of search space denoting the number of various subjects provided.

(ii) Teacher phase: Each teacher puts his best effort to enhance the mean class result in his assigned subject. The teacher is considered to be the highly educated person as he trains the learners and therefore, he is taken to be the best learner. Hence, the best solution (X_{best}) is found out and designtated as teacher. The average or mean value of the marks secured in each subject by different students is computed as:

$$M_d = [m_1, m_2, ..., m_D] \tag{11}$$

The difference between mean value of the grades in a given subject and the grade of respective teacher is determined by:

$$M_{\text{diff}} = \text{rand} \times [X_{\text{best}} - T_F M_d] \tag{12}$$

where, T_F denotes the teaching factor, rand denotes the random number within 0 and 1. The value of T_F maybe 1 or 2 and randomly decided using the equations given below.

$$T_F = \text{round}(1 + \text{rand}) \tag{13}$$

where, rand denotes a positive real random number of value less than 1.

The existing population gets updated by using the following equations.

$$X_{\text{new}} = M_{\text{diff}} + X \tag{14}$$

Elements of X_{new} are retained if $J(X_{i,\text{new}}) < J(X_i)$ otherwise elements of X_{new} are replaced by corresponding elements of X. Here, J denotes the objective function as defined by Eq. (7).

(iii) Learner phase: In this step, a learner randomly selects another learner and tries to enhance his knowledge through mutual interactions with the other learner. The learner enhances his knowledge through mutual interaction when the other learner is more knowledgeable than him. The procedure of learning in this step is described by the equations given below.

$$X_{\text{new}} = \text{rand}(X_i - X_j) + X_i, \text{ if } J(X_i < X_j) \tag{15}$$

Otherwise,

$$X_{\text{new}} = \text{rand}(X_j - X_i) + X_i \tag{16}$$

where, X_i and X_j are two arbitrarily selected learners and $i \neq j$.

If X_{new} performs better than it is kept. Steps (ii) and (iii) will be repeated till the stopping criterion is arrived and lastly, the elements with the best solution are retained.

4 Result Analysis

The considered power system model is depicted in Fig. 1. Different model parameters are depicted in Appendix-1. The power system is modelled and simulated in the MATLAB and Simulink environment. The controllers employed for the LFC analysis of the considered power system are PID and PI$^{\lambda}$D$^{\mu}$ controllers. The control action takes place in the governor of the thermal plant of each area. TLBO algorithm is scripted in them file and integrated with the model under investigation for optimal tuning of the controllers. The numbers of population are taken as 50 (i.e. NP = 50) and the numbers of iteration are taken as 500 in each case.

4.1 Transient Performance Analysis

An abrupt disruption of 0.1 p.u. is imparted in area-1 and the transient system response is examined independently by implementation of TLBO tuned PID and PI$^{\lambda}$D$^{\mu}$ controllers. The tuned parameters of both the controllers obtained by the

injection of an abrupt disturbance of 10% in area-1 are given in Table 1. The transient response of tieline power oscillations and frequency oscillations in both areas with both controllers are depicted in Figs. 4, 5 and 6 and the corresponding transient response specifications with ITAE values for a simulation time of 50 s are depicted in Table 2.

By careful examination of ITAE value and transient performance specifications given in Table 2 and transient responses shown in Figs. 4, 5 and 6, it can be inferred that the TLBO optimised PI$^{\lambda}$D$^{\mu}$ (TLBO-PI$^{\lambda}$D$^{\mu}$) controller delivers superior performance than the TLBO designed conventional PID (TLBO-PID) controller. Comparing the performance of both the controllers, it is evident that, apart from a slight increase in peak undershoot (U_{sh}) in tieline power oscillation and a slight increase in overshoot (O_{sh}) in area-1 frequency oscillation, the TLBO-PI$^{\lambda}$D$^{\mu}$ controller exhibits better transient performance than the TLBO-PID controller. The disturbance injected into the system is 10% which is significantly large. The system considered in this work is extremely nonlinear due to the inclusion of GDB and GRC and yet the magnitude of the disturbance injected is considerably large. Considering the above facts, the settling time of the system response is crucial and it is important to observe that the settling time (T_S) in case of TLBO-PI$^{\lambda}$D$^{\mu}$ controller is considerably less as compared to the TLBO-PID controller. Further, considering the effect of large injected disturbance and system nonlinearities, the slight increase in peak undershoot in tieline power oscillation and the slight increase in overshoot in area-1 frequency oscillation in the case of TLBO-PI$^{\lambda}$D$^{\mu}$ controller can be ignored because finally the TLBO-PI$^{\lambda}$D$^{\mu}$ controller gives very less ITAE value than the TLBO-PID controller. Hence, it is concluded that the recommended TLBO-PI$^{\lambda}$D$^{\mu}$ controller delivers superior performance than the TLBO-PID controller.

4.2 Robustness Analysis

The robustness of the recommended TLBO-PI$^{\lambda}$D$^{\mu}$ controller is verified with the existing controller parameters as depicted in Table 1 by varying the different time constants of the system over a range of -25 to 25% of the nominal value. The time constants varied are (i) time constant of the governor (T_g), (ii) time constant of the turbine (T_C) and (iii) time constant of reheat (T_r). The frequency deviations in both areas (Δf_1 and Δf_2) along with the tieline power oscillation (ΔP_{tie}) due to variations of different time constants are depicted in Figs. 7, 8, 9, 10, 11, 12, 13, 14 and 15. It is obvious from Figs. 7, 8, 9, 10, 11, 12, 13, 14 and 15 that the controller is proficient in retaining the system stability even with the variations of different time constants over a wide range.

Table 1 Optimum parameters of the TLBO optimised controllers

Controllers	Controller parameters of area-1					Controller parameters of area-2				
	A_{P1}	A_{I1}	A_{D1}	λ_1	μ_1	A_{P2}	A_{I2}	A_{D2}	λ_2	μ_2
TLBO-PID	3.4573	0.9626	0.1521	– -	– -	0.2911	0.0100	0.0100	– -	– -
TLBO-PI$^{\lambda}$D$^{\mu}$	4.6583	5.0000	5.0000	0.9556	0.1591	4.4126	1.3766	1.3006	0.2420	1.0000

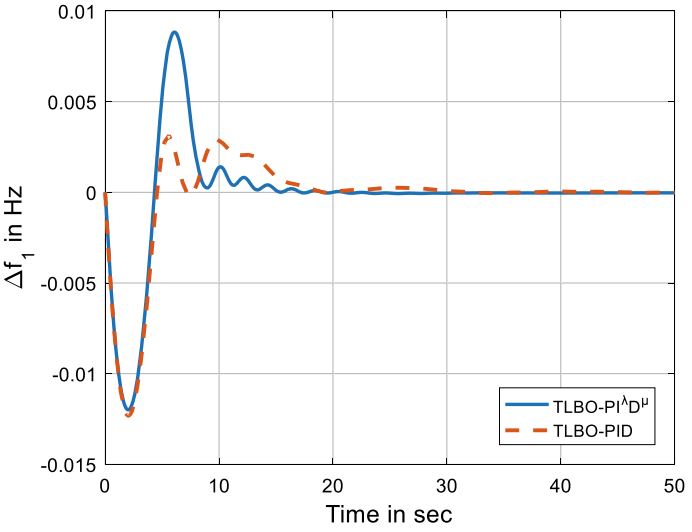

Fig. 4 Frequency oscillations in area-1

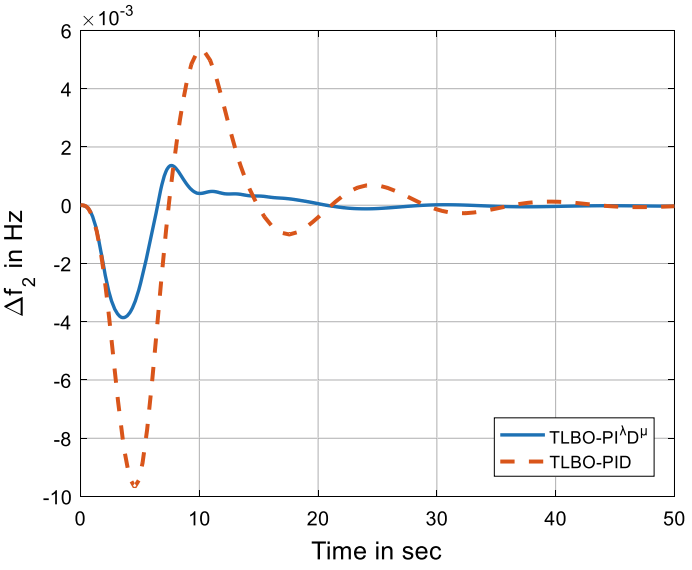

Fig. 5 Frequency oscillations in area-2

5 Conclusion

In this paper, a dual area reheat type nonlinear thermal plant is modelled and PID controller along with $PI^{\lambda}D^{\mu}$ controller are implemented for load frequency control.

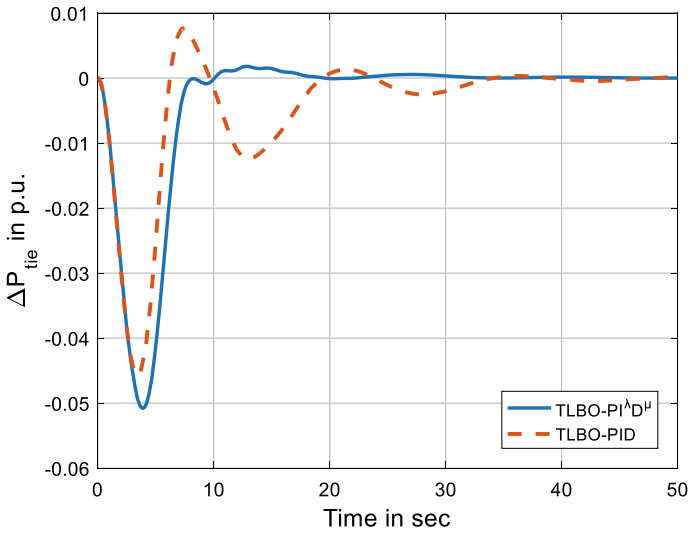

Fig. 6 Tieline power oscillations

The designed system model includes the effect of nonlinearities like GDB and GRC. The controller parameters are optimised by employing TLBO algorithm. A step disruption of 10% is applied in area-1 to examine the transient system response with various controllers. It is found that the proposed TLBO-PI$^{\lambda}$D$^{\mu}$ controller gives the least ITAE value and delivers supreme performance when compared to the TLBO-PID controller. Lastly, the robustness of the proposed controller is verified by varying the different time constants of the system over a wide range.

Table 2 Transient performance specifications due to application of abrupt load in area 1

Controllers	Δf_1			Δf_2			ΔP_{tie}			ITAE
	$U_{\text{sh}} \times 10^{-3}$	$O_{\text{sh}} \times 10^{-3}$	T_S	$U_{\text{sh}} \times 10^{-3}$	$O_{\text{sh}} \times 10^{-3}$	T_S	$U_{\text{sh}} \times 10^{-3}$	$O_{\text{sh}} \times 10^{-3}$	T_S	
TLBO-PID	−12.3170	3.1293	27.8259	−9.6740	5.3249	33.7908	−45.6303	7.6706	45.3922	3.2452
TLBO-PI$^{\lambda}$D$^{\mu}$	−12.0043	8.8329	14.8258	−3.8581	1.3620	17.9315	−50.8009	1.7980	31.1909	1.5222

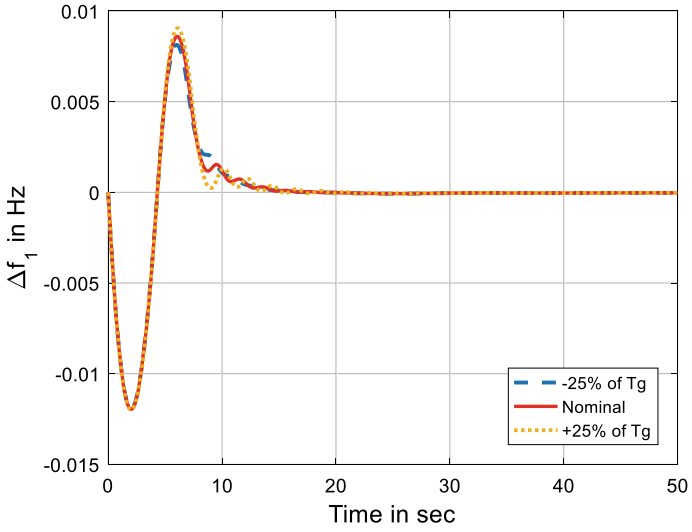

Fig. 7 Frequency oscillations in area-1 due to variation of T_g

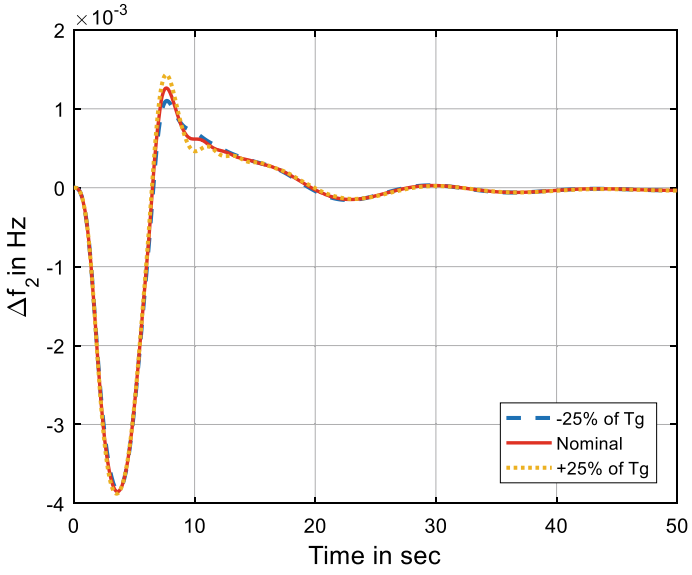

Fig. 8 Frequency oscillations in area-2 due to variation of T_g

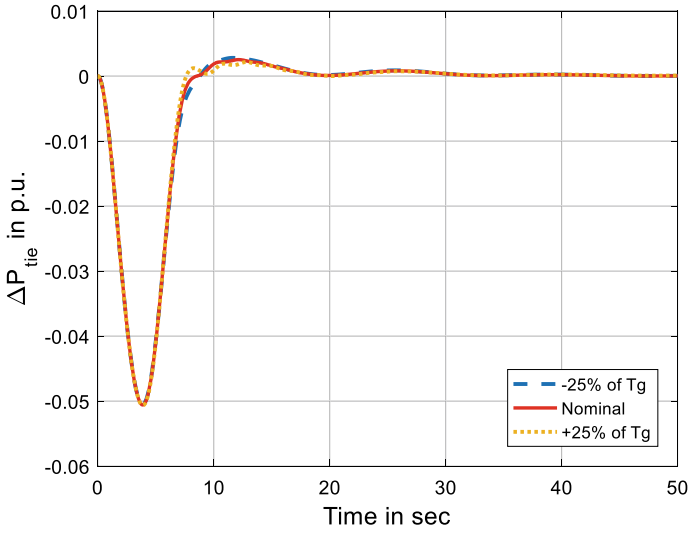

Fig. 9 Tieline power oscillations due to variation of T_g

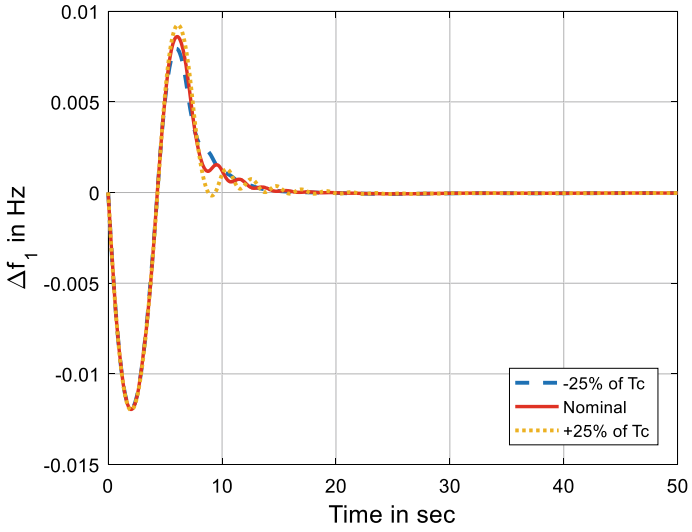

Fig. 10 Frequency oscillations in area-1 due to variation of T_C

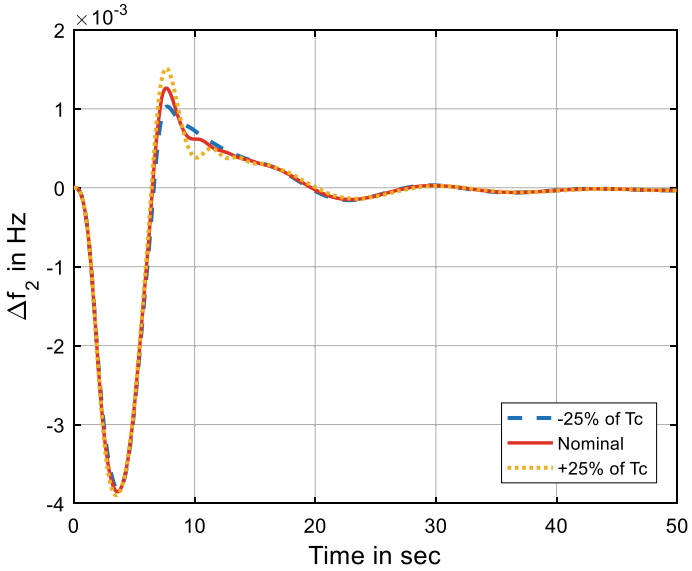

Fig. 11 Frequency oscillations in area-2 due to variation of T_C

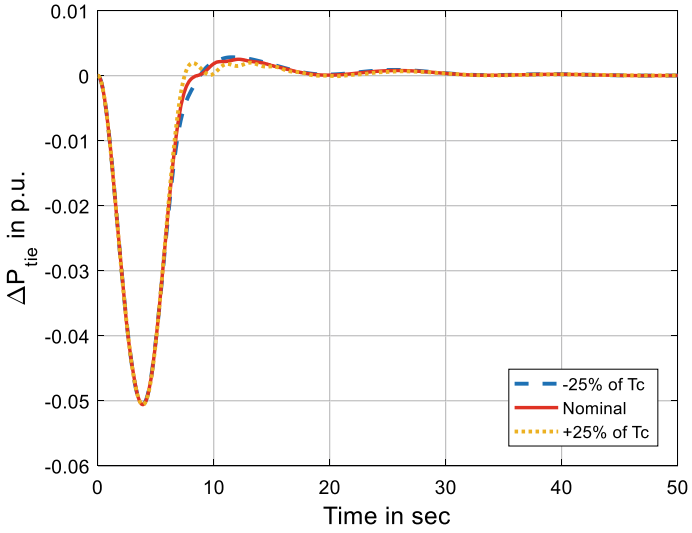

Fig. 12 Tieline power oscillations due to variation of T_C

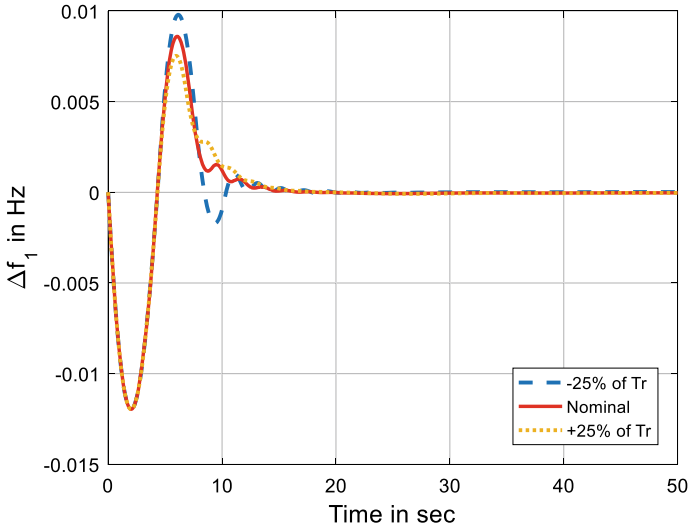

Fig. 13 Frequency oscillations in area-1 due to variation of T_r

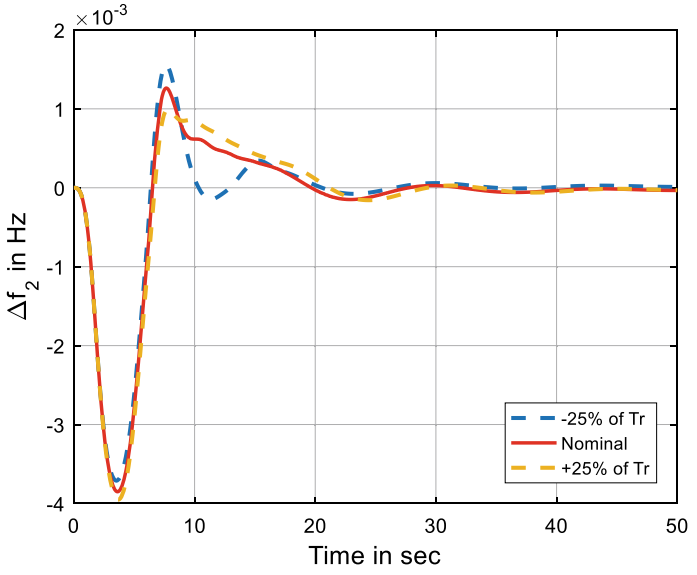

Fig. 14 Frequency oscillations in area-2 due to variation of T_r

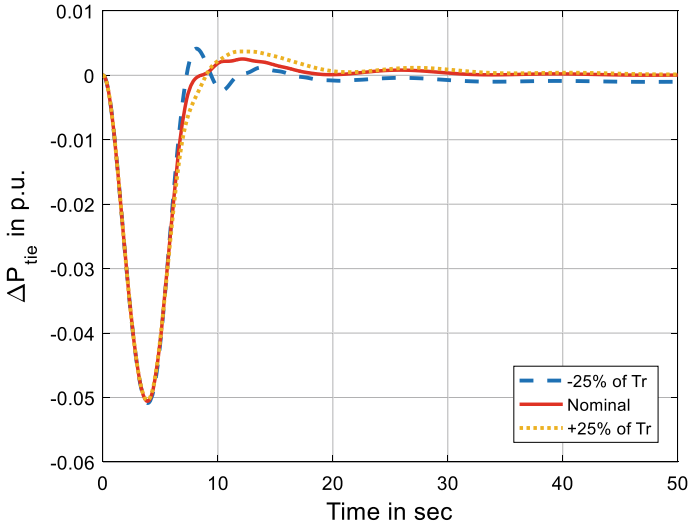

Fig. 15 Tieline power oscillations due to variation of T_r

Appendix-1

Investigated system parameters are given below.

$$B = 21,\ R = {}^{1}\!/_{11},\ F_P = {}^{1}\!/_{6},\ T_r = 12,\ T_C = 0.3,\ T_g = 0.2,\ D = 1,\ M = 8.8\,.$$

References

1. Kundur P, Balu NJ, Lauby MG (1994) Power system stability and control, vol 7. McGraw-Hill, New York
2. Elgard OI (1982) Electric energy systems theory. McGraw-Hill, New York, pp 299–362
3. Saadat H (1999) Power system analysis. McGraw-Hill
4. Cohn N (1956) Some aspects of tie-line bias control on interconnected power systems. Trans Am İnst Electric Eng. Part III: Power Appar Syst 75(3):1415–1436
5. Elgerd OI, Fosha CE (1970) Optimum megawatt-frequency control of multiarea electric energy systems. IEEE Trans Power Appar Syst 4:556–563
6. Chang CS, Fu W (1997) Area load frequency control using fuzzy gain scheduling of PI controllers. Electric Power Syst Res 42(2):145–152
7. Nanda J, Saikia LC (2008) Comparison of performances of several types of classical controller in automatic generation control for an interconnected multi-area thermal system. In: Australasian universities power engineering conference. IEEE, pp 1–6
8. Panigrahi TK, Behera A, Sahoo AK (2017) Novel approach to automatic generation control with various non-linearities using 2-degree-of-freedom PID controller. Energy Procedia 138:464–469

9. Patel NC, Debnath MK, Sahu BK, Dash SS, Bayindir R (2019) Application of invasive weed optimization algorithm to optimally design multi-staged PID controller for LFC analysis. Int J Renew Energy Res 9(1):470–479
10. Patel NC, Debnath MK (2019) Whale optimization algorithm tuned fuzzy integrated PI controller for LFC problem in thermal-hydro-wind interconnected system. Applications of computing automation and wireless systems in electrical engineering. Springer, Singapore, pp 67–77
11. Patel NC, Sahu BK, Bagarty DP, Das P, Debnath MK (2019) A novel application of ALO-based fractional order fuzzy PID controller for AGC of power system with diverse sources of generation. Int J Electric Eng Educ 2019:0020720919829710
12. Patel NC, Debnath MK, Sahu BK, Dash SS (2020) Automatic generation control using novel PD Plus FOPI controller tuned by salp swarm algorithm. Artificial ıntelligence and evolutionary computations in engineering systems. Springer, Singapore, pp 1–13
13. Patel NC, Sahu BK, Debnath MK (2019) Automatic generation control analysis of power system with nonlinearities and electric vehicle aggregators with time-varying delay implementing a novel control strategy. Turk J Electr Eng Comput Sci 27(4):3040–3054
14. Jena NK, Patel NC, Sahoo S, Sahu BK, Dash SS, Bayndir R (2020) Application of fractional order cascaded controller for AGC study in power system integrated with renewable sources. Int J Renew Energy Res 10(1):89–100
15. Rao RV, Savsani VJ, Vakharia DP (2012) Teaching–learning-based optimization: an optimization method for continuous non-linear large scale problems. Inf Sci 183(1):1–5

Author Index

C. Subramani et al. (eds.), *Proceedings of International Conference on Power Electronics and Renewable Energy Systems*, Lecture Notes in Electrical Engineering 795,
https://doi.org/10.1007/978-981-16-4943-1